TECHNISCHE UNIVERSITÄT MÜNCHEN

Lehrstuhl für Flugsystemdynamik

Nonlinear and Adaptive Missile Autopilot Design

Florian Ulrich Peter

Vollständiger Abdruck der von der Fakultät für Maschinenwesen der Technischen Universität München zur Erlangung des akademischen Grades eines

Doktor-Ingenieurs

genehmigten Dissertation.

Vorsitzender:	Prof. Dr.-Ing. Veit Senner
Prüfer der Dissertation:	1. Prof. Dr.-Ing. Florian Holzapfel 2. Prof. Dr.-Ing. Horst Baier

Die Dissertation wurde am 16.11.2017 bei der Technischen Universität München eingereicht und durch die Fakultät für Maschinenwesen am 07.05.2018 angenommen.

Abstract

Missiles for air defense purposes (e.g. surface-to-air missile or air-to-air missile) are characterized by their high agility and fast velocities. In an air defense scenario the missile constitutes the pursuer guiding itself towards the maneuvering threat (evader) with the purpose to intersect the target's trajectory (direct-hit) or to minimize the deviation at the point of intercept. The intercept of a target can be subdivided in three scenario phases: boost, midcourse, and endgame. Within the last phase, the missile system needs to fulfill demanding trajectories to minimize the distance between target and missile at the point of intercept. Based on those trajectories, issued from the missile's guidance unit, the autopilot generate commands for the missile's actuator section. Therefore, the missile autopilot constitutes the key element determining the system's closed-loop performance and tracking characteristics. In traditional design approaches, integrated control architectures are applied with the purpose of setting up the closed-loop characteristics coinciding with a linear reference dynamics. Enforcing the nonlinear missile system to exhibit a linear, uniform behavior at a large set of operating points leads to closed-loop performance characteristics lagging far behind the missile's maximum physical capabilities.

Within this thesis, a novel autopilot architecture is developed based on modern, nonlinear control methodologies with the purpose of fully exploiting the missile airframe's performance capabilities across the entire flight envelope. The autopilot architecture is subdivided in three elements: a nonlinear reference, a baseline control law, and an adaptive augmentation. In contrast to classic, holistic autopilot approaches, the herein developed modular architecture allows an unique assignment of each element with respect to certain system's performance and robustness requirements.

For the layout of the nonlinear reference model and the baseline control law Nonlinear Dynamic Inversion and Backstepping techniques are tailored to match the missile's dynamical peculiarities and fulfill the demanding requirements under nominal conditions. To maintain this closed-loop behavior even in cases of large model deviations, stemming from parametric and sensor uncertainties, a cascaded adaptive structure based on $\mathcal{L}_1$-Piecewise-Constant is incorporated within the autopilot. A nonlinear, six degree of freedom surface-to-air missile simulation model including a realistic aerodynamic data set and dynamic representations of actuator and sensor units is used throughout the entire design and verification process. Linear analysis and nonlinear simulations are utilized for proving the superiority of the herein developed autopilot architecture compared to linear methods. Furthermore, the general validity of the layout process across the entire flight envelope is demonstrated.

The proposed novel autopilot architecture and the corresponding design process are not limited to missile applications only. Certain elements, procedures, and considerations can add significant value in future control design of any aerial platform exhibiting dominant nonlinear characteristics.

Zusammenfassung

Luftabwehrflugkörper zeichnen sich durch ihre hohe Agilität und Geschwindigkeiten aus. In einem Luftabwehrszenario steuert der Flugkörper Richtung manövrierender Bedrohung (Verfolger) mit dem Ziel dessen Trajektorie zu schneiden (Direkttreffer) bzw. die Ablage am Abfangpunkt zu minimieren. Das Abfangen eines Ziels kann dabei in drei Flug Flughasen unterteilt werden: Start-, Übergangs- und Endphase. Um die Trefferablage zwischen Flugkörper und Ziel zu verkleinern, muss der Flugköper in der Lage sein innerhalb der letzten Phase hochagilen Trajektorienverläufen folgen zu können. Auf Basis dieser Trajektorien, welche von der Lenkeinheit ausgegeben werden, errechnet der Autopilotalgorithmus Stellsignale für die Flugkörperaktuatorik. Aufgrund der maßgeblichen Beeinflussung der Leistungsfähigkeit des geschlossenen Kreises und der Qualität der Trajektorienfolge nimmt der Flugkörperautopilot eine Schlüsselrolle im Rahmen der Flugkörperentwicklung ein. In klassischen Autopilotenauslegungen werden integrierte Regelungsansätze verwendet, welche in Übereinstimmung mit einer linearen Übertragungsfunktion des geschlossenen Kreises ausgelegt werden. Das Erzwingen eines linearen, gleichförmigen Verhaltens der nichtlinearen Flugkörperdynamik über große Bereiche der Flugenveloppe führt zu einer Leistungsfähigkeit des geschlossenen Kreises, welche weit unter den maximalen physikalischen Fähigkeiten des Flugköpers zurückbleibt.

Auf Basis moderner, nichtlinearer Regelungsmethoden wird in dieser Arbeit eine neuartige Autopilotenarchitektur mit dem Ziel entwickelt die volle physikalische Leistungsfähigkeit der Flugkörperkonfiguration über den gesamten Flugbereich auszunutzen. Die Architektur ist in drei Elemente unterteilt: ein nichtlineares Referenzmodell, einen Basisregler und eine adaptive Erweiterung. Im Gegensatz zu klassischen, ganzheitlichen Autopilotenansätzen, erlaubt die hier vorgestellte modulare Architektur eine eindeutige Zuordnung der einzelnen Autopilotelemente zu den Leistungs- und Robustheitsanforderungen des Systems.

Für die Auslegung von nichtlinearen Referenzmodells und Basisregler werden Verfahren aus den Bereichen Nonlinear Dynamic Inversion bzw. Backstepping angepasst, um den dynamischen Eigenheiten des Flugkörpersystems und den anspruchsvollen Anforderungen unter nominellen Bedingungen gerecht zu werden. Um das Verhalten des geschlossenen Kreises auch im Falle von großen Modellabweichungen, welche aus parametrischen Unsicherheiten und Sensorfehlern resultieren, aufrechtzuerhalten, wird der Autopilot um eine kaskadierte Adaptionsstrategie basierend auf $\mathcal{L}_1$-Piecewise-Constant erweitert. Ein nichtlineares, sechs-Freiheitsgrad Luft-Boden-Flugkörpersimulationsmodell, welches auf einem realistischen Aerodynamikdatensatz basiert und dynamische Verhaltensmodelle der Sensor- und Aktorsubsysteme beinhaltet, wird über den gesamten Design- und Nachweisprozess verwendet. Lineare Analyse und nichtlineare Simulationen werden bei der Evaluierung angewandt um die Überlegenheit des entwickelten Ansatzes gegenüber linearen Autopiloten aufzuzeigen. Des Weiteren wird die generelle Gültigkeit des Auslegungsprozesses über den gesamten Flugbereich demonstriert.

Die dargestellte neuartige Autopilotenarchitektur und der zugehörige Designprozess sind nicht auf

Flugkörperanwendungen beschränkt. Diverse Elemente, Prozeduren und Betrachtungen können einen bedeuteten Beitrag für zukünftige Reglerauslegungen von fliegenden Systemen mit einer dominant-nichtlinearen Streckencharakteristik liefern.

This page is intentionally left blank.

Acknowledgments

First and foremost I want to express my sincere gratitude to my advisor Professor Florian Holzapfel for the support of my study and related research, for his motivation, inspiration, and sharing his immense knowledge. His ideas and advices helped me in all the time of research. He made it possible to collaborate with the leading researchers in my field. Furthermore, he encouraged us to constantly present our results on international conferences. I could not have imagined having a better advisor and mentor for my doctoral thesis.

Secondly, I would like to express my appreciation to the committee members: Prof. Horst Baier and Dr. Christian Stemmer.

Regarding my research topic I would like to thank Dr. Ralf Lange for providing me with a profound understanding of missile systems, Enric Xargay for sharing his experience in the field of adaptive flight control, and Prof. Stephan Myschik for his continuous assistance. My sincere thanks also goes to my co-workers for the stimulating discussions, for the collaboration in several projects, and all the fun we had. Special thanks go at this point to Bernhard Baur, Farhana Chew, Dr. Sanchito Banerjee, Dr. Thomas Bierling, Stanislaw Braun, Miguel Leitão, Dr. Christian Heise, Onur Celebi, and Simon Schatz.

Finally, I would like to thank my parents, my grandmother, and my sister for all their support, love, and encouragement. Most of all I would like to express my thankfulness to my girlfriend Laura for her great support and patience during the final stages of this thesis.

This page is intentionally left blank.

Content

Directory of Important Formula Symbols

Latin letters

$\left(\boldsymbol{a}_K^A\right)_D^{BC}$	Vector of acceleration of point A derived with respect to coordinate frame B (first derivative) and C (second derivative) denoted in frame D; K denotes its physical origin (here: kinematic)
$\boldsymbol{A}_d$	Desired system matrix
$\boldsymbol{A}(\boldsymbol{x})$	Decoupling matrix of a nonlinear system
$\hat{\boldsymbol{A}}(\boldsymbol{x})$	Estimated decoupling matrix of a nonlinear system
$\boldsymbol{b}_i$	Vector of measurement bias
$\boldsymbol{b}(\boldsymbol{x})$	Vector of assembled system nonlinearities
$\hat{\boldsymbol{b}}(\boldsymbol{x})$	Estimated assembled system nonlinearities
c	Speed of sound
$\boldsymbol{B}_m$, $\boldsymbol{B}_{um}$	Matched and unmatched input matrix
$(C_{i,j})_B$, $(\boldsymbol{C}_i)_B$	Aerodynamic coefficient (scalar, vector) denoted in frame B
$\boldsymbol{C}$	Output matrix
$\boldsymbol{C}(s)$	Transfer matrix of low-pass filter
d_i	Input disturbance noise
e_i, $\boldsymbol{e}$	Control error (scalar, vector)
$\hat{e}_i$, $\hat{\boldsymbol{e}}$	Tracking error (scalar, vector)
$\tilde{e}_i$, $\tilde{\boldsymbol{e}}$	Compensated Tracking Error (scalar, vector)
$f(\boldsymbol{x})$, $\boldsymbol{f}(\boldsymbol{x})$	General dynamics of nonlinear system (scalar, vector)
$\left(F_{i,A}^B\right)_C$, $\left(\boldsymbol{F}_A^B\right)_C$	Force (scalar, vector) acting on point B denoted in frame C; A denotes its physical origin (here: aerodynamics)
$\boldsymbol{F}(\boldsymbol{x}, \boldsymbol{u})$	System input/output characteristic (vector)
$\left(\mathbf{I}^G\right)_{BB}$	Tensor containing the moment of inertia of point G with respect to point B denoted in frame B
$G(s)$, $\boldsymbol{G}(s)$	Transfer function (scalar, matrix)
$\boldsymbol{g}(\boldsymbol{x})$, $\boldsymbol{G}(\boldsymbol{x})$	General control input of nonlinear system (vector, matrix)
h	Altitude above sea level
$h(\boldsymbol{x})$, $\boldsymbol{h}(\boldsymbol{x})$	General output mapping of nonlinear system (scalar, vector)
$\boldsymbol{H}_m(s)$, $\boldsymbol{H}_{um}(s)$	Transfer matrix of matched and unmatched open-loop dynamics
$\mathbb{I}$	Identity matrix of appropriate dimension
k, $\boldsymbol{k}$, $\boldsymbol{K}$	Control gains (scalar, vector, matrix)
l_{ref}	Aerodynamic reference length
$L_{\boldsymbol{f}}\lambda(\boldsymbol{x})$	Lie derivative of λ along $\boldsymbol{f}$
m	Mass of body; number of inputs
M	Mach number

$\left(M_{i,A}^{B}\right)_{C}$, $\left(\boldsymbol{M}_{A}^{B}\right)_{C}$	Moment (scalar, vector) acting on body B denoted in frame C; A denotes its physical origin (here: aerodynamics)
M_S	Maximum sensitivity
n, N	Variable for quantification
n_i	Measurement noise
$(n_i)_K$	Load factor in i-axis of K-frame
$\mathbf{0}$	Matrix of zeros with appropriate dimension
$\left(p_K^{AB}\right)_C$	Roll component (first entry) of angular rates $\left(\boldsymbol{\omega}_K^{AB}\right)_C$ describing rotation between coordinate frame A and B denoted in frame C; K denotes its physical origin (here: kinematic)
$\boldsymbol{p}$	Parameter vector of trim problem
$\boldsymbol{P}_i$	Matrix for error weighting in case of Backstepping/Command Filtered Backstepping control law derivation
$\bar{q}$	Dynamic pressure
q_i^{AB} , $\boldsymbol{q}^{AB}$	Quaternion describing the rotation between coordinate frame A and B; (scalar) components are labeled with $i = 0, \ldots, 3$
$\left(q_K^{AB}\right)_C$	Pitch component (second entry) of angular rates $\left(\boldsymbol{\omega}_K^{AB}\right)_C$ describing rotation between coordinate frame A and B denoted in frame C; K denotes its physical origin (here: kinematic)
r	Relative degree of a system
$\boldsymbol{r}$	Residual vector of trim problem
$\left(r_K^{AB}\right)_C$	Yaw component (third entry) of angular rates $\left(\boldsymbol{\omega}_K^{AB}\right)_C$ describing rotation between coordinate frame A and B denoted in frame C; K denotes its physical origin (here: kinematic)
r_E	Earth radius
$\left(\boldsymbol{r}^{AB}\right)_C$	Vector pointing from point A to point B denoted in frame C
S_{ref}	Aerodynamic reference area
$S_i\,(s)$	Sensitivity transfer function
$S_{N,i}\,(s)$	Noise sensitivity transfer function
$S_{L,i}\,(s)$	Load disturbance sensitivity transfer function
$S_{C,i}\,(s)$	Complementary sensitivity transfer function
t	Time
T	Time constant
T_d	Time delay
T_{rt}	Rise time
T_s	Sampling time
T_{st}	Settling time
$\boldsymbol{T}_\delta$	Matrix of fin mapping between aerodynamic equivalent controls and physical controls of the fins
$\left(u_K^A\right)_C^B$	First component of velocity vector $\left(\boldsymbol{V}_K^A\right)_C^B$ of point A derived with respect to coordinate frame B denoted in frame C; K denotes its physical origin (here: kinematic)
$\boldsymbol{u}$	Vector of aerodynamic equivalent control variables ξ, η, ζ
$\boldsymbol{u}_\delta$	Vector of physical fin deflections δ_i, $i = 1, \ldots, 4$
$\left(v_K^A\right)_C^B$	Second component of velocity vector $\left(\boldsymbol{V}_K^A\right)_C^B$ of point A derived with respect to coordinate frame B denoted in frame C; K denotes its physical origin (here: kinematic)
$V\,(\boldsymbol{x})$	Lyapunov function of autonomous system with state $\boldsymbol{x}$

$\left(\boldsymbol{V}_K^A\right)_C^B$	Vector of velocity of point A derived with respect to coordinate frame B denoted in frame C; K denotes its physical origin (here: kinematic)
$\left(w_K^A\right)_C^B$	Third component of velocity vector $\left(\boldsymbol{V}_K^A\right)_C^B$ of point A derived with respect to coordinate frame B denoted in frame C; K denotes its physical origin (here: kinematic)
$\boldsymbol{w}_i$	Vector of white measurement noise signal
$W_i\left(\boldsymbol{e}\right)$	Limiting function of i-th design step in Backstepping control law design
x, $\boldsymbol{x}$	General state of dynamic system (scalar, vector)
$\boldsymbol{x}_{c,i}$	Center of radial basis function
$x_{IMU,P}$	Distance between Inertial Measurement Unit and virtual sensor location
y, $\boldsymbol{y}$	General output of dynamic system (scalar, vector)
y_c, $\boldsymbol{y}_c$	Command signal (scalar, vector)
y_r, $\boldsymbol{y}_r$	Reference signal (scalar, vector)
$y^{(r)}\left(t\right)$	r-th derivative of y with respect to time t
z_i, $\boldsymbol{z}$	Unachieved portion (scalar, vector)

Mathematical symbols

$\mathcal{N}$	Normal distribution
$\mathcal{O}$	Truncation error of Taylor series expansion
$\Re\left(.\right)$	Real part of a complex number

Greek letters

α_K	Angle of attack
$\alpha_i\left(\boldsymbol{x}\right)$, $\boldsymbol{\alpha}_i\left(\boldsymbol{x}\right)$	Virtual control law used in Backstepping methods (scalar, vector)
β_K	Angle of sideslip
γ_K	Flight path angle
δ_i	Missile's physical control surface deflections $i = 1, \ldots, 4$
Δ	Change of any changeable quantity
$\boldsymbol{\Delta}_m$, $\boldsymbol{\Delta}_{um}$	Matched and unmatched model uncertainties
ζ	Aerodynamic equivalent control variable of the yaw-axis
ζ_i	Damping
η	Aerodynamic equivalent control variable of the pitch-axis
η_i, $\boldsymbol{\eta}$	Internal state (scalar, vector) of system transformed via Nonlinear Dynamic Inversion
ϑ_K	Total incidence angle
Θ^{AB}	Elevation angle (Euler angle convention) between coordinate frame A and B
$\kappa\left(r\right)$	Radial basis function of distance r
$\lambda_{i,j,k}$	Weighting factor of Radial basis function network

$\mu_{i,j}$	Expected value
ν, $\boldsymbol{\nu}$	Pseudo control (scalar, vector)
ν_h, $\boldsymbol{\nu}_h$	Pseudo control hedging signal (scalar, vector)
ξ	Aerodynamic equivalent control variable of the roll-axis
ξ_i^j, $\boldsymbol{\xi}$	External state (scalar, vector) of system transformed via Nonlinear Dynamic Inversion
ς_{ov}	Overshoot
$\sigma_{i,j}$	Standard deviation
$\boldsymbol{\sigma}_m(t)$, $\boldsymbol{\sigma}_{um}(t)$	Vector estimates of matched and unmatched uncertainties
ϕ_K	Rotation angle of the load factor frame L with respect to the body frame B
ϕ_v	Roll angle about velocity vector
Φ	Cost function
Φ^{AB}	Heading angle (Euler angle convention) between coordinate frame A and B
Ψ^{AB}	Bank angle (Euler angle convention) between coordinate frame A and B
ω_i	Bandwidth
$\left(\boldsymbol{\omega}_K^{AB}\right)_C$	Vector of angular rates describing rotation between coordinate frame A and B denoted in frame C; K denotes its physical origin (here: kinematic)

List of Figures

List of Theorems

List of Definitions

List of Assumptions

Abbreviations

AAM air-to-air missile

AoA angle of attack

AoS angle of sideslip

ARW Angular Random Walk

ASM air-to-surface missile

BIBO bounded-input bounded-output

BM ballistic missile

BS Backstepping

BSRBM battlefield short-range ballistic missile

BTT Bank-To-Turn

CFB Command Filtered Backstepping

CFD Computational Fluid Dynamics

CLF Control Lyapunov Function

cog center of gravity

cop center of percussion

CPU Central Processing Unit

CTE Compensated Tracking Error

DOF degree of freedom

ECEF Earth-Centered Earth-Fixed

ECI Earth-Centered Inertial

EOM equation of motion

FAA Federal Aviation Administration

FCS Flight Control System

FGS-X-03 FSD Generic Surface-to-Air Missile

FR functional requirement

FSD Institute of Flight System Dynamics

ICBM intercontinental ballistic missile

IMU Inertial Measurement Unit

IR infrared

IRBM intermediate-range ballistic missile

$\mathcal{L}_1$ **AC** $\mathcal{L}_1$ Adaptive Control

LPV linear parameter-varying

LTI linear time-invariant

MC Monte Carlo

MIMO Multiple-Input-Multiple-Output

MRAC Model Reference Adaptive Control

MRBM medium-range ballistic missile

NDI Nonlinear Dynamic Inversion

NED North-East-Down

NFR non-functional requirement

NRM nonlinear reference model

ODE ordinary differential equation

PCH Pseudo Control Hedging

PE persistent excitation

PIP predicted intercept point

PWC Piecewise-Constant

RBF radial basis function

RMS Root Mean Square

SAM surface-to-air missile

SGT small-gain theorem

SISO Single-Input-Single-Output

SRBM short-range ballistic missile

SSM surface-to-surface missile

STT Skid-To-Turn

TOC tactical operation center

UAV Unmanned Aerial Vehicle

CHAPTER 1

Introduction

> Can the magic of flight ever be carried by words? I think not.
>
> Michael Parfit

It lies in the nature of mankind to constantly improve all aspects of our lives. This evolution also includes advances in defending ourselves from enemies or potential threats. Since advanced developments in computatial power, sensor, and manufacturing technologies, autonomous systems gained more and more importance in strategic defense systems over recent years. Those enhanced capabilities lead to a broader spectrum of threats to be engaged and therefore a wider range of possible scenarios. On the other hand, the increased availability of technology and declining prices of electronic components give rise to an accelerated evolution of autonomous aerial threats, ranging from simple Unmanned Aerial Vehicles to ballistic missiles. Therefore, air defense systems require the representation of the complex engagement chain for intercepting hostile aerial vehicles. In particular, this includes target detection, tracking (illumination), and intercepting. Air defense missiles, guided autonomously towards the target, are used as effectors. In order to intersect the target trajectory, the missile is required to exhibit superior maneuverability compared to the hostile vehicle. Besides the design of the airframe, the interplay of sensors and algorithms has a significant impact on the missile's performance capabilities. Within the algorithmic layout, the autopilot constitutes the key element in ensuring the missile's maximum agility.

In section 1.1, a brief historical overview of missile systems and its categorization according to purpose, airframe, range, etc is given. Section 1.2 introduces the challenges, requirements, and interfaces of the autopilot within a missile system. The state of the art of autopilot design methods is outlined in section 1.3. Within section 1.4 the main contributions of this thesis to the field of missile autopilot are listed. This chapter is concluded by the summary of major findings within this thesis (section 1.5).

1.1 History and Categorization of Missile Systems

In the history of warfare, unmanned propelled devices that can be shot over a large range, has always played a crucial role. A rocket is defined as a propelled, flying, unmanned vehicle. In contrast to

rockets, (guided) missiles include a device for controlling its flight path [1]. Over the centuries, primitive rockets have evolved to advanced missile systems, which fulfill challenging missions by the collaboration of the missile itself with launching, guidance, control, and sensing devices [5, 6, 7, 8].

The first use of rockets dates back to the 13th century, when China used an arrow propelled with gunpowder to repel the Mongols at the city of Kai-fung-fu [1, 9]. A major step in the evolution from simple rockets to advanced missiles was the ability to build trivial electronic circuits and transmit signals. The first steps towards a remote-controlled missile system were inspired by the use of aircraft as military weapons during World War I [1, 8]. Through the first half of the 20th century, Hermann Oberth's idea of rocket travel into outer space inspired rocket and missile scientists all around the world. During this time, parallel to developments in the field of electric signal processing, the first experiments of liquid (gasoline and oxygen) propelled rockets were conducted. With the founding of the "Peenemünde Project" in 1936, Germany decided to intensify the research of guided missiles. Under the technical direction of Wernher von Braun, who was a student of Oberth, the V-1 and V-2 missiles were developed within the "Peenemünde Project" [1, 8, 10]. Those two missiles constitute the origin of advanced missile technology [1]. After World War II, von Braun and a large number of the "Peenemünde Project" team migrated to the USA within the "Operation Paperclip". A similar migration of German scientists took place into Russia. By using the results and experience of the "Peenemünde Project", the USA and Russia became the world's leaders in missile and rocket technology in the middle of the 20th century. Driven by the Cold War, both nations raced for the position of supremacy in terms of military and space technology, which led to a further acceleration in missile and rocket development. Milestones in missile and rocket evolution were the manned and unmanned space missions, which went hand in hand with the development of the first intercontinental ballistic missile (ICBM) (Atlas in 1959) [6]. Besides the growth of research interest stepped up in the field of BMs, efforts were also in other missile applications. With steady improvements in high-tech devices such as radar and sensor units, and with the increased computatial power, steering of missiles became more precise. Therefore, in the mid 1900s, the development of air-defense missile system began with the "Project Nike", which constitutes a line-of-sight antiaircraft missile system developed and manufactured by Bell Telephone and Western Electric [11]. A rapidly increasing technology level in the second half of the 20th century led to more and more realizable scenarios with missiles demonstrating their superior ability. The development and optimization of missiles for novel scenarios resulted in a large diversity of different missile types over the last 60 years [12, 13].

Due to the multiple types of missiles and their use in diverse scenarios, there are several ways of classifying missiles. This fact, combined with mixed nomenclature and differing definitions (e.g. range classification) complicate the task of a unique missile sub-division. The most common divisions of missiles are depicted in table 1.1. These categorizations of missiles (table 1.1) is only a brief overview with the purpose of introducing the background and framework the herein considered missile can be placed. Each class of missile presented in table 1.1 can be further sub-classified in a more detailed breakdown. More information on missile classifications can be found in [1, 7, 14, 15].

Table 1.1 shows that besides the rough classification into *guided* and *unguided* missiles, there exist a few other categories depending on missile and scenario features. Regarding the scenario, missiles are classified according to the launch and target position [5, 16]. For the context of this thesis, it is sufficient to consider only the realms of land and air for launch and target position. Subdividing missiles according to the distance they are able to cover is very common for the group of ballistic surface-to-surface missiles (SSMs). SSMs with a radius below 150km belong to the class of battlefield short-range ballistic missiles (BSRBMs). A ballistic missile is categorized as a short-range ballistic missile (SRBM) if it can travel a distance up to 1000km [1]. Medium-range ballistic missiles (MRBMs) and intermediate-range ballistic missiles (IRBMs) are able to cover a radius of 1000-2400km and

2400-5500km respectively [7, 14].

Launch and Target Position	Range
Air-to-Air Missile (AAM)	Battlefield Short-Range Ballistic Missile (BSRBM)
Air-to-Surface Missile (ASM)	Ballistic Missile (BM)
Surface-to-Air Missile (SAM)	Intermeditate-Range Ballistic Missile (IRBM)
Surface-to-Surface Missile (SSM)	Intercontinental Ballistic Missile (ICBM)

Type	Airframe Configuration	Guidance Concept
Guided	Canard-Controlled	Homing Guidance
Unguided	Tail-Controlled	Command Guidance
	Wing-Controlled	Inertial Navigation

Table 1.1: Examples of missile categorizations

Grouping missiles according to their airframe configuration is especially common for AAMs and ASMs. Those missiles possess movable control surfaces, which are deflected according to commands issued by the Flight Control System (FCS) in order to accelerate the missile in a certain direction. The three most common airframe configurations are shown in fig. 1.1. In addition to the specific aerodynamic advantages [1], each of the configurations (fig. 1.1) exhibits other issues (e.g. control algorithm, heat transfer, assembly, construction, etc.) affecting the design of the entire missile system. Within this thesis, the focus is exclusively on missiles that can alter its flight path actively during flight (*guided* missiles). Therefore, a further subdivision of the guided missile category is helpful to provide the reader with a deeper insight into different guidance concepts. Guided missiles can be sectioned into three different guidance concepts (table 1.1): homing guidance, command guidance, and inertial navigation. In homing guidance concepts, the missile is equipped with an onboard sensor providing the interceptor's FCS with target information. On basis of this data, guidance decisions are made and a command signal is generated, which directs the interceptor (missile) towards the target. Target information is sensed by the radiation (radar, infrared, visual) emanated by the target. The concept of homing guidance incorporates three different types of target illumination: a missile employed with a passive homing guidance system receives the energy emanated from the target (e.g. infrared (IR)). A Missile with an active homing guidance concept includes an illumination device onboard, which reflects the transmitted waves. A semi-active system requires an external source for target illumination [17]. In contrast to homing guidance, a command guidance system generates the commands necessary to alter the missile's flight path based on ground sensor information provided to the missile via data link (wire or radio). In the case of inertial navigation, the missile does not require any external signal. Based on gyroscopic sensor information, the absolute missile position and velocity is estimated via the onboard FCS algorithm and the missile is guided towards the pre-programmed target location [1, 16, 18].

The control task is applied to the generic, tail-controlled SAM model of the Institute of Flight System Dynamics (FSD), called the FSD Generic Surface-to-Air Missile (FGS-X-03). Usually, the family of SAM types exhibit a characteristic scenario depicted in fig. 1.2. If the tactical operation center (TOC) assesses that the intercept situation is within the missile's range, a launch solution is computed, the missile is initialized, and launched (boost phase). The prime goal of the first flight phase is to accelerate the missile to operating velocity. Therefore, the guidance law plays only a minor role. Commonly, inertial navigation is used for the purpose of directing the missile roughly towards the target. During the midcourse phase, the missile shall minimize the distance to the calculated predicted intercept point (PIP). In order to align the onboard sensors to the target, the missile must

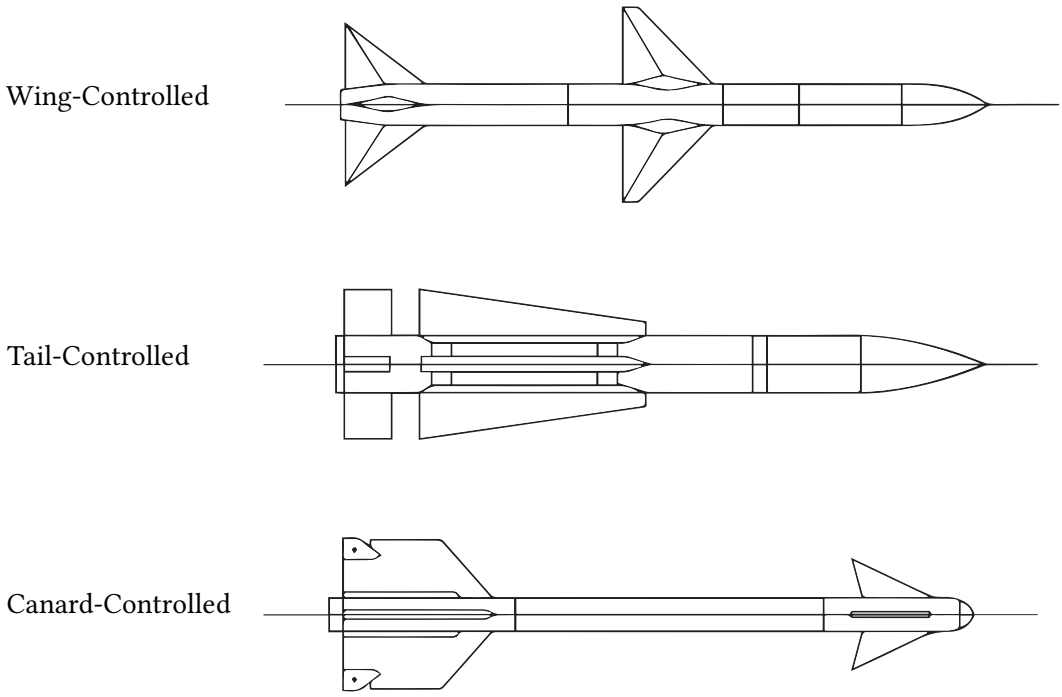

Figure 1.1: Three common airframe configurations. From top to bottom: Sparrow III AIM-7F, Phoenix AIM-54A, Sidewinder AIM-9 [1].

provide a certain relative geometry with respect to the target. In general, the missile is radar guided during this phase. Reaching the lock-on range (handover), the onboard seeker and onboard guidance algorithm are activated in order to guide the missile towards the target (terminal phase). Within the endgame (fig. 1.2), which labels the end of the terminal phase, the guidance demands the missile's maximum maneuverability in order to maximize the intercept lethality probability [7, 18].

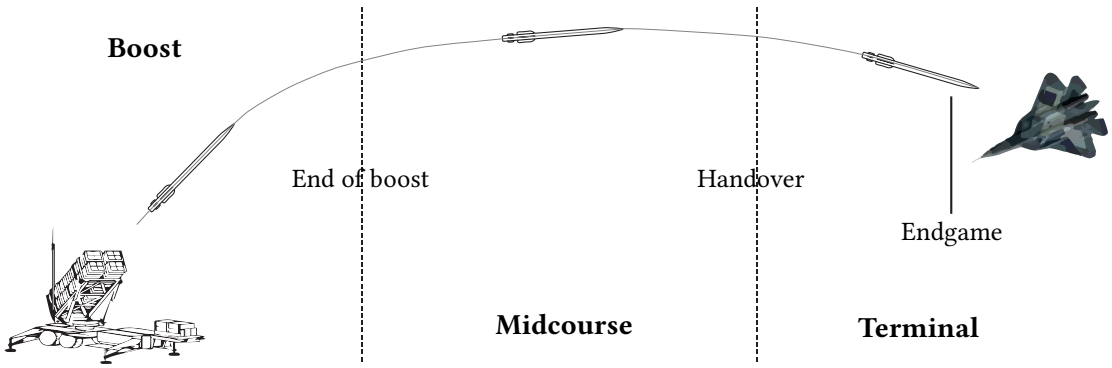

Figure 1.2: Flight phases of a missile engagement scenario. [2, 3]

Missiles of the class AAM or SAM can be further subdivided according to their steering type. The predominant steering technique used for AAM or SAM is labeled as Skid-To-Turn (STT). Missiles, which *skid to turn*, apply the desired aerodynamic force in the desired direction by mixing the control surfaces. Thus, no roll motion to a preferred angle is necessary. Usually, missiles employing STT exhibit identical airframe configuration - and therefore dynamics - in the longitudinal and lateral plane. Aircraft directing the lift vector towards the desired direction by rolling the aircraft body in

the considered plane use the so-called Bank-To-Turn (BTT) steering. This approach is very common for aerial vehicles exhibiting a high lifting capability in one body axis direction (e.g.: fixed-wing aircraft, cruise missiles) [1, 19]. Since the body of the herein considered missile FGS-X-03 is axially symmetric, STT is the designated steering technique.

1.2 Control Challenges of Missile Systems in Endgame Flight Phase

Within this thesis, the term *missile control* describes the process of computing the desired control surface deflections based on higher-level guidance commands. The guidance unit calculates the desired missile outputs based on the current states of the missile and target (fig. 1.3). These outputs constitute the reference of the FCS, which compares this signal with the measured (e.g. Inertial Measurement Unit (IMU)) or estimated control variables. In this context, the guidance and control loop are often referred to as *outer loop* and inner loop, respectively. The guidance law is designed, such that if the provided guidance commands and the missile outputs match, an intercept between missile and target will occur. Therefore, a fast and precise tracking of the guidance outputs by the autopilot running on the FCS is essential for the mission success. Usually, the control variables (outputs) are selected in order to fully cover the missile's three translational degree of freedoms (DOFs). With the continuously evolved sensory capabilities, enhanced computing power, and improved performance of missiles and targets, the guidance and control algorithms become more and more complex.

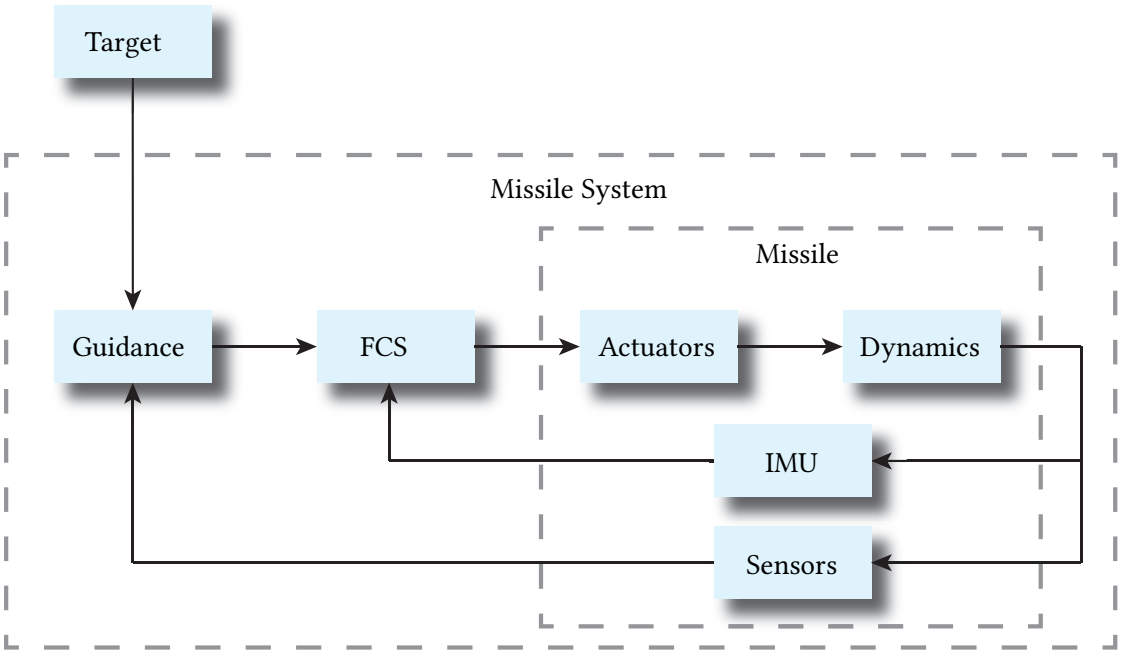

Figure 1.3: Block diagram of missile system emphasizing guidance, control, actuator, and guidance units.

Considering the three phases of a standard engagement scenario (Figure 1.2), the terminal phase and specifically the endgame play a decisive role for achieving the desired distance between missile and target. The maximum maneuverability and performance of the missile is demanded within the endgame flight phase, which is shortly before the intercept occurs. During this phase, the guidance may demand (depending on the target's evasiveness) the maximum performance the missile is physically capable of. Therefore, the FCS shall provide a fast and precise tracking of the desired trajectory without degrading the overall missile's performance capabilities.

Two main challenges arise by designing a flight control law for highly agile AAMs and SAMs: first, as mentioned above, the full physical capabilities and the entire flight envelope of the missile shall be exploited; and second, the control system shall maintain its performance in case of unavoidable modeling and sensor errors [20]. The main source for the mismatch between the assumed model used for control design purposes and the real missile system stems from the complex and expensive identification process of the nonlinear missile aerodynamics. Since flight control laws are generally model based approaches, a mismatch between the considered model and the real system can cause insufficient tracking performance or - in the worst case - lead to an instable closed-loop system. In addition to uncertainties caused by the aerodynamics, other system parameters can be estimated with high accuracy but vary during flight (e.g. missile mass). The transmission of signals and commands through the sensor and actuator system introduce a certain time delay in the closed-loop. Since time delays limit the bandwidth and therefore the overall closed-loop performance of a system, the control designer has to balance between performance and robustness in order to exploit the maximum physical performance by fulfilling the demanding robustness requirements. Furthermore, the saturation effects of the actuator unit constitute additional hard nonlinearities. Those physical limitations (e.g. position, rate limitation) of the control surfaces determine, inter alia, the maximum performance of the missile system. Therefore, the controller shall be designed to fully exploit the maximum actuator capabilities by considering the actuator limitations. Ignoring those limitations in the FCS design leads either to a conservative control design, which does not exploit the full envelope or results in anti-windup effects [21], which may lead to destabilized closed-loop behavior. Due to the demanding agility, significant cross-coupling effects occur, which are owed to the highly nonlinear coupled missile dynamics [1, 17]. These dynamical effects make missile autopilot design more challenging in terms of performance issues compared to other UAVs.

The autopilot architecture, and therefore the control variables, are mainly influenced by the missile's steering type and the available sensor information. For STT-steered SAMs and AAMs it is common to control the missile's roll channel (angle or rate), longitudinal, and lateral acceleration. An approach similar to fixed-wing aircraft is to control the missiles attitude. Controlling the flight-path angles of the missile is a third method to design an inner loop autopilot [22]. Since the FGS-X-03 is a rotationally symmetric SAM, STT steering in combination with lateral and longitudinal acceleration inner loop control is an appropriate approach.

1.3 Nonlinear and Adaptive Missile Control for an Endgame Scenario

As mentioned in section 1.2, control design of missiles is dominated by fulfilling maximum maneuverability and robustness specifications over an extensive flight envelope. These demanding requirements combined with the inherently nonlinear dynamics, a wide spectrum of uncertainties, and fast varying flight conditions require intelligent algorithms in order to fulfill the mission goals even in the case that the system deviates from the one assumed. Within the context of control design, it might be helpful to familiarize the reader with the terms *plant model* and *design model*. *Plant model* describes the identified, high fidelity plant including all available system information and dynamics to adequately reproduce the plant (here: missile) behavior. For the purpose of control design, it is feasible and in many cases necessary to reduce the complexity of the plant model in order to apply analysis or control design techniques. This model is called *design model*.

Due to hardware restrictions and lack of experience, the first FCSs employed classic linear, gain-scheduled control architectures [23, 24]. The design parameters of those control laws are obtained based on a linearization (design model) of the assumed nonlinear missile dynamics at a certain grid of operating points. In the 1980s, the fast growing popularity of robust control techniques for in-

dustry application and the increased onboard computational power led to robust control designs, which provide the methodology to layout multivariable controllers with respect to performance and stability requirements simultaneously [24]. Analogous to classic linear approaches, robust control layout is also based on linear representation of the highly nonlinear missile dynamics at certain envelope points [25, 26, 27]. Both control design methodologies exhibit the advantage that a variety of linear metrics are available in order to analyze the linearized closed-loop behavior. Due to the inherent nonlinear missile dynamics, a linear system representation approximates the dynamic behavior only within a narrow flight envelope region sufficiently well. Therefore, robustness and performance of one of the aforementioned control techniques hold only in the close vicinity of the considered operation point. In the case of these classic linear time-invariant (LTI) approaches, the controller gains are scheduled over a certain grid of fixed operating points. A scheduling algorithm selects the valid gain combination depending on appropriate state variables (e.g. velocity, angle of attack (AoA)). Since multivariable LTI controllers may vary in state order and feedback structure over the flight envelope, scheduling approaches like in classic linear autopilots are impossible. In order to overcome this drawback, some inner loop missile controllers based on robust (multivariable) techniques use blending methods of the controller output [24] or dynamical scheduling of relevant design parameters [28, 29].

By using control methods based on linear parameter-varying (LPV) system representations, autopilots that are able to cover some nonlinear effects of the missile can be designed. LPV systems have a linear structure, whose state-space entries depend on time-varying parameters. This special form of a nonlinear system exhibit several characteristics for which certain control techniques were developed. The resultant controller consists of an LPV system dependent on available parameters. In contrast to gain-scheduling approaches, LPV autopilots guarantee specific performance and robustness criteria for the approximated plant over the entire considered flight envelope [30, 31]. A limiting factor of the LPV framework is the identification of an accurate, low-order system representation, which is required for control design [32]. It is important to emphasize that both approaches - classic linear and LPV autopilot design - exhibit the desired closed-loop behavior only for the considered linear or LPV system, respectively. Therefore, there is no similar guarantee that those controllers fulfill the robustness and performance specifications when applied to the nonlinear plant model or plant itself.

The herein considered class of nonlinear controllers inherently account for the nonlinear system dynamics. Within this thesis, the term *nonlinear control* refers to control methods which can be directly applied to nonlinear, time-variant design models. Two major design methods of the class of nonlinear control constitute Backstepping and Nonlinear Dynamic Inversion (NDI). Although the resultant control law of both approaches show an almost identical structure, the design philosophy is different [33, 34]. A Backstepping controller is obtained by recursively - from the outer most system dynamics to the inner most one - applying Lyapunov's second method of stability subsystem-wise in order to calculate intermediate control laws at each design step [35]. The design idea behind classic NDI is to cancel the entire nonlinear dynamics for the purpose of rendering the input/output dynamics linear. Therefore, NDI is not considered a control method itself but a strategy to transform a nonlinear control problem into a linear one. This conversion offers the possibility to apply a large variety of controllers, which are applicable to linear systems. For the purpose of using those methods in the field of missile control, modifications are necessary in order to tailor those approaches to the complex dynamics and peculiarities of a high-agile missile system. Those changes of the standard control laws lead to an increased employment of these techniques in the field of inner loop missile control [36, 37, 38, 39, 40].

Nevertheless, all NDI- and Backstepping (BS)-based approaches have in common that the considered system has to exhibit a minimum phase input/output characteristic [35, 41, 42]. Since the longitu-

dinal and lateral acceleration outputs of a tail-controlled missile render the system non-minimum phase, several techniques evolved in order to overcome this issue [36, 37, 43]. Other approaches cope with non-minimum phaseness by introducing a time scale separation into the control loop [43, 44]. In contrast to the majority of fixed-wing vehicles (e.g. UAV, cruise missiles), the dynamics of SSMs and AAMs does usually not possess a defined time scale separation. Therefore, an introduction of an artificial time scale separation leads to the undesired reduction of the system's bandwidth. Besides the restriction to minimum phase systems, classic NDI and Backstepping approaches applied to complex dynamics (e.g. missile dynamics) lead to tedious control laws, which are impractical to implement [41]. Due to this apparent disadvantage of those powerful control strategies, several novel extensions and modifications evolved, which make Backstepping especially suitable for complex (aerospace) systems [41, 45, 46, 47, 48].

All the aforementioned autopilots are designed on the basis of an assumed mathematical system representation (design model). The design of the controllers based on the nominal design model (*baseline controller*) involve the complete fulfillment of performance specifications derived from mission requirements. Since a missile system is subject to a large variety of uncertainties, a control design not capable of compensating for those deviations, between assumed (design) model and real plant, may result in a failure of the mission objectives. Therefore, an *augmentation* of the baseline controller is necessary to preserve the desired performance, even in the case of severe model mismatches. As discussed above, the class of robust control is able to guarantee the compliance of certain performance and robustness specifications within the design process simultaneously [25, 28, 30]. With increased computing power and advances in control theory, the field of adaptive control gained more and more significance in manned and unmanned flight control [47, 49, 50, 51, 52, 53**?**]. An adaptive control scheme consists of two elements: an identification algorithm that estimates the deviation between the assumed model used for control design and the real plant. This information is used in a feedback control law in order to compensate for the mismatch between design model and plant. Over the years many different approaches evolved within the field of adaptive control. With Adaptive Backstepping, Model Reference Adaptive Control (MRAC), and $\mathcal{L}_1$-Adaptive Control, only the most relevant adaptive autopilot strategies for aerial applications are considered herein. The interested reader is referred to [54, 55, 56] for further state-of-the-art adaptive control techniques.

The control algorithm calculates the actuator commands (here: fin deflections) based on the difference between the measured output and the desired reference signals. A careful control design reduces the workload of the error controller to a minimum. This avoids control surface fatigue or undesired system behavior. Besides the control algorithm layout, the shape of the reference signals plays a decisive role in terms of tracking quality. The main idea of the reference signal is to provide the control algorithm with a sufficiently smooth signal, that exhibits a trajectory in accordance with the main missile characteristics. Therefore, the *reference model* shall filter the desired trajectory issued by the guidance unit (see fig. 1.3) to a feasible reference signal, which fully explores the missile's physical capabilities over the entire flight envelope. Since a missile is a highly nonlinear system, common approaches using linear filter algorithms (reference models) lead to a closed-loop behavior that is beyond the missile's maximum performance potential [36, 38, 40]. As stated by Wise, Lavretsky and Hovakimyan in [57], the reference models for aerial vehicles with fast changing dynamics remains an open problem in the field of nonlinear and adaptive control.

1.4 Contributions of this Thesis

This thesis contributes to the field of missile autopilot design. Specifically, it introduces novel control techniques and architectures which are modified to fully exploit the physical system capabilities

of the missile. In order to raise the technological readiness of the proposed methodologies, the autopilot design and layout procedure is incorporated in a complete development process. Therefore, demanding requirements are defined based on the in-depth analysis of the FGS-X-03 benchmark model. The assessment and verification of the developed algorithms with respect to the requirements are conducted by utilizing linear and nonlinear metrics covering common industrial standards. Some of the results presented within this thesis are already published by the author in [20, 21, 58]. The major scientific contributions of this thesis are described in the following.

Realistic benchmark model including high fidelity aerodynamic model

The FGS-X-03 simulation model serves as the benchmark model. The novel missile autopilot approach is conducted and verified with respect to elaborate performance and robustness requirements. In available literature, autopilot design and proofs of concept are carried out for simplified nonlinear or even linear missile models [26, 29, 37, 38, 59, 60, 61, 62]. Therefore, characteristic but realistic effects of the missile system such as actuator saturation, available measurements, aerodynamic/kinematic cross-coupling, input-affine aerodynamics, and fast varying uncertainties are not considered. Neglecting those effects simplifies the missile control design tremendously.

The herein examined benchmark model constitutes a realistic six DOF model of a generic SAM including representative sensor and actuator models. As the parametric uncertainties play a crucial role in evaluating the missile's robustness, the primary focus within modeling the six DOF missile dynamics lies in a detailed representation of the uncertainty effects. Thus, the nonlinear aerodynamic data given in tabular data is extended by a state-dependent uncertainty model based on a probabilistic weighted radial basis function (RBF) network.

Modular autopilot architecture

The objective of this thesis is the systematic development and parametrization of a missile autopilot in accordance with requirements demanding the missile's maximum possible performance capabilities. Thus, the design of the autopilot is subdivided in three modular and independent units: a nonlinear reference model, a nonlinear baseline autopilot, and an adaptive augmentation. With this modular approach each specification is covered by one of the three autopilot elements. Therefore, a clear allocation between requirements and algorithms are achieved. This facilitates the interchangeability of certain elements, testing procedures, and the verification process.

Physical motivated output selection

In order to apply the selected nonlinear control techniques, the input/output characteristics of the control variables require to be minimum phase. In case of tail-controlled missiles the acceleration outputs provided by IMU constitute (depending on the airframe configuration) commonly a non-minimum phase output with respect to the aerodynamic controls. In [37, 38] the non-minimumphaseness is circumvented by so-called *output redefinition*, using a blend of the estimated aerodynamic angles and body rates. Other available literature facilitate this problem by selecting the non-measurable aerodynamic angles as control variables [39, 59].

For the purpose of rendering the system dynamics minimum phase, the missile's acceleration is calculated at a virtual point ahead of the IMU location. The selection process of the virtual IMU position is based on linear metrics evaluated for different uncertainty configurations across the entire flight envelope.

Nonlinear reference model

The purpose of the reference model is to mimic the missile's main physical characteristics over the entire flight envelope and provide all necessary reference signals for the control algorithms upstream. In common literature this command filtering is obtained by linear reference models [36, 37, 38, 39]. Therefore, the missile's closed-loop dynamics is transformed to a linear behavior limiting the missile's performance.

For the presented autopilot a nonlinear reference model is developed representing the major nonlinear effects of the missile system. Thus, the provided outputs incorporate the nonlinear, interconnected characteristics of the missile system. These reference trajectories lead to more agile system behavior and therefore to a significant increase in performance characteristics.

Tailoring of baseline control techniques

Two baseline control methodologies, based on NDI and BS theory, are identified for being perfectly suitable to track the nonlinear reference trajectories provided by the reference model. In order to utilize the advantageous characteristics of the reference trajectories and to account for the peculiarities of the missile dynamics, both approaches are customized for the usage within the autopilot algorithm. The validity of the modifications are verified by theoretical considerations with respect to stability properties.

Cascaded adaptive augmentation of the plant dynamics

To preserve the desired closed-loop behavior, set up via the baseline autopilot, even in case of unavoidable modeling effects, an adaptive augmentation is included within the FCS. A modification of the $\mathcal{L}_1$-Adaptive Control methodology (see [63]) constitutes the theoretical foundation for the robustifying adaptive layer. The selected methodology and modification is carefully justified based on the inherent properties of the respective theory, the modular autopilot architecture, and the missile's uncertainties. To achieve independence of the adaptive layer with respect to the structure and parametrization of the baseline autopilot, the adaptive element is designed to directly address deviations between design model and plant dynamics. Based on thorough analysis of the baseline control algorithms, the augmentation incorporates a newly developed cascaded structure to account for uncertainties in both dynamical layers (force and momentum dynamics).

1.5 Outline of this Thesis

Within chapter 2 the FGS-X-03 benchmark model is introduced in detail. This covers the derivation of the missile's equation of motions (EOMs), the introduction of parameter definition, and the specification of the subsystems. The performance capabilities and dynamic properties of this benchmark model are in-depth analyzed within chapter 3. The theoretical background of the algorithms used for the autopilot design (see chapter 5) is outlined in chapter 4. Based on the results from the system analysis (in chapter 3), the first step of the autopilot design in chapter 5 constitutes the derivation of the functional and non-functional performance requirements. Those requirements in combination with the model dynamics serve as main inputs for the layout and parametrization of the autopilot algorithms. The evaluation and analysis of the autopilot design with respect to the aforementioned requirements is conducted in chapter 6. In this analysis linear as well as nonlinear

metrics are utilized to verify the missile's closed-loop robustness and performance. **??** concludes the thesis by summarizing the main results and presenting an outlook on further research in the area of nonlinear missile autopilot design.

CHAPTER 2

Missile Model

> I do not know what I may appear to the world; but to myself I seem to have been only like a boy playing on the seashore, and diverting myself in now and then finding of a smoother pebble or a prettier shell than ordinary, whilst the great ocean of truth lay all undiscovered before me.
>
> Sir Isaac Newton

This chapter introduces the nonlinear, generic missile model of the FSD Generic Surface-to-Air Missile (FGS-X-03) that serves as a benchmark model for the systematic development and evaluation of the autopilot designs. The fidelity of the simulation model accounts for the two main modeling drivers: on the one hand the model is set up in order to design, test, and evaluate different autopilot architectures; on the other hand the specific scenario and missile type demand certain specifications and allow for some feasible simplifications. Control design, model simulation, and analysis are obtained within the simulation framework *MATLAB/Simulink ® 2015b*.

2.1 Introduction

A simulation model is a mathematical, digital representation of a physical system to better analyze its characteristic behavior over time and to develop algorithms or devices for obtaining a desired system behavior. The process of modeling forces the designer to balance in each model layer between accuracy, verifiable characteristics, available information, and execution time. The design depth of the model is chosen to reproduce the major characteristics of real surface-to-air missile (SAM) systems in order to employ the simulation model as a realistic benchmark for autopilot design purposes. Any degree of compliance with current real missile systems is pure coincidence. A schematic of the FGS-X-03 airframe is depicted in fig. 2.1.

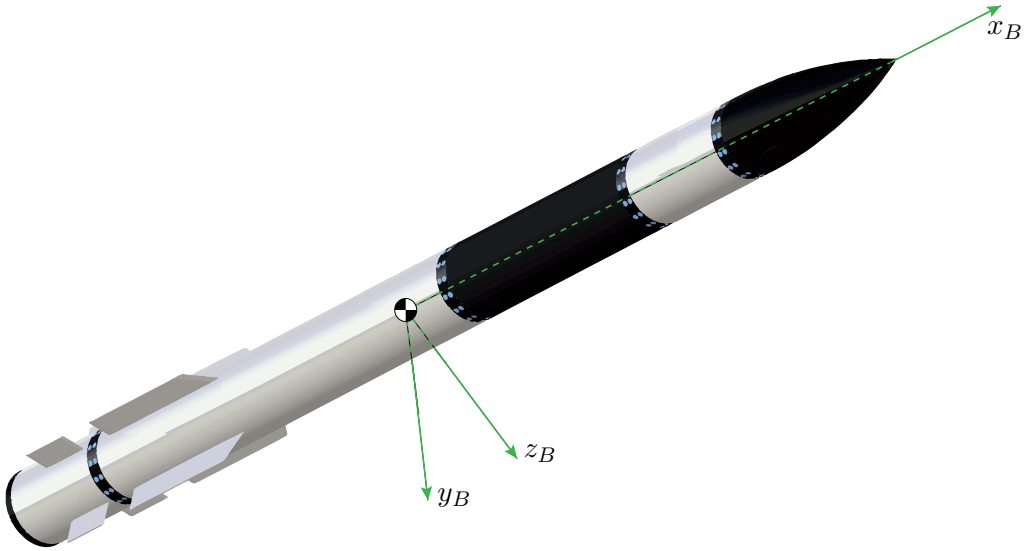

Figure 2.1: View of the benchmark missile FGS-X-03 with the body-fixed coordinate frame.

For deriving the missile's equation of motions (EOMs), the relevant reference frames of the missile system are defined in section 2.2. In section 2.3, the forces and moments acting on the missile body are introduced according to their physical origin (e.g. aerodynamics). In this context the modeling of the aerodynamic and parameter uncertainties are described (section 2.4). Section 2.5 is dedicated to the actuator, sensor, and state estimation unit of the missile system.

2.2 Missile Dynamics

In this section the missile dynamics is derived according to Newton's laws of motion. In order to model the rigid body EOM the choice of the considered reference frames is significant. Therefore, a brief introduction of missile dynamics' underlying coordinate frames is given. For the purpose of reducing complexity and improving the simulation's usability, besides the 6-degree of freedom (DOF) rigid body dynamics, no other dynamical effects (e.g. bending modes) are considered. This chapter presents only the formulas of the rigid body missile dynamics. A detailed derivation of the rigid body dynamics can be found in [1, 64, 65].

2.2.1 Coordinate Frames

In order to provide a complete description of the missile dynamics and all relevant variables essential for control design purposes, the necessary coordinate frames are introduced within this section. All herein presented coordinate systems are right-hand systems. Therefore, the system is sufficiently defined by the origin and two axes (see appendix A.1). The following list provides a brief description of the coordinate frames. Detailed information and illustrations about the herein used coordinate frames can be found in [1, 66].

- *Earth-Centered Inertial (ECI), I-frame*: With the origin of the I-frame attached to the earth sphere, the ECI is rotating on its orbit around the sun. The x_I-axis is pointing towards the vernal equinox and the z_E-axis is aligned with the earth rotational axis.
- *Earth-Centered Earth-Fixed (ECEF), E-frame*: The E-frame's origin is located at the center of

the earth sphere. The x_E-axis intersects the earth sphere at 0° latitude and 0° longitude. The z_E-axis is aligned with the earth rotational axis. $\left(\boldsymbol{\omega}_K^{IE}\right)$ describes the angular velocity, the E-frame is rotating with respect to the I-frame due to earth rotation. This rotation rate is assumed to be constant.

- *North-East-Down (NED), O-frame*: The origin of the NED frame is attached to the missile's center of gravity (cog). Due to earth curvature the O-system rotates with the transportation rate $\left(\boldsymbol{\omega}_K^{EO}\right)$ around the E-frame. The x_0 points in polar direction parallel to the earth reference surface. The z_O-axis is directed antiparallel to the surface normal vector.
- *Body-Fixed, B-frame*: The origin of the Body-Fixed frame is attached to the missile's cog. The x_B-axis is aligned with the missile's rotational symmetry axis and directed toward the missile's cone. The z_B-axis is pointing downwards, perpendicular to the symmetry plane of the missile. A rotation of the missile's B-frame with respect to the underlying O-frame is denoted as $\left(\boldsymbol{\omega}_K^{OB}\right)$.
- *Kinematic, K-frame*: The origin moves with the missile's reference point R. The x_K-axis is coincident in direction with the missile's velocity vector. The y_K-axis is perpendicular to the velocity vector, pointing to the right, and lies in the missile's $x_O y_O$-plane. With the assumption of no wind, the aerodynamic and kinematic frame are equivalent.
- *Rotated Kinematic, $\bar{K}$-frame*: The origin moves with the missile's reference point R. The x_K-axis is coincident in direction with the missile's velocity vector. The y_K-axis is rotated in the $y_K z_K$-plane about the kinematic bank angle μ_K.
- *Load Factor, L-frame*: The origin of the load factor frame is attached to the missile's reference point R. The x_L-axis is aligned with the missile's velocity vector and the load factor vector acting on the missile body is perpendicular to the $x_L y_L$-plane.

2.2.2 Rigid Body Equations of Motion

The rigid body EOM consists of four different dynamical layers: translation, rotation, position, and attitude dynamics. In common aircraft simulation literature [1, 64, 65], the translational and attitude dynamics can usually be described by the use of two different sets of variables, quaternions and Euler angles. In this section, forces F and moments M are considered in a general way. A detailed description of the force and moment composition is given in section 2.3. Taking the given missile type and the considered endgame scenario into account, the model is designed by utilizing the following assumptions:

- *FGS-X-03 is modeled as a rigid body*: The distance between all possible points of the missile body remains constant over time.
- *Constant mass*: By considering the endgame scenario, the missile's propulsion unit is assumed to be fully burned out. Therefore, the missile is not subject to any mass changes or any resulting forces or moments.
- *Constant moment of inertia*: Due to the negligible impact of the fin movement on the moment of inertia and the constant mass, it is feasible to consider the moment of inertia as constant over the entire simulation horizon.
- *Symmetric mass distribution*: The mass distribution of the missile is symmetric with respect to the $x_B y_B$- and $x_B z_B$-plane. Therefore, the entities $I_{xy}, I_{yx}, I_{yz}, I_{zy}$ of the inertia tensor vanish and x_B constitutes the principal axis.

- *Flat and non-rotating earth*: Since the covered distance in the considered SAM endgame scenarios is small compared to the earth radius, it is feasible to consider the earth to be non-rotating and flat. Thus, the transportation rate $\left(\boldsymbol{\omega}_K^{EO}\right)$ and rotation of the earth with respect to the ECI-frame $\left(\boldsymbol{\omega}_K^{IE}\right)$ can be neglected in the following derivation and the ECEF-frame constitutes the inertial frame.
- *Wind is neglected*: Due to the high traveling speeds of the missile, wind effects are neglected within the simulation model.

2.2.2.1 Translation Dynamics

According to Newton's second law of motion

$$\sum \boldsymbol{F} = \boldsymbol{F}_T = m \cdot \left(\boldsymbol{a}^P\right)^{II} \tag{2.1}$$

the sum of forces $\boldsymbol{F}_T$ acting on a body is equal to the body mass multiplied by the body's acceleration [67]. Utilizing the introduced rotational rates and coordinate frames (section 2.2.1), the acceleration of an arbitrary point P with respect to the reference point R, both located at the missiles body, is given by

$$\begin{aligned}\left(\boldsymbol{a}^P\right)^{II} = \left(\dot{\boldsymbol{V}}^R\right)^{EB} + 2 \cdot \left(\boldsymbol{\omega}^{IE}\right) \times \left(\boldsymbol{V}^R\right)^E + \left(\boldsymbol{\omega}^{IE}\right) \times \left[\left(\boldsymbol{\omega}^{IE}\right) \cdot \left(\boldsymbol{r}^R\right)\right] \\ + \left(\dot{\boldsymbol{\omega}}^{IB}\right)^B \times \left(\boldsymbol{r}^{RP}\right) + \left(\boldsymbol{\omega}^{IB}\right) \times \left[\left(\boldsymbol{\omega}^{IB}\right) \cdot \left(\boldsymbol{r}^{RP}\right)\right]\end{aligned} . \tag{2.2}$$

Under the assumption of a non-rotating ($\left(\boldsymbol{\omega}_K^{IE}\right) = \mathbf{0}$) and flat earth ($\left(\boldsymbol{\omega}_K^{EO}\right) = \mathbf{0}$), the rates describing rotation of the missile's body with respect to the ECEF-frame (inertial frame in case of non-rotating earth) becomes

$$\begin{aligned}\left(\boldsymbol{\omega}_K^{IB}\right)_B &= \underbrace{\left(\boldsymbol{\omega}_K^{IE}\right)_B}_{=\mathbf{0}} + \underbrace{\left(\boldsymbol{\omega}_K^{EO}\right)_B}_{=\mathbf{0}} + \left(\boldsymbol{\omega}_K^{OB}\right)_B \\ &= \boldsymbol{\omega}_K^{EB}\end{aligned} . \tag{2.3}$$

Substituting (2.2) in (2.1) by using the body rates defined in (2.3), the translational velocity $\left(\boldsymbol{V}_K^G\right)_B^E = \begin{bmatrix} u_K^G & v_K^G & w_K^G \end{bmatrix}_B^{E,T}$ with respect to the ECEF-frame results in

$$\left(\dot{\boldsymbol{V}}_K^G\right)_B^{EB} = \frac{1}{m} \cdot \left(\boldsymbol{F}_T^G\right)_B - \left(\boldsymbol{\omega}_K^{EB}\right)_B \times \left(\boldsymbol{V}_K^G\right)_B^E . \tag{2.4}$$

(2.4) is obtained by merging the point of interest (P) and reference point (R) in (2.2) in the cog (G). Besides the velocities $\left(u_K^G\right)_B^E, \left(v_K^G\right)_B^E, \left(w_K^G\right)_B^E$, it is necessary in aircraft simulation to provide the translational states, absolute velocity $\left(V_K^G\right)^E = \| \left(\boldsymbol{V}_K^G\right)^E \|$, angle of attack (AoA) α_K, and angle of sideslip (AoS) β_K, for certain subsystems (e.g. calculation of aerodynamic forces and moments). These angles define the attitude of the $\bar{K}$-frame with respect to the aircraft's body frame (see appendix A.1). Within missile simulation the common processing procedure is the calculation of those

alternative states based on the velocities obtained from (2.4) via the following relationship:

$$\begin{aligned}
\left(V_K^G\right)_{\bar{K}}^E &= \sqrt{\left(\left(u_K^G\right)_B^E\right)^2 + \left(\left(v_K^G\right)_B^E\right)^2 + \left(\left(w_K^G\right)_B^E\right)^2} \\
\alpha_K &= \arctan \frac{\left(w_K^G\right)_B^E}{\left(u_K^G\right)_B^E} \\
\beta_K &= \arctan \frac{\left(v_K^G\right)_B^E}{\sqrt{\left(\left(u_K^G\right)_B^E\right)^2 + \left(\left(w_K^G\right)_B^E\right)^2}}
\end{aligned} \tag{2.5}$$

The alternative translation states (2.5) can be directly obtained by integration of the following differential equations [1]

$$\begin{aligned}
\dot{V}_K^G &= \frac{\left(F_x^G\right)_{\bar{K}}}{m} \\
\dot{\alpha}_K &= \frac{\left(F_z^G\right)_{\bar{K}}}{m\left(V_K^G\right)_{\bar{K}}^E \cos\beta_K} + \left(q_K^{EB}\right)_B - \tan\beta_K \left(\left(p_K^{EB}\right)_B \cos\alpha_K + \left(r_K^{EB}\right)_B \sin\alpha_K\right). \\
\dot{\beta}_K &= \frac{\left(F_y^G\right)_{\bar{K}}}{m\left(V_K^G\right)_{\bar{K}}^E} + \left(p_K^{EB}\right)_B \sin\alpha_K - \left(r_K^{EB}\right)_B \cos\alpha_K
\end{aligned} \tag{2.6}$$

F_i denotes the single force components. p_K^{EB}, q_K^{EB}, and r_K^{EB} describe the rotation rates of the B-frame with respect to the E-frame (inertial frame) around x_B-, y_B-, and z_B-axis, respectively. These rotation rates are labeled *roll*, *pitch*, and *yaw rate*, respectively. Based on the velocity $\left(V_K^G\right)^E$, the Mach number is defined as

$$M = \frac{\left|\left(V_K^G\right)^E\right|}{c} \tag{2.7}$$

where c is the speed of sound. The Mach number constitutes another way for describing the missile's absolute velocity.

Due to the fact that the missile is a rotational symmetric body, it is common to employ the L-frame for describing the missile's aerodynamics and certain control tasks. In contrast to the kinematic (K-frame) coordinate system, which is mainly used for fixed-wing configurations, the load factor frame (L-frame) is orientated with respect to the aerodynamic force vector acting on the missile body (see appendix A.1). Since the load factor is perpendicular to the kinematic velocity $\left(V_K^G\right)^E$ (assuming no wind) [64], the attitude of the L-frame with respect to the missile body (B-frame) is defined by a rotation φ_K around the x_B-axis to align the $x_L z_L$-plane with the velocity vector. The total incidence angle ϑ_K describes the second rotation to parallelize the x_L-axis with the velocity vector. Based on the velocities $\left(\boldsymbol{V}_K^G\right)_B^E = \begin{bmatrix} u_K^G & v_K^G & w_K^G \end{bmatrix}_B^{E,T}$, those angles can be calculated by the following algebraic relationship [64]:

$$\begin{aligned}
\vartheta_K &= \arccos\left(\frac{\left(u_K^G\right)_B^E}{\left(V_K^G\right)_{\bar{K}}^E}\right) \\
\phi_K &= \arctan\left(\frac{\left(v_K^G\right)_B^E}{\left(w_K^G\right)_B^E}\right)
\end{aligned} \tag{2.8}$$

An alternative approach to calculate the total incidence ϑ_K and roll angle ϕ_K is obtained by substi-

tuting the aerodynamic angles α_K and β_K from (2.5) into (2.8) [64]:

$$\begin{aligned} \vartheta_K &= \arccos\left(\cos\alpha_K \cos\beta_K\right) \\ \phi_K &= \arctan\left(\frac{\tan\beta_K}{\sin\alpha_K}\right) \end{aligned} \tag{2.9}$$

Remark: The transformation in (2.8) and (2.9) exhibits a singularity at $\left(w_K^G\right)_B^E = 0$ and $\alpha_K = 0$, respectively.

2.2.2.2 Rotation Dynamics

The rotation dynamics of the missile's body according to the ECEF-frame is obtained by applying Newton's second law of motion ([67]) to the conservation of the angular momentum $\boldsymbol{H}^E$. The angular momentum is calculated with respect to the inertial fixed point. With the assumption of flat, non-rotating earth, this fixed point coincides with the earth center E. Newton's second law states, that the variation of the angular momentum $\boldsymbol{H}^E$ over time equals the sum of all moments $\boldsymbol{M}^E$ acting on the body:

$$\sum \boldsymbol{M}^E = \boldsymbol{M}_T^E = \left(\frac{d}{dt}\right)^I \boldsymbol{H}^E \tag{2.10}$$

Based on (2.3), (2.10), and by the selection of cog G as reference point the dynamics of the body rate $\left(\boldsymbol{\omega}_K^{EB}\right)_B = \begin{bmatrix} p_K^{EB} & q_K^{EB} & r_K^{EB} \end{bmatrix}_B^T$ describing the rotational motion of the missile body with respect to the ECEF-frame results in

$$\left(\dot{\boldsymbol{\omega}}_K^{EB}\right)_B^B = \left(\mathbf{I}^G\right)_{BB}^{-1} \left(\left(\boldsymbol{M}_T^G\right)_B - \left(\boldsymbol{\omega}_K^{EB}\right)_B \times \left(\mathbf{I}^G\right)_{BB} \left(\boldsymbol{\omega}_K^{EB}\right)_B\right). \tag{2.11}$$

The complete derivation of the rotational dynamics including all intermediate steps can be found in [64, 65].

2.2.2.3 Position Dynamics

With the aforementioned assumptions the ECI- and the ECEF-frame are coincident. Therefore, the E-frame can be considered as the inertial frame, which constitutes the coordinate system for the missile's global position vector $\left(\boldsymbol{r}^G\right)_E = \begin{bmatrix} x^G & y^G & z^G \end{bmatrix}_E$. Integrating the missile's velocity transformed to the ECEF-frame with respect to time

$$\left(\dot{\boldsymbol{r}}^G\right)_E^E = \mathbf{M}_{EB} \cdot \left(\boldsymbol{V}_K^G\right)_B^E \tag{2.12}$$

results in the position vector $\left(\boldsymbol{r}^G\right)_E$ describing the distance between the cog G and the origin of the E-frame. For flight envelope considerations and atmospheric data calculation within the simulation framework, the distance of the missile with respect to the earth surface is necessary. Thus, with the definition of $\left(r_z^G\right)_E$ and the earth radius r_E, the missile's altitude above sea level is calculated by

$$h = \left(r_z^G\right)_E - r_E. \tag{2.13}$$

2.2.2.4 Attitude Dynamics

In contrast to civil aircraft, SAMs can occupy any possible attitude in space during their mission. The attitude of the missile body-frame with respect to the inertial E-frame can be described via Euler angles Φ^{EB}, Θ^{EB}, Ψ^{EB} or quaternions $\boldsymbol{q}^{EB} = \begin{bmatrix} q_0^{EB} & q_1^{EB} & q_2^{EB} & q_3^{EB} \end{bmatrix}^T$. Since the attitude dynamics of Euler angles

$$\begin{bmatrix} \dot{\Phi}^{EB} \\ \dot{\Theta}^{EB} \\ \dot{\Psi}^{EB} \end{bmatrix} = \begin{bmatrix} 1 & \sin\Phi^{EB}\tan\Theta^{EB} & \cos\Phi^{EB}\tan\Theta^{EB} \\ 0 & \cos\Phi^{EB} & -\sin\Phi^{EB} \\ 0 & \frac{\sin\Phi^{EB}}{\cos\Theta^{EB}} & \frac{\cos\Phi^{EB}}{\cos\Theta^{EB}} \end{bmatrix} \begin{bmatrix} p_K^{EB} \\ q_K^{EB} \\ r_K^{EB} \end{bmatrix}_B \tag{2.14}$$

exhibits a singularity in case the missile's body axis x_B is perpendicular ($\Theta = \pm 90°$) to the $x_O y_O$-plane (see appendix A.1), Euler angles are not suitable for attitude calculation in missile simulation. Utilizing quaternions

$$\boldsymbol{q}^{EB} = q_0^{EB} + q_1^{EB} \cdot \boldsymbol{i} + q_2^{EB} \cdot \boldsymbol{j} + q_3^{EB} \cdot \boldsymbol{k} \tag{2.15}$$

for describing the missile's attitude provides a singularity-free description [64, 65]. $\boldsymbol{i}$, $\boldsymbol{j}$, and $\boldsymbol{i}$ denote the standard orthonormal basis for $\mathbb{R}^3$. The quaternions definition and its dynamical representation

$$\dot{\boldsymbol{q}}^{EB} = \frac{1}{2}\boldsymbol{q}^{EB} \circ \begin{bmatrix} 0 \\ \left(\boldsymbol{\omega}_K^{EB}\right)_B \end{bmatrix} \tag{2.16}$$

is in line with [68], where $\circ$ denotes the quaternion multiplication operator and q_0^{EB}. Due to the fact that Euler angles represent the missile attitude in a more descriptive and intuitive way compared to quaternions, it is common within the post processing procedure to calculate the Euler angles based on quaternions by the following algebraic relationship [68] (indices dropped due to better readability):

$$\begin{aligned} \Phi &= \arctan\left[2\left(q_0 q_1 + q_2 q_3\right), \left(q_0^2 + q_3^2 - q_1^2 - q_2^2\right)\right] \\ \Theta &= \arcsin\left[2\left(q_0 q_2 + q_1 q_3\right)\right] \\ \Psi &= \arctan\left[2\left(q_0 q_3 + q_1 q_2\right), \left(q_0^2 + q_1^2 - q_2^2 - q_3^2\right)\right] \end{aligned} \tag{2.17}$$

For a practical implementation of (2.17) the following two issues have to be considered:

- The arithmetic operation *arctan* shall be conducted by the *atan2* function, which provide the result in the proper quadrant.
- In order to avoid the indetermination (*gimbal lock*) of the bank Ψ^{EB} and heading angle Φ at north ($\Theta^{EB} = +90°$) and south pole ($\Theta^{EB} = -90°$) singularity configuration, a workaround is implemented in accordance with [68].

For Skid-To-Turn (STT) missile application it is very common to control the roll channel by considering the roll angle

$$\phi_v = \int \left(\cos\alpha_K \cdot \cos\beta_K \cdot \left(p_K^{EB}\right)_B + \sin\beta_K \cdot \left(q_K^{EB}\right)_B + \sin\alpha_K \cos\beta_K \cdot \left(r_K^{EB}\right)_B\right) dt \tag{2.18}$$

about the velocity vector $\left(\boldsymbol{V}_K^G\right)_{\bar{K}}^E$ as control variable.

2.2.2.5 Summary

This section summarizes the missile's body dynamics with a detailed breakdown of the introduced rigid body EOMs. The element-wise form of the translation dynamics (2.4) is given by

$$\begin{bmatrix} \dot{u}_K^G \\ \dot{v}_K^G \\ \dot{w}_K^G \end{bmatrix}_B^{EB} = \frac{1}{m} \begin{bmatrix} F_{x,T}^G \\ F_{y,T}^G \\ F_{z,T}^G \end{bmatrix}_B - \begin{bmatrix} \left(q_K^{EB}\right)_B \left(w_K^G\right)_B^E - \left(r_K^{EB}\right)_B \left(v_K^G\right)_B^E \\ \left(r_K^{EB}\right)_B \left(u_K^G\right)_B^E - \left(p_K^{EB}\right)_B \left(w_K^G\right)_B^E \\ \left(p_K^{EB}\right)_B \left(v_K^G\right)_B^E - \left(q_K^{EB}\right)_B \left(u_K^G\right)_B^E \end{bmatrix}_B . \tag{2.19}$$

The assumption of a symmetric mass distribution leads to an inertia matrix $\left(\mathbf{I}^G\right)_{BB}$ of diagonal form. Therefore, the rotational dynamics

$$\begin{bmatrix} \dot{p}_K^{EB} \\ \dot{q}_K^{EB} \\ \dot{r}_K^{EB} \end{bmatrix}_B^B = \begin{bmatrix} 1/I_{xx}^G & 0 & 0 \\ 0 & 1/I_{yy}^G & 0 \\ 0 & 0 & 1/I_{zz}^G \end{bmatrix}_{BB} \begin{bmatrix} \left(L^G\right)_B - \left(q_K^{EB}\right)_B \left(r_K^{EB}\right)_B \left(I_{zz}^G - I_{yy}^G\right)_{BB} \\ \left(M^G\right)_B - \left(r_K^{EB}\right)_B \left(p_K^{EB}\right)_B \left(I_{xx}^G - I_{zz}^G\right)_{BB} \\ \left(N^G\right)_B + \left(p_K^{EB}\right)_B \left(q_K^{EB}\right)_B \left(I_{xx}^G - I_{yy}^G\right)_{BB} \end{bmatrix} \tag{2.20}$$

is decoupled in terms of the moments acting on the missile. Thus, the roll L^G, pitch M^G, and yaw moment N^G influence only the corresponding dynamics. Under nominal assumptions (no uncertainties) the missile body is ideal rotational symmetric. Therefore, the difference $\left(I_{zz}^G\right)_{BB} - \left(I_{yy}^G\right)_{BB}$ in the roll channel vanishes and dynamical interference of the roll motion caused by the yaw and pitch dynamics can be considered as negligible. Due to the equivalence $I_{zz}^G = I_{yy}^G$, the only mutual interference between the axes is caused by the inertia cross-coupling in the pitch and yaw dynamics.

In order to obtain the position dynamics

$$\begin{bmatrix} \dot{r}_x^G \\ \dot{r}_y^G \\ \dot{r}_z^G \end{bmatrix}_E^E = \underbrace{\mathbf{M}_{EO}\mathbf{M}_{OB}}_{\mathbf{M}_{EB}} \begin{bmatrix} u_K^G \\ v_K^G \\ w_K^G \end{bmatrix}_B^E \tag{2.21}$$

the transformation of the velocity vector $\left(V_K^G\right)_B^E$ from body-fixed frame into the ECEF-frame ($\mathbf{M}_{EB}$) is conducted via direction cosine matrix (see [64]) expressed (upper indices denoting rotation are dropped due to better readability)

$$\mathbf{M}_{OB} = \begin{bmatrix} q_0^2 + q_1^2 - q_2^2 - q_3^2 & 2\left(q_1 q_2 - q_0 q_3\right) & 2\left(q_1 q_3 + q_0 q_2\right) \\ 2\left(q_1 q_2 + q_0 q_3\right) & q_0^2 - q_1^2 + q_2^2 - q_3^2 & 2\left(q_2 q_3 - q_0 q_1\right) \\ 2\left(q_1 q_3 - q_0 q_2\right) & 2\left(q_2 q_3 + q_0 q_1\right) & q_0^2 - q_1^2 - q_2^2 + q_3^2 \end{bmatrix} \tag{2.22}$$

and the O-frame's $180°$ rotation about the y_O-axis:

$$\mathbf{M}_{EO} = \begin{bmatrix} -1 & 0 & 0 \\ 0 & 1 & 0 \\ 0 & 0 & -1 \end{bmatrix} \tag{2.23}$$

The quaternion theory is based on the restriction, that the quaternion $\boldsymbol{q}^{EB}$ is of unity length

$$\left(q_0^{EB}\right)^2 + \left(q_1^{EB}\right)^2 + \left(q_2^{EB}\right)^2 + \left(q_3^{EB}\right)^2 = 1. \tag{2.24}$$

Depending on the simulation step size and choice of the solver, the numerical integration of the quaternion differential equation (2.16) can lead to violations of (2.24). Therefore, it is common in

aircraft simulations to preserve the unity-vector condition (2.24) by adding stabilizing term to the quaternion dynamics (2.16):

$$\begin{bmatrix} \dot{q}_0^{EB} \\ \dot{q}_1^{EB} \\ \dot{q}_2^{EB} \\ \dot{q}_3^{EB} \end{bmatrix} = \frac{1}{2} \begin{bmatrix} 0 & -\left(p_K^{EB}\right)_B & -\left(q_K^{EB}\right)_B & -\left(r_K^{EB}\right)_B \\ \left(p_K^{EB}\right)_B & 0 & \left(r_K^{EB}\right)_B & -\left(q_K^{EB}\right)_B \\ \left(q_K^{EB}\right)_B & -\left(r_K^{EB}\right)_B & 0 & \left(p_K^{EB}\right)_B \\ \left(r_K^{EB}\right)_B & \left(q_K^{EB}\right)_B & -\left(p_K^{EB}\right)_B & 0 \end{bmatrix} \begin{bmatrix} q_0^{EB} \\ q_1^{EB} \\ q_2^{EB} \\ q_3^{EB} \end{bmatrix} + \frac{1}{2}\lambda \begin{bmatrix} q_0^{EB} \\ q_1^{EB} \\ q_2^{EB} \\ q_3^{EB} \end{bmatrix} \tag{2.25}$$

The gain

$$\lambda = 1 - \left(q_0^2 + q_1^2 + q_2^2 + q_3^2\right) \tag{2.26}$$

of the quaternion vector $\boldsymbol{q}^{EB}$ describes its distance (*orthonormality error*) to the desired normed value (2.24) [64].

2.3 Forces and Moments

For the purpose of deriving the translational (2.4) and rotational dynamics (2.11) a general description of the forces $\boldsymbol{F}_T$ and moments $\boldsymbol{M}_T^G$ acting on the missile body is used. By considering the missile to be fully burned out in endgame configuration, the total forces and moments are composed by the aerodynamic and gravity parts:

$$\begin{aligned} \boldsymbol{F}_T &= \boldsymbol{F}_A + \boldsymbol{F}_G \\ \boldsymbol{M}_T^G &= \boldsymbol{M}_A^G \end{aligned} \tag{2.27}$$

The gravity part of the total moment $\boldsymbol{M}_T^G$ vanishes due to the choice of cog as reference point for applying the laws of motion (see sections 2.2.2.1 and 2.2.2.2).

2.3.1 Gravity Force

Within an endgame scenario of a SAM an attitude range is covered by the missile that makes it feasible to consider the earth as the only celestial body with a significant impact on the missile dynamics. For the sake of reducing complexity, the gravitational field is assumed to be constant and homogeneous. Therefore, it is assumed to be directed perpendicular with respect to the earth surface and its acceleration g is constant over the entire altitude range. In order to account for both translational dynamic descriptions ((2.4) and (2.6)) the gravitational force vector is depicted in the body-fixed frame

$$\left(\boldsymbol{F}_G\right)_B = \mathbf{M}_{BO} \begin{bmatrix} 0 \\ 0 \\ m \cdot g \end{bmatrix}_O = m \cdot g \begin{bmatrix} 2\left(q_1 q_3 - q_0 q_2\right) \\ 2\left(q_2 q_3 + q_0 q_1\right) \\ q_0^2 - q_1^2 - q_2^2 + q_3^2 \end{bmatrix}_B \tag{2.28}$$

and in the rotated kinematic frame ($\bar{K}$-frame)

$$\left(\boldsymbol{F}_G\right)_{\bar{K}} = \mathbf{M}_{\bar{K}O} \begin{bmatrix} 0 \\ 0 \\ m \cdot g \end{bmatrix}_O = m \cdot g \begin{bmatrix} -\sin\gamma_K \\ \cos\gamma_K \sin\mu_K \\ \cos\gamma_K \cos\mu_K \end{bmatrix}_{\bar{K}}. \tag{2.29}$$

The transformation $\mathbf{M}_{BO}$ is the transpose of (2.22) and $\mathbf{M}_{\bar{K}O}$ (see appendix A.1) is defined by

$$\mathbf{M}_{\bar{K}O} = \mathbf{M}_{\bar{K}K}\mathbf{M}_{KO} \tag{2.30}$$

where

$$\mathbf{M}_{\bar{K}K} = \begin{bmatrix} 1 & 0 & 0 \\ 0 & \cos\mu_K & \sin\mu_K \\ 0 & -\sin\mu_K & \cos\mu_K \end{bmatrix} \tag{2.31}$$

and

$$\mathbf{M}_{KO} = \begin{bmatrix} \cos\chi_K\cos\gamma_K & \sin\chi_K\cos\gamma_K & -\sin\gamma_K \\ -\sin\gamma_K & \cos\chi_K & 0 \\ \cos\chi_K\sin\gamma_K & \sin\chi_K\sin\gamma_K & \cos\gamma_K \end{bmatrix} \tag{2.32}$$

describes the rotation of the K-frame around the x_K-axis and the transformation from O- to K-system, respectively.

2.3.2 Aerodynamic Forces and Moments

Besides the mass distribution and geometry data, the aerodynamic forces and moments constitute the main distinctive feature in simulation of a certain aircraft type. In missile simulation the aerodynamic data set reflects the characteristic in dynamics over the flight envelope. The herein used aerodynamic data set is solely generic and any similarities to existing SAM configurations are purely coincidental.

Within this chapter the aerodynamic data set is introduced by giving the respective coordinate frames, the dependencies of the missile states, and the application rule of the force and moment coefficients. The data set is calculated with the semi-empiric missile aerodynamics prediction software *MISL3* ®. This tool outputs the aerodynamic data set in tabular form given in the body-fixed frame. Therefore, the aerodynamic forces

$$\left(\boldsymbol{F}_A^G\right)_B = \begin{bmatrix} F_{x,A}^G \\ F_{y,A}^G \\ F_{z,A}^G \end{bmatrix}_B = \bar{q}S_{ref} \begin{bmatrix} C_x\left(\vartheta_K, M, \xi, \eta, \zeta\right) \\ C_y\left(\alpha_K, \beta_K, M, \xi, \zeta\right) \\ C_z\left(\alpha_K, \beta_K, M, \xi, \eta\right) \end{bmatrix}_B \tag{2.33}$$

and moments

$$\left(\boldsymbol{M}_A^G\right)_B = \begin{bmatrix} L_A^G \\ M_A^G \\ N_A^G \end{bmatrix}_B = \bar{q}S_{ref}l_{ref} \begin{bmatrix} C_l\left(\alpha_K, \beta_K, M, \xi, \eta, \zeta\right) \\ C_m\left(\alpha_K, \beta_K, M, \xi, \eta\right) \\ C_n\left(\alpha_K, \beta_K, M, \xi, \zeta\right) \end{bmatrix}_B \tag{2.34}$$

are depicted in the body-fixed coordinate frame (B-frame) and the notation is in conformity with [1]. $\bar{q}$, l_{ref}, and S_{ref} denote the dynamic pressure, reference length (diameter), and aerodynamic reference area, respectively. The composition of the respective force and moment coefficients $C_i(.)$, $i = x, y, z$ is described by the application rule. This application rule depends on the software program and the underlying post processing algorithm. For the purpose of modeling and control design the break down of the force and moment coefficients is obtained in an additive way in accordance with their physical origin. Therefore, the force coefficients

$$\begin{bmatrix} C_x \\ C_y \\ C_z \end{bmatrix}_B = \begin{bmatrix} C_{x,0}\left(\alpha, \beta, M\right) + C_{x,\xi}\left(\vartheta, M, \xi, \eta, \zeta\right) \\ C_{y,0}\left(\alpha, \beta, M\right) + C_{y,\zeta}\left(\alpha, \beta, M, \xi, \zeta\right) \\ C_{z,0}\left(\alpha, \beta, M\right) + C_{z,\eta}\left(\alpha, \beta, M, \xi, \eta\right) \end{bmatrix}_B \tag{2.35}$$

consist of the coefficients acting on the plain body $C_{i,0}$ and the ones describing the impact of the control surfaces C_{i,u_j}. $\boldsymbol{u} = \begin{bmatrix}\xi & \eta & \zeta\end{bmatrix}^T$ specifies the equivalent aerodynamic fin deflections. A detailed description of the aerodynamic controls and their relation to the virtual control variables ξ, η, and ζ is presented in section 2.5.1. Considering the moment coefficients

$$\begin{bmatrix} C_l \\ C_m \\ C_n \end{bmatrix}_B = \begin{bmatrix} C_{l,0}(\alpha,\beta,M) + \frac{\left(p_K^{EB}\right)_B l_{ref}}{2\left(V_K^G\right)_B^E} C_{l,p}(\alpha,\beta,M) + C_{l,\xi}(\alpha,\beta,M,\xi,\eta,\zeta) \\ C_{m,0}(\alpha,\beta,M) + \frac{\left(q_K^{EB}\right)_B l_{ref}}{2\left(V_K^G\right)_B^E} C_{m,q}(\alpha,\beta,M) + C_{m,\eta}(\alpha,\beta,M,\xi,\eta) \\ C_{n,0}(\alpha,\beta,M) + \frac{\left(r_K^{EB}\right)_B l_{ref}}{2\left(V_K^G\right)_B^E} C_{n,r}(\alpha,\beta,M) + C_{n,\zeta}(\alpha,\beta,M,\xi,\zeta) \end{bmatrix}_B \tag{2.36}$$

the damping coefficients C_{i,ω_j} constitute an additional physical effect compared to (2.35). For the purpose of a better readability some indexes are dropped in (2.35) and (2.36). All aerodynamic coefficients $(C_i)_B$ are smooth functions in their respective function arguments. The nonlinear, non-affine dependency of aerodynamic moments (and forces) on the equivalent aerodynamic controls u_i in (2.36) (and (2.35)) is a common property of highly nonlinear aerial vehicle aerodynamics. A detailed representation of the generic aerodynamic data set can be found in appendix B.1.

Remark: In aircraft modeling it is very common to describe the aerodynamic forces in the aerodynamic coordinate frame, which coincides in case of no wind with the $\bar{K}$-frame. The definition of the aerodynamic forces in the $\bar{K}$-frame

$$\left(\boldsymbol{F}_A^G\right)_{\bar{K}} = \begin{bmatrix} F_{x,A}^G \\ F_{y,A}^G \\ F_{z,A}^G \end{bmatrix}_{\bar{K}} = \begin{bmatrix} -D \\ Q \\ -L \end{bmatrix}_{\bar{K}} = \bar{q} \cdot S_{ref} \cdot \begin{bmatrix} -C_D \\ C_Q \\ -C_L \end{bmatrix}_{\bar{K}} \tag{2.37}$$

is useful for describing the translational dynamics via the alternative state representation (2.6). D, Q, and L are denoted as drag, lift, and cross-stream force, respectively. The negative signs account for the anti-parallel directions of drag and force with respect to the $x_{\bar{K}}$- and $z_{\bar{K}}$-axis [1, 68]. In case of no wind, the lift L and cross-stream force Q are perpendicular to the free stream airflow (described by $\left(\boldsymbol{V}_K^G\right)^E$). The drag D is anti-parallel to it. Based on this definition the load factor

$$(\boldsymbol{n})_{\bar{K}} = \begin{bmatrix} n_x \\ n_y \\ n_z \end{bmatrix}_{\bar{K}} = \frac{1}{mg} \begin{bmatrix} D \\ Q \\ L \end{bmatrix}_{\bar{K}} \tag{2.38}$$

represents a measure for the stress on the aircraft's body due to the aerodynamic forces. The dimensionless load factor $(\boldsymbol{n})_{\bar{K}}$ is defined by the ratio of the respective aerodynamic force (D, Q, and L) and the weight ($m \cdot g$) of the aircraft.

The aerodynamic data set determines the missile's physical capabilities and limitations. With the given geometry and mass configuration, *MISL3* outputs feasible aerodynamic data for a total incidence angle of $\vartheta_{A,max} = 25°$. Under consideration of the given scenario, the traveling speed and altitude ranges between $M = 0.9 - 4.4$ and $h = 0 - 11km$, respectively. The FGS-X-03's body is assumed to withstand a total acceleration, which is below $\| \left(\boldsymbol{a}^G\right)_B^{II} \| \leq a_{max} = 50g$.

2.4 Model Uncertainties

Control laws, no matter in which field, require a mathematical representation (design model) of the considered plant. The more accurately the design model represents the plant, the smaller is the divergence between the plant's closed-loop behavior and the desired behavior set up via a model based control design approach. The accuracy of the design model increases with the efforts in the parameter identification campaign.

In aerospace applications the divergences between plant and design model can be categorized in geometric/mass, aerodynamic, and measurement/estimation uncertainties. Since the considered missile covers large ranges in altitude, velocity, and total incidence angle (see section 2.3.2), especially the aerodynamic data set contains a source of extensive modeling errors compared to military and civil aircraft applications.

Due to the fact that missiles like the FGS-X-03 have a reduced sensor setup, online state estimation is necessary for providing the algorithms with certain state information. The reduced sensor equipment is a consequence of the lack of space and to preserve the missile's aerodynamic characteristic. Since the estimation process depends on model information, the quality of state estimation correlates with the accuracy of the design model. The above mentioned divergences between design model and plant lead to estimation errors that are propagated (by the estimation algorithm) to the control algorithms. Measurement errors, geometric, and mass variations complete the uncertainty spectrum for the considered missile system. In order to evaluate the herein proposed control design towards robustifying capabilities, the uncertainties need to be considered in their full characteristic.

According to [69], the term *uncertainty* defines a potential lack of knowledge by modeling a certain plant. This vagueness caused by partial information of the respective plant is incorporated within the herein introduced missile model by using normal or Gaussian probability distributions for the missile parameters.

2.4.1 Aerodynamic Uncertainties

In common literature the aerodynamic data set is assumed to exhibit uncertainties that remain constant over the entire flight envelope [20, 36, 40, 62, 70]. In reality, the accuracy of the aerodynamic identification process depends on the considered flight envelope region. Therefore, an aerodynamic uncertainty model is developed displaying the state-dependent confidence level of the aerodynamic data set. Based on this approach the fidelity of the nonlinear missile model is further increased and the control task of stabilizing and robustifying the closed-loop system becomes more challenging compared to conventional uncertainty models.

The aerodynamic uncertainties are modeled in a multiplicative way. Therefore, the aerodynamic coefficient used in the plant model is calculated based on the nominal force and moment coefficients $C_{i,j,nom}$ (see appendix B.1) by the following relationship

$$C_{i,j} = (1 + \Delta C_{i,j}(\boldsymbol{x})) \cdot C_{i,j,nom} + \Delta C_{i,j,off}. \tag{2.39}$$

In order to distinguish between the nominal aerodynamics and the one used in the plant model, the undisturbed data is labeled within this section as $C_{i,j,nom}$. The aerodynamics which is subject to uncertainty is denoted as $C_{i,j}$. All terms $C_{i,j}$ utilized in the rigid body EOM (section 2.2) are calculated by using the multiplicative uncertainty $\Delta C_{i,j}$ and the constant offset $\Delta C_{i,j,off}$. In common aircraft and missile modeling the aerodynamic uncertainties is assumed to be constant [24, 37, 40, 70, 71] or

is accumulated with other uncertainties [62]. Thereafter, the uncertainty of the aerodynamic coefficient is partitioned in an constant offset $\Delta C_{i,j,off}$ and a state dependent multiplicative scaling factor $\Delta C_{i,j}(\boldsymbol{x})$. It is assumed that the main driver of the aerodynamic uncertainty are the total incidence angle and the Mach number, $\boldsymbol{x} = \begin{bmatrix}\vartheta_K & M\end{bmatrix}^T$. Therefore, the divergence of the aerodynamic data set varies with those values and the choice of the constant offset $\Delta C_{i,j,off}$.

2.4.1.1 Multiplicative Uncertainty $\Delta C_{i,j}$

A variation of the scaling factor $\Delta C_{i,j}(\boldsymbol{x})$ dependent on the states ϑ_K and M is modeled by using radial basis function (RBF) networks [72]. A RBF is a scalar function with the distance $r = \|\boldsymbol{x} - \boldsymbol{x}_c\|$ of a point $\boldsymbol{x}$ to a center $\boldsymbol{x}_c$ as argument, $\kappa(r) = \kappa(\|\boldsymbol{x} - \boldsymbol{x}_c\|)$. The RBFs considered herein are of the form

$$\kappa(r) = \exp\left(-\frac{r^2}{\tau}\right). \tag{2.40}$$

This family of curves return a scalar value, which ranges between $\kappa \in [0, 1]$. The RBF $\kappa(r)$ has its maximum value 1 at the center $\boldsymbol{x}_c$ and is monotonically decreasing with increasing distance to the respective center (see fig. 2.2). The parameter $\tau > 0$ regulates the widths of the Gaussian function (2.40).

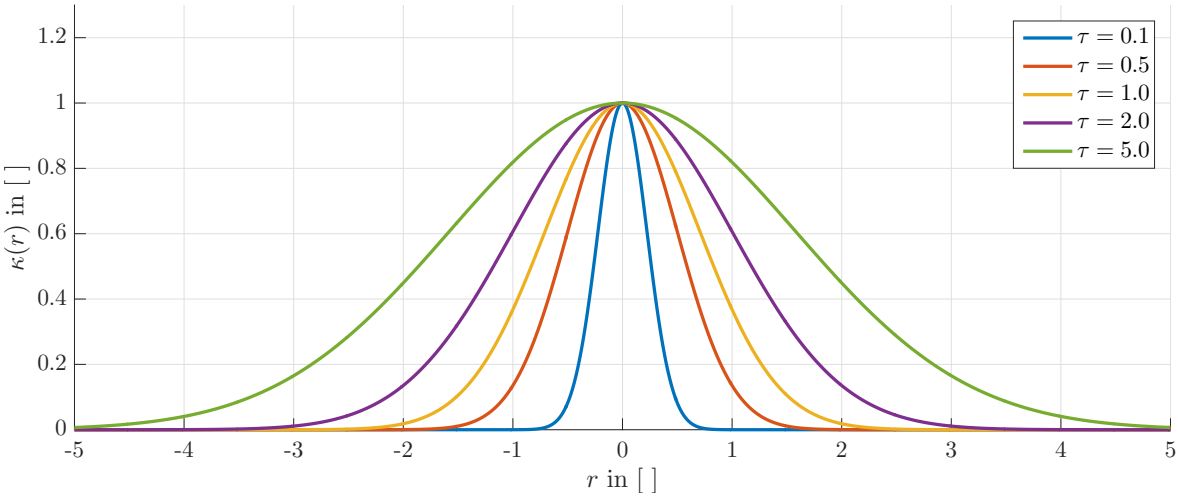

Figure 2.2: Illustration of the RBF candidate (2.40) for different parameters τ.

A RBF network consists of N multiple functions $\kappa(r)$, which are distributed throughout the considered state space around the centers $\boldsymbol{x}_{c,k}$, $k = 1, \ldots, N$ (see fig. 2.4a). In order to cover the respective region with RBFs, a proper choice of the centers $\boldsymbol{x}_{c,k}$ and the parameter τ is crucial. In fig. 2.3 an equidistant distribution of the centers along the state variables is chosen with two different scaling factors τ. An increase in the parameter τ leads to and increased width of the RBFs and therefore a better coverage (overlapping).

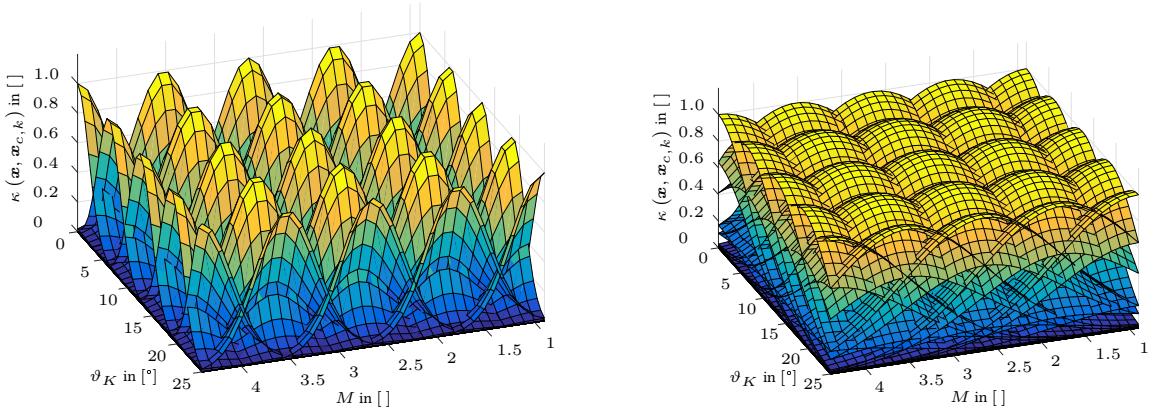

(a) RBFs $\kappa(\boldsymbol{x}, \boldsymbol{x}_{c,k})$ plotted versus ϑ_K and M for $\tau = 0.25$.

(b) RBFs $\kappa(\boldsymbol{x}, \boldsymbol{x}_{c,k})$ plotted versus ϑ_K and M for $\tau = 0.75$.

Figure 2.3: RBFs with different scaling parameters τ.

Based on the above introduced RBFs, the multiplicative uncertainty function

$$\Delta C_{i,j}(\boldsymbol{x}) = k(\boldsymbol{x}) \cdot \sum_{k=1}^{N} \lambda_{i,j,k} \kappa\left(\|\boldsymbol{x} - \boldsymbol{x}_{c,k}\|\right) \tag{2.41}$$

is assembled by weighting each single RBF with the scalar $\lambda_{i,j,k}$ across the N centers $\boldsymbol{x}_{c,k}$. The factor $k(\boldsymbol{x})$ enables a scaling of the uncertainty dependent on the considered missile state.

Since the RBF has its maximum ($\max(\kappa(\boldsymbol{x}_{c,k}, \boldsymbol{x}_{c,k})) = 1$) at the center $\boldsymbol{x}_{c,k}$ and is monotonic decreasing, $\lambda_{i,j,k}$ determines the amplitude of each single neuron. The RBF determines in each successive term (neuron) $\lambda_{i,j,k}\kappa(\|\boldsymbol{x} - \boldsymbol{x}_{c,k}\|)$, depending on the distance $r = \|\boldsymbol{x} - \boldsymbol{x}_{c,k}\|$ of the current state $\boldsymbol{x}$ to the center $\boldsymbol{x}_{c,k}$, the contribution to the overall function value $\Delta C_{i,j}(\boldsymbol{x})$. Therefore, $\kappa(r)$ is denoted as activation function within this context since it determines the *activity* (influence) of each single neuron in the sum of (2.41).

As already mentioned above, the deviation between the nominal aerodynamic coefficient $C_{i,j,nom}$ and the coefficient $C_{i,j}$ at a certain state $\boldsymbol{x}$ is assumed to follow a normal (or Gaussian) distribution [73]. By using the uncertainty modeling approach depicted in (2.41), the weighting factors $\lambda_{i,j,k}$ provide the possibility to assign to each neuron $\lambda_{i,j,k}\kappa(\|\boldsymbol{x} - \boldsymbol{x}_{c,k}\|)$ a defined uncertainty parametrization. Therefore, the amplitude

$$\lambda_{i,j,k} \sim \mathcal{N}\left(\mu_{i,j}, \sigma_{i,j}^2\right) \tag{2.42}$$

of the activation functions κ is selected as a normal distributed value determined by its expected value $\mu_{i,j}$ and its standard deviation $\sigma_{i,j}$. Those two values are determine the uncertainty characteristic a specific aerodynamic coefficient $C_{i,j}$. According to common nomenclature [74], $\mathcal{N}$ labels a random variable (here: $\lambda_{i,j,k}$) that is normally distributed. By using these normally distributed weights $\lambda_{i,j,k}$, the neuron amplitudes of the RBF network $\Delta C_{i,j}$ (2.41) follow a normal probability distribution. The maximum amplitude of each neuron and therefore the maximum multiplicative uncertainty $\Delta C_{i,j}$ is defined via three times the standard deviation 3σ. Since each category of aerodynamic coefficient $C_{i,j}$ exhibits a certain maximum uncertainty threshold ($3\sigma_i$), a categorization according to their respective variance is shown at the end of this section in table 2.1.

Remark: Since 99.73% of the values obtained from a normal distribution lie within the interval $[\mu - 3\sigma, \mu + 3\sigma]$, the standard deviation 3σ is used throughout this thesis to determine the approximate

bounds of the normal distributed multiplicative uncertainties $\Delta C_{i,j}$. With the proposed approach a probability of 0.27% ($100\% - 99.73\%$) remains that one of the neuron amplitudes $\lambda_{i,j,k}$ is not within the given interval $[\mu - 3\sigma, \mu + 3\sigma]$. This desired effect reflects the natural variance of the aerodynamics identification process in reality.

Figure 2.4 depicts a generic example of the uncertainty modeling $\Delta C_{i,j}$ to illustrate the aforementioned theory. Figure 2.4a shows the activation functions κ uniformly distributed along state space determined in this example by ϑ_K and M. The scaling of the activation functions (neurons) with the normally distributed weights $\lambda_{i,j,k}$ are presented in fig. 2.4b. Combining those neurons over the entire state space according to (2.41) results in the generic uncertainty function $\Delta C_{i,j}$.

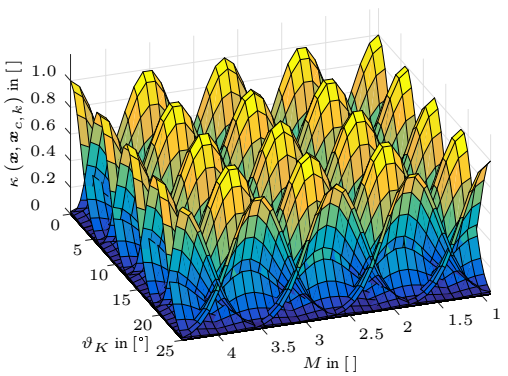

(a) Gaussian activation functions $\kappa(\boldsymbol{x}, \boldsymbol{x}_{c,k})$ plotted versus ϑ_K and M for $\tau = 0.25$.

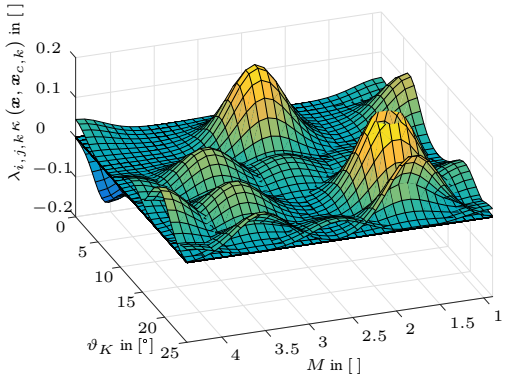

(b) Neurons $\lambda_{i,j,k}\kappa(\boldsymbol{x}, \boldsymbol{x}_{c,k})$ of RBF Network plotted versus ϑ_K and M.

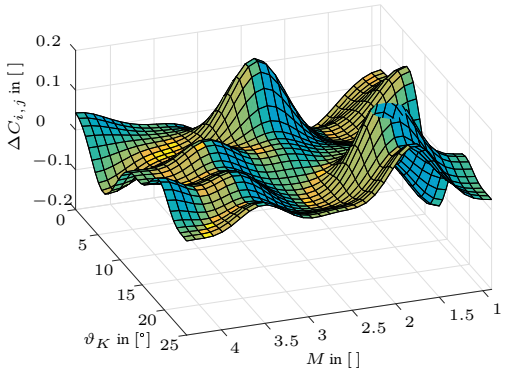

(c) Generic aerodynamic uncertainty $\Delta C_{i,j}$ as a function of ϑ_K and M.

Figure 2.4: Activation Functions, Neurons, and the resulting generic multiplicative uncertainty $\Delta C_{i,j}$ plotted versus ϑ_K and M with 25 centers $\boldsymbol{x}_{c,k}$. The approximate bounds are chosen as $3\sigma = 0.2$.

In the generic example depicted in fig. 2.4 one standard deviation σ (to assign the neuron amplitudes $\lambda_{i,j,k}$) is used for the entire state space. It is reasonable to assume that the accuracy of the aerodynamics identification process (e.g. wind tunnel, Computational Fluid Dynamics (CFD) methods) increases with reduced incidence angle ϑ_K. The impact of the airspeed M on the aerodynamic uncertainty is assumed to exhibit constant probability distribution across the entire Mach range. Therefore, for the purpose of the investigations within this thesis ϑ_K is selected as the variable scaling the uncertainty via $k(\vartheta_K)$ in (2.41).

By using the uncertainty model based on a RBF network (2.41) it is possible to account for different uncertainty levels within certain state space regions. Herein two levels of uncertainty are

considered, which are triggered by ϑ_K. Besides the equally distributed neurons comprising of the amplitudes and parametrized RBFs, the uncertainty is reduced for $\vartheta_K < \vartheta_{K,up}$ in accordance to the following pattern:

$$k\left(\vartheta_A\right) = \begin{cases} k_{low} & \text{if } 0 \leq \vartheta_K \leq \vartheta_{K,low} \\ \frac{1-k_{low}}{\vartheta_{K,up}-\vartheta_{K,low}} & \text{if } \vartheta_{K,low} < \vartheta_K < \vartheta_{K,up} \\ 1 & \text{if } \vartheta_{K,up} \leq \vartheta_{K,max} \end{cases} \tag{2.43}$$

The calculation of k, proposed in (2.43), is illustrated in fig. 2.5. In order to avoid an abrupt parameter change from k_{low} to $k = 1$ a transition zone is introduced, which leads to a smooth change from the distinct values of k.

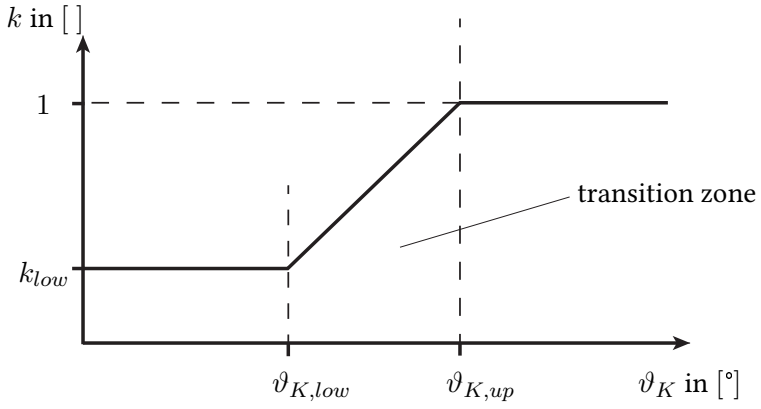

Figure 2.5: Illustration of the dependence of k on ϑ_K (2.43).

Figure 2.6 shows the multiplicative uncertainty $\Delta C_{x,0}$ in order to demonstrate the effect of the scaling factor k. The magenta tube in fig. 2.6a and fig. 2.6b illustrates the ϑ_K-region where the uncertainty is reduced according to (2.43). Considering fig. 2.6c, showing $\Delta C_{x,0}$ versus α_K and M, the region described in (2.43) is illustrated as a corridor in the variable α_K. In case of the fourth plot the value β_K leads to an incidence angle ϑ_K (2.9), which is outside of the chosen scaling region in this example ($\vartheta_K < 11°$).

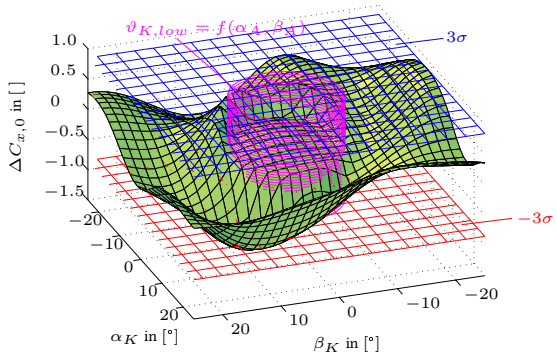

(a) Aerodynamic uncertainty $\Delta C_{x,0}$ plotted versus α_K and β_K at $M = 2.65$.

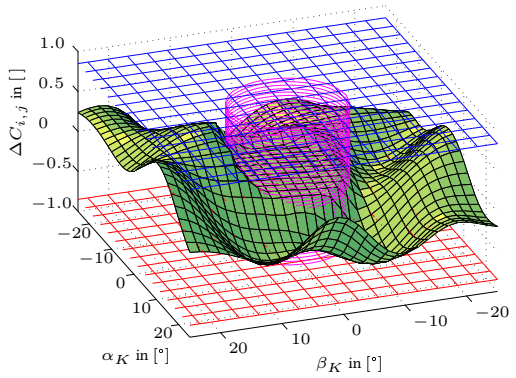

(b) Aerodynamic uncertainty $\Delta C_{x,0}$ plotted versus α_K and β_K at $M = 4.4$.

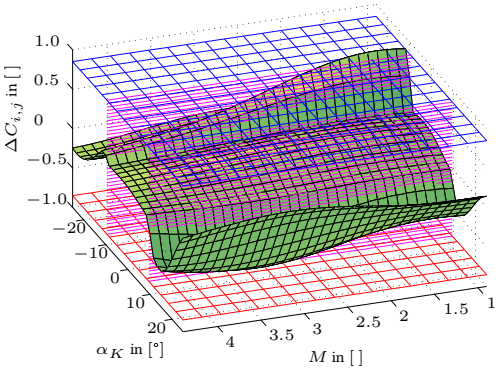

(c) Aerodynamic uncertainty $\Delta C_{x,0}$ plotted versus α_K and M at $\beta_K = -0.81°$.

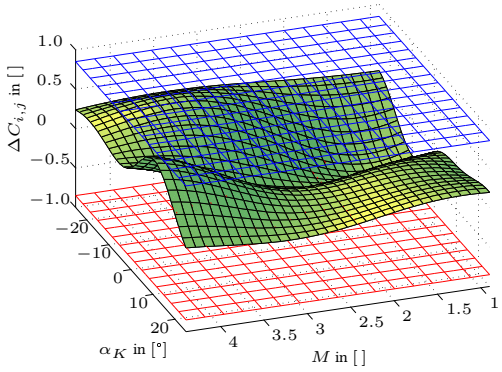

(d) Aerodynamic uncertainty $\Delta C_{x,0}$ plotted versus α_K and M at $\beta_K = 25°$.

Figure 2.6: Plots of the multiplicative uncertainty $\Delta C_{x,0}$ (2.41) versus the state variables α_K, β_K, and M with $k_{low} = 0.15$, $\vartheta_{K,low} = 9°$, and $\vartheta_{K,up} = 11°$.

2.4.1.2 Offset Uncertainty $\Delta C_{i,j,off}$

Besides the state-dependent multiplicative uncertainty $\Delta C_{i,j}$, the offset $\Delta C_{i,j,off}$ is selected as a constant uncertainty over the entire state space region. Since the offset $\Delta C_{i,j,off}$ is an absolute value, it is calculated based on the percentage of the nominal aerodynamics evaluated at $\alpha_K, \beta_K = 0°$, $M = 2.5$, and $u_i = 0°$:

$$\Delta C_{i,j,off} = k_{i,j,off} \cdot C_{i,j} \left(\alpha_K = 0°, \beta_K = 0°, M = 2.5, u_i = 0°\right) \tag{2.44}$$

Therefore, the offset for coefficients exhibiting a zero crossing in the variables α_K, β_K, or u_i vanish. This assumption is feasible since the post processing of the aerodynamic identification process accounts for the characteristics of coefficients. E.g.: $C_{y,0}$ and $C_{z,0}$ considered a certain Mach numbers M reflects point symmetric characteristics with respect to the aerodynamic angles α_K and β_K. Thus, a possible divergence in the origin of the variables α_K and β_K would be compensated within the post processing of the aerodynamic data set.

The parameter $k_{i,j,off}$, which regulates the offset (2.44) is assumed to be normally distributed in the same way like (2.42). Due to its origin, it is assumed that the identification of the respective offset uncertainty $\Delta C_{i,j,off}$ can be estimated with increased accuracy compared to the multiplicative uncertainty $\Delta C_{i,j,off}$. This is reflected by smaller standard deviations 3σ of $k_{i,j,off}$ compared to $\lambda_{i,j,k}$.

All herein considered aerodynamic uncertainties are summarized in table 2.1.

Coefficient	3σ **of** $\lambda_{i,j,k}$	3σ **of** $k_{i,j,off}$
$C_{x,0}$	0.85	0.5
$C_{y,0}$, $C_{z,0}$	0.75	-
$C_{x,\xi}$	0.85	0.5
$C_{y,\zeta}$, $C_{z,\eta}$	0.75	0.4
$C_{l,0}$	0.95	-
$C_{m,0}$, $C_{n,0}$	0.85	-
$C_{l,p}$	0.95	0.5
$C_{m,q}$, $C_{n,r}$	0.85	0.4
$C_{l,\xi}$	0.95	0.5
$C_{m,\eta}$, $C_{n,\zeta}$	0.85	0.4

Table 2.1: Characteristic uncertainty parameters of the aerodynamic coefficients.

2.4.2 Geometric and Mass Uncertainties

Besides the aerodynamic uncertainties presented in section 2.4.1, the missile's geometric and mass parameters are also subject to inaccuracies within the identification process. Since the FGS-X-03 is assumed to be burned out by the beginning of the endgame scenario, no changes in mass and mass distribution is considered during flight. Therefore, the geometry and mass parameters remain constant during the considered scenario. For the purpose of robustness investigations of different autopilot designs, the mass m and moment of inertia $\left(I_{ii}^{G}\right)_{BB}$ of the burned out missile are considered to diverge in a multiplicative way from the nominal values. Considering the nominal parameter p_{nom}, the design model parameter p results as

$$p = p_{nom} \cdot (1 + \Delta p) \tag{2.45}$$

with Δp being the uncertainty. This multiplicative uncertainty is modeled by using the normally distributed factors depicted in table 2.2.

Uncertainty Parameter	3σ **Range**
$\Delta \left(I_{ii}^{G}\right)_{BB}$	0.1
Δm	0.01

Table 2.2: Geometric and mass parameter uncertainties.

2.5 Missile Subsystems

The task of the Flight Control System (FCS) is to command desired fin deflections, in order to follow a certain trajectory computed by the guidance law (see fig. 1.3). The command following is realized within the FCS by comparing the reference trajectory provided by the guidance unit with measurements of the missile's current state. Therefore, in addition to the input of the guidance law the flight control unit receives data from the measurement and estimation unit and the fin deflection of the actuation unit. Considering the context of autopilot investigations, this chapter describes the main characteristics of the missile's upstream and adjacent subsystems.

2.5.1 Actuator System

The herein considered missile is steered in STT mode. For this mode, two cruciform orientations of the missile body are possible, which are determined by the attitude of the fins: in the $+$-orientation the axis of the fins are aligned with the y_B- and z_B-axis of the body fixed frame; the x-orientated missile has the fin arrangement rotated at $45°$ with respect to the body fixed frame [1].

The aerodynamic data set (see appendix B.1) and therefore the missile's rigid body EOMs (section 2.2.2) are obtained by utilizing the aerodynamic equivalent controls: aileron ξ, elevator η, and rudder ζ. The usage of those aerodynamic equivalent controls is due to the fact that the virtual control variables ξ, η, and ζ can be directly assigned to the missile's roll-, pitch-, and yaw-axis, respectively. This aircraft-orientated approach is also very common in missile modeling and missile flight control design [1, 24, 37, 40, 64]. As mentioned above the missile's physical control surfaces consists of four fins $\boldsymbol{u}_\delta = \begin{bmatrix}\delta_1 & \delta_2 & \delta_3 & \delta_4\end{bmatrix}^T$, which are attached to the rear of the missile body (see fig. 2.1). The angular position of each fin can be controlled independently. The numbering of the single fins is conducted clockwise starting with the upper left one as shown in fig. 2.7. Based on the aerodynamic equivalent controls $\boldsymbol{u} = \begin{bmatrix}\xi & \eta & \zeta\end{bmatrix}^T$ the fin deflections δ_i result via the mapping rule

$$\begin{bmatrix}\delta_1\\ \delta_2\\ \delta_3\\ \delta_4\end{bmatrix} = \underbrace{\begin{bmatrix}1 & 1 & 1\\ 1 & -1 & 1\\ 1 & -1 & -1\\ 1 & 1 & -1\end{bmatrix}}_{=\boldsymbol{T}_\delta} \begin{bmatrix}\xi\\ \eta\\ \zeta\end{bmatrix}. \tag{2.46}$$

The aerodynamic equivalent controls $\boldsymbol{u}$ on the basis of the fin deflections δ_i are obtained according to the pseudo-inverse of the (2.46):

$$\begin{bmatrix}\xi\\ \eta\\ \zeta\end{bmatrix} = \underbrace{\frac{1}{4}\begin{bmatrix}1 & 1 & 1 & 1\\ 1 & -1 & -1 & 1\\ 1 & 1 & -1 & -1\end{bmatrix}}_{=\boldsymbol{T}_\delta^{-1}} \begin{bmatrix}\delta_1\\ \delta_2\\ \delta_3\\ \delta_4\end{bmatrix} \tag{2.47}$$

Due to the unsymmetrical mapping of (2.46) and their inverse (2.47), a fourth control variable of $\boldsymbol{u}$ is possible. This fourth conceivable combination produces only drag. It is commonly denoted as *speedbrake* κ [64]. In this study the speedbrake is assumed to be zero. Figure 2.7 depicts an schematic view of the three different fin configurations, which lead to a positive aileron ξ, elevator η, and rudder ζ command.

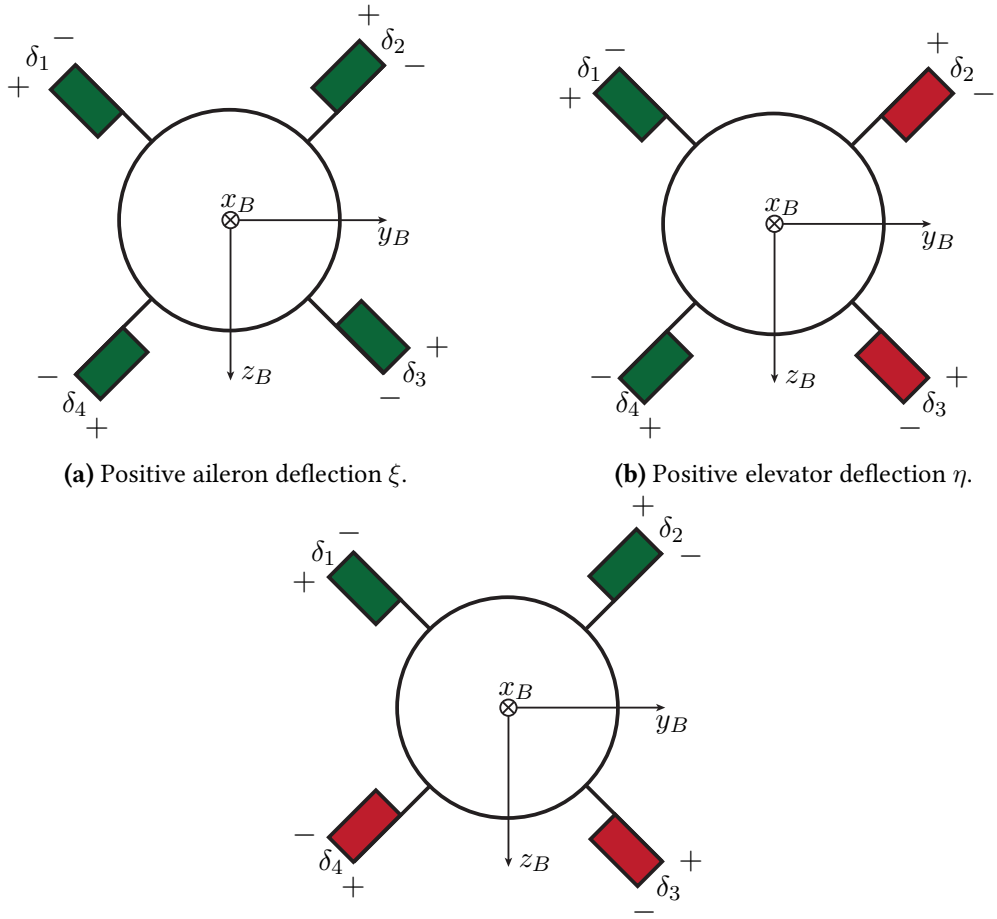

(a) Positive aileron deflection ξ.

(b) Positive elevator deflection η.

(c) Positive rudder deflection ζ.

Figure 2.7: Fin configurations for aerodynamic equivalent aileron, elevator, and rudder deflections (missile view from rear). Positive fin δ_i deflection is marked with green color, a negative fin deflection can be identified by a red labeled fin.

In real missile systems each fin is actuated by an electric actuation unit, which deflects the fin to the desired angle $\delta_{i,c}$. In order to account for the dynamics and the constraints of the fin motors within the simulation model, each fin is modeled as a second order dynamics according to fig. 2.8. Besides the introduced delay defined by the bandwidth ω_{fin} and damping ζ_{fin}, the actuator performance is additionally limited by deflection δ_{max}, deflection rate $\dot{\delta}_{max}$, and deflection acceleration constraints $\ddot{\delta}_{max}$ (see table 2.3). Since all fins are equivalent, each fin section exhibits the same dynamical characteristics.

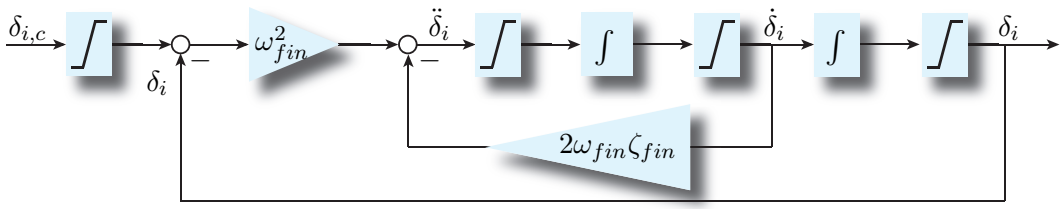

Figure 2.8: Block diagram of second order fin dynamics.

Taking the deflection limitation $|\delta_i| \leq \delta_{max}$ and the fin mapping from (2.47) into account, the sum of the equivalent fin angles absolute values results as $|\xi| + |\eta| + |\zeta| \leq \delta_{max}$.

Parameter	Value	Unit
δ_{max}	25	$[°]$
$\dot{\delta}_{max}$	10	$[\frac{rad}{s}]$
$\ddot{\delta}_{max}$	1500	$[\frac{rad}{s^2}]$
ω_{fin}	50	$[Hz]$
ζ_{fin}	0.7	$[/]$

Table 2.3: Parameters of the actuator subsystem.

2.5.2 Measurement Unit

In short-range tactical missiles like SAMs and surface-to-surface missiles (SSMs) the onboard sensor setup includes an accelerometer and gyroscope measuring the acceleration and body rates, respectively. Both units are incorporated within the Inertial Measurement Unit (IMU), which is assumed to be located along the missile's body axis at $(\boldsymbol{r})_B^{IMU} = \begin{bmatrix} x_{cog,IMU} & 0 & 0 \end{bmatrix}_B^T$. $x_{cog,IMU}$ describes the distance of the IMU with respect to the cog. Thus, the sensor unit (IMU) is aligned with the x_B-axis. Due to the short flight time and the disregard of position estimation based on acceleration signals, misalignment effects of the IMU are neglected within this thesis. Therefore, the axes of the sensor coordinate frame are parallel to the axes of the missile's body-fixed frame (B-frame). For the purpose of a facilitate sensor architecture (heat issues, cable size, etc.) the IMU in common SAM and SSM missile applications is placed between the missile's cog and cone. Besides assembling considerations, the location of the IMU plays also a decisive role by the choice of the autopilot control law.

Considering the assumptions made in section 2.2.2, the IMU processes the body rates $\left(\boldsymbol{\omega}_K^{EB}\right)_B$ (see (2.11)) and the specific aerodynamic force calculated at the IMU. Depending on the IMU location, the measured acceleration results to:

$$\left(\boldsymbol{a}^{IMU}\right)_B^{II} = \frac{1}{m}\left(\boldsymbol{F}_A^G\right)_B + \left(\dot{\boldsymbol{\omega}}^{IB}\right)_B^B \times (\boldsymbol{r})_B^{IMU} + \left(\boldsymbol{\omega}^{IB}\right)_B \times [\left(\boldsymbol{\omega}^{IB}\right)_B (\boldsymbol{r})_B^{IMU}]. \tag{2.48}$$

It is assumed that the acceleration due to gravity is compensated within the sensor unit. Thus, the specific force $\left(\boldsymbol{a}^{IMU}\right)_B^{II}$ calculated at the point $(\boldsymbol{r})_B^{IMU}$ includes the accelerations caused by aerodynamics, the Coriolis term, and the acceleration due to body rate acceleration.

Modeling an IMU can be a tedious task and lead to complex models. Since the IMU output $\boldsymbol{y}_m = \begin{bmatrix} \left(\boldsymbol{a}^{IMU}\right)_{B,m}^{II,T} & \left(\boldsymbol{\omega}_K^{EB}\right)_{B,m}^T \end{bmatrix}^T$ are used for control design, only sensor effects influencing the autopilot controlled missile system are considered. One major sensor behavior affecting the closed-loop stability of the autopilot system is caused by delay of the sensor signals $\boldsymbol{y}_m$. This transmission delay of the actual acceleration to the sensor output is modeled by a linear first order system with the time constant T_{IMU}. Besides the dynamics of the sensor unit, white noise $\boldsymbol{w}_i$ and bias $\boldsymbol{b}_i$ is added to the measurements $\boldsymbol{y}_m$.

$$\begin{bmatrix} \left(\boldsymbol{a}^{IMU}\right)_{B,m}^{II} \\ \left(\boldsymbol{\omega}_K^{EB}\right)_{B,m} \end{bmatrix} = \begin{bmatrix} \frac{1}{1+T_{IMU}s} & 0 \\ 0 & \frac{1}{1+T_{IMU}s} \end{bmatrix} \begin{bmatrix} \left(\boldsymbol{a}^{IMU}\right)_B^{II} \\ \left(\boldsymbol{\omega}_K^{EB}\right)_B \end{bmatrix} + \begin{bmatrix} \boldsymbol{w}_a(t) \\ \boldsymbol{w}_\omega(t) \end{bmatrix} + \begin{bmatrix} \boldsymbol{b}_a \\ \boldsymbol{b}_\omega \end{bmatrix} \tag{2.49}$$

The parametrization of the sensor unit is chosen based on realistic tactical grade IMUs comparable

to [75]. From this data sheet and by taking into account the calculation of the Angular Random Walk (ARW) [76], the relevant parameters are obtained to model a generic but realistic noise and bias characteristics. The parameters of the implemented IMU model are depicted in table 2.4.

Parameter	Value	Unit
T_{IMU}	$7.96 \cdot 10^{-4}$	$[s]$
$3\sigma\left(\boldsymbol{w}_{a,i}(t)\right)$	0.2060	$[\frac{m}{s^2}]$
$3\sigma\left(\boldsymbol{w}_{\omega,i}(t)\right)$	0.0019	$[\frac{rad}{s}]$
$3\sigma\left(\boldsymbol{b}_{a,i}(t)\right)$	0.981	$[\frac{m}{s^2}]$
$3\sigma\left(\boldsymbol{b}_{\omega,i}(t)\right)$	0.05	$[rad]$

Table 2.4: Parameters of IMU subsystem.

It is assumed that each of the four fins include a rotary encoder, which provides the deflection angle δ_i to the FCS. To obtain a high degree of realism deflection rates $\dot{\delta}_i$ and accelerations $\ddot{\delta}_i$ of the aerodynamic actuation surfaces are not passed to FGS-X-03 onboard algorithms.

2.5.3 Estimation Unit

In common SAM and air-to-air missile (AAM) systems, the acceleration and body rates measured by the IMU (see section 2.5.2) constitute the only measurable part of the missile's rigid body state vector (see section 2.2.2). Besides those measurements, which are provided with high accuracy, advanced missile autopilot designs demand additional entries of the missile's state vector. Those signals can be scheduling parameters like aerodynamic angles (e.g. α_K, β_K) or dynamic pressure $\bar{q}$, on which the in-flight selection of controller gains is based on [24]. In case of autopilot layout based on nonlinear or adaptive approaches extended state information - beyond the IMU measurement - constitute an essential prerequisite for the selected theory [37, 38, 40, 61]. Usually, information of the missile velocity, altitude, and aerodynamic angle information is required for applying modern control laws. Therefore, the dynamic pressure $\bar{q}$, the Mach number M, and both aerodynamic angles α_K, β_K are provided to the FCS. All those required but non-measurable signals and states need to be observed or estimated during flight based on IMU measurements and/or model data. Since measurements and especially model data are subject to disturbances and uncertainties the estimates diverge from their actual value. Herein this estimation error is modeled as a multiplicative (Mach number M and dynamic pressure $\bar{q}$) and additive constant uncertainty (aerodynamic angles α_K, β_K). Each uncertainty factor is normally distributed within a certain 3σ range (see table 2.5). An extensive model of the estimation (e.g. navigation) and observation process is not considered due to limited significance for the conducted investigations within this thesis. The uncertainties in table 2.5 are chosen based on the aerodynamic and measurement uncertainties introduced in section 2.5.2 and section 2.4.1.

State Variable	3σ Range	Unit
$\Delta\alpha_K, \beta_K$	± 2.5	$[^\circ]$
$\Delta\bar{q}$	0.05	$[-]$
ΔM	0.1	$[-]$

Table 2.5: Multiplicative and additive constant uncertainties of the estimated signals.

CHAPTER 3

Flight Dynamics Analysis of the FSD Generic Surface-to-Air Missile (FGS-X-03)

> All progress takes place outside the comfort zone.
>
> Michael John Bobak

The previously introduced numerical representation of the FGS-X-03 constitutes the basis for evaluating the developed autopilot architectures. Since the designed flight controller shall fully exploit the performance of the considered plant, a detailed knowledge of the plant's physical capabilities is required. Developing an autopilot without extensive knowledge of the plant's physical limitations and properties may result in a impaired closed-loop performance.

Usually, in aircraft performance analysis the maximum commendable magnitude of the control variables is determined by several state and input constraints. Common state constraints for aerial vehicles are the maximum angle of attack (AoA), the maximum acceleration the structure can withstand, or criteria considering the comfort of passengers and pilots in manned aircraft systems. Limited control surface deflection and thrust level are examples for aircraft input restrictions. The subset of all physically possible state and input combinations is denoted as *flight envelope*.

In addition to the maximum achievable flight envelope of the aerial vehicle, the dynamic performance analysis is the second main driver for the parametrization of the missile's autopilot. Those dynamic properties are described via the input/output characteristics between the respective state variables and the considered actuators. The dynamic closed-loop performance requirements such as transmission bandwidths and eigenmodes are derived based on the results of the dynamic performance analysis.

Dynamic properties and the missile's flight envelope are calculated based on the plant model described in chapter 2. The flight dynamic characteristics of the missile system are determined by the vehicle's parameter configuration (e.g. aerodynamics, mass properties, etc). Since those parameters are subject to large variations (see section 2.4), the flight dynamics properties change accordingly. In order to obtain reliable bounds for the flight dynamics properties, three parameter sets are analyzed, which account for the missile's nominal, least, and most agile flight dynamics.

Considering the effect of the uncertain mass and aerodynamic parameters on the missile's dynam-

ics, each extrema (minimum/maximum) of the parametric uncertainty can be assigned to one agility level (slow, fast) of the missile dynamics. The nominal case describes the missile model without uncertainties. The parameters of these three configurations (slow, nominal, and agile) are summarized in table 3.1. Since all parameters are assumed to be normally distributed, the slow and agile missile configuration are defined by the 3σ deviation (see table 2.1 and table 2.2) of the nominal parameters.

Uncertainty	Slow	Nominal	Agile
$\Delta C_{x,0}$	-0.85	0	0.85
$\Delta C_{y,0}$, $\Delta C_{z,0}$	-0.75	0	0.75
$\Delta C_{x,\xi}$	0.85	0	-0.85
$\Delta C_{y,\zeta}$, $C_{z,\eta}$	0.75	0	-0.75
$\Delta C_{l,0}$	0.95	0	-0.95
$\Delta C_{m,0}$, $\Delta C_{n,0}$	0.85	0	-0.85
$\Delta C_{l,p}$	0.95	0	-0.95
$\Delta C_{m,q}$, $\Delta C_{n,r}$	0.85	0	-0.85
$\Delta C_{l,\xi}$	-0.95	0	0.95
$\Delta C_{m,\eta}$, $\Delta C_{n,\zeta}$	-0.85	0	0.85
$\Delta \left(I_{ii}^{G}\right)_{BB}$	0.1	0	-0.1
Δm	0.01	0	-0.01

Table 3.1: Uncertainty parameters for the slow, agile, and nominal missile configuration.

3.1 Trim Calculations

Identifying the entire set of states and inputs, which belong to a given physical achievable steady-state flight condition is called *trim calculation*. The result of a trim calculation are the entire rigid body states and inputs of an aircraft system for a certain maneuver. In aircraft performance analysis the objective of trim calculations is to determine steady-state flight conditions of the rigid-body dynamics serving as a starting point for linearization or deriving static performance requirements. Therefore, trim calculations are the first step in analyzing the dynamics and performance capabilities of an aerial vehicle.

A steady-state flight condition describes the equilibrium point of a certain flight maneuver, which is maintained by the aircraft in cases of no disturbances. Thus, the forces and moments of the aircraft are constant over time [77], which implies that the aerodynamic angles (e.g. α_K, β_K) and the angular rates remain constant over time. General examples from aircraft applications of steady-state flight conditions are the steady turning flight and the horizontal level flight [4, 68, 77].

In case the change rate of states and inputs necessary to maintain a certain flight condition is negligible with regard to their dynamic characteristics, the flight condition is denoted as quasi-stationary. Fast transitions in the state and input variables are caused by unsteady maneuvers such as accelerated flight or pull-up/push-over maneuvers. Those trim conditions are instantly left by the aerial vehicle. Therefore, those state and input combinations constitute an unstable equilibrium point. The validity of a linear analysis at an non-steady flight condition is limited.

3.1.1 Procedure and Mathematical Background of Trim Calculations

The trim calculation procedure of the aircraft states and inputs varies with the considered flight maneuver. Each flight maneuver has its unique physical constraints regarding the states, its derivatives, and specific state-dependent quantities (e.g. load factor, acceleration) [77]. Besides constraints resulting from the aircraft physics and the selected maneuver, the trim algorithm incorporates other limitations stemming from airframe restrictions like maximum control surface deflection and the stall region. Trim calculations are computed by an optimization algorithm, which calculates a trim solution under the given constraints and a cost function. The cost function describes the trim problem in terms of flight maneuver constraints with respect to the nonlinear rigid body aircraft dynamics by mapping the solver parameters of the optimization algorithm to the considered parts of the state vector and the regarded inputs. Based on the state/input combination the required derivatives and values are calculated and forwarded to the invoking optimization routine.

For further considerations, the following generalized, nonlinear aircraft dynamics

$$\begin{aligned} \dot{\boldsymbol{x}} &= \boldsymbol{f}\left(\boldsymbol{x}, \boldsymbol{u}\right) \\ \boldsymbol{y} &= \boldsymbol{h}\left(\boldsymbol{x}, \boldsymbol{u}\right) \end{aligned} \tag{3.1}$$

is considered. $\boldsymbol{x} \in \mathbb{R}^{n\times 1}$, $\boldsymbol{u} \in \mathbb{R}^{m\times 1}$, and $\boldsymbol{y} \in \mathbb{R}^{r\times 1}$ describe the system's state, input, and output, respectively. Depending on the maneuver, only a certain part of the state vector $\boldsymbol{x}$ and system dynamics $\boldsymbol{f} \in \mathbb{R}^{n\times 1}$ is of interest. The relevant part is denoted with $\boldsymbol{f}_{trim} \in \mathbb{R}^{t\times 1}$ while the part not considered for trim calculations is labeled as $\boldsymbol{f}_{spare} \in \mathbb{R}^{(n-t)\times 1}$. Applying the same separation for the derivative of the state vector, the dynamics of (3.1) can be rewritten as

$$\begin{bmatrix} \dot{\boldsymbol{x}}_{trim} \\ \dot{\boldsymbol{x}}_{spare} \end{bmatrix} = \begin{bmatrix} \boldsymbol{f}_{trim}\left(\boldsymbol{x}, \boldsymbol{u}\right) \\ \boldsymbol{f}_{spare}\left(\boldsymbol{x}, \boldsymbol{u}\right) \end{bmatrix}. \tag{3.2}$$

The trim algorithm solves the quadratic, nonlinear system of equations

$$\boldsymbol{r} = \dot{\boldsymbol{x}}_{trim} - \dot{\boldsymbol{x}}_{trim,des} = \boldsymbol{f}_{trim}\left(\boldsymbol{x}_s^*, \boldsymbol{p}\right) - \dot{\boldsymbol{x}}_{trim,des} \stackrel{!}{=} \boldsymbol{0} \tag{3.3}$$

for the trim solver state $\boldsymbol{x}_s \in \mathbb{R}^{q\times 1}$. The trim parameter vector $\boldsymbol{p} \in \mathbb{R}^{p\times 1}$ contains constant state and input variables, which characterize the trimmed flight maneuver in a specific operating point. $\boldsymbol{r} \in \mathbb{R}^{t\times 1}$ denotes the residual vector describing the difference between the desired state derivative $\dot{\boldsymbol{x}}_{trim,des} \in \mathbb{R}^{q\times 1}$ and the current trim solution $\dot{\boldsymbol{x}}_{trim} \in \mathbb{R}^{q\times 1}$ of the respective maneuver.

Figure 3.1 depicts a diagram of the herein used trim approach. Initialization, storing of the results, and definition of the analyzed flight envelope regions are accomplished by the *Trim Control* segment. From an implementation point of view, the calculation of the solution $\boldsymbol{x}_s$ by the *Trim Solver* can be considered as an optimization problem with the cost function (3.3) and the solution $\boldsymbol{x}_s^*$. The residual vector $\boldsymbol{r}$ contains the evaluated cost function, the *Trim Solver* attempts to minimize (3.3) by modifying $\boldsymbol{x}_s$ in each iteration step. The mapping rule of the trim solver state $\boldsymbol{x}_s$ and trim parameters $\boldsymbol{p}$ to the aircraft system states $\boldsymbol{x}$ and inputs $\boldsymbol{u}$ is defined by the so called *Trim Template*. This interface provides the *Aircraft Model* with the complete state $\boldsymbol{x}$ and input $\boldsymbol{u}$ vectors computed on the basis of the trim solver state $\boldsymbol{x}_s$ and parameter $\boldsymbol{p}$ by considering the maneuver-specific constraints.

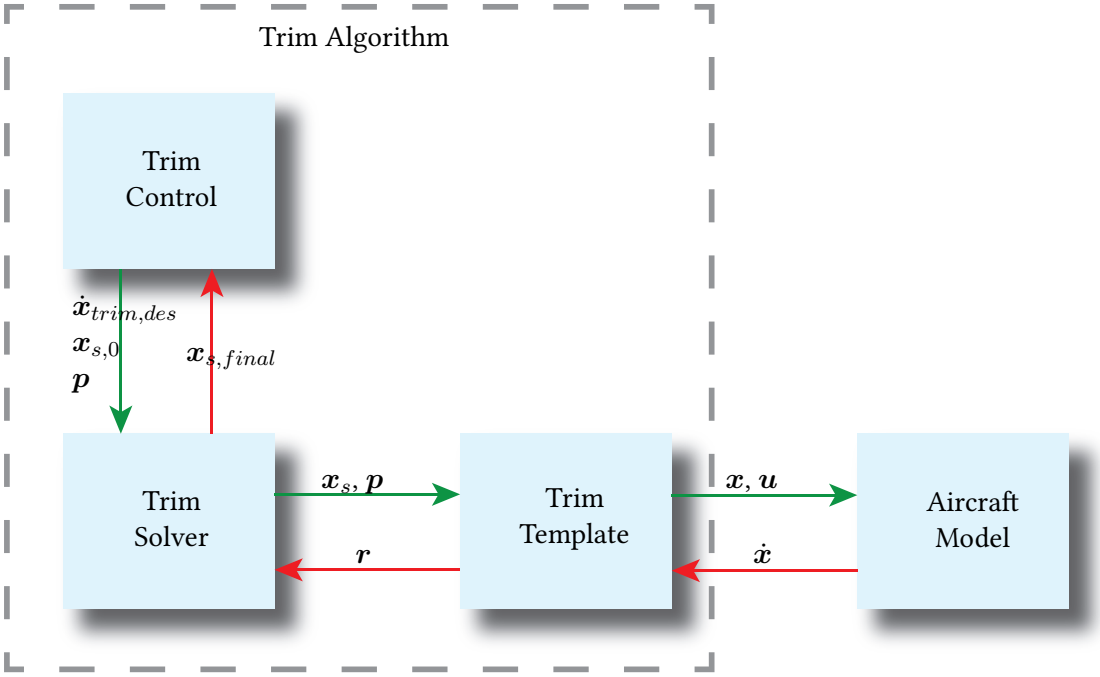

Figure 3.1: Scheme of the herein utilized trim algorithm.

A detailed overview of trim calculations, their applications and implementations can be found in [68, 77]. In the following section the maximum physical capability of the missile with respect to its parameter configuration is determined by using the herein presented trim calculations.

3.1.2 Flight Envelope Determination of FGS-X-03

In order to analyze the missile's performance capabilities two trim calculations are conducted: first, the steady-state horizontal flight is investigated. Even though this calculation offers only a limited amount of information concerning the physical capabilities of the missile, the results are necessary to linearize the missile's nonlinear dynamics. In a second trim approach, the flight envelope is estimated by trim calculations with constant accelerations, so-called pull-up maneuvers. Since the dynamics of the actuator, measurement, and estimation unit will not influence the solution $\boldsymbol{x}_s$ of a trimmed flight condition, only the state equations of the rigid body dynamics (see section 2.2.2.5) are considered. For the analysis, no trim problems are considered in which the rotation described via Euler angles exhibit the singularity (see section 2.2.2.4). Therefore, the description of the missile's attitude - in case of the trim calculations - via Euler angles is valid and reasonable. Thus, the rigid body dynamics comprises of twelve differential equations depending on the equivalent state variables and three inputs combined in the vectors $\boldsymbol{x}$ and $\boldsymbol{u}$, respectively. This means that for the purpose of trim calculation the parameters $\boldsymbol{p}$ and solver states $\boldsymbol{x}_s$ have to cover the 15 variables $\begin{bmatrix}\boldsymbol{x} & \boldsymbol{u}\end{bmatrix}$. As already mentioned in chapter 2, any influences of wind and disturbances on the missile body are not taken into account.

3.1.2.1 Horizontal Steady-State Flight

Horizontal steady-state flight is characterized by a defined altitude $\left(z^G\right)_E$ and a force vector $\left(\boldsymbol{F}^G\right)_B$ compensating the influence of weight force due to gravity. Since the missile is assumed to be burned

out by the beginning of the endgame scenario, no thrust control is taken into account for trim calculations. The force generated by the propulsion unit is the main driver for altering the missile's velocity $\left(V_K^G\right)_{\bar{K}}^{EB}$ in steady-state flight [1, 65]. Therefore, the time derivative of the velocity $\left(V_K^G\right)_{\bar{K}}^{EB}$ cannot be part of the residual vector $\boldsymbol{r}$. In order to maintain horizontal flight, the missiles attitude is not subject to any alterations. This fact requires the body rates $\left(\boldsymbol{\omega}_K^{EB}\right)_B$ and body accelerations $\left(\dot{\boldsymbol{\omega}}_K^{EB}\right)_B^B$ to be zero. With $\left(\boldsymbol{\omega}_K^{EB}\right)_B = \mathbf{0}$, the time derivatives of the Euler angles (see (2.14)) vanish. The above mentioned requirement of a constant force vector $\left(\boldsymbol{F}^G\right)_B$ results in constant aerodynamic angles α_K and β_K. Thus, the state derivatives for a trimmed horizontal flight of an endgame missile scenario are

$$\dot{\boldsymbol{x}}_{trim} = \begin{bmatrix} \left(\dot{r}_z^G\right)_E^E & \dot{\alpha}_K & \dot{\beta}_K & \left(\dot{p}_K^{EB}\right)_B^B & \left(\dot{q}_K^{EB}\right)_B^B & \left(\dot{r}_K^{EB}\right)_B^B \end{bmatrix}^T. \tag{3.4}$$

According to (3.3) the flight condition is fulfilled if $\dot{\boldsymbol{x}}_{trim}$ defined in (3.4) equals the desired state derivatives $\dot{\boldsymbol{x}}_{trim,des} = \mathbf{0}$.

For the purpose of achieving the constraints in (3.4) of a horizontal flight condition the aerodynamic angles α_K, β_K and aerodynamic controls $\boldsymbol{u} = \begin{bmatrix} \xi & \eta & \zeta \end{bmatrix}^T$ are used as solver parameters:

$$\boldsymbol{x}_s = \begin{bmatrix} \alpha_K & \beta_K & \Theta & \xi & \eta & \zeta \end{bmatrix}^T \tag{3.5}$$

The flight envelope point considered for trim calculation is determined via the altitude $h = -\left(z^G\right)_E$, absolute velocity $\left(V_K^G\right)_{\bar{K}}^{EB}$, and the bank angle Φ. Due to the missile's rotational symmetry all trim calculations are conducted for $\Phi = 0$. Since the azimuth angle Ψ, the position $\left(x^G\right)_E$, and $\left(y^G\right)_E$ have no influence on the missile's dynamics, they are set to zero for all trim conditions. Summarizing all trim parameters in the vector

$$\boldsymbol{p} = \begin{bmatrix} \left(V_K^G\right)_{\bar{K}}^E & \left(p_K^{EB}\right)_B & \left(q_K^{EB}\right)_B & \left(r_K^{EB}\right)_B & \left(x^G\right)_E & \left(y^G\right)_E & \left(z^G\right)_E & \Phi & \Psi \end{bmatrix}^T \tag{3.6}$$

leads to a square trim problem, where the dimension $q = 6$ of the trim solver states equals the dimension of the residuals $t = 6$. The summation of the trim parameters $p = 9$ and trim solver states $q = 6$ coincides with the number of system variables (states and inputs) $n + m = 15$. Therefore, all rigid body states $\boldsymbol{x}$ and inputs $\boldsymbol{u}$ are covered by the trim solver state $\boldsymbol{x}_s$ and the trim parameter $\boldsymbol{p}$.

The results of the missile's horizontal trim calculations for the two altitudes $h = 0km$ and $h = 4.5km$ are shown in fig. 3.2.

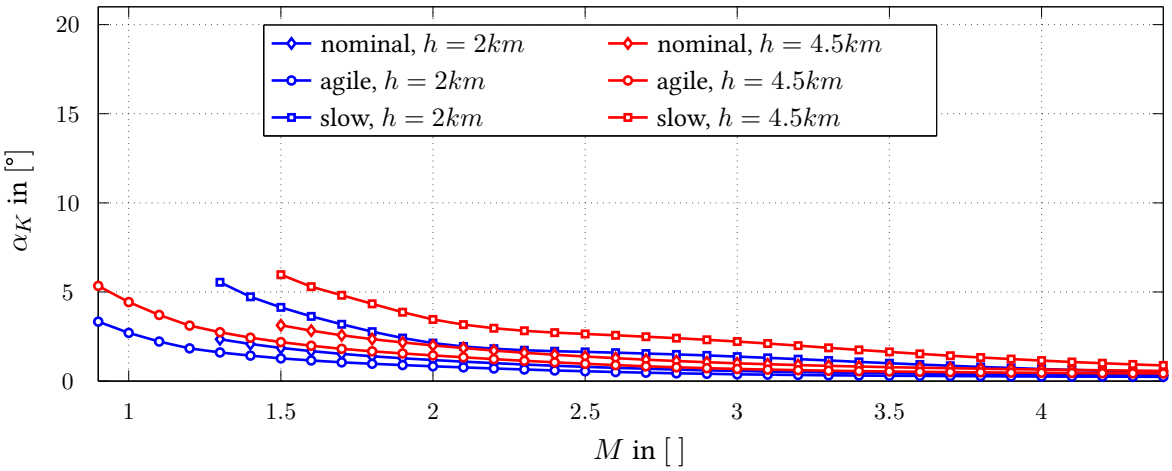

(a) Horizontal flight trim results for AoA α_K versus M.

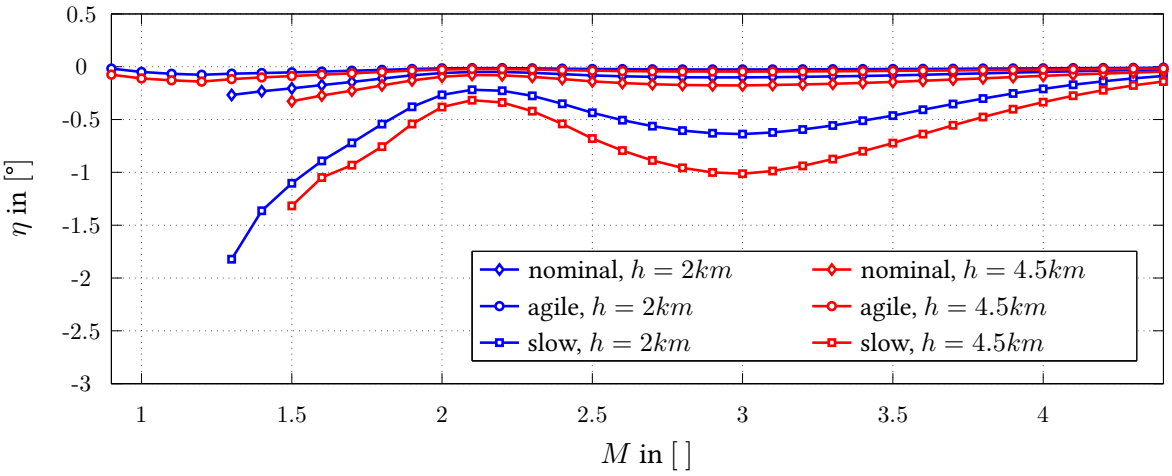

(b) Horizontal flight trim results for fin deflection η versus M.

Figure 3.2: Mach dependency of Trim results of horizontal steady-state flight at the altitudes $h = 2km$ and $h = 4.5km$.

Figure 3.2a and fig. 3.2b depicts the AoA α_K and the control surface deflection η versus Mach number M for the different agile configurations introduced in table 3.1, respectively. The plotted curves in fig. 3.2a and fig. 3.2b exhibit a decline in AoA α_K and increase of the fin deflection η with increasing Mach number M. Since the dynamic pressure $\bar{q}$ depends on the square of the Mach number M, an increase in M leads to an increased control effectiveness of the aerodynamic control surfaces (see appendix B.1). More effective control surfaces require a reduced absolute control surface deflection to achieve zero body acceleration $\left(\boldsymbol{\omega}_K^{EB}\right)_B^B$ (zero moments) acting on the missile. The decline of the necessary AoA α_K to produce a contrary force (downward in B-system) compensating the gravity force, is owed to the increased force effectiveness of the missile body with a rise in velocity.

From the graphs representing the different agile missile configurations it can be seen, that a more agile missile configuration leads to smaller AoA α_K and smaller absolute control surface deflection η. This means, that the more agile the missile is, the less AoA and fin deflection is required to produce zero moment and compensating the gravity force in horizontal flight.

3.1.2.2 Flight with Constant Accelerations

In order to determine the maximum possible maneuver capabilities, trim calculations at constant accelerations are conducted for the entire range of possible operating points ($M = 0.9 - 4.4$, $h = 0 - 11km$). This analysis provides the maximum possible flight envelope for different agile missile configurations. The set of physical achievable flight conditions is limited by the maximum actuator deflection δ_{max}, the maximum total incidence angle $\vartheta_{A,max}$, and the maximum acceleration capability a_{max} of the missile body. Maneuvers with constant accelerations leading to a positive climb angle are denoted as *pull-up* maneuvers (or *push-over* in case of a negative climb angle) [1, 4, 77]. Since a missile is rotation-symmetric body, the acceleration potential is analyzed by a symmetric pull-up maneuver in the pitch plane ($x_{\bar{K}}z_{\bar{K}}$ - plane).

Pull-up trims describe a quasi-stationary flight condition at a defined acceleration given by the load factor $(n_z)_{\bar{K}}$. For maintaining this flight condition a certain pitch angle Θ and pitch rate $\left(q_K^{EB}\right)_B \neq 0$ is required in combination with constant aerodynamic angles α_K, β_K and body rates $\left(\boldsymbol{\omega}_K^{EB}\right)_B$. Since the altitude h is not constant during this maneuver a variation in dynamic pressure takes place, which causes the states to leave the trimmed flight condition. Therefore, the trimmed pull-up flight condition constitutes an unstable equilibrium point.

Based on the assumptions above, the state derivatives used for trim calculations are cumulated in the vector

$$\dot{\boldsymbol{x}}_{trim} = \begin{bmatrix} \dot{\alpha}_K & \dot{\beta}_K & \left(\dot{p}_K^{EB}\right)_B^B & \left(\dot{q}_K^{EB}\right)_B^B & \left(\dot{r}_K^{EB}\right)_B^B \end{bmatrix}^T . \tag{3.7}$$

A trimmed pull-up condition is achieved if the state derivatives in (3.7) vanish: $\dot{\boldsymbol{x}}_{trim,des} = \boldsymbol{0}$. The desired load factor $(n_z)_{\bar{K}}$ at the defined equilibrium point $\boldsymbol{x}_s^*$ ($\dot{\boldsymbol{x}}_{trim} = \boldsymbol{f}_{trim}(\boldsymbol{x}_s^*, \boldsymbol{p}) = \boldsymbol{0}$) is achieved by a unique combination of aerodynamic angles (α_K, β_K) and aerodynamic controls $\boldsymbol{u} = \begin{bmatrix} \xi & \eta & \zeta \end{bmatrix}^T$. Thus, the solver states of the considered trim problem are

$$\boldsymbol{x}_s = \begin{bmatrix} \alpha_K & \beta_K & \xi & \eta & \zeta \end{bmatrix}^T . \tag{3.8}$$

In order to estimate the acceleration capabilities of the missile, the operating points for the trim calculations are determined by the altitude $h = -\left(z^G\right)_E$, absolute velocity $\left(V_K^G\right)_{\bar{K}}^E$, and the load factor $(n_z)_{\bar{K}}$. Usually, in pull-up (acceleration) trim calculations the flight path angle γ_K is considered as a parameter, too. Since the gravitational acceleration of the missile is negligible compared to the missile's acceleration range, a variation in the missile's flight path angle γ_K has less significance for the pull-up trim results. Therefore, γ_K is selected to be zero. According to the explanation in section 3.1.2.1, the states Ψ, $\left(x^G\right)_E$, and $\left(y^G\right)_E$ can be chosen in an arbitrary way without influencing the flight condition and therefore the trim state $\boldsymbol{x}_s^*$. For the reasons of simplicity, those trim parameters are set to zero ($\Psi = 0$, $\left(x^G\right)_E = \left(y^G\right)_E = 0$). Since only the longitudinal motion is of interest, the roll and yaw rate are required to be zero, $\left(p_K^{EB}\right)_B = \left(r_K^{EB}\right)_B = 0$.

Besides the altitude change, the state derivatives and their constraints $\dot{\boldsymbol{x}}_{trim,des}$ are equal for a horizontal steady-state flight (3.4) and a pull-up trim condition (3.7), both considered without propulsion force. The major difference between those flight conditions lies in the constraints of the longitudinal dynamics and therefore in the trim template. The trim parameter $(n_z)_{\bar{K}}$ is not part of the rigid body state vector section 2.2.2. Therefore, a calculation within the trim template is necessary to convert the desired load factor into a subset of the rigid body states for a trimmed symmetric pull-up maneuver. For the purpose of deriving this algebraic state dependencies, the path angle dynamics [66]

for a longitudinal motion

$$\dot{\gamma}_K = \frac{(L)_{\bar{K}}}{m\left(V_K^G\right)_{\bar{K}}^E} - \frac{g}{\left(V_K^G\right)_{\bar{K}}^E} \cdot \cos\left(\gamma_K\right) \tag{3.9}$$

can be rewritten as

$$\dot{\gamma}_K = \frac{g}{\left(V_K^G\right)_{\bar{K}}^E} \left(\left(n_z\right)_{\bar{K}} - \cos\left(\gamma_K\right)\right) \tag{3.10}$$

by using the load factor definition $\left(n_z\right)_{\bar{K}}$ introduced in (2.38). Regarding a leveled flight maneuver along the longitudinal axis, the pitch angle Θ is the sum of the flight path angle γ_K and the AoA α_K:

$$\Theta = \gamma_K + \alpha_K \tag{3.11}$$

Considering the dynamics of the attitude angles (2.17) under the assumption of zero bank angle ($\Phi = 0$), the pitch dynamics results in

$$\dot{\Theta} = \left(q_K^{EB}\right)_B . \tag{3.12}$$

(3.12) is denoted as the rate constraint of the pull-up trim calculation. Based on this rate constraint (3.12), the desired state derivative of AoA ($\dot{\alpha}_K = 0$, see (3.7)), and the path angles dynamics of (3.10), the pitch rate $\left(q_K^{EB}\right)_B$ necessary for achieving a certain load factor $\left(n_z\right)_{\bar{K}}$ is calculated via

$$\begin{aligned} \left(q_K^{EB}\right)_B &= \dot{\Theta} \\ &= \dot{\gamma}_K \\ &= \frac{g}{\left(V_K^G\right)_{\bar{K}}^E} \left(\left(n_z\right)_{\bar{K}} - \cos\left(\gamma_K\right)\right) . \end{aligned} \tag{3.13}$$

Therefore, the trim parameter $\left(n_z\right)_{\bar{K}}$, which is not part of the rigid body state description is converted via the rate constraint (3.13) into a corresponding pitch rate $\left(q_K^{EB}\right)_B$. The vector

$$\boldsymbol{p} = \left[\left(V_K^G\right)_{\bar{K}}^E \quad \left(p_K^{EB}\right)_B \quad \left(q_K^{EB}\right)_B \quad \left(r_K^{EB}\right)_B \quad \left(x^G\right)_E \quad \left(y^G\right)_E \quad \left(z^G\right)_E \quad \Phi \quad \Theta \quad \Psi\right]^T \tag{3.14}$$

summarizes all trim parameters for the herein considered symmetric pull-up maneuver. With $q = 5$ solver states (see (3.8)) and $t = 5$ residuals (see (3.7)) the nonlinear system of equations of the trim problem is fully determined. The number of parameters $p = 10$ in combination with the $q = 5$ solver states cover all $n + m = 15$ ($n = 12$ states, $m = 3$ inputs) variables of the rigid body model used for trim calculations.

Figure 3.3 illustrates the Mach dependencies for pull-up trims of $\left(n_z\right)_{\bar{K}} = 10g$ and $\left(n_z\right)_{\bar{K}} = 35g$ at an altitude of $h = 4.5km$ for the three configuration described in table 3.1. As already discussed for the horizontal flight trim case (see fig. 3.2), the AoA α_K and the absolute elevator deflection $|\eta|$ decrease with increasing Mach number M. With an increase in agility, smaller α_K and $|\eta|$ are necessary to obtain the load factors $\left(n_z\right)_{\bar{K}}$. That characteristic also explains the larger set of trimmable operating points for more agile configurations. The more agile the configuration is, the smaller is the minimum Mach number M, at which a trimmed flight condition is achievable without violating the physical limitations of the missile. In the herein considered pull-up trim flight condition, the maximum elevator deflection η_{max} and the maximum AoA (in case of no lateral motion: $\alpha_{K,max} = \vartheta_{A,max}$) constitute the limiting variables.

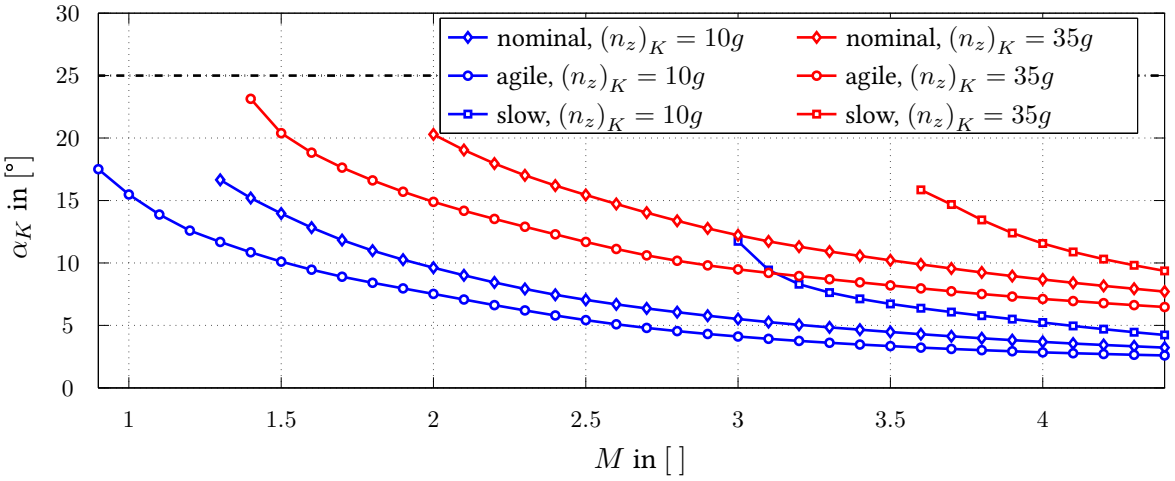

(a) Pull-up trim results for AoA α_K versus M.

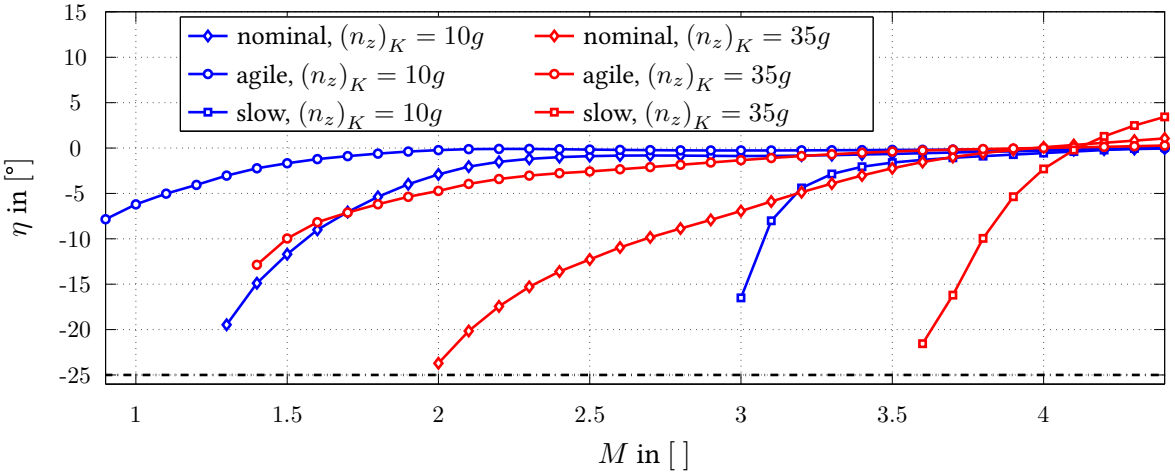

(b) Pull-up trim results for fin deflections η versus M.

Figure 3.3: Mach dependency of trim results for flight with constant accelerations at $h = 4.5km$.

Usually, the aerodynamic coefficient $(C_{m,0})_B$ provides a moment, which counteracts the current AoA (equivalence of a spring in *mass spring damper system* [78]). This negative moment resulting from $(C_{m,0})_B < 0$ is compensated in a trimmed flight condition by a positive moment originating from the fin effectiveness $(C_{m,\eta})_B$, leading to zero pitch moment $\left(\dot{q}_K^{EB}\right)_B^B = 0$. By definition of the elevator deflection, a negative deflection angle $\eta < 0$ causes a positive $(C_{m,\eta})_B > 0$ (see appendix B.1.2). Thus, the trim results in fig. 3.2 and fig. 3.3 exhibit a positive AoA $\alpha_K > 0$ and a negative $\eta < 0$ to maintain zero longitudinal (pitch) moment, which leads to $\left(\dot{q}_K^{EB}\right)_B^B = 0$. Considering fig. 3.3 it is striking that at high Mach numbers ($M > 3.9$) a positive fin deflection is required to obtain the desired load factor in a trimmed condition. This anomaly can be explained by investigating the aerodynamic coefficient $(C_{m,0})_B$ at certain AoAs in the high Mach regime. Figure 3.4 depicts the sign change for $(C_{m,0})_B$ for Mach numbers $M > 3.9$.

Remark: Such aerodynamic anomalies in high Mach regime are typical for missile airframes.

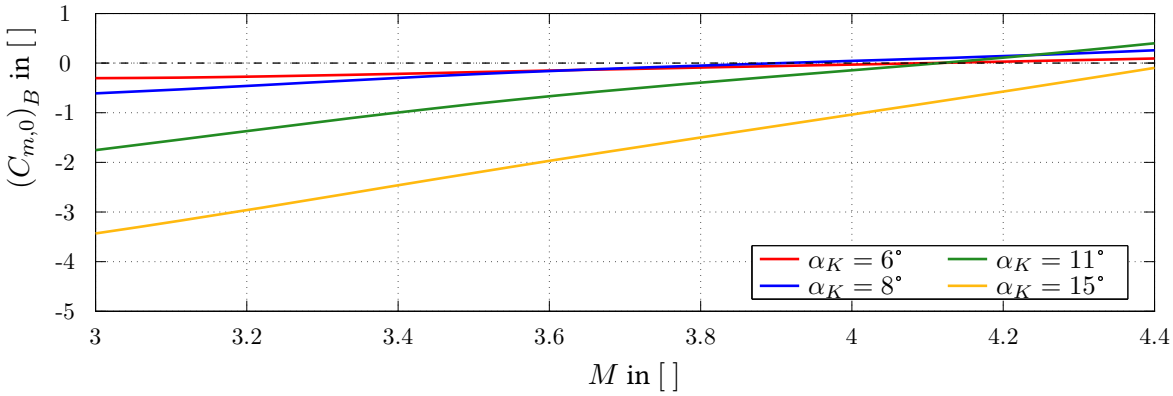

Figure 3.4: High Mach anomaly of the aerodynamic coefficient $(C_{m,0})_B$.

Besides the Mach dependency shown in fig. 3.3, fig. 3.5 illustrates the altitude dependency of AoA α_K and fin deflection η for a trimmed flight with constant load factor $(n_z)_K$. With increasing altitude h the aerodynamic effectiveness (decreasing dynamic pressure $\bar{q}$) of the missile body decreases. Therefore, higher AoAs are necessary to achieve the desired load factors. A growth in AoA leads to an increase in fin deflection to achieve zero longitudinal angular acceleration $\left(\dot{q}_K^{EB}\right)_B^B = 0$.

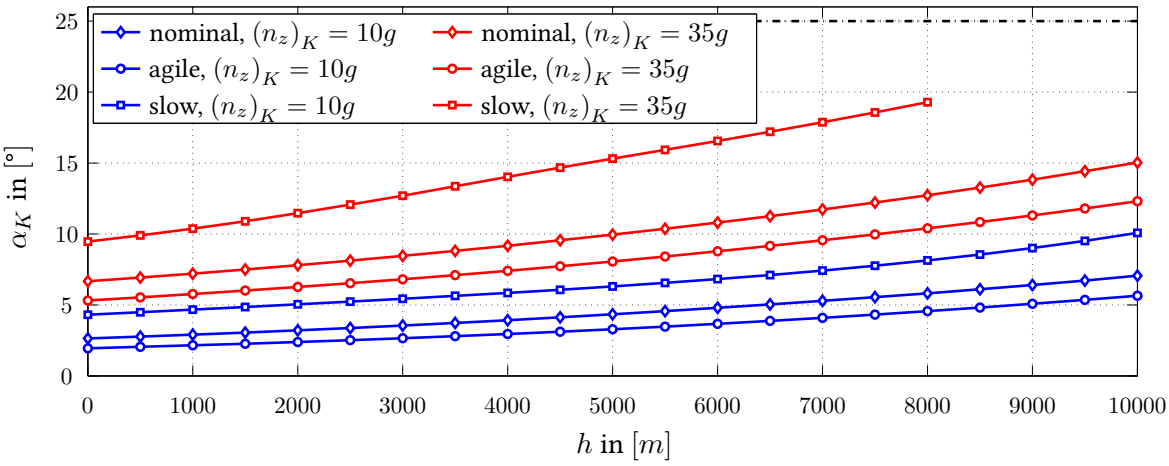

(a) Pull-up trim results for AoA α_K versus M.

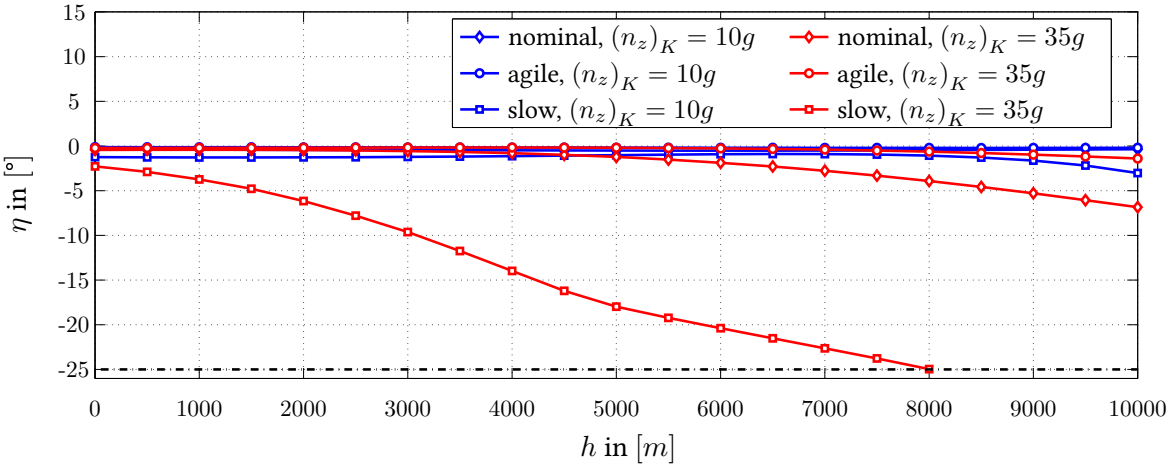

(b) Pull-up trim results for fin deflections η versus M.

Figure 3.5: Altitude dependency of trim results for flight with constant accelerations at $M = 3.7$.

The determination of the physically feasible flight envelope for different configurations is obtained by trim calculations over equidistant flight envelope points ($M = 0.9 - 4.4$ and $h = 0 - 11km$). Figure 3.6 depicts the acceleration trim results of maximum longitudinal acceleration taken into account the limits of fin deflections, the g-limit of the missile, and the maximum permissible AoA (see chapter 2).

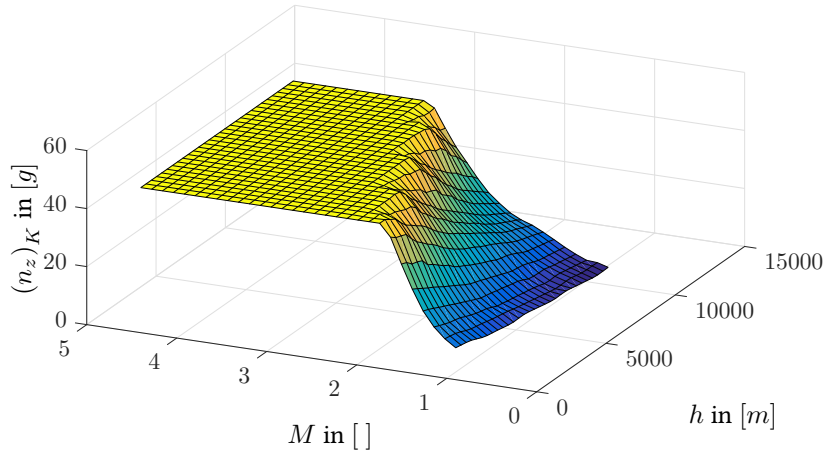

(a) Maximum trimmable load factor $(n_z)_K$ across flight envelope.

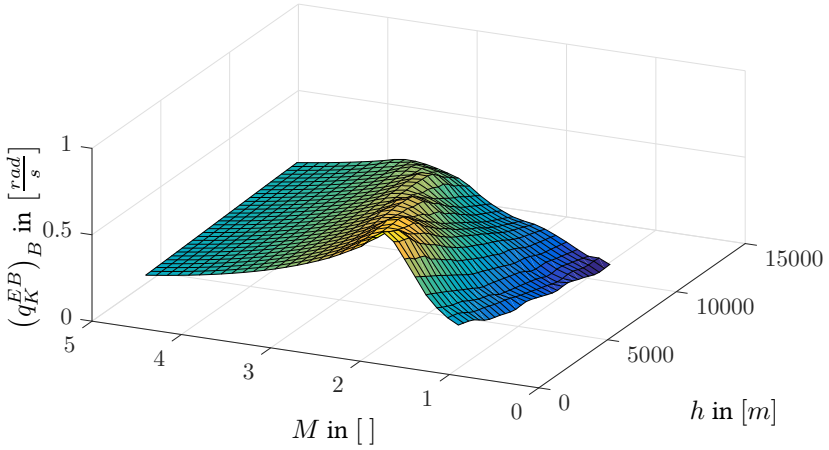

(b) Corresponding pitch rate $\left(q_K^{EB}\right)_B$ of trimmed flight with maximum trimmable load factor.

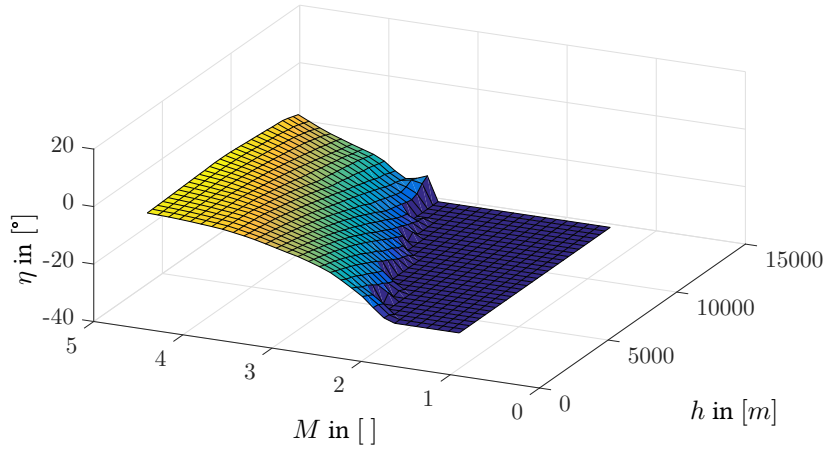

(c) Corresponding fin deflection η of trimmed flight with maximum trimmable load factor.

Figure 3.6: Pitch rate $\left(q_K^{EB}\right)_B$ and fin deflection η of maximum trimmable load factor $(n_z)_K$ in longitudinal direction by respecting the acceleration limits of the missile body.

From fig. 3.6, the representation in fig. 3.7 is derived which shows the physically achievable regions

in terms of Mach M and altitude h for two particular load factors. The curves describe the region hulls, which contain the entire set of possible flight conditions. The graphic illustrates the effect of an enlarged flight envelope due to more agility of the missile. The more agile the considered airframe is, the larger becomes the set of operating points (M and h) the missile can achieve a certain load factor.

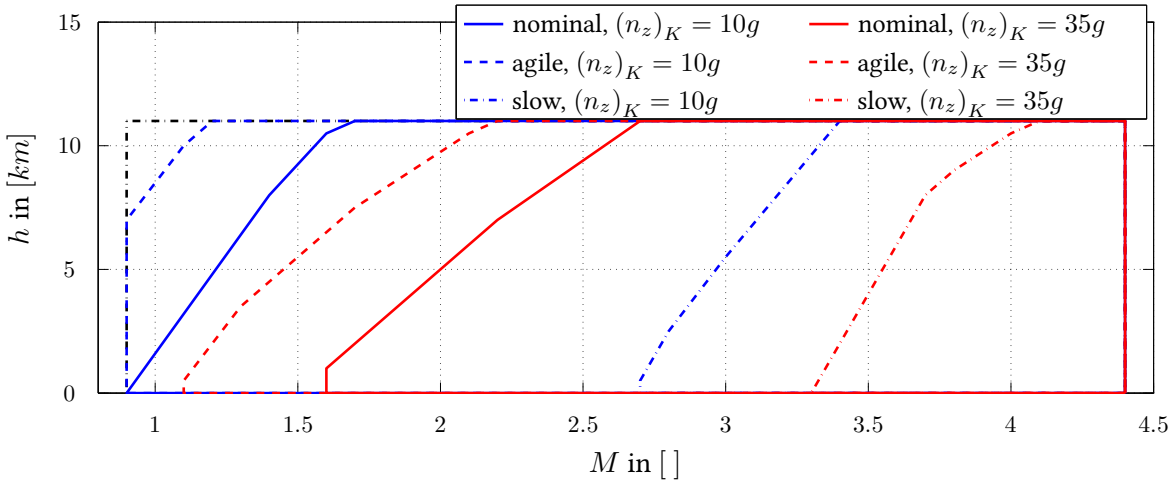

Figure 3.7: Flight envelope for different agile configurations at two load factor levels.

To summarize the missile's non-dynamic, physical capabilities, the entire flight envelope for the nominal configuration is illustrated in fig. 3.8. As already discussed above, the dynamic pressure $\bar{q}$ reaches its maximum for a certain Mach number M at sea level ($h = 0km$). Since the missile's aerodynamic efficiency increases with Mach number M and dynamic pressure $\bar{q}$, the maximum maneuver capability is achieved for $M = 4.4$ and $h = 0km$. Therefore, the flight envelope regions are shrinking with increased load factor towards high Mach number and low altitudes.

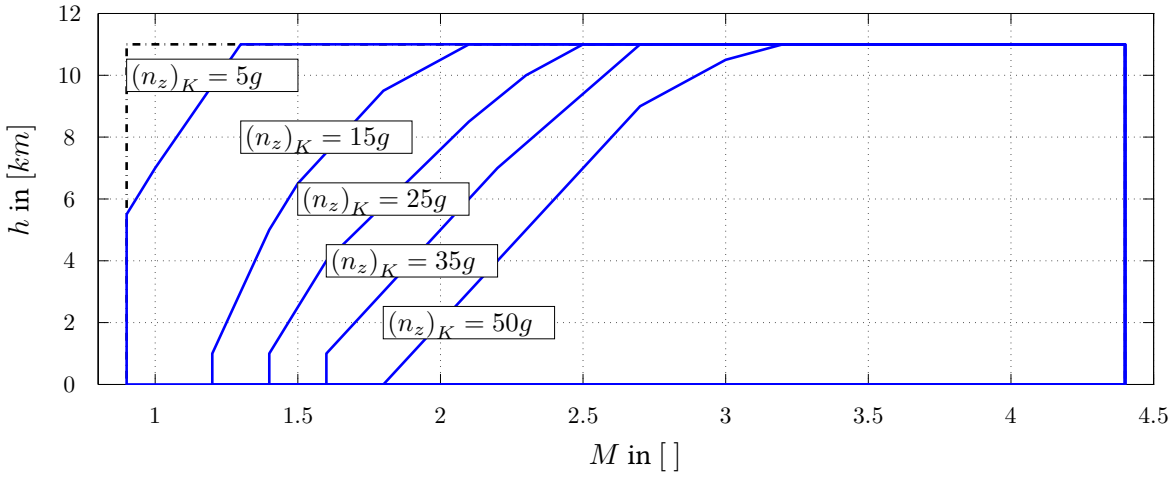

Figure 3.8: Nominal flight envelope for different load factor levels.

3.2 Dynamic Analysis of the Missile via Linearization

The determination of the dynamic properties of a system is of fundamental interest for the control designer. Within the control layout phase, the dynamic properties are taken into account to design a closed-loop behavior, which fully exploits the static and dynamic system capabilities. Thus, for requirement derivation, control design process, and verification, a detailed knowledge about the dynamic system properties is essential.

Nowadays, only a few methods exist for analyzing the dynamic characteristics of a nonlinear system [42, 79, 80]. Besides the method of Singular Perturbation, which provides information about the dynamical coupling of the different dynamic layers, the majority of the methods and tools are designed for analyzing the system stability. Numerical simulations provide another possibility to gain insights in the system dynamics. Due to their extensive nature and the limited value in terms of analyzing open-loop systems, numerical simulations are only suitable for specific investigations regarding the missile's flight dynamics.

In case of linear time-invariant (LTI) systems, a large variety of tools and methods exist to fully quantize the plant's dynamics [81, 82]. Therefore, a standard procedure in the flight dynamics analysis constitute the linearization of the aircraft's dynamics to apply linear analyzing metrics. This section briefly explains the theory of linearization and familiarizes the reader with the basic nomenclature of linearized aircraft systems.

3.2.1 Mathematical Background of Linearization

In order to derive the linearized equation of motion (EOM) of the missile's rigid body dynamics, the generalized nonlinear dynamics depicted in (3.1) is used. The herein introduced procedure of deriving the linearized EOM of a nonlinear dynamics and the according nomenclature are in line with available literature [40, 66, 68, 77, 83].

A linear representation of the nonlinear model dynamics is only valid within a certain state space region around the equilibrium point. The size of the region depends on the nonlinear system characteristics at the considered equilibrium point. The system's equilibrium, denoted by $\boldsymbol{x}_0$, $\boldsymbol{u}_0$, $\boldsymbol{y}_0$, is described by the state, input, and output equilibrium of the nonlinear system (3.1), respectively. Deviations from this equilibrium condition are labeled with δ. Thus, $\delta\boldsymbol{x} = \boldsymbol{x} - \boldsymbol{x}_0$, $\delta\boldsymbol{u} = \boldsymbol{u} - \boldsymbol{u}_0$, $\delta\boldsymbol{y} = \boldsymbol{y} - \boldsymbol{y}_0$ denotes the deviations from the state, input, and output equilibrium, respectively. The differentiation of a vector valued function (e.g. $\boldsymbol{f}$) with respect to a vector (e.g. $\boldsymbol{x}$) results in the *Jacobian* matrix

$$\left(\frac{\partial \boldsymbol{f}}{\partial \boldsymbol{x}}\right) := \begin{bmatrix} \frac{\partial f_1}{\partial x_1} & \frac{\partial f_1}{\partial x_2} & \cdots & \frac{\partial f_1}{\partial x_n} \\ \vdots & \vdots & \ddots & \vdots \\ \frac{\partial f_n}{\partial x_1} & \frac{\partial f_n}{\partial x_2} & \cdots & \frac{\partial f_m}{\partial x_n} \end{bmatrix}. \tag{3.15}$$

The entries of the Jacobian are the partial derivatives of each function element with respect to the vector entries (e.g. $\partial f_i/\partial x_j$). Following the same labeling rules for the equilibrium condition, an evaluation of a vector valued function (exemplarily shown for $\boldsymbol{f}$)

$$\boldsymbol{f}_0 = \boldsymbol{f}\left(\boldsymbol{x} = \boldsymbol{x}_0, \boldsymbol{u} = \boldsymbol{u}_0\right) \tag{3.16}$$

and the Jacobian

$$\left(\frac{\partial \boldsymbol{f}}{\partial \boldsymbol{x}}\right)_0 = \left(\frac{\partial \boldsymbol{f}}{\partial \boldsymbol{x}}\right)_{\boldsymbol{x}=\boldsymbol{x}_0, \boldsymbol{u}=\boldsymbol{u}_0} \tag{3.17}$$

are denoted with the index 0. In order to derive an LTI representation of (3.1), a Taylor series expansion around the equilibrium condition is conducted for the state dynamics

$$\dot{\boldsymbol{x}}_0 + \delta\dot{\boldsymbol{x}} = \boldsymbol{f}_0 + \left(\frac{\partial \boldsymbol{f}}{\partial \boldsymbol{x}}\right)_0 \cdot \delta\boldsymbol{x} + \left(\frac{\partial \boldsymbol{f}}{\partial \boldsymbol{u}}\right)_0 \cdot \delta\boldsymbol{u} + \mathcal{O}\left(\boldsymbol{x}^2\right) + \mathcal{O}\left(\boldsymbol{u}^2\right) \tag{3.18}$$

and the output equation

$$\boldsymbol{y}_0 + \delta\boldsymbol{y} = \boldsymbol{h}_0 + \left(\frac{\partial \boldsymbol{h}}{\partial \boldsymbol{x}}\right)_0 \cdot \delta\boldsymbol{x} + \left(\frac{\partial \boldsymbol{h}}{\partial \boldsymbol{u}}\right)_0 \cdot \delta\boldsymbol{u} + \mathcal{O}\left(\boldsymbol{x}^2\right) + \mathcal{O}\left(\boldsymbol{u}^2\right). \tag{3.19}$$

With the equalities $\dot{\boldsymbol{x}}_0 = \boldsymbol{f}_0$ and $\boldsymbol{y}_0 = \boldsymbol{h}_0$ and by neglecting the higher order terms $\mathcal{O}\left(\boldsymbol{x}^2\right), \mathcal{O}\left(\boldsymbol{u}^2\right)$, the linear dynamics and output equation at $\boldsymbol{x}_0$, $\boldsymbol{u}_0$ results in

$$\delta\dot{\boldsymbol{x}} \approx \left(\frac{\partial \boldsymbol{f}}{\partial \boldsymbol{x}}\right)_0 \cdot \delta\boldsymbol{x} + \left(\frac{\partial \boldsymbol{f}}{\partial \boldsymbol{u}}\right)_0 \cdot \delta\boldsymbol{u} \tag{3.20}$$

and

$$\delta\boldsymbol{y} \approx \left(\frac{\partial \boldsymbol{h}}{\partial \boldsymbol{x}}\right)_0 \cdot \delta\boldsymbol{x} + \left(\frac{\partial \boldsymbol{h}}{\partial \boldsymbol{u}}\right)_0 \cdot \delta\boldsymbol{u}, \tag{3.21}$$

respectively. The "$\approx$" sign in this step emphasizes the fact, that (3.20) and (3.21) are only approximations of the variations $\delta\boldsymbol{y}$ and $\delta\boldsymbol{u}$ due to neglecting the higher order terms $\mathcal{O}\left(.\right)$ containing nonlinear dependencies. For the sake of simplicity in the subsequent formulation of the linear missile dynamics, the "$\approx$" sign is replaced by "$=$" sign. By using the following abbreviations

$$\begin{aligned}
\boldsymbol{A} &:= \left(\frac{\partial \boldsymbol{f}}{\partial \boldsymbol{x}}\right)_0 \\
\boldsymbol{B} &:= \left(\frac{\partial \boldsymbol{f}}{\partial \boldsymbol{u}}\right)_0 \\
\boldsymbol{C} &:= \left(\frac{\partial \boldsymbol{h}}{\partial \boldsymbol{x}}\right)_0 \\
\boldsymbol{D} &:= \left(\frac{\partial \boldsymbol{h}}{\partial \boldsymbol{u}}\right)_0,
\end{aligned} \tag{3.22}$$

which are in coherence with the standard literature [82, 83], the linear state space model of (3.1) can be written as

$$\begin{aligned}
\delta\dot{\boldsymbol{x}} &= \boldsymbol{A} \cdot \delta\boldsymbol{x} + \boldsymbol{B} \cdot \delta\boldsymbol{u} \\
\delta\boldsymbol{y} &= \boldsymbol{C} \cdot \delta\boldsymbol{x} + \boldsymbol{D} \cdot \delta\boldsymbol{u}.
\end{aligned} \tag{3.23}$$

In order to analyze the missile dynamics based on linear EOM, the nonlinear rigid body dynamics (3.1) is linearized at the trim conditions calculated in section 3.1.2.1. The partial derivatives of (3.15) at the equilibrium points are evaluated by using numerical differentiation methods with a fixed step size Δx_i. Because the magnitude of the state $\boldsymbol{x}$ and input vector $\boldsymbol{u}$ vary, the step size Δx_i needs to be scaled with respect to the considered state x_i. The linearization results in this thesis are obtained by using a one dimensional five-point stencil method with a fixed step size Δx_i [84].

3.2.2 Longitudinal Dynamics

Due to the axial symmetry of the missile body, the dynamics of the lateral and longitudinal acceleration outputs are equal. Therefore, it is sufficient to consider only the longitudinal dynamics. For this

purpose the linearized models are obtained at the equilibrium points described by the trim results of the horizontal steady-state flight (see section 3.1.2.1).

3.2.2.1 Linearized System Dynamics of Longitudinal Motion

At first, the missile dynamics is linearized without the influences of the actuator and sensor unit. The general linearized longitudinal dynamics of an aircraft is fully described by $\boldsymbol{x} = \begin{bmatrix} \left(V_K^G\right)^E & \alpha_K & \left(q_K^{EB}\right)_B & \Theta \end{bmatrix}^T$. Since only small deviations from the trimmed horizontal steady state flight condition $\boldsymbol{x}_0$ are considered, the singularity at $\Theta = 90°$ (see section 2.2.2.4) is avoided. With this justification, the linearized longitudinal dynamics is given by

$$\begin{bmatrix} \dot{V} \\ \dot{\alpha} \\ \dot{q} \\ \dot{\Theta} \end{bmatrix} = \begin{bmatrix} X_V & X_\alpha & 0 & -g \cdot \cos(\gamma_0) \\ Z_V & Z_\alpha & 1 & -\frac{g}{V_0} \cdot \sin(\gamma_0) \\ M_V & M_\alpha & M_q & 0 \\ 0 & 0 & 1 & 0 \end{bmatrix} \cdot \begin{bmatrix} V \\ \alpha \\ q \\ \Theta \end{bmatrix} + \begin{bmatrix} X_\eta \\ Z_\eta \\ M_\eta \\ 0 \end{bmatrix} \cdot \eta. \tag{3.24}$$

For the sake of clarity, the labeling of the linearized states by using δ is neglected and the indexes of the state variables are not labeled. Both the derivation of the linearized longitudinal dynamics (3.24) and the nomenclature are in accordance with [4, 40, 66].

Remark: Another possible full description of the longitudinal dynamics is achieved by replacing the pitch angle Θ with the flight path angle γ_K.

The longitudinal dynamics of an aircraft be subdivided into two characteristic modes: the *phugoid* mode is characterized by the continuous exchange of airspeed and altitude at constant AoA and the *short period* mode describes the fast and heavily damped oscillation about the y_B-axis (under the assumption that the short-period dynamics is stable) [4, 66]. Since an endgame scenario demands very agile maneuvers within a relative short time horizon, the slow phugoid mode is of minor interest for air-defense missiles of the type FGS-X-03 [24]. Therefore, the following investigation based on the linearized missile model focuses only on the short period dynamics. By extracting the dynamics of the respective states α_K and $\left(q_K^{EB}\right)_B$ from (3.24) the short period dynamics results to

$$\begin{aligned} \begin{bmatrix} \dot{\alpha} \\ \dot{q} \end{bmatrix} &= \begin{bmatrix} Z_\alpha & 1 \\ M_\alpha & M_q \end{bmatrix} \cdot \begin{bmatrix} \alpha \\ q \end{bmatrix} + \begin{bmatrix} Z_\eta \\ M_\eta \end{bmatrix} \cdot \eta \\ y = a_z^{IMU} &= \begin{bmatrix} \bar{Z}_\alpha & \bar{Z}_q \end{bmatrix} \cdot \begin{bmatrix} \alpha \\ q \end{bmatrix} + \bar{Z}_\eta \cdot \eta \end{aligned} \tag{3.25}$$

with $y = a_z^{IMU}$ being the linearized acceleration output of (2.48). An equivalent description of the linearized short period dynamics of the missile in (3.25) is given by the Laplace transform of (3.25):

$$\begin{aligned} G_{a_z^{IMU},\eta}(s) &= \frac{b_2 s^2 + b_1 s + b_0}{s^2 - (Z_\alpha + M_q)\, s + Z_\alpha M_q} \\ b_0 &= -M_q \left(Z_\alpha Z_\eta + Z_q + M_\eta\right) + Z_q Z_\eta M_\alpha + Z_\alpha M_\eta + \bar{Z}_\eta Z_\alpha M_q \\ b_1 &= -Z_\eta \left(Z_\alpha + M_q\right) + Z_\alpha Z_\eta + Z_q M_\eta \\ b_2 &= \bar{Z}_\eta \end{aligned} \tag{3.26}$$

Remark: The transfer function $G_{a_z^{IMU},\eta}(s)$ covers only the linearized rigid body dynamics. Thus, no sensor or actuator model is incorporated in (3.26).

3.2.2.2 Analysis of the Linearized Longitudinal Motion

Comparing the transfer function in (3.26) with the standard second order transfer function of an under-damped system [85] the two characteristic parameters, natural frequency

$$\omega_{0,SP} = \sqrt{Z_\alpha M_q} \tag{3.27}$$

and damping ratio

$$\zeta_{SP} = \frac{-\left(Z_\alpha + M_q\right)}{2\sqrt{Z_\alpha M_q}} \tag{3.28}$$

can be determined for the short period dynamics (3.26). Figure 3.9 and fig. 3.10 depict the pole-zero maps ([83, 85]) for the linearized short period dynamics in (3.25). Both plots show the pole and zero changes for the three different missile configuration (table 3.1) with respect to altitude h (fig. 3.9) and Mach number M (fig. 3.10). All eigenvalues lie in the left-half complex plane. This is the confirmation that the herein considered FGS-X-03 is inherently stable.

In case of constant Mach number M, the poles and zeros of the short period dynamics migrate towards the origin with higher altitude h (fig. 3.9). As already discussed in section 3.1.2, an increase in altitude h leads to a decrease in dynamic pressure $\bar{q}$ and therefore to a reduced aerodynamic effectiveness of the missile body. This fact results in reduced agility reflected by the decreasing real parts of the short period eigenvalues of the considered configuration.

For constant altitude h the poles and zeros of the missile's short period dynamics exhibit a migration away from the origin (see fig. 3.10). Since the dynamic pressure $\bar{q} \sim M^2$ is proportional to the squared Mach number, traveling with Mach number leads to increased dynamic performance capabilities.

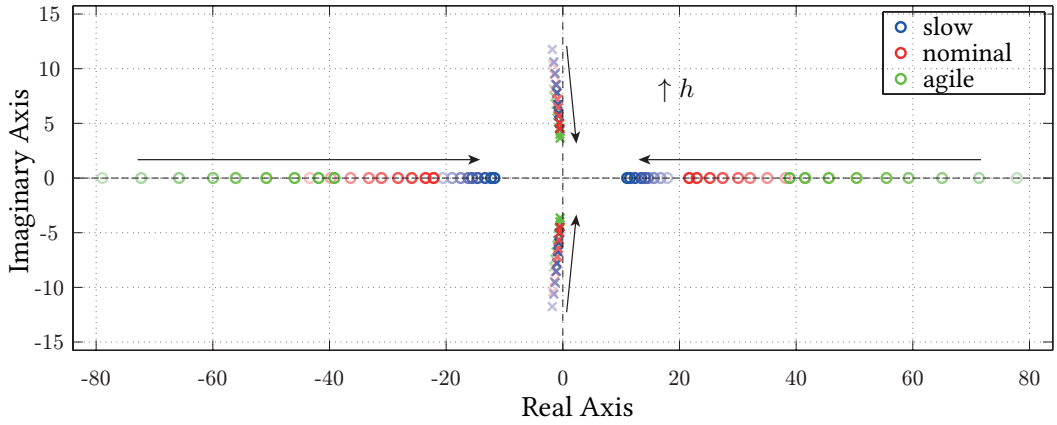

Figure 3.9: Linearized short period dynamics (3.25) for the three different missile configurations (see table 3.1) at the Mach number of $M = 3.7$ and the total altitude range of $h = 0 - 11km$.

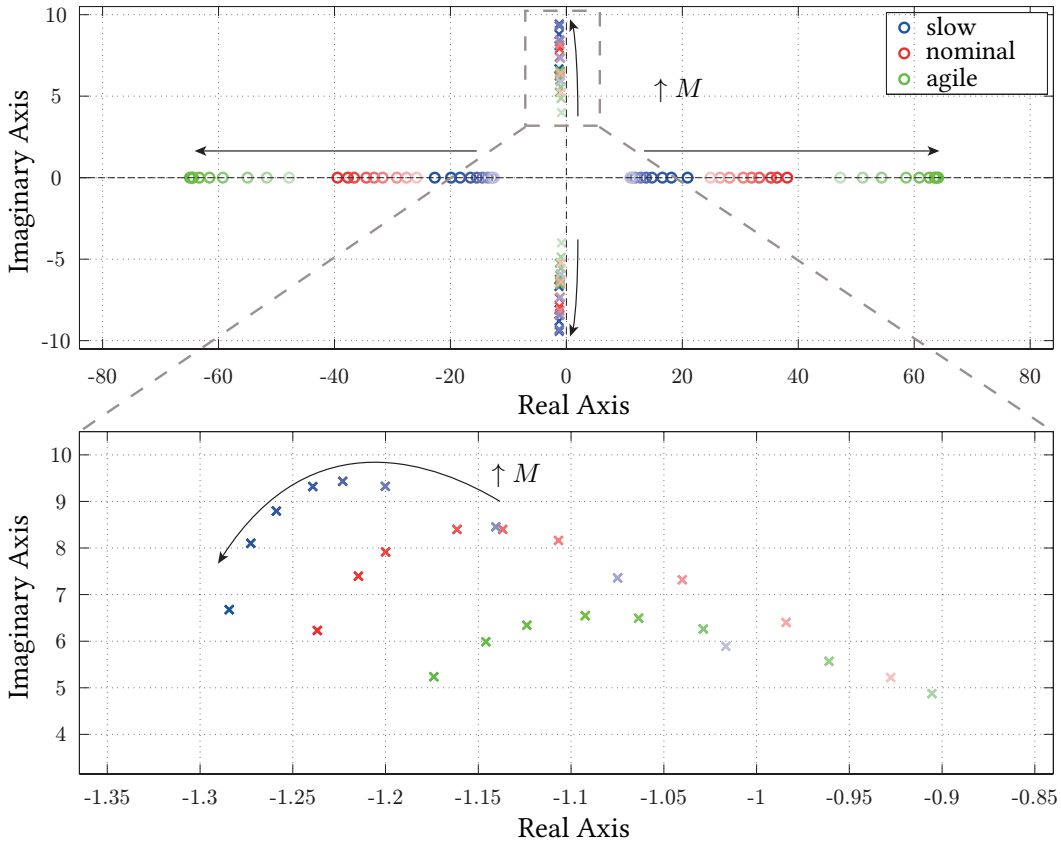

Figure 3.10: Linearized short period dynamics (3.25) for the three different missile configurations (see table 3.1) at the altitude of $h = 3.5km$ and a Mach number range of $M = 2.5-4.4$.

By carefully investigating the location of the system poles for different agile configurations, the interested reader may ask, why an increased agility leads to short period pole pairs with reduced absolute real part. The agility characteristics of a linear system is not only determined by the eigenmotion described by the system's poles, but also characterized by the input effectiveness reflected in the plant's zeros [83]. This is shown by the step responses in fig. 3.11. Figure 3.11a and fig. 3.11b show the response of the AoA α_K and the acceleration $\left(a_z^{IMU}\right)_B$ for a elevator deflection of $\Delta\eta = -1°$, respectively. With an increasing agility, the magnitudes and rise times of the step responses increase, while the settling time decreases [85]. The faster response is due to the increased absolute values of the zeros; the fast transient behavior is related to the smaller real parts of the system's conjugate pole pairs (see fig. 3.9 and fig. 3.10).

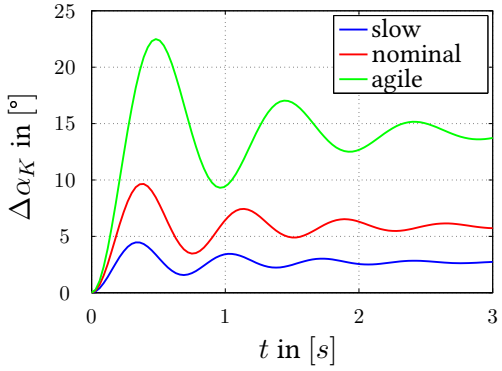

(a) Step responses of the output α_K to an input $\Delta\eta = -1°$.

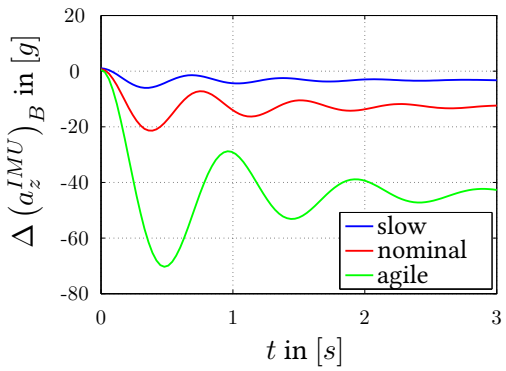

(b) Step responses of the output $\left(a_z^{IMU}\right)_B$ to an input $\Delta\eta = -1°$.

Figure 3.11: Step responses of the linearized short period dynamics (3.25) for a fin deflection of $\Delta\eta = -1°$ at $M = 3.7$ and $h = 3.5km$.

An important parameter of an air defense missile is the bandwidth the system is physically capable of. Fast maneuvering targets or fast altering trajectories require the missile system to exhibit high closed-loop bandwidth. Therefore, the control law on the Flight Control System (FCS) shall be designed to fully exploit the missile's maximum bandwidth. The alteration of bandwidth and phase shift is depicted in fig. 3.12 and fig. 3.13 for the three different agile configurations at a certain altitude h and Mach number M, respectively. Those bandwidths are calculated for the linearized short period dynamics by considering the acceleration $\left(a_z^{IMU}\right)_B$ as output.

As the previous investigations already suggest an increase in dynamic pressure $\bar{q}$ and therefore aerodynamic effectiveness leads to an increase in maneuverability of the missile. With decreasing altitude h and increasing traveling velocity the input/output bandwidth from elevator deflection η to the measured acceleration $\left(a_z^{IMU}\right)_B$ increases. Comparing the magnitudes of different agile configurations at a certain altitude or Mach number, two facts are evident: first, as expected, the bandwidths are larger for more agile configurations due to increased DC gain and second, the *resonant frequency* (also: *cutoff frequency*)

$$\omega_{r,SP} = \omega_{0,SP}\sqrt{1 - 2\zeta_{SP}^2} \tag{3.29}$$

increases for less agile missile parameterizations (see table 3.1). The latter goes hand in hand with the above described eigen dynamics, which tend to be faster in case of reduced agility (see fig. 3.9 and fig. 3.10).

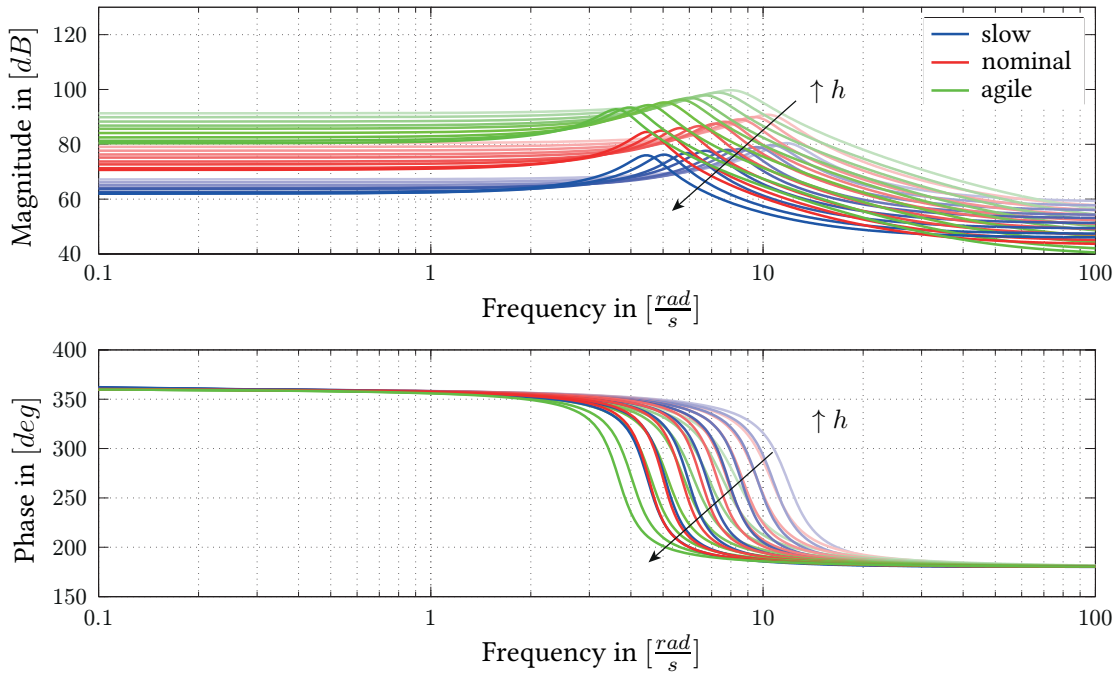

Figure 3.12: Bode plots of short period dynamics (3.25) for the three different missile configurations (see table 3.1) at the Mach number of $M = 3.7$ and the total altitude range of $h = 0 - 11km$.

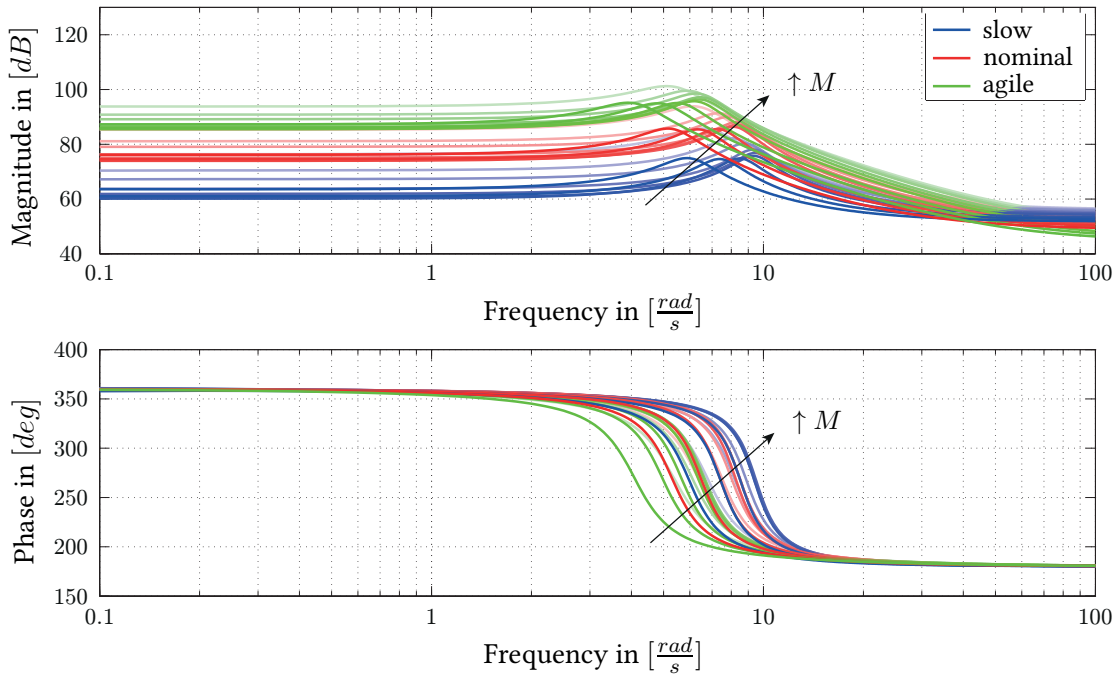

Figure 3.13: Bode plots of short period dynamics (3.25) for the three different missile configurations (see table 3.1) at the altitude of $h = 3.5km$ and a Mach number range of $M = 2.5 - 4.4$.

By considering (3.27) and (3.28), the cutoff frequency of the short period dynamics (3.29) becomes

$$\omega_{r,SP} = \sqrt{Z_\alpha \cdot M_q + (Z_\alpha + M_q)^2}. \tag{3.30}$$

An analytical approximation of the terms Z_α and M_q, which determine $\omega_{r,SP}$, explains the increased resonant frequency for less agile configurations. Those two terms are based on an analytic linearization of the nonlinear short period dynamics. In order to obtain an approximation of the linearized expressions Z_α and M_q, showing the dependencies from aerodynamic and modeling parameters, the AoA and pitch dynamics are considered in the longitudinal plane ($x_B z_B$-plane). Therefore, the rigid body states describing the lateral motion are set to zero: $\beta_K = \left(p_K^{EB}\right)_B = \left(r_K^{EB}\right)_B = \mu_K = 0$. Based on those assumptions, (2.5), and (2.20), the nonlinear short period dynamics result to

$$\dot{\alpha}_K = \frac{-\left(F_{x,A}^G\right)_B \sin\alpha_K + \left(F_{z,A}^G\right)_B \cos\alpha_K}{m\left(V_K^G\right)_{\bar{K}}^E} + \frac{g}{\left(V_K^G\right)_{\bar{K}}^E}\cos\gamma_K + \left(q_K^{EB}\right)_B \tag{3.31a}$$

$$\left(\dot{q}_K^{EB}\right)_B^B = \frac{1}{\left(I_{yy}^G\right)_{BB}}\left(M_A^G\right)_B. \tag{3.31b}$$

The linear approximation Z_α describes the change of the AoA dynamics (3.31) with respect to α_K at a certain trim point. Since the linearization is obtained at horizontal trim conditions (see section 3.1.2.1), the linearization is only valid for small AoA deviations (see fig. 3.2). Thus, the force component $\left(F_{x,A}^G\right)_B \sin\alpha_K$ acting along the missile's rotational axis x_B can be neglected. With this assumption, the substitution $\gamma_K = \Theta - \alpha_K$, and the definition of the aerodynamic force (2.33), the approximated EOM of the AoA short period dynamics is given by

$$\dot{\alpha}_K \approx \frac{(C_z)_B \cos\alpha_K}{m\left(V_K^G\right)_{\bar{K}}^E} + \frac{g}{\left(V_K^G\right)_{\bar{K}}^E}\cos\left(\Theta - \alpha_K\right) + \left(q_K^{EB}\right)_B. \tag{3.32}$$

The approximation sign $\approx$ in (3.32) accounts for the neglected terms compared to (3.31a). An approximation

$$Z_\alpha \approx \frac{\bar{q}_0 S_{ref}}{m\left(V_K^G\right)_{\bar{K},0}^E}\left[-(C_z)_B \cdot \sin\alpha_{K,0} + \left(\frac{\partial (C_z)_B}{\partial \alpha_K}\right)\cdot\cos\alpha_{K,0}\right] + \frac{g}{\left(V_K^G\right)_{\bar{K},0}^E}\sin\gamma_{K,0} \tag{3.33}$$

of the linear expression Z_α is obtained by deriving (3.32) with respect to the AoA, α_K. The index "0" assigns the respective variable to the horizontal trim condition. By pasting the gravity term in (3.33) to the bracket, the three summands in

$$Z_\alpha \approx \frac{\bar{q}_0 S_{ref}}{m\left(V_K^G\right)_{\bar{K},0}^E}\left[\underbrace{-(C_z)_B \cdot \sin\alpha_{K,0}}_{\mathcal{O}(1)} + \underbrace{\left(\frac{\partial (C_z)_B}{\partial \alpha_K}\right)\cdot\cos\alpha_{K,0}}_{\mathcal{O}(10)} + \underbrace{\frac{mg}{\bar{q}_0 S_{ref}}\sin\gamma_{K,0}}_{\mathcal{O}(10^{-3})}\right] \tag{3.34}$$

can be compared according to their order. From this investigation it becomes obvious, that the aerodynamic derivative $\partial(C_z)_B/\partial\alpha_K$ has a dominating effect on the linearization of (3.31a) with respect to α_K. Since the derivative of $(C_z)_B$ with respect to α_K is negative (see appendix B.1.1.3) and dominating the expression (3.34), it follows that $Z_\alpha < 0$. Considering the introduced multiplicative uncertainties in table 3.1, a less agile configuration leads to a reduced absolute value of Z_α. This is consistent with the expectations from flight physics: the body of an agile configuration has increased aerodynamic effectiveness compared to a missile body of a less agile configuration. The second factor M_q describes the dependency of the pitch dynamics from the pitch rate $\left(q_K^{EB}\right)_B$. With

the application rule of the aerodynamic data set (see (2.36)), (3.31b) the pitch rate dynamics can be extended to

$$\left(\dot{q}_K^{EB}\right)_B^B = \frac{\bar{q} S_{ref} l_{ref}}{\left(I_{yy}^G\right)_{BB}} \left(C_{m,0} + \frac{\left(q_K^{EB}\right)_B l_{ref}}{2\left(V_K^G\right)_B^E} C_{m,q} + C_{m,\eta} \right). \tag{3.35}$$

Since the pitch rate $\left(q_K^{EB}\right)_B$ appears linearly in (3.35), the partial derivation $\partial\left(\dot{q}_K^{EB}\right)_B^B / \partial\left(q_K^{EB}\right)_B$ with respect to $\left(q_K^{EB}\right)_B$ is trivial and gives

$$M_q = \frac{\bar{q}_0 S_{ref} l_{ref}^2}{2\left(V_{K,0}^G\right)_B^E \left(I_{yy}^G\right)_{BB}} C_{m,q}. \tag{3.36}$$

Due to the inherently stable FGS-X-03, $C_{m,q} < 0$ is negative over the entire flight envelope. Therefore, according to (3.36) $M_q < 0$ is negative for all trim points. In case of the moment damping coefficients, a more agile missile configuration reduces those aerodynamic parameters.

Since force coefficients can be estimated with higher accuracy compared to moment damping coefficients, the uncertainty $\Delta C_{m,q}$ has a larger standard deviation compared to $\Delta C_{z,0}$. This affects the linearized terms M_q and Z_α in an equal proportion. Due to this inherent uncertainty characteristics, the resonant frequency $\omega_{r,SP}$ (3.30) is more sensitive to changes in M_q. Therefore, the cutoff frequency $\omega_{r,SP}$ increases with reduced agility and decreases for more agile missile configurations.

The investigation so far explains the missile's physical performance capabilities and their change with respect to different operating points based on linearization of the missile's rigid body dynamics. To conclude the missile's performance investigation the effect of the actuator and sensor unit (described in section 2.5) on the open-loop bandwidth and phase shift is considered. The impact of the sensor and actuator unit on the input/output characteristic of the missile provides important information for control design.

The second order actuator dynamics explained in section 2.5.1 has the following linear transfer function $G_{\delta_i,\delta_{i,c}}(s)$, from the commanded $\delta_{i,c}$ to the actual fin deflection δ_i:

$$\delta_i = \frac{\omega_{fin}^2}{s^2 + 2\zeta_{fin}\omega_{fin} + \omega_{fin}^2} \cdot \delta_{i,c} = G_{\delta_i,\delta_{i,c}}(s) \cdot \delta_{i,c} \tag{3.37}$$

$G_{\delta_i,\delta_{i,c}}(s)$ represents the transfer function of a single fin. Since the mapping between the aerodynamic equivalent controls and the actual fin deflections δ_i is linear (see (2.46)), the same transfer function (3.37) holds for the linearized dynamics of the commanded η_c to the actual fictive control η (denoted as $G_{\eta,\eta_c}(s)$). Combining the missile's linearized short period dynamics (3.26) with the actuator dynamics (3.37) and the transfer function of the Inertial Measurement Unit (IMU) (see table 2.4)

$$G_{a_{z,meas}^{IMU},a_z^{IMU}} = \frac{1}{T_{IMU} \cdot s + 1}, \tag{3.38}$$

the overall system linear dynamics $G_{a_z^{IMU},\eta}(s)$ can be written as

$$\begin{aligned} G_{a_{z,meas}^{IMU},\eta_c}(s) &= G_{a_{z,meas}^{IMU},a_z^{IMU}} \cdot G_{a_z^{IMU},\eta}(s) \cdot G_{\eta,\eta_c}(s) \\ &= \frac{1}{T_{IMU}s + 1} \cdot \frac{b_2 s^2 + b_1 s + b_0}{s^2 - (Z_\alpha + M_q)\, s + Z_\alpha M_q} \cdot \frac{\omega_{fin}^2}{s^2 + 2\zeta_{fin}\omega_{fin} + \omega_{fin}^2}. \end{aligned} \tag{3.39}$$

Figure 3.14 compares the frequency responses of the missile configuration with (solid line) and without (dashed line) actuator and sensor subsystem at $M = 3.7$ and $h = 3.5km$. In order to see the

attenuation effect of the sensor and actuator unit the axis scale is changed up to $1000^{rad}/_{s}$ compared to fig. 3.12 and fig. 3.13.

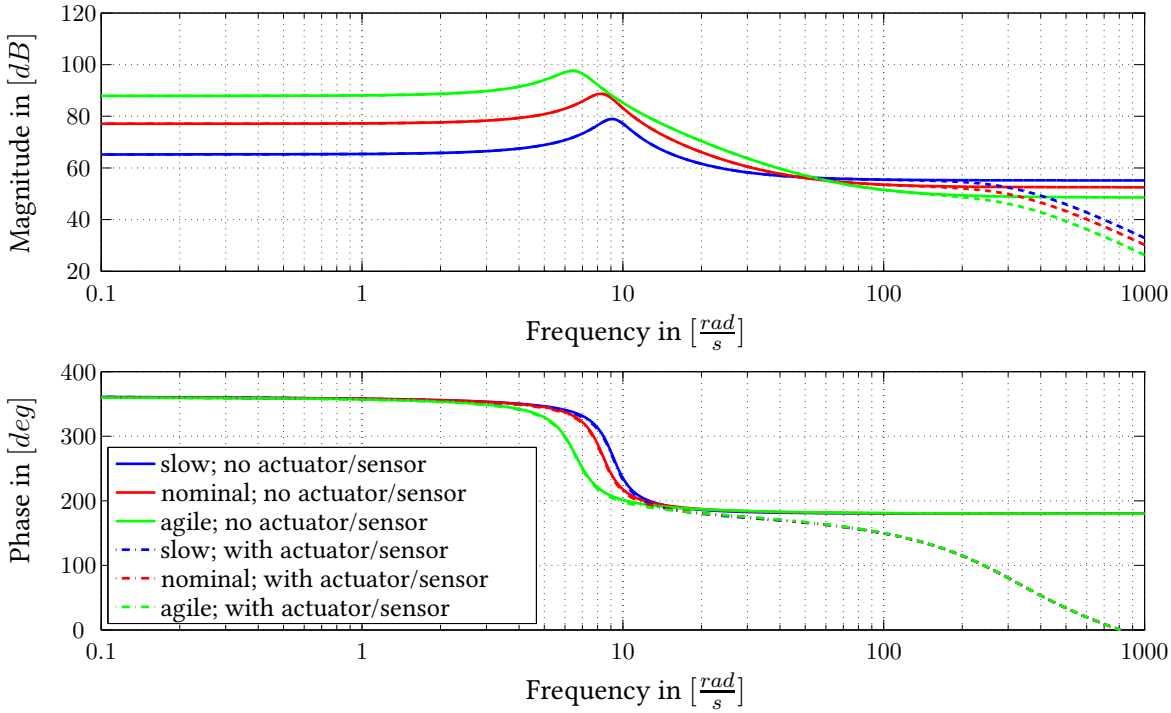

Figure 3.14: Bode plots of short period dynamics (3.25) for the three different missile configurations (see table 3.1) with and without sensor and actuator subsystems at the altitude of $h = 3.5km$ and Mach number $M = 3.7$.

Figure 3.14 shows that the actuator transfer function introduces a further bandwidth attenuation at $\omega \approx 220^{rad}/_{s}$. Due to the fast IMU time constant T_{IMU} another bandwidth reduction occurs around $\omega \approx 1260^{rad}/_{s}$ (see fig. 3.14). Thus, both subsystem have minor influence on the bandwidth and phase shift of the short period dynamics within the frequency domain of $\omega = 0 - 100^{rad}/_{s}$.

3.2.3 Roll Dynamics

Since the herein considered missile is steered in Skid-To-Turn (STT) mode, a fixed roll axis orientation is required to achieve the desired lateral and longitudinal acceleration commands. Therefore, disturbances in the roll channel stemming from the kinematic and aerodynamic cross-coupling need to be compensated fast. The roll angle ϕ_v defined in (2.18) constitutes the control variable. This variable is obtained by integrating the body rates $\left(\boldsymbol{\omega}_K^{EB}\right)_B$ contribution along the velocity vector. Considering (2.18) in combination with the restriction of $\vartheta_K \leq 25°$ it is obvious that the roll angle ϕ_v mainly depends on the roll rate $\left(p_K^{EB}\right)_B$. Thus, the roll rate dynamics is investigated in terms of bandwidth and open-loop behavior for later control layout purposes.

3.2.3.1 Linearized System Dynamics of Roll Motion

A linearized representation of the roll dynamics in time

$$\dot{p} = L_p \cdot p + L_\xi \cdot \xi \tag{3.40}$$

and frequency domain

$$\begin{aligned} p &= \frac{L_\xi}{s - L_p}\xi \\ &= G_{p,\xi}(s)\xi \end{aligned} \tag{3.41}$$

is obtained at the calculated horizontal steady-state conditions in section 3.1.2.1.

3.2.3.2 Analysis of the Linearized Roll Motion

Figure 3.15 and fig. 3.16 depict the pole movement of (3.41) for the three uncertainty configurations in dependency of varying altitude h and Mach number M, respectively. Similar to the pole zero movement in section 3.2.2 high altitudes and lower Mach numbers lead to a movement of the stable poles (left-half complex plane) towards the origin.

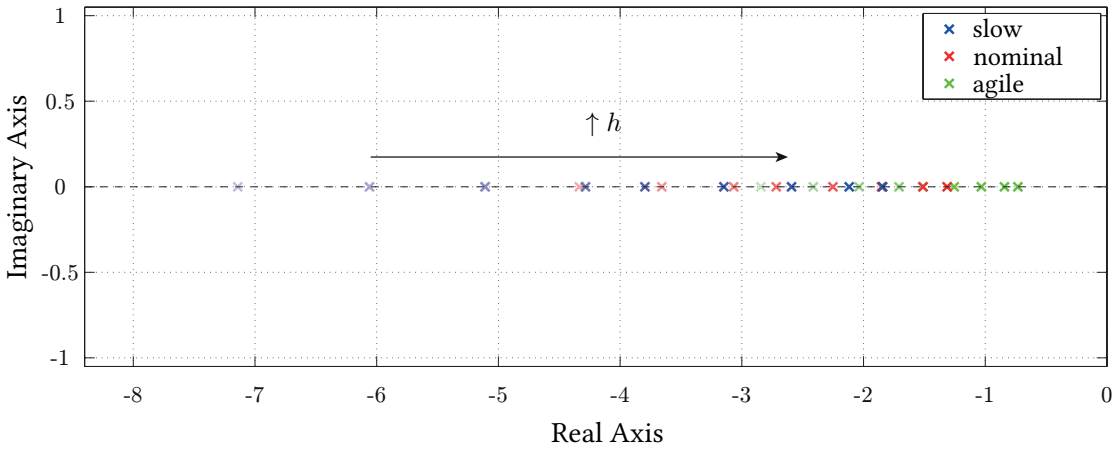

Figure 3.15: Linearized roll dynamics (3.40) for the three different missile configurations (see table 3.1) at the Mach number of $M = 3.7$ and the total altitude range of $h = 0 - 11km$.

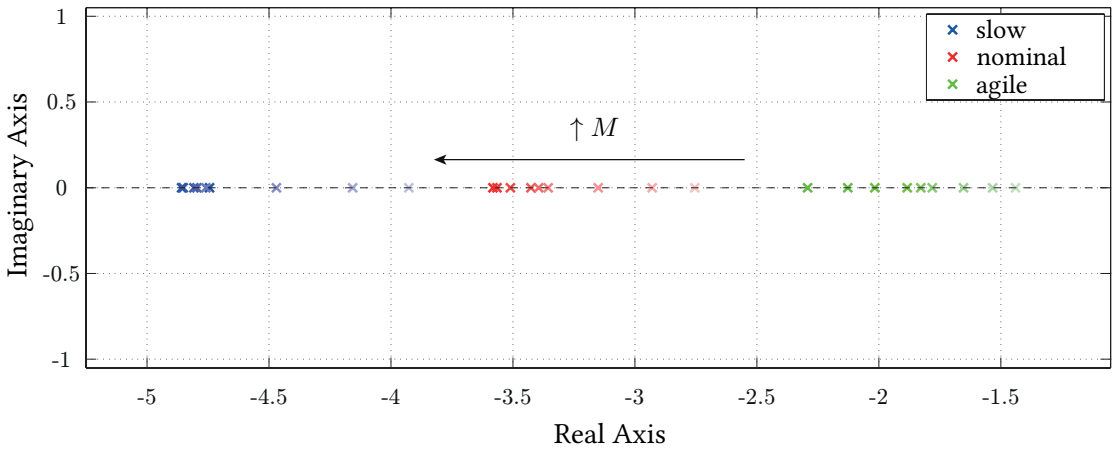

Figure 3.16: Linearized roll dynamics (3.40) for the three different missile configurations (see table 3.1) at the altitude of $h = 3.5km$ and a Mach number range of $M = 2.5 - 4.4$.

As already discussed in section 3.2.2, a more agile configuration entails an increased bandwidth of the transfer function from the aerodynamic equivalent control ξ to the roll rate $\left(p_K^{EB}\right)_B$. At lower altitudes h and Mach numbers M the effectiveness of the aerodynamic control surfaces increases. This physical property is covered by the linearized parameter L_ξ, which increases with enhanced agility of the missile system.

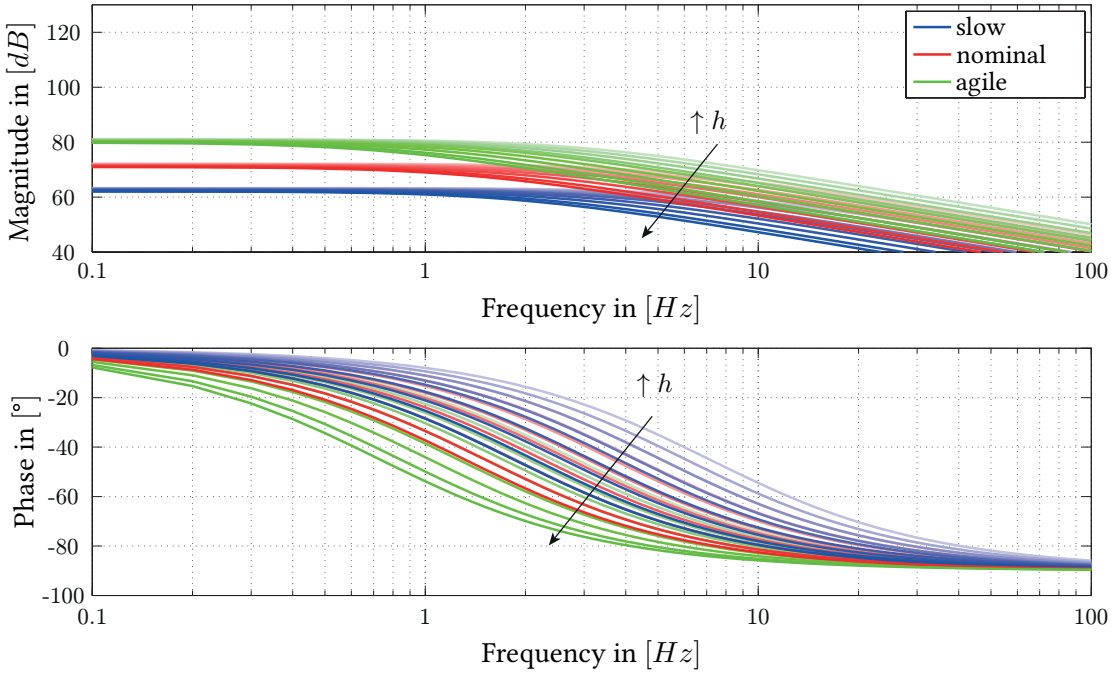

Figure 3.17: Bode plots of roll dynamics (3.25) for the three different missile configurations (see table 3.1) at the Mach number of $M = 3.7$ and the total altitude range of $h = 0-11km$.

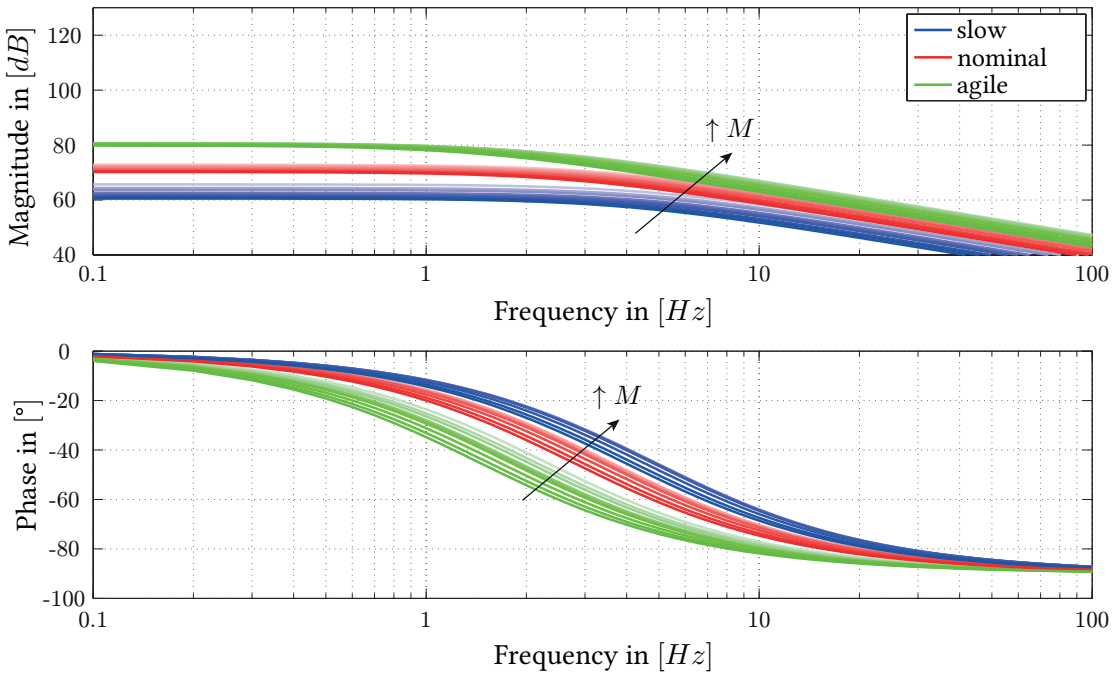

Figure 3.18: Bode plots of roll dynamics (3.25) for the three different missile configurations (see table 3.1) at the altitude of $h = 3.5km$ and a Mach number range of $M = 2.5 - 4.4$.

Finally, the linear input/output characteristic of the roll dynamics is considered under the influence of the actuator and sensor dynamics similar to the investigation at the end of section 3.2.2. The overall linear dynamics from the missile's equivalent aileron control input ξ to the roll rate $\left(p_K^{EB}\right)_B$ including the sensor and actuator dynamics is given by

$$\begin{aligned} G_{p_{meas},\xi_c}(s) &= G_{p_{meas},p} \cdot G_{p,\xi}(s) \cdot G_{\xi,\xi_c}(s) \\ &= \frac{1}{T_{IMU}s + 1} \cdot \frac{L_\xi}{s - L_p} \cdot \frac{\omega_{fin}^2}{s^2 + 2\zeta_{fin}\omega_{fin} + \omega_{fin}^2}. \end{aligned} \tag{3.42}$$

This derivation is obtained analogously to (3.39). Similar to fig. 3.14 the bode plot of the roll dynamics $G_{p_{meas},\xi_c}(s)$ exhibits a bandwidth attenuation due to the actuator dynamics at $\omega \approx 220^{rad/s}$ (fig. 3.19). Like in fig. 3.14 the IMU introduces a further reduction in bandwidth.

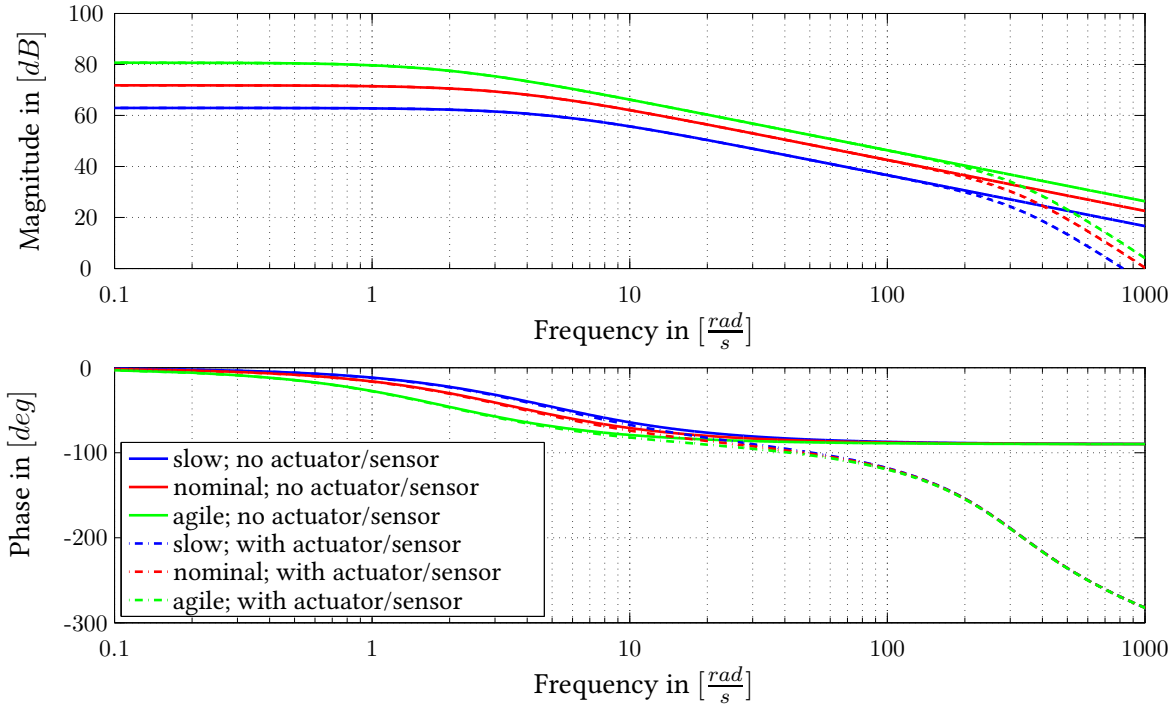

Figure 3.19: Bode plots of roll dynamics for the three different missile configurations (see table 3.1) with and without sensor and actuator subsystems at the altitude of $h = 3.5km$ and Mach number $M = 3.7$.

In summary, the results of section 3.2.2 and section 3.2.3 depict a strong dependency of the dynamical characteristics with respect to the chosen configuration and the considered flight envelope point. Since the missile dynamics is highly nonlinear, the conclusion drawn on linearization techniques needs to be treated with caution. The results presented in section 3.2.2 and section 3.2.3 provide the control designer with a notion about the dynamic system performance and a reference point for the control design phase.

3.3 Nonlinear Analysis of the Missile Dynamics

Deeper insight and more accurate information about the considered missile dynamics can be obtained by nonlinear analysis. Due to its limited applicability only certain aspects of the plant dynamics can be investigated. Within this section the dynamical properties in terms of roll, pitch and yaw time constants are analyzed. These time constants serve as inputs for the control design process, especially the determination of certain performance requirements. By utilizing those accurate information about the nominal dynamics within the control design process, the closed-loop response is expected to better exploit the missile's performance capabilities.

The estimation of roll (T_p), pitch (T_q), and yaw (T_r) time constants is conducted via channel-wise optimization of the error $e_{\boldsymbol{\omega}_i}$ between the trajectory $\left(\boldsymbol{\omega}_K^{EB}\right)_{B,i}(t)$ of the body rates obtained from simulation output and the respective first order reference trajectory $\boldsymbol{\omega}_{i,r}(t)$. The label $i = 1, 2, 3$ refers to the corresponding entry of $\left(\boldsymbol{\omega}_K^{EB}\right)_B = \begin{bmatrix} p_K^{EB} & q_K^{EB} & r_K^{EB} \end{bmatrix}_B^T$. The continuous optimization problem

$$\min_{T_{\boldsymbol{\omega}_i}} \Phi_{\boldsymbol{\omega}_i} = e_{\boldsymbol{\omega}_i}^2 \tag{3.43}$$

is defined by utilizing a quadratic cost function of the error $e_{\boldsymbol{\omega}_i}(t) = \left(\boldsymbol{\omega}_K^{EB}\right)_{B,i}(t) - \boldsymbol{\omega}_{i,r}(t)$.

The reference $\boldsymbol{\omega}_{i,r}(t)$ is given by the linear first order system

$$T_{\boldsymbol{\omega}_{i,r}} \cdot \dot{\boldsymbol{\omega}}_{i,r}(t) + \boldsymbol{\omega}_{i,r}(t) = \boldsymbol{\omega}_{i,trim}. \tag{3.44}$$

$T_{\boldsymbol{\omega}_{i,r}}$ constitutes the time constant and system's input $\boldsymbol{\omega}_{i,trim}$ denotes the maximum trimmable body rate of the respective channel.

By inverting the rotational dynamics (2.20), abbreviated as $\left(\dot{\boldsymbol{\omega}}_K^{EB}\right)_B^B = \boldsymbol{F}_{\boldsymbol{\omega}}(\boldsymbol{C}_{\boldsymbol{M},\boldsymbol{u}})$, the body-rate $\boldsymbol{\omega}_{i,r}(t)$ of one of the three channels is directly mapped to the associated equivalent aerodynamic fin deflection $\boldsymbol{u}_{c,i}$. Applying this as input to the missile plant model (see fig. 3.20) at trimmed condition results in the trajectory $\left(\boldsymbol{\omega}_K^{EB}\right)_{B,i}(t)$.

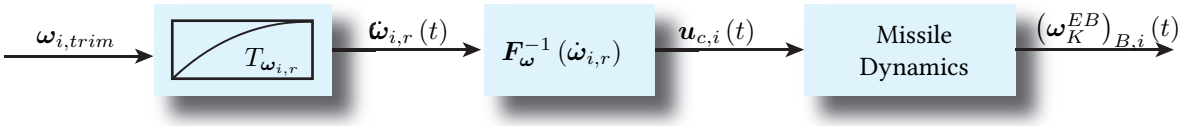

Figure 3.20: Generating $\left(\boldsymbol{\omega}_K^{EB}\right)_{B,i}(t)$ dependent on the time constant $T_{\boldsymbol{\omega}_{i,r}}$ of the first order linear system.

Therefore, by solving the optimization problem (3.43) a time constant $T_{\boldsymbol{\omega}_{i,r}}$ of the linear system (3.44) is identified, which closely approximates the considered body-rate dynamics.

Figure 3.21 shows the resulting time constants of the roll (fig. 3.21a) and pitch channel (fig. 3.21b). Due to the symmetry of the missile body, the dynamic properties of pitch and yaw dynamics can be considered equivalent. Thus, the depiction of the yaw rate's time constant T_r is omitted.

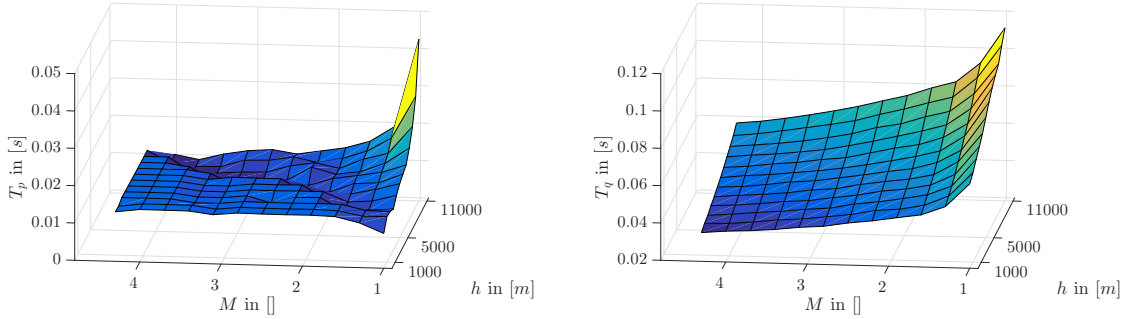

(a) Time constant T_p of approximated roll dynamics. **(b)** Time constant T_q of approximated roll dynamics.

Figure 3.21: Time constant of approximated roll and pitch dynamics using a linear first order system.

As expected, both channels exhibit a rise in the time constant for increased altitude h and reduced Mach number M. This is in line with the expectation that a reduction of dynamic pressure $\bar{q}$ leads to a less agile response of the missile system. According to fig. 3.21, T_p is less sensitive to changes in dynamic pressure than T_q (and therefore T_r). A significant rise in T_p can be observed only at very low speeds $M < 1.5$ and high altitudes $h > 10000m$. The non-monotonic characteristics of T_p over M and h are attributed to numerical inaccuracies within the optimization process. The ratio of the time constant of both control channels ranges between $T_p/T_q = 3 - 6$ (respectively T_p/T_r).

CHAPTER 4

Mathematical Background of Nonlinear Autopilot Design and Analysis

> Imagination is more important than knowledge. Knowledge is limited. Imagination encircles the world.
>
> Albert Einstein

Developments in the field of missile subsystems lead to more agile airframe configurations, more precise actuators, and enhanced measurement units. The perfect interplay of sensors, data processing, actuators, and airframe design result in increased performance capabilities and an extended flight envelope. Due to the enhanced operating domain, the dynamic description of those systems lead to more complex nonlinear system characteristic. Since the success of classic missile autopilot strategies ([24, 64, 86, 87]) rely strongly on the design model of the considered system, an accurate representation of the missile dynamics is necessary to meet the demanding requirements. As already discussed in chapter 2, the identification process of the missile's parameters increases dramatically with an enlarged flight envelope region. In order to fulfill the performance requirements at the entire set of physical possible operating points and to maintain the desired closed-loop response in cases of a large set of parametric uncertainties, an autopilot architecture is necessary, which fully exploits the physical capabilities of the plant even under large deviations between the plant and design model.

The inherently nonlinear, fast changing dynamics of high agile missiles in combination with unknown dependencies in the modeled aerodynamics and a variety of parametric uncertainties (see section 2.4) led over recent years to an increased application of novel nonlinear and adaptive control methodologies for missile autopilot design [20, 21, 38, 58]. This development was supported by theoretical advances in the respective control methodology. In the field of nonlinear control approaches, the two most powerful techniques, Backstepping (BS) and Nonlinear Dynamic Inversion (NDI) ([35, 42]) were tailored to industry needs based on novel sensor equipment and new theoretical considerations. In contrast to the basis methodologies of BS and NDI, advanced versions like [41, 88] result in compact implementations and therefore perfectly suitable for control design of complex nonlinear systems (like missiles).

On the basis of mathematical advances in control theory [63, 89, 90] promising approaches evolved from the first steps and experiences in adaptive flight control [52, 53]. Reliability and applicability

for systems with large uncertainties and changed vehicle configuration has been already proved via various flight tests on different aeroal platforms [91, 92].

It is common in adaptive flight control architectures that the control task is distributed among two elements: on the one hand the *baseline* control law, which is designed to achieve a certain performance for the nominal design model dynamics and on the other hand the robustification of this desired closed-loop response by the so-called *adaptive augmentation* [20, 58, 66, 71]. Nevertheless, holistic approaches based on an integral architecture are justifiable in cases performances is not the main driver of autopilot design and the plant characteristics matches the theoretical requirements of the applied methodology [49, 93].

Along with the control algorithm itself, the Flight Control System (FCS) for high-agile aerial vehicle may include additional elements. Figure 4.1 depicts a generalized missile autopilot scheme. The command signal $\boldsymbol{y}_c$ issued by the guidance unit (see fig. 1.3) is filtered by the *reference model* to obtain a smooth reference signal $\boldsymbol{y}_r$ including potential derivatives $\dot{\boldsymbol{y}}_r, \ldots$ and state trajectories $\boldsymbol{x}_r, \dot{\boldsymbol{x}}_r, \ldots$. Besides filtering the commanded guidance signal $\boldsymbol{y}_c$, the reference model constrains the outputs $\boldsymbol{y}_r, \dot{\boldsymbol{y}}_r, \ldots$ and forwarded reference states $\boldsymbol{x}_r, \dot{\boldsymbol{x}}_r, \ldots$ in accordance to the system's physical capabilities at the considered operating point. Thus, the reference model shall provide the control algorithm with a physically feasible and smooth reference signal. The motivation for *shaping* of the commanded guidance signal lies in the significant workload reduction of the control algorithm, especially integrator parts. In cases where the physical input of the plant $\boldsymbol{u}$ would result in too complex mathematical expressions, a so-called *pseudo-control* variable is used(here: $\boldsymbol{\nu}$) to facilitate the control layout process. The last step within the autopilot data processing comprises of mapping this pseudo-control variable to the physical system input (e.g. fin deflections) and forwarding it to the actuation unit. For the purpose of missile control design it is common to assign one aerodynamic equivalent pseudo-control variable (ξ, η, ζ) per body axis (see section 2.5.1) instead of using the deflections of each single fin (δ_i, $i = 1..4$) [38, 40, 58]. The analytical mapping of the control algorithm's output $\boldsymbol{\nu}$ to the corresponding system input $\boldsymbol{u}_c$ is realized by the *control allocation*.

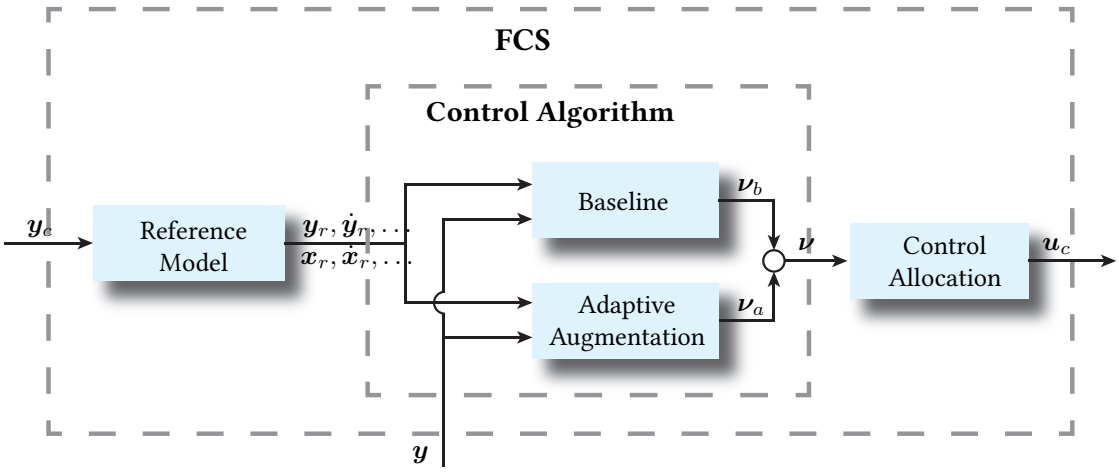

Figure 4.1: Elements of a nonlinear FCS with adaptive augmentation.

Within this chapter the theoretical background of selected control approaches is explained in detail. In the following chapter, the theory is introduced with regard to missile control design. Proofs, which do not provide the reader with additional information are omitted in the text. The interested reader is referred to the cited literature for further information about the respective control theory.

4.1 Stability of Nonlinear Systems

The underlying purpose of each control design approach is the tracking of the reference input by respecting certain stability, robustness, and performance requirements. Since stability is a major driver in the derivation of control methodologies, control design approaches can be categorized according to the underlying stability theorem (e.g.: Lyapunov, contraction theory, small-gain theorem (SGT)) [35, 42, 54, 94]. In case of linear system theory, a wide spectrum of methods and tools exist for evaluating the system's stability characteristics. Considering the class of nonlinear systems, only a few system characteristics can be analyzed. One of the central methods in stability analyzes of nonlinear systems was founded by Lyapunov in 1892, the so-called *Lyapunov's direct method of stability*. While his indirect (first) method uses the linearization of the dynamics, the direct (second) method is is inspired by energy consideration of the nonlinear system [42, 54]. This section briefly introduces the main stability properties of dynamical systems and Lyapunov's direct method of stability following the notation and the concept of [42, 94].

For this purpose the autonomous, nonlinear system

$$\dot{\boldsymbol{x}} = \boldsymbol{f}(\boldsymbol{x}) \tag{4.1}$$

is introduced. The function $\boldsymbol{f}(\boldsymbol{x}) \in \mathbb{R}^{n\times 1}$ describes the system dynamics with $\boldsymbol{x} \in \mathbb{R}^{n\times 1}$ denoting the state vector. Since stability is a property related to a certain equilibrium point $\boldsymbol{x}_0$, the equilibrium condition of the autonomous systems (4.1) is introduced in the following.

Definition 4.1.1 (*Equilibrium Point*)

A state $\boldsymbol{x}_0$ is denoted as an equilibrium point $\boldsymbol{x}_0$ of the autonomous system (4.1) *if*

$$\boldsymbol{f}(\boldsymbol{x}_0) \equiv 0.$$

4.1.1 Stability Properties of Nonlinear Systems

Before introducing different stability properties, the reader needs to be familiarized with the standard nomenclature concerning the solution of (4.1). The state trajectory, which starts from the point $\boldsymbol{x}(t_0)$ at $t_0 \geq 0$ is denoted as $\boldsymbol{x}(t; t_0, \boldsymbol{x}(t_0))$ [54].

Further stability definitions, which are beyond the scope of this thesis, can be found in [42, 80, 95]. The stability characteristics of dynamical systems listed in definitions 4.1.2 to 4.1.5 build the basis for Lyapunov's direct method of stability. The main idea of the following stability definitions is to provide some measure for the trajectory $\boldsymbol{x}(t; t_0, \boldsymbol{x}(t_0))$ in relation to the equilibrium point $\boldsymbol{x}_0$ and under consideration of the solution's starting point $\boldsymbol{x}(t_0)$. Without loss of generality, it can be assumed that equilibrium $\boldsymbol{x}_0 = \boldsymbol{0}$ coincides with the origin.

Definition 4.1.2 (*Stable*)

*The equilibrium point $\boldsymbol{x}_0 = \boldsymbol{0}$ is said to be **stable** (in the sense of Lyapunov) if for every $\epsilon > 0$ there exists a $\delta = \delta(\epsilon) > 0$ such that*

$$\|\boldsymbol{x}(0)\| < \delta \Rightarrow \|\boldsymbol{x}(t)\| < \epsilon, \quad \forall t \geq 0.$$

Definition 4.1.3 (*Asymptotically Stable*)

*The equilibrium point $\boldsymbol{x}_0$ is said to be **asymptotically stable** if it is stable according to definition 4.1.2, and there exists a δ such that*

$$\|\boldsymbol{x}(0)\| < \delta \Rightarrow \lim_{t\to\infty} \boldsymbol{x}(t) = \mathbf{0}.$$

Definition 4.1.4 (*Unstable*)

*The equilibrium point $\boldsymbol{x}_0$ is said to be **unstable** if it is not stable according to definition 4.1.2.*

Definition 4.1.5 (*Bounded*)

*The solution $\boldsymbol{x}(t; t_0, \boldsymbol{x}(t_0))$ of (4.1) is said to be **bounded** if there exists a constant $\gamma(t_0, \boldsymbol{x}(t_0))$, which may depend on each solution such that*

$$\boldsymbol{x}(t; t_0, \boldsymbol{x}(t_0)) < \gamma(t_0, \boldsymbol{x}(t_0)).$$

The stability properties considered in definitions 4.1.2 to 4.1.4 are only valid within a certain state space region containing the equilibrium. All stability conditions (definitions 4.1.2 to 4.1.5) hold globally, if the radius approaches infinity, $\delta \to \infty$.

4.1.2 Lyapunov's Direct Method of Stability

One of the most important stability concepts of nonlinear system theory is Lyapunov's direct method of stability. Inspired by the concept of energy and its dissipation within physical systems, the method only requires the knowledge of the system dynamics $\boldsymbol{f}(\boldsymbol{x})$. Considering the dissipation rate of this generalized system "energy", the stability properties can be categorized according to definitions introduced in section 4.1.1. Thus, the exact solution $\boldsymbol{x}(t; t_0, \boldsymbol{x}(t_0))$ of (4.1) is not necessary to determine the system's stability.

Before defining the stability criteria of nonlinear systems according to Lypaunov's direct method, a few characteristics of scalar functions depending on vector arguments are introduced. Further theoretical background and the according proofs can be found in [42, 54].

Without loss of generality the equilibrium point of (4.1) is assumed to be in the origin, $\boldsymbol{x}_0 = \mathbf{0}$.

Definition 4.1.6 (*Positive Definite Functions*)

*A function $V(\boldsymbol{x}) : \mathbb{R}^{n\times 1} \to \mathbb{R}$ is said to be **positive definite** if*

$$V(\mathbf{0}) = 0, \quad V(\boldsymbol{x}) > 0 \quad \forall \boldsymbol{x} \in \mathbb{R}^{n\times 1} \setminus \{\mathbf{0}\}$$

holds.

Definition 4.1.7 (*Negative Definite Functions*)

*A function $V(\boldsymbol{x}) : \mathbb{R}^{n\times 1} \to \mathbb{R}$ is said to be **negative definite** if $-V(\boldsymbol{x})$ is positive definite according to definition 4.1.6.*

Definition 4.1.8 (*Semidefinite Functions*)

*A function $V(\boldsymbol{x}) : \mathbb{R}^{n\times 1} \to \mathbb{R}$ is said to be **positive (negative) semi-definite** if*

$$V(\boldsymbol{x}) \geq 0 \quad (V(\boldsymbol{x}) \leq 0) \quad \forall \boldsymbol{x} \in \mathbb{R}^{n\times 1}$$

holds.

With the time derivative

$$\dot{V} = \frac{\partial V}{\partial \boldsymbol{x}} \cdot \boldsymbol{f}(\boldsymbol{x}) \tag{4.2}$$

of $V(\boldsymbol{x})$ along the solution of (4.1) Lyapunov's direct method of stability is summarized in the following theorem:

Theorem 4.1.9 (*Lyapunov Second Theorem*)

Let $\boldsymbol{mathexpression}_0 = \mathbf{0}$ *be an equilibrium point for* (4.1) *and* $\mathcal{D} \subset \mathbb{R}^{n\times 1}$. *Suppose there exists a positive definite function* $V(\boldsymbol{x}) : \mathcal{D} \to \mathbb{R}$ *with continuous first-order partial derivative* $\dot{V}$, *and* $V(\mathbf{0}) = 0$. *Then the following statements are true:*

i) $\boldsymbol{x}_0 = \mathbf{0}$ *is* ***stable*** *if*

$$\begin{aligned} V(\boldsymbol{x}) &> 0 \quad \forall \boldsymbol{x} \in \mathcal{D} \setminus \{\mathbf{0}\} \\ \dot{V}(\boldsymbol{x}) &\leq 0 \quad \forall \boldsymbol{x} \in \mathcal{D} \end{aligned}$$

ii) $\boldsymbol{x}_0 = \mathbf{0}$ *is* ***asymptotically stable*** *if*

$$\begin{aligned} V(\boldsymbol{x}) &> 0 \quad \forall \boldsymbol{x} \in \mathcal{D} \setminus \{\mathbf{0}\} \\ \dot{V}(\boldsymbol{x}) &< 0 \quad \forall \boldsymbol{x} \in \mathcal{D} \setminus \{\mathbf{0}\} \end{aligned}$$

The proof can be found in [94].

Remark: Within the context of Lyapuno's stability theory a function $V(\boldsymbol{x}) : \mathbb{R}^{n\times 1} \to \mathbb{R}$ is denoted as a *Lyapunov candidate function* if $V(t\boldsymbol{x}) > 0$ is positive definite and the first time derivative $\dot{V}(\boldsymbol{x}) \leq 0$ is negative semi-definite. Those two properties hold also for energy functions of conservative systems in physics: the total potential of a conservative system is ($V > 0$ for all $\boldsymbol{x} \neq \mathbf{0}$) positive definite and systems without external energy supply conserve ($\dot{V} = 0$) or dissipate ($\dot{V} < 0$) energy. Therefore, a Lyapunov function can be regarded as a generalized energy function of the considered system.

The crucial part in proving stability with Lyapunov's direct method is the finding of a suitable Lyapunov function candidate V. Due to the fact that various functions satisfying the property of a Lyapunov function, the assignment of an appropriate Lyapunov function for a certain dynamical (linear or nonlinear) system is not unique. Due to non-uniqueness of V, it is not possible to conclude system's instability based on theorem 4.1.9.

4.2 Nonlinear Control Theory

At first, the two underlying baseline control techniques, NDI and Command Filtered Backstepping (CFB) are introduced in section 4.2.1 and section 4.2.2, respectively. CFB constitutes a novel modification of the BS approach [41]. For the general purpose of introducing the two state feedback methodologies, the general nonlinear system

$$\begin{aligned} \dot{\boldsymbol{x}} &= \boldsymbol{f}(\boldsymbol{x}) + \boldsymbol{G}(\boldsymbol{x}) \cdot \boldsymbol{u} \\ \boldsymbol{y} &= \boldsymbol{h}(\boldsymbol{x}) \end{aligned} \tag{4.3}$$

is considered. The system (4.3) with the state $\boldsymbol{x} \in \mathbb{R}^{n\times 1}$ and the output vector $\boldsymbol{y} \in \mathbb{R}^{m\times 1}$ is affine in the input $\boldsymbol{u} \in \mathbb{R}^{m\times 1}$ and exhibits no direct feed-through. The nonlinear function $\boldsymbol{f} \in \mathbb{R}^{n\times 1}$, the output mapping $\boldsymbol{h} \in \mathbb{R}^{m\times 1}$, and the rows of the input mapping $\boldsymbol{g}_i \in \mathbb{R}^{1\times m}$, $i = 1, \ldots, n$ are smooth vector fields on $\mathbb{R}^{n\times 1}$. It is assumed, that the number of inputs (entering the system in a linear way) equals the number m of the outputs $\boldsymbol{y}$ to be controlled. The system is assumed to be controllable and observable [42].

Remark: For the sake of simplicity, the term *smooth* denotes in this context an infinitely differentiable function (class C^{∞}).

4.2.1 Nonlinear Dynamic Inversion (NDI)

Per definition NDI is not a control technique. NDI approaches transform a nonlinear input/output characteristics to a linear one. Therefore, a NDI controller consists of two parts: the transformation, which renders the input/output dynamics linear (NDI) and control suitable for the remaining linear system, which drives the control error to zero. This section focuses on the theory of NDI and introduces a simple example of a NDI-based feedback controller (see section 4.2.1.4). The following considerations will be made for $\boldsymbol{x} \in U$, where U describes an open subset of $\mathbb{R}^{n\times 1}$ and without loss of generality it is assumed that $\boldsymbol{x}_0$ is an equilibrium point for which $\boldsymbol{f}(\boldsymbol{x}_0) = \boldsymbol{0}$ and $\boldsymbol{h}(\boldsymbol{x}_0) = \boldsymbol{0}$ holds [42, 94].

4.2.1.1 Lie Derivative and Relative Degree

An important property of nonlinear system is the so-called *relative degree* r. The relative degree r_i of a respective system output y_i describes its dynamical dependence with respect to the input vector $\boldsymbol{u}$. For the purpose of deriving the relative degree and obtaining a compact notation of the input/output transformation, the *Lie Derivative* is introduced in definition 4.2.1, describing the rate of change of a scalar function λ along the flow of a vector field $\boldsymbol{f}$.

Definition 4.2.1 (*Lie Derivative*)

Let $\boldsymbol{f} \in \mathbb{R}^{n\times 1}$ be a smooth vector field and $\lambda \in \mathbb{R}$ be a smooth real-valued function both defined on $\boldsymbol{x} \in \mathbb{R}^{n\times 1}$. The derivative of λ along $\boldsymbol{f}$ is called the Lie Derivative

$$
\begin{aligned}
L_{\boldsymbol{f}}\lambda(\boldsymbol{x}) &= \frac{\partial \lambda}{\partial \boldsymbol{x}} \boldsymbol{f}(\boldsymbol{x}) \\
&= \begin{bmatrix} \frac{\partial \lambda}{\partial x_1} & \cdots & \frac{\partial \lambda}{\partial x_n} \end{bmatrix} \cdot \begin{bmatrix} f_1 \\ \vdots \\ f_n \end{bmatrix}
\end{aligned}
$$

of λ along $\boldsymbol{f}$. The k-th repetition of the derivative of λ along $\boldsymbol{f}$ is denoted as

$$
L_{\boldsymbol{f}}^{k}\lambda(\boldsymbol{x}) = L_{\boldsymbol{f}} L_{\boldsymbol{f}}^{k-1}\lambda(\boldsymbol{x}) = \frac{\partial \left(L_{\boldsymbol{f}}^{k-1}\lambda \right)}{\partial \boldsymbol{x}} \boldsymbol{f}(\boldsymbol{x})
$$

with

$$
L_{\boldsymbol{f}}^{0}\lambda(\boldsymbol{x}) = \lambda(\boldsymbol{x}).
$$

For the sake of completeness, the Lie Derivative of λ along the matrix function $\boldsymbol{F}(\boldsymbol{x})$ is introduced in definition 4.2.2.

Definition 4.2.2 (*Lie Derivative*)

Let $\boldsymbol{F} = \begin{bmatrix} \boldsymbol{f}_1 & \dots & \boldsymbol{f}_m \end{bmatrix} \in \mathbb{R}^{n\times m}$ be a matrix consisting of smooth vector fields $\boldsymbol{f}_i \in \mathbb{R}^{n\times 1}$ and $\lambda \in \mathbb{R}$ be a smooth real-valued function both defined on $\boldsymbol{x} \in \mathbb{R}^{n\times 1}$. The Lie Derivative of λ along $\boldsymbol{F}$ is defined as

$$\begin{aligned} L_{\boldsymbol{F}}\lambda(\boldsymbol{x}) &= \frac{\partial \lambda}{\partial \boldsymbol{x}}\boldsymbol{F}(\boldsymbol{x}) \\ &= \begin{bmatrix} L_{\boldsymbol{f_1}}\lambda(\boldsymbol{x}) & \dots & L_{\boldsymbol{f_m}}\lambda(\boldsymbol{x}) \end{bmatrix} \end{aligned}$$

The k-th repetition of the derivative of λ along $\boldsymbol{F}$ is denoted as

$$L_{\boldsymbol{F}}^{k}\lambda(\boldsymbol{x}) = L_{\boldsymbol{F}}L_{\boldsymbol{F}}^{k-1}\lambda(\boldsymbol{x}) = \frac{\partial\left(L_{\boldsymbol{F}}^{k-1}\lambda\right)}{\partial \boldsymbol{x}}\boldsymbol{F}(\boldsymbol{x})$$

with

$$L_{\boldsymbol{F}}^{0}\lambda(\boldsymbol{x}) = \lambda(\boldsymbol{x}).$$

The advantage of the Lie Derivative's compact notation becomes obvious by multiple consecutive derivation of a scalar function (here: λ) along a vector field (here: $\boldsymbol{f}$) or a matrix function.

Here, the introduction of the relative degree r is obtained for a Single-Input-Single-Output (SISO) system before the theory is expanded to Multiple-Input-Multiple-Output (MIMO) systems. Considering the nonlinear SISO system

$$\begin{aligned} \dot{\boldsymbol{x}} &= \boldsymbol{f}(\boldsymbol{x}) + \boldsymbol{g}(\boldsymbol{x})\cdot u \\ y &= h(\boldsymbol{x}) \end{aligned} \tag{4.4}$$

with the system state $\boldsymbol{x} \in \mathbb{R}^{n\times 1}$, the output $y \in \mathbb{R}$ and the affine system input $u \in \mathbb{R}$. The system is described by the nonlinearity $\boldsymbol{f}(\boldsymbol{x}) \in \mathbb{R}^{n\times 1}$ and the state-dependent input vector $\boldsymbol{g}(\boldsymbol{x}) \in \mathbb{R}^{n\times 1}$. All further derivations are based on the assumption that $\boldsymbol{x} \in U$, an open subset of $\mathbb{R}^{n\times 1}$. This subset contains the equilibrium point $\boldsymbol{x}_0 \in U$ ($\boldsymbol{f}(\boldsymbol{x}_0) = \boldsymbol{0}$) of the undriven system [42].

In the instance that the first time derivative of the output

$$\dot{y} = \frac{\partial h(\boldsymbol{x})}{\partial \boldsymbol{x}}\cdot\dot{\boldsymbol{x}} = \frac{\partial h(\boldsymbol{x})}{\partial \boldsymbol{x}}\cdot\boldsymbol{f} + \frac{\partial h(\boldsymbol{x})}{\partial \boldsymbol{x}}\cdot\boldsymbol{g}\cdot u = L_{\boldsymbol{f}}h + L_{\boldsymbol{g}}h\cdot u \tag{4.5}$$

is independent of the input u ($L_{\boldsymbol{g}}h \equiv 0$) for all $\boldsymbol{x} \in U$, the second time derivative of y leads to

$$\ddot{y} = \frac{\partial L_{\boldsymbol{f}}h}{\partial \boldsymbol{x}}\cdot\dot{\boldsymbol{x}} = \frac{\partial L_{\boldsymbol{f}}h}{\partial \boldsymbol{x}}\cdot\boldsymbol{f} + \frac{\partial L_{\boldsymbol{f}}h}{\partial \boldsymbol{x}}\cdot\boldsymbol{g}\cdot u = L_{\boldsymbol{f}}^{2}h + L_{\boldsymbol{g}}L_{\boldsymbol{f}}h\cdot u. \tag{4.6}$$

If the second derivative of y is also not influenced by the input u ($L_{\boldsymbol{g}}L_{\boldsymbol{f}}h \equiv 0$), the procedure of deriving the output y with respect to time is repeated until the input u appears on the right-hand side ($L_{\boldsymbol{g}}L_{\boldsymbol{f}}^{r-1}h \neq 0$).

$$\begin{aligned} \dddot{y} &= \frac{\partial L_{\boldsymbol{f}}^{2}h}{\partial \boldsymbol{x}}\cdot\dot{\boldsymbol{x}} = \frac{\partial L_{\boldsymbol{f}}^{2}h}{\partial \boldsymbol{x}}\cdot\boldsymbol{f} + \frac{\partial L_{\boldsymbol{f}}^{2}h}{\partial \boldsymbol{x}}\cdot\boldsymbol{g}\cdot u = L_{\boldsymbol{f}}^{3}h + \underbrace{L_{\boldsymbol{g}}L_{\boldsymbol{f}}^{2}h}_{=0}\cdot u \\ &\vdots \\ y^{(r)} &= \frac{\partial L_{\boldsymbol{f}}^{r-1}h}{\partial \boldsymbol{x}}\cdot\dot{\boldsymbol{x}} = \frac{\partial L_{\boldsymbol{f}}^{r-1}h}{\partial \boldsymbol{x}}\cdot\boldsymbol{f} + \frac{\partial L_{\boldsymbol{f}}^{r-1}h}{\partial \boldsymbol{x}}\cdot\boldsymbol{g}\cdot u = L_{\boldsymbol{f}}^{r}h + \underbrace{L_{\boldsymbol{g}}L_{\boldsymbol{f}}^{r-1}h}_{\neq 0}\cdot u \end{aligned} \tag{4.7}$$

The number of necessary differentiations is labeled with r, the so-called *relative degree*. The relative degree r of a SISO system describes the number of derivations with respect to time of the output y which are necessary until the system's input u influences the r-th time derivative of the output ($y^{(r)}$). Therefore, the relative degree r can be seen as an input/output property quantifying the number of integration steps until an input signal u is propagated to the output y of a dynamic system. At this point it needs to be stressed, that the relative degree of a system can be influenced by a careful selection of the regarded output y.

By utilizing the Lie Derivative (definition 4.2.1), the relative degree r of a SISO system is defined in the following way:

Definition 4.2.3 (*Relative Degree of a SISO system*)

The nonlinear, affine SISO system in (4.4) *is said to have a strict relative degree r in a neighborhood $\boldsymbol{x}^0 \in U$ if*

$$\begin{aligned} L_{\boldsymbol{g}} L_{\boldsymbol{f}}^{k} h\left(\boldsymbol{x}\right) &\equiv 0, \qquad \forall \boldsymbol{x} \in U, \quad k = 0, \ldots, r-2 \\ L_{\boldsymbol{g}} L_{\boldsymbol{f}}^{r-1} h\left(\boldsymbol{x}^0\right) &\neq 0. \end{aligned} \tag{4.8}$$

In case of a MIMO system the relative degree r is obtained in an analogue way. For the purpose of deriving the relative degree for a MIMO system, each output y_i has to be derived with respect to time until one of the input elements u_j influences the output derivative.

$$\begin{aligned}
\dot{y}_i &= \tfrac{\partial h_i}{\partial \boldsymbol{x}} \cdot \dot{\boldsymbol{x}} &&= \tfrac{\partial h_i}{\partial \boldsymbol{x}} \cdot \boldsymbol{f}\left(\boldsymbol{x}\right) &&+ \tfrac{\partial h_i}{\partial \boldsymbol{x}} \cdot \boldsymbol{G}\left(\boldsymbol{x}\right) \cdot \boldsymbol{u} \\
&&&= L_{\boldsymbol{f}} h_i &&+ \underbrace{L_{\boldsymbol{G}} h_i}_{=\boldsymbol{0}} \cdot \boldsymbol{u} \\
\ddot{y}_i &= \tfrac{\partial L_{\boldsymbol{f}} h_i}{\partial \boldsymbol{x}} \cdot \dot{\boldsymbol{x}} &&= \tfrac{\partial L_{\boldsymbol{f}} h_i}{\partial \boldsymbol{x}} \cdot \boldsymbol{f}\left(\boldsymbol{x}\right) &&+ \tfrac{\partial L_{\boldsymbol{f}} h_i}{\partial \boldsymbol{x}} \cdot \boldsymbol{G}\left(\boldsymbol{x}\right) \cdot \boldsymbol{u} \\
&&&= L_{\boldsymbol{f}}^2 h_i &&+ \underbrace{L_{\boldsymbol{G}} L_{\boldsymbol{f}} h_i}_{=\boldsymbol{0}} \cdot \boldsymbol{u} \\
&\vdots \\
y_i^{(r_i-1)} &= \tfrac{\partial L_{\boldsymbol{f}}^{r_i-2} h_i}{\partial \boldsymbol{x}} \cdot \dot{\boldsymbol{x}} &&= \tfrac{\partial L_{\boldsymbol{f}}^{r_i-2} h_i}{\partial \boldsymbol{x}} \cdot \boldsymbol{f}\left(\boldsymbol{x}\right) &&+ \tfrac{\partial L_{\boldsymbol{f}}^{r_i-2} h_i}{\partial \boldsymbol{x}} \cdot \boldsymbol{G}\left(\boldsymbol{x}\right) \cdot \boldsymbol{u} \\
&&&= L_{\boldsymbol{f}}^{r_i-1} h_i &&+ \underbrace{L_{\boldsymbol{G}} L_{\boldsymbol{f}}^{r_i-2} h_i}_{=\boldsymbol{0}} \cdot \boldsymbol{u} \\
y_i^{(r_i)} &= \tfrac{\partial L_{\boldsymbol{f}}^{r_i-1} h_i}{\partial \boldsymbol{x}} \cdot \dot{\boldsymbol{x}} &&= \tfrac{\partial L_{\boldsymbol{f}}^{r_i-1} h_i}{\partial \boldsymbol{x}} \cdot \boldsymbol{f}\left(\boldsymbol{x}\right) &&+ \tfrac{\partial L_{\boldsymbol{f}}^{r_i-1} h_i}{\partial \boldsymbol{x}} \cdot \boldsymbol{G}\left(\boldsymbol{x}\right) \cdot \boldsymbol{u} \\
&&&= L_{\boldsymbol{f}}^{r_i} h_i &&+ \underbrace{L_{\boldsymbol{G}} L_{\boldsymbol{f}}^{r_i-1} h_i}_{\neq \boldsymbol{0}} \cdot \boldsymbol{u}
\end{aligned} \tag{4.9}$$

The overall input/output dynamics

$$\begin{bmatrix} y_1^{(r_1)} \\ \vdots \\ y_m^{(r_m)} \end{bmatrix} = \underbrace{\begin{bmatrix} L_{\boldsymbol{f}}^{r_1} h_1\left(\boldsymbol{x}\right) \\ \vdots \\ L_{\boldsymbol{f}}^{r_m} h_m\left(\boldsymbol{x}\right) \end{bmatrix}}_{\boldsymbol{b}(\boldsymbol{x})} + \underbrace{\begin{bmatrix} L_{\boldsymbol{g}_1} L_{\boldsymbol{f}}^{r_1-1} h_1\left(\boldsymbol{x}\right) & \cdots & L_{\boldsymbol{g}_m} L_{\boldsymbol{f}}^{r_1-1} h_1\left(\boldsymbol{x}\right) \\ \vdots & \ddots & \vdots \\ L_{\boldsymbol{g}_1} L_{\boldsymbol{f}}^{r_m-1} h_m\left(\boldsymbol{x}\right) & \ldots & L_{\boldsymbol{g}_m} L_{\boldsymbol{f}}^{r_m-1} h_m\left(\boldsymbol{x}\right) \end{bmatrix}}_{\boldsymbol{A}(\boldsymbol{x})} \cdot \begin{bmatrix} u_1 \\ \vdots \\ u_m \end{bmatrix} \tag{4.10}$$

of the nonlinear system (4.3) is described by summarizing all r_i-th derivatives of the respective outputs y_i. These time derivatives are derived in accordance to (4.9). The *decoupling matrix* $\boldsymbol{A}\left(\boldsymbol{x}\right) \in \mathbb{R}^{m \times m}$ is square in case the system (4.3) exhibits the same numbers m of inputs and outputs. The vector $\boldsymbol{b}\left(\boldsymbol{x}\right) \in \mathbb{R}^{m \times 1}$ denotes the accumulation of the remaining nonlinear terms. With the above derivations, the overall relative degree r of a MIMO system is defined as follows:

Definition 4.2.4 (*Relative Degree of a MIMO system*)

The nonlinear MIMO system in (4.3) *has a vector relative degree of* $\{r_1, \ldots, r_m\}$ *in a neighborhood* $\boldsymbol{x}^0 \in U$ *if*

$$L_{\boldsymbol{g}_j} L_{\boldsymbol{f}}^k h_i(\boldsymbol{x}) = 0 \qquad \forall \boldsymbol{x} \in U, \quad 1 \leq j \leq m, \quad k < r_i - 1, \quad 1 \leq i \leq m$$

and the decoupling matrix (see (4.10)*) is nonsingular*

$$\det \boldsymbol{A}(\boldsymbol{x}) \neq 0$$

at $\boldsymbol{x}^0$*. For the overall relative degree*

$$r = \sum_{i=1}^{m} r_i$$

of a nonlinear MIMO system (see (4.3)*) the inequality* $r \leq n$ *holds.*

In the derivation of (4.10) the distinction between the entire state space $\boldsymbol{x}$ and the neighborhood of $\boldsymbol{x}_0 \in U$ was dropped due to simplicity. It is important to note that for a nonlinear MIMO system the conditions in definition 4.2.4 hold only within a certain neighborhood of $\boldsymbol{x}_0 \in U$. Leaving this set of states can lead to uncontrollable outputs y_i (e.g. sign changes of $\boldsymbol{g}_j$), which lead to $rank(\boldsymbol{A}) < m$, and therefore to an undefined relative degree r.

For certain control problems an artificial modification of the input or output, which aims at a well-defined relative degree r, exhibits advantages in terms of applying feedback linearization (e.g. output decoupling) [80]. Especially, in the case of MIMO systems it might happen that the relative degree of the considered input/output characteristics is undefined in a certain state space region, which leads to singularity of the decoupling matrix $\boldsymbol{A}(\boldsymbol{x})$. By using *Dynamic Extension* the input/output characteristics of the plant is altered by adding additional integrators to certain input channels [42], [80].

4.2.1.2 System Transformation and Internal Dynamics

Within this section a coordinate transformation of the system states $\boldsymbol{x}$ is introduced, leading to a linear input/output dynamics of (4.3). Following the derivation of the relative degree in (4.9), a linear coordinate transformation for the i-th output y_i is given by

$$\begin{array}{lllll} \xi_1^i = \Phi_1^i(\boldsymbol{x}) = L_{\boldsymbol{f}}^0 h_i = y_i \\ \xi_2^i = \Phi_2^i(\boldsymbol{x}) = L_{\boldsymbol{f}} h_i = \dot{y}_i \\ \quad \vdots \qquad\qquad\qquad\qquad\qquad . \\ \xi_{r_i}^i = \Phi_{r_i}^i(\boldsymbol{x}) = L_{\boldsymbol{f}}^{r_i} h_i = y_i^{(r_i)} \end{array} \tag{4.11}$$

The so-called external states $\boldsymbol{\xi} = \begin{bmatrix} \xi_1^1 & \ldots & \xi_{r_1}^1 & \xi_1^2 & \ldots \xi_{r_2}^2 & \ldots \xi_{r_m}^m \end{bmatrix}^T$ only qualify as a local coordinate transformation if the relative degree $r = n$ coincides with the system order n of (4.3). In case the relative degree is smaller ($r < n$) than the system order, $n - r$ additional coordinates

$$\begin{array}{ll} \eta_1 = \Phi_{r+1}(\boldsymbol{x}) \\ \eta_2 = \Phi_{r+2}(\boldsymbol{x}) \\ \quad \vdots \\ \eta_{n-r} = \Phi_n(\boldsymbol{x}) \end{array} \tag{4.12}$$

need to be determined to guarantee a bijective mapping

$$\boldsymbol{\Phi} = \begin{bmatrix} \Phi_1^1 & \dots & \Phi_{r_1}^1 & \dots & \Phi_1^m & \dots & \Phi_{r_m}^m & \Phi_{r+1} & \dots & \Phi_n \end{bmatrix}^T \tag{4.13}$$

between

$$\boldsymbol{z} = \begin{bmatrix} z_1 \\ \vdots \\ z_{r_1} \\ \vdots \\ z_{r_1+r_2} \\ \vdots \\ z_r \\ - - - \\ z_{r+1} \\ \vdots \\ z_{r+n} \end{bmatrix} = \begin{bmatrix} L_{\boldsymbol{f}}^0 h_1 \\ \vdots \\ L_{\boldsymbol{f}}^{r_1-1} h_1 \\ \vdots \\ L_{\boldsymbol{f}}^{r_2-1} h_2 \\ \vdots \\ L_{\boldsymbol{f}}^{r_m-1} h_m \\ - - - \\ \Phi_{r+1} \\ \dots \\ \Phi_{r+n} \end{bmatrix} = \begin{bmatrix} \boldsymbol{\xi} \\ - - \\ \boldsymbol{\eta} \end{bmatrix} \tag{4.14}$$

and the state vector $\boldsymbol{x}$. $\boldsymbol{\eta} \in \mathbb{R}^{(n-r)\times 1}$ constitute the *internal states* of the system (4.3). In case the relative degree $r < n$ is smaller than the system order, it is always possible to find $n - r$ internal states such that the Jacobian is nonsingular $\det \partial\boldsymbol{\Phi}/\partial\boldsymbol{x} \neq 0$ at $\boldsymbol{x}_0 \in U$ and therefore $\boldsymbol{z} = \boldsymbol{\Phi}(\boldsymbol{x})$ establishes a local coordinate transformation [80].

Under the assumption that the system possess a vector relative degree of $\{r_1, \dots, r_m\}$, it can be shown that the row vectors of the differentials $dL_{\boldsymbol{f}}^k h_i(\boldsymbol{x}_0)$ are linearly independent for $0 \leq k \leq r_i - 1$ and $1 \leq i \leq m$ if the outputs y_i are independent. Thus, if the rank equals the system order $n = r$, the Jacobian of the mapping $\boldsymbol{z} = \Phi(\boldsymbol{x})$ has full rank (invertible) and therefore $\Phi(\boldsymbol{x})$ is a valid coordinate transformation in a neighborhood $\boldsymbol{x}_0$. In case the relative degree $r < n$ is less than the system order, the $n - r$ additional coordinates (internal states $\boldsymbol{\eta}$) have to be chosen with the purpose of rendering the Jacobian $\frac{\partial\boldsymbol{\Phi}}{\partial\boldsymbol{x}}$ non-singular at $\boldsymbol{x}_0$. It is important to note that the additional state transformations $\Phi_{r+1}, \dots, \Phi_{n-r}$ require to satisfy a set of $n - r$ partial differential equations in order to be linearly independent of (4.11). A detailed discussion about the choice of $\boldsymbol{\eta}$ can be found in [80].

With the above introduced transformation (4.14) and the state transformation of the abbreviations

$$\begin{array}{lcll} a_{ij}(\boldsymbol{\xi}, \boldsymbol{\eta}) & = & L_{\boldsymbol{g}_j} L_{\boldsymbol{f}}^{r_i-1} h_i\left(\boldsymbol{\Phi}^{-1}(\boldsymbol{z})\right) & \text{for } 1 \leq i, j \leq m \\ b_i(\boldsymbol{\xi}, \boldsymbol{\eta}) & = & L_{\boldsymbol{f}}^{r_i} h_i\left(\boldsymbol{\Phi}^{-1}(\boldsymbol{z})\right) & \text{for } 1 \leq i \leq m \end{array} \tag{4.15}$$

the dynamics

$$\begin{array}{lcl} \dot{\xi}_1^i & = & \xi_2^i \\ \dot{\xi}_2^i & = & \xi_3^i \\ & \vdots & \\ \dot{\xi}_{r_i-1}^i & = & \xi_{r_i}^i \\ \dot{\xi}_{r_i}^i & = & b_i(\boldsymbol{\xi}, \boldsymbol{\eta}) + \sum_{j=1}^m a_{ij}(\boldsymbol{\xi}, \boldsymbol{\eta}) \cdot u_j \\ \dot{\boldsymbol{\eta}} & = & \boldsymbol{q}(\boldsymbol{\xi}, \boldsymbol{\eta}) + \sum_{j=1}^m \boldsymbol{p}_j(\boldsymbol{\xi}, \boldsymbol{\eta}) \cdot u_j = \boldsymbol{q}(\boldsymbol{\xi}, \boldsymbol{\eta}) + \boldsymbol{P}(\boldsymbol{\xi}, \boldsymbol{\eta}) \cdot \boldsymbol{u} \end{array} \tag{4.16}$$

given in the coordinates $\boldsymbol{z} = \begin{bmatrix}\boldsymbol{\xi}^T & \boldsymbol{\eta}^T\end{bmatrix}^T$ define the so-called *normal form* [42]. The dynamics of the $r-1$ external states $\xi_1^i, \ldots, \xi_{r_i-1}^i$ exhibit a linear structure (time derivative of $\dot{\xi}_k^i = \xi_{k+1}^i$ is defined by the previous state ξ_{k+1}^i for $1 \leq k \leq r_i - 1$ and $1 \leq i \leq m$). The internal states $\boldsymbol{\eta}$ are unobservable considering the output $\boldsymbol{y}$.

4.2.1.3 Linearizing State Feedback and Zero Dynamics

In this section the dynamic relationship between the input $\boldsymbol{u}$ and the r_i-th derivative of the output elements y_i is used to calculate a state feedback law

$$\begin{aligned}\boldsymbol{u} &= \boldsymbol{A}^{-1}(\boldsymbol{x}) \cdot [\boldsymbol{\nu} - \boldsymbol{b}(\boldsymbol{x})] \\ &= \boldsymbol{A}^{-1}(\boldsymbol{\xi}, \boldsymbol{\eta}) \cdot [\boldsymbol{\nu} - \boldsymbol{b}(\boldsymbol{\xi}, \boldsymbol{\eta})]\end{aligned} \tag{4.17}$$

which renders the closed-loop input/output characteristics linear. $\boldsymbol{\nu} \in \mathbb{R}^{m \times 1}$ constitutes the external reference input, the so-called *pseudo-control*. Considering the stability of the input/output linearized system, the closed-loop dynamics obtained by zeroing the output $\boldsymbol{y} = \boldsymbol{0}$ plays a crucial role. This so-called *zero dynamics* is introduced in the second part of this section and the conditions for stability of the linearized input/output dynamics (4.16) are derived.

With the decoupling matrix $\boldsymbol{A}(\boldsymbol{x})$ being nonsingular (see definition 4.2.4), the static feedback law (4.17) leads to the linearized map

$$\begin{bmatrix} y_1^{(r_1)} \\ \vdots \\ y_m^{(r_m)} \end{bmatrix} = \begin{bmatrix} \nu_1 \\ \vdots \\ \nu_m \end{bmatrix} \tag{4.18}$$

between the pseudo-control $\boldsymbol{\nu}$ and the considered output $\boldsymbol{y}$. By considering the transformation of the nonlinear system (4.18) in the frequency domain

$$\begin{bmatrix} y_1 \\ y_2 \\ \vdots \\ y_m \end{bmatrix} = \begin{bmatrix} \frac{1}{s^{r_1}} & 0 & \cdots & 0 \\ 0 & \frac{1}{s^{r_2}} & \cdots & 0 \\ 0 & \vdots & \ddots & 0 \\ 0 & 0 & \cdots & \frac{1}{s^{r_m}} \end{bmatrix} \cdot \begin{bmatrix} \nu_1 \\ \nu_2 \\ \vdots \\ \nu_m \end{bmatrix}, \tag{4.19}$$

the linearized system exhibits a decoupled characteristics where the pseudo-controls $\boldsymbol{\nu}$ are separated from the outputs by an integrator chain of length r_i in the respective input/output channel. Therefore, some literature calls this procedure *input/output decoupling* [96, 97].

A system with a relative degree $r = n$ equal the number of states is called *exact input/output linearizable* [42]. In this case the external states $\boldsymbol{\xi}$ form a coordinate transformation $\boldsymbol{z} = \boldsymbol{\xi} = \boldsymbol{\Phi}(\boldsymbol{x})$ transforming the nonlinear dynamics into a linear one:

$$\begin{aligned} \dot{\xi}_1^i &= \xi_2^i \\ \dot{\xi}_2^i &= \xi_3^i \\ &\vdots \\ \dot{\xi}_{r_i}^i &= \nu_i \end{aligned} \tag{4.20}$$

Besides linearity, all states ($\boldsymbol{\xi}$ and therefore $\boldsymbol{x}$) are controllable and observable. On the other hand,

if the relative degree is less than the system order $r < n$, the following dynamics

$$\begin{array}{rcl} \dot{\xi}_1^i & = & \xi_2^i \\ \dot{\xi}_2^i & = & \xi_3^i \\ & \vdots & \\ \dot{\xi}_{r_i-1}^i & = & \xi_{r_i}^i \\ \dot{\xi}_{r_i}^i & = & \nu_i \\ \dot{\boldsymbol{\eta}} & = & \bar{\boldsymbol{q}}\left(\boldsymbol{\xi},\boldsymbol{\eta}\right) + \bar{\boldsymbol{P}}\left(\boldsymbol{\xi},\boldsymbol{\eta}\right)\cdot\boldsymbol{\nu} \end{array} \tag{4.21}$$

with the abbreviations (see (4.16))

$$\begin{array}{rcl} \bar{\boldsymbol{P}}\left(\boldsymbol{\xi},\boldsymbol{\eta}\right) & = & \boldsymbol{P}\left(\boldsymbol{\xi},\boldsymbol{\eta}\right)\boldsymbol{A}^{-1}\left(\boldsymbol{\xi},\boldsymbol{\eta}\right) \\ \bar{\boldsymbol{q}}\left(\boldsymbol{\xi},\boldsymbol{\eta}\right) & = & \boldsymbol{q}\left(\boldsymbol{\xi},\boldsymbol{\eta}\right) - \boldsymbol{P}\left(\boldsymbol{\xi},\boldsymbol{\eta}\right)\boldsymbol{A}^{-1}\left(\boldsymbol{\xi},\boldsymbol{\eta}\right)\boldsymbol{b}\left(\boldsymbol{\xi},\boldsymbol{\eta}\right) \end{array} \tag{4.22}$$

results from (4.16) by application of (4.17). Since the equilibrium point is assumed to lead to $\boldsymbol{h} = \boldsymbol{0}$, it follows from the state transformation in (4.11) that $\boldsymbol{\xi} = \boldsymbol{0}$ at $\boldsymbol{x}_0$. From the representation of (4.21) it is straightforward to find i pseudo-control laws $\nu_i = \nu_i\left(\xi_1^i, \ldots, \xi_{r_i}^i\right)$, which asymptotically stabilizes the origin $\boldsymbol{\xi}^i = \begin{bmatrix}\xi_1^i & \ldots & \xi_{r_i}^i\end{bmatrix}^T = \boldsymbol{0}$ (for an example see [42, 80, 94]). Nevertheless, no conclusion can be drawn about the stability property of the internal states $\boldsymbol{\eta}$. A sufficient condition to conclude stability of the entire closed-loop system (4.21), require the remaining internal dynamics to be stable at the equilibrium point $\begin{bmatrix}\boldsymbol{\xi}_0^T & \boldsymbol{\eta}_0^T\end{bmatrix}^T = \boldsymbol{0}$ ($\boldsymbol{\eta}_0 = \boldsymbol{0}$ can be assumed without loss of generality), which coincides with the output to be zero ($\boldsymbol{y} = \boldsymbol{0}$). Since this stability consideration of the internal dynamics demands the output and its derivatives to be zero for all time, this regulation problem is denoted as *Problem of Zeroing the Output* [80]. Therefore, the system's input vector must solve the set of m equations

$$\boldsymbol{b}\left(\boldsymbol{0},\boldsymbol{\eta}\right) + \boldsymbol{A}\left(\boldsymbol{0},\boldsymbol{\eta}\right)\cdot\boldsymbol{u} = \boldsymbol{0} \tag{4.23}$$

leading to the input law

$$\boldsymbol{u} = -\boldsymbol{A}^{-1}\left(\boldsymbol{0},\boldsymbol{\eta}\right)\boldsymbol{b}\left(\boldsymbol{0},\boldsymbol{\eta}\right). \tag{4.24}$$

Applying (4.24) to the system (4.21), the external dynamics remains zero $\boldsymbol{\xi}\left(t\right) = \boldsymbol{0}$ and the internal dynamics results to

$$\dot{\boldsymbol{\eta}} = \bar{\boldsymbol{q}}\left(\boldsymbol{0},\boldsymbol{\eta}\right). \tag{4.25}$$

Due to its crucial role for deriving stability properties of feedback linearized MIMO systems, the internal dynamics resulting by zeroing the output is called *zero dynamics* [42, 80, 94]. In case of a linear system, the eigenvalues of the zero dynamics coincide with the zeros of the system's open-loop transfer function. In contrast to the SISO case, it must be stressed that for non-exact input/output linearizable MIMO systems ($r < n$) that the requirement of asymptotic stability is not necessary in general [80]. A system exhibiting a stable zero dynamics is referred to as a *minimum phase* system:

Definition 4.2.5 (*Minimum Phaseness*)

The nonlinear MIMO system in (4.3) *is said to be locally asymptotically (exponentially) minimum phase at* $\boldsymbol{x}_0$ *if the equilibrium point of the internal states* $\boldsymbol{\eta} = \boldsymbol{0}$ *is locally asymptotically (exponentially) stable.*

As already mentioned, the minimum phase characteristics of a linear system can be concluded from the zeros of the open-loop plant. In the nonlinear case linearization methods are commonly used to either calculate a linear open-loop system representation or to use Lyapunov's direct method to derive the stability property of the zero dynamics (4.25).

Remark: It is important to point out that the minimum phase characteristics of a system depends on

the chosen inputs and outputs and is a property of the open-loop, uncontrolled system. Regarding nonlinear systems (like (4.3)), the minimum phase characteristics varies over the state space of the system. Therefore, the system can exhibit minimum phaseness at one equilibrium point and non-minimum phaseness at an other one.

4.2.1.4 Linear Error Feedback Control Design

Applying the feedback control law (4.17) to the nonlinear system dynamics (4.3) leads to (4.18), where the r_i-th derivative of the outputs y_i equals the corresponding pseudo-control variables ν_i. Thus, the pseudo-controls ν_i can be used for error feedback in order to track the reference trajectories $y_{r,i}$ by the outputs y_i. Since (4.17) leads to a linear input/output dynamics (4.18), there exists a wide spectrum of linear and nonlinear control approaches that can be used for minimizing the control error

$$e_i = y_{r,i} - y_i. \tag{4.26}$$

The most intuitive approach for designing the pseudo-control laws ν_i is to use linear error feedback in the form

$$\begin{aligned}\nu_i &= y_{r,i}^{(r_i)} + k_{i,0} \cdot (y_{r,i} - y_i) + k_{i,1} \cdot (\dot{y}_{r,i} - \dot{y}_i) + \ldots + k_{i,r_i-1} \cdot \left(y_{r,i}^{(r_i-1)} - y_i^{(r_i-1)}\right) \\ &= y_{r,i}^{(r_i)} + \sum_{j=0}^{r_i-1} k_{i,j} \cdot e_i^{(j)}\end{aligned} \quad . \tag{4.27}$$

By choosing this error feedback law (4.27) with the controller gains $k_{i,j} > 0$, the closed-loop error dynamics

$$e_i^{(r_i)} = -k_{i,0} \cdot e_i - k_{i,1} \cdot \dot{e}_i - \ldots - k_{i,r_i-1} \cdot e_i^{(r_i-1)} \tag{4.28}$$

becomes exponentially asymptotically stable. It is important to note, that the NDI-based control law using a linear error feedback

$$\boldsymbol{u} = \boldsymbol{A}^{-1}(\boldsymbol{x}) \cdot \left[\begin{bmatrix} y_{r,i}^{(r_1)} + \sum_{j=0}^{r_1-1} k_{1,j} \cdot e_1^{(j)} \\ \vdots \\ y_{r,m}^{(r_m)} + \sum_{j=0}^{r_m-1} k_{m,j} \cdot e_m^{(j)} \end{bmatrix} - \boldsymbol{b}(\boldsymbol{x}) \right] \tag{4.29}$$

is widespread in the field of nonlinear control of aerial vehicles [37, 58, 66, 71].

In many practical applications it is not possible to apply the NDI theory with its restrictive conditions like minimum phase characteristics or proper relative degree of the considered system. Thus, several NDI approximation techniques have been evolved over the years, to tailor this powerful methodology to systems, which do not inherently exhibit a well-defined relative degree or a stable zero dynamics. An overview of those approximated NDI approaches can be found in [98, 99]. The presented NDI theory incorporates - like many other model based control approaches - model information to cancel the system's nonlinearities. Therefore, the standard approach introduced here requires a precise design model for control layout purposes. Due to the inherent and inevitable divergence between the design model and the plant robustifying elements are necessary for applying NDI methodologies in missile autopilot design.

4.2.2 Backstepping and Command Filtered Backstepping

BS is a control design methodology developed by Petar Kokotovic in the early 90s. The theory of classic BS and robustifying extensions (Adaptive Backstepping) are summarized in [35]. Both BS- and NDI-based control laws, are nonlinear feedback approaches, which exhibit in their basic version a similar structure. A significant advantage of BS compared to NDI control approaches is the systematic and recursive design methodology based on Lyapunov's direct method of stability. With the inherent recursive design procedure, BS stabilizes the control error between the system's output $\boldsymbol{y}$ and a reference trajectory $\boldsymbol{y}_r$. The derivation of the control law is conducted layer-wise beginning at the system's output dynamics ($\boldsymbol{y}$). An artificial, intermediate control variable is calculated in each design step until the dynamic layer is reached, in which is driven by the system's input ($\boldsymbol{u}$).

All BS-based control laws are designed on the basis of a specified Lyapunov function. The purpose of the control design procedure is to render the time derivative of the Lyapunov function candidate negative definite by selecting a suitable feedback control law $\boldsymbol{u} = \boldsymbol{\alpha}(\boldsymbol{x})$. This special class of Lyapunov functions are introduced in section 4.2.2.1. In the following section, classical BS and CFB are explained starting in both cases with SISO systems before extending the theory to MIMO systems.

4.2.2.1 Control Lyapunov Function

Lyapunov's direct method of stability is introduced in section 4.1.2 as a method to prove stability of linear or nonlinear systems. Besides analyzing the closed-loop form of dynamical systems (4.1), a Lyapunov function can also serve as a starting point for control design. The idea of a Control Lyapunov Function (CLF) is to design a control law $\boldsymbol{u} = \boldsymbol{\alpha}(\boldsymbol{x})$ for the general nonlinear system

$$\dot{\boldsymbol{x}} = \boldsymbol{f}(\boldsymbol{x}, \boldsymbol{u}) \tag{4.30}$$

based on a desired Lyapunov function $V(\boldsymbol{x})$. The Lyapunov function is selected in order that the closed-loop system (4.1) satisfies certain closed-loop stability properties (see theorem 4.1.9).

Definition 4.2.6 (*Control Lyapunov Function*)

A positive definite, continuously differentiable function

$$V(\boldsymbol{x}) > 0 \qquad \forall \boldsymbol{x} \neq \boldsymbol{0} \tag{4.31}$$

is called a CLF for the system (4.30) *if there exists a* $\boldsymbol{u} = \boldsymbol{\alpha}(\boldsymbol{x})$ *such that*

$$\dot{V} = \frac{\partial V}{\partial \boldsymbol{x}} \cdot \boldsymbol{f}(\boldsymbol{x}, \boldsymbol{\alpha}(\boldsymbol{x})) < 0 \qquad \forall \boldsymbol{x} \neq \boldsymbol{0}$$

Thus, the difference between a Lyapunov function (introduced in section 4.1.2) and a CLF is the appearance of the desired control law $\boldsymbol{u} = \boldsymbol{\alpha}(\boldsymbol{x})$ in the Lyapunov candidate function's time derivative $\dot{V}$ (see definition 4.2.6).

4.2.2.2 Backstepping for SISO Systems

The principle of BS is introduced by considering a SISO system in strict-feedback form with the state x_1 being the output:

$$\begin{array}{rcll} \dot{x}_1 & = & f_1(x_1) & + \; g_1(x_1)\cdot x_2 \\ \dot{x}_2 & = & f_2(x_1,x_2) & + \; g_2(x_1,x_2)\cdot x_3 \\ & \vdots & & \\ \dot{x}_{n-1} & = & f_{n-1}(x_1,\ldots,x_{n-1}) & + \; g_{n-1}(x_1,\ldots,x_{n-1})\cdot x_n \\ \dot{x}_n & = & f_n(x_1,\ldots,x_n) & + \; g_n(x_1,\ldots,x_n)\cdot u \end{array} \tag{4.32a}$$

$$y = x_1 \tag{4.32b}$$

A system's structure is denoted as *strict-feedback* if the state x_{i+1} can be considered as the affine control input of the dynamics $\dot{x}_i$ and $\dot{x}_i$ depends only on $x_1,\ldots,x_i$. The state x_{i+1} from the following dynamic layer is considered, in BS-based control design approaches, as *virtual control input* (or pseudo-controls). BS is a recursive design procedure starting at the dynamics closest to the output (*outermost* dynamics, here: x_1-dynamics). In each design step i, a pseudo-control law $x_{i+1,d} = \alpha_i$ is designed, based on a CLF candidate, for the considered dynamics. In the subsequent design step $i+1$, the dynamics $\dot{x}_i$ is extended with the adjacent state dynamics ($\dot{x}_{i+1}$). This consecutive procedure is conducted until the *innermost* equation of motion (EOM) is reached. In the last design step $i = n$, the control law $u = \alpha_{n-1}$ for the physical system input is designed.

Since the missile autopilot is designed to track a certain reference trajectory, the methodology of BS (and CFB) is introduced by considering a control problem of minimizing the tracking error

$$e_1 = y_r - x_1. \tag{4.33}$$

instead of stabilizing the system's origin as described in common literature [35, 42, 94]. In order to stabilize the tracking error in (4.33), the quadratic (in e_1) CLF candidate

$$V_1 = \frac{1}{2}e_1^2. \tag{4.34}$$

is chosen. With the error dynamics (see (4.33))

$$\begin{array}{rl} \dot{e}_1 & = \dot{y}_r - \dot{x}_1 \\ & = \dot{y}_r - f_1(x_1) - g_1(x_1)\cdot x_2 \end{array} \tag{4.35}$$

the time derivative of V_1 (see (4.34)) along the trajectory of (4.33) becomes

$$\begin{array}{rl} \dot{V}_1 & = e_1 \cdot \dot{e}_1 \\ & = e_1 \cdot (\dot{y}_r - f_1(x_1) - g_1(x_1)\cdot x_2) \overset{!}{\leq} W_1(e_1) = -c_1 e_1^2 \end{array} \tag{4.36}$$

$W_1(e_1)$ is selected as negative definite limiting function of $\dot{V}_1$. Thus, if a pseudo-control law $x_{2,d} = \alpha_1(x_1)$ can be found which fulfills the inequality in (4.36), the tracking error $e_1 = 0$ is asymptotically stable in terms of Lyapunov's direct method (see theorem 4.1.9). In order to design a deterministic intermediate control law $x_{2,d} = \alpha_1(x_1)$ for the virtual control input (state) x_2, the maximum value

$$\dot{V}_1 = e_1 \cdot (\dot{y}_r - f_1(x_1) - g_1(x_1)\cdot x_2) \overset{!}{=} W_1(e_1) = -c_1 e_1^2 \tag{4.37}$$

of the limiting function is considered. Thus, the inequality constraint in (4.36) is changed to the

equality constraint in (4.37) which is fulfilled by choosing the virtual control law as

$$\alpha_1(x_1) = \frac{1}{g_1}\left(\dot{y}_r - f_1 + c_1 \cdot e_1\right). \tag{4.38}$$

If the state x_2 follows the desired trajectory $x_{2,d} = \alpha_1$ defined in (4.38), the tracking error e_1 converges exponentially towards zero. Since x_2 is a physical state of the system, which results from the differential equation described in (4.32a), the intermediate control law (4.38) cannot be directly addressed. In order to force x_2 to follow the desired trajectory $x_{2,d} = \alpha_1$, the tracking error is extended by $e_2 = \alpha_1 - x_2$ within the second control design step $i = 2$. Therefore, the considered error system

$$\begin{aligned} e_1 &= y_r - x_1 \\ e_2 &= \alpha_1 - x_2 \end{aligned} \tag{4.39}$$

consists of the previous error state (e_1) and e_2, the difference between the desired α_1 and the physical state x_2. Due to the system's strict-feedback structure (4.32a), the dynamics of x_2 is driven by the state x_3. In the same manner as x_2 was considered as a virtual control for the error dynamics in the first step, a desired intermediate control law $x_{3,d} = \alpha_2$ is calculated in the second design step for the state x_3. Adding the squared tracking error e_2 to the Lyapunov function V_1 results in the CLF candidate

$$V_2 = V_1 + \frac{1}{2}e_2^2. \tag{4.40}$$

This function candidate serves as a starting point for calculating the desired trajectory $x_{3,d} = \alpha_2$ for the state x_3. By representing the state $x_2 = \alpha_1 - e_2$ by the virtual control law from the first step and the tracking error e_2, the following error dynamics results for the subsystem (4.39):

$$\begin{aligned} \dot{e}_1 &= \dot{y}_r - \dot{x}_1 = \dot{y}_r - f_1(x_1) - g_1(x_1) \cdot (\alpha_1 - e_2) \\ \dot{e}_2 &= \dot{\alpha}_1 - \dot{x}_2 = \dot{\alpha}_1 - f_2(x_1, x_2) - g_2(x_1, x_2) \cdot x_3 \end{aligned} \tag{4.41}$$

The intermediate control law $x_{3,d} = \alpha_2$ for this design step is calculated to render the time derivative

$$\begin{aligned} \dot{V}_2 &= \dot{V}_1 + e_2 \cdot \dot{e}_2 \\ &= e_1 \cdot (\dot{y}_r - f_1(x_1) - g_1(x_1) \cdot (\alpha_1 - e_2)) \\ &\quad + e_2 \cdot (\dot{\alpha}_1 - f_2 - g_2 \cdot x_3) \\ &= e_1 \cdot (\dot{y}_r - f_1(x_1) - g_1(x_1) \cdot \alpha_1 + g_1 \cdot e_2) \\ &\quad + e_2 \cdot (\dot{\alpha}_1 - f_2 - g_2 \cdot x_3) \\ &\overset{!}{\leq} W_2(e_1, e_2) = W_1 - c_2 e_2^2 \end{aligned} \tag{4.42}$$

of (4.40) negative definite via the limiting function $W_2(e_1, e_2)$. By substituting α_1 from (4.38) and assigning the term $e_1 \cdot g_1 \cdot e_2$ to the braces of the tracking error e_2, (4.42) becomes

$$\begin{aligned} \dot{V}_2 &= -c_1 e_1^2 \\ &\quad + e_2 \cdot (g_1 \cdot e_1 + \dot{\alpha}_1 - f_2 - g_2 \cdot x_3) \overset{!}{=} W_2(e_1, e_2) = W_1(e_1) - c_2 e_2^2. \end{aligned} \tag{4.43}$$

The cross-coupling term $e_1 \cdot g_1 \cdot e_2$ results from the discrepancy e_2 between the desired virtual control law $x_{2,d} = \alpha_1$ and driven state x_2.

Analogue to the considerations in the first step, one possibility to calculate the desired virtual control law $x_{3,d} = \alpha_2$ for the state x_3 is to consider the maximum of the function W_2 as the upper limit of $\dot{V}_2$. By solving (4.43) the time derivative $\dot{V}_2$ is rendered negative definite and the error dynamics (4.41) is exponentially stable with respect to $e_1 = e_2 = 0$. Therefore, the intermediate control law

of the state x_3 arise from the solution of (4.43) to

$$\alpha_2(x_1, x_2) = \frac{1}{g_2}\left(\dot{\alpha}_1 - f_2 + c_2 \cdot e_2 + g_1 \cdot e_1\right). \tag{4.44}$$

Both pseudo-control laws from the first (4.38) and second step (4.44), exhibit an identical feedback structure with the exception of the cross-coupling term $e_1 \cdot g_1 \cdot e_2$ in $x_{3,d} = \alpha_2$. The information from the pseudo-control $x_{2,d} = \alpha_1$ of the previous step is propagated through the time derivative $\dot{\alpha}_1$. From (4.38) it becomes obvious that the determination of $\dot{\alpha}_1$ requires the time derivative of the dynamic parts f_1, g_1 and the tracking error e_1.

The derivation of the of the pseudo-control laws for $x_4, \ldots, x_n$ follows the same procedure as the one for $x_{3,d} = \alpha_2$ described in design step two. The BS procedure concludes with the derivation of the final control law $u = \alpha_{n-1}(x_1, \ldots, x_n)$ for the system's physical input. Following the procedure from the steps above, the error dynamics in the final step is given by

$$\begin{array}{rcl} e_1 & = & y_r - x_1 \\ e_k & = & \alpha_{k-1} - x_k, \quad k = 2, \ldots, n \end{array}. \tag{4.45}$$

As in (4.34) and (4.40), the sum of the squared error states (4.45) serves as a CLF candidate

$$V_n = V_{n-1} + \frac{1}{2}e_n^2. \tag{4.46}$$

The CLF in (4.46) is the extension of the Lyapunov function candidate $V_{n-1} = \frac{1}{2}\sum_{i=1}^{n-1} e_i^2$ used in the previous step $n-1$. With the dynamics

$$\begin{array}{rcl} \dot{e}_1 & = & \dot{y}_r - \dot{x}_1\dot{y}_r - f_1(x_1) - g_1(x_1)\cdot(\alpha_1 - e_2) \\ \dot{e}_k & = & \dot{\alpha}_{k-1} - \dot{x}_k \\ & = & \dot{\alpha}_{k-1} - f_k(x_1, \ldots, x_k) - g_k(x_1, \ldots, x_k)(\alpha_k - e_{k+1}), \quad k = 2, \ldots, n \end{array} \tag{4.47}$$

of the error states introduced in (4.45), the time derivative of V_n becomes

$$\begin{array}{rcl} \dot{V}_n & = & \dot{V}_{n-1} + e_n \cdot \dot{e}_n \\ & = & -c_1e_1^2 - c_2e_2^2 - \ldots - e_{n-1}\cdot\dot{e}_{n-1} - e_n\cdot\dot{e}_n \\ & = & -c_1e_1^2 - c_2e_2^2 - \ldots - e_{n-1}\cdot(\dot{\alpha}_{n-2} - f_{n-1} - g_{n-1}\cdot(\alpha_{n-1} - e_n)) \\ & & -e_n\cdot(\dot{\alpha}_{n-1} - f_n - g_n\cdot u) \\ & = & -c_1e_1^2 - c_2e_2^2 - \ldots - e_{n-1}\cdot(\dot{\alpha}_{n-2} - f_{n-1} - g_{n-1}\cdot\alpha_{n-1} + g_{n-1}\cdot e_n) \\ & & -e_n\cdot(\dot{\alpha}_{n-1} - f_n - g_n\cdot u) \\ & \overset{!}{\leq} & W_n(e_1, \ldots, e_n) = W_{n-1}(e_1, \ldots, e_{n-1}) - c_ne_n^2. \end{array} \tag{4.48}$$

In the same manner, the CLF in (4.46) is extended, the limiting function W_n is the extension of $W_{n-1} = -c_1e_1^2 - \ldots - c_{n-1}e_{n-1}^2$. Substituting the resulting pseudo-control law

$$\alpha_{n-1} = \frac{1}{g_{n-1}}\cdot(\dot{\alpha}_{n-2} - f_{n-1} + c_{n-1}\cdot e_{n-1} + g_{n-1}\cdot e_{n-1}) \tag{4.49}$$

from design step $i = n-1$ (not shown here), rearranging the term $e_{n-1}\cdot g_{n-1}\cdot e_n$, and considering the maximum of the limiting function $W_n(e_1, \ldots, e_n)$ results in the equation

$$\begin{array}{rcl} \dot{V}_n & = & -c_1e_1^2 - \ldots - c_{n-1}e_{n-1}^2 \\ & & -e_n\cdot(g_{n-1}\cdot e_n + \dot{\alpha}_{n-1} - f_n - g_n\cdot u) \\ & \overset{!}{=} & W_n(e_1, \ldots, e_n) + W_{n-1}(e_1, \ldots, e_{n-1}) - c_ne_n^2. \end{array} \tag{4.50}$$

The final control law

$$u\left(x_1,\ldots,x_n\right)=\frac{1}{g_n}\left(\dot{\alpha}_{n-1}-f_n+c_n\cdot e_n+g_{n-1}\cdot e_{n-1}\right) \tag{4.51}$$

is obtained by solving (4.50) for the system's input u. The structure of (4.51) is equal to the pseudo-control laws $\alpha_2,\ldots,\alpha_{n-2}$ derived within the auxiliary steps $2,\ldots,n-1$. In analogy to step $i=2$, the necessary information to stabilize the intermediate subsystems is provided to the final control law by the time derivative of $\dot{\alpha}_{n-1}$, obtained in step $i=n-1$. The calculation of this term requires the $n-i$-th derivative with respect to time of the pseudo-controls α_i, $i=1,\ldots,n-2$.

4.2.2.3 Block Backstepping for MIMO Systems

In case the considered system has multiple inputs and outputs, the system can be grouped in subsystems of equal dynamical layers with equivalent structures (e.g. rotational, translational dynamics). This section describes - in conformity with the derivation for the SISO case (section 4.2.2.2) - the BS procedure for a coupled MIMO system.

The considered system

$$\begin{array}{lcll}
\dot{\boldsymbol{x}}_1 & = & \boldsymbol{f}_1\left(\boldsymbol{x}_1\right) & + \quad \boldsymbol{G}_1\left(\boldsymbol{x}_1\right)\cdot\boldsymbol{x}_2\\
\dot{\boldsymbol{x}}_2 & = & \boldsymbol{f}_2\left(\boldsymbol{x}_1,\boldsymbol{x}_2\right) & + \quad \boldsymbol{G}_2\left(\boldsymbol{x}_1,\boldsymbol{x}_2\right)\cdot\boldsymbol{x}_3\\
 & \vdots & & \\
\dot{\boldsymbol{x}}_{N-1} & = & \boldsymbol{f}_{N-1}\left(\boldsymbol{x}_1,\ldots,\boldsymbol{x}_{N-1}\right) & + \quad \boldsymbol{G}_{N-1}\left(\boldsymbol{x}_1,\ldots,\boldsymbol{x}_{N-1}\right)\cdot\boldsymbol{x}_N\\
\dot{\boldsymbol{x}}_N & = & \boldsymbol{f}_N\left(\boldsymbol{x}_1,\ldots,\boldsymbol{x}_N\right) & + \quad \boldsymbol{G}_N\left(\boldsymbol{x}_1,\ldots,\boldsymbol{x}_N\right)\cdot\boldsymbol{u}
\end{array} \tag{4.52a}$$

$$\boldsymbol{y}=\boldsymbol{x}_1 \tag{4.52b}$$

is described in $N<n$ interconnected subsystems with the restriction that the state vectors of each subsequent subsystem is equal or larger in dimension $\boldsymbol{x}_i\in\mathbb{R}^{n_i\times 1}$, $n_1\leq n_2\leq\ldots\leq n_N$. Since $\boldsymbol{f}_i$ and $\boldsymbol{G}_i$ of each subsystem dynamics $\dot{\boldsymbol{x}}_i$ depend only on states from the same or preceding dynamical layers $\boldsymbol{x}_1,\ldots,\boldsymbol{x}_i$ and the previous state $\boldsymbol{x}_{i+1}$ appears linearly (affine), the system (4.52) is in strict-feedback form. The dimension of the entire set of states $\boldsymbol{x}=\begin{bmatrix}\boldsymbol{x}_1 & \ldots,\boldsymbol{x}_n\end{bmatrix}^T\in\mathbb{R}^{n\times 1}$ is given by the summation of the subsystem dimensions: $n=\sum_{i=1}^{N}n_i$. Similar to section 4.2.2.2, a control law for the system's input $\boldsymbol{u}\in\mathbb{R}^{m\times 1}$, $m\geq n_N$ is derived, for the purpose of output tracking the reference signal $\boldsymbol{y}_r$. For the case that the input matrix $\boldsymbol{G}_i\in\mathbb{R}^{n_i\times n_{i+1}}$ ($\boldsymbol{G}_N\in\mathbb{R}^{n_N\times n_m}$) is non-square $n_i<n_{i+1}$ ($n_N\neq n_m$), the inverse is calculated via the Moore-Penrose-Inverse $\boldsymbol{G}_i'=\left(\boldsymbol{G}_i^T\boldsymbol{G}_i\right)^{-1}\boldsymbol{G}_i^T$ [100, 101].

Since the explanation of the MIMO BS follows the same didactic scheme as section 4.2.2.2, the derivation of the MIMO BS control law is depicted in a brief way with highlighting the main differences for block-wise considerations of the subsystems. Further consideration about BS in case of MIMO systems can be found in [40, 102, 103, 104].

By defining the vector tracking error

$$\boldsymbol{e}_1=\boldsymbol{y}_r-\boldsymbol{x}_1 \tag{4.53}$$

the CLF

$$V_1=\boldsymbol{e}_1^T\boldsymbol{P}_1\boldsymbol{e}_1 \tag{4.54}$$

of the first design step is chosen as a quadratic function of the tracking error $\boldsymbol{e}_1$ with the symmetric, positive definite matrix $\boldsymbol{P}_1\in\mathbb{R}^{n_1\times n_1}>0$. As in section 4.2.2.2, $\boldsymbol{x}_{2,d}=\boldsymbol{\alpha}_1$ is designed to render the

time derivative of the CLF negative definite. Substituting the error dynamics of the tracking error

$$\begin{aligned} \dot{\boldsymbol{e}}_1 &= \dot{\boldsymbol{y}}_r - \dot{\boldsymbol{x}}_1 \\ &= \dot{\boldsymbol{y}}_r - \boldsymbol{f}_1(\boldsymbol{x}_1) - \boldsymbol{G}_1(\boldsymbol{x}_1) \cdot \boldsymbol{x}_2 \end{aligned} \tag{4.55}$$

in (4.54) results in the time derivative

$$\begin{aligned} \dot{V}_1 &= \dot{\boldsymbol{e}}_1^T \boldsymbol{P}_1 \boldsymbol{e}_1 + \boldsymbol{e}_1^T \boldsymbol{P}_1 \dot{\boldsymbol{e}}_1 \\ &= \left(\dot{\boldsymbol{y}}_r - \boldsymbol{f}_1(\boldsymbol{x}_1) - \boldsymbol{G}_1(\boldsymbol{x}_1) \cdot \boldsymbol{x}_2\right)^T \boldsymbol{P}_1 \boldsymbol{e}_1 + \\ &\quad \boldsymbol{e}_1^T \boldsymbol{P}_1 \left(\dot{\boldsymbol{y}}_r - \boldsymbol{f}_1(\boldsymbol{x}_1) - \boldsymbol{G}_1(\boldsymbol{x}_1) \cdot \boldsymbol{x}_2\right) \\ &\overset{!}{\leq} W_1(\boldsymbol{e}_1) = -\boldsymbol{e}_1^T \boldsymbol{Q}_1 \boldsymbol{e}_1. \end{aligned} \tag{4.56}$$

Under consideration of the rendering function's (W_1) maximum, the pseudo-control law is obtained by

$$\boldsymbol{\alpha}_1(\boldsymbol{x}_1) = \boldsymbol{G}_1' \left(\dot{\boldsymbol{y}}_r - \boldsymbol{f}_1(\boldsymbol{x}_1) + \boldsymbol{K}_1 \boldsymbol{e}_1\right). \tag{4.57}$$

Substituting (4.57) in (4.55) the time derivative (4.56) of the CLF becomes

$$\begin{aligned} \dot{V}_1 &= -\boldsymbol{e}_1^T \boldsymbol{K}_1^T \boldsymbol{P}_1 \boldsymbol{e} - \boldsymbol{e}_1^T \boldsymbol{P}_1 \boldsymbol{K}_1 \boldsymbol{e}_1 \\ &= -\boldsymbol{e}_1^T \left(\boldsymbol{K}_1^T \boldsymbol{P}_1 + \boldsymbol{P}_1 \boldsymbol{K}_1\right) \boldsymbol{e}_1 \overset{!}{=} -\boldsymbol{e}_1^T \boldsymbol{Q}_1 \boldsymbol{e}_1 \end{aligned}. \tag{4.58}$$

Based on the positive definite symmetric matrices $\boldsymbol{Q}_1 > 0$ and $\boldsymbol{P}_1 > 0$ the feedback gain matrix $\boldsymbol{K}_1$ must fulfill the matrix Lyapunov equation [42]

$$\boldsymbol{K}_1^T \boldsymbol{P}_1 + \boldsymbol{P}_1 \boldsymbol{K}_1 = \boldsymbol{Q}_1. \tag{4.59}$$

Therefore, the convergence rate of the tracking error $\boldsymbol{e}_1$ for the equilibrium $\boldsymbol{e}_1 = \boldsymbol{0}$ depends on the weighting matrices $\boldsymbol{Q}_1$ and $\boldsymbol{P}_1$, which determine via (4.59) the amplification $\boldsymbol{K}_1$ of the error feedback.

In order to track the intermediate control law $\boldsymbol{\alpha}_1$ (4.57) from the previous step by the physical state variable $\boldsymbol{x}_2$, a desired pseudo-control law $\boldsymbol{\alpha}_2$ for the state $\boldsymbol{x}_3$ is designed. Following the concept from the SISO case section 4.2.2.2, the considered error from the first design step (4.53) is extended by $\boldsymbol{e}_2$, describing the difference between the desired and the real state $\boldsymbol{x}_2$. Thus, the considered error states are

$$\begin{aligned} \boldsymbol{e}_1 &= \boldsymbol{y}_r - \boldsymbol{x}_1 \\ \boldsymbol{e}_2 &= \boldsymbol{\alpha}_1 - \boldsymbol{x}_2 \end{aligned}. \tag{4.60}$$

Extending the Lyapunov function V_1 (4.54) from the first design step by the additional error state $\boldsymbol{e}_2$ results in

$$\begin{aligned} V_2 &= V_1 + \boldsymbol{e}_2^T \boldsymbol{P}_2 \boldsymbol{e}_2 \\ &= \boldsymbol{e}_1^T \boldsymbol{P}_1 \boldsymbol{e}_1 + \boldsymbol{e}_2^T \boldsymbol{P}_2 \boldsymbol{e}_2 \end{aligned}. \tag{4.61}$$

Based on the error dynamics

$$\begin{aligned} \dot{\boldsymbol{e}}_1 &= \dot{\boldsymbol{y}}_r - \dot{\boldsymbol{x}}_1 &&= \dot{\boldsymbol{y}}_r - \boldsymbol{f}_1(\boldsymbol{x}_1) - \boldsymbol{G}_1(\boldsymbol{x}_1) \cdot (\boldsymbol{\alpha}_1 - \boldsymbol{e}_2) \\ \dot{\boldsymbol{e}}_2 &= \dot{\boldsymbol{\alpha}}_1 - \dot{\boldsymbol{x}}_2 &&= \dot{\boldsymbol{\alpha}}_1 - \boldsymbol{f}_2(\boldsymbol{x}_1, \boldsymbol{x}_2) - \boldsymbol{G}_2(\boldsymbol{x}_1, \boldsymbol{x}_2) \cdot \boldsymbol{x}_3 \end{aligned}, \tag{4.62}$$

obtained by substituting (4.52a) in the time derivative (4.60), and the definition (4.57), the pseudo-

control law $\boldsymbol{x}_{3,d} = \boldsymbol{\alpha}_2$ is designed to render

$$\begin{aligned}
\dot{V}_2 &= \dot{V}_1 + \dot{\boldsymbol{e}}_2^T \boldsymbol{P}_2 \boldsymbol{e}_2 + \boldsymbol{e}_2^T \boldsymbol{P}_2 \dot{\boldsymbol{e}}_2 \\
&= -\boldsymbol{e}_1^T \boldsymbol{Q}_1 \boldsymbol{e}_1 + \boldsymbol{e}_1^T \boldsymbol{P}_1 \boldsymbol{G}_1 \boldsymbol{e}_2 + \boldsymbol{e}_2^T \boldsymbol{G}_1^T \boldsymbol{P}_1 \boldsymbol{e}_1 + \dot{\boldsymbol{e}}_2^T \boldsymbol{P}_2 \boldsymbol{e}_2 + \boldsymbol{e}_2^T \boldsymbol{P}_2 \dot{\boldsymbol{e}}_2 \\
&= -\boldsymbol{e}_1^T \boldsymbol{Q}_1 \boldsymbol{e}_1 + \left(\dot{\boldsymbol{\alpha}}_1 - \boldsymbol{f}_2 - \boldsymbol{G}_2 \cdot \boldsymbol{x}_3 + \boldsymbol{P}_2^{-1} \boldsymbol{G}_1^T \boldsymbol{P}_1 \boldsymbol{e}_1\right)^T \cdot \boldsymbol{P}_2 \boldsymbol{e}_2 + \\
&\quad \boldsymbol{e}_2^T \boldsymbol{P}_2 \cdot \left(\dot{\boldsymbol{\alpha}}_1 - \boldsymbol{f}_2 - \boldsymbol{G}_2 \cdot \boldsymbol{x}_3 + \boldsymbol{P}_2^{-1} \boldsymbol{G}_1^T \boldsymbol{P}_1 \boldsymbol{e}_1\right) \\
&\overset{!}{\leq} W_2(\boldsymbol{e}_1, \boldsymbol{e}_2) = W_1(\boldsymbol{e}_1) - \boldsymbol{e}_2^T \boldsymbol{Q}_2 \boldsymbol{e}_2
\end{aligned} \tag{4.63}$$

negative definite. The appearance of the term $\boldsymbol{e}_1^T \boldsymbol{P}_1 \boldsymbol{G}_1 \boldsymbol{e}_2$ in (4.63) is due to the fact that the desired pseudo-control law $\boldsymbol{\alpha}_1$ (rendering the error $\boldsymbol{e}_1$ stable) needs to be propagated through the dynamics of $\boldsymbol{x}_2$.

Following the derivation of BS for the scalar case, the maximum $W_2 = -\boldsymbol{e}_1^T \boldsymbol{Q}_1 \boldsymbol{e}_1 - \boldsymbol{e}_2^T \boldsymbol{Q}_2 \boldsymbol{e}_2$ of the limiting function is considered in (4.63) for the purpose of designing the intermediate control law. Thus, the pseudo-control law

$$\boldsymbol{\alpha}_2 = \boldsymbol{G}_2' \left(\dot{\boldsymbol{\alpha}}_1 - \boldsymbol{f}_2 + \boldsymbol{K}_2 \boldsymbol{e}_2 + \boldsymbol{P}_2^{-1} \boldsymbol{G}_1^T \boldsymbol{P}_1 \boldsymbol{e}_1\right), \tag{4.64}$$

renders the time derivative (4.63) of the CLF candidate

$$\begin{aligned}
\dot{V}_2 &= -\boldsymbol{e}_1^T \boldsymbol{Q}_1 \boldsymbol{e}_1 - \boldsymbol{e}_2^T \boldsymbol{K}_2^T \boldsymbol{P}_2 \boldsymbol{e}_2 - \boldsymbol{e}_2^T \boldsymbol{P}_2 \boldsymbol{K}_2 \boldsymbol{e}_2 \\
&= -\boldsymbol{e}_1^T \boldsymbol{Q}_1 \boldsymbol{e}_1 - \boldsymbol{e}_2^T \left(\boldsymbol{K}_2^T \boldsymbol{P}_2 + \boldsymbol{P}_2 \boldsymbol{K}_2\right) \boldsymbol{e}_2 \overset{!}{=} -\boldsymbol{e}_1^T \boldsymbol{Q}_1 \boldsymbol{e}_1 - \boldsymbol{e}_2^T \boldsymbol{Q}_2 \boldsymbol{e}_2
\end{aligned} \tag{4.65}$$

negative definite if the feedback gain $\boldsymbol{K}_2$ fulfills the matrix Lyapunov equation

$$\boldsymbol{K}_2^T \boldsymbol{P}_2 + \boldsymbol{P}_2 \boldsymbol{K}_2 = \boldsymbol{Q}_2 \tag{4.66}$$

for $\boldsymbol{P}_2, \boldsymbol{Q}_2 > 0$.

The derivation of the pseudo-control laws $\boldsymbol{\alpha}_i$ is conducted in an analogous manner for the design steps $i = 2, \ldots, N-1$. Therefore, and due to reasons of clarity the derivations of the $i = 2, \ldots, N-1$ intermediate control laws is representatively depicted for the $N-1$-th design step with the considered pseudo-control $\boldsymbol{x}_N = \boldsymbol{\alpha}_{N-1}$. Following the procedure of the previous design steps, the error states

$$\begin{aligned}
\boldsymbol{e}_1 &= \boldsymbol{y}_r - \boldsymbol{x}_1 \\
\boldsymbol{e}_k &= \boldsymbol{\alpha}_{k-1} - \boldsymbol{x}_k, \quad k = 2, \ldots, N-1, \quad ,
\end{aligned} \tag{4.67}$$

which are subject to stabilization around the equilibrium $\boldsymbol{e}_k = \boldsymbol{0}$, $k = 1, \ldots, N-1$, are obtained by an extension of the error states in each design step i. The CLF candidate

$$V_{N-1} = V_{N-2} + \boldsymbol{e}_{N-1}^T \boldsymbol{P}_{N-1} \boldsymbol{e}_{N-1} \tag{4.68}$$

used for control design within this design step, is constructed by extending the Lyapunov function $V_{N-2} = \sum_{i=1}^{N-2} \boldsymbol{e}_i^T \boldsymbol{P}_i \boldsymbol{e}_i$ from the previous step $i = N-2$ with $\boldsymbol{e}_{N-1}^T \boldsymbol{P}_{N-1} \boldsymbol{e}_{N-1}$. Inserting the EOM from (4.52a) in the time derivative of the error definition (4.67) results in the error dynamics

$$\begin{array}{lllll}
\dot{\boldsymbol{e}}_1 & = \dot{\boldsymbol{y}}_r - \dot{\boldsymbol{x}}_1 & = \dot{\boldsymbol{y}}_r - \boldsymbol{f}_1 - \boldsymbol{G}_1 \cdot (\boldsymbol{\alpha}_1 - \boldsymbol{e}_2) & & \\
\dot{\boldsymbol{e}}_k & = \dot{\boldsymbol{\alpha}}_{k-1} - \dot{\boldsymbol{x}}_k & = \dot{\boldsymbol{\alpha}}_{k-1} - \boldsymbol{f}_k - \boldsymbol{G}_k \cdot (\boldsymbol{\alpha}_k - \boldsymbol{e}_{k+1}), & k = 2, \ldots, N-2 \ . & (4.69) \\
\dot{\boldsymbol{e}}_{N-1} & = \dot{\boldsymbol{\alpha}}_{N-2} - \dot{\boldsymbol{x}}_{N-1} & = \dot{\boldsymbol{\alpha}}_{N-2} - \boldsymbol{f}_{N-1} - \boldsymbol{G}_{N-1} \cdot \boldsymbol{x}_N & &
\end{array}$$

The derivation of the Lyapunov function (4.68) with respect to time along the trajectories of (4.69)

leads to

$$\begin{aligned}
\dot{V}_{N-1} &= \dot{V}_{N-2} + \dot{\boldsymbol{e}}_{N-1}^T \boldsymbol{P}_{N-1}\boldsymbol{e}_{N-1} + \boldsymbol{e}_{N-1}^T \boldsymbol{P}_{N-1}\dot{\boldsymbol{e}}_{N-1} \\
&= -\boldsymbol{e}_1^T \boldsymbol{Q}_1 \boldsymbol{e}_1 - \ldots - \boldsymbol{e}_{N-2}^T \boldsymbol{Q}_{N-2}\boldsymbol{e}_{N-2} + \boldsymbol{e}_{N-2}^T \boldsymbol{P}_{N-2}\boldsymbol{G}_{N-2}\boldsymbol{e}_{N-1} + \\
&\quad \boldsymbol{e}_{N-1}^T \boldsymbol{G}_{N-2}^T \boldsymbol{P}_{N-2}\boldsymbol{e}_{N-2} + \dot{\boldsymbol{e}}_{N-1}^T \boldsymbol{P}_{N-1}\boldsymbol{e}_{N-1} + \boldsymbol{e}_{N-1}^T \boldsymbol{P}_{N-1}\dot{\boldsymbol{e}}_{N-1} \\
&= -\boldsymbol{e}_1^T \boldsymbol{Q}_1 \boldsymbol{e}_1 - \ldots - \boldsymbol{e}_{N-2}^T \boldsymbol{Q}_{N-2}\boldsymbol{e}_{N-2} + \\
&\quad \left(\dot{\boldsymbol{\alpha}}_{N-2} - \boldsymbol{f}_{N-1} - \boldsymbol{G}_{N-1}\cdot\boldsymbol{x}_N + \boldsymbol{P}_{N-1}^{-1}\boldsymbol{G}_{N-2}^T \boldsymbol{P}_{N-2}\boldsymbol{e}_{N-2}\right)^T \cdot \boldsymbol{P}_{N-1}\boldsymbol{e}_{N-1} + \\
&\quad \boldsymbol{e}_{N-1}^T \boldsymbol{P}_{N-1}\cdot\left(\dot{\boldsymbol{\alpha}}_{N-2} - \boldsymbol{f}_{N-1} - \boldsymbol{G}_{N-1}\cdot\boldsymbol{x}_N + \boldsymbol{P}_{N-1}^{-1}\boldsymbol{G}_{N-2}^T \boldsymbol{P}_{N-2}\boldsymbol{e}_{N-2}\right) \\
&\overset{!}{\leq} W_{N-1}\left(\boldsymbol{e}_1,\ldots,\boldsymbol{e}_{N-1}\right) = W_{N-2}\left(\boldsymbol{e}_1,\ldots,\boldsymbol{e}_{N-2}\right) - \boldsymbol{e}_{N-1}^T \boldsymbol{T}_{N-1}\boldsymbol{e}_{N-1}
\end{aligned} \quad . \tag{4.70}$$

Considering the maximum of the limiting function W_{N-1}, the pseudo-control law

$$\boldsymbol{\alpha}_{N-1} = \boldsymbol{G}_{N-1}'\left(\dot{\boldsymbol{\alpha}}_{N-2} - \boldsymbol{f}_{N-1} + \boldsymbol{K}_{N-1}\boldsymbol{e}_{N-1} + \boldsymbol{P}_{N-1}^{-1}\boldsymbol{G}_{N-2}^T \boldsymbol{P}_{N-2}\boldsymbol{e}_{N-2}\right), \tag{4.71}$$

renders (4.70) negative definite if the matrix Lyapunov equation

$$\boldsymbol{K}_{N-1}^T \boldsymbol{P}_{N-1} + \boldsymbol{P}_{N-1}\boldsymbol{K}_{N-1} = \boldsymbol{Q}_{N-1} \tag{4.72}$$

is fulfilled for the positive definite matrices $\boldsymbol{P}_{N-1}, \boldsymbol{Q}_{N-1} > 0$. Within the last design step $i = N$, the control law of the physical system input $\boldsymbol{u}$ is derived by stabilizing the error states

$$\begin{aligned}
\boldsymbol{e}_1 &= \boldsymbol{y}_r - \boldsymbol{x}_1 \\
\boldsymbol{e}_k &= \boldsymbol{\alpha}_{k-1} - \boldsymbol{x}_k, \quad k = 2,\ldots,N,
\end{aligned} \tag{4.73}$$

around the equilibrium $\boldsymbol{e}_k = \boldsymbol{0}$, $k = 1,\ldots,N$. Based on (4.67), the error states in (4.73) are obtained by adding the difference $\boldsymbol{e}_N = \boldsymbol{\alpha}_{N-1} - \boldsymbol{x}_N$. Extending the Lyapunov function $V_{N-1} = \sum_{i=1}^{N-1} \boldsymbol{e}_i^T \boldsymbol{P}_i \boldsymbol{e}_i$ from the previous step $N-1$ by $\boldsymbol{e}_N^T \boldsymbol{P}_N \boldsymbol{e}_N$, the CLF candidate for $i = N$ becomes

$$V_N = V_{N-1} + \boldsymbol{e}_N^T \boldsymbol{P}_N \boldsymbol{e}_N. \tag{4.74}$$

Substituting the state vector $\boldsymbol{x}_{k+1}$, utilized as pseudo-control, in each subsystem by $\boldsymbol{x}_{k+1} = \boldsymbol{\alpha}_k - \boldsymbol{e}_{k+1}$, $k = 1,\ldots,N-1$, the error dynamics of (4.73) has the following form

$$\begin{aligned}
\dot{\boldsymbol{e}}_1 &= \dot{\boldsymbol{y}}_r - \dot{\boldsymbol{x}}_1 &&= \dot{\boldsymbol{y}}_r - \boldsymbol{f}_1 - \boldsymbol{G}_1\cdot(\boldsymbol{\alpha}_1 - \boldsymbol{e}_2) \\
\dot{\boldsymbol{e}}_k &= \dot{\boldsymbol{\alpha}}_{k-1} - \dot{\boldsymbol{x}}_k &&= \dot{\boldsymbol{\alpha}}_{k-1} - \boldsymbol{f}_k - \boldsymbol{G}_k\cdot(\boldsymbol{\alpha}_k - \boldsymbol{e}_{k+1}), \quad k = 2,\ldots,N-1 \\
\dot{\boldsymbol{e}}_N &= \dot{\boldsymbol{\alpha}}_{N-1} - \dot{\boldsymbol{x}}_N &&= \dot{\boldsymbol{\alpha}}_{N-1} - \boldsymbol{f}_N - \boldsymbol{G}_N\cdot\boldsymbol{u}.
\end{aligned} \tag{4.75}$$

In the final design step, the system's input $\boldsymbol{u}$ is designed to render the time derivative of V_N

$$\begin{aligned}
\dot{V}_N &= \dot{V}_{N-1} + \dot{\boldsymbol{e}}_N^T \boldsymbol{P}_N \boldsymbol{e}_N + \boldsymbol{e}_N^T \boldsymbol{P}_N \dot{\boldsymbol{e}}_N \\
&= -\boldsymbol{e}_1^T \boldsymbol{Q}_1 \boldsymbol{e}_1 - \ldots - \boldsymbol{e}_{N-1}^T \boldsymbol{Q}_{N-1}\boldsymbol{e}_{N-1} + \boldsymbol{e}_{N-1}^T \boldsymbol{P}_{N-1}\boldsymbol{G}_{N-1}\boldsymbol{e}_N + \\
&\quad \boldsymbol{e}_N^T \boldsymbol{G}_{N-1}^T \boldsymbol{P}_{N-1}\boldsymbol{e}_{N-1} + \dot{\boldsymbol{e}}_N^T \boldsymbol{P}_N \boldsymbol{e}_N + \boldsymbol{e}_N^T \boldsymbol{P}_N \dot{\boldsymbol{e}}_N \\
&= -\boldsymbol{e}_1^T \boldsymbol{Q}_1 \boldsymbol{e}_1 - \ldots - \boldsymbol{e}_{N-1}^T \boldsymbol{Q}_{N-1}\boldsymbol{e}_{N-1} + \\
&\quad \left(\dot{\boldsymbol{\alpha}}_{N-1} - \boldsymbol{f}_N - \boldsymbol{G}_N\cdot\boldsymbol{u} + \boldsymbol{P}_N^{-1}\boldsymbol{G}_{N-1}^T \boldsymbol{P}_{N-1}\boldsymbol{e}_{N-1}\right)^T \cdot \boldsymbol{P}_N \boldsymbol{e}_N + \\
&\quad \boldsymbol{e}_N^T \boldsymbol{P}_N \cdot \left(\dot{\boldsymbol{\alpha}}_{N-1} - \boldsymbol{f}_N - \boldsymbol{G}_N\cdot\boldsymbol{u} + \boldsymbol{P}_N^{-1}\boldsymbol{G}_{N-1}^T \boldsymbol{P}_{N-1}\boldsymbol{e}_{N-1}\right) \\
&\overset{!}{\leq} W_N\left(\boldsymbol{e}_1,\ldots,\boldsymbol{e}_N\right) = W_{N-1}\left(\boldsymbol{e}_1,\ldots,\boldsymbol{e}_{N-1}\right) - \boldsymbol{e}_N^T \boldsymbol{T}_N \boldsymbol{e}_N
\end{aligned} \tag{4.76}$$

negative definite.

Assuming the maximum of the limiting function $W_N = -\boldsymbol{e}_1^T \boldsymbol{Q}_1 \boldsymbol{e}_1 - \ldots - \boldsymbol{e}_N^T \boldsymbol{Q}_N \boldsymbol{e}_N$, the control law

$$\boldsymbol{u} = \boldsymbol{G}_N'\left(\dot{\boldsymbol{\alpha}}_{N-1} - \boldsymbol{f}_N + \boldsymbol{K}_N \boldsymbol{e}_N + \boldsymbol{P}_N^{-1}\boldsymbol{G}_{N-1}^T \boldsymbol{P}_{N-1}\boldsymbol{e}_{N-1}\right) \tag{4.77}$$

renders the time derivative

$$\begin{aligned}\dot{V}_N &= -\boldsymbol{e}_1^T\boldsymbol{Q}_1\boldsymbol{e}_1 - \ldots - \boldsymbol{e}_{N-1}^T\boldsymbol{Q}_{N-1}\boldsymbol{e}_{N-1} - \boldsymbol{e}_N^T\boldsymbol{K}_N^T\boldsymbol{P}_N\boldsymbol{e}_N - \boldsymbol{e}_N^T\boldsymbol{P}_N\boldsymbol{K}_N\boldsymbol{e}_N \\ &= -\boldsymbol{e}_1^T\boldsymbol{Q}_1\boldsymbol{e}_1 - \ldots - \boldsymbol{e}_{N-1}^T\boldsymbol{Q}_{N-1}\boldsymbol{e}_{N-1} - \boldsymbol{e}_N^T\left(\boldsymbol{K}_N^T\boldsymbol{P}_N + \boldsymbol{P}_N\boldsymbol{K}_N\right)\boldsymbol{e}_N \\ &\overset{!}{=} -\boldsymbol{e}_1^T\boldsymbol{Q}_1\boldsymbol{e}_1 - \ldots - \boldsymbol{e}_N^T\boldsymbol{Q}_N\boldsymbol{e}_N\end{aligned} \tag{4.78}$$

of (4.75) negative definite if $\boldsymbol{K}_N$ fulfills the matrix Lyapunov equation

$$\boldsymbol{P}_N\boldsymbol{K}_N + \boldsymbol{K}_N^T\boldsymbol{P}_N = \boldsymbol{Q}_N \tag{4.79}$$

for $\boldsymbol{P}_N, \boldsymbol{Q}_N > 0$. Therefore, the equilibrium $\boldsymbol{e} = \begin{bmatrix}\boldsymbol{e}_1 & \ldots, \boldsymbol{e}_N\end{bmatrix}^T = \boldsymbol{0}$ of the overall error states (4.73) is asymptotically stable.

The presented classical BS control design procedure (SISO and MIMO) includes several degrees of freedom considering the parametric and structural design of the control law. The selected parameters and structure affect the error convergence rate and therefore the overall tracking performance significantly. In the following, all degree of freedoms of the BS control design are listed:

- *CLF*: The BS procedure was introduced by selecting the CLF as a quadratic function in the error states. This choice simplified the derivation of the pseudo-control and final control laws for SISO and MIMO cases. Besides a quadratic function, any other potential CLF candidate is possible. Each variation in the CLF may result in different control structures and closed-loop performances.
- *Feedback Gains*: As in any control design methodology, the gains used to feedback the system states or tracking errors play a crucial role in terms of closed-loop robustness and performance. In the presented BS control structure the increase of the controller gains lead to a faster decay of states towards the considered equilibrium (here: $\boldsymbol{e} = \boldsymbol{0}$). In case of the MIMO system the controller gains cannot be defined directly but are determined via the matrix Lyapunov function and the corresponding weighting matrices $\boldsymbol{P}_i$ and $\boldsymbol{Q}_i$.
- *Limiting Function*: In each design step, the limiting function was chosen as a quadratic function and the upper limit was considered for the pseudo-control and final control laws. As already discussed for the selection of the CLF, the limiting function influence the structure (and therefore the closed-loop behavior) of the control laws in a similar way.

  Remark: It is not required, that the function structure of the limiting function matches with the one of the CLF candidate. Any negative definite rendering function is possible.

4.2.2.4 Command Filtered Backstepping for SISO Systems

By considering the classical BS procedure described in section 4.2.2.2 and section 4.2.2.3, the $n-i$-th time derivative of the intermediate control law α_i enters the final control law u (in case of a MIMO system the $N-i$-th time derivative enters the final control law $\boldsymbol{u}$). This control structure requires the derivation of model data and the n-th time derivative of the reference trajectory y_r. In case of systems with complex dynamics (e.g. nonlinear aerodynamics) the offline calculated derivatives of model data may lead to extensive analytical expressions for the final control law [40]. Besides the impracticalness of those feedback laws for real systems, the numerical derivation of tabular data (e.g. aerodynamic data) is a significant source for mismatch between plant and design model. Another drawback of classical BS is its limited applicability to systems, which exhibit a feedback form [35, 94].

In recent years, further BS-based approaches were designed to overcome the aforementioned major drawbacks of the theoretical methodology developed by Kokotovic in the early 1990s [105]. A collection of novel adaptive and non-adaptive approaches concerning the shortcomings of conventional BS can be found in [48]. A promising methodology, avoiding cumbersome expressions stemming from derivations of system dynamics, is called *Command Filtered Backstepping* and was published by Farrel in 2009 [41]. The analytical expressions of the intermediate control laws with respect to time are generated by filters [41].

This novel approach does not require the system to be in (strict) feedback form anymore. Thus, for the purpose of introducing CFB the system is assumed to be in the following form

$$\begin{array}{rcl} \dot{x}_1 &=& f_1(\boldsymbol{x}) + g_1(\boldsymbol{x}) \cdot x_2 \\ \dot{x}_2 &=& f_2(\boldsymbol{x}) + g_2(\boldsymbol{x}) \cdot x_3 \\ &\vdots& \\ \dot{x}_{n-1} &=& f_{n-1}(\boldsymbol{x}) + g_{n-1}(\boldsymbol{x}) \cdot x_n \\ \dot{x}_n &=& f_n(\boldsymbol{x}) + g_n(\boldsymbol{x}) \cdot u \end{array} \tag{4.80a}$$

$$y = x_1 \tag{4.80b}$$

with $\boldsymbol{x} = \begin{bmatrix} x_1 & \dots & x_n \end{bmatrix}^T \in \mathbb{R}^{n \times 1}$ being the system's state vector, $u \in \mathbb{R}$ is the scalar input, and y constitutes the system's output, which is equal to the outermost state x_1. Since the methodology of CFB is based on BS, a repetition of design steps which are already described in section 4.2.2.2 are omitted in this section. In contrast to Farrell's explanation [41], the depicted derivation of CFB is in accordance with the recursive design procedure of the foregoing sections 4.2.2.2 and 4.2.2.3.

For the purpose of overcoming the tedious and impractical analytical expression of the final control law u stemming from the consecutive time derivations of the pseudo-control laws (see (4.44) or (4.51)), CFB introduces filters to calculate a filtered version $\alpha_{fil,i}$ and $\dot{\alpha}_{fil,i}$ based on the intermediate control laws α_i. For the sake of simplicity the principle of filtering the intermediate control α_i is illustrated by linear filters described in the frequency domain. Thus, for the design steps $i = 1, \dots, n$ the filtered version of the $n-1$ pseudo-controls

$$\begin{array}{rcl} \alpha_1 &=& \frac{1}{g_1}\left(\dot{y}_r - f_1 + c_1 \cdot \hat{e}_1\right) \\ \alpha_k &=& \frac{1}{g_k}\left(\dot{\alpha}_{k-1,fil} - f_k + c_k \cdot \hat{e}_k + g_{k-1} \cdot \tilde{e}_{k-1}\right), \quad k = 2, \dots, i-1 \end{array} \tag{4.81}$$

and its corresponding time derivative result as

$$\begin{array}{rcl} \alpha_{k,fil} &=& G_{fil,k}(s) \cdot \alpha_k \\ \dot{\alpha}_{k,fil} &=& sG_{fil,k}(s) \cdot \alpha_k, \quad k = 1, \dots, i-1. \end{array} \tag{4.82}$$

Due to the usage of filters for obtaining the intermediate control signals, two different error definitions are used throughout the theory of CFB: one is the *tracking error*

$$\hat{e}_i = \alpha_{i-1,fil} - x_i \tag{4.83}$$

describing the difference between the filtered pseudo-control law $\alpha_{i-1,fil}$ and the corresponding state x_i. In contrast to the error definition in section 4.2.2.2 (see (4.39) or (4.45)), the error with respect to the filtered version of $\alpha_{i-1,fil}$ is labeled by using the $\hat{}$-symbol. The second error is called *Compensated Tracking Error (CTE)*

$$\begin{array}{rcl} \tilde{e}_i &=& \alpha_{i-1,fil} - x_i - z_i \\ &=& \hat{e}_i - z_i \end{array} \tag{4.84}$$

and describes the tracking error compensated by the unachieved portion z_i. In case of $i = 1$, $\alpha_{0,fil} = y_r$ holds.

This unachieved portion z_i plays a crucial role in CFB: Due to the dynamic characteristics of the command filters, the filtered intermediate control variable $\alpha_{i,fil}$ exhibits a delayed response compared to α_i. Those filtered versions $\alpha_{i,fil}$ replace the intermediate controls α_i in the subsequent BS design steps. For compensating the deviating response (unachieved portion) caused by the lagged intermediate controls, the unachieved portion z_i is removed from the tracking error $\hat{e}_i$ (see (4.84)). In contrast to classical BS, the intermediate control variable *and* the dynamics of the unachieved portion z_i is calculated in each design step i to render the control error stable in terms of Lyapunov's direct method.

Since CFB follows the same recursive design methodology as classical BS, the pseudo-control law α_i is calculated in each i design step. Due to the fact that the filtering of α_i is part of the subsequent design step $i + 1$, the unachieved portion z_i (depending on the difference $\alpha_{i,fil} - \alpha_i$) is considered as zero ($z_i = 0$) for deriving the intermediate control law α_i in design step i. In step $i + 1$, the pseudo-control α_i is filtered to obtain $\alpha_{fil,i}$. Therefore, the dynamics of the unachieved portion z_i is calculated in the following design step $i + 1$ under the restriction to render the relevant subsystem - based on the respective CLF - stable. According to the error definitions in (4.83) and (4.84) and under consideration of $z_i = 0$ the CTE and the tracking error are equal for the considered design step i.

Therefore, the CLF in the i-th design step includes the CTE from the previous steps $1, \ldots, i-1$ and the tracking error of the current design step i:

$$V_i = \frac{1}{2}\sum_{k=1}^{i-1} \tilde{e}_k^2 + \frac{1}{2}\hat{e}_i^2 \tag{4.85}$$

In order to calculate the time derivative of V_i, the dynamics of the tracking error (4.83)

$$\begin{aligned} \dot{\hat{e}}_i &= \dot{\alpha}_{i-1,fil} - \dot{x}_i \\ &= \dot{\alpha}_{i-1,fil} - f_i(\boldsymbol{x}) - g_i(\boldsymbol{x}) \cdot x_{i+1} \end{aligned} \tag{4.86}$$

and the CTE (4.84)

$$\begin{aligned} \dot{\tilde{e}}_i &= \dot{\alpha}_{i-1,fil} - \dot{x}_i - \dot{z}_i \\ &= \dot{\alpha}_{i-1,fil} - f_i(\boldsymbol{x}) - g_i(\boldsymbol{x}) \cdot x_{i+1} - \dot{z}_i \end{aligned} \tag{4.87}$$

are necessary. Both dynamic expressions are obtained by substituting the state EOM from (4.80a) into the time derivative of the respective tracking errors. Reorganizing (4.84) and adding/subtracting the respective pseudo-control α_{i-1}, the state variable becomes

$$x_i = \alpha_{i-1,fil} - \tilde{e}_i - z_i + \alpha_{i-1} - \alpha_{i-1}. \tag{4.88}$$

Substituting (4.88) in (4.86) and (4.87) the tracking error and its compensated version result as

$$\dot{\hat{e}}_i = \dot{\alpha}_{i-1,fil} - f_i(\boldsymbol{x}) - g_i(\boldsymbol{x}) \cdot (\alpha_{i,fil} - \tilde{e}_{i+1} - z_{i+1} + \alpha_i - \alpha_i) \tag{4.89}$$

and

$$\dot{\tilde{e}}_i = \dot{\alpha}_{i-1,fil} - f_i(\boldsymbol{x}) - g_i(\boldsymbol{x}) \cdot (\alpha_{i,fil} - \tilde{e}_{i+1} - z_{i+1} + \alpha_i - \alpha_i) - \dot{z}_i, \tag{4.90}$$

respectively. Considering (4.89) and (4.90), the time derivative of the CLF (4.85) becomes

$$\begin{aligned}\dot{V}_i &= \tilde{e}_1 \cdot (\dot{y}_r - f_1 - g_1 \cdot (\alpha_{1,fil} - \tilde{e}_2 - z_2 + \alpha_1 - \alpha_1) - \dot{z}_1) \\ &\quad +\tilde{e}_2 \cdot (\dot{\alpha}_{1,fil} - f_2 - g_2 \cdot (\alpha_{2,fil} - \tilde{e}_3 - z_3 + \alpha_2 - \alpha_2) - \dot{z}_2) \\ &\quad +\dots \\ &\quad +\tilde{e}_{i-1} \cdot (\dot{\alpha}_{i-2,fil} - f_{i-1} - g_{i-1} \cdot (\alpha_{i-1,fil} - \hat{e}_i + \alpha_{i-1} - \alpha_{i-1}) - \dot{z}_{i-1}) \\ &\quad +\hat{e}_i \cdot (\dot{\alpha}_{i-1,fil} - f_i - g_i \cdot x_{i+1}) \\ &\overset{!}{\leq} W_i(\tilde{e}_1, \dots, \tilde{e}_{i-1}, \hat{e}_i) = -\textstyle\sum_{k=1}^{i-1} c_k \tilde{e}_k^2 + -c_i \hat{e}_i^2.\end{aligned} \tag{4.91}$$

Applying the pseudo-control laws (4.81) from the design steps $k \leq i-1$, (4.91) can be written as

$$\begin{aligned}\dot{V}_i &= \tilde{e}_1 \cdot (-c_1 \cdot \hat{e}_1 - g_1 \cdot (\alpha_{1,fil} - z_2 - \alpha_1) - \dot{z}_1) \\ &\quad +\tilde{e}_2 \cdot (-c_2 \cdot \hat{e}_2 - g_2 \cdot (\alpha_{2,fil} - z_3 - \alpha_2) - \dot{z}_2) \\ &\quad +\dots \\ &\quad +\tilde{e}_{i-1} \cdot (-c_{i-1} \cdot \hat{e}_{i-1} - g_{i-1} \cdot (\alpha_{i-1,fil} - \alpha_{i-1}) - \dot{z}_{i-1}) \\ &\quad +\hat{e}_i \cdot (\dot{\alpha}_{i-1,fil} + g_{i-1} \cdot \tilde{e}_{i-1} - f_i - g_i \cdot x_{i+1}) \\ &\overset{!}{=} W_i(\tilde{e}_1, \dots, \tilde{e}_k, \hat{e}_i) = -\textstyle\sum_{k=1}^{i-1} c_k \tilde{e}_k^2 + -c_i \hat{e}_i^2.\end{aligned} \tag{4.92}$$

As discussed in the previous sections (see sections 4.2.2.2 and 4.2.2.3), the maximum of the limiting function W_i is considered to facilitate the derivation of the pseudo-control laws (final control law) and unachieved portions. For the purpose of rendering (4.92) negative definite, the unachieved portions and the desired state variable $x_{i+1,d}$ (pseudo-control) of design step i result as

$$\begin{aligned}\dot{z}_k &= -c_k \cdot z_k - g_k(\alpha_{k,fil} - \alpha_k) + g_k \cdot z_{k+1}, \quad k = 1, \dots, i-2 \\ \dot{z}_{i-1} &= -c_{i-1} \cdot z_{i-1} - g_{i-1}(\alpha_{i-1,fil} - \alpha_{i-1}) \\ \dot{z}_i &= 0\end{aligned} \tag{4.93}$$

and

$$x_{i+1,d} = \alpha_i = \frac{1}{g_i}(\dot{\alpha}_{i-1,fil} - f_i + c_i \cdot \hat{e}_i + g_{i-1} \cdot \tilde{e}_{i-1}), \tag{4.94}$$

respectively. In the final design step $i = n$, the CLF is extended to

$$V_n = \frac{1}{2}\sum_{k=1}^{n-1} \tilde{e}_k^2 + \frac{1}{2}\hat{e}_n^2 \tag{4.95}$$

and by following the same procedure as for the pseudo-control laws (see (4.86) to (4.94)), the final control law is

$$u = \frac{1}{g_n}(\dot{\alpha}_{n-1,fil} - f_n + c_n \cdot \hat{e}_n + g_{n-1} \cdot \tilde{e}_{n-1}). \tag{4.96}$$

Analogous to the discussion at the end of section 4.2.2.3, the structure of the CLF, the limiting function W_i, and the choice of the feedback gains determine the dynamics of the unachieved portion, intermediate, and final control laws.

With the derivation above, the Lyapunov function guarantees only stability for the CTE. By using the properties of singular perturbed systems [106], the stability of the additional states (tracking error $\hat{e}_i$, unachieved portion z_i, filter states) involved within the control design process can be proven. Since this prove is beyond the scope of this thesis, the interested reader is referred to [41].

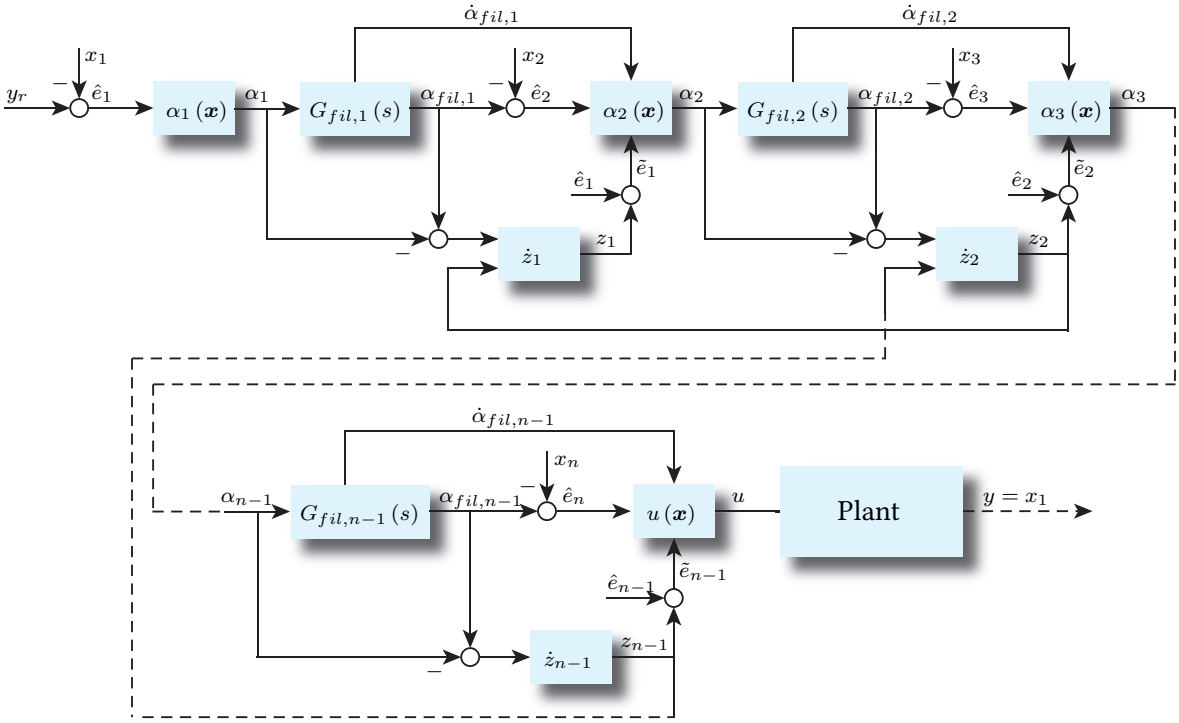

Figure 4.2: Block diagram of CFB-based control law.

4.2.2.5 Command Filtered Backstepping for MIMO Systems

This section briefly introduces CFB for the case that the considered system has the following MIMO dynamics:

$$\begin{aligned}
\dot{\boldsymbol{x}}_1 &= \boldsymbol{f}_1(\boldsymbol{x}) + \boldsymbol{G}_1(\boldsymbol{x}) \cdot \boldsymbol{x}_2 \\
\dot{\boldsymbol{x}}_1 &= \boldsymbol{f}_2(\boldsymbol{x}) + \boldsymbol{G}_2(\boldsymbol{x}) \cdot \boldsymbol{x}_3 \\
&\vdots \\
\dot{\boldsymbol{x}}_{N-1} &= \boldsymbol{f}_{N-1}(\boldsymbol{x}) + \boldsymbol{G}_{N-1}(\boldsymbol{x}) \cdot \boldsymbol{x}_N \\
\dot{\boldsymbol{x}}_N &= \boldsymbol{f}_N(\boldsymbol{x}) + \boldsymbol{G}_N(\boldsymbol{x}) \cdot \boldsymbol{u}
\end{aligned} \tag{4.97a}$$

$$\boldsymbol{y} = \boldsymbol{x}_1 \tag{4.97b}$$

The notations and dimensions are in accordance with the system representation (4.52b) in section 4.2.2.3. The CFB-based control law is derived for the considered system dynamics (4.97a) to fulfill the tracking task $\boldsymbol{y} \overset{!}{=} \boldsymbol{y}_r$. The presentation follows the same didactic structure as the control law design described for the SISO case (see section 4.2.2.4).

Since the main idea of CFB is already presented in the previous section (section 4.2.2.4), the purpose of the depicted derivation is to highlight the main peculiarities in CFB control design for MIMO systems.

The i-th design step requires the filtered version

$$\begin{aligned}
\boldsymbol{\alpha}_{k,fil} &= \boldsymbol{G}_{fil,k}(s) \cdot \boldsymbol{\alpha}_k \\
\dot{\boldsymbol{\alpha}}_{k,fil} &= s\boldsymbol{G}_{fil,k}(s) \cdot \boldsymbol{\alpha}_k, \quad k = 1, \ldots, i-1.
\end{aligned} \tag{4.98}$$

of the $N-1$ pseudo-control laws

$$\begin{array}{rcl} \boldsymbol{\alpha}_1 & = & \boldsymbol{G}_1' \left(\dot{\boldsymbol{y}}_r - \boldsymbol{f}_1 + \boldsymbol{K}_1 \cdot \hat{\boldsymbol{e}}_1 \right) \\ \boldsymbol{\alpha}_k & = & \boldsymbol{G}_k' \left(\dot{\boldsymbol{\alpha}}_{k-1,fil} - \boldsymbol{f}_k + \boldsymbol{K}_k \cdot \hat{\boldsymbol{e}}_k + \boldsymbol{P}_k^{-1} \boldsymbol{G}_{k-1}^T \boldsymbol{P}_{k-1} \tilde{\boldsymbol{e}}_{k-1} \right), \quad k = 2, \ldots, i-1 \end{array} \tag{4.99}$$

obtained in the previous $i-1$ design steps. With the tracking error

$$\hat{\boldsymbol{e}}_i = \boldsymbol{\alpha}_{i-1,fil} - \boldsymbol{x}_i \tag{4.100}$$

and its compensated version (CTE)

$$\begin{array}{rcl} \tilde{\boldsymbol{e}}_i & = & \boldsymbol{\alpha}_{i-1,fil} - \boldsymbol{x}_i - \boldsymbol{z}_i \\ & = & \hat{\boldsymbol{e}}_i - \boldsymbol{z}_i \end{array} \tag{4.101}$$

the CLF

$$V_i = \sum_{k=1}^{i-1} \tilde{\boldsymbol{e}}_k^T \boldsymbol{P}_k \tilde{\boldsymbol{e}}_k + \hat{\boldsymbol{e}}_i^T \boldsymbol{P}_i \hat{\boldsymbol{e}}_i \tag{4.102}$$

is selected as a quadratic function including both errors, $\tilde{\boldsymbol{e}}_k$, $k \leq i-1$ and $\hat{\boldsymbol{e}}_i$. As already explained in section 4.2.2.3, $\boldsymbol{P}_i \in \mathbb{R}^{n_i \times n_i}$ describes the positive definite weighting of the respective error states.

By analogy to section 4.2.2.4 and taking the system's state space representation (4.97a) into account, the dynamics of the tracking error and the CTE result to

$$\begin{array}{rcl} \dot{\hat{\boldsymbol{e}}}_i & = & \dot{\boldsymbol{\alpha}}_{i-1,fil} - \dot{\boldsymbol{x}}_i \\ & = & \dot{\boldsymbol{\alpha}}_{i-1,fil} - \boldsymbol{f}_i(\boldsymbol{x}) - \boldsymbol{G}_k(\boldsymbol{x}) \cdot \boldsymbol{x}_{i+1} \end{array} \tag{4.103}$$

and

$$\begin{array}{rcl} \dot{\tilde{\boldsymbol{e}}}_i & = & \dot{\boldsymbol{\alpha}}_{i-1,fil} - \dot{\boldsymbol{x}}_i - \dot{\boldsymbol{z}}_i \\ & = & \dot{\boldsymbol{\alpha}}_{i-1,fil} - \boldsymbol{f}_i(\boldsymbol{x}) - \boldsymbol{G}_i(\boldsymbol{x}) \cdot \boldsymbol{x}_{i+1} - \dot{\boldsymbol{z}}_i, \end{array} \tag{4.104}$$

respectively. Rearranging (4.101) and adding/subtracting the pseudo-control law $\boldsymbol{\alpha}_{i-1}$, the state variable $\boldsymbol{x}_{i+1}$ in (4.104) can be written as

$$\boldsymbol{x}_{i+1} = \boldsymbol{\alpha}_{i,fil} - \tilde{\boldsymbol{e}}_{i+1} - \boldsymbol{z}_{i+1} + \boldsymbol{\alpha}_i - \boldsymbol{\alpha}_i. \tag{4.105}$$

Thus, the dynamics of the tracking error (4.103) and the CTE (4.104) becomes

$$\dot{\hat{\boldsymbol{e}}}_i = \dot{\boldsymbol{\alpha}}_{i-1,fil} - \boldsymbol{f}_i(\boldsymbol{x}) - \boldsymbol{G}_i(\boldsymbol{x}) \cdot (\boldsymbol{\alpha}_{i,fil} - \tilde{\boldsymbol{e}}_{i+1} - \boldsymbol{z}_{i+1} + \boldsymbol{\alpha}_i - \boldsymbol{\alpha}_i) \tag{4.106}$$

and

$$\dot{\tilde{\boldsymbol{e}}}_i = \dot{\boldsymbol{\alpha}}_{i-1,fil} - \boldsymbol{f}_i(\boldsymbol{x}) - \boldsymbol{G}_i(\boldsymbol{x}) \cdot (\boldsymbol{\alpha}_{i,fil} - \tilde{\boldsymbol{e}}_{i+1} - \boldsymbol{z}_{i+1} + \boldsymbol{\alpha}_i - \boldsymbol{\alpha}_i) - \dot{\boldsymbol{z}}_i, \tag{4.107}$$

respectively.

Based on the error dynamics (4.106), (4.107) and the pseudo-control laws $\boldsymbol{\alpha}_k$, $k = 1, \ldots, i-1$ (see (4.99)) the time derivative

$$\begin{array}{rcl} \dot{V}_i & = & \dot{\tilde{\boldsymbol{e}}}_1^T \boldsymbol{P}_1 \tilde{\boldsymbol{e}}_1 + \tilde{\boldsymbol{e}}_1^T \boldsymbol{P}_1 \dot{\tilde{\boldsymbol{e}}}_1 + \ldots + \dot{\tilde{\boldsymbol{e}}}_{i-1}^T \boldsymbol{P}_{i-1} \tilde{\boldsymbol{e}}_{i-1} + \tilde{\boldsymbol{e}}_{i-1} \boldsymbol{P}_{i-1} \dot{\tilde{\boldsymbol{e}}}_{i-1}^T \\ & & + \dot{\hat{\boldsymbol{e}}}_i^T \boldsymbol{P}_i \hat{\boldsymbol{e}}_i + \hat{\boldsymbol{e}}_i^T \boldsymbol{P}_i \dot{\hat{\boldsymbol{e}}}_i \\ & \overset{!}{\leq} & W_i(\tilde{\boldsymbol{e}}_1, \ldots, \tilde{\boldsymbol{e}}_k, \hat{\boldsymbol{e}}_i) = -\sum_{k=1}^{i-1} \tilde{\boldsymbol{e}}_k^T \boldsymbol{Q}_k \tilde{\boldsymbol{e}}_k - \hat{\boldsymbol{e}}_i^T \boldsymbol{Q}_i \hat{\boldsymbol{e}}_i \end{array} \tag{4.108}$$

of V_i (4.102) becomes:

$$\begin{aligned}
\dot{V}_i &= \left(-\boldsymbol{K}_1 \cdot \hat{\boldsymbol{e}}_1 - \boldsymbol{G}_1 \cdot (\boldsymbol{\alpha}_{1,fil} - \boldsymbol{z}_2 - \boldsymbol{\alpha}_1) - \dot{\boldsymbol{z}}_1\right)^T \cdot \boldsymbol{P}_1 \tilde{\boldsymbol{e}}_1 \\
&\quad + \tilde{\boldsymbol{e}}_1^T \boldsymbol{P}_1 \cdot \left(-\boldsymbol{K}_1 \cdot \hat{\boldsymbol{e}}_1 - \boldsymbol{G}_1 \cdot (\boldsymbol{\alpha}_{1,fil} - \boldsymbol{z}_2 - \boldsymbol{\alpha}_1) - \dot{\boldsymbol{z}}_1\right) \\
&\quad + \ldots \\
&\quad + \tilde{\boldsymbol{e}}_{i-1}^T \boldsymbol{P}_{i-1} \cdot \left(-\boldsymbol{K}_{i-1} \cdot \hat{\boldsymbol{e}}_{i-1} - \boldsymbol{G}_{i-1} \cdot (\boldsymbol{\alpha}_{i-1,fil} - \boldsymbol{\alpha}_{i-1}) - \dot{\boldsymbol{z}}_{i-1}\right) \\
&\quad + \left(-\boldsymbol{K}_{i-1} \cdot \hat{\boldsymbol{e}}_{i-1} - \boldsymbol{G}_{i-1} \cdot (\boldsymbol{\alpha}_{i-1,fil} - \boldsymbol{\alpha}_{i-1}) - \dot{\boldsymbol{z}}_{i-1}\right)^T \cdot \boldsymbol{P}_{i-1} \tilde{\boldsymbol{e}}_{i-1} \cdot \\
&\quad + \left(\dot{\boldsymbol{\alpha}}_{i-1,fil} - \boldsymbol{f}_i - \boldsymbol{G}_i \cdot x_{i+1} + \boldsymbol{P}_i^{-1} \boldsymbol{G}_{i-1}^T \boldsymbol{P}_{i-1} \tilde{\boldsymbol{e}}_{i-1}\right)^T \boldsymbol{P}_i \hat{\boldsymbol{e}}_i \\
&\quad + \hat{\boldsymbol{e}}_i^T \boldsymbol{P}_i \cdot \left(\dot{\boldsymbol{\alpha}}_{i-1,fil} - \boldsymbol{f}_i - \boldsymbol{G}_i \cdot x_{i+1} + \boldsymbol{P}_i^{-1} \boldsymbol{G}_{i-1}^T \boldsymbol{P}_{i-1} \tilde{\boldsymbol{e}}_{i-1}\right) \\
&\overset{!}{\leq} W_i\left(\tilde{\boldsymbol{e}}_1, \ldots, \tilde{\boldsymbol{e}}_k, \hat{\boldsymbol{e}}_i\right) = -\sum_{k=1}^{i-1} \tilde{\boldsymbol{e}}_k^T \boldsymbol{Q}_k \tilde{\boldsymbol{e}}_k - \hat{\boldsymbol{e}}_i^T \boldsymbol{Q}_i \hat{\boldsymbol{e}}_i
\end{aligned} \tag{4.109}$$

In order to be in line with the derivation in section 4.2.2.5, the limiting function's maximum $W_i = -\sum_{k=1}^{i-1} \tilde{\boldsymbol{e}}_k^T \boldsymbol{Q}_k \tilde{\boldsymbol{e}}_k - \hat{\boldsymbol{e}}_i^T \boldsymbol{Q}_i \hat{\boldsymbol{e}}_i$ is considered for rendering the time derivative of V_i (see (4.109)) negative definite. Based on this assumption the equality constraint from (4.109) restricts the unachieved portions and the pseudo-control law in the i-th design step to

$$\begin{aligned}
\dot{\boldsymbol{z}}_k &= -\boldsymbol{K}_k \cdot \boldsymbol{z}_k - \boldsymbol{G}_k\left(\boldsymbol{\alpha}_{k,fil} - \boldsymbol{\alpha}_k\right) + \boldsymbol{G}_k \cdot \boldsymbol{z}_{k+1}, \quad k = 1, \ldots, i-2 \\
\dot{\boldsymbol{z}}_{i-1} &= -\boldsymbol{K}_{i-1} \cdot \boldsymbol{z}_{i-1} - \boldsymbol{G}_{i-1}\left(\boldsymbol{\alpha}_{i-1,fil} - \boldsymbol{\alpha}_{i-1}\right) \\
\dot{\boldsymbol{z}}_i &= \boldsymbol{0}
\end{aligned} \tag{4.110}$$

and

$$\boldsymbol{\alpha}_i = \boldsymbol{G}_i'\left(\dot{\boldsymbol{\alpha}}_{i-1,fil} - \boldsymbol{f}_i + \boldsymbol{K}_i \cdot \hat{\boldsymbol{e}}_i + \boldsymbol{P}_i^{-1} \boldsymbol{G}_{i-1}^T \boldsymbol{P}_{i-1} \tilde{\boldsymbol{e}}_{i-1}\right), \tag{4.111}$$

respectively. Substituting (4.110) and (4.111) in (4.109), the time derivative of the CLF

$$\begin{aligned}
\dot{V}_i &= -\sum_{k=1}^{i-1} \tilde{\boldsymbol{e}}_k^T \boldsymbol{Q}_k \tilde{\boldsymbol{e}}_k - \hat{\boldsymbol{e}}_i^T \left(\boldsymbol{K}_i^T \boldsymbol{P}_i + \boldsymbol{P}_i \boldsymbol{K}_i\right) \hat{\boldsymbol{e}}_i \\
&\overset{!}{=} -\sum_{k=1}^{i-1} \tilde{\boldsymbol{e}}_k^T \boldsymbol{Q}_k \tilde{\boldsymbol{e}}_k - \hat{\boldsymbol{e}}_i^T \boldsymbol{Q}_i \hat{\boldsymbol{e}}_i
\end{aligned} \tag{4.112}$$

is negative definite if $\boldsymbol{K}_k$ fulfills the matrix Lyapunov equation

$$\boldsymbol{K}_k^T \boldsymbol{P}_k + \boldsymbol{P}_k \boldsymbol{K}_k = \boldsymbol{Q}_k \tag{4.113}$$

for $\boldsymbol{P}_k = \boldsymbol{P}_k^T > 0, \boldsymbol{Q}_k > 0$.

Conducting the above described procedure for the final design step $i = N$ using CLF

$$V_N = \sum_{k=1}^{n-1} \tilde{\boldsymbol{e}}_k^T \boldsymbol{P}_k \tilde{\boldsymbol{e}}_k + \frac{1}{2} \hat{\boldsymbol{e}}_n^T \boldsymbol{P}_n \hat{\boldsymbol{e}}_n, \tag{4.114}$$

the control law results as

$$\boldsymbol{u} = \boldsymbol{G}_N'\left(\dot{\boldsymbol{\alpha}}_{N-1,fil} - \boldsymbol{f}_N + \boldsymbol{K}_N \cdot \hat{\boldsymbol{e}}_N + \boldsymbol{P}_N^{-1} \boldsymbol{G}_{N-1}^T \boldsymbol{P}_{N-1} \tilde{\boldsymbol{e}}_{N-1}\right). \tag{4.115}$$

4.2.3 Reference Model and Pseudo Control Hedging (PCH)

In the flight control architecture depicted in fig. 4.1 the commanded signal $\boldsymbol{y}_c$, issued by the guidance unit is filtered by the so called *reference model*. The resulting reference signal and its corresponding derivatives $y_{1,r}, \dot{y}_{1,r}, \ldots, y_{1,r}^{(r_1)}, \ldots, y_{m,r}, \dot{y}_{m,r}, \ldots, y_{m,r}^{(r_m)}$ serve as the reference input of the subsequent flight control algorithm (FCS). The filtering of the commanded signal $\boldsymbol{y}_c$ has the main purpose to provide the control algorithm with a smooth trajectory, that is coherent with the physical capa-

bilities of the aerial vehicle at the considered flight envelope point and airframe configuration. A smooth reference trajectory $\boldsymbol{y}_r\,(t)$, which reflects the missile's physical characteristics reduces the workload of the control algorithm and therefore leads to an attenuation of undesirable effects (e.g. overshoot, undershoot, slow settling time) of the closed-loop system. Thus, the reference model in combination with the autopilot constitutes a key element by representing the system's performance requirements within the algorithmic design process. Those performance requirements, which are assigned to the FCS and in particular to the reference model, incorporate rise time, settling time, axes decoupling, and transmission bandwidth. For high-agile aerial systems, an ideal layout of the reference model would guarantee the full exploitation of the system's performance capabilities at all operating points without violating the boundaries of the flight envelope. A reference model for high-agile configurations (like the considered FSD Generic Surface-to-Air Missile (FGS-X-03)) shall be able to mimic the following physical features:

- nonlinear axes coupling
- saturation effects of the actuator unit
- main nonlinear aerodynamic effects
- non-uniform response for different command amplitudes

In common control approaches utilized in several aerial applications, the reference model is designed as a linear dynamical system [36, 37, 60]. Linear reference model lack the ability to fully exploit the aerial vehicle's nonlinear physics over the entire flight envelope. Thus, effects like the nonlinear kinematics or main aerodynamic effects are not represented by those classical, linear approaches.

In the context of model reference command filters, Johnson and Calise invented a method called Pseudo Control Hedging, which has the primary purpose to compensate the actuator dynamics [107]. Over recent years, PCH became a standard anti wind-up technique within autopilots of Unmanned Aerial Vehicles (UAVs) [66]. PCH protects the control algorithm, especially the summation elements, from counter-acting the actuator dynamics or actuator saturation effects. The main idea of this anti wind-up strategy is to compensate the influence of the actuator unit by removing the reaction deficit, caused by the difference of the commanded ($\boldsymbol{u}_c$) and measured (estimated) actuator deflection, ($\boldsymbol{u}$) from the reference signal $\boldsymbol{y}_r 0$.

The theoretical background is explained based on the NDI control design scheme and nomenclature (see section 4.2.1). Transferring the strategy of PCH to a Backstepping control design using a reference model is straight forward [21].

In order to obtain a compact notation, the important expressions from section 4.2.1 are summarized here.

Based on the nomenclature defined in section 4.2.1 the plant's input/output characteristics is abbreviated by

$$\begin{bmatrix} y_1^{(r_1)}\,(\boldsymbol{x},\boldsymbol{u}) \\ \vdots \\ y_m^{(r_m)}\,(\boldsymbol{x},\boldsymbol{u}) \end{bmatrix} = \boldsymbol{F}\,(\boldsymbol{x},\boldsymbol{u})\,. \tag{4.116}$$

Considering (4.17), the NDI-based feedback control law $\boldsymbol{u}_c = \boldsymbol{A}^{-1}\,(\boldsymbol{x}) \cdot [\boldsymbol{\nu} - \boldsymbol{b}\,(\boldsymbol{x})]$ fulfills

$$\begin{bmatrix} y_1^{(r_1)}\,(\boldsymbol{x},\boldsymbol{u}_c) \\ \vdots \\ y_m^{(r_m)}\,(\boldsymbol{x},\boldsymbol{u}_c) \end{bmatrix} = \boldsymbol{F}\,(\boldsymbol{x},\boldsymbol{u}_c) = \boldsymbol{\nu}. \tag{4.117}$$

Recall that the feedback control $\boldsymbol{u}_c$ is designed to render the closed-loop system's input/output characteristic linear with the pseudo-control $\boldsymbol{\nu}$ constituting the input of the transformed (linear) system (see section 4.2.1.2). This pseudo-control

$$\boldsymbol{\nu} = \boldsymbol{\nu}_r + \boldsymbol{\nu}_c \tag{4.118}$$

introduced in section 4.2.1, can be separated in a feed-forward part ($\boldsymbol{\nu}_r$) generated by the reference model and a feedback signal ($\boldsymbol{\nu}_c$). As the feed-forward signal $\boldsymbol{\nu}_r$ is used to guarantee fast transient response, the feedback portion $\boldsymbol{\nu}_c$ is designed to set up certain performance and robustness properties of the closed-loop. The control term $\boldsymbol{\nu}_c$ is inevitable when the dynamics of the assumed design model and the plant deviates. For introducing the principle of PCH within this section, the control portion $\boldsymbol{\nu}_c$ in (4.118) is not necessary and is therefore omitted from further considerations.

To fulfill the tracking control task in terms of NDI, the system's nonlinear input/output characteristic $\boldsymbol{F}(\boldsymbol{x}, \boldsymbol{u})$ is required to match the corresponding reference model derivatives:

$$\begin{aligned} \boldsymbol{F}(\boldsymbol{x}, \boldsymbol{u}) &\overset{!}{=} \begin{bmatrix} y_{1,r}^{(r_1)}(\boldsymbol{x}_r, \boldsymbol{y}_c) \\ \vdots \\ y_{m,r}^{(r_m)}(\boldsymbol{x}_r, \boldsymbol{y}_c) \end{bmatrix} \\ &= \boldsymbol{F}_r(\boldsymbol{x}_r, \boldsymbol{y}_c). \end{aligned} \tag{4.119}$$

The reference model's states are summarized by $\boldsymbol{x}_r = \left[y_{1,r},\, \dot{y}_{1,r},\, \ldots, y_{1,r}^{(r_1-1)}, \ldots,\, y_{m,r},\, \dot{y}_{m,r},\, \ldots,\, y_{m,r}^{(r_m-1)}\right]^T \in \mathbb{R}^{r\times 1}$. Obviously, if (4.119) is fulfilled, the output $\boldsymbol{y} = \boldsymbol{y}_r$ tracks the reference signal and the main control goal is fulfilled. Based on the definitions (4.117) and (4.119), the reaction deficit

$$\begin{aligned} \boldsymbol{\nu}_h &= \boldsymbol{F}(\boldsymbol{x}, \boldsymbol{u}_c) - \boldsymbol{F}(\boldsymbol{x}, \boldsymbol{u}) \\ &= \boldsymbol{\nu} - \boldsymbol{F}(\boldsymbol{x}, \boldsymbol{u}) \end{aligned} \tag{4.120}$$

between the command $\boldsymbol{u}_c$ and the input $\boldsymbol{u}$ expressed in terms of the respective r_i-th output derivative defines the PCH-signal, $\boldsymbol{\nu}_h$. By rearranging the reaction deficit (4.120), the system's input/output characteristics can be expressed as

$$\boldsymbol{F}(\boldsymbol{x}, \boldsymbol{u}) = \boldsymbol{\nu} - \boldsymbol{\nu}_h. \tag{4.121}$$

With this result and the control goal $\boldsymbol{F}(\boldsymbol{x}, \boldsymbol{u}) \overset{!}{=} \boldsymbol{F}_r(\boldsymbol{x}_r, \boldsymbol{y}_c)$, the input/output characteristics of the reference signal results as

$$\boldsymbol{F}_r(\boldsymbol{x}_r, \boldsymbol{y}_c) = \boldsymbol{\nu} - \boldsymbol{\nu}_h. \tag{4.122}$$

This equation depicts the main idea of PCH: the reaction deficit $\boldsymbol{\nu}_h$ (4.120) resulting from the mismatch between $\boldsymbol{u}_c$ and $\boldsymbol{u}$ is removed from the input of the reference model's dynamics. Figure 4.3 illustrates a FCS including a model reference system with actuator compensation via PCH. Those modified reference signals are forwarded to the flight control algorithm.

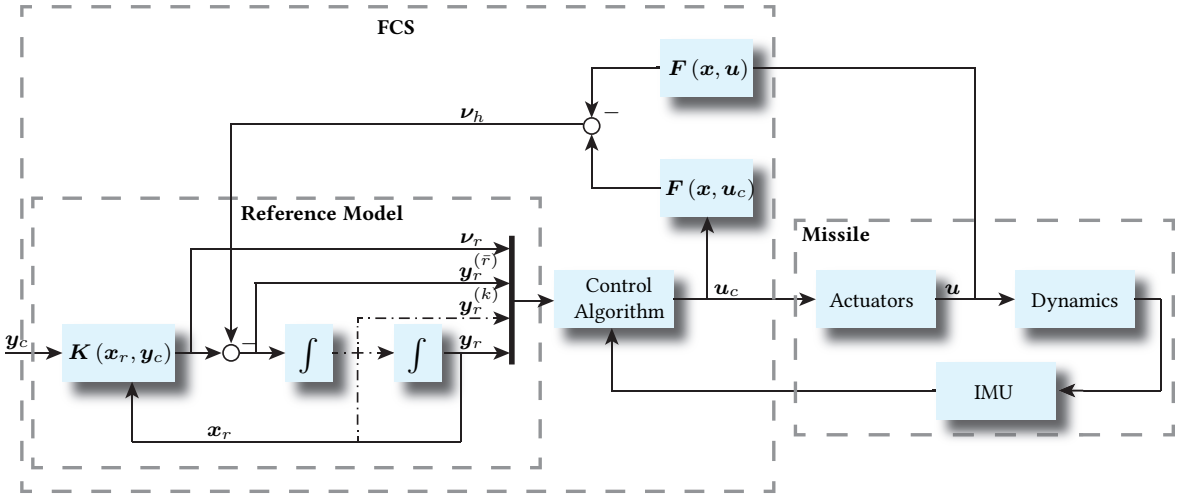

Figure 4.3: Block diagram of FCS architecture including autopilot and reference model. Remark: In order to facilitate the scheme, it is assumed that the relative degrees $r_1 = \cdots = r_k = \ldots = r_m = \bar{r}$ are equal.

At this point it is emphasized that the feed-forward signal $\boldsymbol{\nu}_r$ is not algebraically dependent of the PCH signal. $\boldsymbol{\nu}_r$ is influenced by $\boldsymbol{\nu}_h$ via the interconnected (feedback) structure of the reference model's dynamics.

4.3 $\mathcal{L}_1$ Adaptive Control ($\mathcal{L}_1$ AC) - Piecewise-Constant (PWC) Adaptation

Due to their extensive flight envelope including high angle of attacks and large traveling speeds, UAV in general and missiles in particular exhibit a wide spectrum of unmodeled and uncertain dynamics. Even though advanced computational methods are available and wind tunnel campaigns covering a large flight envelope are possible, the missile's aerodynamics still poses the most significant source of uncertainties within the modeling process.

In terms of missile autopilot design this large spectrum of parametric uncertainties and unmodeled dynamics (e.g. phantom yaw effects [108]) demand counter measures to preserve the closed-loop stability and desired performance characteristics. Besides classical robust control methods, which evolved in design and analysis process during the 1980s and 1990s [24, 28, 109], novel adaptive control theory mainly motivated by robust autopilot design for aerial platforms and experience gained from flight tests led to a variety of adaptive control approaches [49, 53, 54, 93, 110]. Model Reference Adaptive Control (MRAC) and $\mathcal{L}_1$ AC constitute the two main adaptive schemes widely used in the field of adaptive autopilot design.

MRAC tries to compensate the parametric uncertainties of a linear, minimum phase plant by updating (adapting) the parameters based on the error between the plant and a desired reference system. Over the years, four different MRAC schemes evolved using several modification methods to modify certain closed-loop characteristics. Only a short overview of the different MRAC architectures and their peculiarities are given [52, 54, 111, 112].

In classical *direct MRAC* design (see fig. 4.5) the feedback (and feed forward) gains of the controller are the outputs of an adaption algorithm. Those adaptive gains are calculated in a dynamical process

based on the error $\boldsymbol{e}$ between the states of a reference system $\boldsymbol{x}_{ref}$ and the closed-loop plant $\boldsymbol{x}$. The controller gains are modified by the adaption law to obtain an equal response between the closed-loop system and the desired reference dynamics [52, 54].

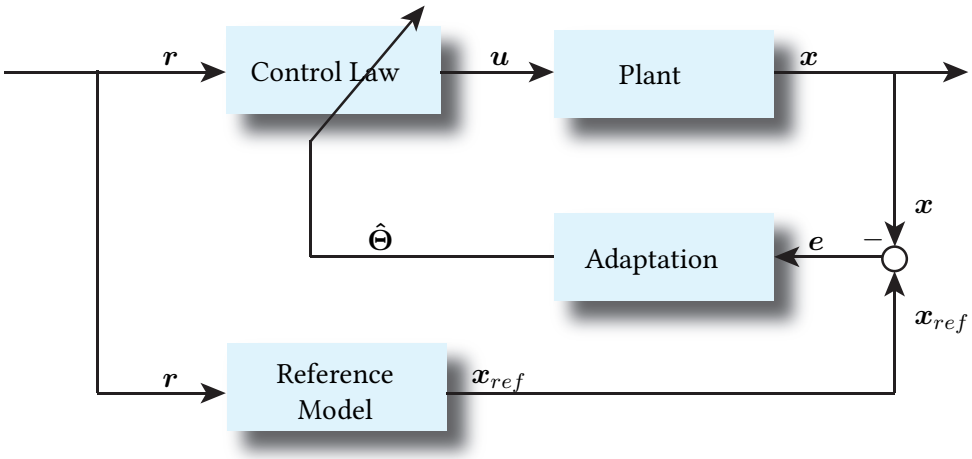

Figure 4.4: Block diagram of MRAC state feedback controller.

An *indirect MRAC* approach consists of two stages: in the first stage the uncertain plant parameters are estimated considering the error between the identification model and the closed-loop plant. Based on the estimated plant parameters, the controller gains are synthesized either using an algebraic relationship or a dynamic update (second stage) [52, 54, 111, 112]. *Composite MRAC* describes the combination of indirect and direct MRAC [113]. Besides the above mentioned schemes, *predictor based MRAC* identifies the difference between the closed-loop plant and the assumed plant dynamics (state predictor). This difference is applied to the control input of both: the state predictor and the plant [52, 111].

In general, all MRAC schemes calculate their on-line adaptive estimate based on the error between the plant's state vector and the state of a dynamic system, which serves as reference or identification system. Despite these slight variations in architecture, all MRAC approaches are derived based on the same stability concept. Lyapunov's direct method of stability (see section 4.1.2) is utilized in combination with the *MIT* rule for updating the adaptive parameters. The MIT rule constitute the basic concept within MRAC methodologies [52]. This approach guarantees only stability but no asymptotic stability of the error between closed-loop system and reference or identification model. Therefore, Barbalat's Lemma is used for proving asymptotic stability of the error [52].

The theory of MRAC, similar to other adaptive control approaches like Adaptive Pole Placement or Adaptive BS, exhibit some adverse characteristics considering the dependency between the rate of adaptation (performance) and the closed-loop robustness [114]. On the one hand, fast adaption lead to fast compensation of the undesired uncertainties with the possible drawback of introducing high-frequencies and large amplitudes into the control channel. On the other hand, slow adaption may lead to an unsatisfactory uncertainty compensation and therefore to undesired closed-loop performance.

Inspired by the concept of MRAC, Naira Hovakimyan and Chengyu Cao developed in the late 2000s the theory of $\mathcal{L}_1$ AC. Their concept is summarized in [63]. In $\mathcal{L}_1$ AC a predictor-based adaption scheme using an high learning rate is decoupled from the feedback path by a low-pass filter. This approach does not only guarantee that the bandwidth-limited portion of the adaptive estimate is

forwarded to the control signal $\boldsymbol{u}$, but also allows an adaptation rate, which is only constraint by computation capacities [63, 115]. At this point it should be noted, that both adaptive control theories (the same holds for Adaptive Pole Placement or Adaptive BS) are derived to minimize the control error between the closed-loop system and the desired dynamics (reference model or state predictor). The convergence of the adaptive estimates to the true uncertainties can only be achieved if the excitation of the closed-loop system is sufficiently rich [52]. In order to fulfill the persistent excitation (PE) condition, the reference signal is required to contain a specific set of frequencies.

Within the $\mathcal{L}_1$ AC framework, two different estimation schemes exist: a continuous one based on the MIT rule and a piecewise constant update law, which calculates the uncertainty estimate at a constant frequency depending on the available CPU sampling time T_s. Due to its inherent discrete structure and the capability of compensating uncertainties and unmodeled dynamics with the maximum allowable bandwidth, $\mathcal{L}_1$-PWC (see fig. 4.5) is perfectly suitable for agile systems exhibiting fast varying plant uncertainties such as the FGS-X-03.

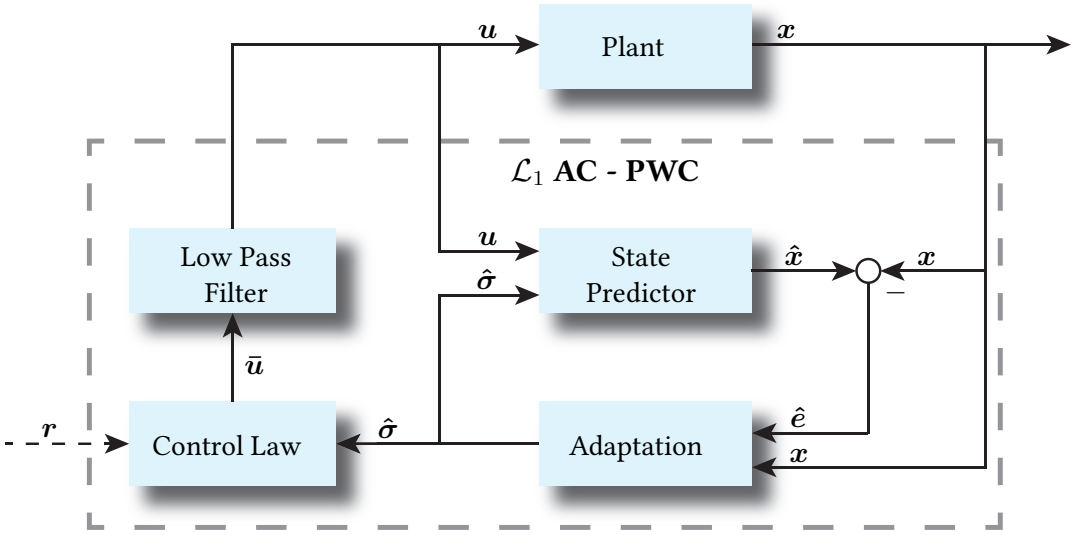

Figure 4.5: Block diagram of $\mathcal{L}_1$ AC - PWC.

Within section 4.3, the theory of $\mathcal{L}_1$ AC is derived and the main idea of the relevant proofs are presented. The book [63] of Naira Hovakimyan and Chengyu Cao constitute the main source for the following derivations and the interested reader can find the complete proofs of the herein considered theory in there. Since $\mathcal{L}_1$ AC - PWC is derived without introducing the MIT rule-based update law of $\mathcal{L}_1$ AC beforehand, the didactic organization in presenting the control law differs from [63].

At first, the control law including the update law is derived in section 4.3.1. The derivation of the control law is followed by the explanation of the according proofs, performance, and stability analysis section 4.3.2.

4.3.1 Derivation of Control Law

Before deriving the update and control law, the control problem including the plant's structure and its assumptions are defined in section 4.3.1.1. The idea of the state predictor and the resulting parameter estimate incorporating the CPU sampling time is depicted in section 4.3.1.2. The derivation of the final control law concludes this section.

4.3.1.1 Definition of Control Problem

The linear, non-autonomous system

$$\begin{aligned} \dot{\boldsymbol{x}} &= \boldsymbol{A}_d\boldsymbol{x} + \boldsymbol{B}_m\left(\boldsymbol{\Lambda}\boldsymbol{u} + \boldsymbol{\Delta}_m\left(t, \boldsymbol{x}, \boldsymbol{x}_z\right)\right) + \boldsymbol{B}_{um}\boldsymbol{\Delta}_{um}\left(t, \boldsymbol{x}, \boldsymbol{x}_z\right) \\ \dot{\boldsymbol{x}}_z &= \boldsymbol{f}_z\left(t, \boldsymbol{x}, \boldsymbol{x}_z\right) \end{aligned} \tag{4.123a}$$

$$\begin{aligned} \boldsymbol{y} &= \boldsymbol{C}\boldsymbol{x} \\ \boldsymbol{y}_z &= \boldsymbol{h}_z\left(t, \boldsymbol{x}_z\right) \end{aligned} \tag{4.123b}$$

with the desired closed-loop dynamic matrix $\boldsymbol{A}_d \in \mathbb{R}^{n\times n}$, the system's state vector $\boldsymbol{x} \in \mathbb{R}^{n\times 1}$, the input $\boldsymbol{u} \in \mathbb{R}^{m\times 1}$, and the output $\boldsymbol{y} \in \mathbb{R}^{n\times 1}$ is subject to the uncertainties $\boldsymbol{\Delta}_m : \mathbb{R}\times\mathbb{R}^n\times\mathbb{R}^p \to \mathbb{R}^m$ and $\boldsymbol{\Delta}_{um} : \mathbb{R}\times\mathbb{R}^n\times\mathbb{R}^p \to \mathbb{R}^{(n-m)}$, which are functions of the system state $\boldsymbol{x}$ and the unmodeled dynamics $\boldsymbol{x}_z \in \mathbb{R}^{p\times 1}$. The uncertainties are subdivided in a *matched* $\boldsymbol{\Delta}_m$ and an *unmatched* portion $\boldsymbol{\Delta}_{um}$ corresponding to the constant matched and unmatched input matrices and $\boldsymbol{B}_m \in \mathbb{R}^{n\times m}$ and $\boldsymbol{B}_{um} \in \mathbb{R}^{n\times(n-m)}$, respectively. The matched uncertainty lies within the span of the input $\boldsymbol{B}_m$ and can be directly compensated via the input $\boldsymbol{u}$. In contrast to the matched uncertainty $\boldsymbol{\Delta}_m$, the unmatched portion $\boldsymbol{\Delta}_{um}$ is mapped to a subset (via $\boldsymbol{B}_{um}$), which is not directly "accessible" by the input $\boldsymbol{u}$. The uncertainty of the system's input effectiveness is labeled with $\boldsymbol{\Lambda} \in \mathbb{R}^{m\times m}$. $\boldsymbol{y}_z \in \mathbb{R}^{l\times 1}$ describes the output of the nonlinear unmodeled dynamics.

For a compact notation, the index j is introduced denoting the matched ($j = m$) and unmatched ($j = um$) version of the uncertainty $\boldsymbol{\Delta}_j$ and the corresponding input matrix $\boldsymbol{B}_j$, respectively. The assumptions 4.3.1 to 4.3.8 characterize the uncertain system dynamics depicted in (4.123). With the assumptions 4.3.1 to 4.3.4 the properties of the undisturbed, nominal system are defined. The remaining assumptions consider the unmodeled dynamics (assumption 4.3.7), the input effectiveness (assumption 4.3.8), and the matched/unmatched uncertainties (assumptions 4.3.5 and 4.3.6) [63].

Assumption 4.3.1 (*Stability and observability*)

$\boldsymbol{A}_d$ is a Hurwitz matrix defining the desired closed-loop eigen dynamics of the system. The system $(\boldsymbol{A}_d, \boldsymbol{C})$ is assumed to be observable.

Assumption 4.3.2 (*Initial condition*)

The initial condition $\boldsymbol{x}(0)$ is assumed to be in inside an arbitrary known set $\|\boldsymbol{x}(0)\|_\infty \leq \rho_0$ for an arbitrary $\rho_0 > 0$.

Assumption 4.3.3 (*Input matrix*)

For the constant matched $\boldsymbol{B}_m$ and unmatched input matrix $\boldsymbol{B}_{um}$, the following condition hold:

- $\boldsymbol{B}_m^T\boldsymbol{B}_{um} = \boldsymbol{0}$.
- $\operatorname{rank}\left(\begin{bmatrix}\boldsymbol{B}_m & \boldsymbol{B}_{um}\end{bmatrix}\right) = n$

Assumption 4.3.4 (*Minimum phase characteristics*)

The open-loop transmission zeros of the transfer matrix $\boldsymbol{H}_m(s) = \boldsymbol{C}\left(s\boldsymbol{I} - \boldsymbol{A}_d\right)^{-1}\boldsymbol{B}_m$ lie in the open left-half complex plane.

Assumption 4.3.5 (*Boundedness of $\boldsymbol{\Delta}_j(t, \boldsymbol{0}, \boldsymbol{0})$*)

There exists $\boldsymbol{B}_j$, such that $\|\boldsymbol{\Delta}_j(t, \boldsymbol{0}, \boldsymbol{0})\|_\infty \leq \boldsymbol{B}_j$ holds for all $t \geq 0$.

Assumption 4.3.6 (*Semi-global Lipschitz condition*)

For arbitrary $\delta > 0$, there exists $K_{j,\delta} > 0$, such that

$$\left\|\boldsymbol{\Delta}_j\left(t, \boldsymbol{x}_1, \boldsymbol{x}_{z,1}\right) - \boldsymbol{\Delta}_j\left(t, \boldsymbol{x}_2, \boldsymbol{x}_{z,2}\right)\right\|_\infty \leq K_{j,\delta} \left\| \begin{bmatrix} \boldsymbol{x}_1 - \boldsymbol{x}_2 \\ \boldsymbol{x}_{z,1} - \boldsymbol{x}_{z,2} \end{bmatrix} \right\|_\infty \tag{4.124}$$

holds for all $\begin{bmatrix} \boldsymbol{x}_i \\ \boldsymbol{x}_{z,i} \end{bmatrix} \leq \delta$, $i = 1, 2$, uniformly in t.

Assumption 4.3.7 (*Stability of unmodeled dynamics*)

The unmodeled $\boldsymbol{x}_z$-dynamics are bounded-input bounded-output (BIBO) stable with respect to both initial conditions $\boldsymbol{x}_z(0)$ and input $\boldsymbol{x}(t)$, i.e. there exist $L_z, B_z > 0$ such that for all $t \geq 0$

$$\left\|(\boldsymbol{x}_z)_t\right\|_{\mathcal{L}_\infty} \leq L_z \left\|\boldsymbol{x}_t\right\|_{\mathcal{L}_\infty} + B_z \tag{4.125}$$

Assumption 4.3.8 (*Partial knowledge of the system input gain*)

The unknown system input effectiveness matrix $\boldsymbol{\Lambda}$ fulfills the following requirements:

- *strictly diagonally dominant matrix with the (known) sign of each diagonal element $\operatorname{sgn}(\boldsymbol{\Lambda}_{ii})$ with $j = i, \ldots, m$.*
- *there exists a known compact convex set $\boldsymbol{\Omega} \subset \mathbb{R}^{m \times m}$, such that $\boldsymbol{\Lambda} \in \boldsymbol{\Omega}$ and that a nominal system input gain $\boldsymbol{\Lambda}_0 \in \boldsymbol{\Omega}$ is known.*

In [63] $\mathcal{L}_1$ AC is derived for a tracking problem. The adaptive control algorithm is utilized as an augmentation of the baseline autopilot in order to increase the robustness under preserving the nominal performance. Under this constraint the adaptive control task is reduced to stabilize the tracking error. Therefore, the following derivation of the $\mathcal{L}_1$-PWC theory is conducted under the objective of stabilizing the state of the system (4.123) at $\boldsymbol{x} = \boldsymbol{0}$.

4.3.1.2 State Predictor and Update Law

Within the class of MRAC schemes (to which $\mathcal{L}_1$ AC belongs to), a control error is generated between the closed-loop system and the reference or identification model. This control error is processed within the update law to calculate the considered uncertainty estimate or adaptive gain. This dynamical model constitutes a core element within all MRAC schemes. In case of $\mathcal{L}_1$ AC, the so called state predictor depicted in (4.126) serves as an identification model for (4.123a).

$$\dot{\hat{\boldsymbol{x}}} = \boldsymbol{A}_d \hat{\boldsymbol{x}} + \boldsymbol{B}_m\left(\boldsymbol{\Lambda}_0 \boldsymbol{u} + \hat{\boldsymbol{\sigma}}_m(t)\right) + \boldsymbol{B}_{um} \hat{\boldsymbol{\sigma}}_{um}(t) \tag{4.126a}$$

$$\hat{\boldsymbol{y}} = \boldsymbol{C} \hat{\boldsymbol{x}} \tag{4.126b}$$

The predicted state vector is denoted with $\hat{\boldsymbol{x}} \in \mathbb{R}^{n \times n}$. $\hat{\boldsymbol{\sigma}}_m \in \mathbb{R}^{m \times 1}$ and $\hat{\boldsymbol{\sigma}}_{um} \in \mathbb{R}^{(n-m) \times 1}$ represent the matched and unmatched estimates, respectively. Even though the nominal system input gain $\boldsymbol{\Lambda}_0$ equals the identity matrix $\boldsymbol{I}_{m \times m}$ it is considered here for the sake of completeness.

Since both states $\boldsymbol{x}(t)$ and $\boldsymbol{x}_z(t)$ are functions of time, the respective uncertainty (matched or unmatched)

$$\bar{\boldsymbol{\Delta}}_j(t) = \boldsymbol{\Delta}_j\left(t, \boldsymbol{x}, \boldsymbol{x}_z\right) \tag{4.127}$$

can be expressed as a function of time only. As mentioned above, the adaptive update law is based on the error $\hat{\boldsymbol{e}} = \hat{\boldsymbol{x}} - \boldsymbol{x}$ between the state vector of the plant (4.123) and the one of the predictor system (4.126). Taking into account the dynamics (4.123a) and (4.126a), the error dynamics becomes

$$\begin{aligned}
\dot{\hat{\boldsymbol{e}}} &= \boldsymbol{A}_d\hat{\boldsymbol{e}} + \boldsymbol{B}_m\big(\hat{\boldsymbol{\sigma}}_m(t) + \underbrace{(\boldsymbol{\Lambda}_0 - \boldsymbol{\Lambda})\,\boldsymbol{u} - \bar{\boldsymbol{\Delta}}_m(t)}_{-\tilde{\boldsymbol{\Delta}}_m(t)}\big) + \boldsymbol{B}_{um}\left(\hat{\boldsymbol{\sigma}}_{um}(t) - \bar{\boldsymbol{\Delta}}_{um}(t)\right) \\
&= \boldsymbol{A}_d\hat{\boldsymbol{e}} + \boldsymbol{B}_m\left(\hat{\boldsymbol{\sigma}}_m(t) - \tilde{\boldsymbol{\Delta}}_m(t)\right) + \boldsymbol{B}_{um}\left(\hat{\boldsymbol{\sigma}}_{um}(t) - \bar{\boldsymbol{\Delta}}_{um}(t)\right) \\
&= \boldsymbol{A}_d\hat{\boldsymbol{e}} + \begin{bmatrix}\boldsymbol{B}_m & \boldsymbol{B}_{um}\end{bmatrix} \cdot \left(\begin{bmatrix}\hat{\boldsymbol{\sigma}}_m(t) \\ \hat{\boldsymbol{\sigma}}_{um}(t)\end{bmatrix} - \begin{bmatrix}\tilde{\boldsymbol{\Delta}}_m(t) \\ \bar{\boldsymbol{\Delta}}_{um}(t)\end{bmatrix}\right).
\end{aligned} \tag{4.128}$$

The peculiarity of $\mathcal{L}_1$-PWC compared to adaption schemes using the MIT-rule, is the CPU sample-based error consideration and compensation. In order to derive the uncertainty effect within one time sample T_s, the linear ordinary differential equation (ODE) of the error dynamics (4.128) is integrated (over the time t) starting at a multiple of the sample time, iT_s:

$$\begin{aligned}
\hat{\boldsymbol{e}}(iT_s + t) = e^{\boldsymbol{A}_d \cdot t} \cdot \hat{\boldsymbol{e}}(iT_s) &+ \int_{iT_s}^{iT_s+t} e^{\boldsymbol{A}_d\cdot(iT_s+t-\lambda)} \cdot \begin{bmatrix}\boldsymbol{B}_m & \boldsymbol{B}_{um}\end{bmatrix} \cdot \begin{bmatrix}\hat{\boldsymbol{\sigma}}_m(\lambda) \\ \hat{\boldsymbol{\sigma}}_{um}(\lambda)\end{bmatrix} d\lambda \\
&- \int_{iT_s}^{iT_s+t} e^{\boldsymbol{A}_d\cdot(iT_s+t-\lambda)} \cdot \begin{bmatrix}\boldsymbol{B}_m & \boldsymbol{B}_{um}\end{bmatrix} \cdot \begin{bmatrix}\tilde{\boldsymbol{\Delta}}_m(\lambda) \\ \bar{\boldsymbol{\Delta}}_{um}(\lambda)\end{bmatrix} d\lambda
\end{aligned} \tag{4.129}$$

The estimates $\hat{\boldsymbol{\sigma}}_m$ and $\hat{\boldsymbol{\sigma}}_{um}$ constitute the modifiable input of the error dynamics (4.128) and are designed to compensate for undesired, measurable errors of the system (4.129).

By substituting the integration arguments with

$$\begin{aligned}
\varrho(\lambda) &= \lambda - iT_s \Leftrightarrow \lambda(\varrho) = \varrho + iT_s \\
\varrho'(\lambda) &= \frac{d\varrho}{d\lambda} = 1 \rightarrow d\varrho = d\lambda
\end{aligned} \tag{4.130}$$

the integration limits and function arguments result as

$$\begin{aligned}
\int_{iT_s}^{iT_s+t} f(\lambda)\,d\lambda &= \int_{\varrho(iT_s)}^{\varrho(iT_s+t)} f(\lambda(\varrho))\,d\varrho \\
&= \int_0^t f(\varrho + iT_s)\,d\varrho.
\end{aligned} \tag{4.131}$$

Applying the substitution (4.130) with the corresponding limits (4.131) to the error system dynamics in (4.129) leads to

$$\begin{aligned}
\hat{\boldsymbol{e}}(iT_s + t) = e^{\boldsymbol{A}_d \cdot t} \cdot \hat{\boldsymbol{e}}(iT_s) &+ \int_0^t e^{\boldsymbol{A}_d\cdot(t-\varrho)} \begin{bmatrix}\boldsymbol{B}_m & \boldsymbol{B}_{um}\end{bmatrix} \begin{bmatrix}\hat{\boldsymbol{\sigma}}_m(\varrho + iT_s) \\ \hat{\boldsymbol{\sigma}}_{um}(\varrho + iT_s)\end{bmatrix} d\varrho \\
&- \int_0^t e^{\boldsymbol{A}_d\cdot(t-\varrho)} \begin{bmatrix}\boldsymbol{B}_m & \boldsymbol{B}_{um}\end{bmatrix} \begin{bmatrix}\tilde{\boldsymbol{\Delta}}_m(\varrho + iT_s) \\ \bar{\boldsymbol{\Delta}}_{um}(\varrho + iT_s)\end{bmatrix} d\varrho.
\end{aligned} \tag{4.132}$$

In order to consider the error propagation within one sampling period the integration horizon is chosen to be $t \in [iT_s, (i+1)T_s[$. Due to the sample-based approach the estimates are assumed to be constant $\hat{\boldsymbol{\sigma}}_i = const$ within the time span of a sampling interval $t \in [iT_s, (i+1)T_s[$. Since they are updated at each multiple of T_s, they are denoted as a function of the sampling time, $\hat{\boldsymbol{\sigma}}_i(iT_s)$.

Thus, the error (4.132) becomes

$$\begin{aligned}\hat{\boldsymbol{e}}\left(iT_s+T_s\right) = e^{\boldsymbol{A}_d\cdot T_s}\cdot\hat{\boldsymbol{e}}\left(iT_s\right) &+ \int_0^{T_s} e^{\boldsymbol{A}_d\cdot(T_s-\varrho)}\begin{bmatrix}\boldsymbol{B}_m & \boldsymbol{B}_{um}\end{bmatrix}\begin{bmatrix}\hat{\boldsymbol{\sigma}}_m\left(iT_s\right)\\ \hat{\boldsymbol{\sigma}}_{um}\left(iT_s\right)\end{bmatrix}d\varrho\\ &- \int_0^{T_s} e^{\boldsymbol{A}_d\cdot(T_s-\varrho)}\begin{bmatrix}\boldsymbol{B}_m & \boldsymbol{B}_{um}\end{bmatrix}\begin{bmatrix}\tilde{\boldsymbol{\Delta}}_m\left(\varrho+iT_s\right)\\ \bar{\boldsymbol{\Delta}}_{um}\left(\varrho+iT_s\right)\end{bmatrix}d\varrho\end{aligned} \tag{4.133}$$

with $\hat{\boldsymbol{e}}\left(iT_s\right)$ constituting the accumulated prediction error from previous time intervals $t < iT_s$ (initial condition of integration). Therefore, the first addend in (4.133) describes the measurable effect of the propagated error within one sampling interval $t \in [iT_s, (i+1)T_s[$. The second addend constitutes the effect of the customizable estimates $\hat{\boldsymbol{\sigma}}_i$, which are constant within one sampling interval $t \in [iT_s, (i+1)T_s[$. The prediction error resulting from the matched $\tilde{\boldsymbol{\Delta}}_m$ and unmatched $\bar{\boldsymbol{\Delta}}_{um}$ system uncertainties within the considered time span is given by the third addend in (4.133).

The idea of $\mathcal{L}_1$-PWC control is to compensate the effect of the propagated error $e^{\boldsymbol{A}_d\cdot T_s}\cdot\hat{\boldsymbol{e}}\left(iT_s\right)$, resulting from the previous time step $t < iT_s$, by the control inputs $\hat{\boldsymbol{\sigma}}_m$ and $\hat{\boldsymbol{\sigma}}_{um}$. Based on the representation of the prediction error transient in (4.133), the algebraic equation for the estimates are

$$\begin{bmatrix}\hat{\boldsymbol{\sigma}}_m\left(iT_s\right)\\ \hat{\boldsymbol{\sigma}}_{um}\left(iT_s\right)\end{bmatrix} = -\begin{bmatrix}\mathbb{I}_m & \boldsymbol{0}_{m\times(n-m)}\\ \boldsymbol{0}_{(n-m)\times m} & \mathbb{I}_{n-m}\end{bmatrix}\begin{bmatrix}\boldsymbol{B}_m & \boldsymbol{B}_{um}\end{bmatrix}^{-1}\boldsymbol{\Phi}^{-1}\left(T_s\right)e^{\boldsymbol{A}_d\cdot T_s}\cdot\hat{\boldsymbol{e}}\left(iT_s\right). \tag{4.134}$$

It is emphasized at this point that the propagated error $e^{\boldsymbol{A}_d\cdot T_s}\cdot\hat{\boldsymbol{e}}\left(iT_s\right)$ is compensated by (4.134) only within the considered time interval $t \in [iT_s, (i+1)T_s[$.

$\boldsymbol{\Phi}\left(T_s\right)$ describes the transition matrix of the linear system dynamics (4.133):

$$\begin{aligned}\boldsymbol{\Phi}\left(T_s\right) &= \int_0^{T_s} e^{\boldsymbol{A}_d\cdot(T_s-\varrho)}d\varrho\\ &= \left[-\boldsymbol{A}_d^{-1}\cdot e^{\boldsymbol{A}_d\cdot(T_s-\varrho)}\right]_0^{T_s} = -\boldsymbol{A}_d^{-1}\cdot\left(e^{\boldsymbol{A}_d\cdot(0)} - e^{\boldsymbol{A}_d\cdot(T_s)}\right)\cdot\\ &= \boldsymbol{A}_d^{-1}\cdot\left(e^{\boldsymbol{A}_dT_s} - \mathbb{I}_n\right)\end{aligned} \tag{4.135}$$

Applying the update law (4.134) to (4.133), the prediction error within the interval of one time sample T_s exhibits the following closed-loop form:

$$\hat{\boldsymbol{e}}\left(iT_s+T_s\right) = -\int_0^{T_s} e^{\boldsymbol{A}_d\cdot(T_s-\varrho)}\begin{bmatrix}\boldsymbol{B}_m & \boldsymbol{B}_{um}\end{bmatrix}\begin{bmatrix}\tilde{\boldsymbol{\Delta}}_m\left(\varrho+iT_s\right)\\ \bar{\boldsymbol{\Delta}}_{um}\left(\varrho+iT_s\right)\end{bmatrix}d\varrho \tag{4.136}$$

The remaining closed-loop error consists only of the integration of the matched and unmatched modeling errors summarized in $\tilde{\boldsymbol{\Delta}}_m$ and $\bar{\boldsymbol{\Delta}}_{um}$, respectively. The time integration of this error over one sampling interval constitutes the initial condition of the subsequent time step $(i+1)\,T_s$ and is compensated within the following sampling period $t \in [(i+1)T_s, (i+2)T_s[$ by the adaptive law (4.134).

Two things should be noted at the end of this section: first, the magnitude of the closed-loop error depicted in (4.136) correlates with the length of the sampling interval T_s. Therefore, it can be clearly seen, that with smaller sampling time T_s the magnitude of the error $\hat{\boldsymbol{e}}\left(iT_s+T_s\right)$ decreases. Second, the error feedback introduced via the update law of the estimates (4.134) constitutes a proportional

feedback with the gain

$$\boldsymbol{K}_{pwc} = -\begin{bmatrix} \mathbb{I}_m & \boldsymbol{0}_{m\times(n-m)} \\ \boldsymbol{0}_{(n-m)\times m} & \mathbb{I}_{n-m} \end{bmatrix} \begin{bmatrix} \boldsymbol{B}_m & \boldsymbol{B}_{um} \end{bmatrix}^{-1} \boldsymbol{\Phi}^{-1}\left(T_s\right) e^{\boldsymbol{A}_d \cdot T_s}. \tag{4.137}$$

This gain increases to infinity in case the sampling time goes to zero, $T_s \to 0$. Thus, a fast update of the estimates (small sampling time T_s) results in high gain control if this signal is directly used to close the control loop. In common control theory, high gain control is undesirable due to negative influence on robustness (noise amplification, limited bandwidth of actuators). Therefore, the advantage of fast adaption and error compensation is accompanied by a reduced robust performance.

For the purpose of decoupling the fast estimation loop from the feedback part, $\mathcal{L}_1$ AC theory uses low-pass filter to guarantee a bandwidth which is in line with the physical properties of the actuation unit and plant.

4.3.1.3 Control Law

In order to exploit the maximum possible estimation rate constrained by the used hardware without violating desired robustness characteristics, the core idea of $\mathcal{L}_1$-PWC consists in separating the estimation loop from the system input by a low-pass filter. Based on this design philosophy, the control signal of $\mathcal{L}_1$-PWC is generated by the output of the following dynamical system

$$\boldsymbol{u} = -\boldsymbol{K}_{fil}\boldsymbol{D}\left(s\right) \cdot \left(\boldsymbol{\Lambda}_0 \boldsymbol{u} + \hat{\boldsymbol{\sigma}}_m + \boldsymbol{H}_m^{-1}\left(s\right)\boldsymbol{H}_{um}\left(s\right)\hat{\boldsymbol{\sigma}}_{um}\right) \tag{4.138}$$

with

$$\boldsymbol{H}_m\left(s\right) = \boldsymbol{C} \cdot \underbrace{\left(s\mathbb{I}_n - \boldsymbol{A}_d\right)^{-1} \cdot \boldsymbol{B}_m}_{\boldsymbol{H}_{xm}(s)} \tag{4.139a}$$

$$\boldsymbol{H}_{um}\left(s\right) = \boldsymbol{C} \cdot \underbrace{\left(s\mathbb{I}_n - \boldsymbol{A}_d\right)^{-1} \cdot \boldsymbol{B}_{um}}_{\boldsymbol{H}_{xum}(s)}, \tag{4.139b}$$

being the input/output transfer functions of the matched and unmatched dynamics, respectively. $\boldsymbol{D}\left(s\right)$ is a strictly proper transfer matrix leading to the strictly proper $\mathcal{L}_1$ low-pass filter

$$\boldsymbol{C}\left(s\right) = \left(\mathbb{I}_m + \boldsymbol{\Lambda}_0 \boldsymbol{K}_{fil}\boldsymbol{D}\left(s\right)\right)^{-1}\boldsymbol{K}_{fil}\boldsymbol{D}\left(s\right). \tag{4.140}$$

Under the feasible assumption that the nominal control effectiveness equals the identity matrix $\boldsymbol{\Lambda}_0 = \mathbb{I}_m$ and by substituting the filter equation (4.140) into (4.138) the final control law of $\mathcal{L}_1$-PWC is given by:

$$\boldsymbol{u} = -\boldsymbol{C}\left(s\right) \cdot \left(\hat{\boldsymbol{\sigma}}_m + \boldsymbol{H}_m^{-1}\left(s\right)\boldsymbol{H}_{um}\left(s\right)\hat{\boldsymbol{\sigma}}_{um}\right) \tag{4.141}$$

Remark: As already mentioned in section 4.3.1.1 the derivation of the presented adaptive law, in contrast to [63], does not consider any reference signal $\boldsymbol{r}\left(t\right)$.

4.3.2 Analysis of $\mathcal{L}_1$ controller

The analysis section contains only the major steps of the proof of the $\mathcal{L}_1$-PWC control law presented in section 4.3.1. A detailed derivation of the proofs in a more general form can be found in [63].

The proof is subdivided into three parts: first, the stability of the prediction error $\hat{\boldsymbol{e}}\left(t\right)$ is considered (section 4.3.2.1). The second step includes the stability analysis of the ideal closed-loop refer-

ence system and the derivation of corresponding performance bounds (section 4.3.2.2). Based on both foregoing proofs, the last step comprises of analyzing the overall closed-loop dynamics (section 4.3.2.3).

4.3.2.1 Stability of Prediction Error $\hat{\mathbf{e}}(t)$

Within this section the transient and steady-state performance of the prediction error $\hat{\boldsymbol{e}}(iT_s + T_s)$ is considered. This analysis leads to an upper limit of the prediction error.

For the purpose of defining a general bound for the prediction error $\hat{\boldsymbol{e}}(t)$ the following functions

$$\bar{\alpha}_1(T_s) := \max_{t\in[0,T_s]} \left(\left\| e^{A_d \cdot t} \right\|_2 \right) \tag{4.142a}$$

$$\bar{\alpha}_2(T_s) := \max_{t\in[0,T_s]} \left(\int_0^t \left\| e^{A_d\cdot(t-\tau)} \cdot \boldsymbol{\Phi}^{-1}(T_s) \cdot e^{A_d \cdot T_s} \right\|_2 d\tau \right) \tag{4.142b}$$

$$\bar{\alpha}_3(T_s) := \max_{t\in[0,T_s]} \left(\int_0^t \left\| e^{A_d\cdot(t-\tau)} \cdot \boldsymbol{B}_m \right\|_2 d\tau \right) \tag{4.142c}$$

$$\bar{\alpha}_4(T_s) := \max_{t\in[0,T_s]} \left(\int_0^t \left\| e^{A_d\cdot(t-\tau)} \cdot \boldsymbol{B}_{um} \right\|_2 d\tau \right) \tag{4.142d}$$

are introduced describing the input bounds of the error transient (see (4.133)) with respect to the prediction error's initial condition $\hat{\boldsymbol{e}}(iT_s)$, the prediction error $\hat{\boldsymbol{e}}(iT_s)$ due to feedback by the update law (4.134), the matched and unmatched uncertainty, respectively.

With these input bounds the overall bound of the prediction error $\hat{\boldsymbol{e}}(iT_s + T_s)$ within one sampling interval (4.133) results as

$$\|\hat{\boldsymbol{e}}(iT_s + T_s)\|_2 \leq (\bar{\alpha}_1(T_s) + \bar{\alpha}_2(T_s)) \cdot \varsigma(T_s) + \bar{\alpha}_3(T_s) \cdot \Xi_m + \bar{\alpha}_4(T_s) \cdot \Xi_{um} := \gamma_0(T_s). \tag{4.143}$$

Ξ_m and Ξ_{um} defining the bounds of the matched and unmatched uncertainties, respectively. The upper bound of $\gamma_0(T_s)$ in (4.143) depends only on the sampling period T_s. This relationship between the control error $\hat{\boldsymbol{e}}(iT_s)$ and the sampling time T_s is one of the key results of $\mathcal{L}_1$-PWC control theory. It states that with smaller sampling time T_s (increased computation power), which leads to faster updates of the control estimates, the prediction error $\hat{\boldsymbol{e}}$ becomes smaller. Based on the definition of the integral functions (4.142) and $\gamma_0(T_s)$ in (4.143), this property is described mathematically by $\lim_{T_s\to 0} \gamma_0(T_s) = 0$. With this limiting relationship a constant $\bar{\gamma}_0$ is associated with each sample time $T_s > 0$ which satisfies

$$\gamma_0(T_s) < \bar{\gamma}_0. \tag{4.144}$$

Based on this relationship the prediction error's $\mathcal{L}_\infty$-norm is bounded by $\bar{\gamma}_0$:

$$\|\hat{\boldsymbol{e}}\|_{\mathcal{L}_\infty} \leq \bar{\gamma}_0 \tag{4.145}$$

Remark: It shall be emphasized at this point that $\bar{\gamma}_0$ constitutes an upper bound of $\gamma_0(T_s)$. Therefore, even if the upper bound does not explicitly depend on T_s, an implicit dependency of $\bar{\gamma}_0$ from the sampling time is given via (4.144).

4.3.2.2 Closed-Loop Reference System and Performance Bounds

In $\mathcal{L}_1$ AC theory the term *closed-loop reference system* defines the achievable closed-loop control objectives. It is an ideal representation of the closed-loop system dynamics assuming the uncertainties $\boldsymbol{\Delta}_m$ and $\boldsymbol{\Delta}_{um}$ are known and can be incorporated via the control law. This reference system uses the full filter dynamics to compute performance bounds. The closed-loop reference system for the herein considered control task (see section 4.3.1.1) is described by the following system:

$$\dot{\boldsymbol{x}}_{ref} = \boldsymbol{A}_d \boldsymbol{x}_{ref} + \boldsymbol{B}_m \left(\boldsymbol{\Lambda} \boldsymbol{u}_{ref} + \boldsymbol{\Delta}_m \left(t, \boldsymbol{x}_{ref}, \boldsymbol{x}_z \right) \right) + \boldsymbol{B}_{um} \boldsymbol{\Delta}_{um} \left(t, \boldsymbol{x}_{ref}, \boldsymbol{x}_z \right) \tag{4.146a}$$

$$\boldsymbol{u}_{ref} = \boldsymbol{\Lambda}^{-1} \boldsymbol{C} \left(s \right) \left(\boldsymbol{\Delta}_m + \boldsymbol{H}_m^{-1} \left(s \right) \boldsymbol{H}_{um} \left(s \right) \boldsymbol{\Delta}_{um} \right) \tag{4.146b}$$

$$\boldsymbol{y}_{ref} = \boldsymbol{C} \boldsymbol{x}_{ref} \tag{4.146c}$$

In the subsequent analysis part those ideal performance bounds derived from the closed-loop reference system are linked to the real closed-loop system incorporating the estimates $\boldsymbol{\sigma}_m$ and $\boldsymbol{\sigma}_{um}$. This comparison is used to establish conditions with respect to the sampling time T_s, which describe the divergence between both system from a performance perspective. Therefore, the stability properties of the closed-loop reference system are derived in a first step. In the following second step, those properties of the closed-loop reference system build the basis for performance investigations on the real closed-loop system.

Based on the input/output transfer functions (4.139), the closed-loop transfer functions of the matched and unmatched uncertainties $\boldsymbol{\Delta}_m$, $\boldsymbol{\Delta}_{um}$ to the system state $\boldsymbol{x}_{ref}$ is given by

$$\boldsymbol{G}_m \left(s \right) = \boldsymbol{H}_{xm} \left(s \right) \cdot \left(\mathbb{I}_m - \boldsymbol{C} \left(s \right) \right) \tag{4.147a}$$

$$\boldsymbol{G}_{um} \left(s \right) = \left(\mathbb{I}_n - \boldsymbol{H}_{xm} \boldsymbol{C} \left(s \right) \boldsymbol{H}_m^{-1} \left(s \right) \boldsymbol{C} \right) \cdot \boldsymbol{H}_{xum} \tag{4.147b}$$

, respectively. Using the $\mathcal{L}_1$-norm of $\boldsymbol{G}_m$ and $\boldsymbol{G}_{um}$, it is shown in [63] that the following stability bounds hold for the closed-loop reference system:

$$\left\| \boldsymbol{x}_{ref} \right\|_{\mathcal{L}_\infty} < \rho_r \tag{4.148a}$$

$$\left\| \boldsymbol{u}_{ref} \right\|_{\mathcal{L}_\infty} < \rho_{ur} \tag{4.148b}$$

The bounds of the prediction error (4.145) and the reference system (4.148) build the basis for the proof of the closed-loop system performance bounds. Herein, only the key ideas of this proof, which is depicted in detail in [63], are presented. The term *performance bound* denotes the upper limit of the corresponding errors between the reference and $\mathcal{L}_1$-PWC closed-loop system state, input, and output. Those performance bounds are given by

$$\left\| \boldsymbol{x}_{ref} - \boldsymbol{x} \right\|_{\mathcal{L}_\infty} < \gamma_1 \tag{4.149a}$$

$$\left\| \boldsymbol{u}_{ref} - \boldsymbol{u} \right\|_{\mathcal{L}_\infty} < \gamma_2 \tag{4.149b}$$

$$\left\| \boldsymbol{y}_{ref} - \boldsymbol{y} \right\|_{\mathcal{L}_\infty} < \left\| C \right\|_\infty \gamma_1 \tag{4.149c}$$

with the definitions

$$\gamma_1 := \frac{\left\| \boldsymbol{H}_{xm} \left(s \right) \boldsymbol{C} \left(s \right) \boldsymbol{H}_m^{-1} \left(s \right) \boldsymbol{C} \right\|_{\mathcal{L}_\infty}}{1 - \left\| \boldsymbol{G}_m \left(s \right) \right\|_{\mathcal{L}_1} L_{m\rho_r} - \left\| \boldsymbol{G}_{um} \left(s \right) \right\|_{\mathcal{L}_1} L_{um\rho_r}} \bar{\gamma}_0 + \beta \tag{4.150a}$$

$$\begin{aligned} \gamma_2 := & \left(\left\| \boldsymbol{\Lambda}^{-1} \boldsymbol{C} \left(s \right) \right\|_{\mathcal{L}_1} L_{m\rho_r} + \left\| \boldsymbol{\Lambda}^{-1} \boldsymbol{C} \left(s \right) \boldsymbol{H}_m^{-1} \left(s \right) \boldsymbol{H}_{um}^{-1} \left(s \right) \right\|_{\mathcal{L}_1} L_{um\rho_r} \right) \gamma_1 \\ & + \left\| \boldsymbol{\Lambda}^{-1} \boldsymbol{C} \left(s \right) \boldsymbol{H}_m^{-1} \left(s \right) \boldsymbol{C} \right\|_{\mathcal{L}_1} \bar{\gamma}_0, \end{aligned} \tag{4.150b}$$

, where $\bar{\gamma}_0$, defined in (4.145), and β are positive constants such that $\bar{\gamma}_1 \geq \gamma_1$ describes the upper bound of (4.150a). The definitions in (4.150) are based on the transfer functions introduced in (4.139). Considering assumption 4.3.6, the Lipschitz constant $L_{j\rho_r}$ is defined as

$$\left\|\left(\boldsymbol{\Delta}_j\left(t, \boldsymbol{x}_{ref}, \boldsymbol{x}_z\right) - \boldsymbol{\Delta}_j\left(t, \boldsymbol{x}, \boldsymbol{x}_z\right)\right)_\tau\right\|_{\mathcal{L}_\infty} < L_{j\rho_r}\left\|\left(\boldsymbol{x}_{ref} - \boldsymbol{x}\right)_\tau\right\|_{\mathcal{L}_\infty}. \tag{4.151}$$

In [63] the proof of the bounds (4.149a) and (4.149b) follows the principle of contradiction.

4.3.2.3 Closed-Loop Stability of $\mathcal{L}_1$ Controller

Considering the stability properties of the reference system (4.148) and the performance bounds (4.150), the uniform boundedness of the system states $\boldsymbol{x}$ and the input $\boldsymbol{u}$

$$\|\boldsymbol{x}\|_{\mathcal{L}_\infty} < \rho_r + \bar{\gamma}_1 \tag{4.152a}$$

$$\|\boldsymbol{u}\|_{\mathcal{L}_\infty} < \rho_{ur} + \gamma_2 \tag{4.152b}$$

can be derived. The above mentioned link between the system's closed-loop stability and boundedness properties of the closed-loop reference system (4.149) and the prediction error (4.143) is reflected in the composed bounds of (4.152).

The proof of (4.152) underlies the mathematical concept of contradiction in a similar way as indicated in the proof of (4.150).

CHAPTER 5

Flight Control System for the FGS-X-03 Model

> Doubt is the origin of wisdom.
>
> René Descartes

Within this chapter the architecture and parametrization of the FCS is derived and fundamental decisions concerning the control design are examined in detail. Designing a missile autopilot requires the control engineer to have a full understanding of the physical capabilities and characteristics of the considered system. Therefore, the derivation of the FCS is in line with the system and performance analysis presented in chapter 3. Before starting the control design development the first step consists of deriving the autopilot requirements. Those requirements, listed in section 5.1, are divided in functional requirements (FRs) and non-functional requirements (NFRs).

The FCS architecture consists of the nonlinear reference model (NRM), the baseline control algorithm, and an $\mathcal{L}_1$-Piecewise-Constant (PWC) augmentation. The motivation for the usage of these three elements within the missile's FCS and their evolution from the requirements considering the missile's physical capabilities are described in detail within section 5.2.

Since the considered approaches are model-based control methods, a suitable choice of the design model plays a key role in designing and parameterizing the flight control algorithms. Thus, a detailed description and derivation of the design model, which has to be compliant with system requirements (section 5.1) and requirements stemming from control theory, is presented in section 5.3. Based on the design model the NRM (section 5.4) and the control algorithms (section 5.5) are parametrized and designed in compliance to the requirements section 5.1.

5.1 Requirements

Before developing software algorithms in any field, a detailed specification is necessary, which is subdivided in FRs, NFRs, and use cases. The process of defining the requirements, their dependencies, and the methods to verify and validate them take up a great amount of time within the FCS development. Since a full requirement specification would go far beyond the scope of this thesis, only the main driving requirements are briefly introduced within this section.

As mentioned above, the requirements for the missile's FCS are subdivided into FRs and NFRs. While

FRs specify the behavior and function of a system's component, NFRs define criteria, property, or quality of the entire system [116]. In terms of interfaces to the guidance algorithm, the sensor unit, and the fin section, the FRs define the input and output signals of the missile's autopilot. Since NFRs define stability, robustness, and performance issues, they mainly influence the parameter design process. Both, FRs and NFRs have an impact on certain architectural design decisions. For the purpose of signifying single requirements several key words are recommended by responsible authorities like the Federal Aviation Administration (FAA) [117]. The three key words "must", "can", and "should" are used to prioritize main requirements of the control design process [118]. Their exact definition is given in the following:

- The word *must* means that the definition is an mandatory requirement of the specification.
- The word *should* denotes a recommended requirement, which is not formally tested.
- The word *can* indicates a permissible procedure, which facilitates the fulfillment of superior requirements.

5.1.1 Functional requirement (FR)

The FRs define the inputs (FR_6), sensor outputs (FR_4), and state estimates (FR_5) for controlling the roll, lateral, and longitudinal motion (FR_2) of the missile body across the entire flight envelope (FR_10).

FR_1: The FCS must allow Skid-To-Turn (STT) steering.

FR_2: The FCS must allow tracking of the following variables:

a) the roll angle about the velocity vector ϕ_v to control the roll channel.

b) The lateral acceleration with respect to the body frame at the Inertial Measurement Unit (IMU) location $\left(a_y^{IMU}\right)_B^{II}$ to control the missile's lateral motion.

c) The longitudinal acceleration with respect to the body frame at the IMU location $\left(a_z^{IMU}\right)_B^{II}$ to control the missile's longitudinal motion.

FR_3: The FCS must fulfill the herein specified control task even under the uncertainties and disturbances defined in chapter 3.

FR_4: The FCS can utilize the sensor outputs $\left(\boldsymbol{a}^{IMU}\right)_{B,meas}^{II}$, $\left(\boldsymbol{\omega}_K^{EB}\right)_{B,meas}$.

FR_5: The FCS can utilize the following missile state estimates: $\bar{q}$, α_k, β_k, M.

FR_6: The FCS must utilize the missile's four aerodynamic control surfaces δ_1, δ_2, δ_3, δ_4 or their equivalent controls ξ, η, ζ.

FR_7: The FCS must exhibit a modular architecture with an independent implementation of the model reference, baseline controller, and adaptive augmentation.

FR_8: The FCS must exhibit an independent implementation of the adaptive augmentation with respect to the baseline controller and reference model.

FR_9: The baseline autopilot (reference model + baseline controller) must fulfill all FRs and NFRs requirements under nominal conditions.

FR_10: The FCS must cover the entire flight envelope of the missile. The flight envelope is defined as the hull of the missile's maximum performance capabilities (see chapter 3).

Requirement FR_7 aims to an independent layout, separate testing, and a straightforward interchange of FCS elements. To address the design philosophy of a full augmentation, FR_9 requires the baseline architecture to fulfill all performance and certain robustness requirements under nominal conditions without an adaptive augmentation. This adaptive augmentation is meant to recover the nominal closed-loop performance established by the baseline autopilot in the case of deviations between design model and plant. Herein, the term *baseline autopilot* refers to the non-adaptive feedback control structure together with the reference model providing the filtered reference signals.

5.1.2 Non-functional requirement (NFR)

Within the NFRs, robustness and performance criteria are addressed. Herein overshoot (NFR_4), bandwidth (NFR_2), rise time (NFR_5), and settling time (NFR_6) constitute the metrics to quantize the missile's closed-loop performance. A common linear metric for robust stability is given by the maximum sensitivity function (NFR_9) of the linearized open-loop system. The minimum time delay T_d introduced at the system's input at which the closed-loop system maintains stable defines the *time delay margin* (NFR_7). In contrast to phase and gain margin, the time delay margin constitutes a robustness measure for nonlinear systems.

NFR_1: The FCS must account for bending modes by attenuating frequencies in the range between $f_{bending} = 80Hz - 100Hz$ with a roll-off of at least $20dB/dec$.

NFR_2: The FCS must achieve for the longitudinal and lateral control channels the minimum closed-loop crossover frequency $\omega_{cr} \geq \omega_{cr,min}$ at the corresponding flight envelope point. ω_{cr} (also *cut-off frequency*) is defined as the frequency where the magnitude of the longitudinal/lateral transfer function $G_{a_{i,c},a_{i,IMU}}(s)$ is below 0.707 (or $-3dB$). The minimum crossover frequency over Mach and altitude is depicted in fig. 5.1.

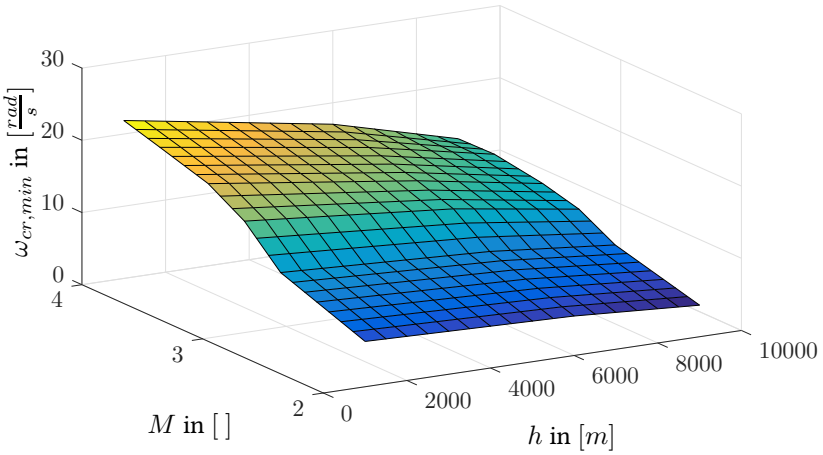

Figure 5.1: Minimum crossover frequency $\omega_{cr,min}$ of lateral and longitudinal acceleration channels with respect to Mach M and altitude h.

NFR_3: The FCS must achieve the following decoupling properties:

a) The roll angle error of the closed-loop system must remain within $\|e_{\phi_v}(t)\| \leq 2°$ in the event of a step input command to the lateral or longitudinal acceleration channel. The amplitude of the acceleration command step input must not exceed the maximum trim acceleration (see chapter 3) at the corresponding flight envelope point.

b) In the event of a step input command to the lateral or longitudinal acceleration channel, the absolute error of the non-stimulated axis must remain below 10% (compared to the initial value) of the step amplitude, $\| \left(\Delta a_i^{IMU}\right)_B^{II}(t) \| \leq 0.10 \cdot \left(a_{j,amp}^{IMU}\right)_B^{II}{}^{\circ}$, $i = y, z$, $j = z, y$. The amplitude of the acceleration command step input must not exceed the maximum trim acceleration (see chapter 3) at the corresponding flight envelope point. The amplitude of the acceleration command step input must not exceed the maximum trim acceleration (see chapter 3) at the corresponding flight envelope point.

NFR_4: The undershoot/overshoot $\varsigma_{i,ov} = a_{i,ov}/a_{i,amp}$ of the closed-loop system in the event of a step input command to the lateral or longitudinal acceleration channel must remain within 20% (compared to the initial value) of the step input's amplitude $a_{i,amp}$.

NFR_5: The rise time T_{rt} of the nominal closed-loop system in the event of a step input command to the lateral or longitudinal axis must satisfy $T_{rt} < T_{rt,max}(M, h)$. The maximum allowable rise time $T_{rt,max}(M, h)$ is depicted in fig. 5.2.

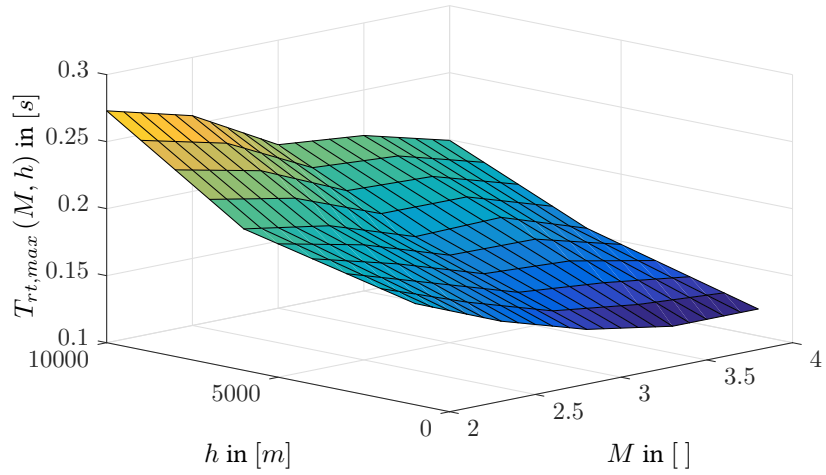

Figure 5.2: Maximum allowable rise time $T_{rt,max}(M, h)$ for lateral and longitudinal acceleration channels with respect to Mach M and altitude h.

NFR_6: The time span (settling time) T_{st} of the response to a step input command to the lateral or longitudinal axis to remain within $\| \left(a_i^{IMU}\right)_B^{II}(t) \| \leq 0.1 \cdot \left(a_{i,amp}^{IMU}\right)_B^{II}$, $i = y, z$ must be $T_{st} \leq 4 \cdot T_{rt,max}$.

NFR_7: The time delay margin T_d at the FCS output must at least be $T_d > 15 \cdot T_s$ (T_s denotes the sample time of the control algorithm).

NFR_8: The gain (GM) and phase margin (PM) at the sensor loop opening $\boldsymbol{y}_m$ (transfer function $G_{y_{m,i},ol}(s)$) and the actuator loop opening $\boldsymbol{u}$ (transfer function $G_{u_i,ol}(s)$) must at least be

$$GM\left(G_{y_{m,i},ol}(s)\right), GM\left(G_{u_i,ol}(s)\right) \geq 6dB \tag{5.1}$$

and

$$PM\left(G_{y_{m,i},ol}(s)\right), PM\left(G_{u_i,ol}(s)\right) \geq 30^{\circ}, \tag{5.2}$$

respectively.

NFR_9: The maximum

$$M_S = \max_{\omega_{min} \leq \omega} |S(j\omega)| \tag{5.3}$$

of the sensitivity function $S(j\omega)$ [119] must exhibit an upper limit of $M_S \leq 2.5$ in the desired frequency range $\omega_{min} \leq \omega, \omega_{min} = 0.1^{rad/s}$.

The evaluation criteria used to impose and quantify the performance requirements (e.g. NFR_4, NFR_6) are depicted in fig. 5.3. The undershoot and overshoot value reflect the offset between the amplitude of the commanded step and the considered control variable. The negative undershoot of the IMU acceleration signal due to the instant fin deflection is not subject to analysis. The reason is the non-minimum phase characteristics of the missile and the physical inherent acceleration undershoot in case of a fin configuration assigned to an acceleration in the opposite direction (see $t = 1s$ in fig. 5.3). Agile maneuvers demanding fast fin response lead to significant undershoot. Restricting this kind of undershoot would collide with the requirements of a fast rise time and a large bandwidth.

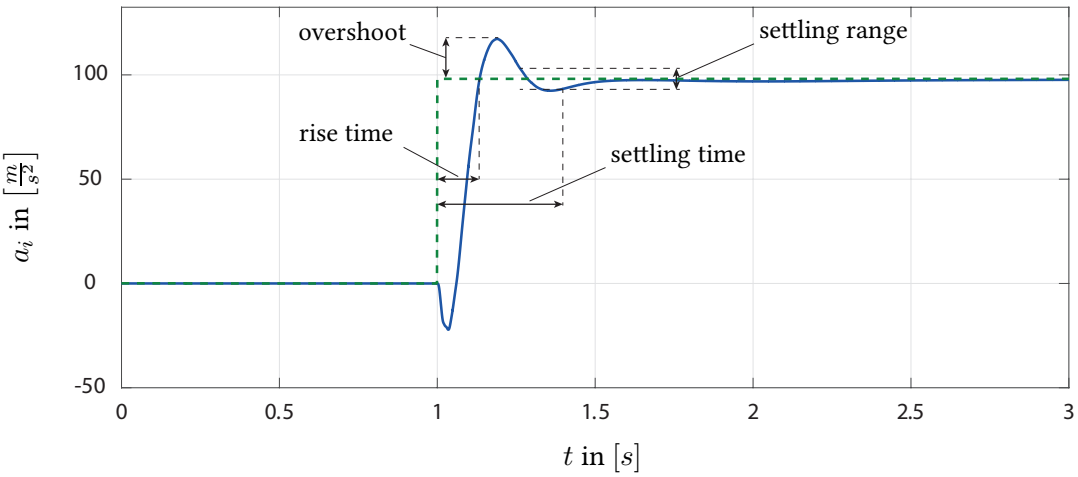

Figure 5.3: Visualization of the quantifiable performance criteria undershoot, overshoot, rise time, settling time, and settling range for a commanded step input within the acceleration command.

5.2 FCS Architecture

The term architecture, related to missile autopilot design include both, the algorithmic structure of the specific control law and the served/available interfaces. The interfaces of the FCS are determined on the one hand by the specified inputs and outputs of the actuator and sensor unit and on the other hand by the available estimated states. The algorithmic design decisions of the flight control law is mainly driven by the missile's steering mode (see FR_1) in combination with the selected control variables (see FR_2) to modify the motion of all three missile axis. Figure 5.4 illustrates the elements of the FCS and their interconnection.

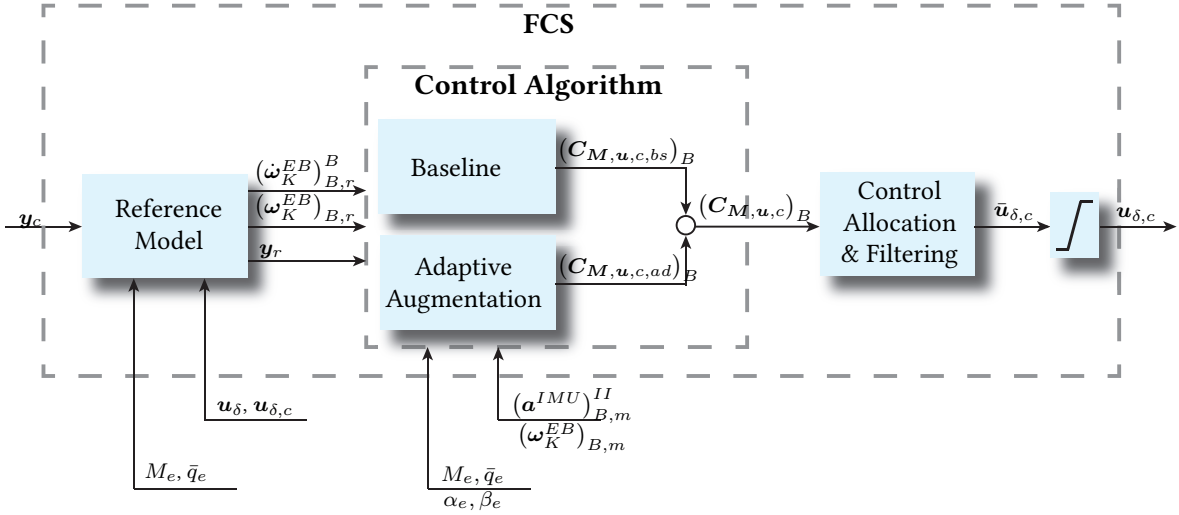

Figure 5.4: Elements, signals, and interconnection of FCS architecture.

The control commands

$$\boldsymbol{y}_c = \begin{bmatrix} \phi_{v,c} \\ (a_{z,c})_B^{II} \\ (a_{y,c})_B^{II} \end{bmatrix}, \tag{5.4}$$

calculated within the guidance laws constitute the input of the FCS. According to the requirements in section 5.1.1 $\boldsymbol{y}_c$ contains the desired transient of the roll, longitudinal, and lateral control channel summarized in

$$\boldsymbol{y} = \begin{bmatrix} \phi_v \\ (a_z^{IMU})_B^{II} \\ (a_y^{IMU})_B^{II} \end{bmatrix} \tag{5.5}$$

In order to reduce the workload of the controller and to provide a physical feasible reference signal sequence, the reference model also transforms the trajectory of $\boldsymbol{y}_c$ to a smooth and physically accessible reference signal $\boldsymbol{y}_r$. Besides, the filtered version $\boldsymbol{y}_r$ of the commanded variables the reference model provides the control algorithm with the reference body rate $\left(\boldsymbol{\omega}_K^{EB}\right)_{B,r}$ and the angular acceleration $\left(\dot{\boldsymbol{\omega}}_K^{EB}\right)_{B,r}^B$. In order to account for the varying physical performance capabilities of the missile with respect to altitude and speed (see section 3.2), the estimated dynamic pressure $\bar{q}$ and Mach number M are utilized to adapt the reference model dynamics to the respective flight envelope point. This feedback of those two state estimates is a direct consequence of the performance requirements listed within the NFRs (section 5.1.2) and an example how the requirements have an impact on the control algorithm and architecture.

As already indicated in chapter 4, the control algorithm consists of a baseline algorithm and an adaptive augmentation. Those two elements receive the estimated missile states and the IMU measurements. The commanded aerodynamic control coefficient

$$(\boldsymbol{C}_{\boldsymbol{M},\boldsymbol{u},c})_B = \begin{bmatrix} C_{l,\xi,c} \\ C_{m,\eta,c} \\ C_{n,\zeta,c} \end{bmatrix}_B \tag{5.6}$$

constitutes the intermediate control input used for control design purposes. The reason for this choice is the straight-forward assignment of each control input to the missile axes. This choice facilitates the design and layout of the autopilot. Within the control allocation, those variables are

transformed to the fin deflection commands $\boldsymbol{u}_{\delta,c}$ of the missile's actuator system by using the inverse of the approximated aerodynamic control coefficients and the mapping rule introduced in (2.46):

$$\boldsymbol{u}_{\delta,c} = \boldsymbol{T}_{\delta} \cdot \begin{bmatrix} \xi_c \\ \eta_c \\ \zeta_c \end{bmatrix} = \begin{bmatrix} \xi\left(\alpha_K, \beta_K, M, \left(C_{l,\xi,c}\right)_B\right) \\ \eta\left(\alpha_K, \beta_K, M, \left(C_{m,\eta,c}\right)_B\right) \\ \zeta\left(\alpha_K, \beta_K, M, \left(C_{n,\zeta,c}\right)_B\right) \end{bmatrix} \tag{5.7}$$

Those auxiliary controls and their link to the considered system dynamics used for the layout of the algorithmic FCS elements (reference model, baseline controller, adaptive augmentation) are defined in the following section section 5.3.

The requirements FR_7 and FR_8, requiring modularity and independent subsystem layout, play a crucial role in designing the baseline controller, the adaptive augmentation, and the interconnection of the autopilot elements (depicted in fig. 5.4). Those requirements demand the elements to be implemented in a modular, independent, and therefore interchangeable way. This guarantees a straight forward mapping of the requirements (see section 5.1) to the respective elements and a simplified verification process on subsystem basis.

Remark: For the purpose of a compact notation within the control design, the indices of states, inputs, and parameters are dropped in case the meaning of the variable is clear from context. The reader is referred to chapter 2 for a detailed description of all relevant missile states, inputs, and parameters.

5.3 Definition of Design Model

The development of each control algorithm starts with the definition of a reduced plant model (so-called *design model*), which serves for architectural and parameterization purposes. By defining the design model based on the plant's model the control engineer has to face the trade-off between modeling depth and simplification. The degree of accuracy depend strongly on the quality of the identified parameters, the complexity of the plant model dynamics, and the chosen control approach. Strict-feedback form in case of Backstepping (section 4.2.2.2), minimum phase characteristics in case of Nonlinear Dynamic Inversion (NDI) (section 4.2.1), or linear system representations in case of linear control theory are examples of how the used control technique implies certain requirements considering the mathematical representation of the design model.

A common approach by defining the design model is to reduce the system's state vector to states which have a major impact on the control variables only. An example is the reduction of the aircraft's nonlinear equation of motion (EOM) to the respective linear short-period dynamics, which is used for longitudinal autopilot design and analysis.

Besides the selection of the design model dynamics, the choice of the considered control input and output plays a crucial role from a control point of view and has to be in line with the requirements of the control task and the selected algorithm.

Remark: The *control inputs* and *outputs* used within the control algorithm may differ from the physical inputs (actuators) and outputs (sensors) provided by the considered system. Nevertheless, by using different inputs and outputs for control design purposes, it has to be assured that the overall control goals are fulfilled and the closed-loop requirements are met.

The consideration of a control input or output different from the physical one may introduce beneficial properties which facilitates the layout process, fulfills certain requirements stemming from

the applied control theory, and may lead to increased robustness and performance characteristics. Examples for deviating control inputs and outputs can be found in [36, 37, 120]. In case of civil aircraft, a common approach for longitudinal autopilot design is to use the blending of the pitch rate and the load factor [121].

As already mentioned in section 4.2.1.3, classical NDI approaches require the system's input/output characteristics to be minimum phase. In general, tail-controlled missiles tend to exhibit a non-minimum phase characteristics by considering the IMU acceleration as output. The following section describes a physical motivated approach for rendering the missile's input/output characteristics minimum phase.

5.3.1 Minimum Phase Output

Whether a system exhibits minimum phase characteristics depends on the stability properties of the system's zero dynamics (see section 4.2.1.3). A minimum phase system exhibits a zero dynamics which is stable with respect to Lyapunov's stability definition. In case of an linear time-invariant (LTI) system, the transfer zeros of the open-loop correlate with the system's minimum phaseness. An LTI system is called minimum phase if the system's zeros lie in the left-half complex plane. Considering a nonlinear mathematical description of the respective system, the stability proof of the remaining zero dynamics by finding an appropriate Lyapunov function candidate might be cumbersome. Therefore, the investigation of the zero dynamics of the linearized system dynamics of interest is an appropriate procedure in determining the minimum phase characteristics of a nonlinear system.

Commonly, the transfer characteristics of a tail-controlled missile from the aerodynamic equivalent control inputs η and ζ to the corresponding accelerations $\left(a_z^{IMU}\right)_{B,meas}^{II}$ and $\left(a_y^{IMU}\right)_{B,meas}^{II}$, depend on the location of the IMU along the missile body-axis, the layout of the fins, and the missile's operating point within the flight envelope. In order to overcome these inherent input/output characteristics several approaches evolved over recent years in the field of missile autopilot design. In [36, 37] a method called *output redefinition* is proposed using a blend of aerodynamic angles in combination with the body-rates to create an alternative, minimum phase output with equivalent properties compared to the measured acceleration. Since the aerodynamic angles (α_A and β_A) possess equivalent dynamical properties by exhibiting minimum phase characteristics, a common approach is to consider those angles as control variables [59]. Both concepts require accurate information of the aerodynamic angles, which is not feasible for high-agile missile configurations. A physically motivated approach, presented in [58], considers the position of the acceleration measurements (IMU position) and its influence on the minimum phase characteristics. For a non-minimum phase characteristics there is a point at which the impact of the forces acting in the opposite direction are compensated by the rotational acceleration. This point is called *center of percussion (cop)* and the positive distance along the x_B-axis is labeled as x_{cop}. Due to the compact and space-saving missile's construction the location of the IMU is subject to requirements stemming from structural engineering. Thus, a virtual sensor position P is calculated within the FCS to render the missile's input/output transfer behavior minimum phase (see fig. 5.5).

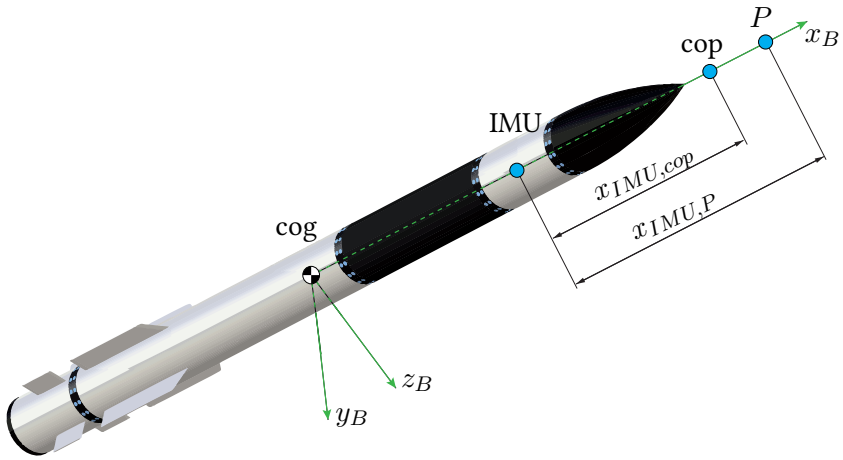

Figure 5.5: Location of the IMU and the virtual sensor location P.

Based on the mathematical description of the IMU measurements (2.48), the occurring longitudinal and lateral acceleration at P can be calculated as

$$\begin{bmatrix} \left(a_z^P\right)_B^{II} \\ \left(a_y^P\right)_B^{II} \end{bmatrix} = \begin{bmatrix} \left(a_z^{IMU}\right)_{B,m}^{II} \\ \left(a_y^{IMU}\right)_{B,m}^{II} \end{bmatrix} + \underbrace{x_{IMU,P} \cdot \begin{bmatrix} -\left(\dot{q}_K^{EB}\right)_B^B + \left(p_K^{EB}\right)_{B,m} \cdot \left(r_K^{EB}\right)_{B,m} \\ \left(\dot{r}_K^{EB}\right)_B^B + \left(p_K^{EB}\right)_{B,m} \cdot \left(q_K^{EB}\right)_{B,m} \end{bmatrix}}_{\begin{bmatrix} \Delta a_z \\ \Delta a_y \end{bmatrix}}. \tag{5.8}$$

The distance between the IMU and the virtual sensor location is labeled with $x_{IMU,P}$. By calculating the acceleration at a point P ahead of the cop only a shift along the x_B-axis is considered. This is due to the fact that offsets between the position of the IMU and the point P along the other body axes has no significant influence on the minimum phase characteristic of the outputs $\left(a_z^P\right)_B^{II}$ and $\left(a_y^P\right)_B^{II}$ as control variables. The additional increments in (5.8) added to the IMU acceleration are denoted with Δa_z and Δa_y for longitudinal and lateral channels, respectively.

Using the transformed acceleration signal (5.8) as control variable to overcome the inherent non-minimum phase characteristics of the missile requires a careful selection of the position of the virtual point P. In order to investigate the influence of the design parameter $x_{IMU,P}$ on the missile's minimum phase characteristics, a linearized representation of the missile's longitudinal dynamics is used. Due to the symmetry properties of the missile body, the longitudinal and lateral dynamics are equivalent and analysis results obtained for one channel are also valid for the other one (see section 3.2.2). Based on the linearized model of the short period dynamics and the acceleration output at the virtual point P, the linear representation results as

$$\begin{aligned} \begin{bmatrix} \dot{\alpha} \\ \dot{q} \end{bmatrix} &= \begin{bmatrix} Z_\alpha & 1 \\ M_\alpha & M_q \end{bmatrix} \cdot \begin{bmatrix} \alpha \\ q \end{bmatrix} + \begin{bmatrix} Z_\eta \\ M_\eta \end{bmatrix} \cdot \eta \\ y = a_z^P &= \begin{bmatrix} \bar{Z}_\alpha - x_{IMU,P} \cdot M_\alpha & \bar{Z}_q - x_{IMU,P} \cdot M_q \end{bmatrix} \cdot \begin{bmatrix} \alpha \\ q \end{bmatrix} \cdot \\ &\quad + \left(\bar{Z}_\eta - x_{IMU,P} \cdot M_\eta\right) \cdot \eta \end{aligned} \tag{5.9}$$

The design parameter $x_{IMU,P}$ has an impact on the output equation of (5.9). In order to determine the minimum distance necessary for rendering the longitudinal and lateral acceleration channel minimum phase, the critical position, denoted as cop, is calculated based on the linear longitudinal

dynamics (5.9). Considering the transfer function of (5.9)

$$G_{a_z^P}(s) = \frac{a_z^P(s)}{\eta(s)} = \frac{p(s)}{q(s)}, \tag{5.10}$$

the transmission zeros $z_{1,2}$ are defined as the roots of the second order polynomial $p(s)$. According to (5.9) the transfer characteristics and therefore the transmission zeros $z_{1,2}$ from the fin deflection η to the acceleration $(a_z)_B^P$ at the position P depend, for a given missile configuration and operating point, only on the parameter $x_{IMU,P}$. The cop is determined as the distance $x_{IMU,P} = x_{IMU,cop}$ between the IMU and the cop at which the real part of the conjugate complex zero $z_{1,2}$ vanishes:

$$\Re(z_{1,2}(x_{IMU,P})) = 0 \tag{5.11}$$

In case there exists a distance $x_{IMU,P} = x_{IMU,cop}$ solving (5.11), an increase in distance $x_{IMU,P} > x_{IMU,cop}$ leads to a negative real part of the short period transmission zeros and therefore to an acceleration signal at the virtual point P rendering the linear system minimum phase. If the point P is located closer to the IMU than the cop ($x_{IMU,P} < x_{IMU,cop}$), the linear system representing the longitudinal dynamics exhibits non-minimum phase characteristics.

Remark: Those characteristics of the cop derived from a system theory point of view is coherent with the observations of the nonlinear acceleration equation given in (5.8). Inserting the EOM of the expanded pitch rate dynamics (2.20) and the acceleration (2.48) into (5.8) the longitudinal acceleration (the same consideration holds for the lateral acceleration) becomes:

$$\begin{aligned} a_z^P \;=\; & \tfrac{\bar{q}S_{ref}}{m}\left(C_{z,0} + C_{z,\eta}\right) \\ & + x_{cog,P} \cdot \tfrac{1}{I_{yy}} \cdot \left(\bar{q}S_{ref}l_{ref}\left(C_{m,0} + \tfrac{q_K l_{ref}}{2V}C_{m,q} + C_{m,\eta}\right)\right) \\ & - x_{cog,P} \cdot \tfrac{1}{I_{yy}} \cdot r_K p_K \left(I_{xx} - I_{zz} - 1\right) \end{aligned} . \tag{5.12}$$

Since the aerodynamic data set (see section 2.3) is defined at the cog, the distance $x_{cog,P} = x_{cog,IMU} + x_{IMU,P}$ between the cog and the virtual point P has to be considered (by considering the acceleration at the IMU only the distance $x_{IMU,P}$ is relevant).

At the cop ($x_{IMU,P} = x_{IMU,cop}$) the impact of the fin deflection η on a_z^P (via $C_{z,\eta}$) is compensated by the fin induced rotational acceleration via $C_{m,\eta}$:

$$\frac{\bar{q}S_{ref}}{m}C_{z,\eta} + x_{cog,P} \cdot \frac{1}{I_{yy}}\bar{q}S_{ref}l_{ref}C_{m,\eta} = 0 \tag{5.13}$$

This cancellation of the aerodynamic force by the forces due to rotational acceleration acting in P is in line with the interpretation of the transmission zero at the origin as described in (5.11).

This different input/output characteristics dependent on the design parameter $x_{IMU,P}$ is illustrated in fig. 5.6 and fig. 5.7. Figure 5.6 shows pole-zero plots of the longitudinal channel with varying distances $x_{IMU,P} = 0, \ldots, 2m$ and longitudinal IMU accelerations for the three different missile configuration introduced in chapter 3. Increases in agility and in lift (and therefore angle of attack (AoA)) leads for a constant distance $x_{IMU,P}$ to a decrease of the real part of the transmission zeros (shift to the left half complex plane). The agile configuration exhibits at almost each operating point a minimum phase characteristics. In case of the slow configuration the considered interval $x_{IMU,P} = 0, \ldots, 2m$ for increased acceleration is too small to render the longitudinal missile dynamics at P minimum phase.

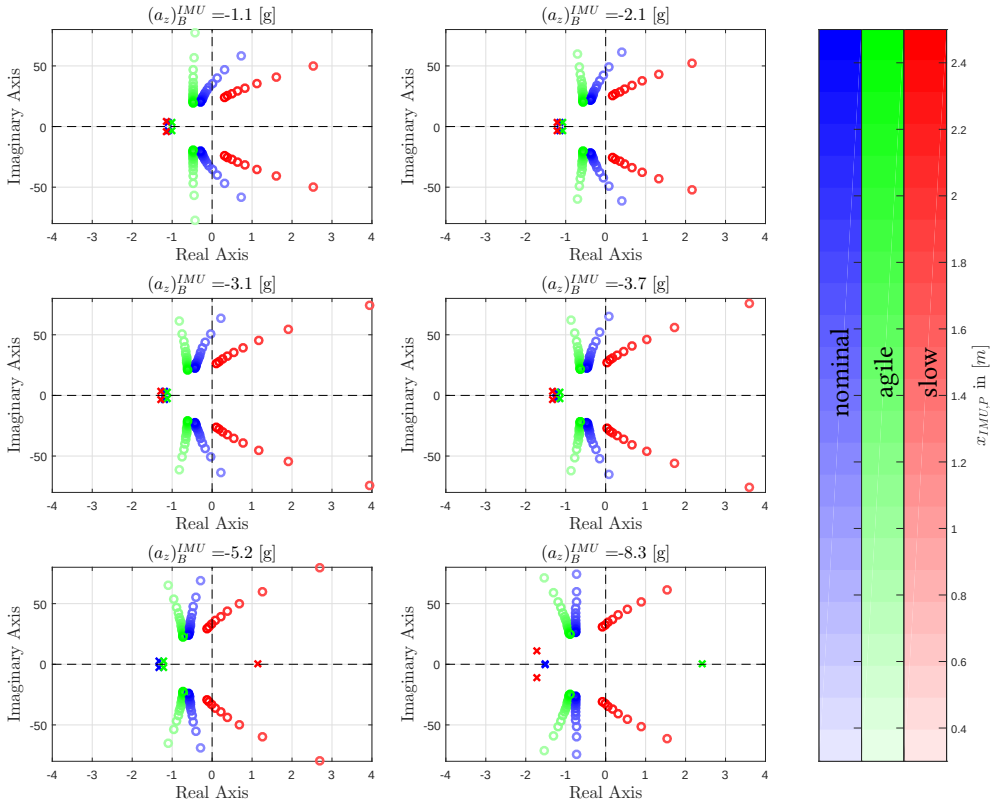

Figure 5.6: Poles and zeros of longitudinal missile dynamics for different IMU accelerations and for variations in $x_{IMU,P}$.

The critical distance $x_{IMU,cop}$ between the IMU location and the cop for the entire flight envelope is depicted in fig. 5.7. The illustration of the distance versus Mach and altitude for the agile configuration is omitted due to the fact that the acceleration at the IMU constitutes already a minimum phase output. It can be concluded from the discussion above that the distance $x_{IMU,cop}$ has its maximum in case no forces are acting on the missile body. Thus, fig. 5.7 depicts the critical distance $x_{IMU,P} = x_{IMU,cop}$ over the flight envelope for the trimmed flight at $(a_z)_B^{IMU} = 0$. From fig. 5.7 it can be concluded that the sensitivity of cop location over the flight envelope is moderate compared to variations in trimmed acceleration.

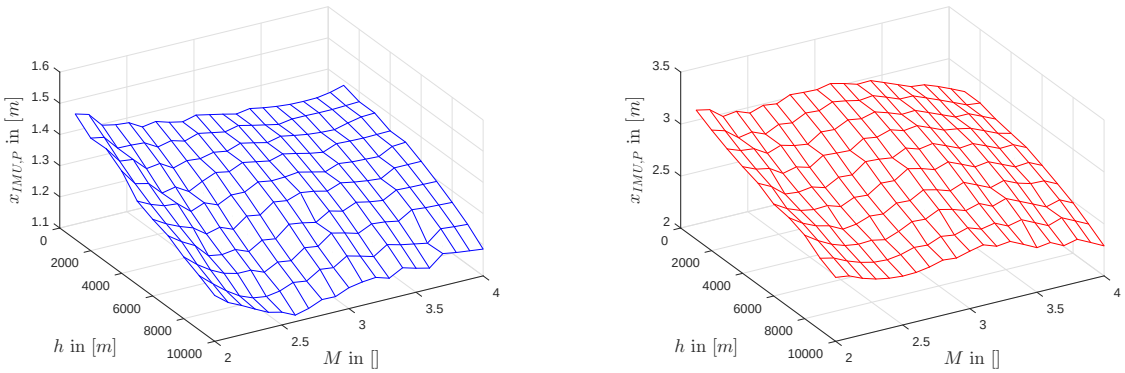

(a) Nominal configuration

(b) Slow configuration

Figure 5.7: Critical distance $x_{IMU,P} = x_{IMU,cop}$ for nominal and slow configuration at trimmed flight with zero acceleration $(a_z)_B^{IMU} = 0$ plotted versus altitude and Mach.

In summary the main influencing factors on the missile's cop constitute the (trimmed) acceleration and the missile parameter configuration leading to variations in agility. With an increase in lift and therefore AoA, the cop decreases and the transmission zeros of the linearized missile model migrate towards the left half complex plane (see fig. 5.6). The distance between IMU position and cop constitutes the critical limit ($x_{IMU,P} = x_{IMU,cop}$) at which the acceleration at P exhibits minimum $x_{IMU,P} > x_{IMU,cop}$ or non-minimum phase ($x_{IMU,P} < x_{IMU,cop}$) input/output characteristics.

A limiting factor by selecting the location of the virtual acceleration at the point P represents the fact that with increased distance $x_{IMU,P}$ the properties of the acceleration output (5.8) differs from the original control variable measured by the IMU. According to section 5.1.1, especially FR_2, the reader is reminded that the overall control goal with respect to the longitudinal and lateral accelerations is to track the commanded trajectory by the corresponding IMU acceleration channels (see (5.5)). Considering (5.8) the acceleration at the IMU and at the point P are equal in case the rate accelerations for pitch $\left(\dot{q}_K^{EB}\right)_B^B$ and yaw $\left(\dot{r}_K^{EB}\right)_B^B$ vanish and no roll cross-coupling ($\left(p_K^{EB}\right)_{B,m} = 0$) occurs. This is the case for a trimmed flight condition. Thus, the virtual shift of the IMU acceleration to a point P (5.8) rendering the missile minimum phase incorporates two drawbacks: First, the difference $\Delta a_y, \Delta a_z$ between the transient characteristics $\left(a_y^{IMU}\right)_{IMU}^{II}$, $\left(a_z^{IMU}\right)_{IMU}^{II}$ and $\left(a_y^P\right)_B^{II}$, $\left(a_z^P\right)_B^{II}$ depends on the choice of $x_{IMU,P}$. An increase in $x_{IMU,P}$ leads to increased divergences $\Delta a_y, \Delta a_z$ during transient response. Second, the calculation of the offset $\Delta a_y, \Delta a_z$, which renders the output minimum phase, requires the pitch $\left(\dot{q}_K^{EB}\right)_B^B$ and yaw angular accelerations $\left(\dot{r}_K^{EB}\right)_B^B$. Since those angular accelerations are non-measurable, they need to be reconstructed based on model data (aerodynamic data) and sensor signals. In the nominal case, a suitable choice of the parameter $x_{IMU,P}$ guarantees a negligible error in transient response by maintaining minimum phase characteristics of (5.8). In case of parametric uncertainties (see section 2.4), the calculated pitch and yaw accelerations lead to a virtual acceleration which does not fulfill the specified transient characteristics nor the required properties at trimmed flight condition.

Therefore, in order to reduce the error in transient response and to match acceleration at trimmed flight condition with the one provided at the IMU, the low-pass part (denoted with $G_{LP}(s)$) of the addend $\begin{bmatrix}\Delta a_z & \Delta a_y\end{bmatrix}^T$ is removed from (5.8) [58]:

$$\begin{bmatrix}\left(a_z^P\right)_{B,fil}^{II} \\ \left(a_y^P\right)_{B,fil}^{II}\end{bmatrix} = \begin{bmatrix}\left(a_z^P\right)_B^{II} \\ \left(a_y^P\right)_B^{II}\end{bmatrix} - \begin{bmatrix}G_{LP}(s) & 0 \\ 0 & G_{LP}(s)\end{bmatrix} \cdot \begin{bmatrix}\Delta a_z \\ \Delta a_y\end{bmatrix} \tag{5.14}$$

By analogy to $\boldsymbol{y}$, defined in (5.5), the roll control variable and the minimum phase accelerations of (5.14) are summarized to the redefined version of the primary control variable as

$$\boldsymbol{y}^P = \begin{bmatrix}\phi_v \\ \left(a_z^P\right)_{B,fil}^{II} \\ \left(a_y^P\right)_{B,fil}^{II}\end{bmatrix}. \tag{5.15}$$

With this redefined output the filter parameter and the distance $x_{IMU,P}$ need to be selected in a suitable way to guarantee the following design goals:

- The minimum phase input/output characteristics for the nominal missile configuration has to be assured.
- Transient and trimmed flight properties of the redefined output (5.14) need to be coherent with the overall control requirements stated in section 5.1.

- The filter layout and the location of the virtual point are fixed parameters over the entire flight envelope (no scheduling required).

The acceleration increments $\begin{bmatrix}\Delta a_z & \Delta a_y\end{bmatrix}$ are filtered by a linear second order low-pass filter. With a damping of $\zeta_{LP} = 0.7$ and a cut-off frequency of $\omega_{LP} = 10Hz$ the filter bandwidth is in line with the missile's maximum transmission bandwidth investigated in section 3.2.

Based on the minimum phase characteristics investigated in fig. 5.6 and fig. 5.7 the choice of parameter $x_{IMU,P}$ defining the acceleration at the virtual point P exhibits insensitive properties with respect to the considered operating point and demanded acceleration. Thus, the parameter is selected in coherence with the nominal missile configuration to $x_{IMU,P} = 1.3m$.

The selection of only one parametric set over the entire flight envelope qualifies the herein presented approach compared to the output redefinition suggested in [36, 37].

5.3.2 EOM of Design Model

Based on the missile system dynamics described in chapter 2, the mathematical description of an appropriate model for control design is derived in this section. The nonlinear and adaptive control methods discussed in chapter 4 require the design model to be evaluated online based on state measurements and estimations. In case of common classical control design methods, the parameters of the control law are calculated offline based on a linear approximation of the nonlinear system dynamics. Thus, no online evaluation of the dynamic model (or parts of it) is required.

Due to the advantages discussed in chapter 4, the selected nonlinear and adaptive control methods are well suited for control of high agile systems exhibiting a wide spectrum of uncertainties. Within the family of Backstepping and NDI, the control design model plays a significant role within the formulation of the feedback laws (see section 4.2.1 and section 4.2.2). Therefore, the requirements of the applied control law have to be considered by defining the design model (e.g. minimum phase characteristics). Besides the restrictions of the considered control methodology, the selection of the design model is also driven by the trade-off between mimicking the system dynamics and the major nonlinear effects on the one hand side, and the reduction of the computational costs on the other side. For the purpose of finding a design model which approximates the system dynamics with sufficient accuracy, dynamical parts have to be identified which have minor/major impact on the main missile characteristics compared to others. The following criteria can give the control designer some guidelines by identifying a suitable design model for the considered control task:

- *minor/major influence*: Certain dynamical parts exhibit a minor/major contribution to the considered dynamics.
- *states not accessible*: Due to the system's sensor setup, reliable estimation or measurement of states necessary for a full description of the system dynamics may not be available.
- *uncertain information*: Measurements or estimates of the system states or dynamical parts can exhibit certain uncertainty characteristics which neutralize the considered dynamical effect.
- *computational effort*: In case the control algorithm requires parts of the design model (e.g. Backstepping, NDI) to be assessed onboard, each dynamical part has to be evaluated carefully with respect to computational load.
- *requirements of control methodology*: The description of the design model dynamics has to be coherent with the requirements of the applied control law.

The manifestation of the above-mentioned criteria depend strongly on the system dynamics, the applied control technique, and the requirements of the closed-loop system. The design model describes in general the dynamical relationship between the control variables and the specific inputs used for autopilot design by respecting the restrictions of the utilized control law.

For the considered control task, the redefined control variable $\boldsymbol{y}$ (see (5.15)) and the aerodynamic moment coefficients $(\boldsymbol{C}_{\boldsymbol{M},\boldsymbol{u},c})_B$ (5.6) constitute the design model's outputs and affine inputs, respectively. In order to describe the dynamic influence of the pseudo controls $(\boldsymbol{C}_{\boldsymbol{M},\boldsymbol{u},c})_B$ on the missile's outputs, the EOM of the control variables are derived. Starting point for the derivation of the design model constitutes the compact notation (indices of coordinate frame dropped) of the outer dynamics described by the roll angle (see (2.18)) and the unfiltered accelerations (see (5.8)):

$$\begin{bmatrix} \phi_v \\ a_z^P \\ a_y^P \end{bmatrix} = \begin{bmatrix} \int \left(\cos\alpha_K \cdot \cos\beta_K \cdot p_K + \sin\beta_K \cdot q_K + \sin\alpha_K \cos\beta_K \cdot r_K\right) dt \\ \frac{\bar{q}S_{ref}}{m} \cdot C_z\left(\alpha_K, \beta_K, M, \xi, \eta\right) + x_{cog,P} \cdot \left(-\dot{q}_K + p_K \cdot r_K\right) \\ \frac{\bar{q}S_{ref}}{m} \cdot C_y\left(\alpha_K, \beta_K, M, \xi, \zeta\right) + x_{cog,P} \cdot \left(\dot{r}_K + p_K \cdot q_K\right) \end{bmatrix} \tag{5.16}$$

In accordance with the aforementioned criteria the dynamics of the control variables (5.16) is derived with respect to time based by considering the following, physically motivated simplifications:

- *dynamic pressure, Mach number / velocity*: As indicated in chapter 2 and chapter 3, the missile dynamics constitutes of different *dynamic layers* which are characterized by different time constants. Body rates, aerodynamic angles, absolute velocity, and position (altitude) dynamics are the layers of interest in descending order of their time constant. States stemming from environment description, like dynamic pressure and Mach number, are analytically linked to the missile's altitude and absolute velocity (see(2.7)). Therefore, those states evolve on a slow time scale, too. Compared to the body rates and accelerations measured by the missile's sensor units and used within the feedback control algorithm, the states belonging to the slow dynamic layer can be regarded as constant within the endgame engagement.
- *constant mass properties*: The missile motor is burned out and the missile is not propelled in endgame flight phase (see section 2.4.2). This results in no alteration of mass properties (mass, moment of inertia).
- *damping moment*: The relative contribution of the moment due to roll, pitch, and yaw damping is negligible compared to the moments produced by the aerodynamic angles and the fin deflection. In case of longitudinal direction the relative magnitude of the pitch damping moment

$$\bar{c}_{m,q} = \frac{\left|\frac{q_K l_{ref}}{2V} \cdot C_{m,q}\right|}{\left|C_{m,0}\right| + \left|\frac{q_K l_{ref}}{2V} \cdot C_{m,q}\right| + \left|C_{m,\eta}\right|} \tag{5.17}$$

  is depicted for pull-up trim configurations across the entire flight envelope in fig. 5.8.

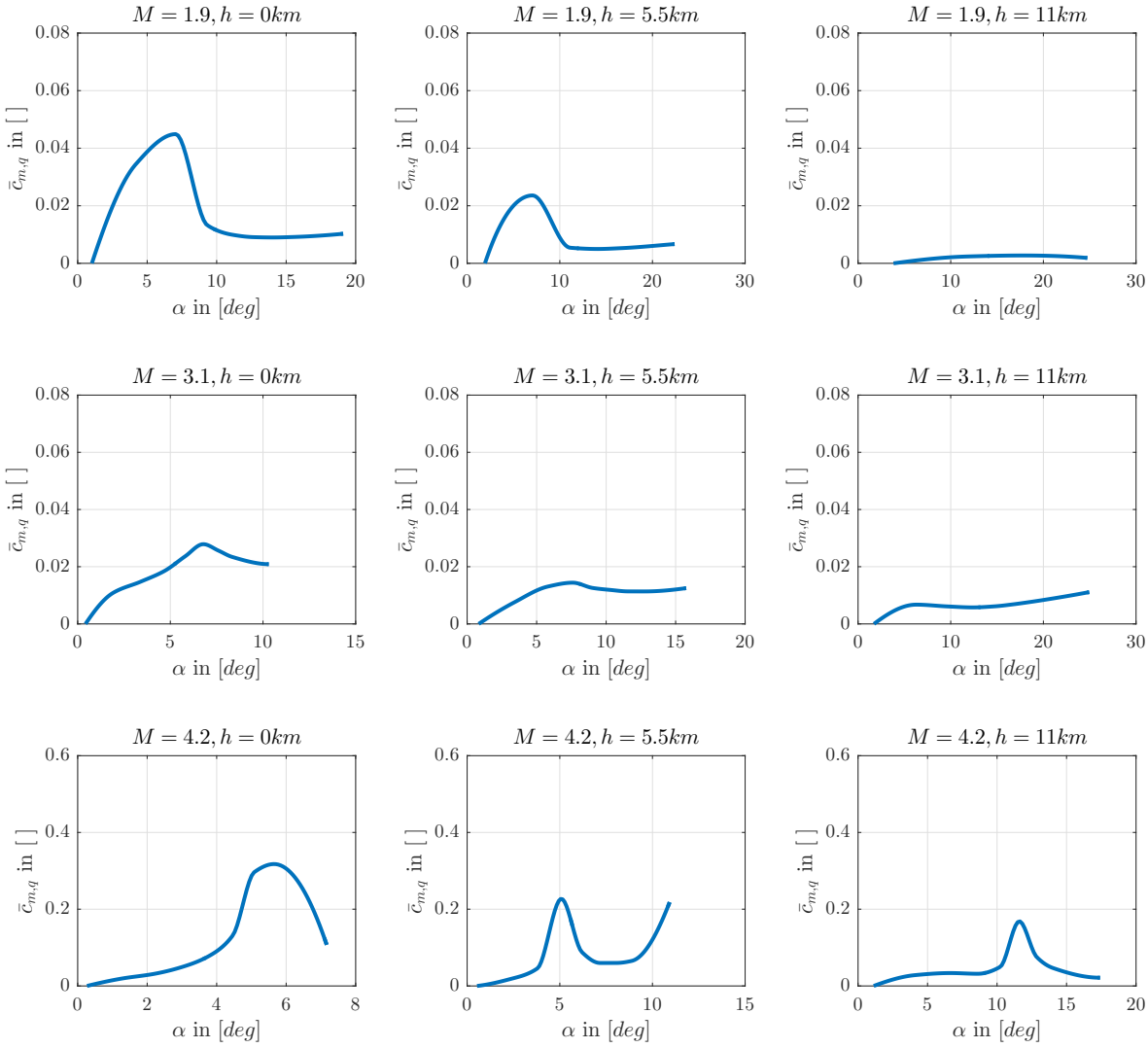

Figure 5.8: Relative magnitude of the pitch damping moment $C_{m,q}$ compared to the summed aerodynamic moment coefficients.

Figure 5.8 supports the assumption that the moment induced by the respective body rate has minor influence on the overall aerodynamic moment.

- *roll rate in STT maneuver*: In STT steering mode zero roll angle ϕ_v is commanded to the missile autopilot from the upstream guidance unit. It can be seen from the definition of the roll angle ϕ_v (2.18) that cross-coupling effects causing undesired roll angles can occur at large aerodynamic angles regimes. In order to avoid those effects, the roll rates p_K are restricted low magnitudes within the FCS, compared to the maximum feasible roll rates resulting in significant cross-coupling effects. Therefore, the influence of those roll rates on the pitch and yaw accelerations via $p_K r_K \left(I_{xx} - I_{zz}\right)$ and $p_K q_K \left(I_{xx} - I_{yy}\right)$ (see (2.20)) can be neglected.
- *control deflection rates*: Within the autopilot design only the fin position is used. The fin rates are not measurable. Estimating the fin rates would require a fast filtering of the fin position measurements. This differentiating filter would result in high frequency feedback due to measurement noise.
- *filtered acceleration increments*: The feedback law is derived without considering the the low-

pass filtered version of the acceleration increments $\begin{bmatrix}\Delta a_z & \Delta a_y\end{bmatrix}$ of the design model's outer dynamics (see (5.16)). This is due to the fact that the fast dynamics and transient characteristics of the longitudinal and lateral accelerations at the virtual point P are only marginally influenced by those increments.

- *gravity force*: Since the gravitational influence is negligible compared to the missile's maximum load factors in an endgame scenario, the gravitational force (see section 2.3.1) is neglected for deriving the design model. Therefore, the flight path angles γ_K and μ_K, transforming the vector of gravitational force to the $\bar{K}$-frame (see (2.29)), are obsolete.
- *influence of fin deflection on acceleration*: As discussed in section 5.3.1, the longitudinal and lateral accelerations for control design (5.16) are considered in the vicinity of the cop. By taking into account the neutralization of fin deflections (5.13) within those channels, the force $C_{z,\eta}$ and moment coefficient $C_{m,\eta}$ can be neglected. Therefore, the fin deflection $\boldsymbol{u}_\delta$ is not considered within the design model.

Based on the simplifications and assumptions described above, the outer dynamics of the design model establishes the time derivative of the control variables (5.16):

$$\begin{bmatrix}\dot{\phi}_v\\ \dot{a}_z^P\\ \dot{a}_y^P\end{bmatrix} = \begin{bmatrix}\cos\alpha_K\cos\beta_K\cdot p_K + \sin\beta_K\cdot q_K + \sin\alpha_K\cos\beta_K\cdot r_K\\ \frac{\bar{q}S_{ref}}{m}\cdot\left(\frac{\partial C_{z,0}}{\partial\alpha_K}\cdot\dot{\alpha}_K + \frac{\partial C_{z,0}}{\partial\beta_K}\cdot\dot{\beta}_K\right) - x_{cog,P}\cdot\ddot{q}_K\\ \frac{\bar{q}S_{ref}}{m}\cdot\left(\frac{\partial C_{y,0}}{\partial\alpha_K}\cdot\dot{\alpha}_K + \frac{\partial C_{y,0}}{\partial\beta_K}\cdot\dot{\beta}_K\right) + x_{cog,P}\cdot\ddot{r}_K\end{bmatrix} \tag{5.18}$$

As mentioned above, changes of roll angle and roll rates are negligible due to STT steering. Therefore, the influence of the roll rate on the acceleration is omitted in (5.18).

The dynamics of the AoA

$$\begin{aligned}\dot{\alpha}_K &= \underbrace{\frac{a_z\cdot\cos\alpha_K - a_x\cdot\sin\alpha_K}{V_K\cdot\cos\beta_K} - \tan\beta_K\cdot(\cos\alpha_K\cdot p_K + \sin\alpha_K\cdot r_K)}_{=b_{\dot{\alpha}}} + q_K\\ &= b_{\dot{\alpha}} + q_K\end{aligned} \tag{5.19}$$

and angle of sideslip (AoS)

$$\begin{aligned}\dot{\beta}_K &= \underbrace{\frac{-a_x\cdot\cos\alpha_K\sin\beta_K + a_y\cdot\cos\beta_K - a_z\cdot\sin\alpha_K\cos\beta_K}{V_K} + \sin\alpha_K\cdot p_K}_{=b_{\dot{\beta}}}\\ &\quad - \cos\alpha_K\cdot r_K\\ &= b_{\dot{\beta}} - \cos\alpha_K\cdot r_K\end{aligned} \tag{5.20}$$

is reconstructed within the algorithm by substituting the forces with the accelerations measured at the IMU. The usage of the axial, lateral, and longitudinal accelerations provided by the IMU exhibits the advantages of obtaining more reliable estimates of $\dot{\alpha}_K$ and $\dot{\beta}_K$ compared to reconstruction via uncertain aerodynamic force coefficients.

The substitutions $b_{\dot{\alpha}}$ and $b_{\dot{\beta}}$ are introduced with the purpose of a compact notation. In order to calculate the acceleration increments in (5.18) which accounts for the virtual accelerations at P, the approximated acceleration increments require the estimation of the pitch

$$\ddot{q}_K = \frac{\bar{q}S_{ref}l_{ref}}{I_{yy}}\cdot\left(\frac{\partial C_{m,0}}{\partial\alpha_K}\cdot\dot{\alpha}_K + \frac{\partial C_{m,0}}{\partial\beta_K}\cdot\dot{\beta}_K\right) \tag{5.21}$$

and yaw accelerations

$$\ddot{r}_K = \frac{\bar{r} S_{ref} l_{ref}}{I_{zz}} \cdot \left(\frac{\partial C_{n,0}}{\partial \alpha_K} \cdot \dot{\alpha}_K + \frac{\partial C_{n,0}}{\partial \beta_K} \cdot \dot{\beta}_K \right). \tag{5.22}$$

Substituting the estimates (5.21), (5.22), (5.19), and (5.20) in (5.18) and separating the body rates of each channel, the approximated input/output dynamics of the outer loop is given in abbreviated form by

$$\dot{\boldsymbol{y}}^P = \begin{bmatrix} \dot{\phi}_v \\ \dot{a}_z^P \\ \dot{a}_y^P \end{bmatrix} = \underbrace{\hat{\boldsymbol{A}}_{\boldsymbol{y}} \cdot \boldsymbol{\omega}_K^{EB} + \hat{\boldsymbol{b}}_{\boldsymbol{y}}}_{\hat{\boldsymbol{F}}_{\boldsymbol{y}}(\boldsymbol{\omega}_K^{EB})} + \boldsymbol{\Delta}_{\boldsymbol{y}} \tag{5.23}$$

with the diagonal input matrix

$$\hat{\boldsymbol{A}}_{\boldsymbol{y}} = \begin{bmatrix} \cos\alpha_K \cos\beta_K & 0 & 0 \\ 0 & \bar{q} S_{ref} \cdot \left(\frac{1}{m} \cdot \frac{\partial C_{z,0}}{\partial \alpha_K} - \frac{x_{cog,P} l_{ref}}{I_{yy}} \cdot \frac{\partial C_{m,0}}{\partial \alpha_K} \right) & 0 \\ 0 & 0 & -\cos\alpha_K \bar{q} S_{ref} \cdot \left(\frac{1}{m} \cdot \frac{\partial C_{y,0}}{\partial \beta_K} + \frac{x_{cog,P} l_{ref}}{I_{zz}} \cdot \frac{\partial C_{n,0}}{\partial \beta_K} \right) \end{bmatrix} \tag{5.24}$$

and the accumulation of the system's nonlinearities

$$\hat{\boldsymbol{b}}_{\boldsymbol{y}} = \begin{bmatrix} \sin\beta_K \cdot q_K \\ \frac{\bar{q} S_{ref}}{m} \cdot \left(\frac{\partial C_{z,0}}{\partial \alpha_K} \cdot b_{\dot{\alpha}} + \frac{\partial C_{z,0}}{\partial \beta_K} \cdot \left(b_{\dot{\beta}} - \cos\alpha_K r_K \right) \right) \\ \frac{\bar{q} S_{ref}}{m} \cdot \left(\frac{\partial C_{y,0}}{\partial \alpha_K} \cdot (b_{\dot{\alpha}} + q_K) + \frac{\partial C_{y,0}}{\partial \beta_K} \cdot b_{\dot{\beta}} \right) \\ + \sin\alpha_K \cos\beta_K \cdot r_K \\ -\frac{x_{cog,P} \bar{q} S_{ref} l_{ref}}{I_{yy}} \cdot \left(\frac{\partial C_{m,0}}{\partial \alpha_K} \cdot b_{\dot{\alpha}} + \frac{\partial C_{m,0}}{\partial \beta_K} \cdot \left(b_{\dot{\beta}} - \cos\alpha_K \cdot r_K \right) \right) \\ + \frac{x_{cog,P} \bar{q} S_{ref} l_{ref}}{I_{zz}} \cdot \left(\frac{\partial C_{n,0}}{\partial \alpha_K} \cdot (b_{\dot{\alpha}} + q_K) + \frac{\partial C_{n,0}}{\partial \beta_K} \cdot b_{\dot{\beta}} \right) \end{bmatrix}. \tag{5.25}$$

In order to mark the parts of the design model as an approximation of the plant dynamics, the physical relevant terms ($\hat{\boldsymbol{A}}_i, \hat{\boldsymbol{b}}_i, i = \boldsymbol{y}, \boldsymbol{\omega}$) are labeled with $\hat{}$. The divergence between the design and plant model of the respective dynamic layer is denoted by $\boldsymbol{\Delta}_i \in \mathbb{R}^{3\times 1}$, $i = \boldsymbol{y}, \boldsymbol{\omega}$.

The body rate dynamics

$$\begin{bmatrix} \dot{p}_K \\ \dot{q}_K \\ \dot{r}_K \end{bmatrix} = \begin{bmatrix} 1/I_{xx} & 0 & 0 \\ 0 & 1/I_{yy} & 0 \\ 0 & 0 & 1/I_{zz} \end{bmatrix} \begin{bmatrix} \left(L^G\right)_B \\ \left(M^G\right)_B - r_K p_K \left(I_{xx} - I_{zz}\right) \\ \left(N^G\right)_B + p_K q_K \left(I_{xx} - I_{yy}\right) \end{bmatrix} \tag{5.26}$$

constitute the underlying fast dynamic layer of the outer loop dynamics (5.23). Separating the aerodynamic moment control effectiveness (5.6) of (5.26) diagonal input matrix

$$\hat{\boldsymbol{A}}_{\boldsymbol{\omega}} = \begin{bmatrix} \frac{1}{I_{xx}} & 0 & 0 \\ 0 & \frac{1}{I_{yy}} & 0 \\ 0 & 0 & \frac{1}{I_{zz}} \end{bmatrix} \tag{5.27}$$

and the inner layer nonlinearities

$$\hat{\boldsymbol{b}}_{\boldsymbol{\omega}} = \begin{bmatrix} \frac{\bar{q}S_{ref}l_{ref}}{I_{xx}} \cdot C_{l,0} \\ \frac{\bar{q}S_{ref}l_{ref}}{I_{yy}} \cdot C_{m,0} - p_K \cdot r_K \cdot (I_{xx} - I_{zz}) \\ \frac{\bar{q}S_{ref}l_{ref}}{I_{zz}} \cdot C_{n,0} + p_K \cdot q_K \cdot (I_{xx} - I_{yy}) \end{bmatrix} \tag{5.28}$$

describe the body rate dynamics (5.26) of the design model

$$\dot{\boldsymbol{\omega}} = \begin{bmatrix} \dot{p}_K \\ \dot{q}_K \\ \dot{r}_K \end{bmatrix} = \underbrace{\hat{\boldsymbol{A}}_{\boldsymbol{\omega}} \cdot \boldsymbol{C}_{\boldsymbol{M},\boldsymbol{u}} + \hat{\boldsymbol{b}}_{\boldsymbol{\omega}}}_{\hat{\boldsymbol{F}}_{\boldsymbol{\omega}}(\boldsymbol{C}_{\boldsymbol{M},\boldsymbol{u}})} + \boldsymbol{\Delta}_{\boldsymbol{\omega}} \tag{5.29}$$

Remark: The aerodynamic force and moment coefficients are implemented within the autopilot using linear interpolation of tabulated data. Based on this aerodynamic data set, the partial derivatives of the aerodynamic coefficients are calculated online using forward finite differences:

$$\frac{\partial C_{i,j}\left(x_1, \ldots, x_k, \ldots, x_n\right)}{\partial x_k} = \frac{C_{i,j}\left(x_1, \ldots, x_k + h, \ldots, x_n\right) - C_{i,j}\left(x_1, \ldots, x_k, \ldots, x_n\right)}{h} \tag{5.30}$$

In (5.30) the index i denotes the axis of the force or moment coefficient, j labels the category of the respective coefficient, and h is the differentiation step size. For the calculation of all partial derivatives within the FCS the step size is chosen to $h = 10^{-3}$.

5.4 Nonlinear Reference Model

As shown in fig. 5.4, the NRM provides the subsequent elements within the autopilot with the required reference signals. Therefore, the reference model determines the overall performance characteristics of the closed-loop system.

In section 4.2.3, general properties of reference models serving as command filters are outlined. In common missile autopilot designs linear filters are used as reference models to represent the desired closed-loop dynamics [36, 38, 40]. Since the nonlinear missile dynamics incorporates strong axes coupling, saturation effects, varying dynamical properties, and nonlinear aerodynamics in combination with an extensive flight envelope, linear reference models limit the closed-loop performance capabilities by far.

In order to avoid the deficiencies of linear reference models and to fully exploit the missile's nonlinear dynamics across the entire flight envelope, it is inevitable to incorporate the main nonlinear effects within the reference model.

A scheme of the reference model providing the set signals $\boldsymbol{y}_r$, $\boldsymbol{\omega}_r$, and $\dot{\boldsymbol{\omega}}_r$ for the presented autopilot approach is depicted in fig. 5.9. It consists of two elements, the *Reference Model Control* and *Reference Model Dynamics*. Based on the command signal $\boldsymbol{y}_c$ and the current operating point, defined via $\bar{q}$ and M, the *Reference Model Control* calculates the respective fin deflections $\boldsymbol{u}_{\delta,r,c}$, which are necessary to guarantee fast tracking (of the commanded signal) by the dynamics of the reference model. Applying those fin deflections to the *Reference Model Dynamics* lead to the reference model outputs $\boldsymbol{y}_r$, $\boldsymbol{\omega}_r$, $\dot{\boldsymbol{\omega}}_r$ which are shaped by incorporating the main nonlinear effects, dynamics, and limitations of the missile system within the reference model. The structure of the nonlinear terms ($\hat{\boldsymbol{F}}_{r,\boldsymbol{y}}$, $\hat{\boldsymbol{F}}_{r,\boldsymbol{\omega}}$, $\hat{\boldsymbol{A}}_{r,\boldsymbol{y}}$, $\hat{\boldsymbol{A}}_{r,\boldsymbol{\omega}}$) approximating the missile dynamics are equivalent to those of the design model (see (5.23) and (5.29)). The index r indicates that the terms are built up by states from the reference model's

State Estimation subsystem (see fig. 5.9).

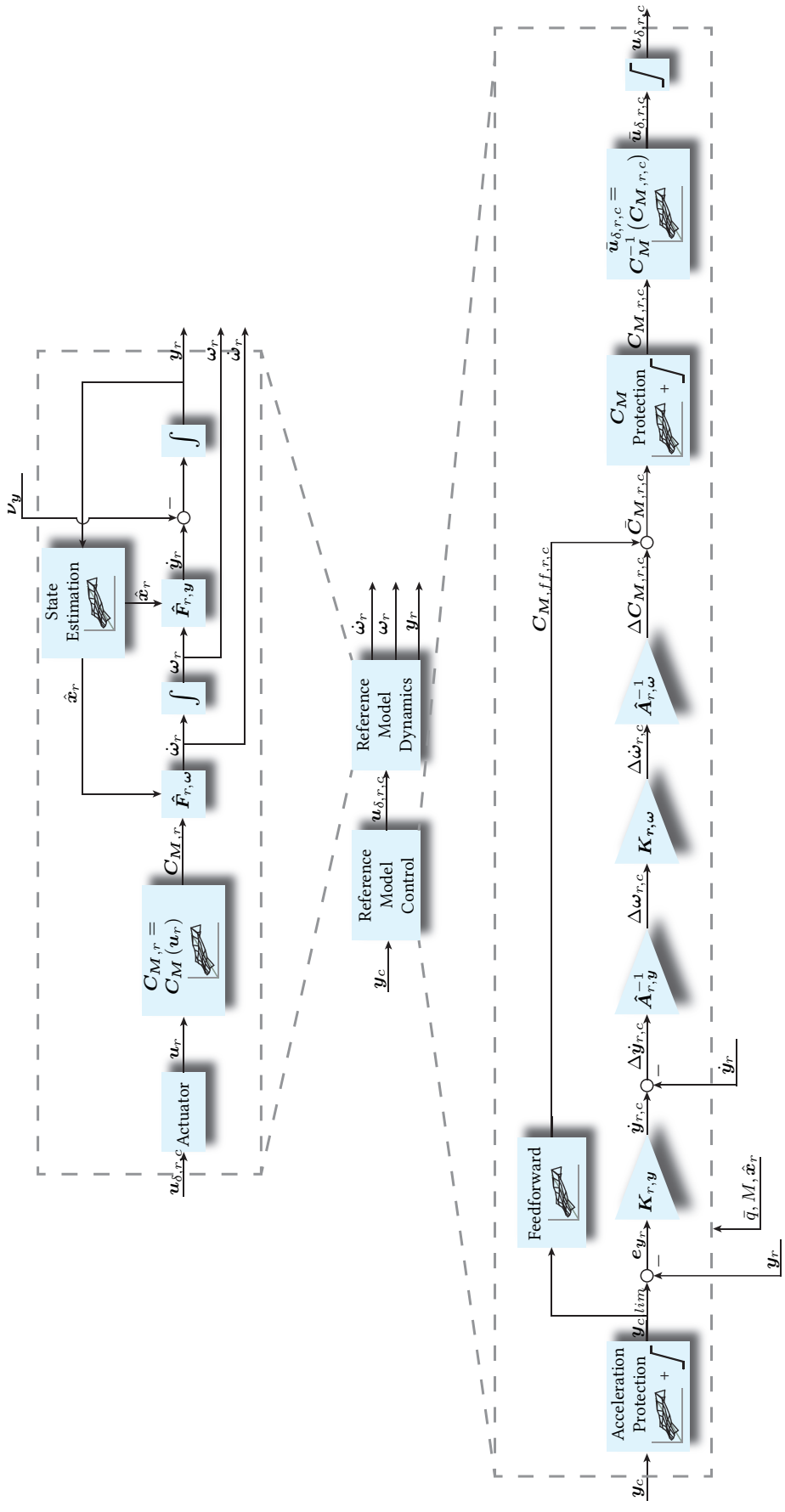

Figure 5.9: Detailed schematic of the nonlinear, interconnected reference model.

Within the *Reference Model Control* the acceleration vector $\boldsymbol{a}_c = \begin{bmatrix} a_{z,c} & a_{y,c} \end{bmatrix}^T$ extracted from the command (5.4) (perpendicular to the missile's x_B-axis) is scaled according to the maximum possible missile acceleration $a_{max}\left(\|\boldsymbol{a}_c\|_2, h, M\right)$ (see chapter 3) at the given flight envelope point:

$$\boldsymbol{a}_{c,lim} = \frac{\left\| \begin{bmatrix} \|\boldsymbol{a}_c\|_2 & a_{max}\left(h, M\right) \end{bmatrix} \right\|_\infty}{\|\boldsymbol{a}_c\|_2} \cdot \boldsymbol{a}_c \tag{5.31}$$

The maximum missile acceleration a_{max} depicted in fig. 5.10 is obtained from acceleration trim calculations by considering the total allowable AoA and maximum fin deflection (for further details see chapter 3; same holds for lateral acceleration).

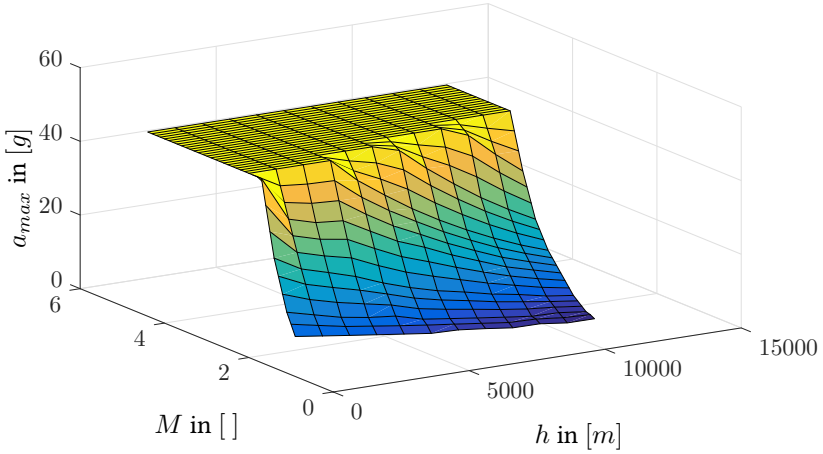

Figure 5.10: Maximum absolute missile acceleration over entire flight envelope with respect to Mach M and altitude h.

A limitation of the roll angle $\phi_{v,c}$ is not required since the missile is steered in STT-mode, which demands $\phi_{v,c} = 0rad$. The desired moment coefficient $\bar{\boldsymbol{C}}_{\boldsymbol{M},r,c}$ for the reference dynamics are calculated in the downstream algorithm of the acceleration protection. This algorithm is subdivided into a feedforward and an incremental feedback branch calculating $\boldsymbol{C}_{\boldsymbol{M},ff,r,c}$ and $\Delta\boldsymbol{C}_{\boldsymbol{M},r,c}$, respectively (see fig. 5.9).

Within the feedforward branch the moment coefficients $C_{l,ff,r,c}$, $C_{m,ff,r,c}$, and $C_{n,ff,r,c}$ are calculated for each missile axes based on the commanded (desired) acceleration $a_{z,c}$, $a_{y,c}$ via tabulated trim results. Those trim results are obtained from trim calculations of the Reference Model Dynamics. Therefore, the moment coefficients of the feedforward branch result in the desired steady-state acceleration. Since the reference model is fully known and not subject to any uncertainties, the reason for steady-state errors between the accelerations of the reference model $a_{z,r}$, $a_{y,r}$ and the commanded ones ($a_{z,c}$, $a_{y,c}$) result from the linear interpolation of the tabulated data set.

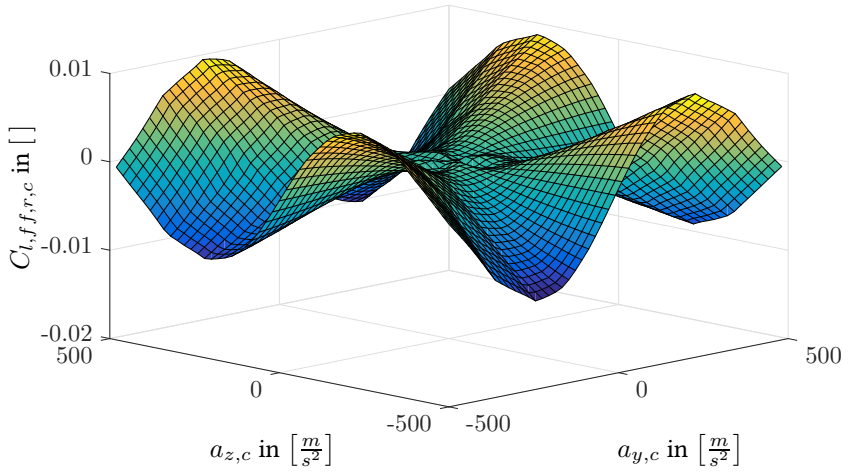

(a) Roll channel moment coefficient $C_{l,ff,r,c}$ of reference model feedforward branch based on commanded accelerations.

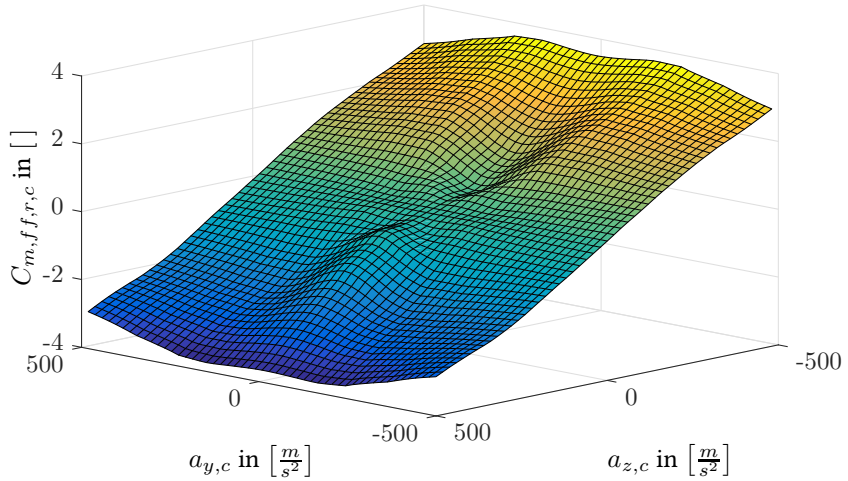

(b) Pitch channel moment coefficient $C_{m,ff,r,c}$ of reference model feedforward branch based on commanded accelerations.

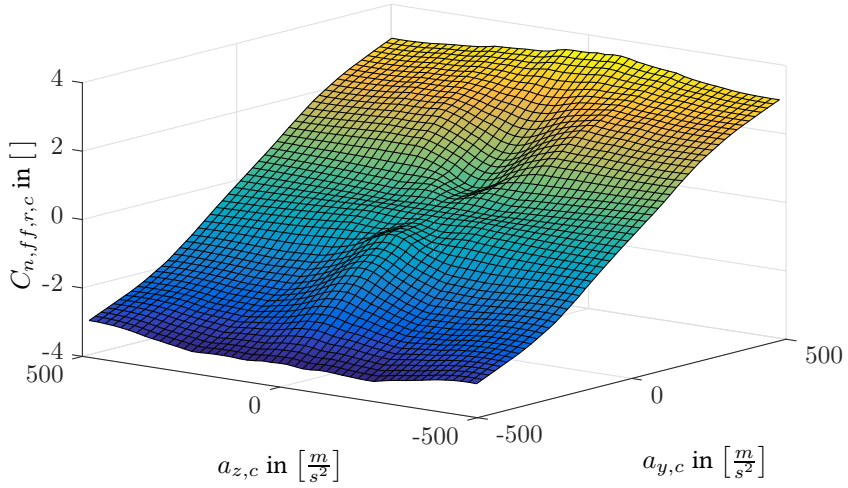

(c) Yaw channel moment coefficient $C_{n,ff,r,c}$ of reference model feedforward branch based on commanded accelerations.

Figure 5.11: Moment coefficients $C_{\boldsymbol{M},ff,r,c}$ of reference model feedforward branch based on commanded accelerations $a_{y,c}$, $a_{z,c}$.

Besides the feedforward signal $\boldsymbol{C_{M,ff,r,c}}$ guaranteeing perfect steady-state characteristics, the feedback branch, issuing $\Delta\boldsymbol{C_{M,r,c}}$, determines the transient behavior of the reference model outputs. Due to the properties of the feedforward structure, $\Delta\boldsymbol{C_{M,r,c}}$ is calculated by using proportional (no integral) error feedback only. Based on the error $\boldsymbol{e_{y_r}} = \boldsymbol{y_{c,lim}} - \boldsymbol{y_r}$ between the commanded and the reference signal and the time derivative $\dot{\boldsymbol{y}}_r$ the cascaded structure of the feedback branch is given by

$$\Delta\boldsymbol{C_{M,r,c}} = \hat{\boldsymbol{A}}_{\boldsymbol{\omega}}^{-1} \cdot \boldsymbol{K}_{\omega}\left(\bar{q}, M\right) \cdot \Delta\boldsymbol{\omega}_{r,c}. \tag{5.32}$$

The incremental approach calculates the desired rate increment

$$\Delta\boldsymbol{\omega}_{r,c} = \hat{\boldsymbol{A}}_{\boldsymbol{y}}^{-1} \cdot \left(\boldsymbol{K}_{r,\boldsymbol{y}}\left(\bar{q}, M\right) \cdot \boldsymbol{e_{y_r}} - \dot{\boldsymbol{y}}_r\right). \tag{5.33}$$

feeding back the difference $\dot{\boldsymbol{y}}_{r,c} - \dot{\boldsymbol{y}}_r$. The time derivative of the reference signals $\dot{\boldsymbol{y}}_r$ is calculated in the preceding cascade with $\dot{\boldsymbol{y}}_{r,c} = \boldsymbol{K}_{r,\boldsymbol{y}}\boldsymbol{e_{y_r}}$. Since the proportional gains $\boldsymbol{K_y}$ and $\boldsymbol{K_\omega}$ establish the desired missile closed-loop transient characteristics, their design has to be in compliance with the required performance characteristics in section 5.1.2 across the entire flight envelope. NFR_3 and NFR_4 constitute the main drivers for the gain layout. The layout is accomplished using nonlinear optimization method. Based on the linearized design model, an initial guess is obtained serving as a starting point for the optimization problem.

The desired moment coefficients

$$\bar{\boldsymbol{C}}_{\boldsymbol{M},r,c} = \boldsymbol{C_{M,ff,r,c}} + \Delta\boldsymbol{C_{M,r,c}}. \tag{5.34}$$

result from addition of the feedforward $\boldsymbol{C_{M,ff,r,c}}$ and feedback $\Delta\boldsymbol{C_{M,r,c}}$ signal. Based on the limited version $\boldsymbol{C_{M,r,c}}$ of the moment coefficients $\bar{\boldsymbol{C}}_{\boldsymbol{M},r,c}$ the fin deflections $\boldsymbol{u_{\delta,r,c}}$ for the simplified actuator model (within the *Reference Model Dynamics*) are calculated in the downstream process by inverting the moment coefficients of the aerodynamic dataset. In order to assure that the demanded fin deflections $\boldsymbol{u_{\delta,r,c}}$ are compliant with the missile's maximum performance capabilities, the limitation of the moment coefficients is accomplished with respect to the magnitude of the physical feasible body angular acceleration. The limits are based on acceleration trim results (see section 3.1.2.2) depending on the current flight envelope point. The saturation of $\bar{\boldsymbol{C}}_{\boldsymbol{M},r,c}$ is depicted in fig. 5.9 by the $\boldsymbol{C_M}Protection$ block ahead of the inversion of the moment coefficients. For a detailed derivation of the algebraic relationship between angular accelerations and aerodynamic moments acting on the missile's body the reader is referred to section 2.2.2.2.

Since the autopilot is designed for STT steering mode, the control demand of pitch and yaw channel requires prioritization compared to the roll channel. Those requirements need to be incorporated within the reference signals for the downstream control law. In order to account for this prioritization within the reference model, the limitation of the moment coefficients $\boldsymbol{C_{M,r,c}}$ need to be implemented by a different weighting of roll and pitch/yaw channel. The limits

$$\begin{aligned} C_{l,limit} \;=\; & C_{l,0}\left(\alpha = 0°, \beta = 0°, M_{trim}\right) \\ & + \tfrac{p_{trim} l_{ref}}{2V_{trim}} C_{l,p}\left(\alpha = 0°, \beta = 0°, M\right) \\ & + C_{l,\eta}\left(\alpha = 0°, \beta = 0°, M_{trim}, \xi = \pm 5°, \eta_{trim} = 0°, \zeta = 0°\right). \end{aligned} \tag{5.35}$$

for the roll moment coefficient C_l are calculated based on trim results considering the roll axis as isolated. In order to account for the minor control authority in roll channel commands, the trim problem solves $\dot{p} = 0$ with respect to the roll rate p_{trim} for $\xi = \pm 5°$ and with zero incidence angles ($\alpha = 0°$, $\beta = 0°$). Conducting those calculations over the entire flight envelope leads to upper and lower limits for the roll moment coefficients C_l, depicted in fig. 5.12. The lower prioritization compared to the longitudinal and lateral channel is realized through allocating reduced control authority

for ξ.

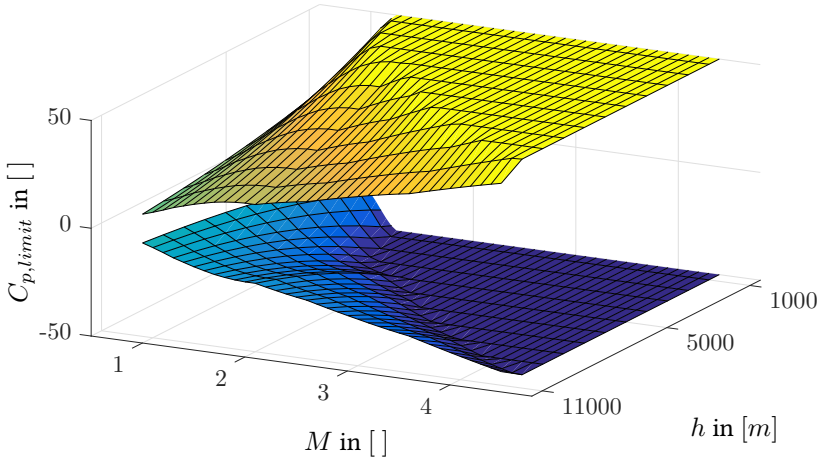

Figure 5.12: Lower and upper limit of absolute angular acceleration $\dot{p}$ in roll direction over Mach M and altitude h.

For the moment coefficients in longitudinal and lateral direction the lower and upper limits are determined by considering the minimum and maximum physical feasible acceleration trim configuration. As already discussed in section 3.1 such a trim configuration is characterized by the aerodynamic angle (α_{trim}, β_{trim}), the body rate (q_{trim}, r_{trim}), and the corresponding fin deflection (η_{trim}, ζ_{trim}) evaluated at the considered operating point, which is described by Mach number M_{trim} and altitude h_{trim}. The limits of the equivalent pitch C_m and yaw moment coefficients C_n are calculated based on (2.36). Equation (5.36) shows the calculation of the limits for the pitch channel.

$$\begin{aligned} C_{m,limit} \quad = \quad & C_{m,0}\left(\alpha_{trim}, \beta = 0°, M_{trim}\right) \\ & + \frac{q_{trim} l_{ref}}{2V_{trim}} C_{m,q}\left(\alpha_{trim}, \beta = 0°, M_{trim}\right) \\ & + C_{m,\eta}\left(\alpha_{trim}, \beta = 0°, M_{trim}, \xi = 0°, \eta_{trim}\right) \end{aligned} \quad . \tag{5.36}$$

Due to the symmetry property of the missile body, the limits of the aerodynamic yaw moment coefficient are calculated in analogy to fig. 5.13 with $\alpha = 0°$ and $\beta = \beta_{trim}$. The upper and lower limits for the pitch channel versus Mach an AoA are depicted in an exemplary manner in fig. 5.13.

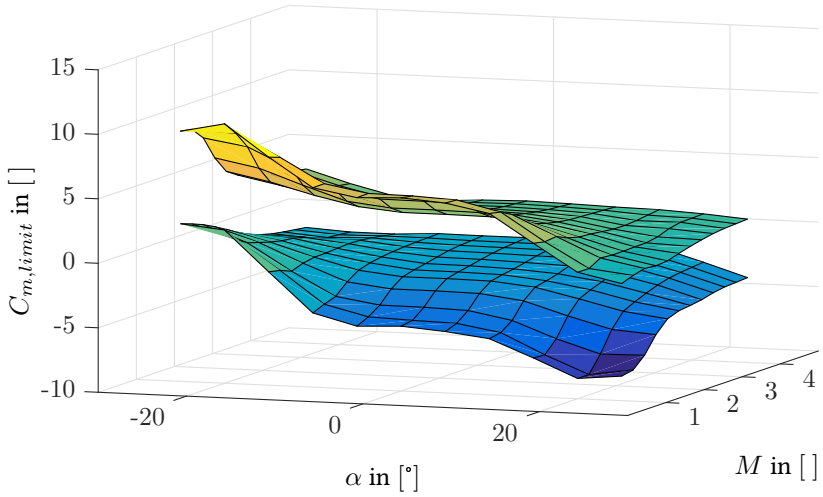

Figure 5.13: Lower and upper limit of absolute angular acceleration $\dot{q}$ in longitudinal direction over Mach M and AoA α at an altitude of $h = 1000m$.

The second part of the reference model consists of a nonlinear approximation of the missile dynamics based on the design model derived in section 5.3.2. $\boldsymbol{u}_{\delta,r,c}$ can be considered as the input to the *Reference Model Dynamics*. With the use of a simplified actuator model and the mapping rule (see (2.46)), the fin deflections are delayed and limited according to the time constants and limits of the actuator model introduced in section 2.5.1. The resulting aerodynamic equivalent fin deflections $\boldsymbol{u}_r$ are transformed to the aerodynamic moment coefficients by

$$\boldsymbol{C}_{\boldsymbol{M},r} = \boldsymbol{C}_{\boldsymbol{M}}\left(\boldsymbol{u}_r\right). \tag{5.37}$$

With those moment coefficients and the implementation of the missile's inner (5.29) and outer dynamic layer (5.23), the reference model outputs result to

$$\dot{\boldsymbol{\omega}}_r = \hat{\boldsymbol{A}}_{\boldsymbol{\omega}} \cdot \boldsymbol{C}_{\boldsymbol{M},r} + \hat{\boldsymbol{b}}_{\boldsymbol{\omega}} \tag{5.38a}$$

$$\boldsymbol{\omega}_r = \int \left(\hat{\boldsymbol{A}}_{\boldsymbol{\omega}} \cdot \boldsymbol{C}_{\boldsymbol{M},r} + \hat{\boldsymbol{b}}_{\boldsymbol{\omega}}\right) dt \tag{5.38b}$$

$$\boldsymbol{y}_r = \int \left(\hat{\boldsymbol{A}}_{\boldsymbol{y}} \cdot \boldsymbol{\omega}_r + \hat{\boldsymbol{b}}_{\boldsymbol{y}}\right) dt \tag{5.38c}$$

. As described in section 5.3.2, the nonlinear functions in (5.25) and (5.28) approximating the missile dynamics depend on a subset of the missile's state vector. Besides the slow entities $\bar{q}$ and M describing the current flight envelope point, an online calculation of the AoA and AoS within the reference model is necessary in order to compute the respective coefficients and their partial derivatives. An estimation of the aerodynamic angles is accomplished by using the longitudinal and lateral accelerations (without influence of gravity) $a_{z,A,r}$ and $a_{y,A,r}$, obtained within the reference model via (5.38c). These accelerations are algebraically linked to the AoA and AoS by the aerodynamic force equation (see (2.33)).

From (2.33) the accumulated aerodynamic force coefficients

$$C_{z,r} = \frac{a_{z,A,r}}{\bar{q} m l_{ref}} \tag{5.39a}$$

$$C_{y,r} = \frac{a_{y,A,r}}{\bar{q} m l_{ref}} \tag{5.39b}$$

, in lateral and longitudinal direction of the body-frame can be calculated based on the accelerations $a_{z,A,r}$ and $a_{y,A,r}$ stemming from the aerodynamic forces expressed in B-frame. By inverting those aerodynamic force coefficients C_z and C_y with respect to α and β

$$\alpha_r = \alpha\left(M, C_{z,r}, C_{y,r}, \eta\right) \tag{5.40a}$$

$$\beta_r = \beta\left(M, C_{z,r}, C_{y,r}, \zeta\right) \tag{5.40b}$$

the two aerodynamic angles are obtained. Due to the fact that both force coefficients C_z and C_y are monotonically increasing with respect to α and β, the inversion (5.40) is unique in the lateral and longitudinal accelerations.

Within the design model (see section 5.3) and therefore the *Reference Model Dynamics* the accelerations are considered without the influence of gravity. Thus, the accelerations $a_{z,r}$ and $a_{y,r}$ obtained via integration of (5.23) can be directly used to estimate α and β by utilizing the inverse functions (5.40).

In summary, the *Reference Model Control* in combination with the *Reference Model Dynamics* shapes the command vector $\boldsymbol{y}_c$ to the physically interconnected signals $\boldsymbol{y}_r$, $\boldsymbol{\omega}_r$, and $\dot{\boldsymbol{\omega}}_r$ for application in the downstream control algorithm. Since only the inner and outer loop missile dynamics is relevant for generating the demanded reference output entities, an incorporation of velocity and altitude (or dynamic pressure) dynamics is not required. The estimates of those two variables are used to adjust the closed-loop dynamics of the reference model to the current flight envelope point.

Since the reference model generates the trajectory $\boldsymbol{y}_r$ which is tracked by the autopilot, it primarily determines the overall closed-loop response of the missile system. Therefore, it is inevitable that the stand-alone reference model is compliant with requirements concerning performance and transient response. This section is concluded by verifying the NFRs of axis decoupling (see NFR_3), overshoot/undershoot (see NFR_4), rise time (see NFR_5), and settling time (see NFR_6) across the entire flight envelope. For this purpose, step inputs with amplitudes close to the maximal trimmable acceleration of the considered operating point are applied to the longitudinal and lateral channels. The roll angle is commanded to $\phi_{v,c} = 0rad$. This is conducted for operating points in the Mach and altitude range of $M = 2 - 4$ and $h = 1 - 10km$, respectively. The responses of all three channels are depicted in fig. 5.14. In order to compare the different trajectories across the range of operating points, the acceleration responses are normalized with respect to amplitude of the commanded step input.

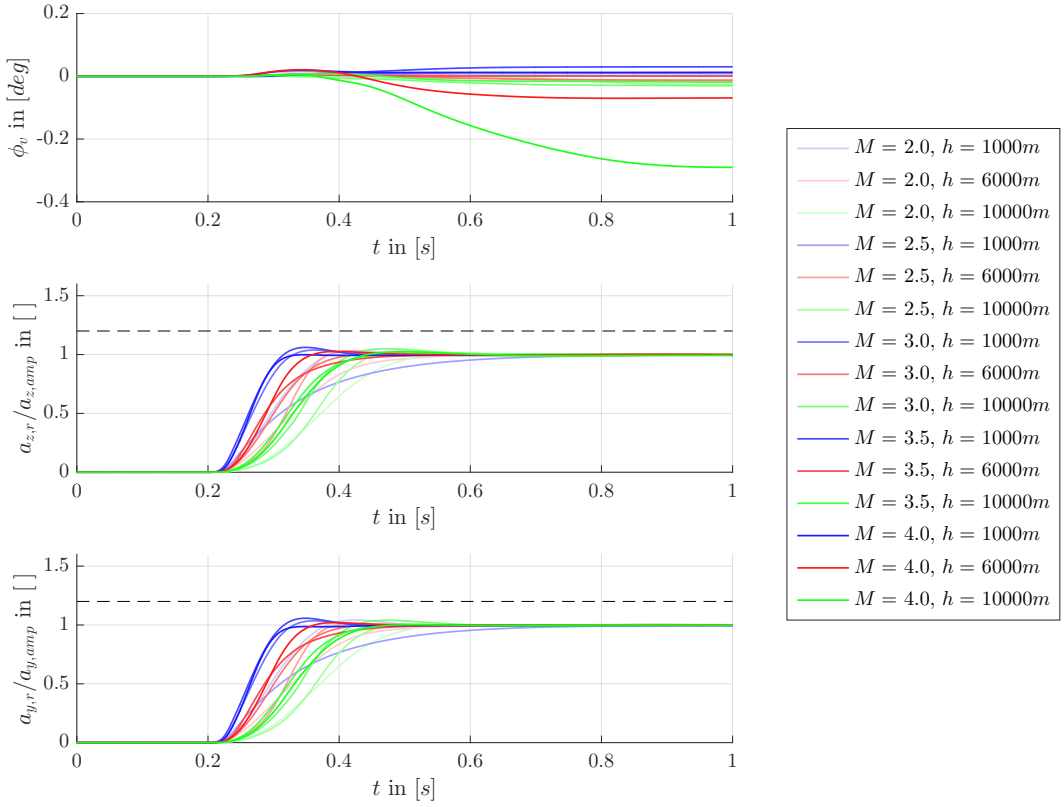

Figure 5.14: Normalized responses of simultaneous step commands to lateral and longitudinal acceleration channel. The dashed line depicts the overshoot limit.

From the evaluation of the reference model's outputs $\boldsymbol{y}_r$ (fig. 5.14) it can be concluded that all acceleration responses of both channels stay below the maximum allowable overshoot threshold (plotted as dashed black line at $a_{i,r}/a_{i,amp} = 1.2,\ i = y, z$). The roll angle never exceeds the defined limits of $\phi_v = \pm 2°$ (see NFR_3). For the sake of completeness, fig. 5.15 shows the overshoot/undershoot evaluation at the considered flight envelope as a fraction of the commanded amplitude $a_{i,amp}$.

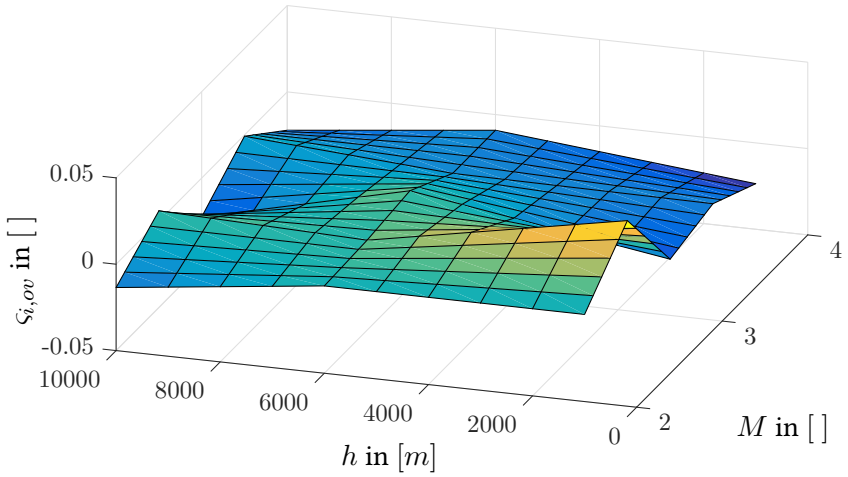

Figure 5.15: Overshoot $\varsigma_{q,ov}$ and $\varsigma_{r,ov}$ of longitudinal and lateral acceleration channel calculated from step responses (see fig. 5.14).

Based on fig. 5.14 and the criteria depicted in fig. 5.3, the resulting rise times T_q and T_r of the reference model's acceleration channels are pictured in fig. 5.16 over Mach and altitude. A comparison with the maximum rise time at each flight envelope point defined in fig. 5.2 shows that the rise time of the step responses generated by the reference model is below the maximum allowable one.

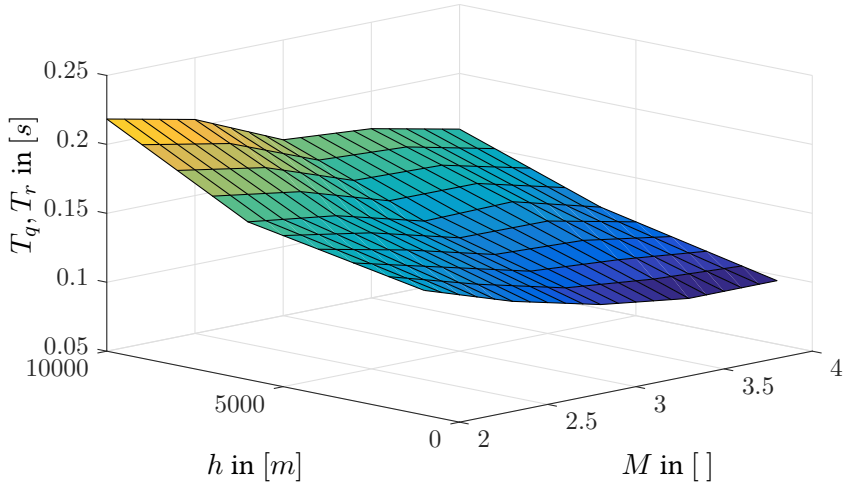

Figure 5.16: Rise time T_q and T_r of longitudinal and lateral acceleration calculated from step responses (see fig. 5.14).

Considering the settling time requirement defined in NFR_6, the calculated settling times of longitudinal and lateral acceleration channel are below the required threshold for all flight envelope points.

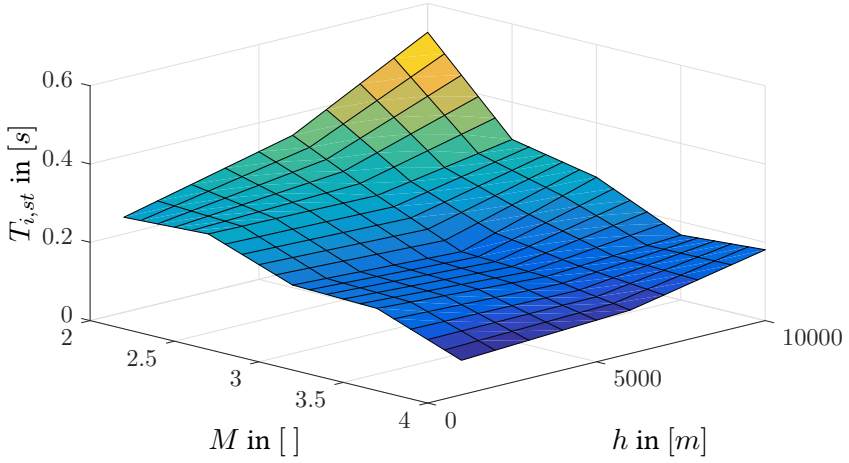

Figure 5.17: Settling time $T_{q,st}$ and $T_{r,st}$ of longitudinal and lateral acceleration calculated from step responses (see fig. 5.14).

Therefore, the evaluation of the step responses allow the conclusion that the reference model is compliant with the transient response, decoupling, and performance requirements defined in NFR_4, NFR_5, NFR_6, and NFR_3, respectively.

5.5 Control Algorithm

Besides the *Reference Model*, the *Control Algorithm* constitutes the second major subsystem within the FCS architecture (see fig. 5.4) with a dominant impact on the performance and robustness.

In short, the overall control goal of the *Control Algorithm* is to track the reference model's output vector $\boldsymbol{y}_r$ even in case of unavoidable modeling and sensor errors. From a mathematical perspective, this is accomplished by minimizing the tracking error between $\boldsymbol{y}_r$ and the considered output $\boldsymbol{y}^P$ under extensive variations of the plant parameters. Thus, the main challenge in missile control design is to be compliant with demanding robustness and performance requirements and the inherent trade-off between those two across a large set of operating points.

In common missile applications one control strategy covers robustness and performance requirements within one integrated approach [26, 29, 40, 122]. A separated, deterministic autopilot design strategy is presented, which consists of two elements (compliant to FR_7): a baseline control law and an adaptive augmentation (see fig. 5.4). Thus, the auxiliary output

$$\boldsymbol{C}_{\boldsymbol{M},\boldsymbol{u},c} = \boldsymbol{C}_{\boldsymbol{M},\boldsymbol{u},c,bs} + \boldsymbol{C}_{\boldsymbol{M},\boldsymbol{u},c,ad} \tag{5.41}$$

of the control algorithm (5.6) consists of a baseline and an adaptive portion, labeled with $\boldsymbol{C}_{\boldsymbol{M},\boldsymbol{u},c,bs}$ and $\boldsymbol{C}_{\boldsymbol{M},\boldsymbol{u},c,ad}$, respectively (the index B denoting the body-fixed coordinate frame is dropped due to better readability).

The advantage of a modular autopilot architecture lies in the clear allocation of certain requirements to each element, streamlined testing, and an adaptive augmentation which is independent of the used baseline control law. Since only the endgame flight phase is regarded, the autopilot design focuses only on this phase (endgame mode). Nevertheless, the modular design demanded in fig. 5.4 would allow a straightforward extension to different baseline control modes for different flight phases (e.g. boost, midcourse) by using the same adaptive element.

The model-based control approaches introduced in section 4.2 and section 4.3 constitute the theoretical framework for deriving the algorithms within autopilot (see fig. 5.4). Thus, the design model derived in section 5.3 constitutes the model used within the layout process of the baseline algorithm as well as the adaptive augmentation.

Due to the modular structure and the clear separation of the contributing autopilot elements, certain requirements (see section 5.1) in terms of performance and robustness are assigned to the baseline controller and the adaptive element, respectively. While the performance requirements are exclusively referred to the baseline controller, the adaptive element can influence the robustness properties only within the bounds preset by the baseline control design. Therefore, it is important in the baseline design phase to incorporate certain robustness properties which can be extended to the desired closed-loop robustness characteristics defined in section 5.1.

First of all, this section describes the derivation, analysis, and comparison of two different baseline strategies, which are tailored to be consistent with the nonlinear structure of the reference model (see section 5.4). In the second part, an adaptive augmentation is designed based on the theory of $\mathcal{L}_1$ Adaptive Control ($\mathcal{L}_1$ AC) - PWC Adaption explained in section 4.3.

5.5.1 Baseline Control Algorithm

In order to fully exploit the physical capabilities of the missile reference model, the subsequent control algorithm must be designed by utilizing the physically related reference model outputs. Since the baseline controller is the key element within the control algorithm in determining the performance characteristics, an exact tailoring to peculiarities of the reference model dynamics has to be considered in the layout of the baseline controller. Due to the fact that the reference model (see section 5.4) is developed as an integrated system providing physically linked reference signals of different dynamical layers, the classical approaches of Command Filtered Backstepping (CFB) and NDI has to be modified to be in line with the reference model interfaces and the beneficial performance characteristics.

Although the main focus of the baseline control law design concentrates on being compliant with performance requirements, robustness characteristics cannot be neglected. The robustness considerations in the baseline design is due to two reasons: first, the design model derived in section 5.3, constitutes an approximation of the missile system. Due to this reduced representation of the missile dynamics uncertainties of significant magnitude are introduced within the closed-loop, consisting of the baseline control law (with reference model) and the missile system. In order to be compliant with all performance requirements in nominal case, the baseline controller must compensate for the deviations between design and plant model. Second, as already mentioned above, the robustness characteristics of the baseline controller influences the overall achievable closed-loop robustness set up via the adaptive augmentation.

The representation of the missile nominal ($\boldsymbol{\Delta}_{m,i} = \mathbf{0}$) inner and outer dynamical layers depicted in (5.23) and (5.29) constitute the basis for deriving the autopilot control laws.

Even though two different control approaches are considered as baseline autopilot, the structure of both designs consists of a proportional-integral error feedback for the outer layer variables ($\boldsymbol{y}$) and a proportional feedback of the inner layer variables (body rates). The usage of integral feedback for the outer layer variables is due to the fact that the transient characteristics of the control variables ($\boldsymbol{y}$) are prioritized over the body rate states (see NFR_3, NFR_4, NFR_5).

5.5.1.1 NDI-based Baseline Control Law

In common missile and aircraft applications which utilize a NDI-based autopilot, the derivation of the control law follows a layer-wise approach. For this purpose the architecture of the autopilot consists of a cascaded structure coherent with the system's dynamic layers, each with a defined relative degree. The underlying assumption of this subdivision is that the dynamics of the N layers exhibit a significant time scale separation and an appropriate relative degree (an elaborate survey of the Singular Perturbation theory and its relevance for guidance and control problems in aerospace applications can be found in [123]). In contrast to applying a NDI control law to the entire system with its full relative degree $r = \sum_{j=1}^{N} r_j = n$, a control design based on separated dynamic layers facilitates the derivation, implementation, and debugging. For the majority of the systems considered in aerospace, an autopilot design using full inversion is impracticable due to complex partial derivatives of aerodynamic data.

In case of standard implementations of NDI-based control design in the field of aerospace, linear reference models separate the control loops (two loops in most applications) of the dynamic layers (e.g. outer/inner loop) [37, 38, 66, 124]. The holistic reference model is used (see section 5.4) which interconnects the relevant dynamic layers by respecting the missile's main physical effects. Thus, the standard two-loop NDI architecture is not applicable in combination with the integrated reference

model approach. This demands the modification of the NDI control theory (section 5.5.1.1) in order to preserve the beneficial structure of the NRM.

The NDI-based autopilot is derived in two steps, beginning with the derivation of the pseudo-control law $\boldsymbol{\omega}_{c,bs}$ for the outer dynamics. Within the second design step this signal is integrated in the final control law $\boldsymbol{C}_{\boldsymbol{M},\boldsymbol{u},c,bs}$ under consideration of the reference model outputs. At the end of this subsection the closed-loop error dynamics is analyzed.

Based on the design model of the outer dynamics (5.23) and by extending the control error by an integral part, the intermediate control law exhibits the following structure:

$$\boldsymbol{\omega}_{c,bs} = \hat{\boldsymbol{A}}_{\boldsymbol{y}}^{-1} \cdot \left(-\hat{\boldsymbol{b}}_{\boldsymbol{y}} + \begin{bmatrix} \boldsymbol{K}_{\boldsymbol{y},P} & \boldsymbol{K}_{\boldsymbol{y},I} \end{bmatrix} \cdot \boldsymbol{E}_{\boldsymbol{y}} + \dot{\boldsymbol{y}}_r \right) \tag{5.42}$$

This control law is in line with the intermediate control law of the standard cascaded NDI approach [66, 124].

The error vector

$$\boldsymbol{E}_{\boldsymbol{y}} = \begin{bmatrix} \boldsymbol{e}_{\boldsymbol{y}} \\ \boldsymbol{e}_{\boldsymbol{y},I} \end{bmatrix} = \begin{bmatrix} \boldsymbol{y}_r - \boldsymbol{y}^P \\ \int \left(\boldsymbol{y}_r - \boldsymbol{y}^P \right) dt \end{bmatrix}, \tag{5.43}$$

is defined as the difference between the reference model's output (5.38c) and the control variables (5.15), extended by the integral version.

Based on (5.42), the final control law for the $\boldsymbol{C}_{\boldsymbol{M},\boldsymbol{u}}$ is derived in the subsequent step. Within the final control law

$$\boldsymbol{C}_{\boldsymbol{M},\boldsymbol{u},c,bs} = \hat{\boldsymbol{A}}_{\boldsymbol{\omega}}^{-1} \left(-\hat{\boldsymbol{b}}_{\boldsymbol{\omega}} + \boldsymbol{K}_{\boldsymbol{\omega},P} \cdot \boldsymbol{e}_{\boldsymbol{\omega}} + \dot{\boldsymbol{\omega}}_r \right) \tag{5.44}$$

the angular acceleration $\dot{\boldsymbol{\omega}}_r$ stemming from the reference model constitutes the feedforward portion. As already mentioned above, the error

$$\boldsymbol{e}_{\boldsymbol{\omega}} = \boldsymbol{\omega}_{c,bs} - \boldsymbol{\omega}_K^{EB} \tag{5.45}$$

between the measured body rate and the desired one resulting from (5.42) describes the feedback part of the final control law. Within standard NDI approaches the feedforward part is given by the time derivative $\dot{\boldsymbol{\omega}}_{c,bs}$ of the intermediate control (5.42).

For the purpose of analyzing the NDI-based approach, the closed-loop error dynamics is obtained by a layer-wise consideration. Applying (5.42) under the idealized assumption $\boldsymbol{\omega}_K^{EB} = \boldsymbol{\omega}_{c,bs}$ to (5.23) the error dynamics of $\boldsymbol{e}_{\boldsymbol{y}}$ becomes

$$\begin{aligned} \dot{\boldsymbol{e}}_{\boldsymbol{y}} = \dot{\boldsymbol{y}}_r - \dot{\boldsymbol{y}}^P &= \dot{\boldsymbol{y}}_r - \hat{\boldsymbol{A}}_{\boldsymbol{y}} \left(\hat{\boldsymbol{A}}_{\boldsymbol{y}}^{-1} \cdot \left(-\hat{\boldsymbol{b}}_{\boldsymbol{y}} + \begin{bmatrix} \boldsymbol{K}_{\boldsymbol{y},P} & \boldsymbol{K}_{\boldsymbol{y},I} \end{bmatrix} \cdot \boldsymbol{E}_{\boldsymbol{y}} + \dot{\boldsymbol{y}}_r \right) \right) - \hat{\boldsymbol{b}}_{\boldsymbol{y}} \\ &= - \begin{bmatrix} \boldsymbol{K}_{\boldsymbol{y},P} & \boldsymbol{K}_{\boldsymbol{y},I} \end{bmatrix} \cdot \boldsymbol{E}_{\boldsymbol{y}} \end{aligned}. \tag{5.46}$$

For the sake of completeness, the dynamics of $\boldsymbol{e}_{\boldsymbol{y},I}$ is given by

$$\dot{\boldsymbol{e}}_{\boldsymbol{y},I} = \boldsymbol{y}_r - \boldsymbol{y}^P = \boldsymbol{e}_{\boldsymbol{y},I}. \tag{5.47}$$

In analogy to (5.43), both error dynamics (5.46) and (5.47) can be accumulated to

$$\dot{\boldsymbol{E}}_{\boldsymbol{y}} = - \underbrace{\begin{bmatrix} \boldsymbol{K}_{\boldsymbol{y},P} & \boldsymbol{K}_{\boldsymbol{y},I} \\ -\boldsymbol{I}_{3\times 3} & \boldsymbol{0}_{3\times 3} \end{bmatrix}}_{=\bar{\boldsymbol{K}}_{\boldsymbol{y}}} \cdot \boldsymbol{E}_{\boldsymbol{y}}. \tag{5.48}$$

The error dynamics exhibits an asymptotic stable equilibrium $\boldsymbol{E_y} = \mathbf{0}$ if $\bar{\boldsymbol{K}}_{\boldsymbol{y}} > 0$ holds.

The error dynamics of the inner layer is obtained in a similar way. Under the assumption that $\boldsymbol{C_{M,u,cbs}} = \boldsymbol{C_{M,u}}$ (no actuator dynamics) and by adding and subtracting $\dot{\boldsymbol{\omega}}_{bs}$, the body rate dynamics can be written as

$$\begin{aligned} \dot{\boldsymbol{\omega}}_K^{EB} &= \boldsymbol{K}_{\boldsymbol{\omega},P} \cdot \boldsymbol{e}_{\boldsymbol{\omega}} + \dot{\boldsymbol{\omega}}_r \\ &= \dot{\boldsymbol{\omega}}_{bs} - \dot{\boldsymbol{\omega}}_{bs} + \boldsymbol{K}_{\boldsymbol{\omega},P} \cdot \boldsymbol{e}_{\boldsymbol{\omega}} + \dot{\boldsymbol{\omega}}_r \end{aligned} . \tag{5.49}$$

Based on (5.49) and the error definition (5.45) the closed-loop (idealized assumption) error dynamics

$$\dot{\boldsymbol{e}}_{\boldsymbol{\omega}} = -\boldsymbol{K}_{\boldsymbol{\omega},P} \cdot \boldsymbol{e}_{\boldsymbol{\omega}} + \underbrace{\dot{\boldsymbol{\omega}}_{bs} - \dot{\boldsymbol{\omega}}_r}_{=\boldsymbol{g}_{\boldsymbol{\omega}}} \tag{5.50}$$

contains the time and state dependent nonlinear source term $\boldsymbol{g}_{\boldsymbol{\omega}} = \dot{\boldsymbol{\omega}}_{bs} - \dot{\boldsymbol{\omega}}_r$. This term describes the difference between the angular acceleration obtained from the pseudo-control law (5.42) and the reference model output. The appearance of this expression within the closed-loop error dynamics is owed to the utilization of $\dot{\boldsymbol{\omega}}_r$ instead of $\dot{\boldsymbol{\omega}}_{bs}$ as in standard NDI designs [33, 66]. In order to analyze the effect of the introduced error excitation $\boldsymbol{g}_{\boldsymbol{\omega}}$ on (5.50), $\boldsymbol{\omega}_{c,bs}$ is substituted by (5.42) and $\dot{\boldsymbol{y}}_r$ is replaced in $\boldsymbol{g}_{\boldsymbol{\omega}}$ using (5.38c):

$$\begin{aligned} \boldsymbol{g}_{\boldsymbol{\omega}} &= \dot{\boldsymbol{\omega}}_{c,bs} - \dot{\boldsymbol{\omega}}_r \\ &= \frac{d}{dt}\left(\boldsymbol{\omega}_{c,bs}\right) - \dot{\boldsymbol{\omega}}_r \\ &= \frac{d}{dt}\left(\hat{\boldsymbol{A}}_{\boldsymbol{y}}^{-1} \cdot \left(-\hat{\boldsymbol{b}}_{\boldsymbol{y}} + \begin{bmatrix} \boldsymbol{K}_{\boldsymbol{y},P} & \boldsymbol{K}_{\boldsymbol{y},I} \end{bmatrix} \cdot \boldsymbol{E}_{\boldsymbol{y}} + \dot{\boldsymbol{y}}_r\right)\right) - \dot{\boldsymbol{\omega}}_r \\ &= \frac{d}{dt}\left(\hat{\boldsymbol{A}}_{\boldsymbol{y}}^{-1} \cdot \left(-\hat{\boldsymbol{b}}_{\boldsymbol{y}} + \begin{bmatrix} \boldsymbol{K}_{\boldsymbol{y},P} & \boldsymbol{K}_{\boldsymbol{y},I} \end{bmatrix} \cdot \boldsymbol{E}_{\boldsymbol{y}} + \hat{\boldsymbol{A}}_{\boldsymbol{y},r}\boldsymbol{\omega}_r + \hat{\boldsymbol{b}}_{\boldsymbol{y},r}\right)\right) - \dot{\boldsymbol{\omega}}_r \end{aligned} \tag{5.51}$$

Under the assumption that the reference model (see section 5.4) approximates the design model sufficiently close and the output $\boldsymbol{y}^P$ tracks the reference signal $\boldsymbol{y}_r$, the expressions $\hat{\boldsymbol{A}}_{\boldsymbol{y},r} \approx \hat{\boldsymbol{A}}_{\boldsymbol{y}}$ and $\hat{\boldsymbol{b}}_{\boldsymbol{y},r} \approx \hat{\boldsymbol{b}}_{\boldsymbol{y}}$ vanish and, under consideration of (5.48), (5.51) is reduced to

$$\begin{aligned} \boldsymbol{g}_{\boldsymbol{\omega}} &= \dot{\boldsymbol{\omega}}_{c,bs} - \dot{\boldsymbol{\omega}}_r \\ &\approx \frac{d}{dt}\left(\hat{\boldsymbol{A}}_{\boldsymbol{y}}^{-1} \cdot \begin{bmatrix} \boldsymbol{K}_{\boldsymbol{y},P} & \boldsymbol{K}_{\boldsymbol{y},I} \end{bmatrix} \cdot \boldsymbol{E}_{\boldsymbol{y}}\right) \\ &\approx \frac{d}{dt}\left(\hat{\boldsymbol{A}}_{\boldsymbol{y}}^{-1}\right) \cdot \begin{bmatrix} \boldsymbol{K}_{\boldsymbol{y},P} & \boldsymbol{K}_{\boldsymbol{y},I} \end{bmatrix} \cdot \boldsymbol{E}_{\boldsymbol{y}} + \hat{\boldsymbol{A}}_{\boldsymbol{y}}^{-1} \cdot \begin{bmatrix} \boldsymbol{K}_{\boldsymbol{y},P} & \boldsymbol{K}_{\boldsymbol{y},I} \end{bmatrix} \cdot \dot{\boldsymbol{E}}_{\boldsymbol{y}} \\ &\approx \frac{d}{dt}\left(\hat{\boldsymbol{A}}_{\boldsymbol{y}}^{-1}\right) \cdot \begin{bmatrix} \boldsymbol{K}_{\boldsymbol{y},P} & \boldsymbol{K}_{\boldsymbol{y},I} \end{bmatrix} \cdot \boldsymbol{E}_{\boldsymbol{y}} - \hat{\boldsymbol{A}}_{\boldsymbol{y}}^{-1} \cdot \begin{bmatrix} \boldsymbol{K}_{\boldsymbol{y},P} & \boldsymbol{K}_{\boldsymbol{y},I} \end{bmatrix} \cdot \bar{\boldsymbol{K}}_{\boldsymbol{y}} \cdot \boldsymbol{E}_{\boldsymbol{y}} \end{aligned} \tag{5.52}$$

With the identity

$$\boldsymbol{A}_{\boldsymbol{y}}^{-1}\boldsymbol{A}_{\boldsymbol{y}} = \boldsymbol{I}_{3\times 3} \tag{5.53}$$

the matrix $\frac{d}{dt}\boldsymbol{A}_{\boldsymbol{y}}^{-1}$ can be expressed as

$$\frac{d}{dt}\boldsymbol{A}_{\boldsymbol{y}}^{-1} = -\boldsymbol{A}_{\boldsymbol{y}}^{-1}\dot{\boldsymbol{A}}_{\boldsymbol{y}}\boldsymbol{A}_{\boldsymbol{y}}^{-1}. \tag{5.54}$$

Substituting (5.54) in (5.52) and bracketing $\boldsymbol{A}_{\boldsymbol{y}}^{-1}$ and $\boldsymbol{E}_{\boldsymbol{y}}$, leads to

$$\boldsymbol{g}_{\boldsymbol{\omega}} \approx -\boldsymbol{A}_{\boldsymbol{y}}^{-1} \cdot \left(\dot{\boldsymbol{A}}_{\boldsymbol{y}}\boldsymbol{A}_{\boldsymbol{y}}^{-1} \cdot \begin{bmatrix} \boldsymbol{K}_{\boldsymbol{y},P} & \boldsymbol{K}_{\boldsymbol{y},I} \end{bmatrix} + \begin{bmatrix} \boldsymbol{K}_{\boldsymbol{y},P} & \boldsymbol{K}_{\boldsymbol{y},I} \end{bmatrix} \cdot \bar{\boldsymbol{K}}_{\boldsymbol{y}}\right) \cdot \boldsymbol{E}_{\boldsymbol{y}} \quad . \tag{5.55}$$

In case the inequality

$$\boldsymbol{K}_{\boldsymbol{y},P} \gg \dot{\boldsymbol{A}}_{\boldsymbol{y}} \boldsymbol{A}_{\boldsymbol{y}}^{-1} \tag{5.56}$$

holds, (5.55) can be further simplified to

$$\boldsymbol{g}_{\boldsymbol{\omega}} \approx -\boldsymbol{A}_{\boldsymbol{y}}^{-1} \cdot \begin{bmatrix} \boldsymbol{K}_{\boldsymbol{y},P} & \boldsymbol{K}_{\boldsymbol{y},I} \end{bmatrix} \cdot \bar{\boldsymbol{K}}_{\boldsymbol{y}} \cdot \boldsymbol{E}_{\boldsymbol{y}} \quad . \tag{5.57}$$

It can be concluded from (5.57) that the term $\boldsymbol{g}_{\boldsymbol{\omega}}$ in (5.50) (describing the difference between $\dot{\boldsymbol{\omega}}_{bs} - \dot{\boldsymbol{\omega}}_{r}$) exhibits dynamic properties which are coincident with the outer layer error dynamics. Therefore, the impact on the inner layer error dynamics (5.50) can be regarded as negligible.

Considering the inequality (5.56) the lower bound of the proportional feedback gain matrix can be quantified by taking into account the structure of $\boldsymbol{A}_{\boldsymbol{y}}$ and its contributing entities. Since $\boldsymbol{A}_{\boldsymbol{y}}$ (see (5.24)) is in diagonal form, the product $\dot{\boldsymbol{A}}_{\boldsymbol{y}} \boldsymbol{A}_{\boldsymbol{y}}^{-1}$ is also a diagonal matrix with the elements

$$\left(\dot{\boldsymbol{A}}_{\boldsymbol{y}} \boldsymbol{A}_{\boldsymbol{y}}^{-1} \right)_{(1,1)} = -\tan\alpha \cdot \dot{\alpha} - \tan\beta \cdot \dot{\beta} \tag{5.58a}$$

$$\left(\dot{\boldsymbol{A}}_{\boldsymbol{y}} \boldsymbol{A}_{\boldsymbol{y}}^{-1} \right)_{(2,2)} = \frac{\frac{1}{m} \cdot \left(\frac{\partial^2 C_{z,0}}{\partial \alpha^2} \dot{\alpha} + \frac{\partial^2 C_{z,0}}{\partial \alpha \partial \beta} \dot{\beta} \right) - \frac{x_{cog,P} l_{ref}}{I_{yy}} \cdot \left(\frac{\partial^2 C_{m,0}}{\partial \alpha^2} \dot{\alpha} + \frac{\partial^2 C_{m,0}}{\partial \alpha \partial \beta} \dot{\beta} \right)}{\frac{1}{m} \cdot \frac{\partial C_{z,0}}{\partial \alpha_K} - \frac{x_{cog,P} l_{ref}}{I_{yy}} \cdot \frac{\partial C_{m,0}}{\partial \alpha_K}} \quad . \tag{5.58b}$$

$$\left(\dot{\boldsymbol{A}}_{\boldsymbol{y}} \boldsymbol{A}_{\boldsymbol{y}}^{-1} \right)_{(3,3)} = + \frac{\frac{1}{m} \cdot \left(\frac{\partial^2 C_{y,0}}{\partial \alpha \partial \beta} \dot{\alpha} + \frac{\partial^2 C_{y,0}}{\partial \beta^2} \dot{\beta} \right) + \frac{x_{cog,P} l_{ref}}{I_{zz}} \cdot \left(\frac{\partial^2 C_{n,0}}{\partial \alpha \partial \beta} \dot{\alpha} + \frac{\partial^2 C_{n,0}}{\partial \beta^2} \dot{\beta} \right)}{\frac{1}{m} \cdot \frac{\partial C_{y,0}}{\partial \beta_K} + \frac{x_{cog,P} l_{ref}}{I_{zz}} \cdot \frac{\partial C_{n,0}}{\partial \beta_K}} - \tan\alpha \cdot \dot{\alpha} \tag{5.58c}$$

For the purpose of defining a lower bound of $\boldsymbol{K}_{\boldsymbol{y},P}$, the maximum values of (5.58) are calculated based on numerical differentiation of the aerodynamic data set (see appendix B.1) and the results from trim calculation regarding acceleration (see fig. 3.6a) and body rate (see fig. 3.6b). The maximum trimmable acceleration is used to calculated the derivatives of the aerodynamic angles via (5.19) and (5.20).

The maximum absolute values of (5.58a) and (5.58b) across the flight envelope are depicted in fig. 5.18.

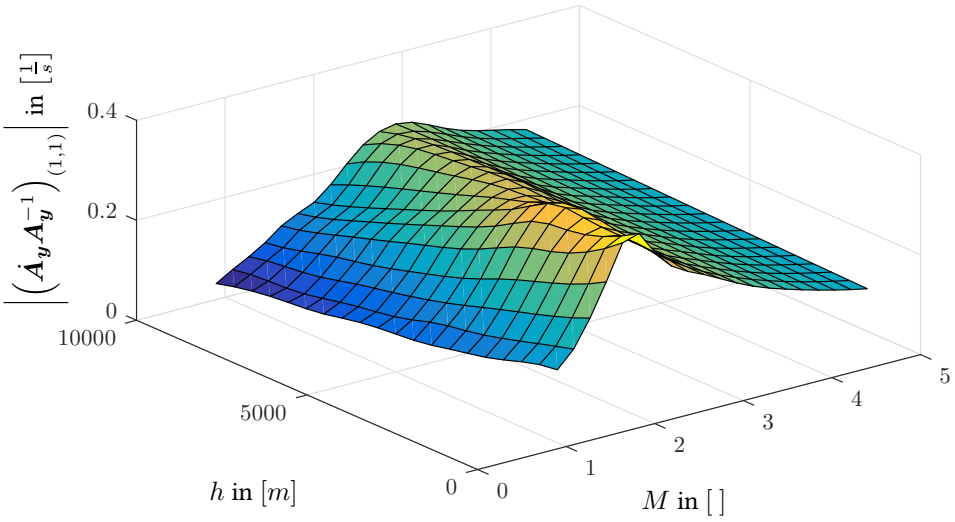

(a) Maximum value of $\left|\left(\dot{\boldsymbol{A}}_{\boldsymbol{y}}\boldsymbol{A}_{\boldsymbol{y}}^{-1}\right)_{(1,1)}\right|$ over Mach M and altitude h.

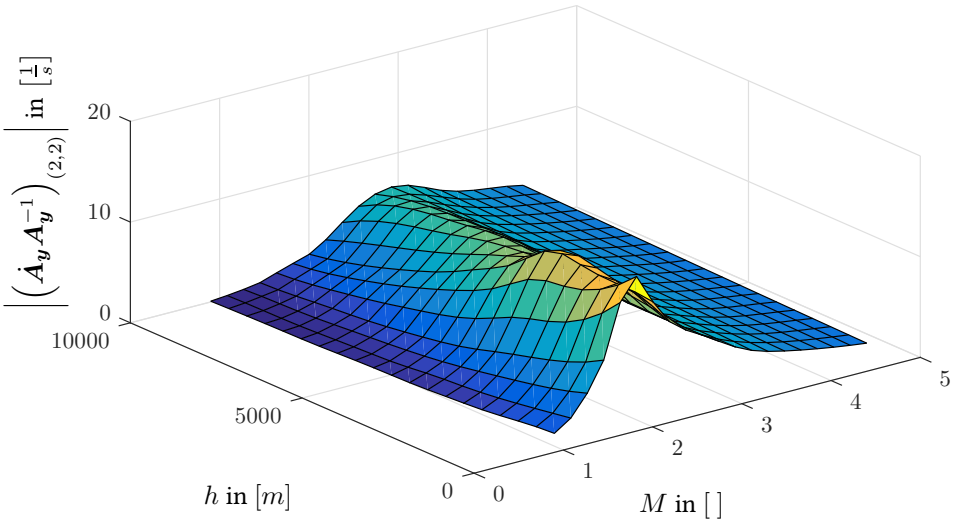

(b) Maximum value of $\left|\left(\dot{\boldsymbol{A}}_{\boldsymbol{y}}\boldsymbol{A}_{\boldsymbol{y}}^{-1}\right)_{(2,2)}\right|$ over Mach M and altitude h.

Figure 5.18: Maximum absolute values of (5.58) over Mach M and altitude h.

Due to the symmetry properties of the missile, the longitudinal and lateral acceleration channel exhibit equivalent characteristics and dependencies. Therefore, the presentation of the maximum absolute values of (5.58c) is omitted.

Based on the derivation from above, this section is concluded with the concatenation of the idealized error dynamics (5.48) and (5.50). Thus, the overall closed-loop error differential equation of the inner and outer layer is given by

$$\begin{bmatrix} \dot{\boldsymbol{e}}_{\boldsymbol{\omega}} \\ \dot{\boldsymbol{e}}_{\boldsymbol{y}} \\ \dot{\boldsymbol{e}}_{\boldsymbol{y},I} \end{bmatrix} = \begin{bmatrix} -\boldsymbol{K}_{\boldsymbol{\omega},P} & \boldsymbol{0}_{3\times3} & \boldsymbol{0}_{3\times3} \\ \hat{\boldsymbol{A}}_{\boldsymbol{y}} & -\boldsymbol{K}_{\boldsymbol{y},P} & -\boldsymbol{K}_{\boldsymbol{y},I} \\ \boldsymbol{0}_{3\times3} & \boldsymbol{I}_{3\times3} & \boldsymbol{0}_{3\times3} \end{bmatrix} \cdot \begin{bmatrix} \boldsymbol{e}_{\boldsymbol{\omega}} \\ \boldsymbol{e}_{\boldsymbol{y}} \\ \boldsymbol{e}_{\boldsymbol{y},I} \end{bmatrix}. \tag{5.59}$$

5.5.1.2 CFB-based Baseline Control Law

The cumbersome analytical expression in case of nonlinear systems with system orders $n > 1$ and the lack of introducing certain requirements within the holistic approach are the main drawbacks which disqualify classical Backstepping (BS) (see [35]) approaches in the field of aircraft applications. In case of missile applications, the nonlinear structure of the system including complex aerodynamic data are the main drivers for utilizing a modified BS version, leading to a less complex and error-prone implementation as in [40]. Over recent years different BS approaches [41, 46, 48, 125] were developed to account for certain drawbacks of classical theory and new developments in the field of measurement and filtering techniques. As explained in section 4.2.2.4 and section 4.2.2.5 CFB constitutes an approach incorporating the beneficial characteristics of Backstepping (no time scale separation) by overcoming the disadvantages of complex implementation.

The derivation of the CFB control law for the inner and outer layer dynamics of the considered FGS-X-03 follows the structure presented in section 4.2.2.5.

Based on (5.23), the Compensated Tracking Error (CTE) of the outer layer, including integral error, and the control error of the inner layer are defined as

$$\tilde{\boldsymbol{E}}_{\boldsymbol{y}} = \begin{bmatrix} \tilde{\boldsymbol{e}}_{\boldsymbol{y}} \\ \tilde{\boldsymbol{e}}_{\boldsymbol{y},I} \end{bmatrix} = \boldsymbol{E}_{\boldsymbol{y}} - \begin{bmatrix} \boldsymbol{z}_{\boldsymbol{y}} \\ \boldsymbol{z}_{\boldsymbol{y},I} \end{bmatrix} \tag{5.60}$$

and

$$\hat{\boldsymbol{e}}_{\boldsymbol{\omega}} = \boldsymbol{\alpha}_{\boldsymbol{\omega},fil} - \boldsymbol{\omega}_K^{EB}, \tag{5.61}$$

respectively. The filtered version of

$$\alpha_{\boldsymbol{\omega},fil,i} = \frac{\omega_{fil}^2}{s^2 + 2\zeta_{fil}\omega_{fil}s + \omega_{fil}^2} \cdot \alpha_{\boldsymbol{\omega},i} \tag{5.62}$$

is calculated based on a second order linear system with equal parametric setup (frequency ω_{fil} and damping ζ_{fil}) for each entry of the pseudo control variable $\alpha_{\boldsymbol{\omega},i}$. In order to derive the outer loop control law $\boldsymbol{\alpha}_{\boldsymbol{\omega}}$, the quadratic Control Lyapunov Function (CLF) of CTE

$$V_1 = \tilde{\boldsymbol{E}}_{\boldsymbol{y}}^T \boldsymbol{P}_{\boldsymbol{y}} \tilde{\boldsymbol{E}}_{\boldsymbol{y}} \tag{5.63}$$

and its corresponding time derivative

$$\dot{V}_1 = \dot{\tilde{\boldsymbol{E}}}_{\boldsymbol{y}}^T \boldsymbol{P}_{\boldsymbol{y}} \tilde{\boldsymbol{E}}_{\boldsymbol{y}} + \tilde{\boldsymbol{E}}_{\boldsymbol{y}}^T \boldsymbol{P}_{\boldsymbol{y}} \dot{\tilde{\boldsymbol{E}}}_{\boldsymbol{y}} \tag{5.64}$$

are used. The positive definite matrix $\boldsymbol{P}_{\boldsymbol{y}} \in \mathbb{R}^{6\times 6}$ is assumed to be in diagonal form. With (5.61) and by adding and subtracting $\boldsymbol{\alpha}_{\boldsymbol{\omega}}$ the body rate can be expressed as $\boldsymbol{\omega}_K^{EB} = \boldsymbol{\alpha}_{\boldsymbol{\omega},fil} - \hat{\boldsymbol{e}}_{\boldsymbol{\omega}} + \boldsymbol{\alpha}_{\boldsymbol{\omega}} - \boldsymbol{\alpha}_{\boldsymbol{\omega}}$. Substituting this expression in the time derivative of (5.60) the dynamics of the CTE results to

$$\dot{\tilde{\boldsymbol{E}}}_{\boldsymbol{y}} = \begin{bmatrix} \dot{\boldsymbol{y}}_r - \hat{\boldsymbol{A}}_{\boldsymbol{y}} \cdot (\boldsymbol{\alpha}_{\boldsymbol{\omega},fil} - \hat{\boldsymbol{e}}_{\boldsymbol{\omega}} + \boldsymbol{\alpha}_{\boldsymbol{\omega}} - \boldsymbol{\alpha}_{\boldsymbol{\omega}}) + \hat{\boldsymbol{b}}_{\boldsymbol{y}} \\ \boldsymbol{e}_{\boldsymbol{y}} \end{bmatrix} - \dot{\boldsymbol{Z}}_{\boldsymbol{y}}. \tag{5.65}$$

Under consideration of (5.65), the intermediate control law and the dynamics of the unachieved portion are selected to

$$\boldsymbol{\alpha}_{\boldsymbol{\omega}} = \hat{\boldsymbol{A}}_{\boldsymbol{y}}^{-1} \cdot \left(-\hat{\boldsymbol{b}}_{\boldsymbol{y}} + \begin{bmatrix} \boldsymbol{K}_{\boldsymbol{y},P} & \boldsymbol{K}_{\boldsymbol{y},I} \end{bmatrix} \cdot \boldsymbol{E}_{\boldsymbol{y}} + \dot{\boldsymbol{y}}_r \right) \tag{5.66}$$

and

$$\dot{\boldsymbol{Z}}_{\boldsymbol{y}} = \begin{bmatrix} -\begin{bmatrix} \boldsymbol{K}_{\boldsymbol{y},P} & \boldsymbol{K}_{\boldsymbol{y},I} \end{bmatrix} \cdot \boldsymbol{Z}_{\boldsymbol{y}} - \hat{\boldsymbol{A}}_{\boldsymbol{y}} \cdot (\boldsymbol{\alpha}_{\boldsymbol{\omega},fil} - \boldsymbol{\alpha}_{\boldsymbol{\omega}}) \\ \boldsymbol{z}_{\boldsymbol{y}} \end{bmatrix}, \tag{5.67}$$

respectively. With (5.66) and (5.67) the dynamics of the CTE (5.65)

$$\dot{\tilde{\boldsymbol{E}}}_{\boldsymbol{y}} = -\underbrace{\begin{bmatrix} \boldsymbol{K}_{\boldsymbol{y},P} & \boldsymbol{K}_{\boldsymbol{y},I} \\ -\boldsymbol{I}_{3\times3} & \boldsymbol{0}_{3\times3} \end{bmatrix}}_{=\bar{\boldsymbol{K}}_{\boldsymbol{y}}} \cdot \tilde{\boldsymbol{E}}_{\boldsymbol{y}} + \begin{bmatrix} \hat{\boldsymbol{A}}_{\boldsymbol{y}} \\ \boldsymbol{0}_{3\times3} \end{bmatrix} \cdot \hat{\boldsymbol{e}}_{\boldsymbol{\omega}} \tag{5.68}$$

consists of a asymptotic linear part and the nonlinear cross-coupling term accounting for delayed response of the physical state $\boldsymbol{\omega}_K^{EB}$ with respect to its desired value $\boldsymbol{\alpha}_{\boldsymbol{\omega}}$. Solving the matrix Lyapunov equation

$$\bar{\boldsymbol{K}}_{\boldsymbol{y}}^T \boldsymbol{P}_{\boldsymbol{y}} + \boldsymbol{P}_{\boldsymbol{y}} \bar{\boldsymbol{K}}_{\boldsymbol{y}} = \boldsymbol{Q}_{\boldsymbol{y}} \tag{5.69}$$

based on the positive definite matrix $\boldsymbol{Q}_{\boldsymbol{y}} \in \mathbb{R}^{6\times6}$, the time derivative of the CLF (5.63) results to

$$\dot{V}_1 = -\tilde{\boldsymbol{E}}_{\boldsymbol{y}}^T \boldsymbol{Q}_{\boldsymbol{y}} \tilde{\boldsymbol{E}}_{\boldsymbol{y}} + \hat{\boldsymbol{e}}_{\boldsymbol{\omega}}^T \begin{bmatrix} \hat{\boldsymbol{A}}_{\boldsymbol{y}} \\ \boldsymbol{0}_{3\times3} \end{bmatrix}^T \boldsymbol{P}_{\boldsymbol{y}} \tilde{\boldsymbol{E}}_{\boldsymbol{y}} + \tilde{\boldsymbol{E}}_{\boldsymbol{y}}^T \begin{bmatrix} \hat{\boldsymbol{A}}_{\boldsymbol{y}} \\ \boldsymbol{0}_{3\times3} \end{bmatrix} \boldsymbol{P}_{\boldsymbol{y}} \hat{\boldsymbol{e}}_{\boldsymbol{\omega}}. \tag{5.70}$$

In the second design step, the regarded system is extended by the tracking error of the inner layer (5.61). Thus, for the purpose of designing the final control law, the CLF (5.63) is extended by the error state $\hat{\boldsymbol{e}}_{\boldsymbol{\omega}}$ to become

$$V_2 = V_1 + \hat{\boldsymbol{e}}_{\boldsymbol{\omega}}^T \boldsymbol{P}_{\boldsymbol{\omega}} \hat{\boldsymbol{e}}_{\boldsymbol{\omega}}. \tag{5.71}$$

As in the first step, $\boldsymbol{P}_{\boldsymbol{\omega}} \in \mathbb{R}^{3\times3}$ constitutes a diagonal positive definite weighting matrix. With (5.70) the time derivative of (5.71) becomes

$$\dot{V}_2 = -\tilde{\boldsymbol{E}}_{\boldsymbol{y}}^T \boldsymbol{Q}_{\boldsymbol{y}} \tilde{\boldsymbol{E}}_{\boldsymbol{y}} + \hat{\boldsymbol{e}}_{\boldsymbol{\omega}}^T \begin{bmatrix} \hat{\boldsymbol{A}}_{\boldsymbol{y}} \\ \boldsymbol{0}_{3\times3} \end{bmatrix}^T \boldsymbol{P}_{\boldsymbol{y}} \tilde{\boldsymbol{E}}_{\boldsymbol{y}} + \tilde{\boldsymbol{E}}_{\boldsymbol{y}}^T \begin{bmatrix} \hat{\boldsymbol{A}}_{\boldsymbol{y}} \\ \boldsymbol{0}_{3\times3} \end{bmatrix} \boldsymbol{P}_{\boldsymbol{y}} \hat{\boldsymbol{e}}_{\boldsymbol{\omega}} + \dot{\hat{\boldsymbol{e}}}_{\boldsymbol{\omega}}^T \boldsymbol{P}_{\boldsymbol{\omega}} \hat{\boldsymbol{e}}_{\boldsymbol{\omega}} + \hat{\boldsymbol{e}}_{\boldsymbol{\omega}}^T \boldsymbol{P}_{\boldsymbol{\omega}} \dot{\hat{\boldsymbol{e}}}_{\boldsymbol{\omega}}. \tag{5.72}$$

Based on the definition of (5.61) and under consideration of (5.29), the dynamics of tracking error $\hat{\boldsymbol{e}}_{\boldsymbol{\omega}}$ (5.61) becomes

$$\dot{\hat{\boldsymbol{e}}}_{\boldsymbol{\omega}} = \dot{\boldsymbol{\alpha}}_{\boldsymbol{\omega},fil} - \hat{\boldsymbol{A}}_{\boldsymbol{\omega}} \cdot \boldsymbol{C}_{\boldsymbol{M},\boldsymbol{u}} - \hat{\boldsymbol{b}}_{\boldsymbol{\omega}}. \tag{5.73}$$

In order to render the time derivative (see (5.72)) of V_2 negative definite, the final CFB-based control law results to

$$\boldsymbol{C}_{\boldsymbol{M},\boldsymbol{u},c,bs} = \hat{\boldsymbol{A}}_{\boldsymbol{\omega}}^{-1} \cdot \left(-\hat{\boldsymbol{b}}_{\boldsymbol{\omega}} + \boldsymbol{K}_{\boldsymbol{\omega}} \boldsymbol{e}_{\boldsymbol{\omega}} + \boldsymbol{P}_{\boldsymbol{\omega}}^{-1} \begin{bmatrix} \hat{\boldsymbol{A}}_{\boldsymbol{y}} \\ \boldsymbol{0}_{3\times3} \end{bmatrix}^T \boldsymbol{P}_{\boldsymbol{y}} \tilde{\boldsymbol{E}}_{\boldsymbol{y}} + \dot{\boldsymbol{\alpha}}_{\boldsymbol{\omega},fil} \right). \tag{5.74}$$

The closed-loop error dynamics

$$\dot{\hat{\boldsymbol{e}}}_{\boldsymbol{\omega}} = -\boldsymbol{K}_{\boldsymbol{\omega}} \boldsymbol{e}_{\boldsymbol{\omega}} - \boldsymbol{P}_{\boldsymbol{\omega}}^{-1} \begin{bmatrix} \hat{\boldsymbol{A}}_{\boldsymbol{y}} \\ \boldsymbol{0}_{3\times3} \end{bmatrix}^T \boldsymbol{P}_{\boldsymbol{y}} \tilde{\boldsymbol{E}}_{\boldsymbol{y}} \tag{5.75}$$

of the tracking error (5.61) is obtained by substituting the control law (5.74) in (5.73).

Under the constraint of the matrix Lyapunov equation

$$\boldsymbol{K}_{\boldsymbol{\omega}}^T \boldsymbol{P}_{\boldsymbol{\omega}} + \boldsymbol{P}_{\boldsymbol{\omega}} \boldsymbol{K}_{\boldsymbol{\omega}} = \boldsymbol{Q}_{\boldsymbol{\omega}} \tag{5.76}$$

the Lyapunov function's time derivative

$$\dot{V}_2 = -\tilde{\boldsymbol{E}}_{\boldsymbol{y}}^T \boldsymbol{Q}_{\boldsymbol{y}} \tilde{\boldsymbol{E}}_{\boldsymbol{y}} - \hat{\boldsymbol{e}}_{\boldsymbol{\omega}}^T \boldsymbol{Q}_{\boldsymbol{\omega}} \hat{\boldsymbol{e}}_{\boldsymbol{\omega}} \tag{5.77}$$

is rendered negative definite. Besides $\boldsymbol{P}_{\boldsymbol{\omega}}$, the solution $\boldsymbol{K}_{\boldsymbol{\omega}}$ of (5.76) is driven by the matrix $\boldsymbol{Q}_{\boldsymbol{\omega}} \in \mathbb{R}^{3\times3}$. In order to simplify the parametrization and to guarantee a channel-wise feedback of the respective control errors via $\boldsymbol{K}_{\boldsymbol{\omega}}$, $\boldsymbol{Q}_{\boldsymbol{\omega}}$ is assumed be of diagonal form.

this section is finalized by outlining the closed-loop dynamics of the CFB baseline control design:

$$\begin{bmatrix} \dot{\tilde{\boldsymbol{e}}}_{\boldsymbol{y}} \\ \dot{\tilde{\boldsymbol{e}}}_{\boldsymbol{y},I} \\ \dot{\hat{\boldsymbol{e}}}_{\boldsymbol{\omega}} \end{bmatrix} = \begin{bmatrix} -\boldsymbol{K}_{\boldsymbol{y}} & -\boldsymbol{K}_{\boldsymbol{y},I} & \hat{\boldsymbol{A}}_{\boldsymbol{y}} \\ \boldsymbol{I} & \boldsymbol{0} & \boldsymbol{0} \\ -\boldsymbol{P}_{\boldsymbol{\omega}}^{-1} \begin{bmatrix} \hat{\boldsymbol{A}}_{\boldsymbol{y}}^T & \boldsymbol{0}_{3\times3} \end{bmatrix} \boldsymbol{P}_{\boldsymbol{y}} & -\boldsymbol{P}_{\boldsymbol{\omega}}^{-1} \begin{bmatrix} \hat{\boldsymbol{A}}_{\boldsymbol{y}}^T & \boldsymbol{0}_{3\times3} \end{bmatrix} \boldsymbol{P}_{\boldsymbol{y}} & -\boldsymbol{K}_{\boldsymbol{\omega}} \end{bmatrix} \begin{bmatrix} \tilde{\boldsymbol{e}}_{\boldsymbol{y}} \\ \tilde{\boldsymbol{e}}_{\boldsymbol{y},I} \\ \hat{\boldsymbol{e}}_{\boldsymbol{\omega}} \end{bmatrix} \tag{5.78}$$

Comparing the two baseline control approaches it becomes apparent that the intermediate control laws (5.42) and (5.66) are equivalent. Differences between both derivations arise from the processing of the intermediate controls $\boldsymbol{\omega}_{c,bs}$ and $\boldsymbol{\alpha}_{\boldsymbol{\omega}}$ to compute the moment coefficient $\boldsymbol{C}_{\boldsymbol{M},\boldsymbol{u},c,bs}$. The final control law in case of the NDI-based approach is calculated by utilization of $\dot{\boldsymbol{\omega}}_r$. Considering the CFB autopilot, the derivative of the desired body-rates $\boldsymbol{\alpha}_{\boldsymbol{\omega}}$ is generated by the command filter (see (5.62)). The effect of those different architectures on the closed-loop characteristics is discussed in detail in section 6.1.

5.5.1.3 Parameters of Baseline Controllers

In combination with the respective baseline control strategies (NDI, CFB) the parameters of the control laws guarantee the conformity with the performance and robustness requirements (see section 5.1). Since both control laws presented in section 5.5.1.1 and section 5.5.1.2 exhibit a certain architectural similarity, the layout approach for the feedback gains is identical for NDI and CFB. Therefore, the derivation and considerations in designing the feedback gains is presented only for the NDI case within this subsection.

The physical insights of the missile system dynamics gained from extensive analysis in chapter 3 provide enough information for a suitable initial guess on the basis of the linearized model dynamics. Based on this initial guess, optimization routines are utilized to fulfill the multiple design goals stemming from the NFRs (see section 5.1.2). In order to account for both, robustness and performance design goals, a performance-based cost function is realized with constraints incorporating robustness requirements. This approach avoids multiple phase optimization and complex weighting amongst different metrics.

The cost function

$$\begin{aligned} \min_{\boldsymbol{k}} \quad \Phi = \quad & c_{stab} \cdot \left\| \begin{bmatrix} e_z(\tau_{stab}) & e_y(\tau_{stab}) \end{bmatrix}^T \right\|_{\mathcal{L}_2} \\ + \quad & c_{track} \cdot \left\| \begin{bmatrix} e_z(\tau_{track}) & e_y(\tau_{track}) \end{bmatrix}^T \right\|_{\mathcal{L}_2} \\ + \quad & c_{settle} \cdot \left\| \begin{bmatrix} e_z(\tau_{settle}) & e_y(\tau_{settle}) \end{bmatrix}^T \right\|_{\mathcal{L}_\infty} \\ \text{subject to} \quad |\delta_i| \leq \quad & \delta_{max} \qquad \text{for } i = 1, \ldots, 4 \\ M_S \leq \quad & 2.5 \end{aligned} \tag{5.79}$$

used for gain optimization is based on the time response of the full nonlinear dynamics of the closed-loop system with respect to a reference acceleration trajectory $a_{i,r}(t)$ in longitudinal and lateral direction. Thus, the closed-loop tracking error $e_i(t) = a_i(t) - a_{i,r}(t)$, $i = z, y$ between the refer-

ence signal $a_{i,r}(t)$ and the corresponding acceleration control variable in longitudinal and lateral direction $a_i(t)$ is evaluated in each iteration of the optimization process. To account for different performance goals defined in section 5.1.2, the cost function (5.79) is assembled by signal norms of the tracking error e_i within three different time sections: stabilizing $\tau_{stab} \in [0, t_{stab}[$, tracking $\tau_{track} \in [t_{stab}, t_{settle}[$, and settling $\tau_{settle} \in [t_{settle}, t_{end}[$. t_{end} marks the end of the time horizon at which the cost function (5.79) is evaluated. Those three regions correspond to the signal-based performance goals NFR_4, NFR_5, NFR_3, and NFR_6. For the purpose of summarizing the norms of different time frames to one scalar cost function (5.79), a normalization of the three parts is necessary. In order to account for the different signal norms and time sections, the norms in (5.79) are scaled by the coefficient c_{stab}, c_{stab}, and c_{stab}.

Due to the missile's symmetry, the gains of the longitudinal and lateral baseline control channel are identical. Thus, the optimization parameters

$$\boldsymbol{k} = \begin{bmatrix} k_{a,P} & k_{a,I} & k_{\omega,P} \end{bmatrix}, \tag{5.80}$$

are mapped to the respective baseline gains by

$$\begin{aligned} k_{a_z,P}, k_{a_y,P} &= k_{a,P} \\ k_{a_z,I}, k_{a_z,I} &= k_{a,I} \\ k_{q,P}, k_{r,P} &= k_{\omega,P} \end{aligned} . \tag{5.81}$$

The optimization task (5.80) includes two constraints: the maximum limitations of the fin deflections and the maximum sensitivity (5.3) denoted with M_S.

The sensitivity function

$$S_{a_z}(s) = \frac{1}{1 + P_{a_z}(s)\, C_{a_z}(s)} \tag{5.82}$$

derived from the basic feedback loop in fig. 5.19 constitutes a feasible metric for disturbance attenuation. It represents the Single-Input-Single-Output (SISO)-transfer function of the measurement noise $n_{a_z}(s)$ to the control error $e_{a_z}(s)$ where $P_{a_z}(s)$ and $C_{a_z}(s)$ label the transfer function of the linearized missile dynamics and controller, respectively.

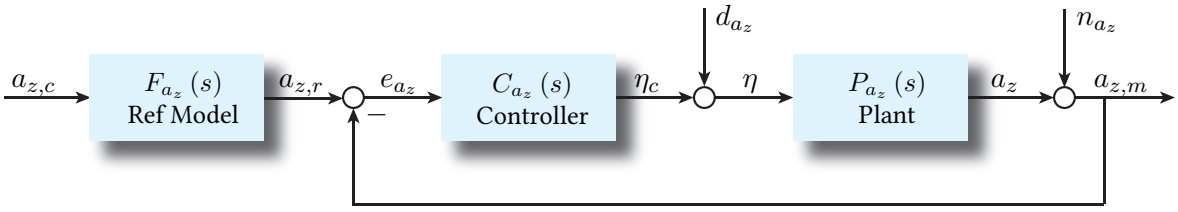

Figure 5.19: Linear basic feedback loop for a SISO-system.

In order to incorporate the maximum sensitivity constraint in (5.79), the linear transfer function (see (5.82)) is evaluated in each iteration of the optimization process (with the current gain combination).

Remark: Since the concept of the sensitivity function is derived for the idealized linear SISO feedback loop (fig. 5.19), an application to nonlinear systems provide only limited absolute measure about the system's sensitivity. Using this metric as a relative measure across different flight conditions provides an important and comparable characteristic estimate for closed-loop robustness towards process variations.

The optimization problem (5.79) is solved with Mathworks' ® genetic algorithm from the *Global*

Optimization Toolbox® [126].

Figure 5.20 illustrates the reference signal $a_{z,r}$ (red) and the considered acceleration in longitudinal direction a_z (blue) in descending order of the cost function Φ. Besides, the three evaluation time frames are depicted as hatched areas.

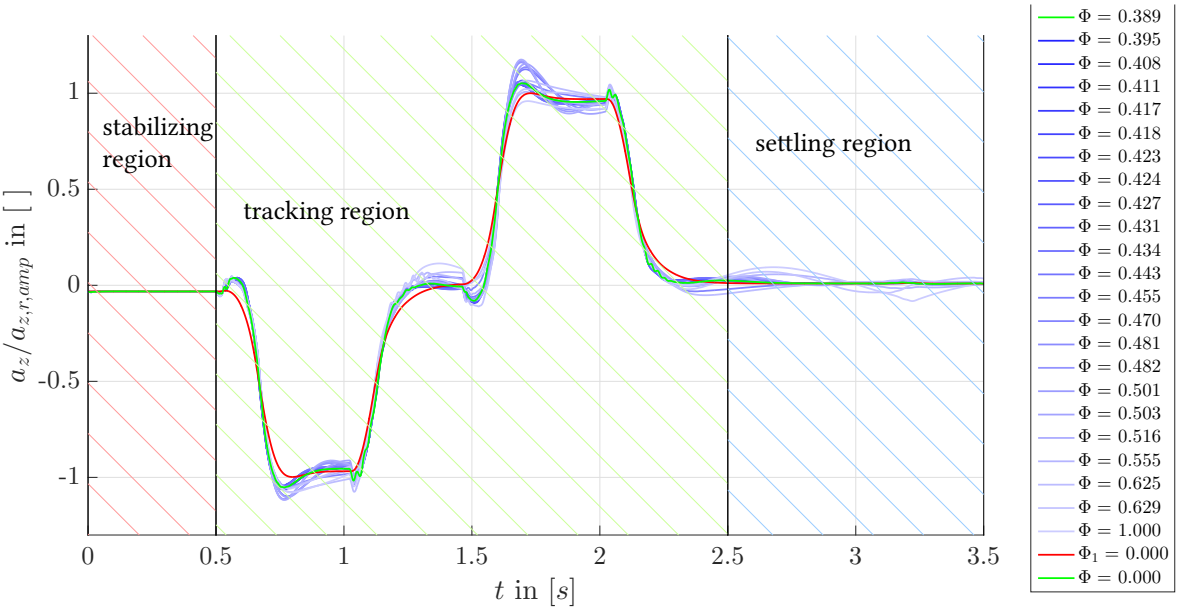

Figure 5.20: Different values of the cost function Φ and the corresponding signals of the control variable a_z with respect to the reference trajectory (red) for different gain configurations. The operating point is $M = 2.5$, $h = 6km$.

The trajectories of $a_z\,(t)$ are extracted from different iterations of the optimization algorithm. With increased number of iterations (increased color intensity) the cost function Φ descends until the optimization algorithms converges and a minimum is reached under the sensitivity and fin deflection constraints (see (5.79)). The trajectory of the resulting in the minimum cost function Φ is colored in green. From fig. 5.20 it can be concluded that the stabilizing region is less sensitive to gain variations (5.80) compared to the closed-loop tracking and settling region.

The corresponding sensitivity functions of each iteration are depicted in fig. 5.21 with different line styles (dashed and solid) to mark the compliance status (rejected and compliant) with the optimization constraint (see (5.3)).

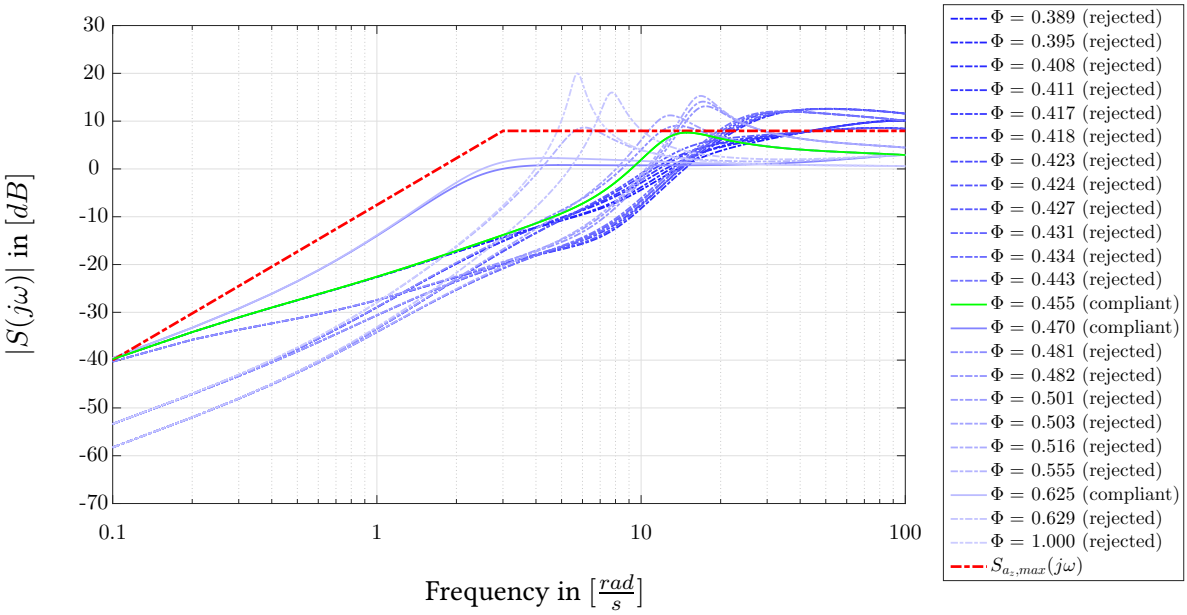

Figure 5.21: Evaluation of the sensitivity function $S\,(j\omega)$ of different iterations of the optimization algorithm including the compliance status (rejected and compliant) and corresponding cost function value Φ ($M = 2.5$, $h = 6km$).

Applying the optimization problem (5.79) to a feasible set of equidistant flight envelope points results in the gain parametrization for lateral and longitudinal channel ($\boldsymbol{k} = \begin{bmatrix} k_{a,P} & k_{a,I} & k_{\omega,P} \end{bmatrix}$) plotted in fig. 5.22.

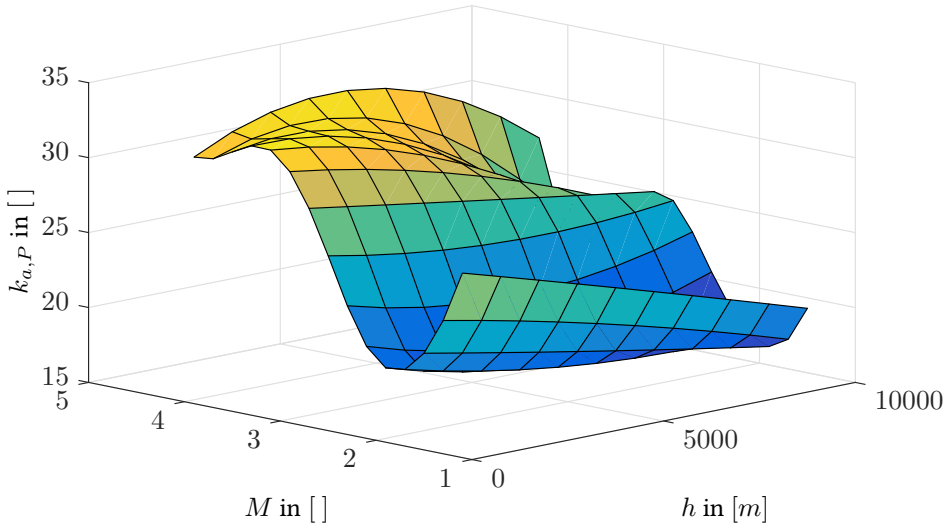

(a) Proportional gain $k_{a,I}$ of outer loop over Mach M and altitude h.

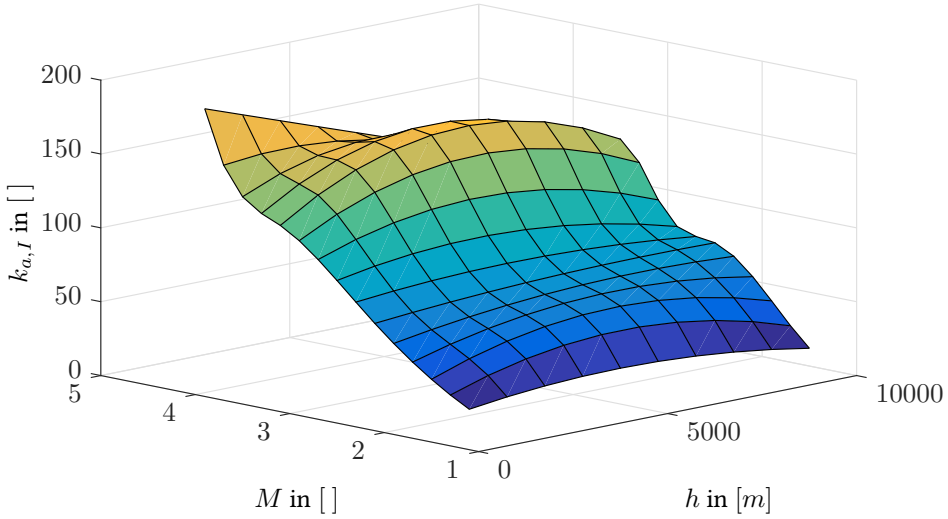

(b) Integral gain $k_{a,I}$ of outer loop over Mach M and altitude h.

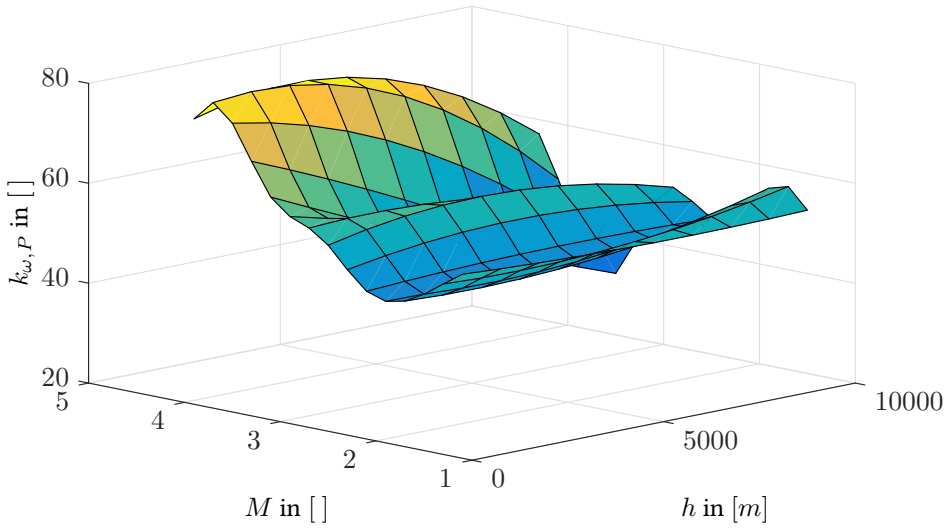

(c) Proportional gain $k_{\omega,P}$ of inner loop over Mach M and altitude h.

Figure 5.22: Pitch channel gain layout over flight envelope for NDI control law.

This section is concluded by describing the parametrization of the roll channel. The analysis in section 3.2.3 indicates that the control efficiency of the aerodynamic control ξ with respect to the roll moment is significantly high compared to longitudinal or lateral dynamics. Besides the high control effectiveness, the large transmission bandwidth and low demands on the control variable ϕ_v lead to a less critical selection of the corresponding parameters. The roll autopilot exhibits the identical structure as the longitudinal and lateral channel. The gain design is conducted solely on basis of the linearized roll channel dynamics. Due to the high control effectiveness and large bandwidth, a very conservative interpretation of the performance and robustness requirements is considered.

The resulting roll channel gains are depicted in fig. 5.23.

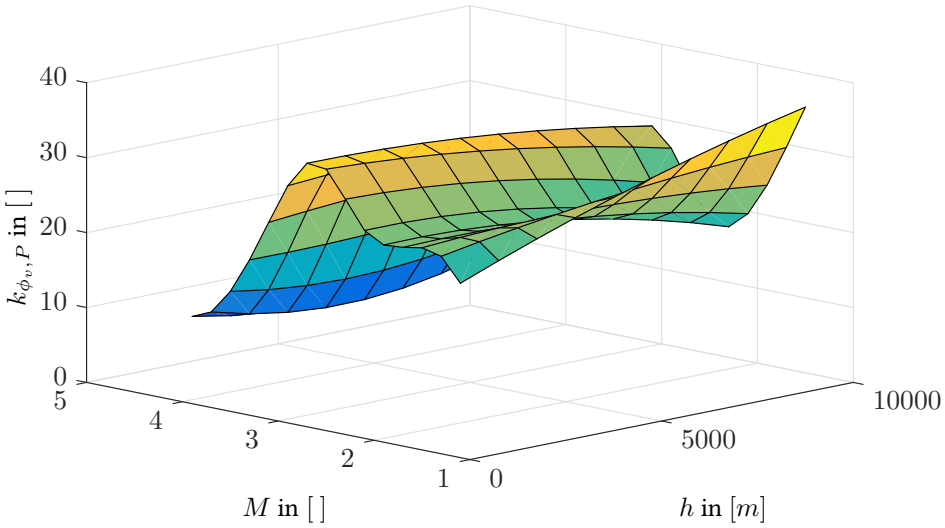

(a) Proportional gain $k_{\phi_v,P}$ of outer loop over Mach M and altitude h.

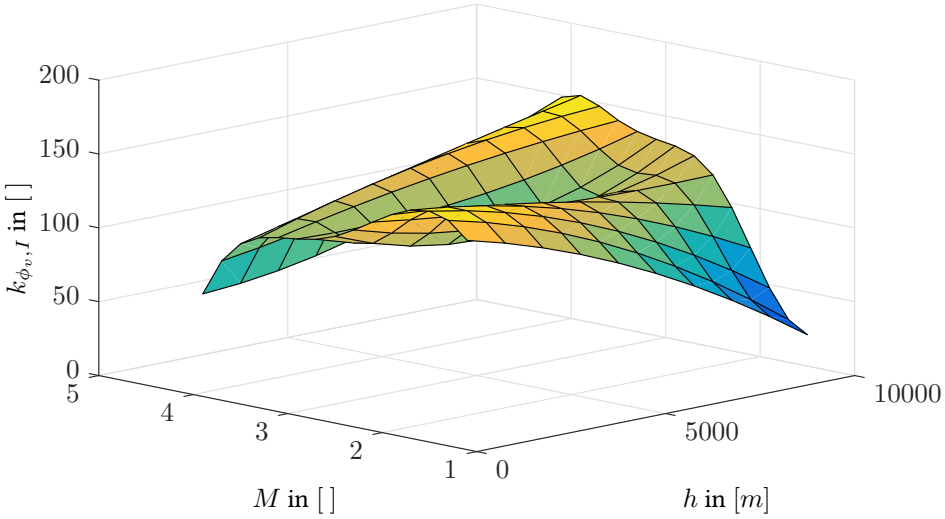

(b) Integral gain $k_{\phi_v,I}$ of outer loop over Mach M and altitude h.

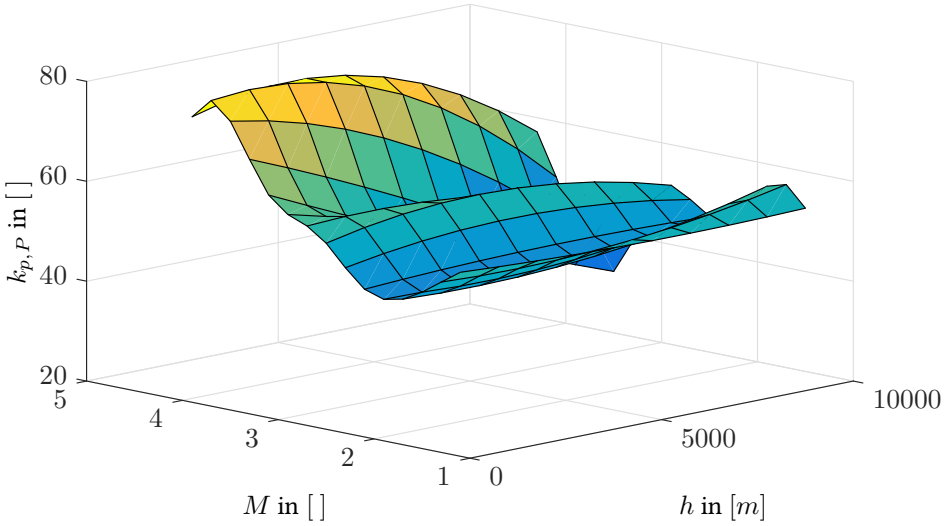

(c) Proportional gain $k_{p,P}$ of inner loop over Mach M and altitude h.

Figure 5.23: Roll channel gain layout over flight envelope for NDI control law.

5.5.2 Adaptive Augmentation based on $\mathcal{L}_1$ AC - PWC

The derivation of the novel autopilot architecture is concluded by describing the design and parameterization of the adaptive augmentation. The layout of the adaptive augmentation is mainly driven by FR_3 and FR_8. Those two requirements demand an independent implementation of the adaptive augmentation and a preservation of the closed-loop characteristics, set up via the baseline autopilot (reference model and baseline controller), in case the design model deviates from the plant. A modular, robustifying augmentation (FR_8) requires an architecture independent of the baseline controller. Besides the demand of a modular implementation, the impact of the specified parametric uncertainties (see section 2.4) on the plant behavior are also influencing the structure of the adaptive element. Thus, the first step in designing a suitable augmentation, which coincides with the aforementioned requirements, comprises of analyzing the sensitivity of the closed-loop baseline dynamics with respect to the considered uncertainties.

5.5.2.1 Sensitivity Analysis

In order to counteract deviations from the design model via an adaptive augmentation, the source and impact of the deviations need to be determined and quantified. Due to its relevance considering the adaption strategy and its architecture, the investigation shall provide an estimate whether the parametric uncertainties within each layer exhibit significant influence with respect to the overall control goal.

The baseline autopilot applied to the nominal (undisturbed) plant model constitute the desired closed-loop characteristics. Therefore, this nominal closed-loop system serves as basis for identifying the impact of the parametric system uncertainties.

Within the sensitivity analysis the variation of a suitable cost function $\Phi\left(\boldsymbol{p}\right)$ with respect to a defined set of parameters $\boldsymbol{p} \in \mathbb{R}^{n_p \times 1}$ is quantified [127]. A certain combination of the parameters according to their distribution is called *sample*.

Due to the large number of considered parameters and samples, *global sensitivity analysis* is the method of choice [127]. This method allows to investigate how parametric changes affect a certain cost function of the model outputs. In contrast to the derivative-based *local sensitivity analysis* the global approach is based using Monte Carlo techniques. In case of global sensitivity analysis a sample space is created by combining all possible parameter samples. Based on this sample space the cost function $\Phi\left(\boldsymbol{p}\right)$ is evaluated sample-wise via simulation.

In order to apply global sensitive analysis to the nominal closed-loop system, the cost function

$$\Phi_{a_z} = \int_{t=0}^{t_{end}} \left(a_{z,nom}^{P}\left(\tau\right) - a_z^P\left(\tau\right)\right)^2 d\tau, \tag{5.83}$$

of the squared tracking error $e_{a_z} = a_{z,nom}^{P}\left(t\right) - a_z^P\left(t\right)$ is considered. The tracking error e_{a_z} describes the difference between the nominal closed-loop response $a_{z,nom}^{P}\left(t\right)$ and the response $a_z^P\left(t\right)$ of the closed-loop system, which is subject to the respective parametric uncertainty. A step input $a_{z,c}$ with amplitude $a_{z,amp}$ serves as a stimulus to the baseline autopilot. The amplitude $a_{z,amp}$ is selected in accordance with the trimmable acceleration of the considered flight envelope point (see section 3.1.2.2).

Since the plant model of the FGS-X-03 depends on a multitude of independent uncertain parameters, a suitable selection of the sample space is required to avoid extensive cost function evaluations. In

order to assess the effect of parametric uncertainties based on closed-loop performance metrics with feasible computational effort, the uncertainties are subdivided in two groups:

- aerodynamic uncertainties: the multiplicative factors

$$\boldsymbol{p}_a = \begin{bmatrix} \Delta C_{z,0} & \Delta C_{z,\eta} & \Delta C_{m,0} & \Delta C_{m,\eta} \end{bmatrix}$$

  are sampled using an equidistant grid with $[\boldsymbol{p}_i - 2 \cdot \sigma_i, \boldsymbol{p}_i + 2 \cdot \sigma_i]$ (see table 2.1) as the respective lower and upper bounds.

- mass and air flow related parameters: the independent parametric uncertainties

$$\boldsymbol{p}_m = \begin{bmatrix} \Delta m & \Delta I_{yy}^G & \Delta \alpha & \Delta \bar{q} \end{bmatrix}$$

  of mass, moment of inertia, AoA, and dynamic pressure are combined in a separate sample space (see table 2.2 and table 2.5). An equidistant grid with $[\boldsymbol{p}_i - \sigma_i, \boldsymbol{p}_i + \sigma_i]$ as the upper and lower bounds was selected.

All parameters in both sampling spaces are subject to an equidistant distribution with gird dimension $n_g = 5$. Thus, each sampling space comprises of $n_g^{n_p} = 5^4 = 625$ samples.

Figure 5.24 depicts the scatter plots of the aerodynamic uncertainty factors (abscissa) against the cost function Φ_{a_z}. Those plots indicate (as expected) that variations $\Delta C_{m,\eta}$ in the missile's control effectiveness $C_{m,\eta}$ have the most significant impact on the cost function Φ_{a_z} and therefore on the closed-loop characteristics. Uncertainties in the aerodynamic force $\Delta C_{z,0}$ and moment coefficient $\Delta C_{m,0}$ have a similar impact on the regarded metric Φ_{a_z}. The consideration of $\Delta C_{z,\eta}$ suggests that uncertainties in the aerodynamic force coefficient $C_{z,\eta}$ have negligible impact on the closed-loop time response of the longitudinal channel (less sensitivity of Φ_{a_z} with respect to $\Delta C_{z,\eta}$).

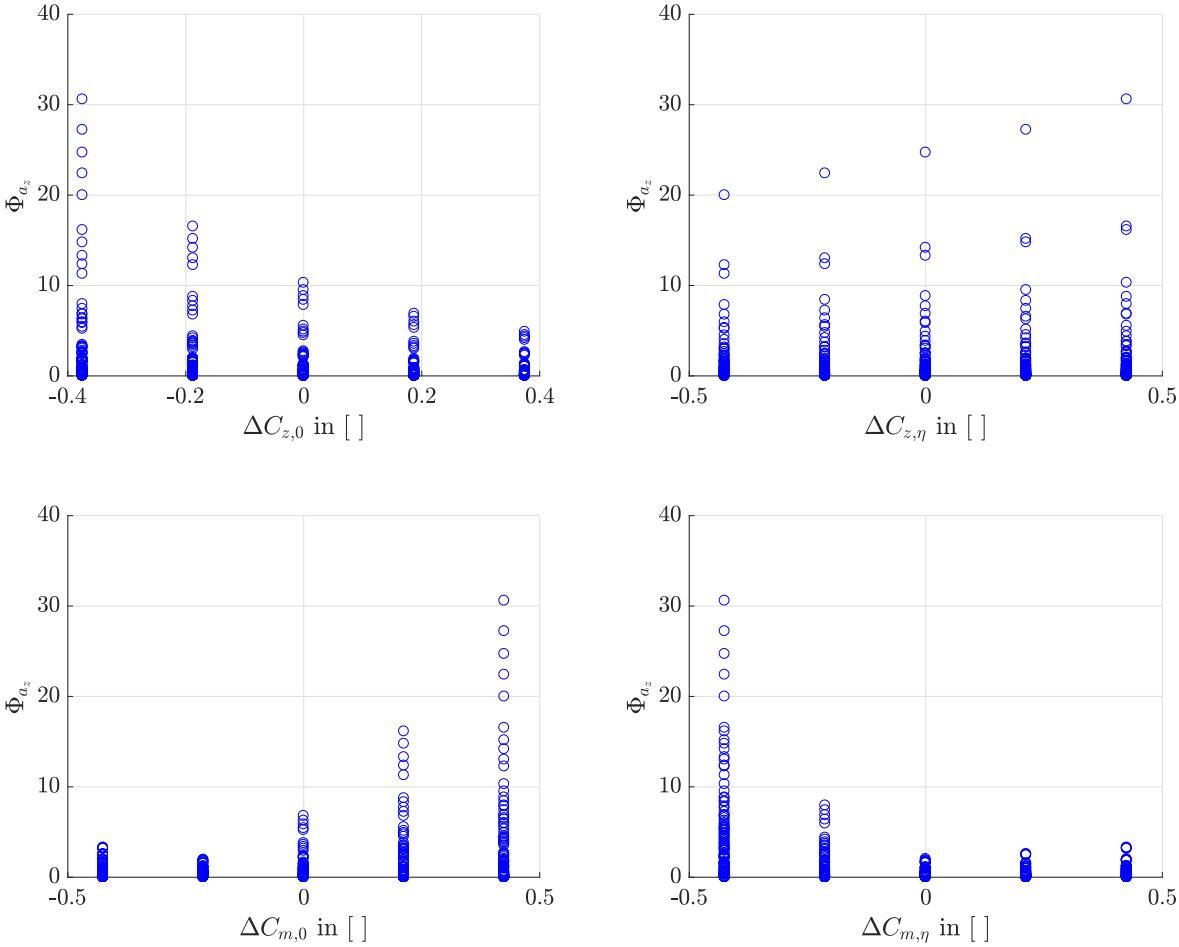

Figure 5.24: Scatter plots of the cost function Φ_{a_z} with respect to aerodynamic uncertainty factors $\Delta C_{z,0}$, $\Delta C_{z,\eta}$, $\Delta C_{m,0}$, and $\Delta C_{m,\eta}$ at $M = 3.3$ and $h = 1km$

For a clearer presentation of the respective aerodynamic uncertainty factors and their effect on the closed-loop response, the correlations and partial correlations of each uncertainty factor are illustrated in the tornado plot in fig. 5.25. This plot reinforces the aforementioned categorization of the uncertainty factors based on fig. 5.24.

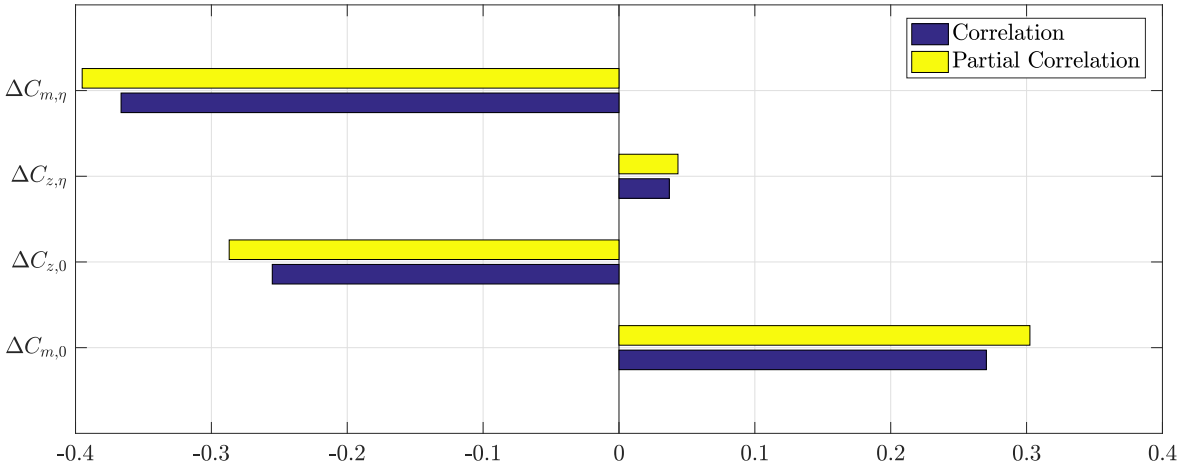

Figure 5.25: Correlation and partial correlation between aerodynamic uncertainty factors $\Delta C_{z,0}$, $\Delta C_{z,\eta}$, $\Delta C_{m,0}$, and $\Delta C_{m,\eta}$ and cost function Φ_{a_z} at $M = 3.3$ and $h = 1km$

For the sake of completeness, the acceleration trajectory resulting in $\max_{\boldsymbol{p}} \Phi_{a_z}$ is depicted in fig. 5.26.

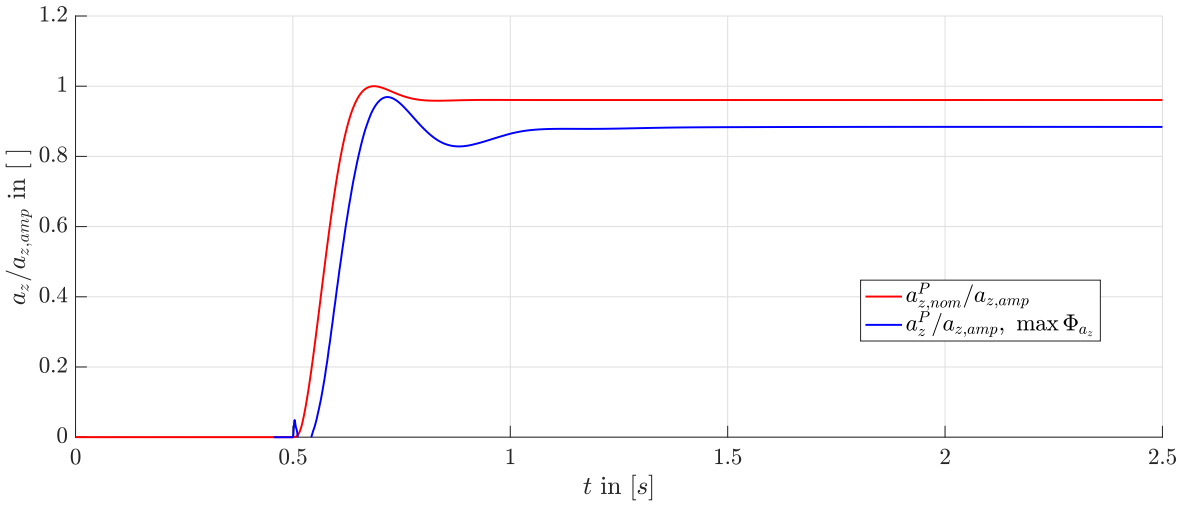

Figure 5.26: Normalized responses of $a^P_{z,nom}(t)$ and $a^P_z(t)$, which result in $\max_{\boldsymbol{p}} \Phi_{a_z}$

Considering the sensitivity analysis of the second uncertainty sampling space ($\boldsymbol{p}_m$), the scatter plots in fig. 5.27 suggests that the closed-loop response is mainly affected by variations in AoA α. Compared to $\Delta\alpha$, the uncertainty $\Delta\bar{q}$ exhibits a diminished impact on Φ_{a_z} but still of higher significance compared to mass Δm and moment of inertia ΔI^G_{yy}.

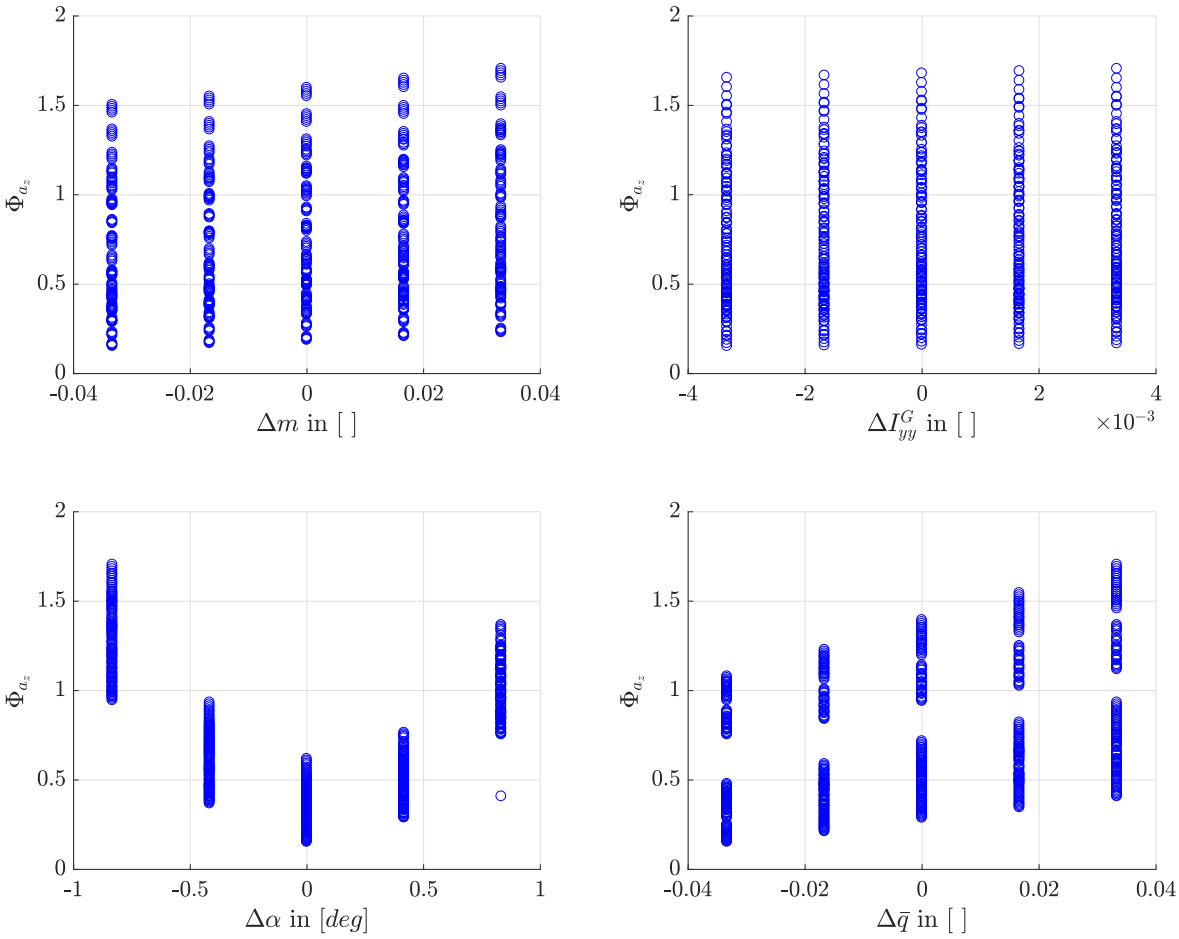

Figure 5.27: Scatter plots of the cost function Φ_{a_z} with respect to aerodynamic uncertainties Δm, ΔI^G_{yy}, $\Delta\alpha$, and $\Delta\bar{q}$ at $M = 3.3$ and $h = 1km$

The ranking of the uncertainties with respect to their impact on Φ_{a_z} becomes more evident by plotting the correlation and partial correlations between the variation in the respective uncertainty and the cost function Φ_{a_z} (see fig. 5.28).

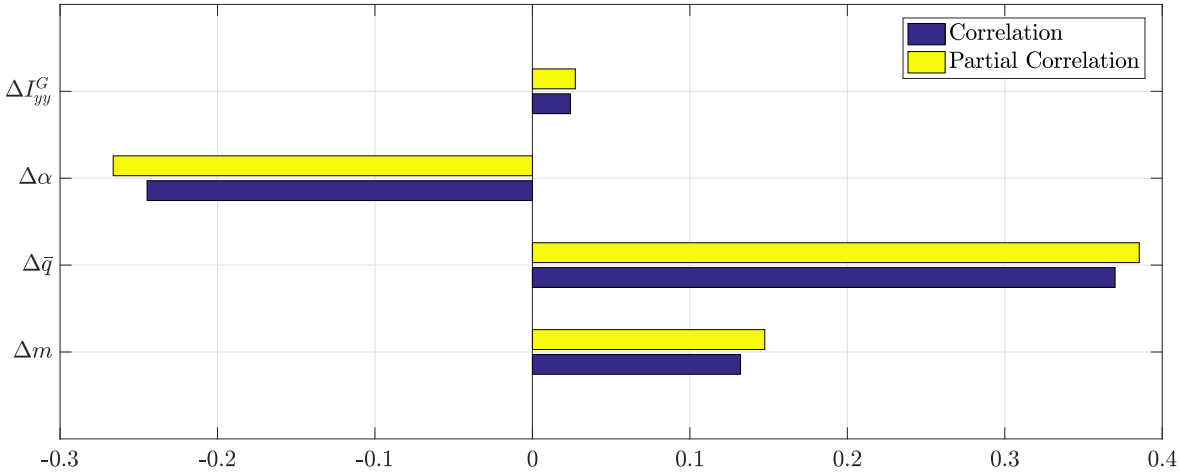

Figure 5.28: Correlation and partial correlation between aerodynamic uncertainty factors Δm, ΔI^G_{yy}, $\Delta\alpha$, and $\Delta\bar{q}$ at $M = 3.3$ and $h = 1km$

In order to associate the results from above with the characteristics of the underlying time responses, the trajectory leading to $\max_{\boldsymbol{p}} \Phi_{a_z}$ is depicted in fig. 5.29.

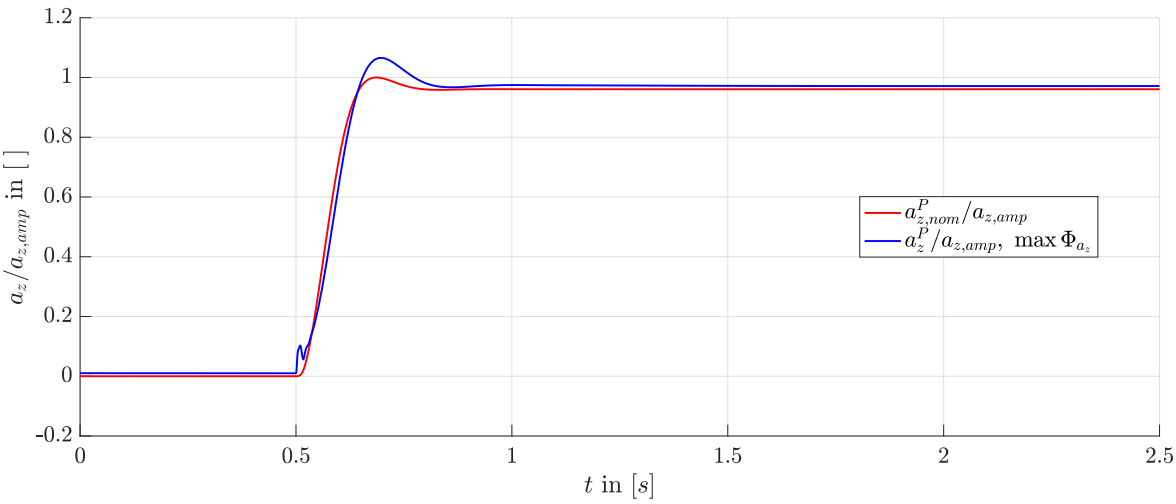

Figure 5.29: Normalized responses of $a^P_{z,nom}(t)$ and $a^P_z(t)$, which result in $\max_{\boldsymbol{p}} \Phi_{a_z}$

It can be concluded from the sensitivity analysis above, that the considered parametric and estimation uncertainties stemming from both dynamic layers exhibit a significant impact on the closed-loop baseline dynamics.

Remark: Commonly, the main effect of changes in weight and balance in missile application is due to the combustion within boost and midcourse phase. This continuous mass flow (changes) leads to a significant change in the missile dynamics (see chapter 2). The missile is considered within the endgame scenario, which is characterized by depleted propellant. Thus, uncertainty in weight and balance parameters are constant over the entire missile flight.

Due to the fact that longitudinal and lateral control channels exhibit the same characteristics and dependencies, the obtained results apply also for the control variable a_y and its dependency on the equivalent uncertain parameters and entities.

5.5.2.2 Cascaded Structure of $\mathcal{L}_1$ AC - PWC for Adaptation of the Plant Dynamics

In order to address the effect of uncertainties in both layers a cascaded structure is designed based on $\mathcal{L}_1$ AC - PWC theory. An augmentation which exhibits independence in design and parametrization of the baseline autopilot is obtained by using a nonlinear state predictor mimicking the missile inner and outer dynamics. With the nonlinear state predictor emulating the plant dynamics and the reduced set of tuning parameters two open problems of classical adaptive flight control are circumvented [57].

The derivation of the adaptive $\mathcal{L}_1$ AC - PWC augmentation is subdivided in the estimation loops of the two dynamical layers, the adaptive control law, and the parametrization of the relevant parameters.

Outer Layer State Predictor

At first the algorithm for estimating the outer layer uncertainties, which are summarized in $\boldsymbol{\Delta}_{\boldsymbol{y}}$, are introduced. On the basis of (5.23), the dynamics of the outer layer is slightly modified for the usage within the state predictor:

$$\dot{\boldsymbol{y}}^P = \hat{\boldsymbol{A}}_{\boldsymbol{y}} \cdot (\boldsymbol{\omega}_{bs} + \boldsymbol{\omega}_{ad}) + \underbrace{\left(\hat{\boldsymbol{b}}_{\boldsymbol{y},lin} \cdot \boldsymbol{y}^P + \hat{\boldsymbol{b}}_{\boldsymbol{y},nonl}\right)}_{\hat{\boldsymbol{b}}_{\boldsymbol{y}}} + \boldsymbol{\Delta}_{\boldsymbol{y}} \tag{5.84a}$$

$$\dot{\boldsymbol{y}}_I^P = \boldsymbol{y}^P \tag{5.84b}$$

The nonlinear part $\hat{\boldsymbol{b}}_{\boldsymbol{y}}$ in (5.84) is subdivided in a portion $\hat{\boldsymbol{b}}_{\boldsymbol{y},lin} \cdot \boldsymbol{y}^P$ which is affine with respect to the output variables $\boldsymbol{y}^P$ and the term $\hat{\boldsymbol{b}}_{\boldsymbol{y},nonl}$ describing the remaining nonlinearities. This distribution is conducted by separating the relevant longitudinal and lateral accelerations of the abbreviations (5.19), (5.20), and (5.25). For the purpose of clarity the body rate $\boldsymbol{\omega} = \boldsymbol{\omega}_{bs} + \boldsymbol{\omega}_{ad}$ is separated in a portion originating from the baseline $\boldsymbol{\omega}_{bs}$ and one from the adaptive augmentation, $\boldsymbol{\omega}_{ad}$. The usage of the time integral of $\boldsymbol{y}^P$ within the baseline autopilot (see section 5.5.1) constitutes a dynamic extension of the plant dynamics. Thus, (5.23) is extended by the integral part of the output variables (5.84b) as well.

In order to mimic the nonlinear plant dynamics described by (5.84) the state predictor of the outer layer exhibits the following structure:

$$\dot{\hat{\boldsymbol{y}}}^P = \hat{\boldsymbol{A}}_{\boldsymbol{y}} \cdot (\boldsymbol{\omega}_{bs} + \boldsymbol{\omega}_{ad}) + \hat{\boldsymbol{b}}_{\boldsymbol{y},lin} \cdot \hat{\boldsymbol{y}}^P + \hat{\boldsymbol{b}}_{\boldsymbol{y},nonl} + \hat{\boldsymbol{\Delta}}_{\boldsymbol{y}} + \boldsymbol{K}_{\boldsymbol{y},SP} \cdot \hat{\boldsymbol{e}}_{\boldsymbol{y}} + \boldsymbol{K}_{\boldsymbol{y},I,SP} \cdot \hat{\boldsymbol{e}}_{\boldsymbol{y},I} \tag{5.85a}$$

$$\dot{\hat{\boldsymbol{y}}}_I^P = \hat{\boldsymbol{y}}^P + \hat{\boldsymbol{\Delta}}_{\boldsymbol{y},I} \tag{5.85b}$$

The estimated versions of $\boldsymbol{y}^P$ and $\boldsymbol{y}_I^P$ calculated via the state predictor(s) are labeled as $\hat{\boldsymbol{y}}^P$ and $\hat{\boldsymbol{y}}_I^P$, respectively. Due to the separation of $\hat{\boldsymbol{b}}_{\boldsymbol{y}}$ in two parts (5.84), the state $\boldsymbol{y}^P$ appears in an affine form on the left-hand side of the state predictor dynamics (5.85). This leads to a better approximation of the plant dynamics by the state predictor and therefore to a more accurate estimate of the uncertainties $\hat{\boldsymbol{\Delta}}_{\boldsymbol{y}}$ and $\hat{\boldsymbol{\Delta}}_{\boldsymbol{y},I}$. Introducing the estimate $\hat{\boldsymbol{\Delta}}_{\boldsymbol{y},I}$ is only motivated by simplification of the following update laws and has no physical origin (compare (5.84) with (5.85)). Therefore, it has no influence on the final control law. By using proportional feedback of the prediction error

$$\hat{\boldsymbol{e}}_{\boldsymbol{y}} = \hat{\boldsymbol{y}}^P - \boldsymbol{y}^P \tag{5.86a}$$

$$\hat{\boldsymbol{e}}_{\boldsymbol{y},I} = \hat{\boldsymbol{y}}_I^P - \boldsymbol{y}_I^P = \int \left(\hat{\boldsymbol{y}}^P - \boldsymbol{y}^P\right) dt \tag{5.86b}$$

in (5.85), two additional degrees of freedom (via $\boldsymbol{K}_{\boldsymbol{y},SP}$ and $\boldsymbol{K}_{\boldsymbol{y},I,SP}$) are introduced per control variable. The prediction error $\hat{\boldsymbol{e}}_{\boldsymbol{y}}$ (5.86a) and its integral version (5.86b) are described by the difference between the plant's output $\boldsymbol{y}^P$ and the estimated response $\hat{\boldsymbol{y}}^P$. Based on (5.84) and (5.85) the dynamics of the prediction error (5.86) becomes

$$\begin{bmatrix} \dot{\hat{\boldsymbol{e}}}_{\boldsymbol{y}} \\ \dot{\hat{\boldsymbol{e}}}_{\boldsymbol{y},I} \end{bmatrix} = \begin{bmatrix} \boldsymbol{K}_{\boldsymbol{y},SP} + \boldsymbol{b}_{\boldsymbol{y},lin} & \boldsymbol{K}_{\boldsymbol{y},I,SP} \\ \mathbb{I}_{3\times3} & \boldsymbol{0}_{3\times3} \end{bmatrix} \cdot \begin{bmatrix} \hat{\boldsymbol{e}}_{\boldsymbol{y}} \\ \hat{\boldsymbol{e}}_{\boldsymbol{y},I} \end{bmatrix} + \begin{bmatrix} \hat{\boldsymbol{\Delta}}_{\boldsymbol{y}} - \boldsymbol{\Delta}_{\boldsymbol{y}} \\ \hat{\boldsymbol{\Delta}}_{\boldsymbol{y},I} \end{bmatrix}. \tag{5.87}$$

Based on the time evolution of the prediction error within one sampling period, the sample-based

update law of the estimates within one sampling interval $t \in [iT_s, (i+1)T_s[$ is given as

$$\begin{aligned}\begin{bmatrix}\hat{\boldsymbol{\Delta}}_{\boldsymbol{y}}(iT_s)\\ \hat{\boldsymbol{\Delta}}_{\boldsymbol{y},I}(iT_s)\end{bmatrix} &= \underbrace{-\begin{bmatrix}\mathbb{I}_{3\times3} & \mathbf{0}_{3\times3}\\ \mathbf{0}_{3\times3} & \mathbb{I}_{3\times3}\end{bmatrix}\boldsymbol{\Phi}_{\boldsymbol{y}}^{-1}(T_s)\, e^{\boldsymbol{A}_{\boldsymbol{y},SP}\cdot T_s}}_{=\boldsymbol{K}_{\boldsymbol{y},PWC}} \cdot \begin{bmatrix}\hat{\boldsymbol{e}}_{\boldsymbol{y}}(iT_s)\\ \hat{\boldsymbol{e}}_{\boldsymbol{y},I}(iT_s)\end{bmatrix}\\ \boldsymbol{\Phi}_{\boldsymbol{y}}(T_s) &= \boldsymbol{A}_{\boldsymbol{y},SP}^{-1}\cdot\left(e^{\boldsymbol{A}_{\boldsymbol{y},SP}T_s} - \mathbb{I}_{3\times3}\right)\end{aligned}. \tag{5.88}$$

The theoretical considerations behind the update law (5.88) can be found in section 4.3.1.2.

Inner Layer State Predictor

The estimation law of the inner layer uncertainties $\hat{\boldsymbol{\Delta}}_{\boldsymbol{\omega}}$ is derived in analogy to the previous section. By considering the design model of the inner layer dynamics (5.26), the corresponding state predictor dynamics results as

$$\dot{\hat{\boldsymbol{\omega}}} = \hat{\boldsymbol{A}}_{\boldsymbol{\omega}}\cdot(\boldsymbol{C}_{\boldsymbol{M},\boldsymbol{u},bs} + \boldsymbol{C}_{\boldsymbol{M},\boldsymbol{u},ad}) + \hat{\boldsymbol{b}}_{\boldsymbol{\omega}} + \hat{\boldsymbol{\Delta}}_{\boldsymbol{\omega}} + \boldsymbol{K}_{\boldsymbol{\omega},SP}\cdot\hat{\boldsymbol{e}}_{\boldsymbol{\omega}}. \tag{5.89}$$

Remark: In case the effect of aerodynamic pitch damping would exhibit a more significant impact on the inner layer dynamics (see fig. 5.8), a separation of $\boldsymbol{b}_{\boldsymbol{\omega}}$ in $\boldsymbol{b}_{\boldsymbol{\omega},lin}\cdot\boldsymbol{\omega}$ and $\boldsymbol{b}_{\boldsymbol{\omega},nonl}$ - in analogy to (5.85) - could be taken into account.

The time derivative of the prediction error

$$\hat{\boldsymbol{e}}_{\boldsymbol{\omega}} = \hat{\boldsymbol{\omega}} - \boldsymbol{\omega} \tag{5.90}$$

leads to

$$\dot{\hat{\boldsymbol{e}}}_{\boldsymbol{\omega}} = \boldsymbol{K}_{\boldsymbol{\omega},SP}\cdot\hat{\boldsymbol{e}}_{\boldsymbol{\omega}} + \hat{\boldsymbol{\Delta}}_{\boldsymbol{\omega}} - \boldsymbol{\Delta}_{\boldsymbol{\omega}}. \tag{5.91}$$

Based on (5.91), the update law of the inner layer - in accordance to section 4.3.1.2 - is given by

$$\begin{aligned}\hat{\boldsymbol{\Delta}}_{\boldsymbol{\omega}}(iT_s) &= \underbrace{-\boldsymbol{\Phi}_{\boldsymbol{\omega}}^{-1}(T_s)\, e^{\boldsymbol{K}_{\boldsymbol{\omega},SP}\cdot T_s}}_{=\boldsymbol{K}_{\boldsymbol{\omega},PWC}}\cdot\hat{\boldsymbol{e}}_{\boldsymbol{\omega}}(iT_s)\\ \boldsymbol{\Phi}_{\boldsymbol{\omega}}(T_s) &= \boldsymbol{K}_{\boldsymbol{\omega},SP}^{-1}\cdot\left(e^{\boldsymbol{K}_{\boldsymbol{\omega},SP}T_s} - \mathbb{I}_{3\times3}\right).\end{aligned} \tag{5.92}$$

Control Law of Adaptive Augmentation

Both uncertainty estimates $\hat{\boldsymbol{\Delta}}_{\boldsymbol{\omega}}$ (5.88) and $\hat{\boldsymbol{\Delta}}_{\boldsymbol{y}}$ (5.92) are incorporated within a cascaded version of $\mathcal{L}_1$ AC - PWC control law. The intermediate control law for compensating the outer layer uncertainties $\boldsymbol{\Delta}_{\boldsymbol{y}}$ is obtained in accordance to the $\mathcal{L}_1$ AC - PWC standard approach presented in section 4.3.1.2:

$$\boldsymbol{\omega}_{c,ad} = \boldsymbol{C}_{\boldsymbol{y}}(s)\cdot\left(-\hat{\boldsymbol{A}}_{\boldsymbol{y}}^{-1}\cdot\hat{\boldsymbol{\Delta}}_{\boldsymbol{y}}\right) \tag{5.93}$$

Since the outer dynamics state predictor (5.85) is designed to account for the effectiveness $\hat{\boldsymbol{A}}_{\boldsymbol{y}}$ of the body rate $\boldsymbol{\omega}$, the control law in (5.93) includes the inverse of $\hat{\boldsymbol{A}}_{\boldsymbol{y}}$. Thus, the outer layer uncertainty estimate is mapped to the adaptive portion of the intermediate control variable $\boldsymbol{\omega}_{c,ad}$. This follows the same pattern as in the pseudo-control law of the baseline autopilot design (see section 5.5.1). The low-pass filter $\boldsymbol{C}_{\boldsymbol{y}}(s)$ within the adaptive law is a linear. A detailed description including the parametrization is presented in the subsequent paragraph.

The final adaptive pseudo-control law

$$\boldsymbol{C}_{\boldsymbol{M},\boldsymbol{u},ad} = \hat{\boldsymbol{A}}_{\boldsymbol{\omega}}^{-1}\left(-\boldsymbol{C}_{\boldsymbol{\omega}}\left(s\right)\cdot\hat{\boldsymbol{\Delta}}_{\boldsymbol{\omega}} + \boldsymbol{K}_{\boldsymbol{\omega},SP}\cdot\boldsymbol{\omega}_{c,ad} + \dot{\boldsymbol{\omega}}_{c,ad}\right) \tag{5.94}$$

consists of three parts: the first term $(-\boldsymbol{C}_{\boldsymbol{\omega}}\left(s\right)\cdot\hat{\boldsymbol{\Delta}}_{\boldsymbol{\omega}})$ in (5.94) compensates the inner layer uncertainty $\boldsymbol{\Delta}_{\boldsymbol{\omega}}$. The proportional $(\boldsymbol{K}_{\boldsymbol{\omega},SP}\cdot\boldsymbol{\omega}_{c,ad})$ and feedforward part $(\dot{\boldsymbol{\omega}}_{c,ad})$ propagate the intermediate outer layer control law (5.93), and therefore the uncertainty estimate $\hat{\boldsymbol{\Delta}}_{\boldsymbol{y}}$, to the control variable $\boldsymbol{C}_{\boldsymbol{M},\boldsymbol{u},ad}$. The feedforward portion $\dot{\boldsymbol{\omega}}_{c,ad}$ is a product of the linear filtering process in (5.93).

In contrast to standard adaptive schemes [52, 128**?**], the designed architecture of the adaptive augmentation does not require any feedforward terms provided by the NRM. Since those feedforward signals determine the closed-loop bandwidth, no performance limitation is introduced through the low-pass filtering of the adaptive signals. Thus, the closed-loop bandwidth setup via the baseline autopilot is fully preserved.

Remark: The additional terms in (5.94) resulting from the intermediate control $\boldsymbol{\omega}_{c,ad}$ could also be added to the baseline autopilot's control signal. In this case $\boldsymbol{\omega}_{c,ad}$ and $\dot{\boldsymbol{\omega}}_{c,ad}$ are added to the reference signals output $\boldsymbol{\omega}_r$ and $\dot{\boldsymbol{\omega}}_r$. This would lead to an equivalent mathematical closed-loop characteristics.

Parameters of Adaptive Augmentation

The design parameters influencing the cascaded $\mathcal{L}_1$ AC - PWC control law, presented in section 5.5.2.2, are depicted in table 5.1.

Parameter	Description
$\boldsymbol{K}_{\boldsymbol{y},SP}$, $\boldsymbol{K}_{\boldsymbol{y},I,SP}$, $\boldsymbol{K}_{\boldsymbol{\omega},SP}$	State predictor feedback gains to setup desired dynamical properties of state predictor dynamics.
T_s	Sampling time of the flight control computer.
$\boldsymbol{C}_{\boldsymbol{\omega}}\left(s\right)$, $\boldsymbol{C}_{\boldsymbol{y}}\left(s\right)$	Transfer functions of inner and outer loop low-pass filters.

Table 5.1: Degrees of freedom of the $\mathcal{L}_1$ AC - PWC control law.

The parameters $\boldsymbol{K}_{\boldsymbol{y},SP}$, $\boldsymbol{K}_{\boldsymbol{y},I,SP}$, and $\boldsymbol{K}_{\boldsymbol{\omega},SP}$ determine the prediction error dynamics of the respective dynamic layer (see (5.85) and (5.89)) and have major impact on the gain $\boldsymbol{K}_{i,PWC}$ of the update laws (5.88) and (5.92). From the error dynamics (5.87) and (5.91), it becomes obvious that high feedback ($\boldsymbol{K}_{\boldsymbol{y},SP}$ and $\boldsymbol{K}_{\boldsymbol{\omega},SP}$) lead to a fast decay in the considered prediction errors and therefore less error information is passed to the corresponding uncertainty estimates. Conversely, small gains of the state predictor feedback ($\boldsymbol{K}_{\boldsymbol{y},SP}$, $\boldsymbol{K}_{\boldsymbol{\omega},SP}$) result in a small gain of the respective update law $\boldsymbol{K}_{i,PWC}$ (see (5.88) and (5.92)) and therefore reduced amplification of the considered prediction error $\hat{\boldsymbol{e}}_i$. In order to obtain a well-balanced performance of the estimation loops, the feedback gains need to be selected by taking the plant's dynamics - of the respective inner and outer layer - into account. Since the tracking problem of the baseline controller also considers a stabilizing problem, the entries $\boldsymbol{K}_{\boldsymbol{y},SP} + \boldsymbol{b}_{\boldsymbol{y},lin}$, $\boldsymbol{K}_{\boldsymbol{y},I,SP}$, and $\boldsymbol{K}_{\boldsymbol{\omega},SP}$ of the dynamic matrix in (5.87) and (5.91) are selected in accordance to (5.48) and (5.49). Thus, the closed-loop prediction error dynamics is in line with the missile dynamical properties.

The sampling time is selected to be $T_s = 0.001s$. This value coincides with common missile avionic hardware.

Remark: The effect of the sampling time parametrizationis further investigated within the subsequent chapter 6.

Based on the bandwidth investigations of the missile system in sections 3.2.2.2 and 3.2.3.2, the structure and parametrization of the low-pass filters used in (5.93) and (5.94) are depicted in

$$\boldsymbol{C}_{y_i}(s) = \frac{a_0}{a_3 s^3 + a_2 s^2 + a_1 s + a_0} \tag{5.95a}$$

$$\boldsymbol{C}_{\omega_i}(s) = \frac{\omega_{0,\omega_i}^2}{s^2 + 2\zeta_{\omega_i}\omega_{0,\omega_i} s + \omega_{0,\omega_i}^2} \tag{5.95b}$$

and table 5.2, respectively.

Filter	Parameters
$\boldsymbol{C}_{y_i}(s)$	$a_0 = 150$, $a_1 = 53$, $a_2 = 8.86$, $a_3 = 0.012$ (cut-off frequency: $\omega_{c,y_i} = 5.9\frac{rad}{s}$)
$\boldsymbol{C}_p(s)$	$\omega_{0,p} = 50\frac{rad}{s}$, $\zeta_p = \sqrt{2}$
$\boldsymbol{C}_q(s)$	$\omega_{0,q} = 35\frac{rad}{s}$, $\zeta_q = \sqrt{2}$

Table 5.2: Parametrization of low-pass filters used in $\mathcal{L}_1$ AC - PWC control law.

Figure 5.30 depicts the magnitude of the different filters over frequency.

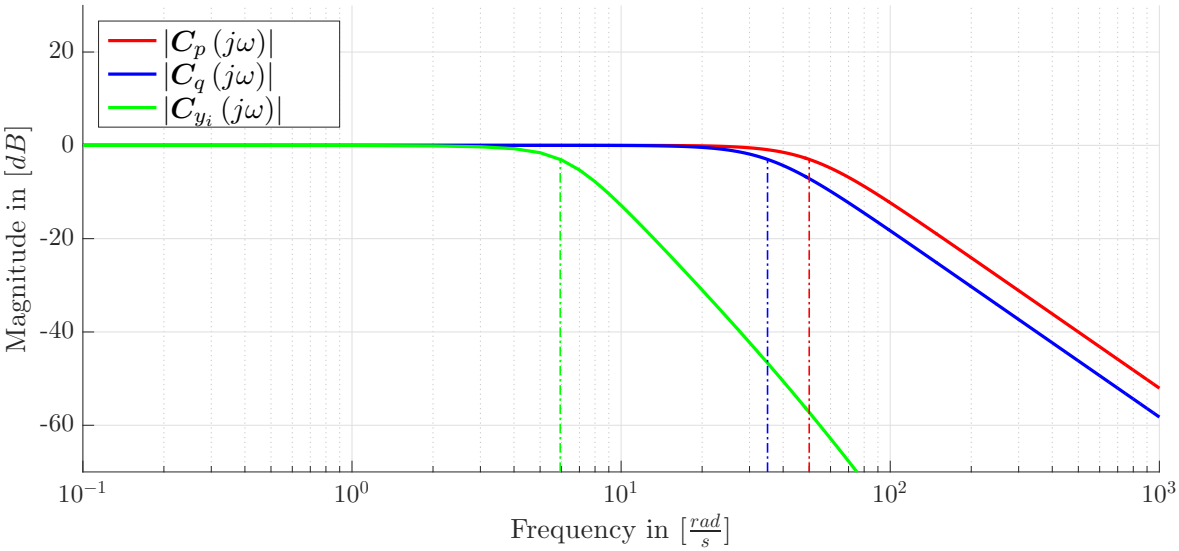

Figure 5.30: Low-pass filter of the cascaded $\mathcal{L}_1$ AC - PWC implementation.

5.5.3 Bending Mode Filters

A band-stop filter is required in order to account for the frequency range of the first bending mode. Due to lack of data, the modes of the missile body are not considered within the modeling chapter (see chapter 2). Even though the autopilot must attenuate the signal commanded to the missile's aerodynamic controls within the frequency range specified in NFR_1. For this reason, the following filter structure

$$\boldsymbol{F}_{band}(s) = \frac{s^2 + a_0}{s^2 + a_1 s + a_0} \tag{5.96}$$

with the parametrization $a_0 = 3.19 \cdot 10^5$ and $a_1 = 113.1$ is integrated in the FCS (see fig. 5.4) to attenuate frequencies in the range between $\omega_{0,low} = 80Hz$ to $\omega_{0,high} = 100Hz$. The magnitude of the bending mode filters is depicted in fig. 5.31).

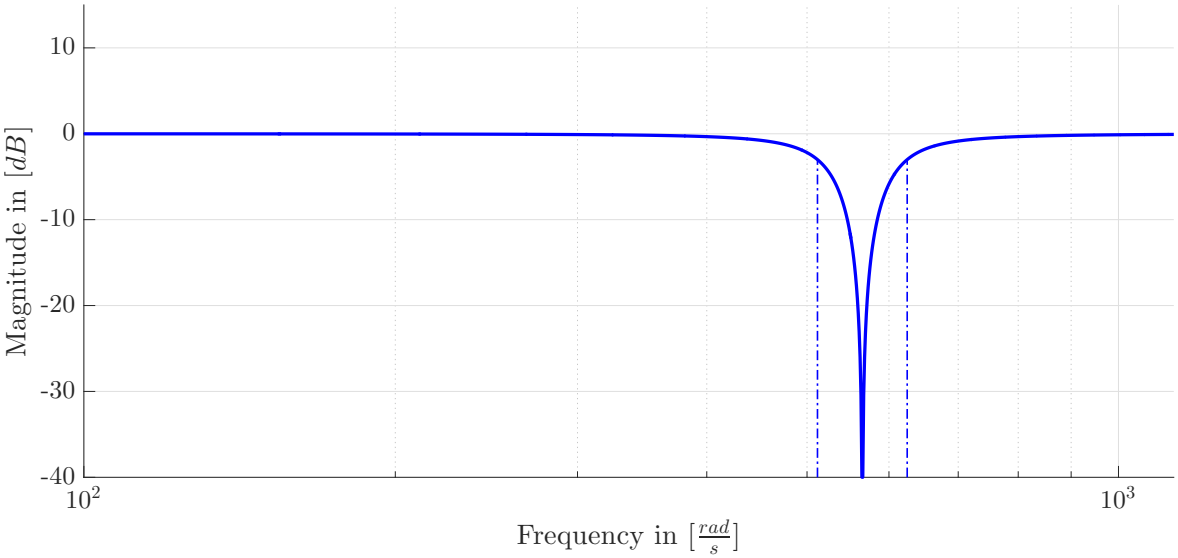

Figure 5.31: Band-stop filter to avoid critical frequency range of first missile bending mode within the control signal commanded to actuators.

CHAPTER 6

Analysis and Evaluation of the Flight Control System (FCS)

> It is a capital mistake to theorize before one has data. Insensibly one begins to twist facts to suit theories instead of theories to suit facts.
>
> Sherlock Holmes, the fictional creation of Arthur Conan Doyle

Within this chapter the FCS designed in chapter 5 is evaluated based on the underlying requirements (see section 5.1), Monte Carlo (MC) simulations, and a realistic missile scenario. Since each element of the autopilot (Reference Model, Baseline, and Adaptive Control Law) comprises of novel algorithmic structures and architectures, the analysis and evaluation is conducted element-wise via a gradually approach. Thus, the two baseline control law are analyzed in section 6.1 and compared to a classical linear implementation of the autopilot. In section 6.2, the robustification effect of the adaptive augmentation is compared to the baseline control design.

Besides the evaluation and comparison of the autopilot elements based on quantifiable metrics, the novel approaches are also investigated concerning the implementation complexity and the computational demand.

Since the non-functional requirements (NFRs) regarding the roll-channel (see section 5.1.2) are less demanding compared to the physical capabilities (fast dynamics in combination with high control effectiveness), the analysis and evaluation is only focused on the longitudinal and lateral acceleration channel.

Remark: Since the missile is a highly nonlinear system, linear metrics remain only valid within the vicinity of the considered trim condition.

6.1 Evaluation and Comparison of Baseline Autopilot

In section 5.5.1 two different control laws are implemented for the baseline autopilot: a modified Nonlinear Dynamic Inversion (NDI) approach and a standard Command Filtered Backstepping (CFB) implementation. Apart from these two control approaches, the nonlinear reference model represents the key element within the autopilot regarding the demanding performance requirements. This

nonlinear reference model was designed with the motivation to realize a better exploitation of the missile's physical capabilities compared to linear reference models or autopilots [36, 37, 38, 40, 43]. Thus, for the purpose of performance evaluation the following linear reference system is considered:

$$G_{a_{i,c},a_{i,m}} = \frac{\omega_{cl}^2}{s^2 + 2\zeta_{cl}\omega_{cl} \cdot s + \omega_{cl}^2} \tag{6.1}$$

This linear dynamics in (6.1) approximates the closed-loop characteristics of the missile controlled via a linear autopilot approach. In order to mimic the closed-loop characteristics for the herein considered missile, the parameters ω_{cl} and ζ_{cl} of the linear transfer function (6.1) are calculated based on the settling time T_{st} (NFR_6) and overshoot requirement $\varsigma_{i,ov}$ (NFR_4), respectively. Since those requirements vary with the operating point, the frequency ω_{cl} and damping ζ_{cl} are functions of Mach M and altitude h:

$$\zeta_{cl}(M,h) = \frac{-\ln\left(\varsigma_{i,ov}(M,h)\right)}{\sqrt{\pi^2 + \ln^2\left(\varsigma_{i,ov}(M,h)\right)}} \tag{6.2a}$$

$$\omega_{cl}(M,h) = -\frac{-\ln\left(c_{st}\sqrt{1-\zeta_{cl}(M,h)^2}\right)}{\zeta_{cl}(M,h) \cdot T_{st}(M,h)} \tag{6.2b}$$

c_{st} describes the constant fraction of the settling time range with respect to the step input amplitude $a_{i,c}$. Thus, the acceleration output stays within $a_{i,m} \leq c_{st} \cdot a_{i,c}$ for all $t \geq T_{st}$.

Besides performance investigations, the two nonlinear baseline control laws are also analyzed with respect to robustness characteristics.

The design and parametrization strategy of the missile autopilot (see chapter 5) exhibits a generic characteristics where the parameters are calculated in an automated way based on the performance and robustness NFRs given in section 5.1.2. In order to demonstrate the generic layout approach, the selected points at which the autopilot is evaluated are spread over a large area of the flight envelope (fig. 6.1). The subset of the flight envelope is selected with the purpose to cover a wide spectrum of agility and to demand the maximum acceleration capabilities ($50g$) in the herein regarded test cases.

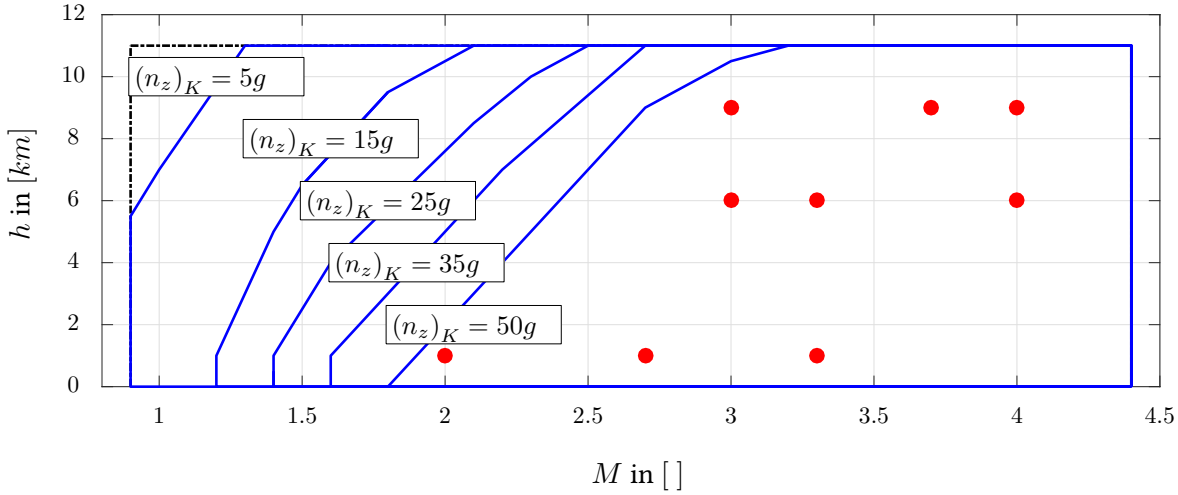

Figure 6.1: Flight envelope points selected for evaluation (red dots) within nominal flight envelope for different load factor levels.

Performance and robustness of control algorithm depend strongly on their parametrization. It might always be possible to find a parametrization which outperforms a given controller setup. Thus, the evaluation and analysis of the closed-loop baseline missile system has two main objectives:

- automated parametrization and consistency with requirements: evaluating both approaches and the automated parametrization (see section 5.5.1.3) with respect to fulfilling the requirements (section 5.1) across the entire flight envelope (section 5.5.1.3).
- architectural differences: investigation of certain trends stemming from architectural differences between both approaches.

6.1.1 Performance Evaluation

Due to the nonlinear characteristics of the missile dynamics, all performance criteria (and requirements), except bandwidth, are evaluated based on nonlinear simulations. For this purpose the missile system controlled via the baseline autopilot is stimulated with a simultaneous step input for both acceleration channels (lateral $a_{z,c}$ and longitudinal $a_{y,c}$) over the time horizon of $t_{sim} = 4s$. The amplitude of the overall commanded acceleration $a_c = \sqrt{a_{z,c}^2 + a_{y,c}^2}$ is within the limits of the maximum trimmable acceleration (see fig. 6.1).

Figure 6.2 displays the normalized responses of both acceleration control channels with respect to the aforementioned step input command for the NDI-, CFB-based, and the linear reference autopilot.

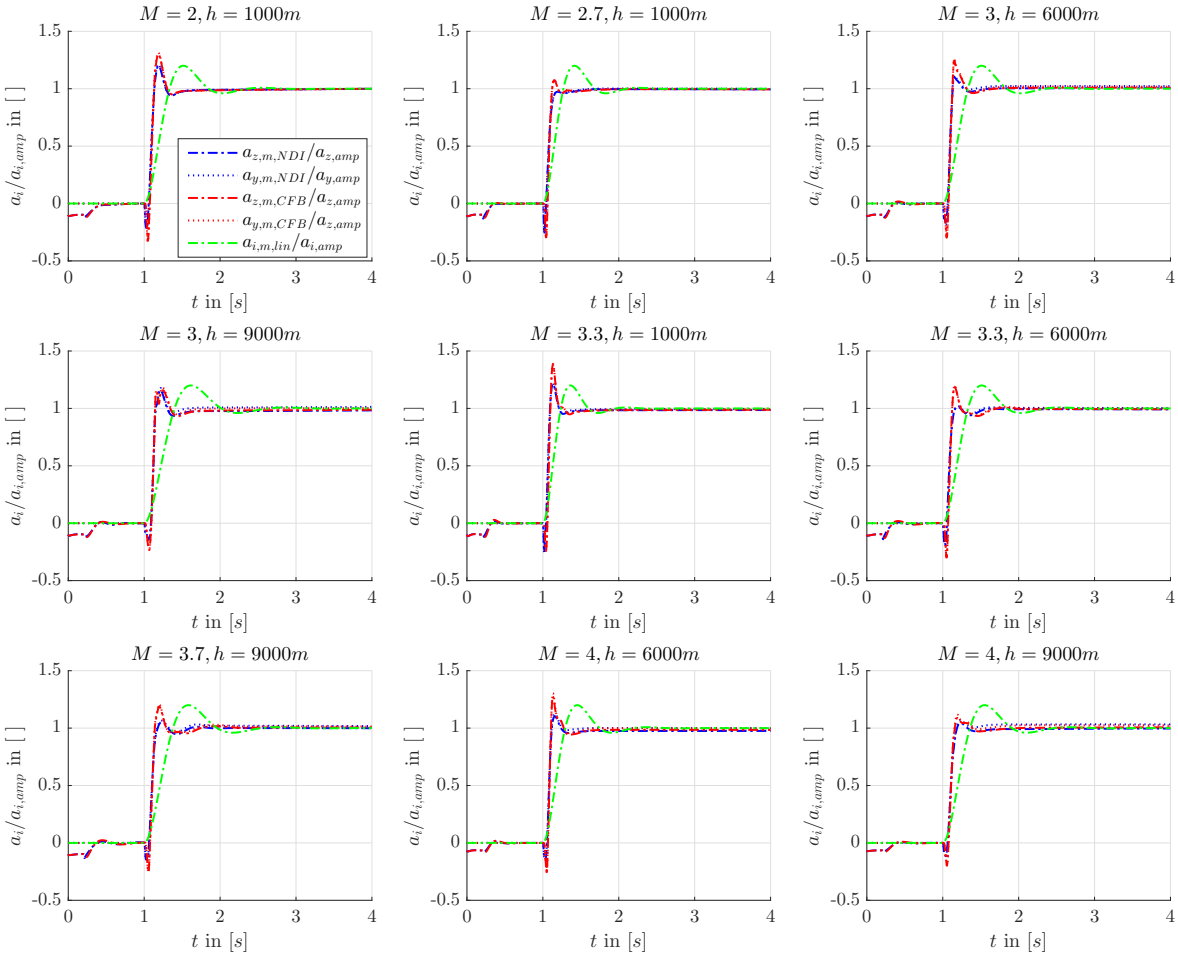

Figure 6.2: Normalized step responses of both acceleration channels across entire flight envelope for NDI, CFB, and the linear reference autopilot.

For reasons of clarity, the respective fin deflections and the corresponding rates are given in figs. 6.3 and 6.4, respectively. Due to better readability, the sums $\sum_{i=1}^{3} |u_i| \leq \delta_{max}$ of the fin deflections and deflection rates $\sum_{i=1}^{3} |\dot{u}_i| \leq \dot{\delta}_{max}$) are depicted.

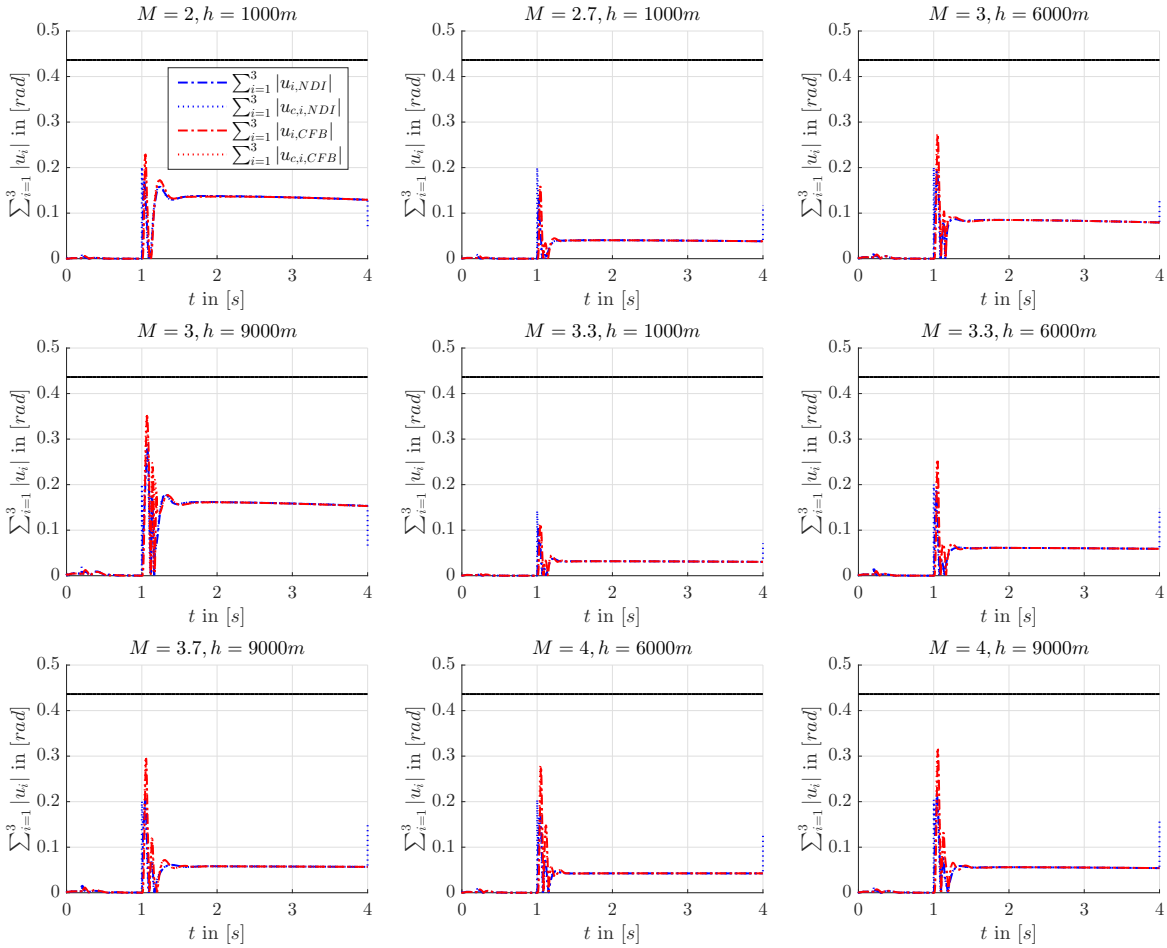

Figure 6.3: Sum of commanded $\boldsymbol{u}_c$ and realized $\boldsymbol{u}$ equivalent fin deflections of the corresponding step responses (see fig. 6.2) for NDI and CFB baseline implementation.

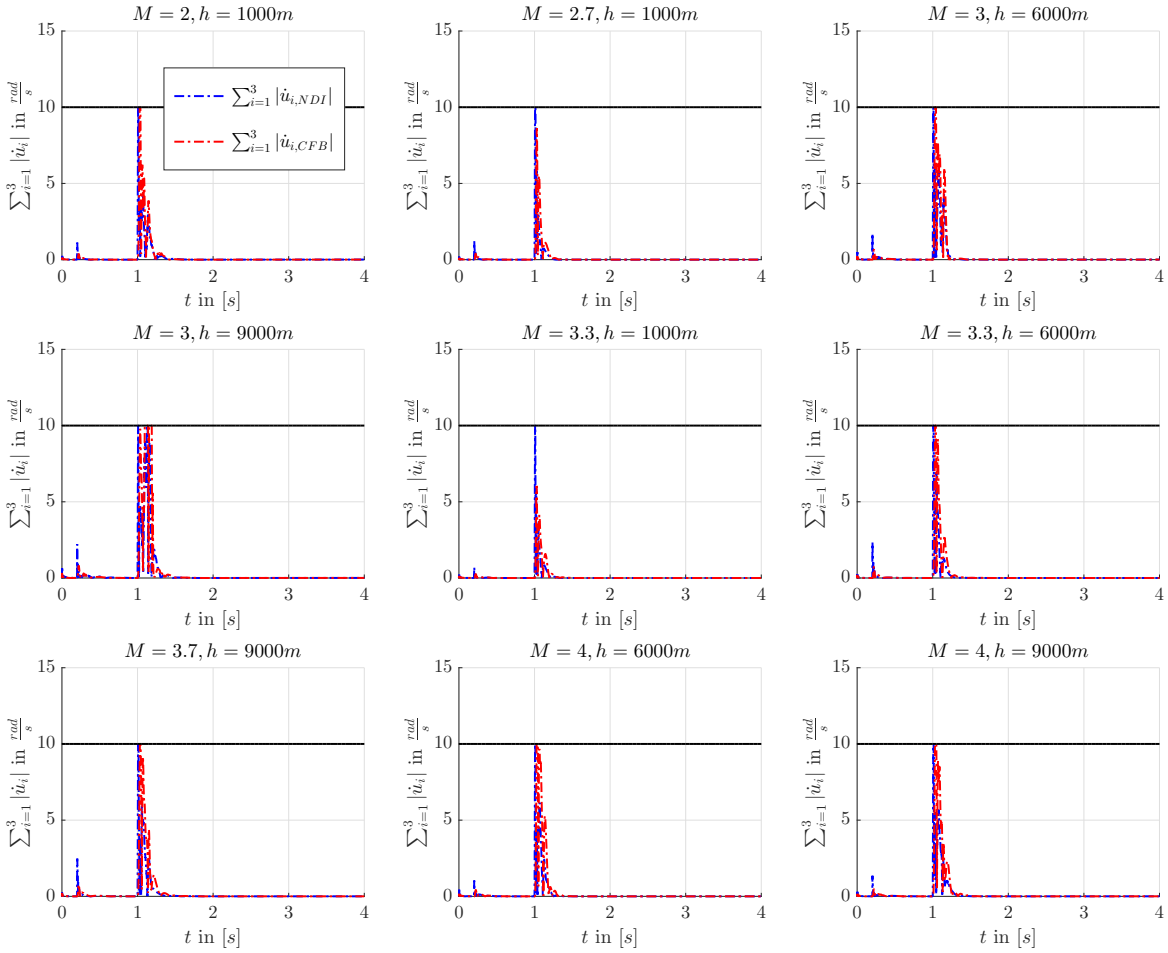

Figure 6.4: Sum of resulting $\dot{\boldsymbol{u}}$ fin deflection rates of the corresponding step responses (see fig. 6.2) for NDI and CFB.

While the sum of the fin rate deflections (see fig. 6.3) stays below the maximum deflection limit, the control signal of both nonlinear autopilot design lead to utilization of the maximum rate limits (see fig. 6.4). Thus, the autopilot exploits the full actuator capabilities at each flight envelope point.

In fig. 6.5 the magnitude of the linearized closed-loop transfer function $\left|G_{a_{z,c},a_{z,IMU}}(j\omega)\right|$ of the longitudinal control channel is depicted for the three considered baseline autopilots. The transfer functions are calculated based on horizontal flight conditions by considering the command $a_{z,c}$ as input and the Inertial Measurement Unit (IMU) measurement $a_{z,IMU}$ as output. Due to the missile's symmetry the same results hold for the linearized transfer function $\left|G_{a_{y,c},a_{y,IMU}}(j\omega)\right|$ of the lateral channel.

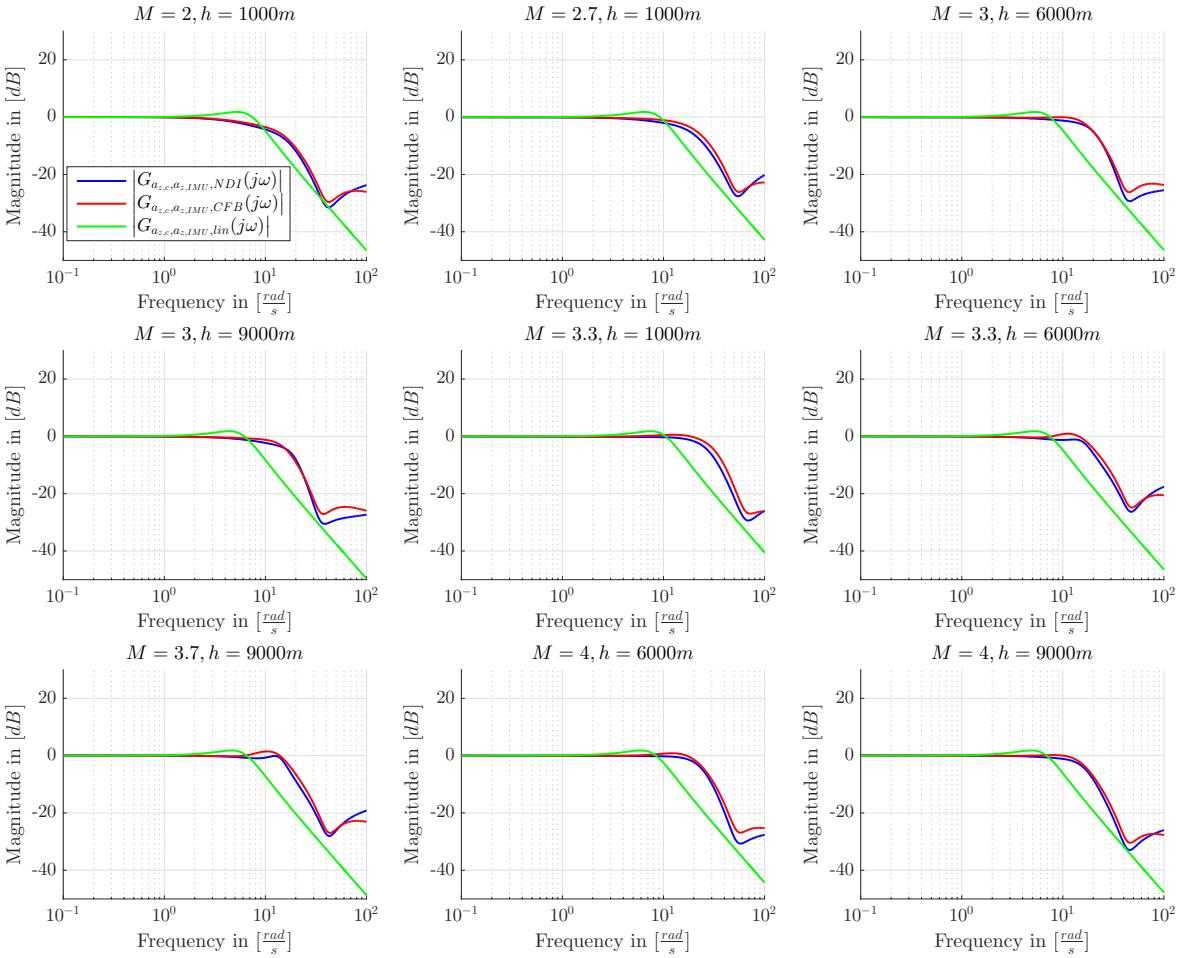

Figure 6.5: Magnitude of linearized closed-loop transfer function $G_{a_{z,c},a_{z,IMU}}(s)$ at the selected flight envelope points for NDI, CFB, and the linear reference autopilot.

The nonlinear closed-loop response of the acceleration outputs are analyzed based on the following metrics:

- overshoot: the arithmetic mean of the overshoots $\varsigma_{i,ov}$ of both channels.

$$\varsigma_{ov} = \frac{1}{2} \cdot \left(\left\| \frac{a_{z,m}(t)}{a_{z,c,amp}} \right\|_{\mathcal{L}_\infty} + \left\| \frac{a_{y,m}(t)}{a_{y,c,amp}} \right\|_{\mathcal{L}_\infty} \right), \quad t \leq t_{sim} \tag{6.3}$$

- rise time: arithmetic mean

$$T_{rt} = \frac{1}{2} \cdot (T_{z,rt} + T_{y,rt}) \tag{6.4}$$

of the smallest time values $T_{i,rt}$ at which the measurement is equal or above 80% of the commanded amplitude $a_{i,c,amp}$:

$$\begin{aligned} T_{i,rt} &= \min_t t \\ \text{subject to} \quad a_{i,m}(t) &\geq 0.8 \cdot a_{i,c,amp} \end{aligned} \tag{6.5}$$

- settling time: arithmetic mean

$$T_{st} = \frac{1}{2} \cdot (T_{z,st} + T_{y,st}) \tag{6.6}$$

of the smallest time values $T_{i,st}$ at which the measurement $a_{i,m}$ stays within the limits $0.9 \cdot a_{i,c,amp} \leq a_{i,m} \leq 1.1 \cdot a_{i,c,amp}$:

$$\begin{aligned} T_{i,st} &= \min_{t} t \\ \text{subject to} \quad t &\in \{t_d \mid t_d \in \mathbb{R}^+, \quad 0.9 \cdot a_{i,c,amp} \leq a_{i,m}(t_d) \leq 1.1 \cdot a_{i,c,amp}\} \end{aligned} \tag{6.7}$$

- bandwidth: crossover frequency of the longitudinal control channel:

$$\begin{aligned} \omega_{z,cr} &= \min_{\omega} \omega \\ \text{subject to} \quad \omega &\in \left\{\omega_d \mid \omega_d \in \mathbb{R}^+, \quad \left|G_{a_{z,c},a_{z,IMU}}(j\omega_d)\right| \leq 3dB\right\} \end{aligned} \tag{6.8}$$

The performance evaluation based on the nonlinear simulation results (see fig. 6.2) and the closed-loop transfer functions (see fig. 6.5) with respect to the aforementioned metrics are summarized in the following bar charts, fig. 6.6. The statistics calculated based on the time and frequency metrics (6.3) to (6.8) are given in fig. 6.6a and fig. 6.6b, respectively. The ordinate and abscissa in each histogram contains the value of the particular metric and the corresponding flight envelope point, respectively.

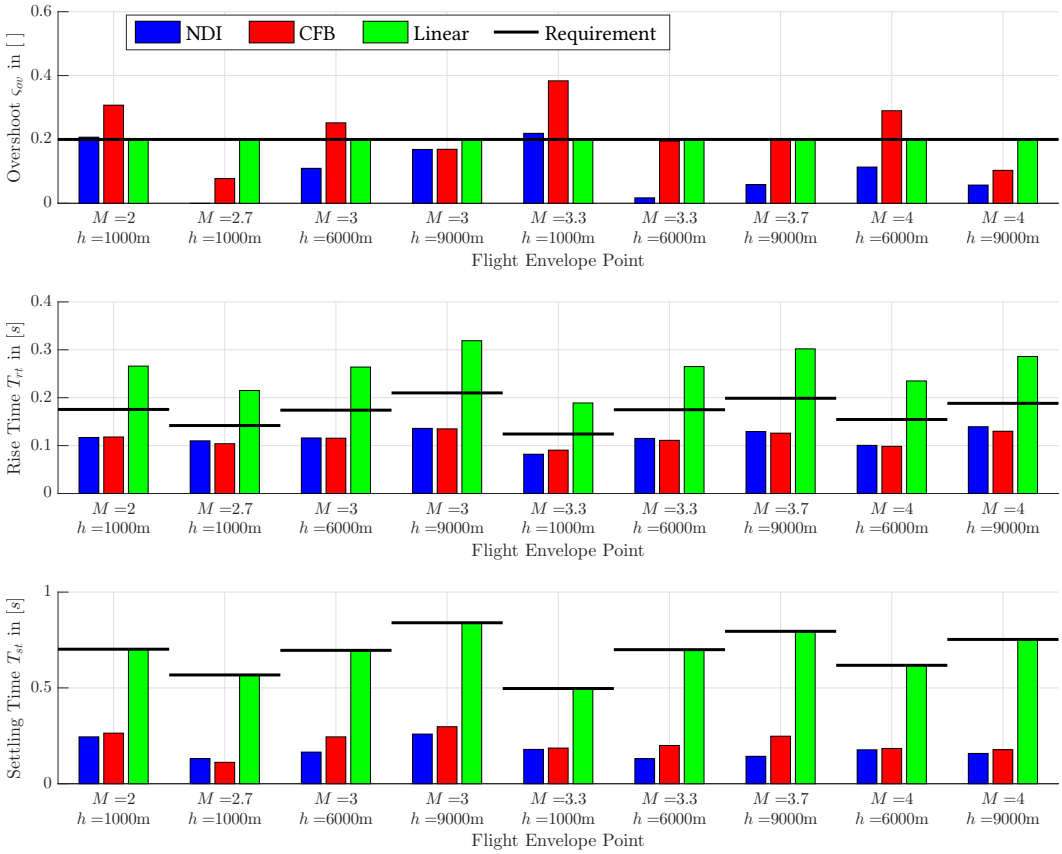

(a) Statistics of the three time-based performance metrics (overshoot, rise time, and settling time) of both acceleration channels at the selected flight envelope points for NDI, CFB, and the linear reference autopilot.

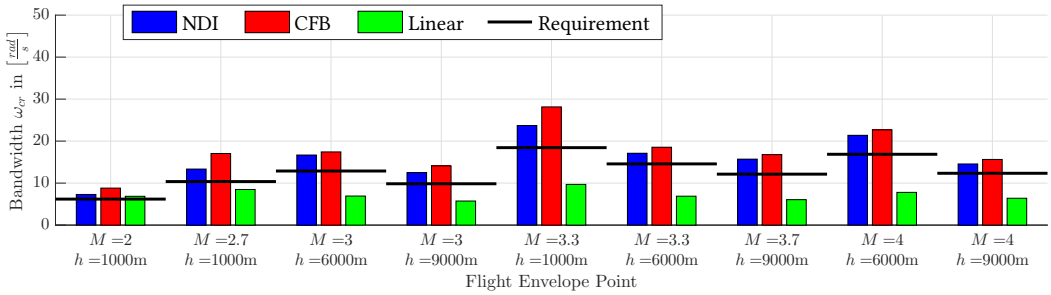

(b) Statistics of the bandwidth analysis of the longitudinal channel at the selected flight envelope points for NDI, CFB, and the linear reference autopilot.

Figure 6.6: Statistics of the performance analysis based on nonlinear simulation and linearized closed-loop transfer function.

From fig. 6.6 it can be concluded that the modular and generic layout approach presented in chapter 5 led to a closed-loop behavior of both baseline autopilots which is in line with the NFRs (see section 5.1.2). Due to the calculation of the frequency and damping parameters in (6.2b), the linear closed-loop reference system matches with the overshoot and settling time boundary as described in (6.2). Considering the two nonlinear autopilots (labeled with NDI and CFB), only the overshoot criteria is violated at a small number of flight envelope points. Both nonlinear baseline autopilots (NDI

and CFB) exhibit significantly faster closed-loop responses in each criteria over the entire flight envelope compared to the linear closed-loop reference system. This is concluded by smaller rise times T_{rt}, smaller settling times T_{st}, and a broader closed-loop bandwidth, which is indicated by the larger crossover frequency ω_{cr} (see fig. 6.6b). By comparing the overshoot metric (see fig. 6.6a), it becomes obvious that the superior performance of the nonlinear autopilots (NDI and CFB) is to the detriment of higher overshoot tendency.

Considering only the two nonlinear approaches, the NDI baseline control law lead to less overshoot and reduced settling times while exhibiting similar rise time characteristics compared to the CFB architecture.

All in all, both nonlinear autopilots exhibit superior performance behavior compared to the linear closed-loop reference characteristics. At (almost) all considered flight envelope points the challenging performance requirements (see section 5.1.2) are fulfilled. The minor differences in overshoot and bandwidth characteristics can be balanced by including the filter parameters of CFB within the parameter optimization process (avoided here due to uniform interface of optimization algorithm).

6.1.2 Robustness Evaluation

Since both baseline autopilots are designed and parametrized to fulfill the robustness requirements under nominal conditions, the concepts of sensitivity, phase, and gain margin is applied to the closed-loop baseline autopilot.

Figure 6.7 depicts the evaluated sensitivity function (5.82) in steady state flight condition across the selected flight envelope points including the upper limit of the sensitivity magnitude $|S_{a_z,max}(j\omega)|$.

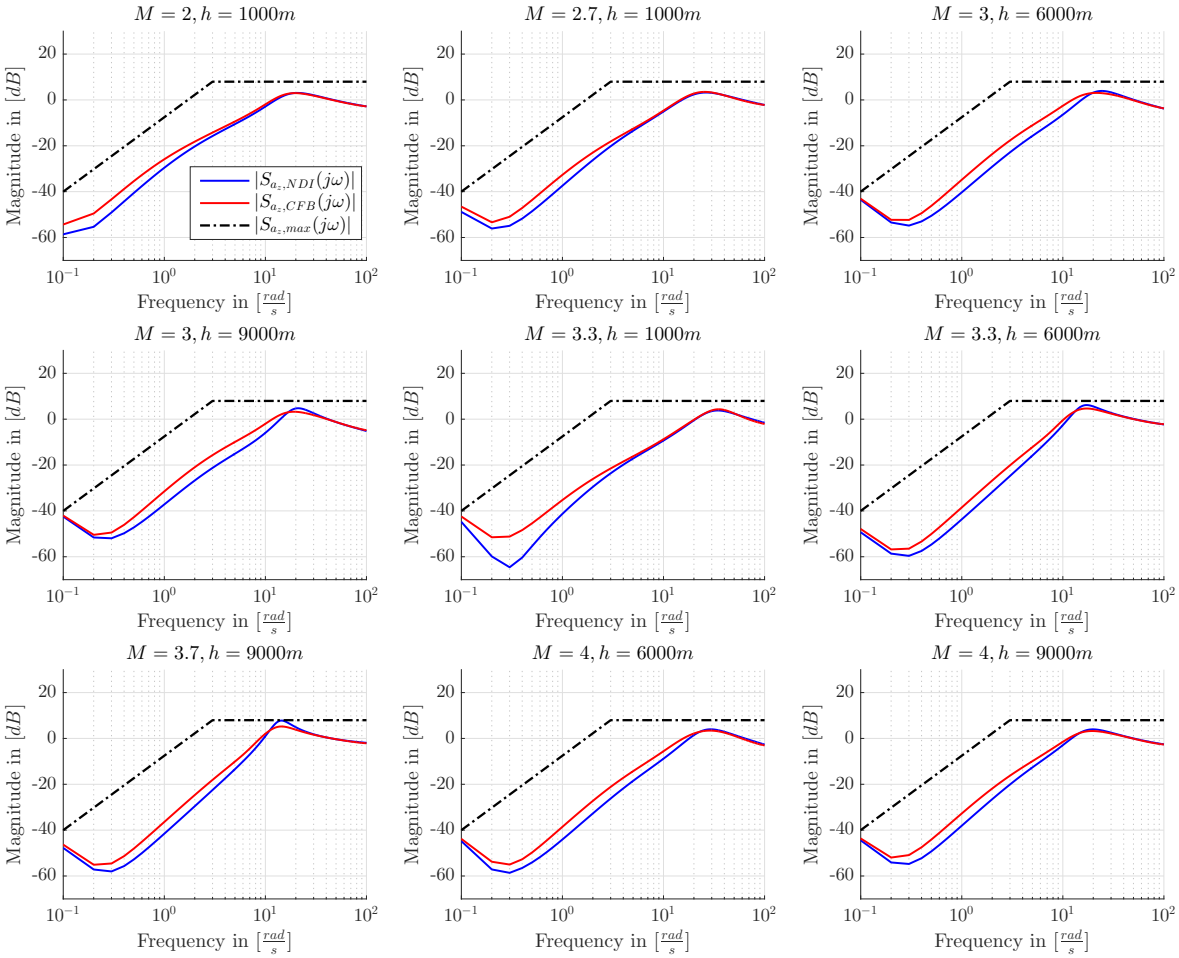

Figure 6.7: Magnitudes of the sensitivity function $S_{a_z}(j\omega)$ at the selected flight envelope points for NDI and CFB baseline autopilots.

According to fig. 6.7 the parametrization (see section 5.5.1.3) of both approaches is perfectly in line with the required disturbance attenuation. The gain curve characteristics of $|S_{a_z,NDI}(j\omega)|$ exhibits less magnitude compared to $|S_{a_z,CFB}(j\omega)|$ for frequencies below $f < 10\frac{rad}{s}$. The remaining curve progression is almost identical. This fact leads to the conclusion that the NDI baseline controller exhibits a superior disturbance attenuation.

Besides the principle of sensitivity, phase PM and gain margin GM constitute another metric to quantify the robustness of a controlled system. Gain and phase margin provide information about how much phase lag and additional gain a linear system can tolerate. The reader is referred to [85] for detailed information. For a complete assessment of robust stability using phase and gain margin, the input (actuator) and output (sensor) of the plant has to be considered as a source of possible uncertainty and delay. Therefore, phase and gain margin are calculated on two separate loop openings: between control output and actuator (*actuator cut*) and at the plant's output (*sensor cut*) constituting the control variable used for feedback. A schematic of those two openings is shown in fig. 6.8. The linear transfer functions characterizing the open-loop system at actuator and sensor opening are denoted as $G_{\eta,ol}(s)$ and $G_{a_{z,m},ol}(s)$, respectively.

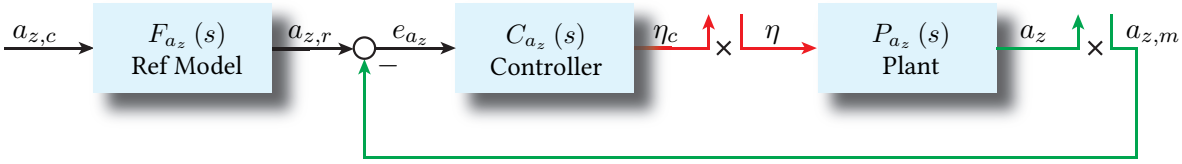

Figure 6.8: Linear basic SISO feedback loop with actuator (red) and sensor (green) loop openings.

The statistics of the phase and gain margin for sensor and actuator loop opening are illustrated in fig. 6.9 and fig. 6.10, respectively.

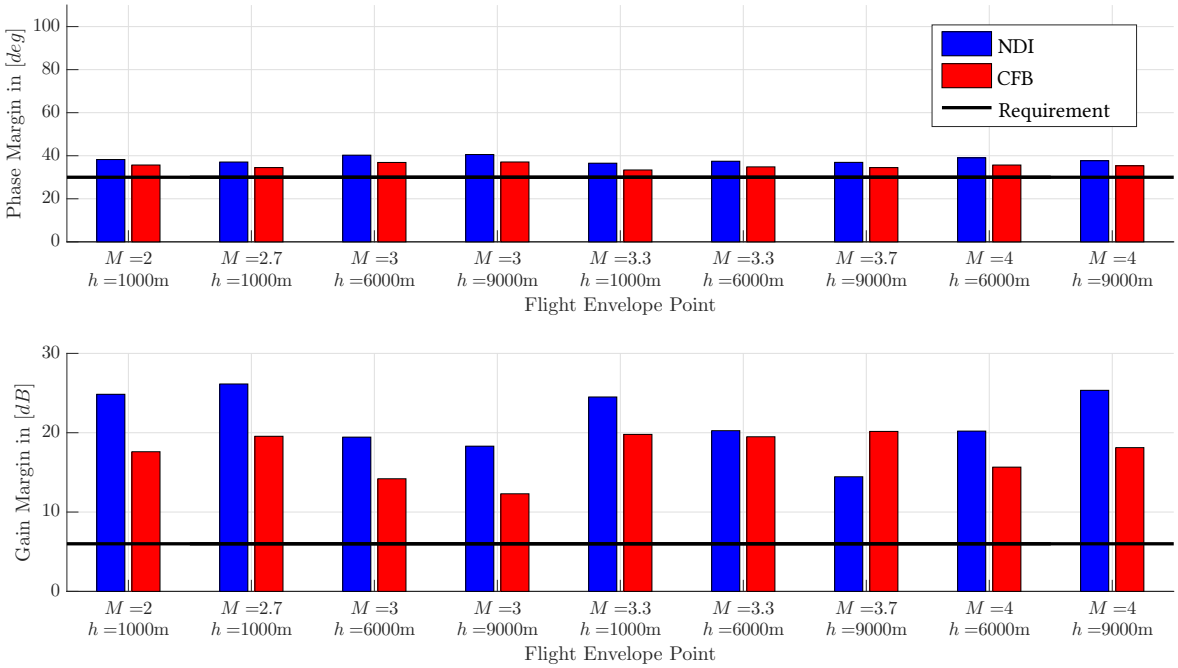

Figure 6.9: Statistics of phase and gain margin (actuator cut) of the longitudinal channel at the selected flight envelope points for the NDI-based and CFB-based autopilot.

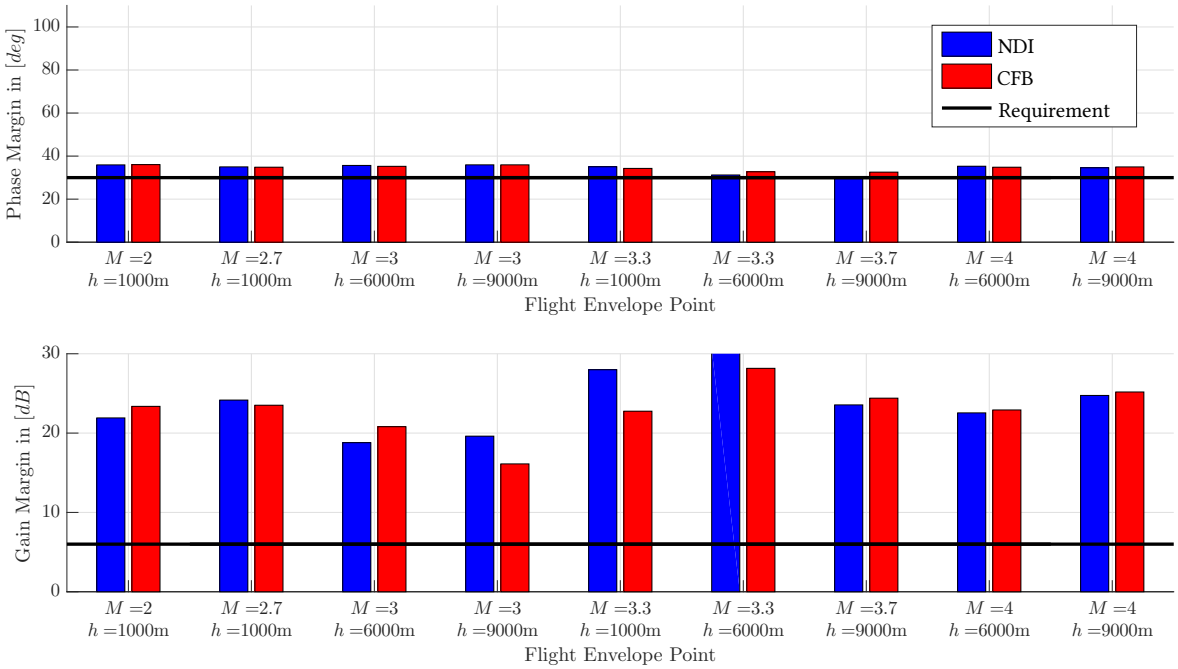

Figure 6.10: Statistics of phase and gain margin (sensor cut) of the longitudinal channel at the selected flight envelope points for the NDI-based and CFB-based autopilot.

With exception of small number of outliers, which could be traced back to numerical issues in linearizing the nonlinear system, both baseline autopilots fulfill the respective robustness requirement (NFR_8) across the entire flight envelope. The remarkable large gain margin in comparison to the narrow phase margin, for both control designs at both openings, lead to the conclusion that each closed-loop system is less sensitive to uncertainties occurring at input and output as to delays of sensor and actuator signals. The trend of a more robust closed-loop characteristics of the NDI approach compared to CFB is confirmed by considering the phase and gain margins in figs. 6.9 and 6.10.

Besides the aforementioned gain margin (see figs. 6.9 and 6.10), the time delay margin obtained from the linear model constitutes a common measure of the closed-loop sensitivity with respect to delays in the system input path. This important robust stability measure quantifies the maximum allowable time delay between autopilot and actuator a closed-loop system can tolerate. The evaluation of the time delay margin across the selected flight envelope points is depicted in fig. 6.11.

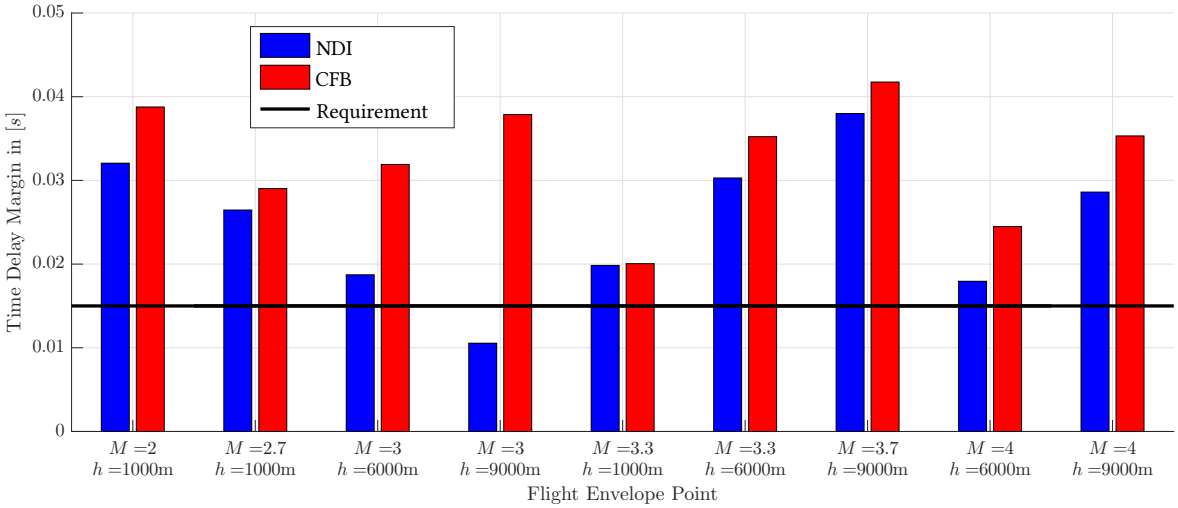

Figure 6.11: Statistics of time delay margin (sensor cut) of the longitudinal channel at the selected flight envelope points for NDI and CFB.

From fig. 6.11 it can be deduced that the CFB-based autopilot provides a higher tolerance of delays within the control signal compared to the NDI version.

This section is concluded by investigating the impact of the virtual IMU location $x_{IMU,P}$, denoting the distance between the IMU and the virtual point P (see section 5.3.1), with respect to the robustness metrics. Based on the extensive analysis of the missile's minimum phase characteristics in section 5.3.1, this parameter is selected as constant ($x_{IMU,P} = 1.3m$) over the entire flight envelope. In order to investigate how variations in the location of P influences the robustness properties of the closed-loop system, the aforementioned metrics (sensitivity analysis, gain, and phase margins) are calculated for a distance ranging between the nominal value $x_{IMU,P} = 1.3m$ and $x_{IMU,P} = 2.6m$. Since the qualitative characteristics of the effect is independent of the considered baseline autopilot, the evaluations are based on the NDI approach. The magnitude $|S_{a_z,NDI}(j\omega)|$ of the sensitivity function $S_{a_z,NDI}(j\omega)$ and the phase PM and gain margins GM at the missile's input and output for different distances $x_{IMU,P}$ are depicted in fig. 6.12 and fig. 6.13, respectively.

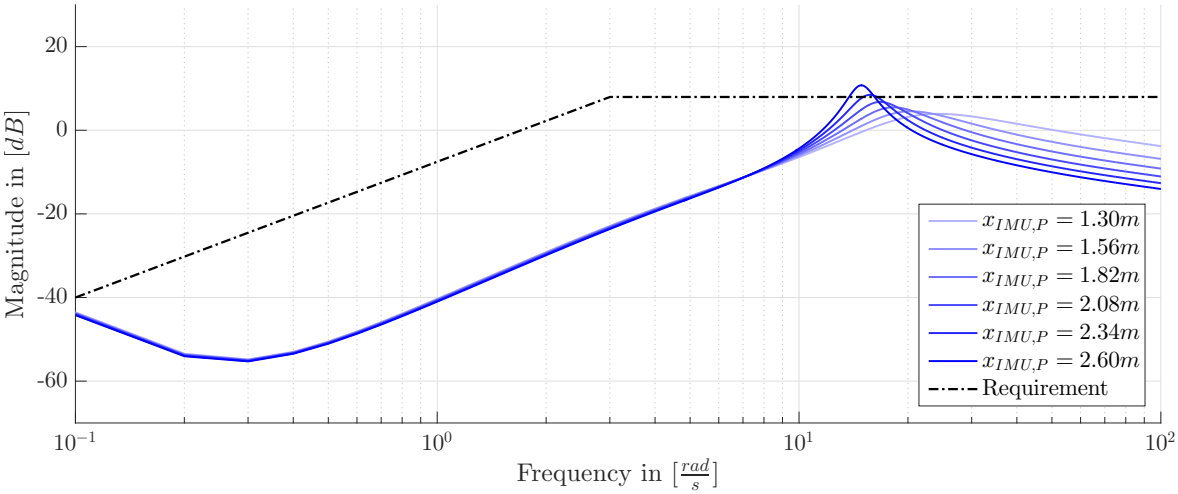

Figure 6.12: Magnitudes of the sensitivity function $S_{a_z}(j\omega)$ for different virtual IMU locations $x_{IMU,P}$ evaluated at the flight envelope point $M = 3$, $h = 6km$ for the NDI baseline autopilot.

Increasing the distance between the IMU and P lead to a reduction of the sensitivity crossover frequency and an increase of the maximum magnitude (see fig. 6.12).

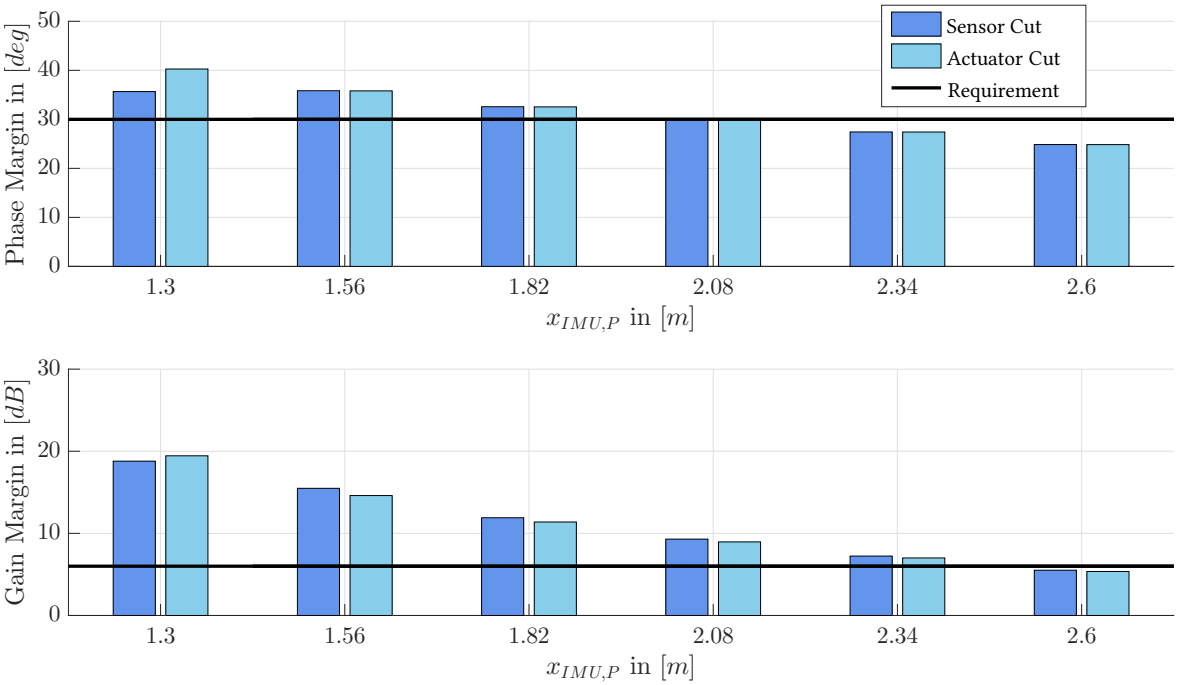

Figure 6.13: Statistic of phase and gain margin for different virtual IMU locations $x_{IMU,P}$ of the longitudinal channel at the flight envelope point $M = 3$, $h = 6km$ for the NDI autopilot.

From fig. 6.13 it becomes obvious that with increased distance $x_{IMU,P}$ phase and gain margin at the sensor and actuator location decreases.

It can therefore be concluded from fig. 6.12 and fig. 6.13 that an increase in $x_{IMU,P}$ lead to less

robustness of the closed-loop system.

6.1.3 Summary of Baseline Autopilot Evaluation and Analysis

Within this section a detailed performance (section 6.1.1) and robustness analysis (section 6.1.2) are conducted for the two baseline approaches including the novel structure of the nonlinear reference model. Since the parameter optimization for both autopilot versions is based on identical metrics, a comparison regarding general characteristics and trends between the NDI and CFB approach is feasible.

The results show that the undertaken design decision lead to closed-loop systems which are in line with the robustness requirement and outperform the stringent performance requirements.

In order to demonstrate the benefit of the nonlinear control strategies within the baseline autopilots in terms of performance a linear closed-loop system is considered as reference. The purpose of this reference system is to represent the closed-loop missile system characteristics of a conventional linear autopilot design. Thus, the layout of the linear transfer function is aligned to the settling time and overshoot performance requirements. The results in section 6.1.1 show that the nonlinear structure of the baseline autopilots (NDI and CFB) exhibits less overshoot, shorter rise, and settling times compared to the behavioral model of the linear autopilot. In terms of performance, the NDI autopilot displays less overshoot and slightly improved settling times across the entire flight envelope compared to the CFB version. Since both approaches incorporate the identical nonlinear reference model (see section 5.4), the rise time statistics reveal no significant differences. Considering the bandwidth of both autopilots (see fig. 6.6b), the CFB controlled missile exhibits increased closed-loop bandwidth compared to the NDI autopilot. The increased bandwidth of the CFB autopilot is to the detriment of larger overshoots (see fig. 6.6a). From those results, it can be assumed that under equal overshoot characteristics NDI would exhibit a larger closed-loop bandwidth compared to CFB.

In terms of sensitivity, the NDI autopilot leads to reduced magnitudes (see fig. 6.7) in low frequency ranges ($f < 10^{rad/s}$) by featuring similar crossover frequency and maximum sensitivity compared to the CFB version. Considering the robust stability metrics, it becomes obvious that the NDI control law provides increased robustness with respect to input amplification (see fig. 6.9) but reduced tolerance towards time delay (see fig. 6.11).

At last the influence of the parameter $x_{IMU,P}$ rendering the missile minimum phase (see section 5.3.1) is presented for the sensitivity, phase, and gain margin at one representative flight envelope point. From fig. 6.12 and fig. 6.13 it becomes obvious that $x_{IMU,P}$ has considerable impact on the closed-loop system regarding robust performance (sensitivity, see fig. 6.12) and stability (phase and gain margin, see fig. 6.13). This underlines the importance of an elaborate analysis phase (see section 5.3.1) in the selection of this parameter.

6.2 Analysis and Evaluation of the Adaptive Augmentation

By developing the missile autopilot architecture the purpose of the adaptive augmentation consists in the preservation of the nominal closed-loop response which is set up via the baseline autopilot. Therefore, the analysis and evaluation of the adaptive element is predominantly orientated toward robustness investigations. The assessment of the augmentation is separated in two parts: first, an analysis based on linear metrics which also investigates the influence of the parametrization with respect to robust performance and stability (section 6.2.1); and second, nonlinear simulations (sec-

tion 6.2.2) are conducted under consideration of measurement noise and extensive MC analysis at different flight envelope points.

6.2.1 Linear Robustness Analysis and Evaluation of Adaptive Augmentation

One of the advantages of the applied $\mathcal{L}_1$-Piecewise-Constant (PWC) augmentation is its linear characteristics in contrast to conventional adaptive control laws presented in [35, 52]. Therefore, the entire spectrum of linear metrics can be applied to analyze stability and robustness. For the linear analysis the metrics belonging to the *Gang of Four* are utilized [71, 129]. The Gang of Four captures the main properties concerning disturbance rejection based on the linear SISO feedback loop (see fig. 5.19). The sensitivity functions and their interpretation are listed in the following:

- the sensitivity function $S_{a_z}(s) = \frac{1}{1+P_{a_z}(s)C_{a_z}(s)}$: response of the measurement output $a_{z,m}$ to measurement noise n_{a_z}.
- the noise sensitivity function $S_{N,a_z}(s) = \frac{C_{a_z}(s)}{1+P_{a_z}(s)C_{a_z}(s)}$: response of the actuator command η_c to measurement noise n_{a_z}.
- the load disturbance sensitivity function $S_{L,a_z}(s) = \frac{P_{a_z}(s)}{1+P_{a_z}(s)C_{a_z}(s)}$: response of the measurement output $a_{z,m}$ to input disturbances noise d_{a_z}.
- the complementary sensitivity function $S_{C,a_z}(s) = \frac{P_{a_z}(s)C_{a_z}(s)}{1+P_{a_z}(s)C_{a_z}(s)}$: response of the actuator command η_c to input disturbances noise d_{a_z}.

The reader is referred to [119] for a more detailed explanation and interpretation of those four transfer functions.

6.2.1.1 Comparison of Adaptive and Baseline Autopilot

For the purpose of a qualitative statement based on the Gang of Four, only the two flight envelope points $M = 2$, $h = 1km$ and $M = 4$, $h = 9km$ from fig. 6.1 are considered in the analysis. The NDI baseline autopilot is used throughout all the investigations. Results with the CFB baseline exhibit similar characteristics.

First, the magnitudes of the Gang of Four sensitivity functions are depicted in fig. 6.14 and fig. 6.15 for the different missile configurations (*slow* to *agile*) introduced in section 3.2.

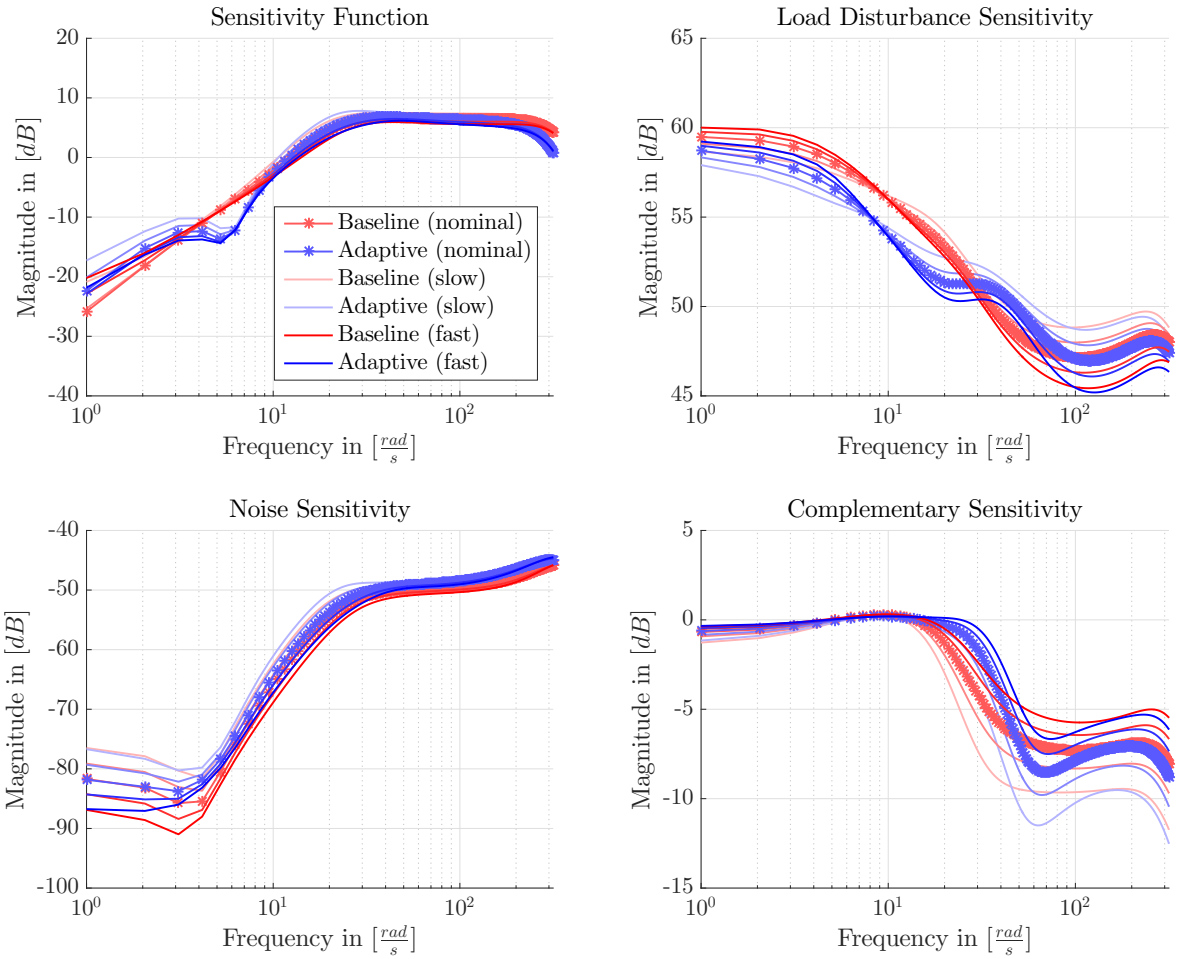

Figure 6.14: Gang of Four for NDI baseline autopilot and its $\mathcal{L}_1$-PWC augmented version considering the three different missile configurations (slow, nominal, and fast) at the flight envelope point $M = 2$, $h = 1km$.

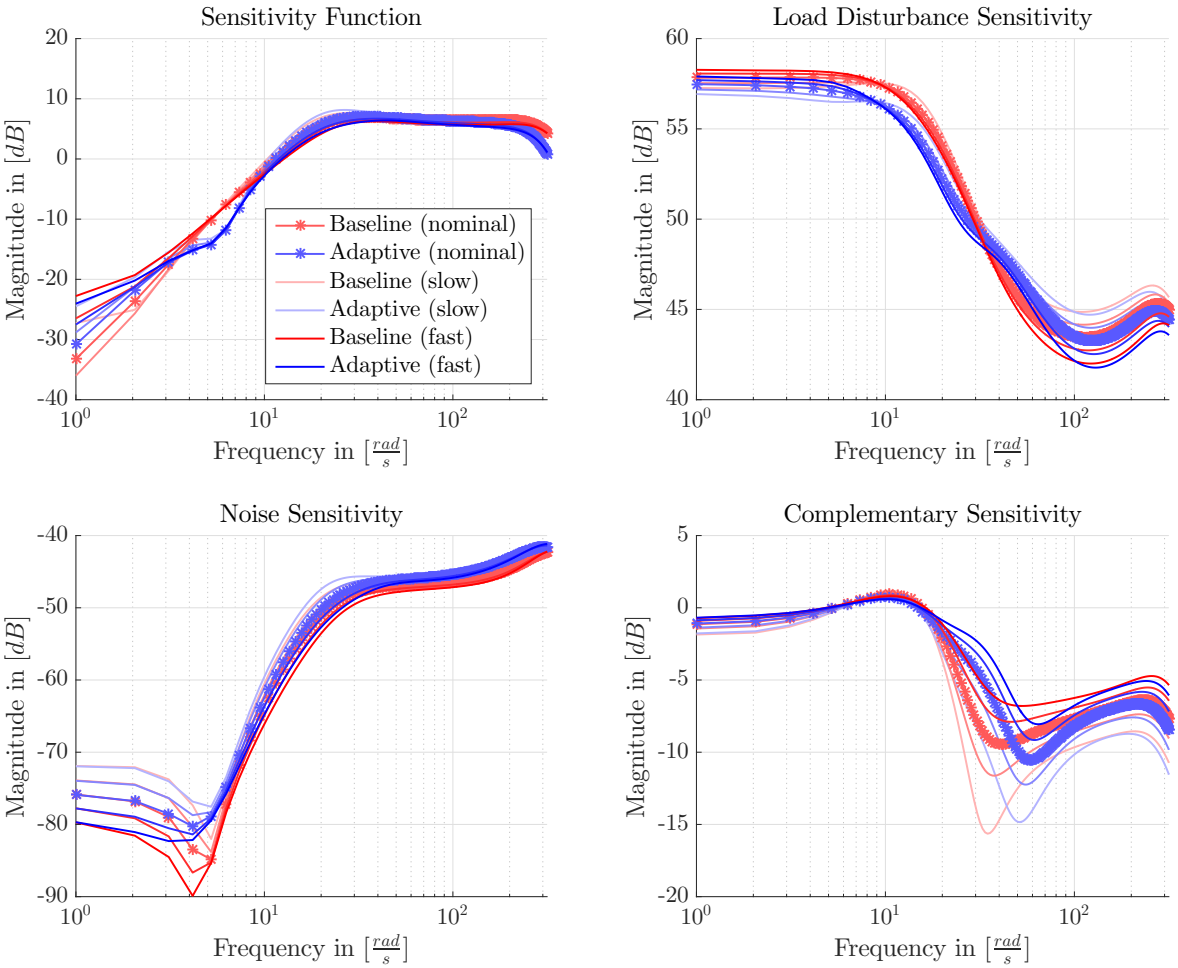

Figure 6.15: Gang of Four for NDI baseline autopilot and its $\mathcal{L}_1$-PWC augmented version considering the three different missile configurations (slow, nominal, and fast) at the flight envelope point $M = 4$, $h = 9km$.

By comparing the two Gang of Four plots in fig. 6.14 and fig. 6.15 evaluated at different flight envelope points, the curve characteristics is identical independent of the flight envelope point.

From the magnitudes in fig. 6.14 and fig. 6.15 it can be concluded that the adaptive augmentation leads to a response which is closer to the nominal response compared to the baseline autopilot. This becomes particularly obvious regarding the noise and complementary sensitivity function. Generally, the augmented autopilot (blue curves) exhibits better attenuation of input d_{a_z} and output n_{a_z} disturbances with respect to the measurement $a_{z,m}$ output (sensitivity and load disturbance sensitivity). Those enhanced robustness properties of the measurement are to the detriment of the closed-loop noise sensitivity, which exhibits minor amplifications compared to the baseline response (red curves). Considering the attenuation of the input disturbance d_{a_z} with respect to the autopilot's output η_c (complementary sensitivity), no clear trend can be identified. In some frequency ranges the augmented autopilot shows better noise rejection while in other ranges the baseline attenuates the disturbance d_{a_z} to a larger extent.

Besides the Gang of Four, the phase and gain margins of actuator and sensor cuts conducted for the nominal missile configuration are depicted in fig. 6.16 and fig. 6.17.

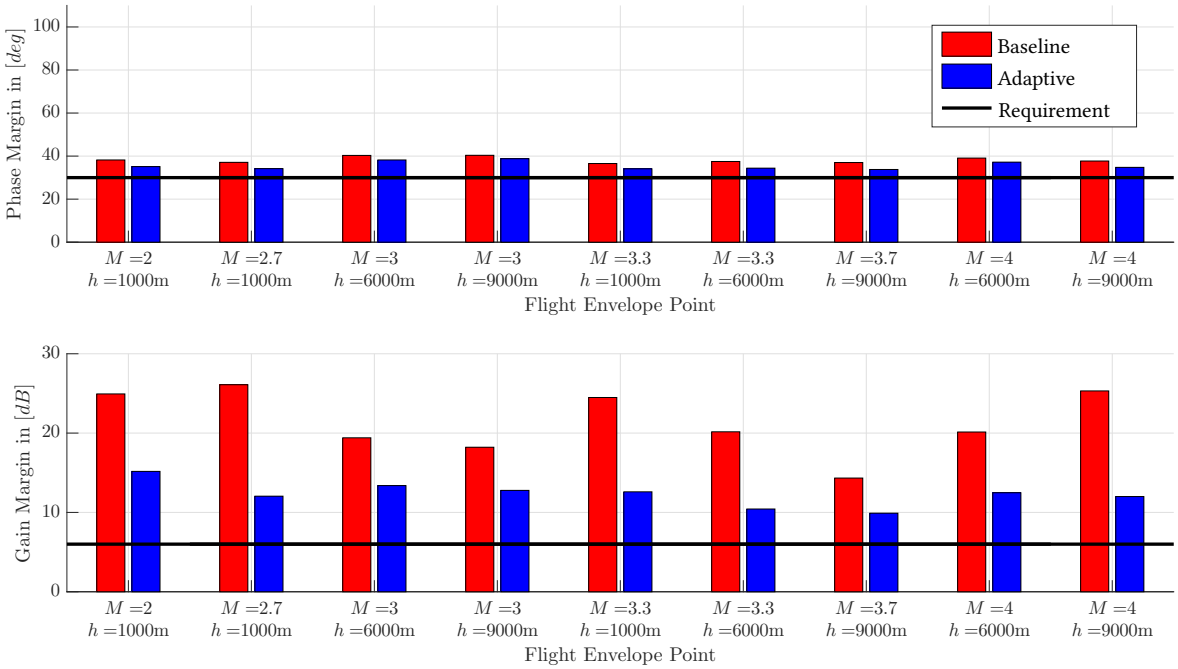

Figure 6.16: Statistics of phase and gain margin (actuator cut) of the longitudinal channel at the selected flight envelope points for the NDI-based and augmented autopilot.

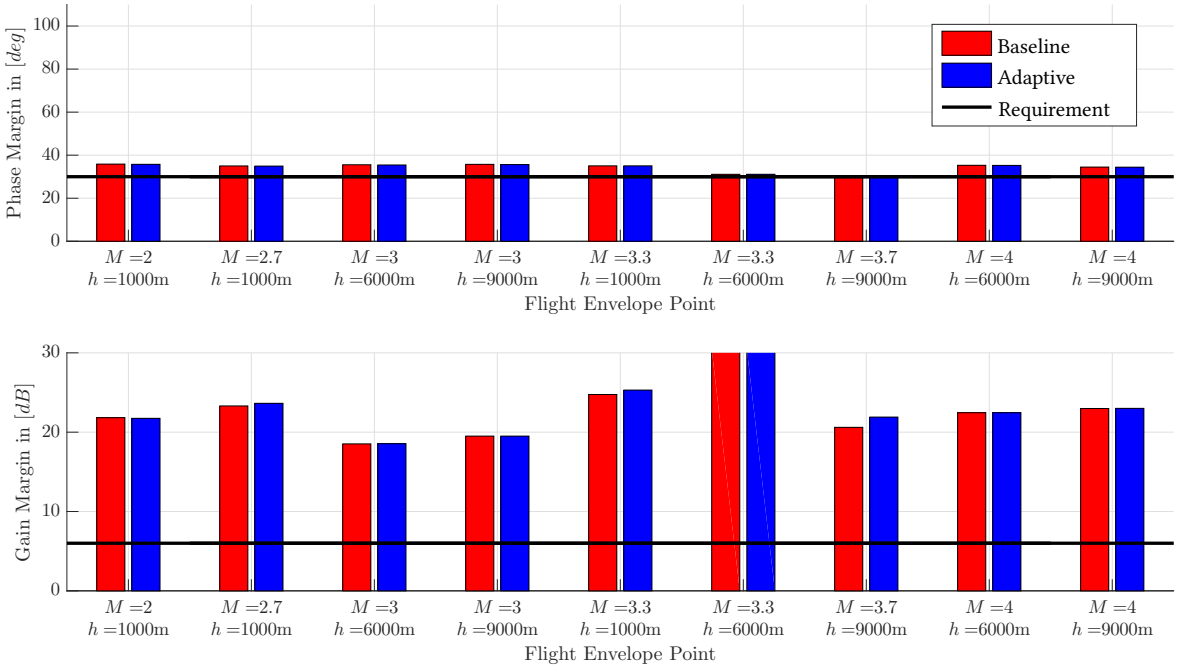

Figure 6.17: Statistics of phase and gain margin (sensor cut) of the longitudinal channel at the selected flight envelope points for the NDI-based and augmented autopilot.

Independent of the considered loop opening (sensor and actuator cuts), the phase margins of the baseline and adaptive controller exhibit minimal differences. In terms of the actuator input gain, the baseline autopilot exhibits larger margins compared to the adaptive version (see fig. 6.16). Nevertheless, the gain margins (actuator cut) of the augmented autopilot fulfill the required minimum

margin defined in NFR_8 for all flight envelope points.

The robust stability investigation of the adaptive augmentation is concluded by comparing the time delay margins at the actuator location of both autopilot versions (see fig. 6.18).

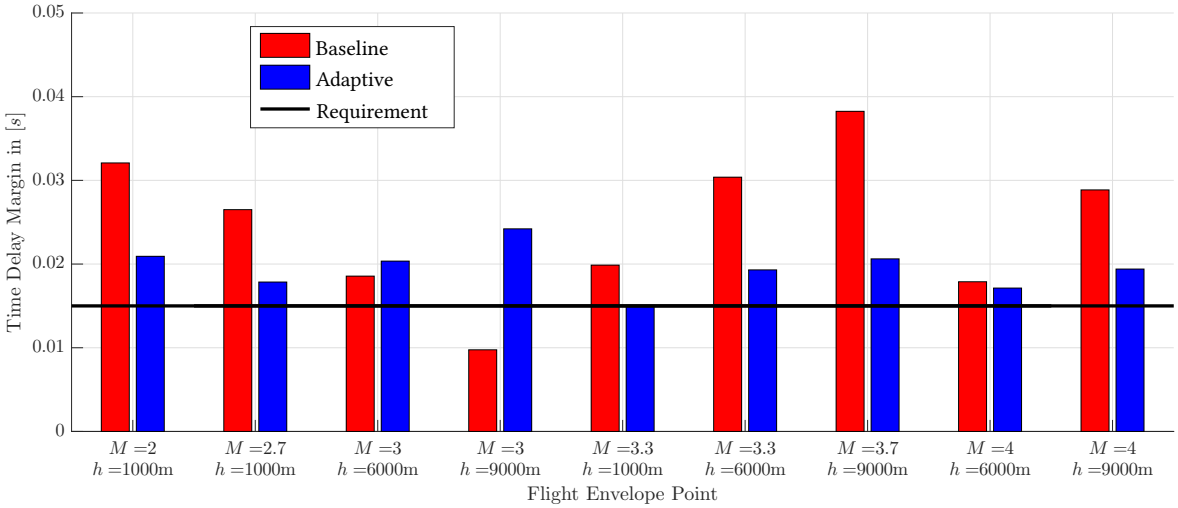

Figure 6.18: Statistics of time delay margin (sensor cut) of the longitudinal channel at the selected flight envelope points for the NDI-based and augmented autopilot.

The maximum tolerable time delay at the actuator input (estimated via the linearized open loop system) of the $\mathcal{L}_1$-PWC augmented controller is slightly decreased at the majority of the considered flight envelope points. Nevertheless, the adaptive autopilot exhibits a more uniform time delay margin across the entire flight envelope. Thus, the time delay requirement NFR_7 is fulfilled for all considered operating points.

6.2.1.2 Parameters of $\mathcal{L}_1$-PWC and their Impact on Robustness

As presented in section 5.5.2.2, the $\mathcal{L}_1$-PWC augmentation introduces additional degrees of freedom (parameters), which influence the robustness properties of the closed-loop (and open-loop) system. The key parameters of the adaptive augmentation and their impact on robustness properties are analyzed based on the aforementioned metrics belonging to the Gang of Four.

First, the gains $\boldsymbol{K}_{i,SP}$ for shaping the predictor dynamics are investigated. For this purpose all feedback gains $\boldsymbol{K}_{\boldsymbol{y},SP}$, $\boldsymbol{K}_{\boldsymbol{y},I,SP}$, $\boldsymbol{K}_{\boldsymbol{\omega},SP}$ in section 5.5.2.2 are varied simultaneously based on the nominal (labeled with $\boldsymbol{K}_{i,SP}$) parametrization by

$$\boldsymbol{K}^{*}_{i,SP} = \gamma_{SP} \cdot \boldsymbol{K}_{i,SP}. \tag{6.9}$$

The multiplier γ_{SP} ranges between $\gamma_{SP} = [0.1, \ldots, 1]$.

Figure 6.19 and fig. 6.20 illustrate the sensitivity functions obtained by variation of the state predictor feedback gains for the envelope points $M = 2$, $h = 1km$ and $M = 4$, $h = 9km$, respectively.

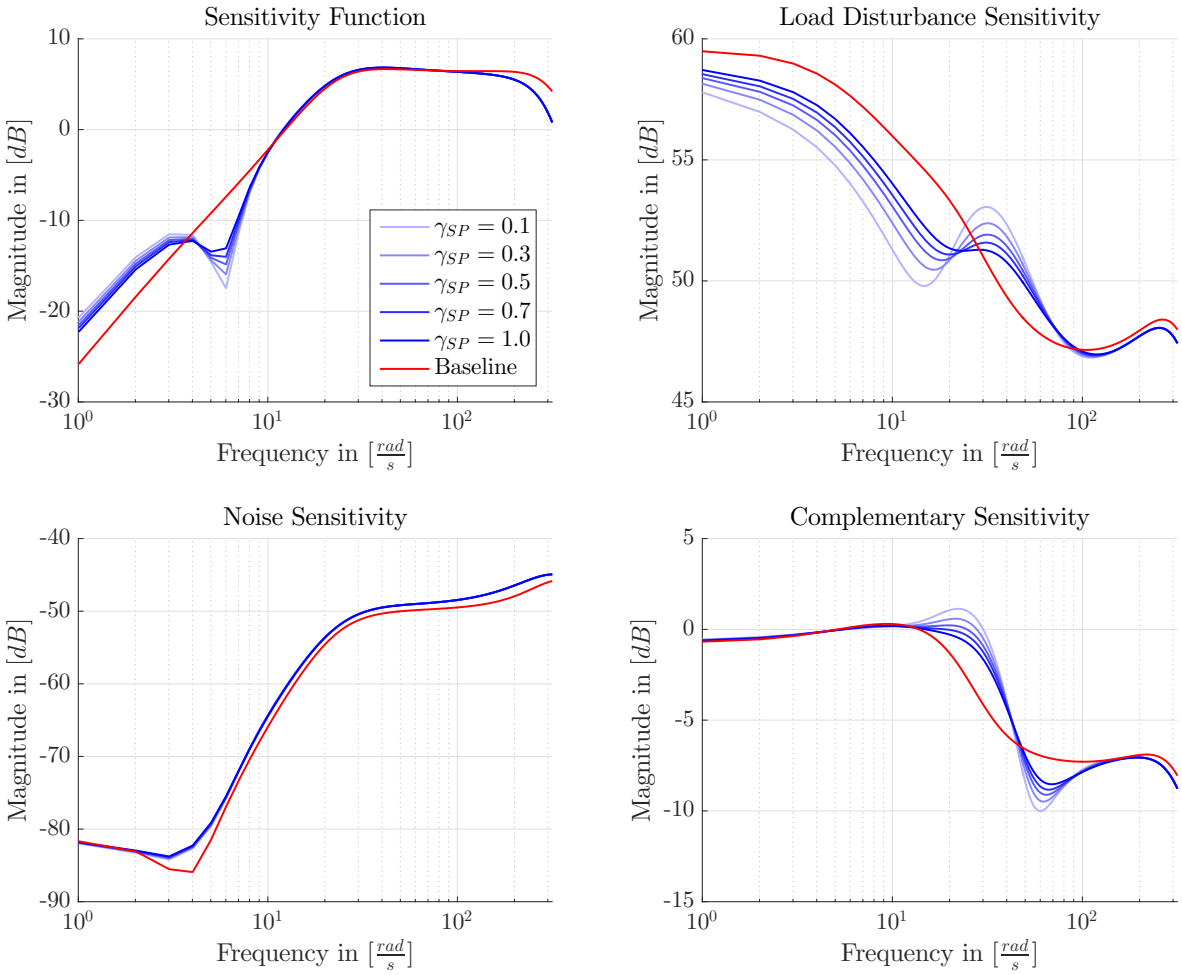

Figure 6.19: Gang of Four of the NDI baseline and its $\mathcal{L}_1$-PWC augmented version considering fractions γ_{SP} of the nominal feedback gains $\boldsymbol{K}_{i,SP}$ at the flight envelope point $M = 2$, $h = 1km$.

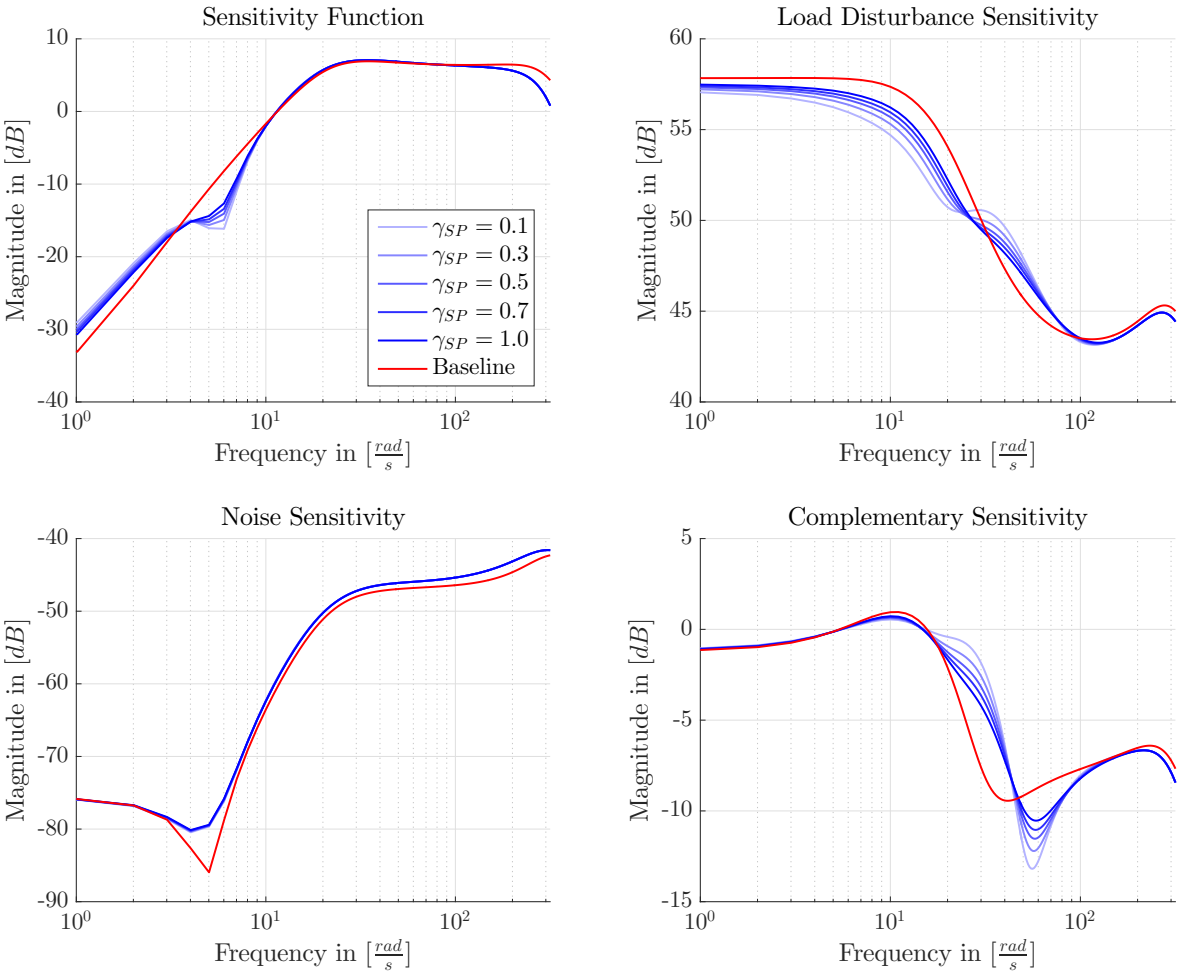

Figure 6.20: Gang of Four of the NDI baseline and its $\mathcal{L}_1$-PWC augmented version considering fractions γ_{SP} of the nominal feedback gains $\boldsymbol{K}_{i,SP}$ at the flight envelope point $M = 4$, $h = 9km$.

Figure 6.19 and fig. 6.20 indicate that the state predictor feedback gains have almost no influence on the sensitivity and noise sensitivity functions. Thus, the impact of the output disturbance n_{a_z} with respect the measurement $a_{z,m}$ and the controller output η_c can not be altered through the choice of $\boldsymbol{K}_{i,SP}$. By contrast, the load disturbance and complementary sensitivity depend strongly on the feedback gains of the prediction errors. From fig. 6.19 and fig. 6.20 it can be concluded that an increase in $\boldsymbol{K}_{i,SP}$ lead to a reduced complementary sensitivity which is closely interlinked with an increased of the load disturbances in designated frequency ranges.

As mentioned in section 5.5.2, the autopilot's sampling time T_s influences the parametrization of the adaptive update law (see (5.88)). This dependency with respect to the Gang of Four is depicted in fig. 6.21 and fig. 6.22.

Remark: It should be stressed here that the sampling time is determined by the utilized FCS and usually not arbitrarily selectable in the autopilot tuning process.

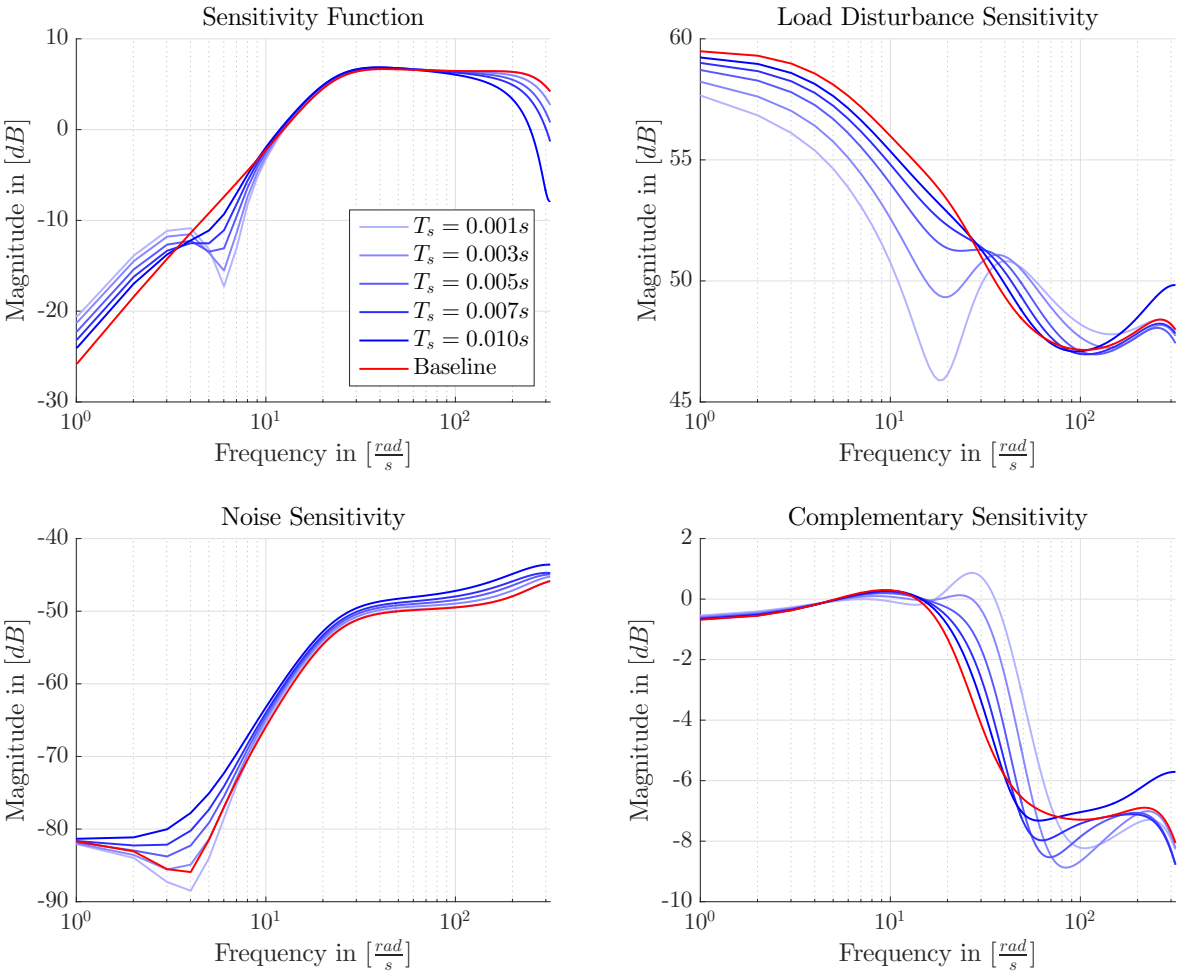

Figure 6.21: Gang of Four of the NDI baseline and its $\mathcal{L}_1$-PWC augmented version considering different sampling times T_s at the flight envelope point $M = 2$, $h = 1km$.

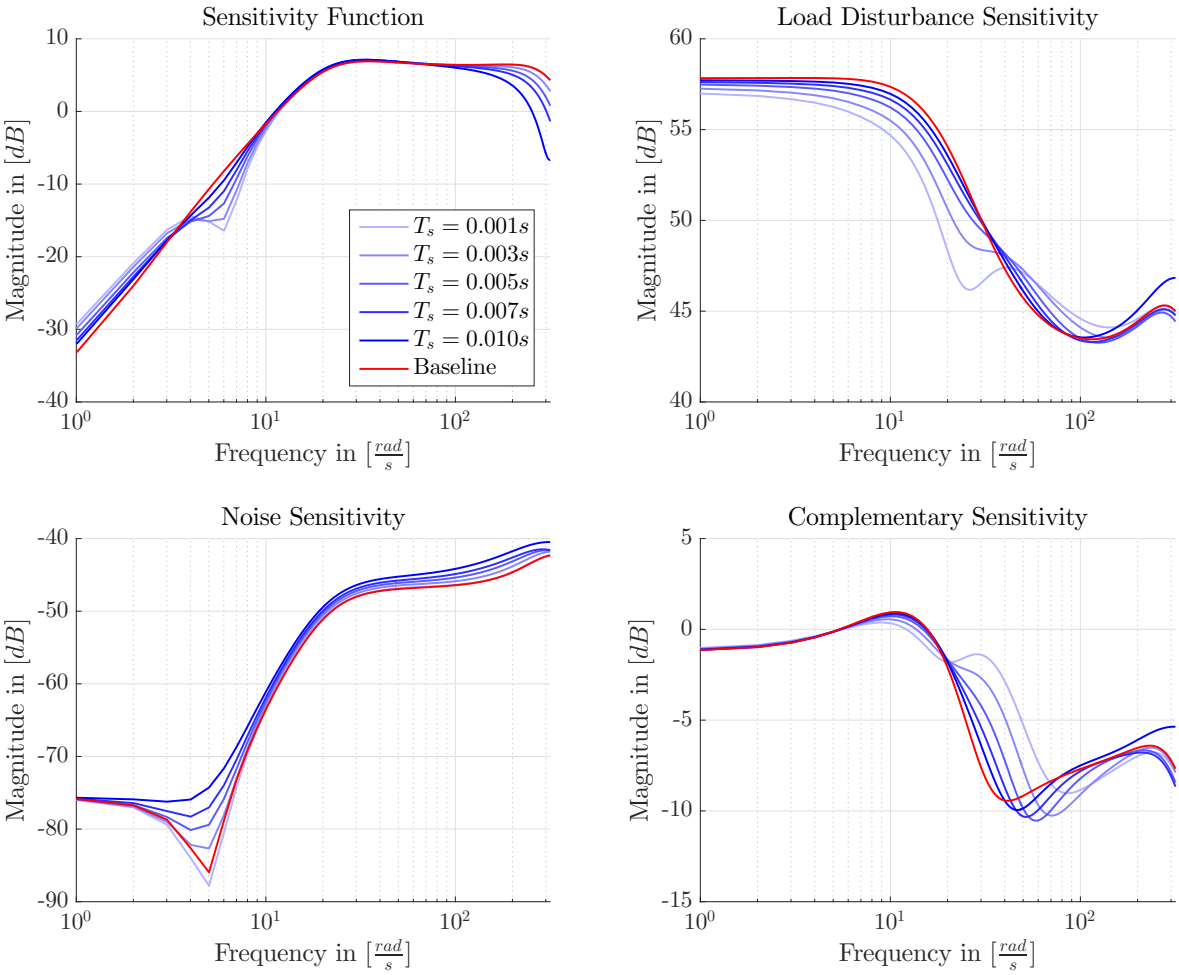

Figure 6.22: Gang of Four of the NDI baseline and its $\mathcal{L}_1$-PWC augmented version considering different sampling times T_s at the flight envelope point $M = 4$, $h = 9km$.

A larger sampling interval (increase in T_s) results in better output disturbance n_{a_z} attenuation regarding the measurement output $a_{z,m}$ (sensitivity function) and an amplification towards the control output η_c (noise sensitivity function) compared to the non-augmented autopilot. Faster sampling (smaller T_s) leads to a considerable suppressing of input disturbances d_{a_z} with respect to the output measurement $a_{z,m}$ (load disturbance sensitivity function). On the downside, fast processing times T_s increase the frequency range of the complementary sensitivity magnitude. As a consequence, the control signal η_c becomes more sensitive to input disturbances d_{a_z}.

At last, the bandwidth $\omega_{0,q}$ of the longitudinal inner loop filter $\boldsymbol{C}_q(s)$ (see table 5.2) is varied from $\omega_{0,q} = \left[3.5\frac{rad}{s}, \ldots, 35\frac{rad}{s}\right]$.

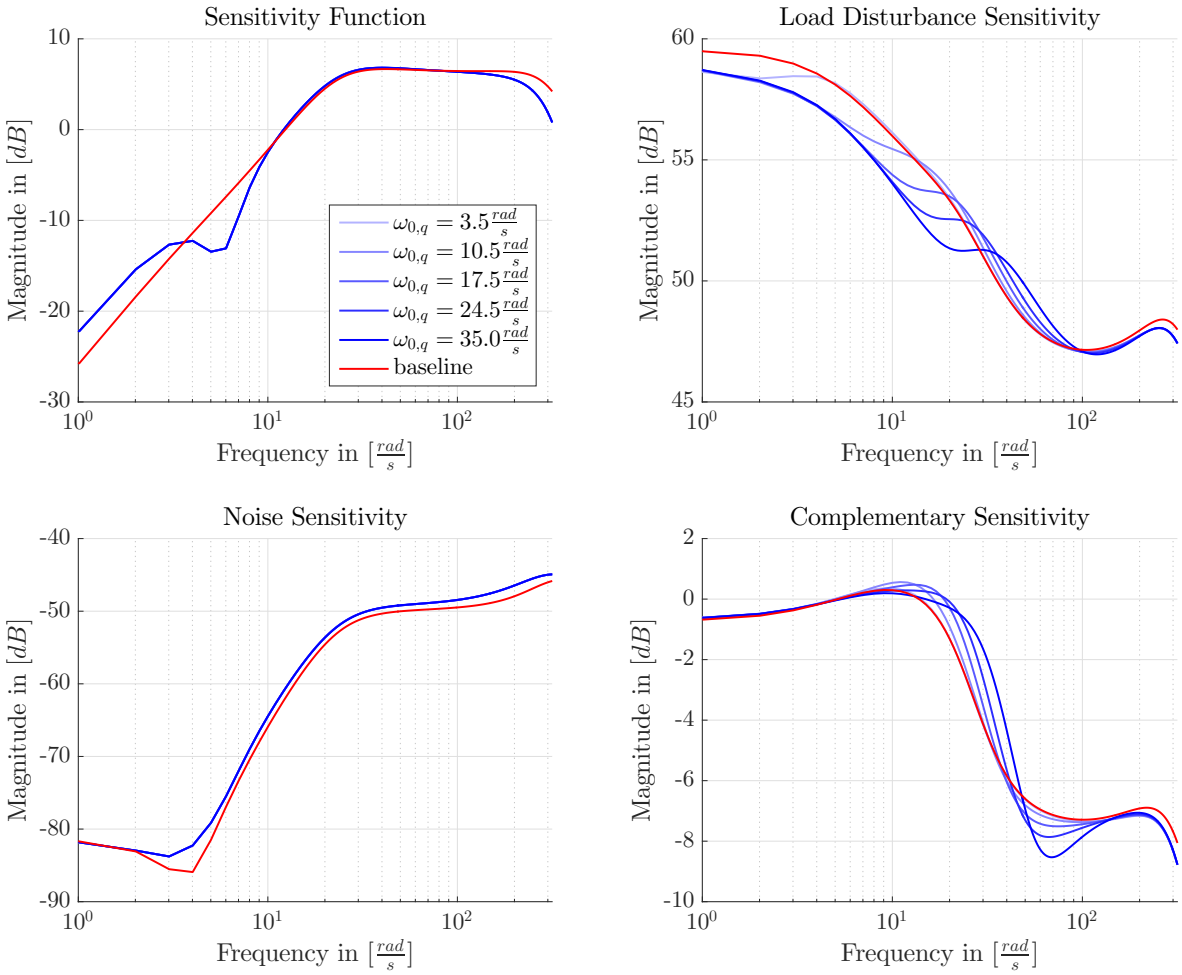

Figure 6.23: Gang of Four of the NDI baseline and its $\mathcal{L}_1$-PWC augmented version considering different inner loop filter bandwidths $\omega_{0,q}$ at the flight envelope point $M = 2$, $h = 1km$.

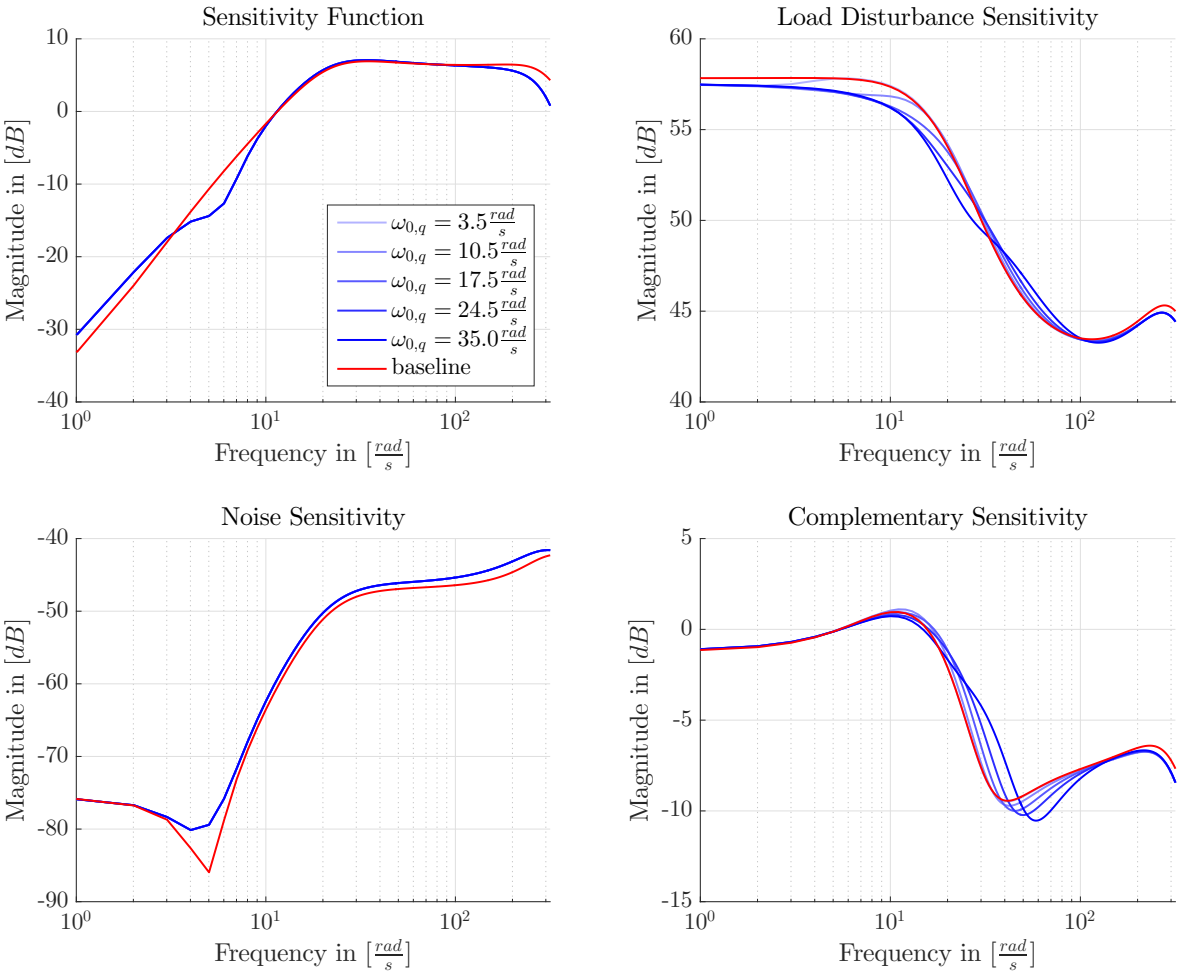

Figure 6.24: Gang of Four for NDI baseline and its $\mathcal{L}_1$-PWC augmented version considering different inner loop filter bandwidths $\omega_{0,q}$ at the flight envelope point $M = 4$, $h = 9km$.

From the magnitude plots in fig. 6.23 and fig. 6.24 it can be concluded that a variation in $\omega_{0,q}$ has no impact on the sensitivity and noise sensitivity transfer function. This characteristics is in analogy to the variation of $\boldsymbol{K}_{i,SP}$ (see fig. 6.19 and fig. 6.20).

6.2.1.3 Summary of Linear Robustness Evaluation and Analysis

The detailed linear analysis of the augmented baseline autopilot conducted within this section revealed some beneficial robustness properties compared to the non-augmented baseline version. In general, the given architecture exhibits considerable attenuation of input d_{a_z} and output disturbances n_{a_z} towards the sensor output $a_{z,m}$. The improved robustness in those transfer functions is obtained at the cost of less attenuated noise sensitivity (see section 6.2.1.1). In terms of the investigated robust stability metrics (gain, phase, and time delay margin) the results in figs. 6.16 to 6.18 based on the linearized open loop dynamics show that significant differences occur only in actuator gain and time delay margin. As discussed in [71, 130] the time delay margin is mainly driven by the selection of filter bandwidth $\boldsymbol{C_\omega}(s)$, $\boldsymbol{C_y}(s)$ and sampling time T_s of the PWC algorithm. With the selected sampling time $T_s = 0.001s$ and corresponding cut-off frequencies of the low-pass filters (see section 5.5.2.2) satisfying and uniform robust stability properties across the entire flight envelope are achieved.

Besides the general robustness comparison with respect to the baseline autopilot, the tuning parameters of the augmentation and their impact on closed-loop robustness are investigated in section 6.2.1.2. The degree of freedoms (DOFs) of the augmentation can be categorized in three groups: the sampling time T_s, the feedback $\boldsymbol{K}_{i,SP}$ of the state-predictor dynamics, and the bandwidth of the low-pass filter.

From the results in section 6.2.1.2 it is notable that only the sampling time T_s has a significant influence on all four robustness metrics (see figs. 6.21 and 6.22). Variation of the filter bandwidth $\omega_{0,q}$ and the inner/outer loop feedback gains $\boldsymbol{K}_{i,SP}$ show that these parameters have no impact on noise attenuation characteristics (see figs. 6.19, 6.20, 6.23, and 6.24). With those parameters only the transfer characteristics from input disturbances d_{a_z} to the command η_c and the sensor measurement $a_{z,m}$ can be modified. Thus, the attenuation of measurement noise depends solely on the selected sampling time T_s.

6.2.2 Nonlinear Simulations

The linear metrics in sections 6.1 and 6.2 are all evaluated by linearizing the nonlinear system with the given parametrization at the steady-state flight condition of the considered flight envelope point. Those linear metrics provide sufficient indications and are perfectly suitable for incorporating robustness metrics within parameter optimization and assessment of the closed-loop verification process. Nevertheless, for a complete performance and robustness analysis of the closed-loop missile system the conduct of nonlinear simulations are inevitable.

For investigating and analyzing the robustness of the nonlinear closed-loop via MC simulations, demanding Skid-To-Turn (STT) commands are applied. Both acceleration channels are stimulated with simultaneous step inputs over a time span of $T_{sim} = 7s$. The commanded signal of roll channel, normalized longitudinal, and normalized lateral acceleration (with respect to the step input amplitude) are depicted in fig. 6.25.

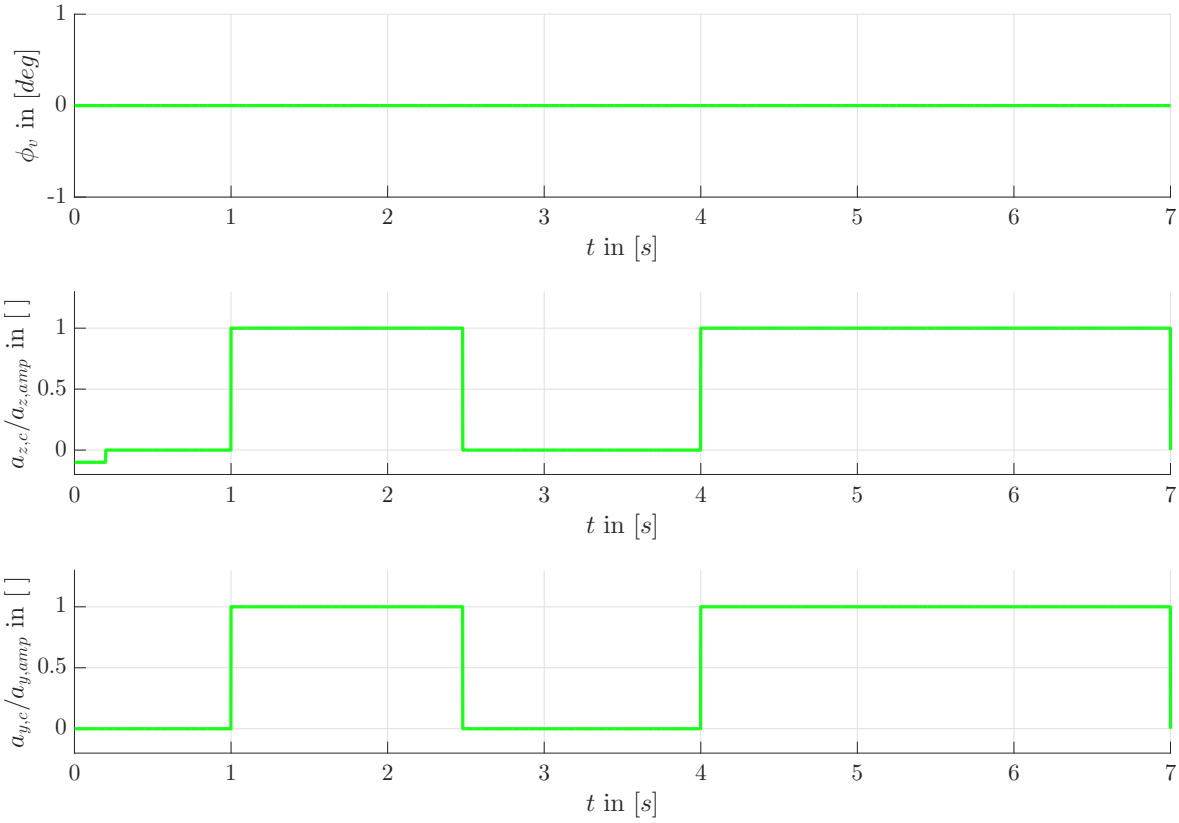

Figure 6.25: Normalized command sequence of roll, lateral, and longitudinal acceleration channel serving as stimuli for nonlinear simulations.

6.2.2.1 Measurement Noise Analysis

As explained in section 2.5.2, the measurement process of the IMU is subject to noise. For the purpose of investigating the noise sensitivity and to support the linear analysis in section 6.2.1.2, the influence of measurement noise with respect to the autopilot's output $\boldsymbol{u}_c$ (actuator command) is considered. In order to evaluate the effect of acceleration and body rate measurement noise independently, two sets of simulation are performed at the selected flight envelope points (see fig. 6.1). Each simulation set is conducted with the baseline (NDI) autopilot and the augmented baseline version. To stimulate the adaptive augmentation, all simulations realized with a defined set of parameter uncertainties.

The time responses of the adaptive and non-adaptive autopilot across the selected flight envelope points is depicted for the case of acceleration and body rate measurement noise in figs. 6.26 and 6.27, respectively.

For better illustrations of the measurement noise influence on the accumulated actuator commands $\sum_{i=1}^{3} |u_{i,c}|$, only the first step $T_{sim} = [1.4s, 2.45s]$ of the command sequence (see fig. 6.25) is depicted for IMU acceleration and body measurement noise in figs. 6.26 and 6.27, respectively. For evaluating the Root Mean Square (RMS) of each signal's noise component the smoothed version $\sum_{i=1}^{3} |u_{i,c,smooth}|$ of the autopilot's output $u_{i,c}$ is calculated [131].

From the time responses in figs. 6.26 and 6.27 it can be concluded that the peak-to-peak noise level in case of the adaptive and baseline autopilot is similar.

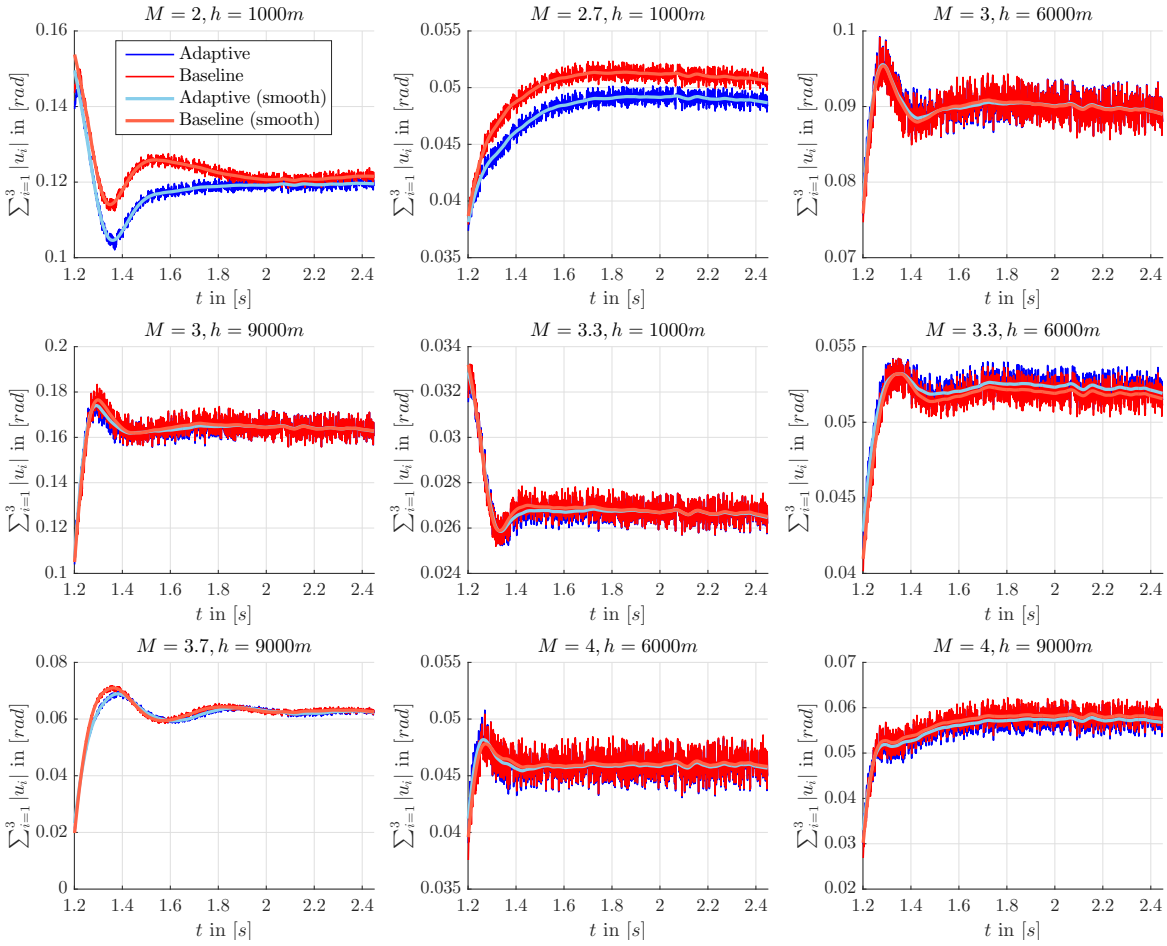

Figure 6.26: Actuator responses of the closed-loop baseline autopilot and the augmented version. Noise is applied to the IMU acceleration measurements. The plots illustrate the accumulated actuator response at the selected flight envelope points within $T_{sim} = [1.4s, 2.45s]$.

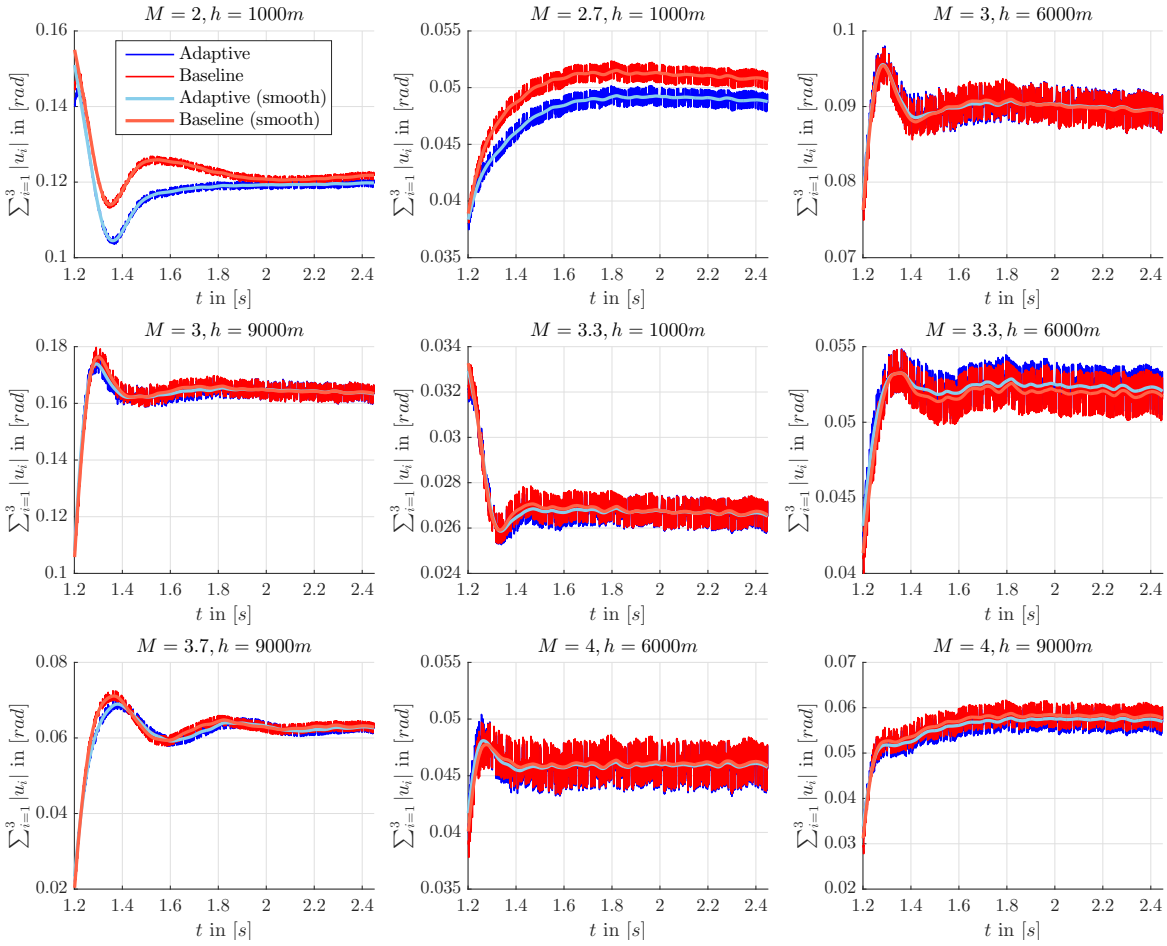

Figure 6.27: Actuator responses of the closed-loop baseline autopilot and the augmented version. Noise is applied to the IMU body rate measurements. The plots illustrate the accumulated actuator response at the selected flight envelope points within $T_{sim} = [1.4s, 2.45s]$.

To evaluate the noise component of the signals, the RMS is calculated based on the summed difference $\sum_{i=1}^{3} |u_{i,c} - u_{i,c,smooth}|$ between the actuator command $u_{i,c}$ and its smoothed version $u_{i,c,smooth}$. The statistics for acceleration and body rate sensor noise are depicted in figs. 6.28 and 6.29, respectively.

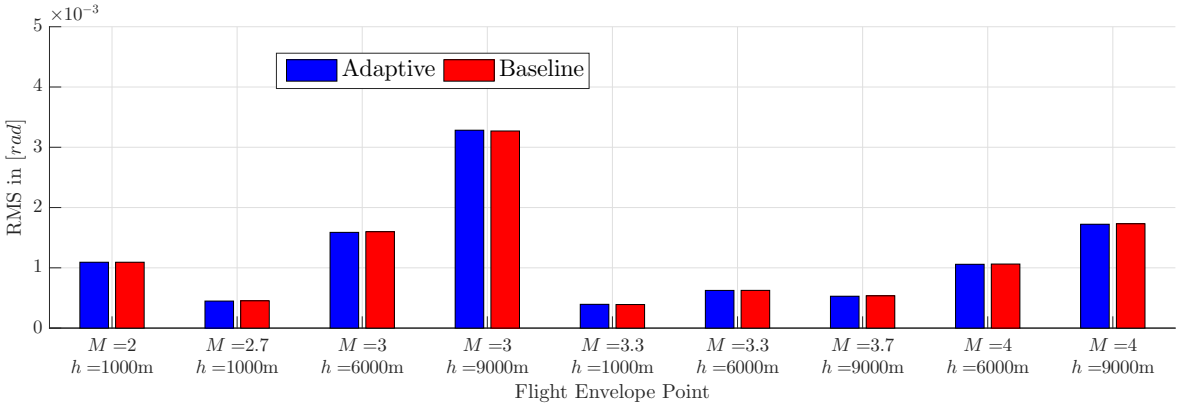

Figure 6.28: Statistics of the RMS of the actuator responses with noise applied on IMU acceleration measurements.

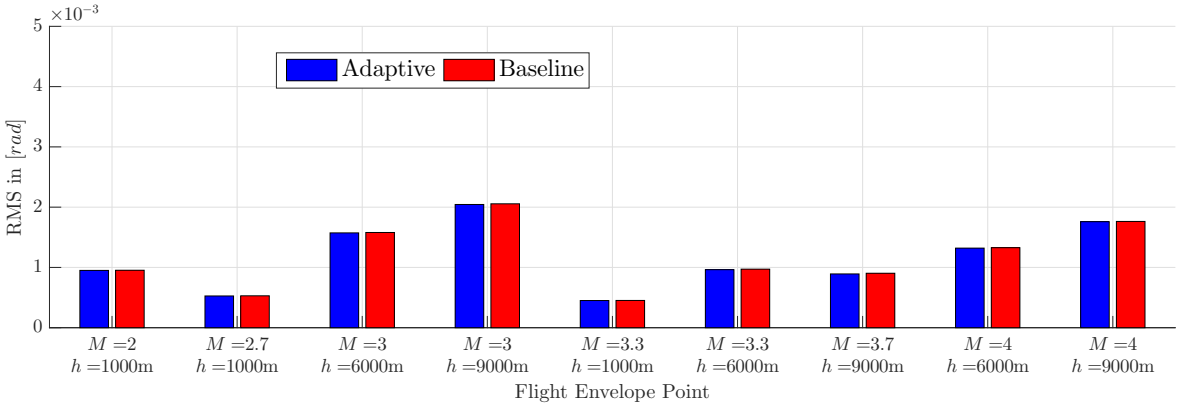

Figure 6.29: Statistics of the RMS of the actuator responses with noise applied on IMU body rate measurements.

The statistics of RMS reveal no significant difference in terms of noise attenuation between the augmented and non-augmented autopilot implementation at the considered flight envelope points. The different RMS values across the flight envelope points (figs. 6.28 and 6.29) result from numerical properties of the smoothing algorithm. Thus, the RMS used to analyze the simulation snapshot is only a metric for comparing two simulation runs at one particular operating point.

6.2.2.2 Monte Carlo Analysis

MC simulations are a standard method to evaluate models (here: tracking accuracy) over a large set of probabilistic distributed model parameters (see section 2.4) with respect to a designated cost function. MC methods are commonly applied within the verification and analysis procedure to investigate the impact of statistically distributed model parameters on the model output. Since the number of model runs for one MC simulation correlates with the number of examined parameter combinations, MC methods can lead to computational extensive simulation campaigns [132].

As discussed in section 2.4, the missile system exhibits a wide spectrum of parametric uncertainties. The ability of preserving the nominal performance even under severe plant variations (uncertainties) plays a key role within the autopilot design of high agile missile systems and is assigned in

section 5.5.2 to the $\mathcal{L}_1$-PWC element. This robust performance property of the augmented autopilot is analyzed with respect to the non-augmented baseline controller by evaluating the deviation from the nominal closed-loop response. For those investigations, the NDI autopilot is selected as the baseline control law.

Remark: the term *nominal closed-loop* designates the closed-loop missile system consisting of the baseline autopilot and the undisturbed (no uncertainties) missile dynamics.

Monte Carlo Simulations

One MC simulation campaign at a given flight envelope point comprises of $n = 1000$ runs with both autopilot configurations ($2 \cdot n = 2000$ runs per flight envelope point): the NDI baseline and the $\mathcal{L}_1$-PWC augmented version. The sequence depicted in fig. 6.25 serves as command vector for the three control channels. The amplitude of the acceleration channels is scaled with respect to the maximum achievable acceleration.

The uncertainties and disturbances defined in section 2.4 are normally distributed in each simulation run with respect to the defined limits. In order to guarantee repeatability of single runs out of the MC simulations and establish equal parametrization for both autopilot configurations, a deterministic stream of random variables is used.

Monte Carlo Evaluation Criteria

For the purpose of analyzing and quantifying robust performance properties of the augmented autopilot, both acceleration channels are evaluated considering several performance and tracking metrics:

- The truncated $\mathcal{L}_2$-norm

$$\left\| e_{a_i,nom} \right\|_{\mathcal{L}_2} = \int_{t_{eval}} \left(a_{i,m}\left(t\right) - a_{i,m,nom}\left(t\right) \right)^2 dt \tag{6.10}$$

  of the deviation $e_{a_i,nom}$ between the respective acceleration signal $a_{i,m}\left(t\right)$ and the corresponding time response $a_{i,m,nom}$ of the nominal closed-loop evaluated over the time horizon t_{eval}.

- Categorization of the acceleration signal quality $a_{i,m}$ based on three different signal regions determined by overshoot, settling time, and steady-state error requirements (see section 5.1.2) of the respective flight envelope point.
- Settling time T_{st}: considered only for signals within signal category 1 and 2.
- Rise time T_{rt}: considered only for signals within signal category 1 and 2.
- Overshoot/undershoot $\varsigma_{i,ov}$: considered only for signals within signal category 1 and 2.

The above mentioned metrics are evaluated for the time interval $t_{eval} = [4, 5.2s]$, which incorporates the second commanded step sequence (see fig. 6.25).

Monte Carlo Evaluation

Since the performed MC simulations exhibit similar characteristics for all flight envelope points in fig. 6.1, the comprehensive evaluation of the MC simulations is presented only for the flight envelope point at $M = 2$ and $h = 1km$. An acceleration of $a_{z,amp} = a_{y,amp} = 10g$ (total acceleration $\begin{bmatrix} a_{z,amp} & a_{y,amp} \end{bmatrix}^T$) is commanded to the longitudinal and lateral axes, respectively. This operating point is representative for the entire missile flight envelope. To analyze the difference between the two autopilot configurations, the cumulative distribution of each metric is depicted in addition to its (normalized) probability density.

For evaluating the ability of preserving the nominal closed-loop response, the truncated $\mathcal{L}_2$-norm (see (6.10)) is considered for both acceleration channels. In fig. 6.30 and fig. 6.31 the probability distribution and the cumulative version of $\|e_{a_i,nom}\|_{\mathcal{L}_2}$ are depicted for the baseline (red) and the adaptive augmented autopilot (blue). Both cumulative probability graphs (fig. 6.30b and fig. 6.30b) show in case of the adaptive autopilot higher probabilities that the value of $\|e_{a_i,nom}\|_{\mathcal{L}_2}$ is below a certain threshold. For example, considering the $\|e_{a_z,nom}\|_{\mathcal{L}_2}$ of longitudinal channel: 59.7% of all runs obtained with the baseline autopilot lie below $300\left[\frac{m}{s^2}\right]$, while 66.1% of the simulations obtained with the adaptive augmentation lie below the same threshold (see fig. 6.30b). In case of the lateral acceleration (see fig. 6.31b), 57.1% of the runs obtained with the baseline autopilot and 66.1% of the simulations based on the augmented autopilot lie below $300\left[\frac{m}{s^2}\right]$.

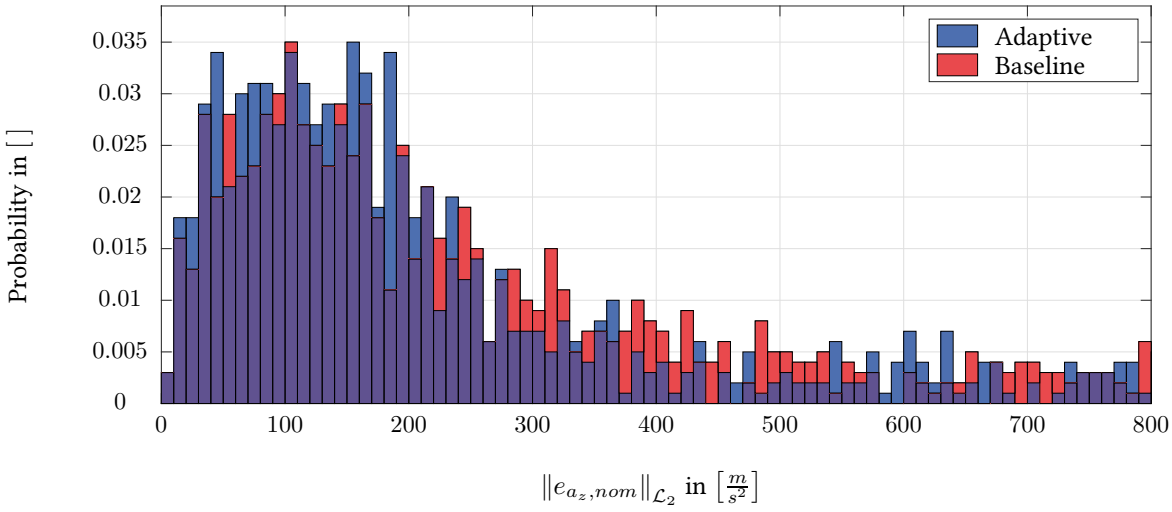

(a) Probability of the $\mathcal{L}_2$-norm of the error $a_{z,m} - a_{z,m,nom}$.

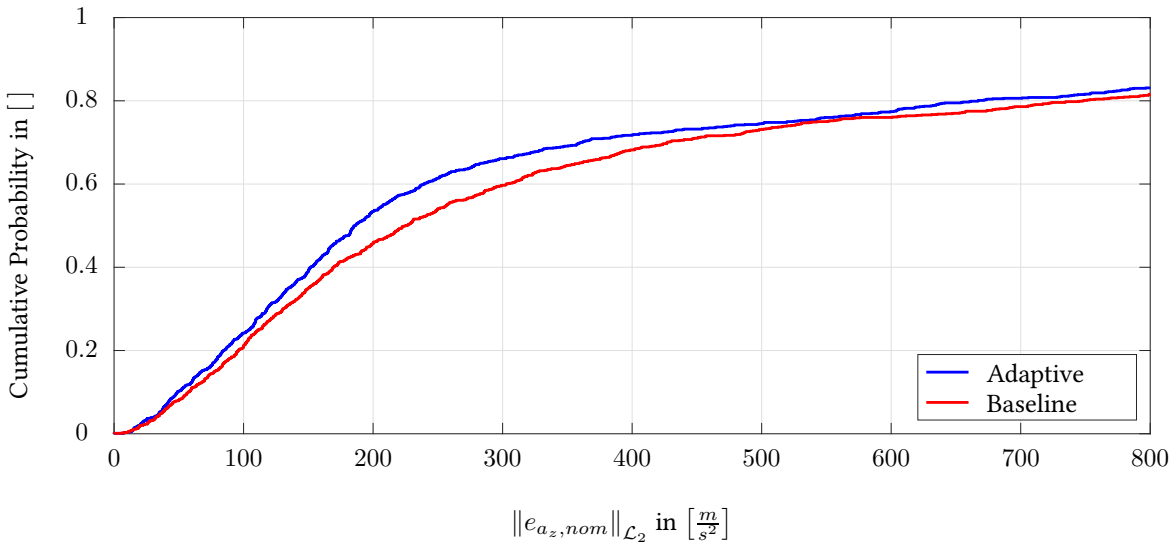

(b) Cumulative Probability of the $\mathcal{L}_2$-norm of the error $a_{z,m} - a_{z,m,nom}$.

Figure 6.30: Probability and cumulative probability of the $\mathcal{L}_2$-norm of the error $a_{z,m} - a_{z,m,nom}$ obtained from MC analysis executed at the flight envelope point $M = 2$, $h = 1km$.

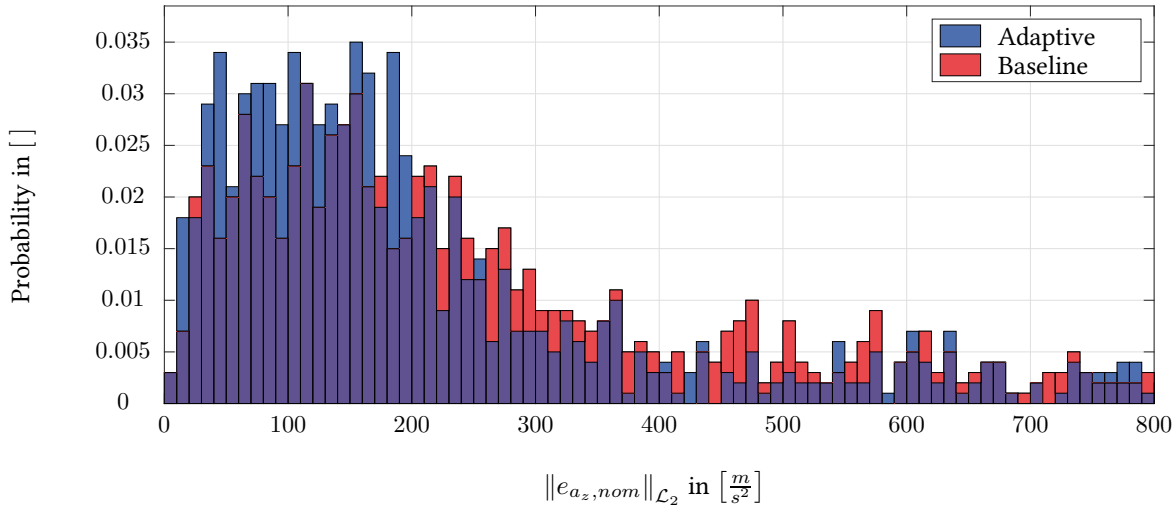

(a) Probability of the truncated $\mathcal{L}_2$-norm of the error $a_{y,m} - a_{y,m,nom}$.

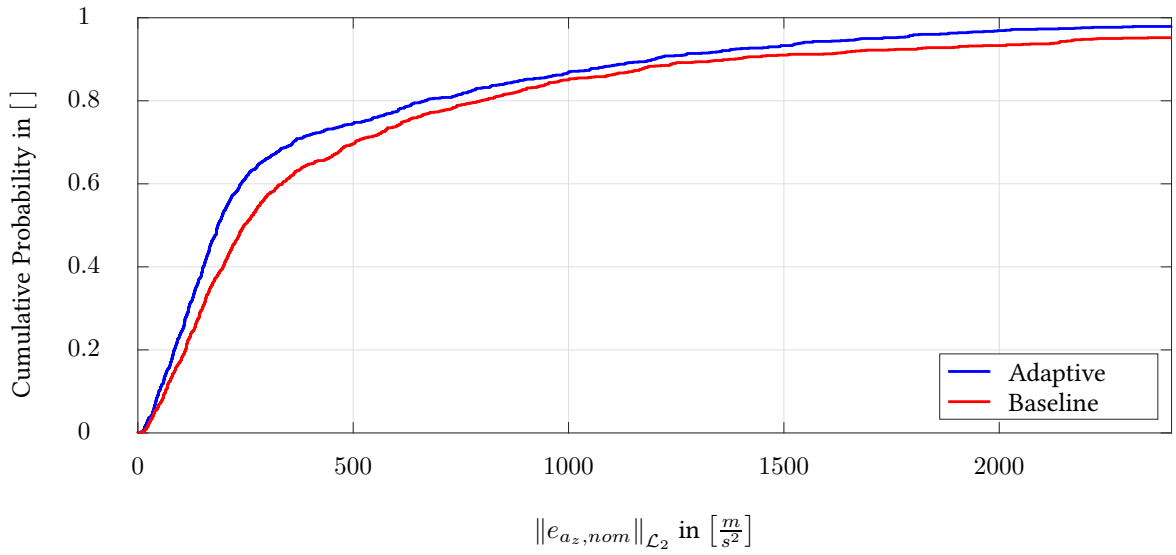

(b) Cumulative Probability of the $\mathcal{L}_2$-norm of the error $a_{y,m} - a_{y,m,nom}$.

Figure 6.31: Probability and cumulative probability of the truncated $\mathcal{L}_2$-norm of the error $a_{y,m} - a_{y,m,nom}$ obtained from MC analysis executed at the flight envelope point $M = 2$, $h = 1km$.

Based on different settling time, overshoot, and defined steady state error levels, the four different regions (fourth region is outside the others) for categorizing the closed-loop performance are shown in fig. 6.32.

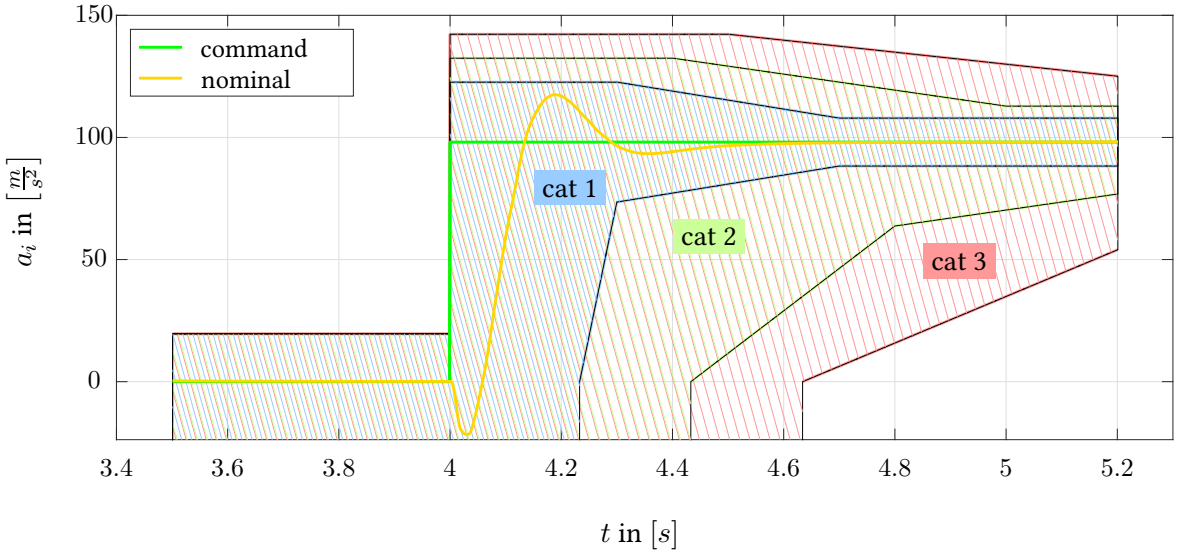

Figure 6.32: Signal regions for categorizing step responses at the flight envelope point $M = 2$, $h = 1km$.

In order to show the proportions of the categories with respect to the acceleration trajectories, both, the commanded acceleration and its nominal closed-loop response are illustrated in fig. 6.32. The regions are defined by the time intervals $t_{eval,st}$, $t_{eval,ov}$ and signal ratios $\varsigma_{i,st}$, $\varsigma_{i,ov}$ for settling time and overshoot (with respect to the acceleration amplitude $a_{i,amp}$), respectively. These parameters, which are in line with the performance requirements section 5.1.2, are listed in table 6.1.

Criteria	Cat 1	Cat 2	Cat 3
$t_{eval,st}$ in $[s]$	$[4.7, 5.2]$	$[5.0, 5.2]$	5.3
$t_{eval,ov}$ in $[s]$	$[4, 4.3]$	$[4, 4.4]$	$[4, 4.5]$
$\varsigma_{i,st}$ in $[\,]$	0.03	0.08	0.12
$\varsigma_{i,ov}$ in $[\,]$	0.25	0.35	0.45

Table 6.1: Parameters defining the regions for categorizing signal quality of longitudinal and lateral acceleration time responses.

For the purpose of verification of the automated categorization routines and to show the different signal trajectories fulfilling category 1, the respective responses of the MC simulations are exemplarily depicted in fig. 6.33.

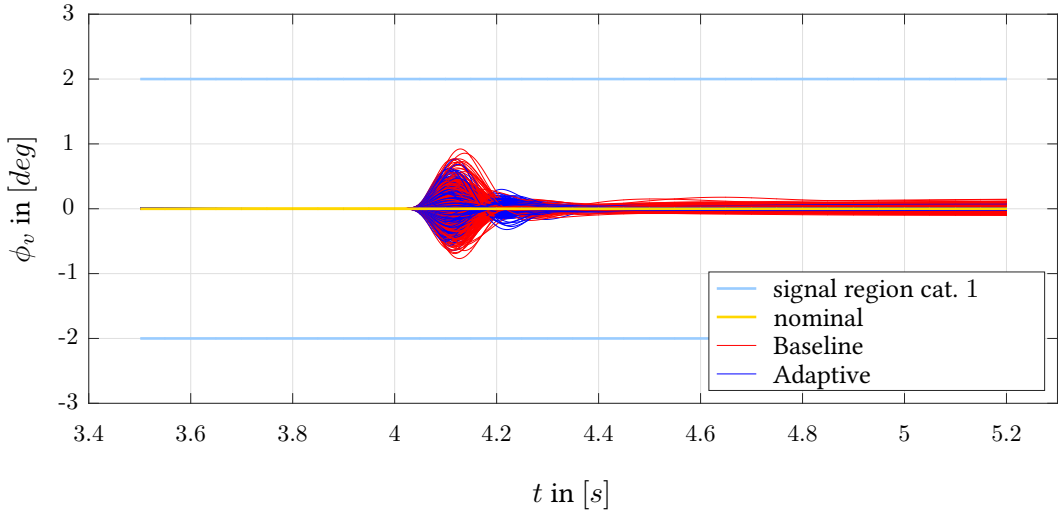

(a) Responses of MC analysis for roll channel (category 1).

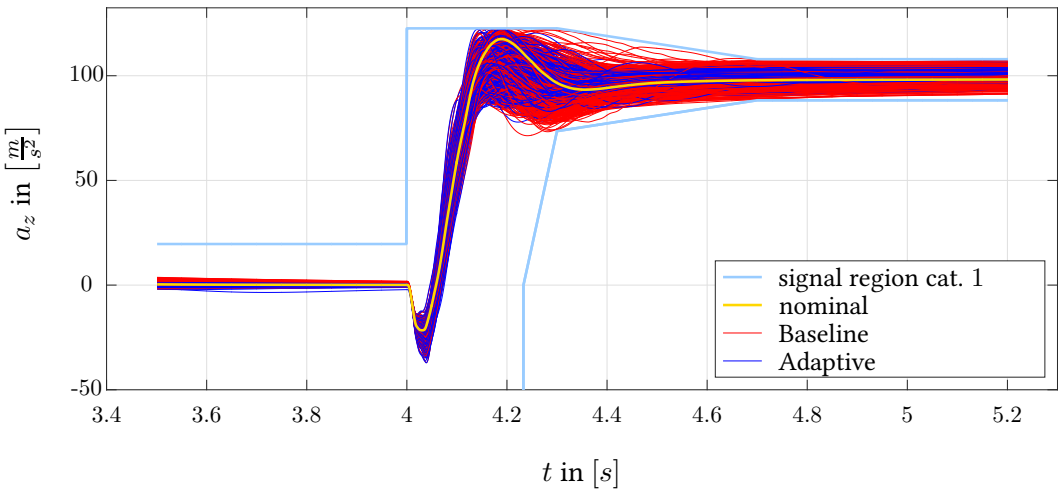

(b) Responses of MC analysis for pitch channel (category 1).

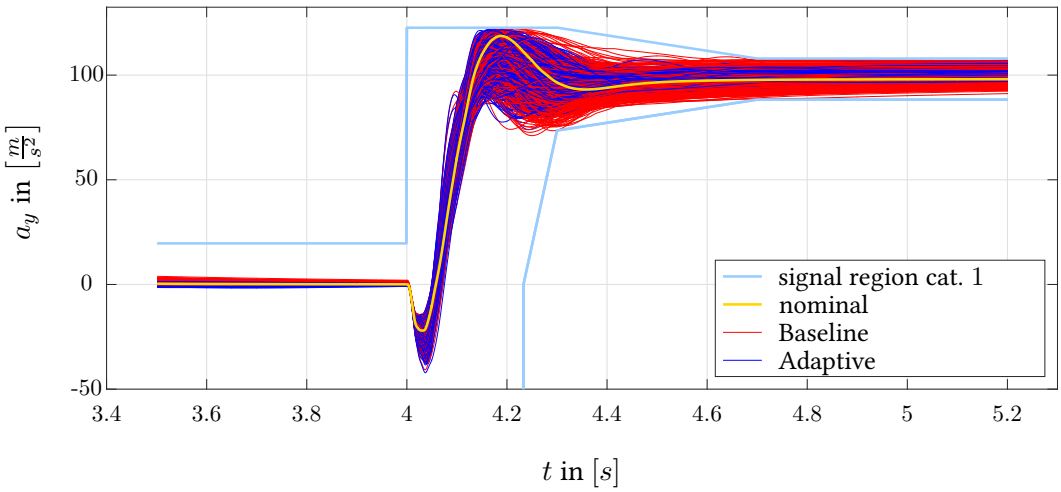

(c) Responses of MC analysis for yaw channel (category 1).

Figure 6.33: Responses of MC analysis of baseline (NDI) and augmented autopilot at the flight envelope point $M = 2, h = 1km$ fulfilling signal category 1; nominal closed-loop response (yellow) serves as a reference.

Categorizing each MC simulation run into the categories of fig. 6.32 lead to the probability distributions and the cumulative probability graphs of the four categories shown in fig. 6.34 and fig. 6.35.

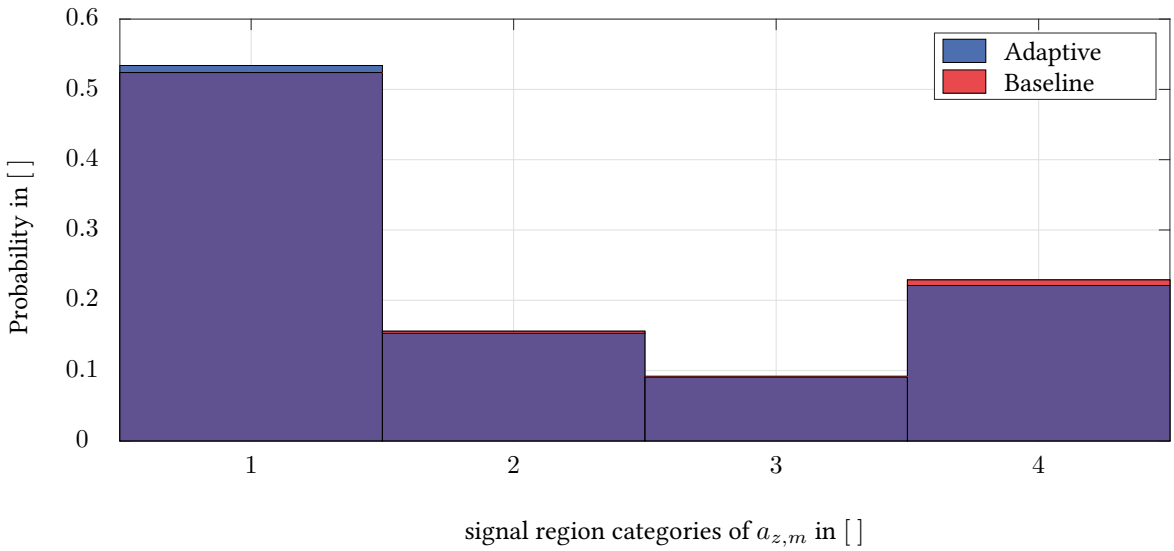

(a) Probability of the signal region category for the response of the longitudinal acceleration channel $a_{z,m}$

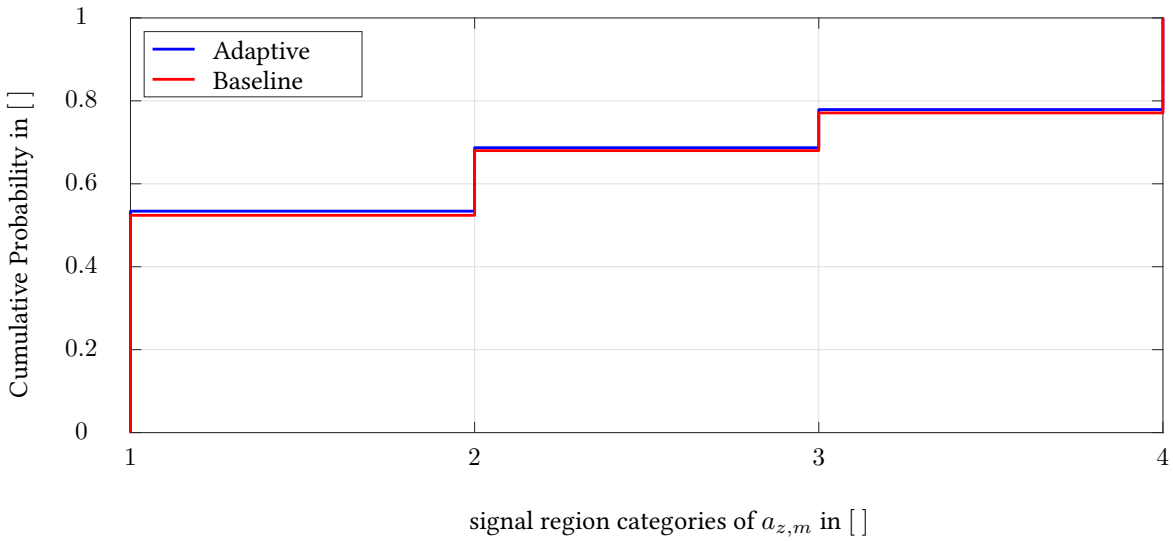

(b) Cumulative probability of the signal region categories for the longitudinal acceleration channel $a_{z,m}$

Figure 6.34: Probability and cumulative probability of the signal region categories of the longitudinal acceleration channel $a_{z,m}$ obtained from MC analysis executed at the flight envelope point $M = 2$, $h = 1km$.

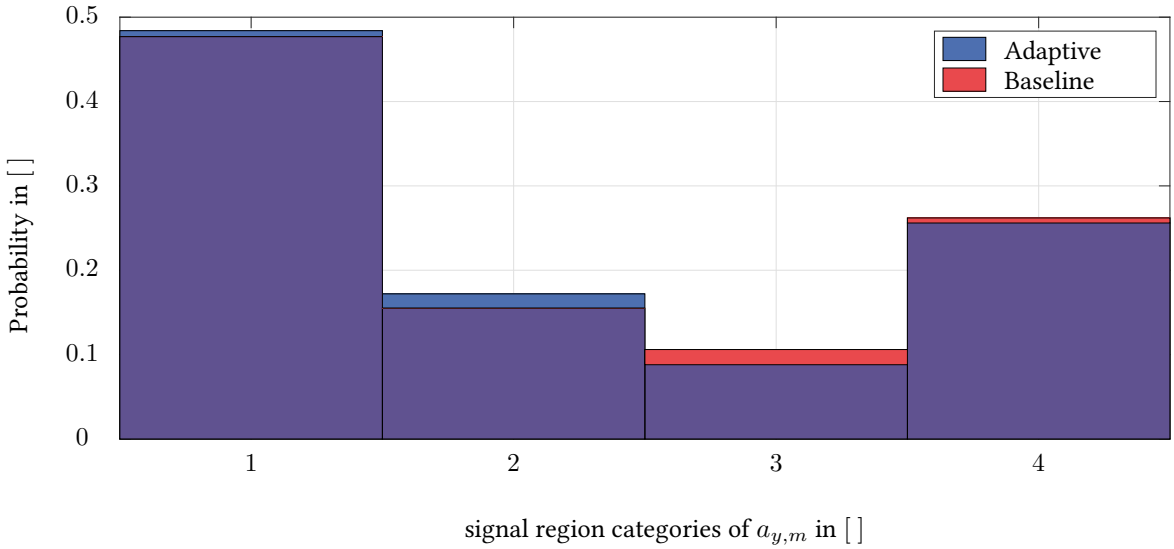

(a) Probability of the signal region category for the response of the lateral acceleration channel $a_{y,m}$.

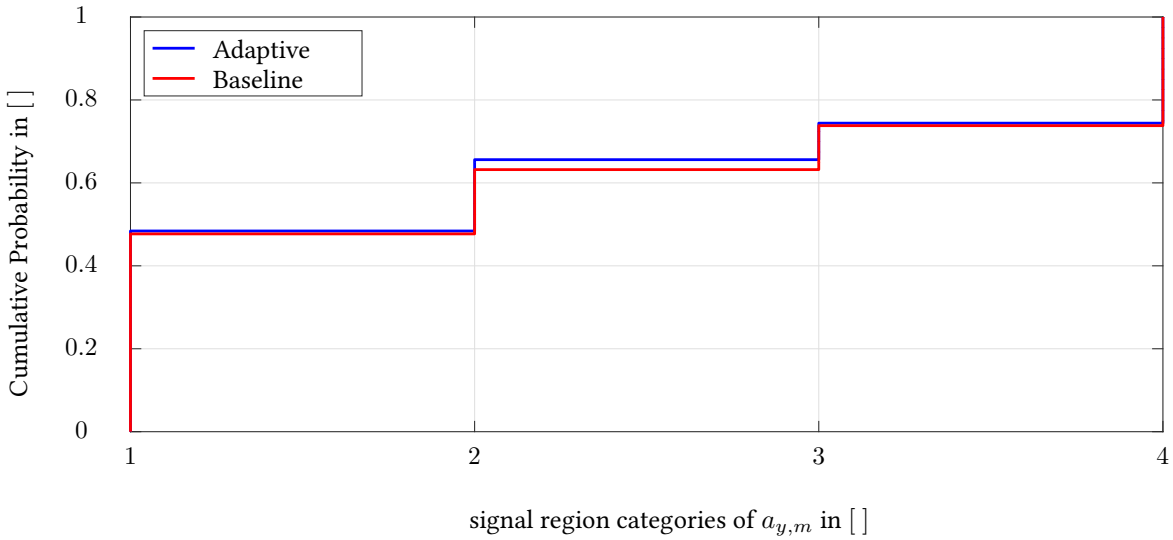

(b) Cumulative probability of the signal region categories of the lateral acceleration channel $a_{y,m}$.

Figure 6.35: Probability and cumulative probability of the signal region categories of the lateral acceleration channel $a_{y,m}$ obtained from MC analysis executed at the flight envelope point $M = 2$, $h = 1km$.

Although those results constitute only a rough categorizations of the MC simulations, they reinforce the trend of the normed error (see fig. 6.30 and fig. 6.31): the response of the augmented autopilot lead to a (slightly) better closed-loop response compared to the baseline controlled missile.

The distribution of the settling time T_{st} of the MC runs is depicted in fig. 6.36 and fig. 6.37 for the longitudinal and lateral acceleration channel, respectively.

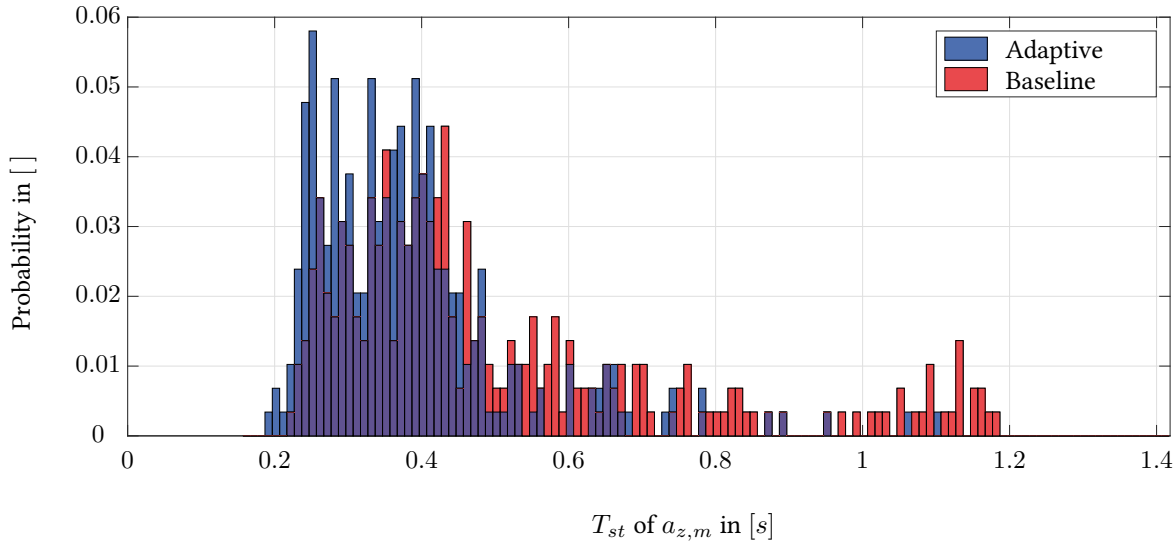

(a) Probability of settling time T_{st} of the longitudinal acceleration channel $a_{z,m}$.

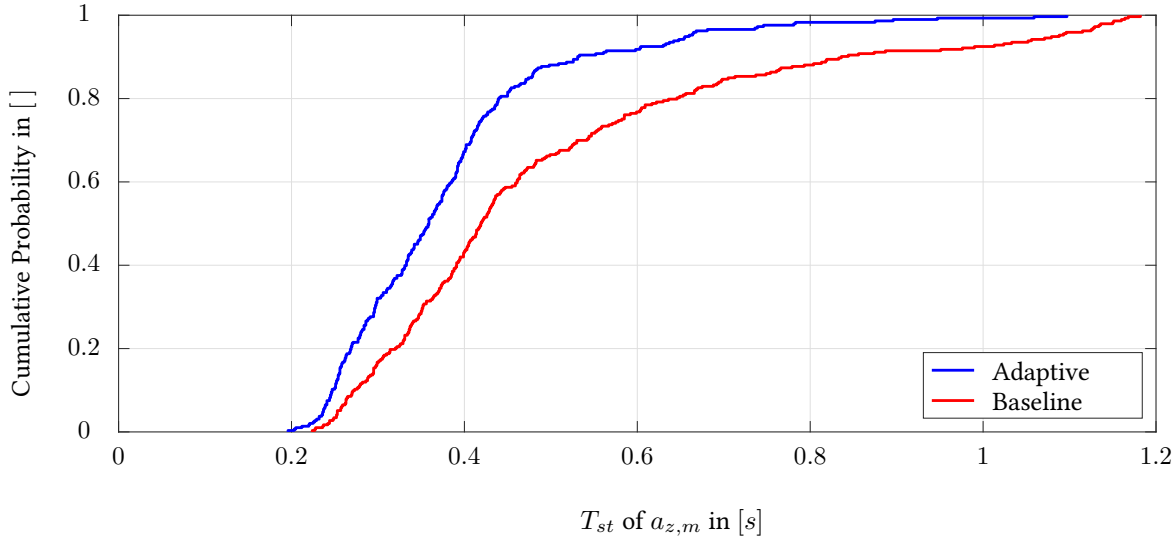

(b) Cumulative probability of settling time T_{st} of the longitudinal acceleration channel $a_{z,m}$.

Figure 6.36: Probability and cumulative probability of settling time T_{st} of the longitudinal acceleration channel $a_{z,m}$ obtained from MC analysis executed at the flight envelope point $M = 2, h = 1km$.

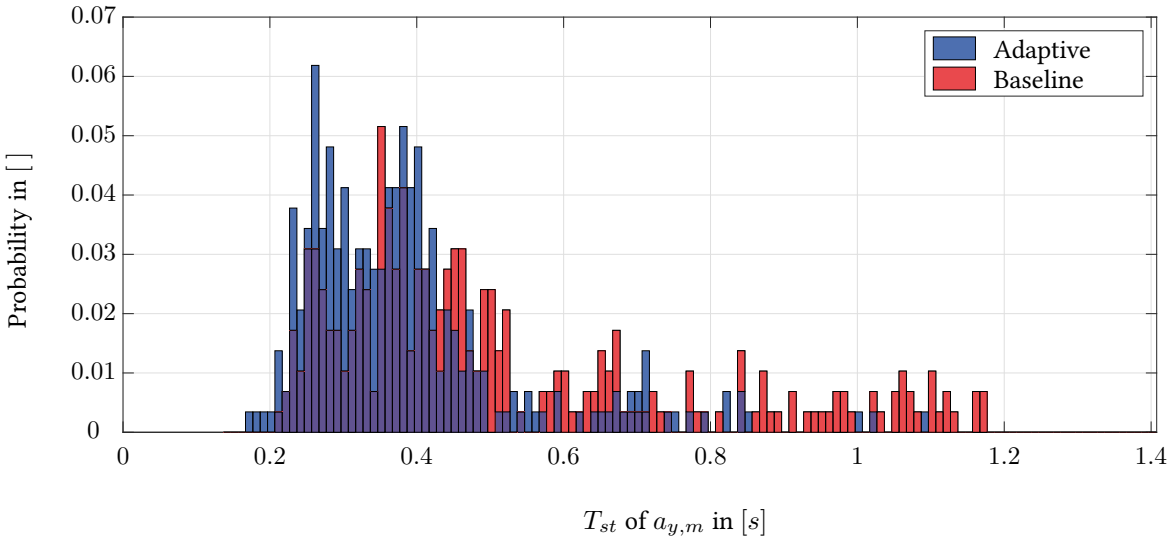

(a) Probability of settling time T_{st} of the lateral acceleration channel $a_{y,m}$.

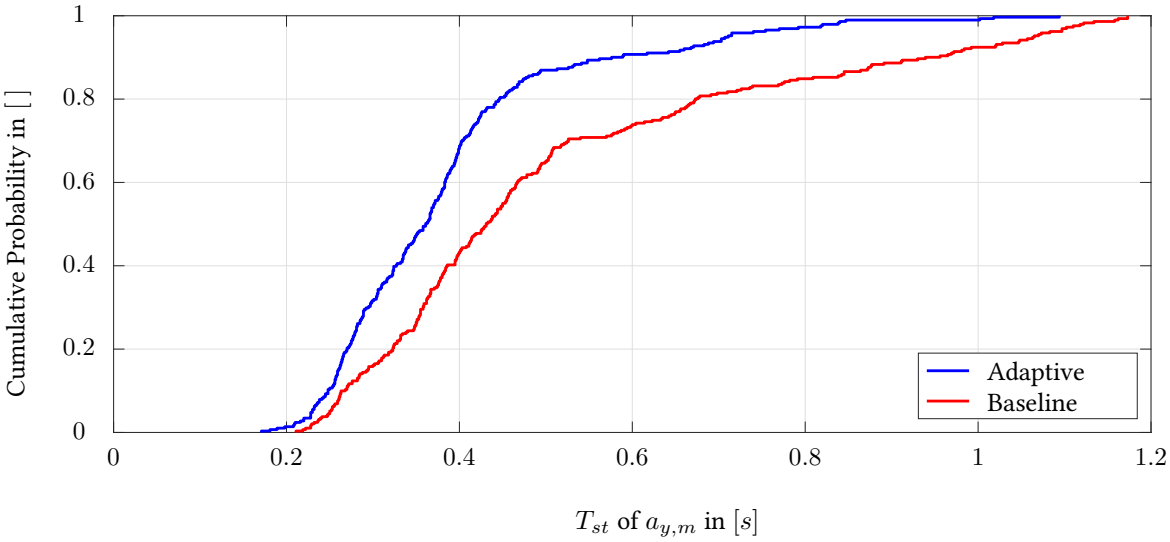

(b) Cumulative probability of settling time T_{st} of the lateral acceleration channel $a_{y,m}$.

Figure 6.37: Probability and cumulative probability of settling time T_{st} of the lateral acceleration channel $a_{y,m}$ obtained from MC analysis executed at the flight envelope point $M = 2$, $h = 1km$.

Based on the cumulative probability of both channels (see fig. 6.36 and fig. 6.37), the adaptive augmented autopilot lead to significant better signal convergence (reduced settling time T_{st}) compared to the non-augmented autopilot. Considering $T_{st} = 0.4s$ as threshold for example, 43.3% of the MC simulations exhibit a smaller settling time in both channels for the baseline autopilot. In case of the adaptive augmented autopilot, 68.4% (a_z) and 67.2% (a_y) are below $T_{st} = 0.4s$.

In case of the rise time evaluation shown in fig. 6.38 and fig. 6.39, both autopilot concepts exhibit almost identical probability distributions in each channel.

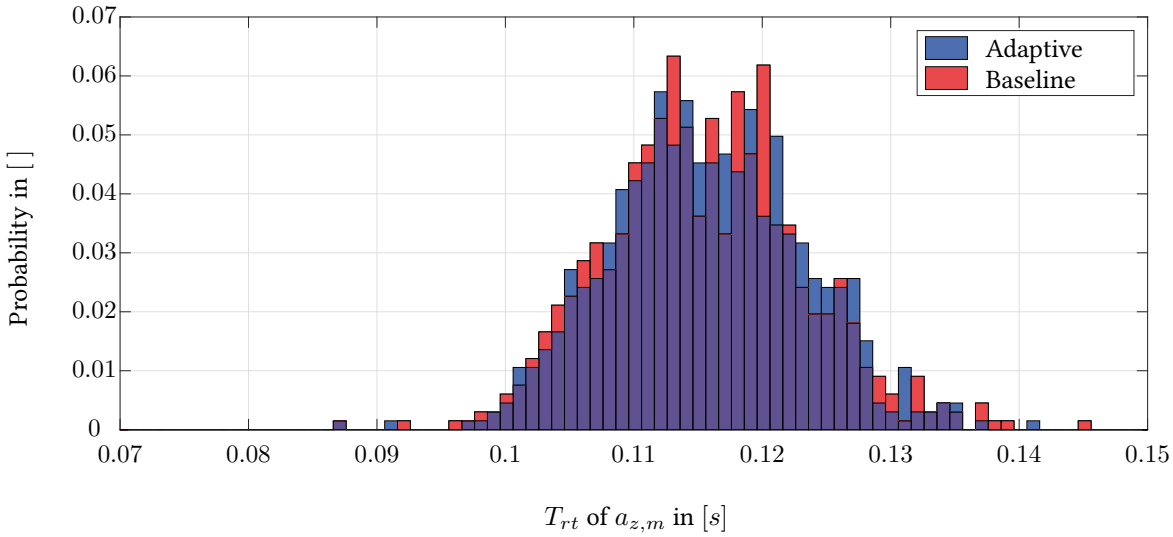

(a) Probability of rise time T_{rt} of the longitudinal acceleration channel $a_{z,m}$.

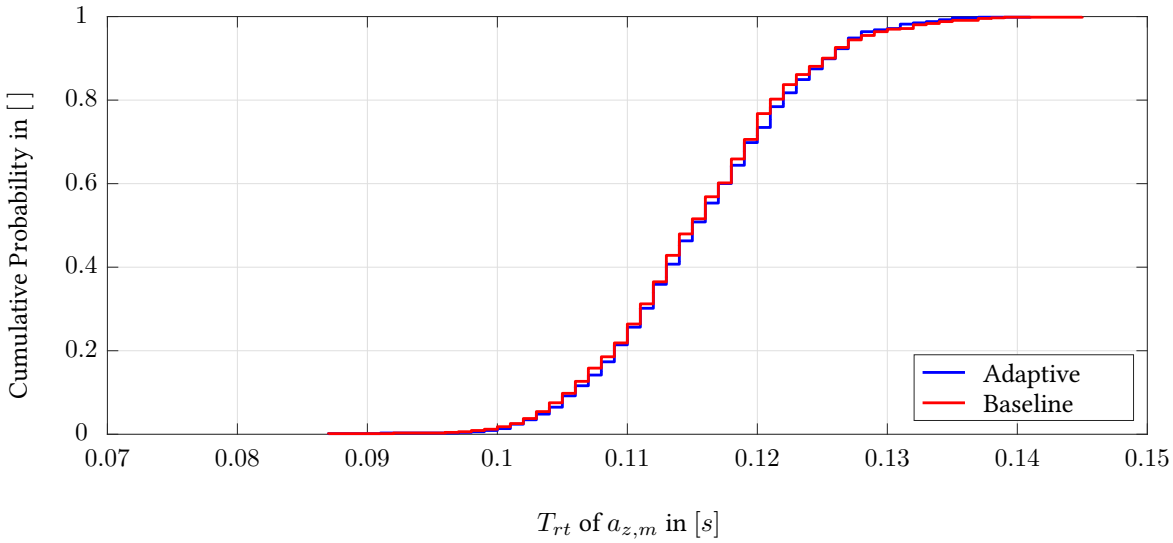

(b) Cumulative probability of rise time T_{rt} of the longitudinal acceleration channel $a_{z,m}$.

Figure 6.38: Probability and cumulative probability of rise time T_{rt} of the longitudinal acceleration channel $a_{z,m}$ obtained from MC analysis executed at the flight envelope point $M = 2$, $h = 1km$.

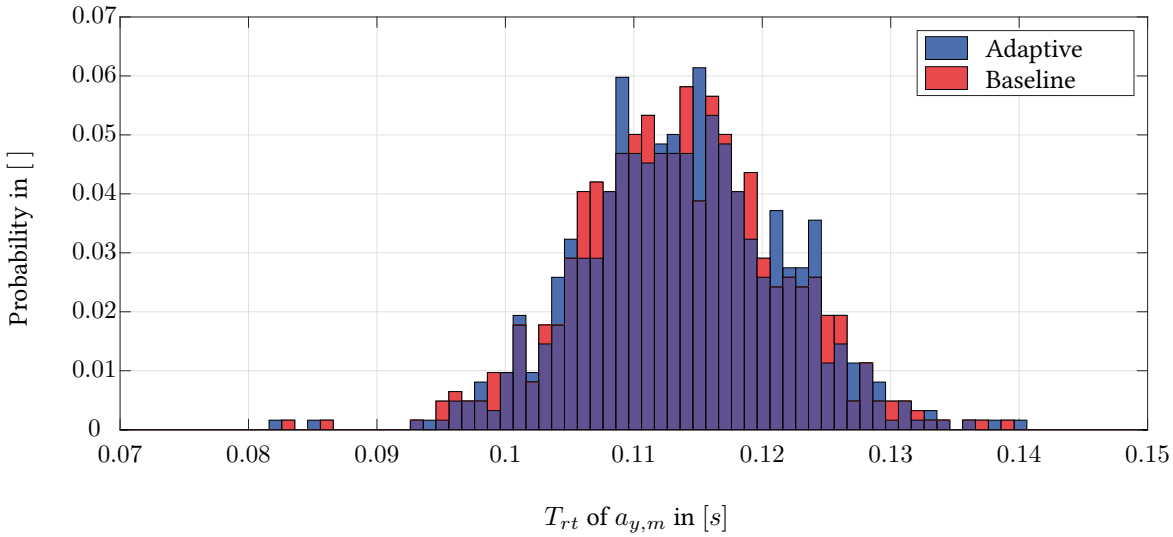

(a) Probability of rise time T_{rt} of the lateral acceleration channel $a_{y,m}$.

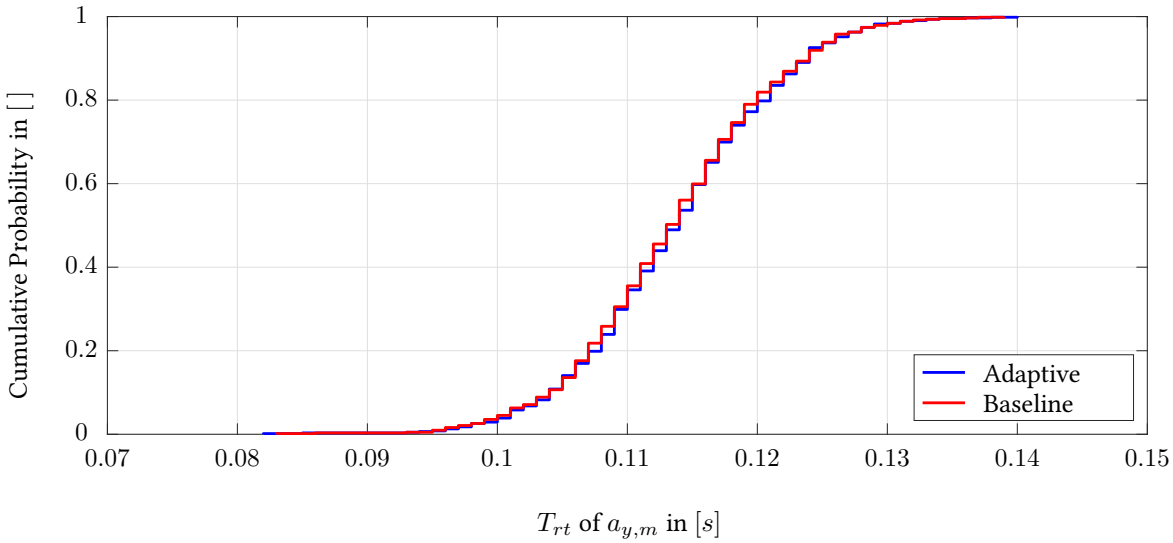

(b) Cumulative probability of rise time T_{rt} of the lateral acceleration channel $a_{y,m}$.

Figure 6.39: Probability and cumulative probability of rise time T_{rt} of the lateral acceleration channel $a_{y,m}$ obtained from MC analysis executed at the flight envelope point $M = 2$, $h = 1km$.

The evaluation of the MC simulations with respect to overshoot is illustrated in fig. 6.40 and fig. 6.41 for the longitudinal and lateral channel, respectively.

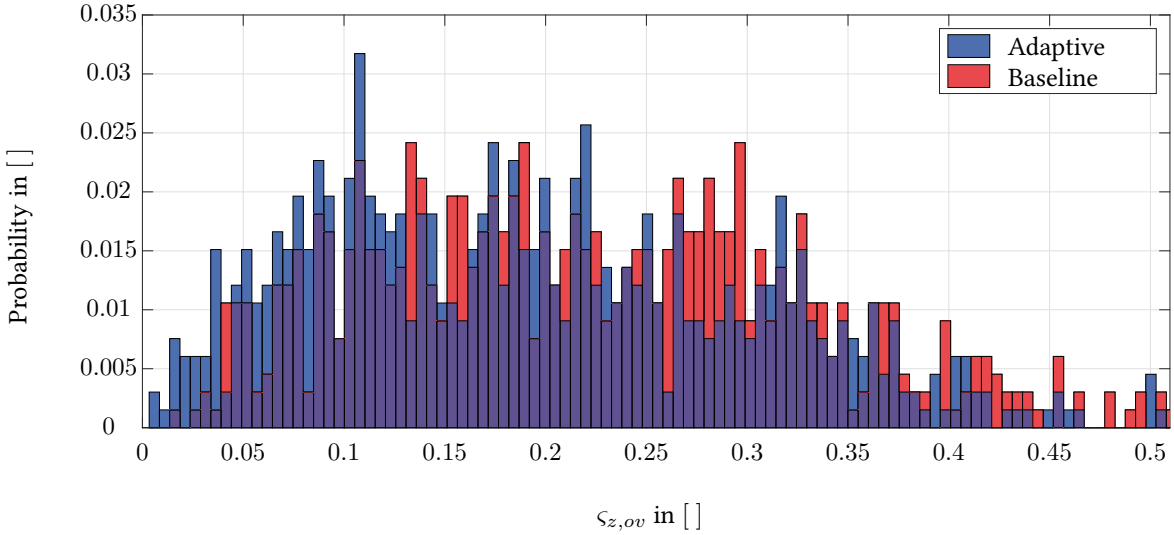

(a) Probability of overshoot $\varsigma_{z,ov}$ of the longitudinal acceleration channel $a_{z,m}$.

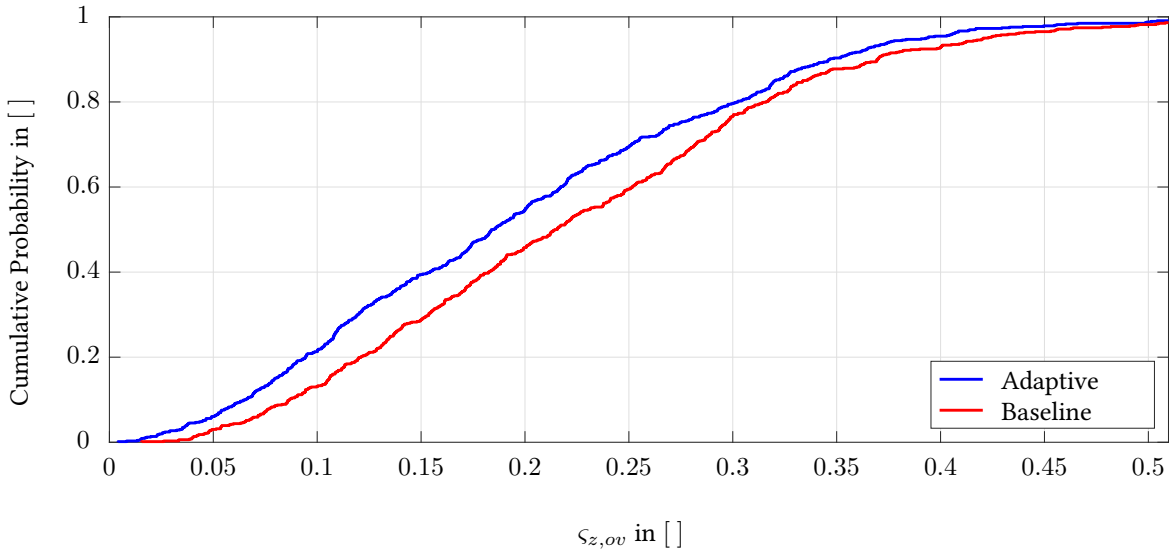

(b) Cumulative probability of overshoot $\varsigma_{z,ov}$ of the longitudinal acceleration channel $a_{z,m}$.

Figure 6.40: Probability and cumulative probability of overshoot $\varsigma_{z,ov}$ of the longitudinal acceleration channel $a_{z,m}$ obtained from MC analysis executed at the flight envelope point $M = 2, h = 1km$.

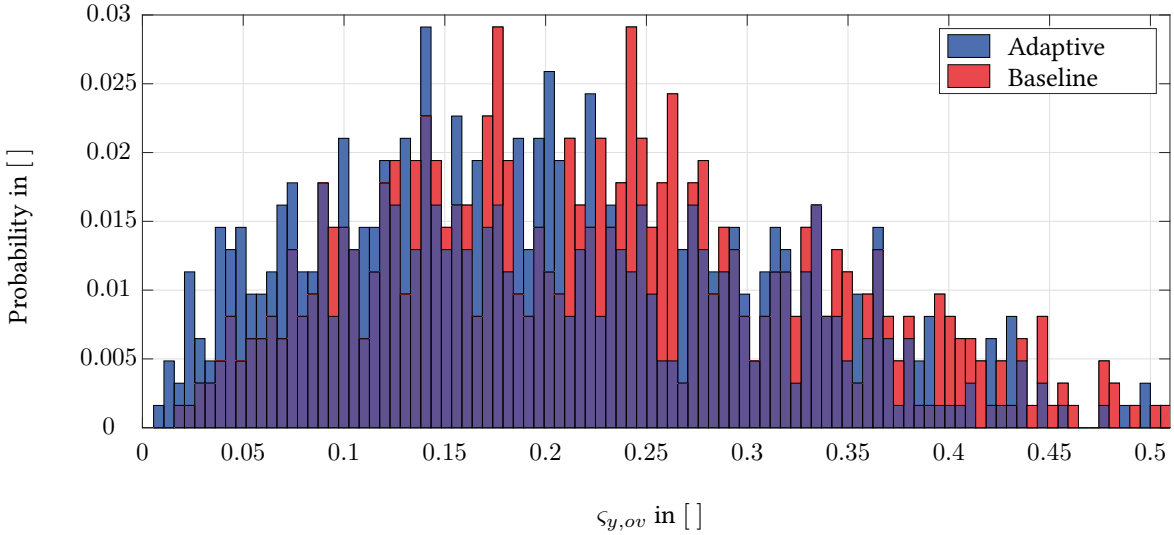

(a) Probability of overshoot $\varsigma_{y,ov}$ of the lateral acceleration channel $a_{y,m}$.

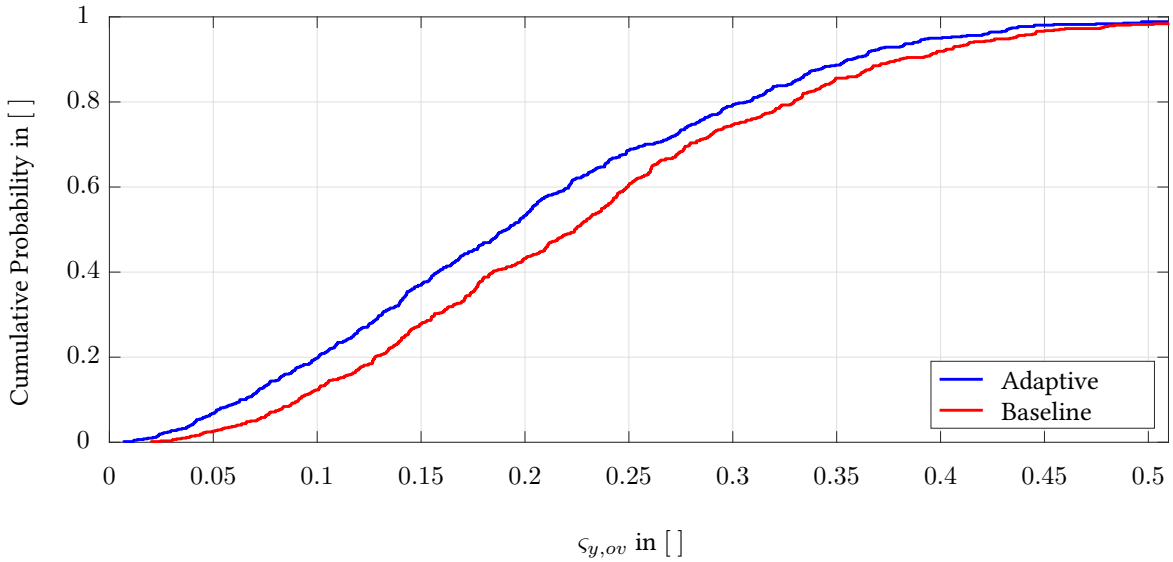

(b) Cumulative probability of overshoot $\varsigma_{y,ov}$ of the lateral acceleration channel $a_{y,m}$.

Figure 6.41: Probability and cumulative probability of overshoot $\varsigma_{y,ov}$ of the lateral acceleration channel $a_{y,m}$ obtained from MC analysis executed at the flight envelope point $M = 2$, $h = 1km$.

The cumulative probability exhibits for both acceleration channels (a_z and a_y) over the range $0.1 \leq \varsigma_{i,ov} \leq 0.25$ an almost constant offset between the baseline and the adaptive autopilot. Around 60% of simulations runs obtained with the adaptive autopilot and ca. 50% resulting from the closed-loop system via the baseline controller lie below $\varsigma_{i,ov} = 0.25$.

6.2.2.3 Summary of Nonlinear Simulations

In accordance with the linear analysis in sections 6.2.1.1 and 6.2.1.2, the nonlinear simulations considering IMU measurement noise exhibit expected responses of both autopilot versions. This characteristics is mainly due to the less progressive layout of the low-pass filters (see section 5.5.2.2).

Section 6.2.2.2 presents the evaluation of the 1000 closed-loop MC simulations (see section 6.2.2.2) for each autopilot configuration based on the metrics summarized in section 6.2.2.2.

The closed-loop system incorporating the adaptive augmentation exhibits a more uniform response of the controlled signals in comparison to the non-augmented version. Therefore, the augmented autopilot leads to smaller deviations from the nominal closed-loop transients in both acceleration channels (see figs. 6.30 and 6.31). The categorization of the signals according to their quality with respect to different levels of performance requirements (see table 6.1) confirm this tendency in a less significant way. In contrast to the rough categorization of the signal quality in figs. 6.34 and 6.35, the illustrations of the truncated $\mathcal{L}_2$ error norm provide a more precise picture of the quantity the advantageous effect of the augmented autopilot by preserving the nominal response figs. 6.30 and 6.31.

The evaluation with respect to overshoot and settling time reinforce the advantageous properties of the augmented autopilot for maintaining the desired nominal performance even in cases of a large spectrum of uncertainties and disturbances. Especially in terms of settling time (see figs. 6.36 and 6.37), the augmented autopilot version shows much faster convergence of a_z and a_y with respect to the commanded acceleration ($a_{z,c}$, $a_{y,c}$).

6.3 Summary

The analysis and evaluation within this chapter has two main goals: first, to assess whether the deterministic parametrization and physically motivated architecture of the control laws and the upstream reference model fulfill the demanding requirements (defined in section 5.1) across the entire flight envelope. Second, to analyze whether the adaptive augmentation is able to preserve the nominal performance for the large spectrum of possible model uncertainties. Furthermore, the impact with respect to robust performance and stability criteria (Gang of Four) is investigated for the parameters of the novel $\mathcal{L}_1$-PWC architecture.

From the evaluation in section 6.1 it can be concluded that the novel baseline autopilot architecture, incorporating the reference model and the baseline controller, leads to a increase in terms of closed-loop performance properties compared to the linear reference closed-loop system. Regarding the actuator responses in figs. 6.3 and 6.4, the novel approaches fully exploit the missile's actuator capabilities and therefore makes use of the missile's maximum performance potential. Considering the evaluation of the two baseline autopilots in section 6.1, it can be seen that slightly increased closed-loop bandwidth of the CFB autopilot goes hand-in-hand with significant disadvantageous overshoot characteristics (see fig. 6.6), reduced robust stability margins (see fig. 6.9), and (slightly) increased affinity to noise sensitivity (see fig. 6.7). The affinity to increased noise amplification of CFB is due to the differentiation of the intermediate control variable $\boldsymbol{\alpha}_{\boldsymbol{\omega}}$ (see (5.66)) and their usage (of $\dot{\boldsymbol{\alpha}}_{\boldsymbol{\omega},fil}$) within the final control law (5.74). In case of NDI (see (5.44)), the derivative of the intermediate control law is replaced with the desired angular accelerations $\dot{\boldsymbol{\omega}}_r$ from the reference model.

The investigations in section 6.2.1 and section 6.2.2 analyzes the autopilot's robustness properties by covering a large set of linear and nonlinear robustness metrics. The baseline controller serves for this evaluation as a reference. In order to analyze the robust performance, sensitivity functions incorporated in the Gang of Four metric are used for the linearized closed-loop (see section 6.2.1), while Monte Carlo analysis and simulations including measurement noise are considered for the nonlinear case (see section 6.2.2). Robust stability is investigated via time delay, phase, and gain margins of the linear system (see section 6.2.1.1). Based on those metrics, it can be concluded that the adaptive augmentation exhibits advantageous characteristics in terms of load disturbance and

sensitivity (see section 6.2.1.1). Remarkable in this context is that the herein designed adaptive augmentation exhibits similar noise characteristics as the baseline autopilot (see section 6.2.2.1). This behavior is in accordance with the linear investigations of noise sensitivity (see section 6.2.1.1). By evaluating the MC simulations in section 6.2.2.2 the $\mathcal{L}_1$-PWC augmentation shows its beneficial property of a uniform closed-loop response even in case of major deviations from the nominal plant. Since in contrast to the standard architectures of $\mathcal{L}_1$ adaptive control [63], the augmentation strategy presented herein (see section 5.5.2) is intentionally designed without the low-pass filtering of any feedforward signals. This circumstance preserves the closed-loop bandwidth set up via the baseline autopilot.

In terms of robust stability, the augmented version leads to uniform time delay margin which is mostly smaller compared to the baseline controlled missile (see 6.2.1.1). Besides the time delay margin, only the gain margin at the actuator location is significantly reduced by still maintaining the requirements.

The novel architecture tailored to the missile's dynamics and the specific control task in combination with the careful considered parameter optimization (which is in accordance with the main specification), lead to a closed-loop response which fulfills the challenging performance and robustness requirements across the entire flight envelope.

CHAPTER 7

Summary, Conclusion, and Outlook

I am a slow walker, but I never walk back.

Abraham Lincoln

This thesis is concluded by summarizing the main results and discussing its major contributions, limitations, and important directions of future research. The chapter is subdivided into two sections: Within section 7.1, a brief summary of the autopilot design process is given, focusing on its underlying assumptions and motivations. The key ideas introduced in section 1.4 are discussed in section 7.2 including further research recommendation.

7.1 Summary

Within this thesis an innovative, systematic approach of designing a modular autopilot architecture for a representative surface-to-air missile (SAM) benchmark model is presented. This novel autopilot structure provides convincing results in terms of baseline performance and robustification.

The entire development process, analysis, and verification of the autopilot was conducted based on the generic simulation model of the tail-controlled FSD Generic Surface-to-Air Missile (FGS-X-03) described in chapter 2. The detailed analysis in chapter 3 marks the starting point of the development process. Based on the information of the missile dynamics and the scenario, the functional and non-functional requirements of the closed-loop missile system were derived in section 5.1. Novel control techniques introduced in chapter 4 build the foundation of the missile autopilot design presented in chapter 5. The verification and analysis of the autopilot with respect to the defined requirements was conducted in chapter 6.

The main focus of the autopilot design lies in fully utilizing the missile's performance capabilities by respecting standard robustness criteria. In common missile autopilot designs (see [22, 24, 27, 28, 37, 38, 39, 40]), holistic architectures are used. Therefore, the entire set of the mutual conflicting performance and robustness requirements needs to be fulfilled by the integral autopilot.

Herein, the autopilot is subdivided into three elements: reference model (see section 5.4), baseline controller (see section 5.5.1), and adaptive augmentation (see section 5.5.2). In case of the reference model, a nonlinear, integrated approach is selected considering both dynamical layers. Therefore,

the reference signal trajectories represent the major nonlinear effects of the nominal missile model. For the purpose of the control algorithm of the subsequent baseline autopilot, a Nonlinear Dynamic Inversion (NDI)-based version is compared to a Command Filtered Backstepping (CFB)-based approach. To account for the nonlinear reference model and the prerequisites of the underlying control theory, physically motivated customization and simplification are conducted in section 5.3 and section 5.5.1. One major modification of the underlying design model constitutes the virtual sensor location ahead of the missile's center of percussion to avoid non-minimum phase characteristics (see section 5.3.1). The parametrization of the reference model and baseline control law were conducted based on standardized optimization routines by incorporating the main performance and robustness requirements. This leads to an automatic parameter layout process across the entire flight envelope.

For the purpose of preserving the baseline performance in case of the large spectrum of uncertainties (see section 2.4), an adaptive layer based on $\mathcal{L}_1$-Piecewise-Constant (PWC) is selected. In contrast to other adaptive control methodologies like Model Reference Adaptive Control (MRAC), classical $\mathcal{L}_1$ Adaptive Control, or Adaptive Backstepping (BS), $\mathcal{L}_1$-PWC exhibit special features which makes this approach perfectly suitable for missile autopilot design. Reasons for this are (discussed in 4.3), inter alia, the absence of basis functions, the straightforward tuning process, and the applicability of linear metrics for analyzing and verification of the control algorithm.

Linear and nonlinear metrics are used for evaluating and verifying the missile autopilot design over the entire flight envelope by using nine representative operating points (see chapter 6). The analysis phase is subdivided into two parts: first, the two novel baseline architectures are compared and evaluated under nominal conditions (see 6.1); second, the robustness characteristics of the adaptive element are assessed (see section 6.2).

Besides fulfilling the challenging requirements (under nominal conditions), both baseline autopilots lead to superior performance behavior (e.g. rise time, bandwidth) compared to conventional linear autopilots represented by a closed-loop reference transfer characteristics (see section 6.1.1). The main reason for the major performance improvement can be traced back to the nonlinear, coupled reference model providing demanding, but physically feasible, reference signal trajectories.

For analyzing the effect of the adaptive layer and its parametrization, the augmented autopilot is evaluated based on linear metrics (see section 6.2.1) and nonlinear simulations (see section 6.2.2). The linear analysis revealed that robust performance properties are mutually conflicting amongst each other. Considering the nonlinear Monte Carlo (MC) simulations, the augmented autopilot exhibits a more uniform transient response of the control variables compared to the non-augmented version.

7.2 Conclusion and Outlook

The main contributions of the herein developed autopilot design and layout process are presented in the following paragraphs. Possible improvements and future research tasks, which are beyond the scope of this thesis, are addressed.

Modular autopilot architecture

With the subdivision of the autopilot, a direct and unique mapping of certain requirement subsets (see section 5.1) to the respective autopilot element is possible. This modular design enables separate execution of the design, tuning, and verification phase for each of the three elements. Due to its generic and interchangeable characteristics, the herein derived autopilot architecture is not re-

stricted to Skid-To-Turn (STT) SAM types. The application of certain elements or the entire modular approach to any flying platform exhibiting nonlinear characteristics, will yield significant advantages over conventional holistic, linear designs.

Physical motivated tailoring of design model

Any autopilot design process starts with the definition of a suitable representation (design model) of the system of interest (plant model). The selection process of the design model is subject to trade offs between accuracy, requirements of the underlying control methodology, and limited onboard processing power. In terms of accuracy, the design model shall mimic the most significant plant characteristics with sufficient accuracy. Herein, all three autopilot elements incorporate a representation of the plant dynamics within their algorithm. The design model was thus carefully selected based on scenario insights, minimum phase input/output characteristics, and a detailed analysis of the missile physics. The accuracy of the design model with respect to the plant model was evaluated based on the consideration of certain aerodynamic effects (see section 5.3).

Metrics quantifying the accuracy of the design model with respect to the plant model offer additional potential for improving the selection process.

Increased performance due to nonlinear reference model

The superior closed-loop performance can be traced back to the representation of the major nonlinear characteristics within the reference model. The coupled reference signals provided to the downstream error control algorithm lead to an autopilot which fully exploits the missile's performance capabilities. Due to the modular architecture, an independent consideration of the reference model was possible, facilitating the design procedure and allowing for automatic testing and verification.

The herein designed reference model mimics the nominal missile dynamics. In case the missile dynamics deviates from the assumed reference dynamics, the closed-loop performance does not match the performance capabilities of the plant. An online adaptation scheme updating the reference model to match the plant's characteristics would therefore lead to a more suitable reference model behavior. This feature could be inevitable in case the nonlinear reference model is applied to aircraft with the tendency to exhibit severe degradation.

Baseline autopilots

In order to realize the beneficial performance properties of the reference signal, the baseline control algorithm was designed with regard to perfect tracking under adherence of the robustness requirements. For this task modern baseline control techniques were considered which are suitable for highly nonlinear applications fulfilling demanding tracking tasks. Nevertheless, only a customization of the classic NDI and CFB schemes led to extended bandwidth and tracking capabilities of the baseline algorithm. The command filters in case of CFB led to slightly increased implementation and tuning effort (increase in degree of freedom) compared to the compact structure of the NDI scheme.

The separate selection of the design model for the purpose of control layout was not considered herein. A detailed modification may result in beneficial robustness and stability properties of the closed-loop. Continuing research should consider a physically-motivated selection of the underlying design model with respect to certain robustness and performance metrics.

Cascaded adaptive structure using nonlinear state predictor models

Detailed analysis of the closed-loop sensitivity (see section 5.5.2.1) suggested a novel cascaded adaptive architecture compensating uncertainties in both dynamical layers. The nominal missile model is considered as reference (state predictor) within the adaptation law. Therefore, the layout and parametrization of the adaptive element is independent of the baseline autopilot (see section 5.5.2). Since the missile dynamics constitute the considered dynamics within the adaptive scheme, bandwidth-limiting filtering of any feedforward signal is avoided. The closed-loop bandwidth of the baseline autopilot is thus preserved. Common control architectures incorporating a $\mathcal{L}_1$-PWC augmentation amplify measurement noise in a significant manner [71]. The herein presented adaptive architecture changes the noise level sensitivity at the autopilot's output with respect to measurement noise. With the given architecture incorporating the nonlinear state predictor and considering the missile system instead of the baseline closed-loop dynamics, tedious and complex scheduling of the state predictor dynamics (reference dynamics) is avoided. This addresses one of the open problems in modern adaptive flight control design [57].

Appendix

A.1 Coordinate Frames

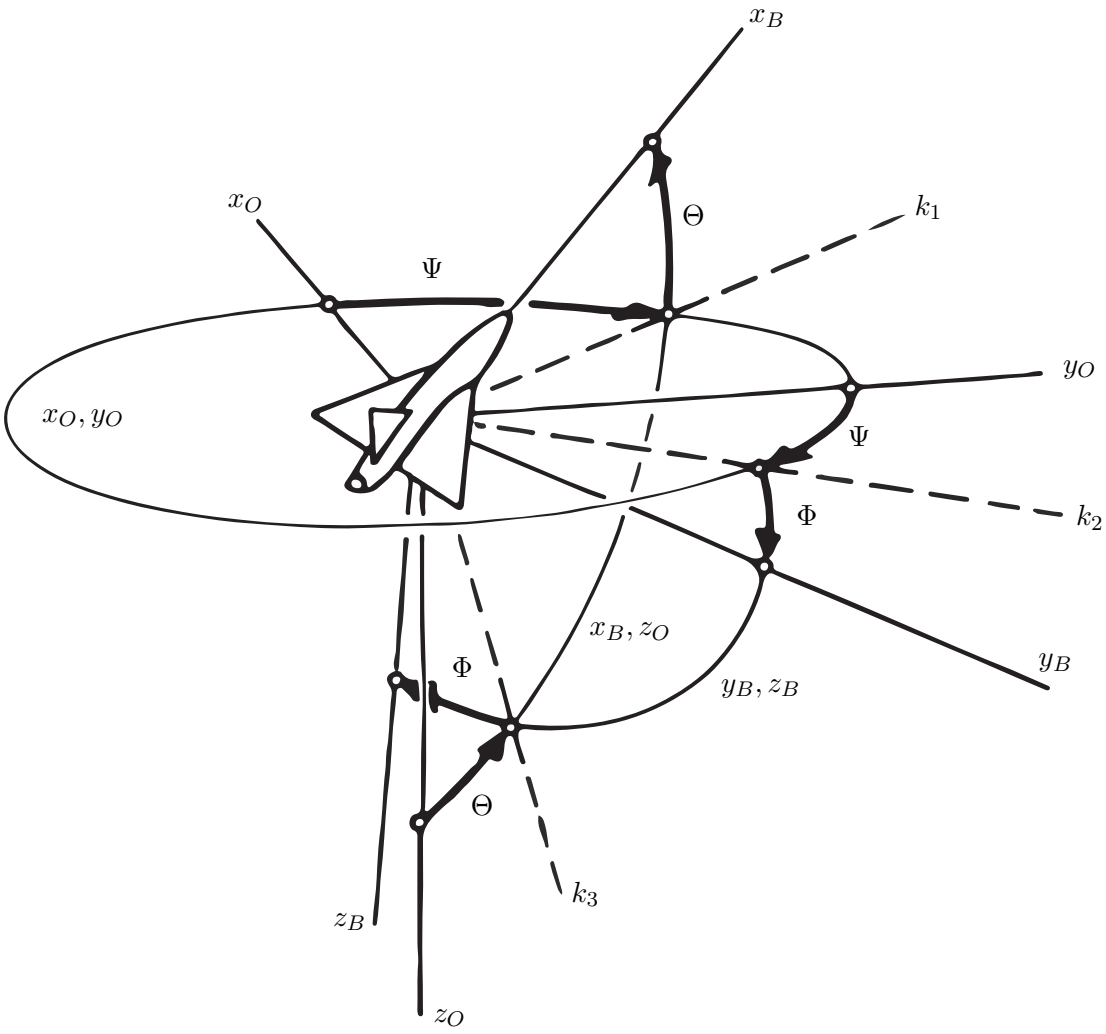

Figure A.1: Orientation of body-fixed frame with respect to NED-frame described by Euler angles Φ, Θ, and Ψ [4].

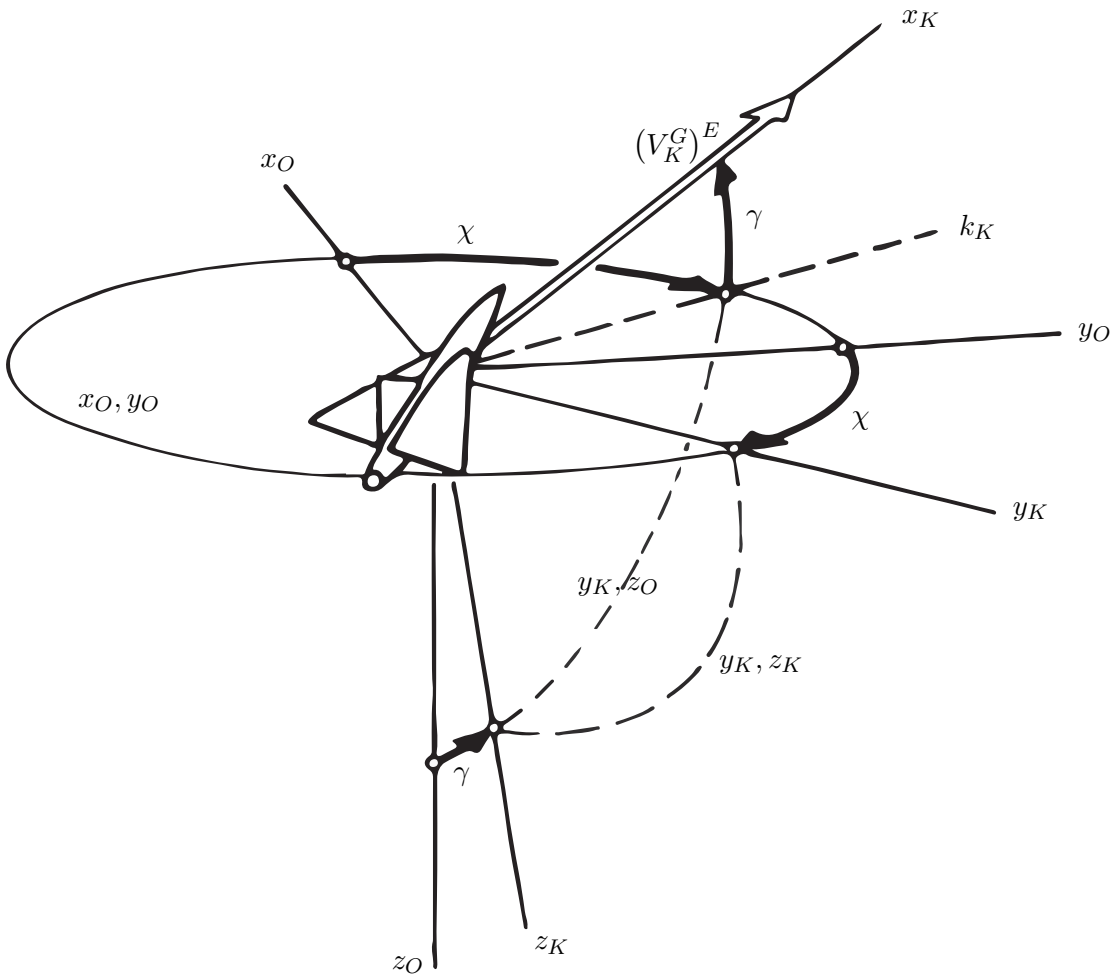

Figure A.2: Orientation of kinematic frame with respect to NED-frame described by the path angles γ and χ [4].

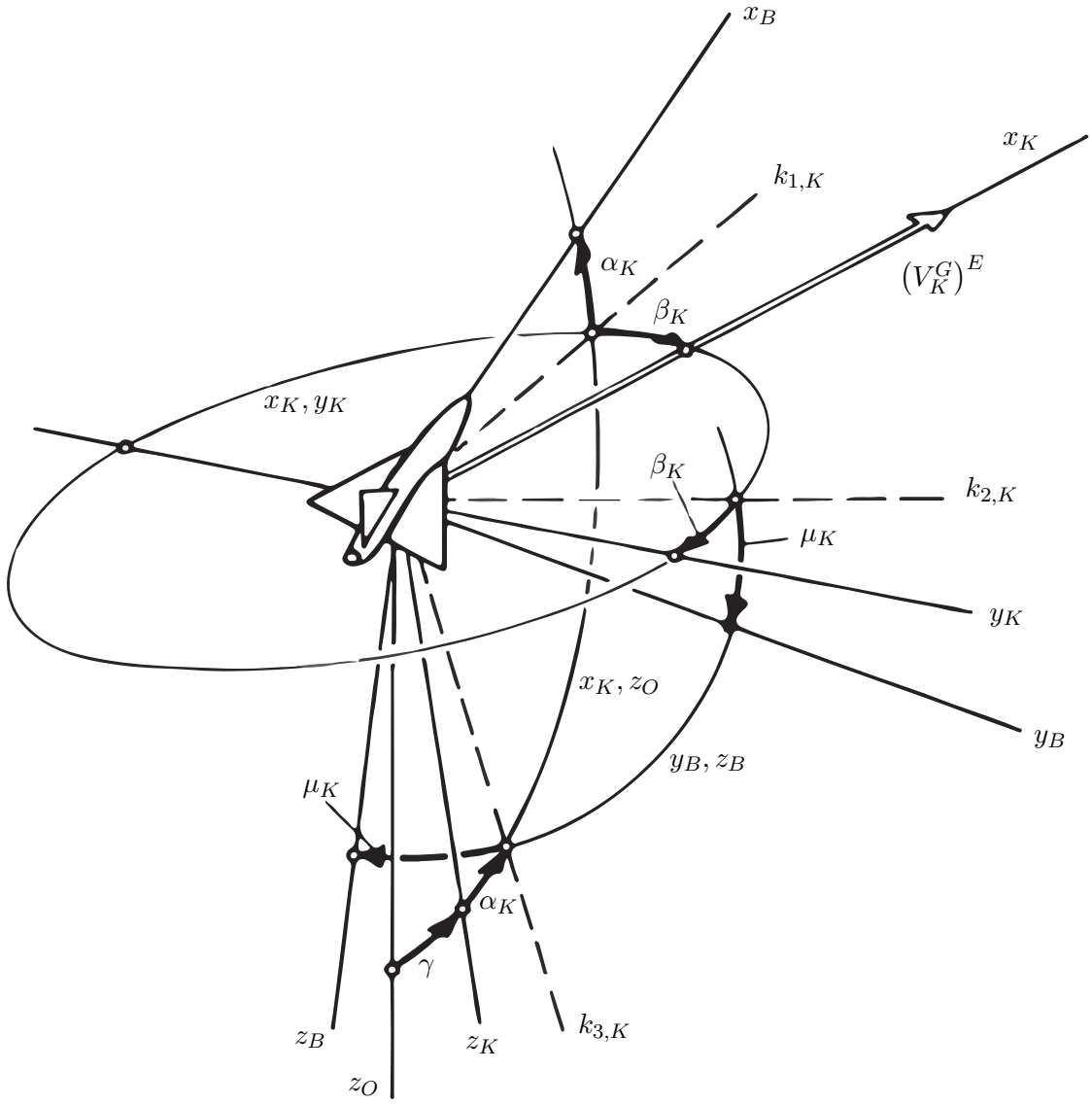

Figure A.3: Orientation of body-fixed frame with respect to kinematic frame described by angles α_K, β_K, and μ_K [4].

B.1 Aerodynamic Data Set

B.1.1 Aerodynamic Force Coefficients

B.1.1.1 Axial Aerodynamic Force Coefficients

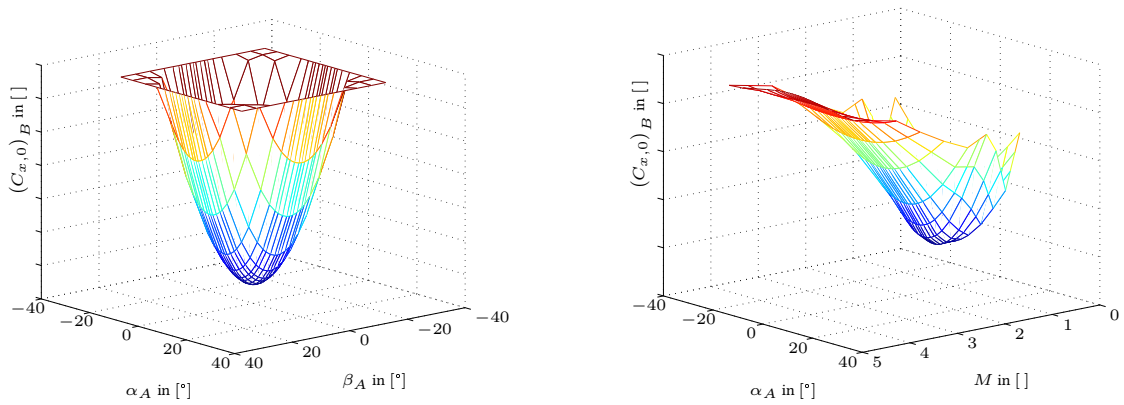

(a) Aerodynamic coefficient $(C_{x,0})_B$ plotted versus α_A and β_A at $M = 0.9$

(b) Aerodynamic coefficient $(C_{x,0})_B$ plotted versus α_A and M at $\beta_A = 5.0°$

Figure B.1: Aerodynamic coefficient $(C_{x,0})_B$ plotted versus its dependencies α_A, β_A, and M at the configuration $\beta = 5.0°$ and $M = 0.9$.

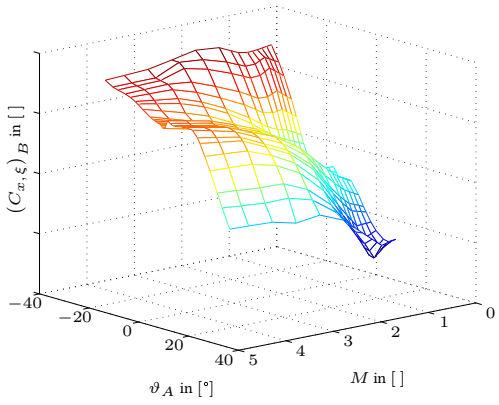

(a) Aerodynamic coefficient $(C_{x,\xi})_B$ plotted versus ϑ_A and M at $\xi = -15.0°$, $\eta = 20.0°$, $\zeta = 4.0°$

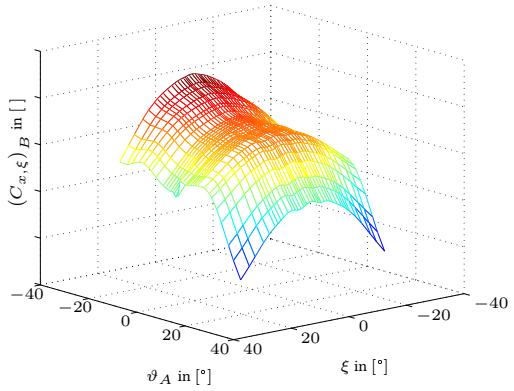

(b) Aerodynamic coefficient $(C_{x,\xi})_B$ plotted versus ϑ_A and ξ at $M = 4.0$, $\eta = 20.0°$, $\zeta = 4.0°$

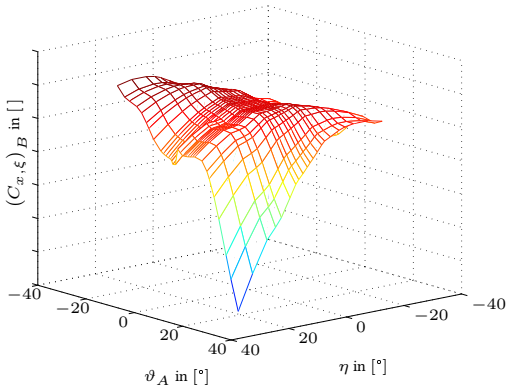

(c) Aerodynamic coefficient $(C_{x,\xi})_B$ plotted versus ϑ_A and η at $M = 4.0$, $\xi = -15.0°$, $\zeta = 4.0°$

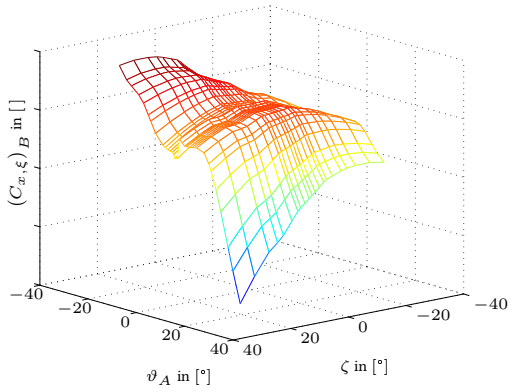

(d) Aerodynamic coefficient $(C_{x,\xi})_B$ plotted versus ϑ_A and ζ at $M = 4.0$, $\xi = -15.0°$, $\eta = 20.0°$

Figure B.2: Aerodynamic coefficient $(C_{x,\xi})_B$ plotted versus its dependencies ϑ_A, M, ξ, η, and ζ at the configuration $\xi = -15.0°$, $M = 4.0$, $\eta = 20.0°$, $\zeta = 4.0°$.

B.1.1.2 Lateral Aerodynamic Force Coefficients

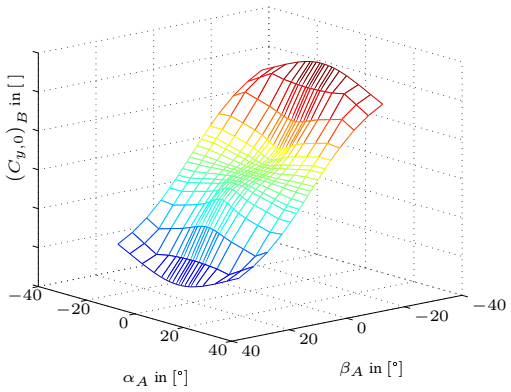

(a) Aerodynamic coefficient $(C_{y,0})_B$ plotted versus α_A and β_A at $M = 1.0$

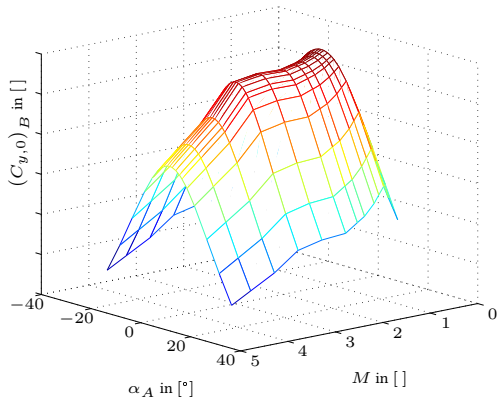

(b) Aerodynamic coefficient $(C_{y,0})_B$ plotted versus α_A and M at $\beta_A = -25.0°$

Figure B.3: Aerodynamic coefficient $(C_{y,0})_B$ plotted versus its dependencies α_A, β_A, and M at the configuration $\beta = -25.0°$ and $M = 1.0$.

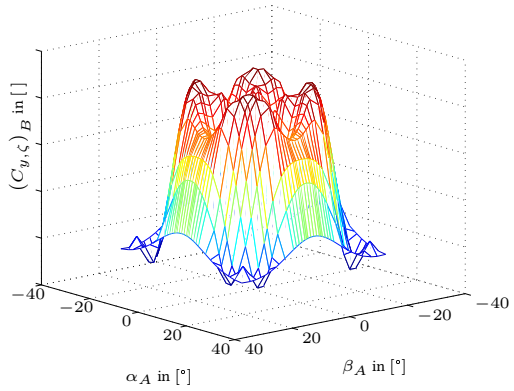

(a) Aerodynamic coefficient $(C_{y,\zeta})_B$ plotted versus α_A and β_A at $M = 1.75, \xi = 22.0°, \zeta = -12.0°$

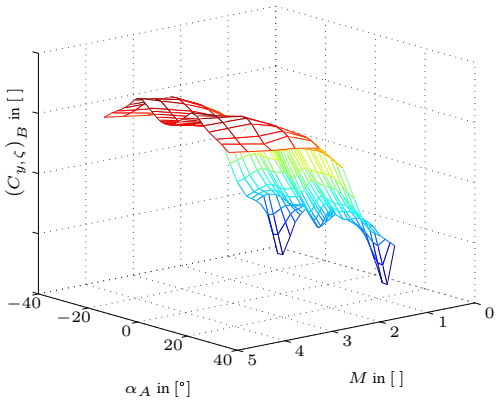

(b) Aerodynamic coefficient $(C_{y,\zeta})_B$ plotted versus α_A and M at $\beta_A = -6.0°$, $\xi = 22.0°$, $\zeta = -12.0°$

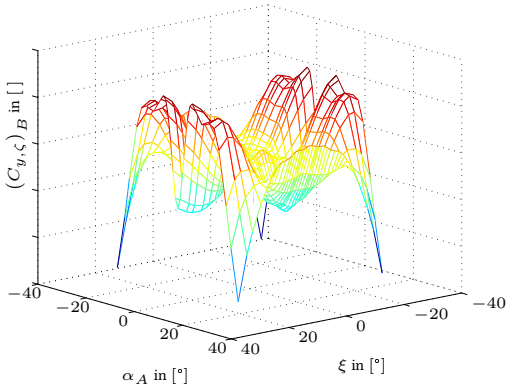

(c) Aerodynamic coefficient $(C_{y,\zeta})_B$ plotted versus α_A and ξ at $\beta_A = -6.0°, M = 1.75, \zeta = -12.0°$

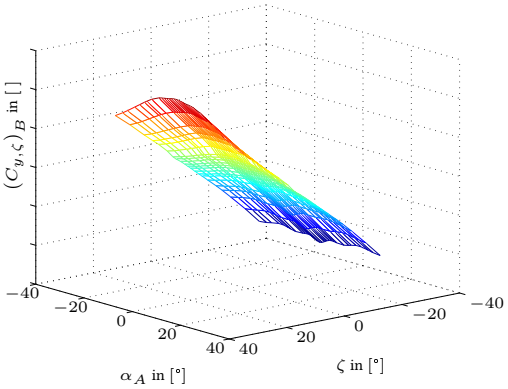

(d) Aerodynamic coefficient $(C_{y,\zeta})_B$ plotted versus α_A and ζ at $\beta_A = -6.0°, M = 1.75, \xi = 22.0°$

Figure B.4: Aerodynamic coefficient $(C_{y,\zeta})_B$ plotted versus its dependencies α_A, β_A, M, ξ, and ζ at the configuration $\beta_A = -6.0°$, $M = 1.75$, $\xi = 22.0°$, $\zeta = -12.0°$.

B.1.1.3 Longitudinal Aerodynamic Force Coefficients

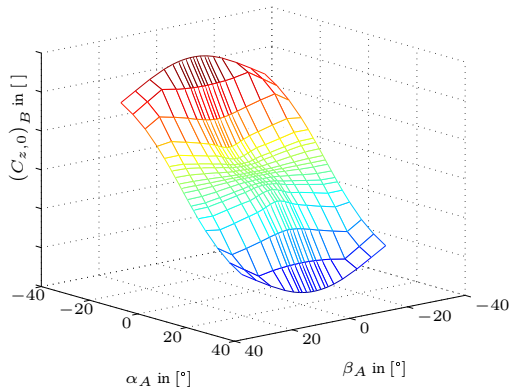

(a) Aerodynamic coefficient $(C_{z,0})_B$ plotted versus α_A and β_A at $M = 1.3$

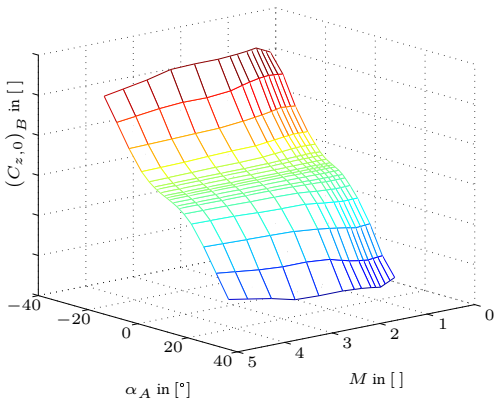

(b) Aerodynamic coefficient $(C_{z,0})_B$ plotted versus α_A and M at $\beta_A = 5.0°$

Figure B.5: Aerodynamic coefficient $(C_{z,0})_B$ plotted versus its dependencies α_A, β_A, M at the configuration $\beta_A = 5.0°$, $M = 1.3$.

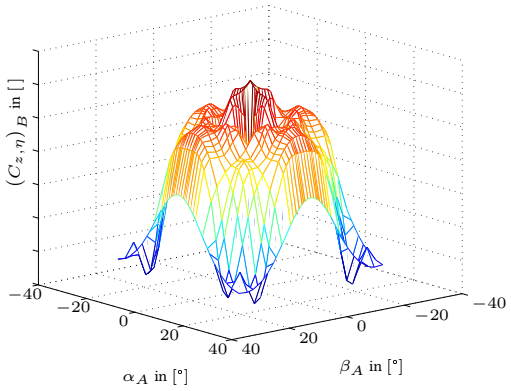

(a) Aerodynamic coefficient $(C_{z,\eta})_B$ plotted versus α_A and β_A at $M = 1.6$, $\xi = 11.0°$, $\eta = -15.0°$

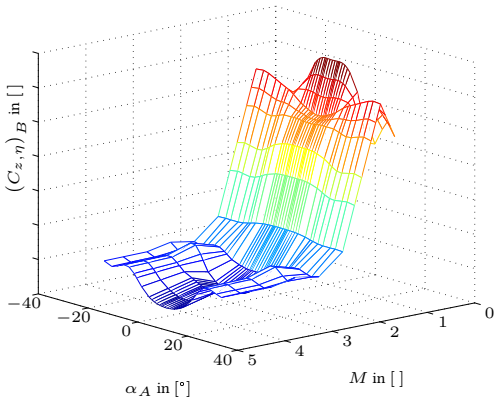

(b) Aerodynamic coefficient $(C_{z,\eta})_B$ plotted versus α_A and M at $\beta_A = 22.0°$, $\xi = 11.0°$, $\eta = -15.0°$

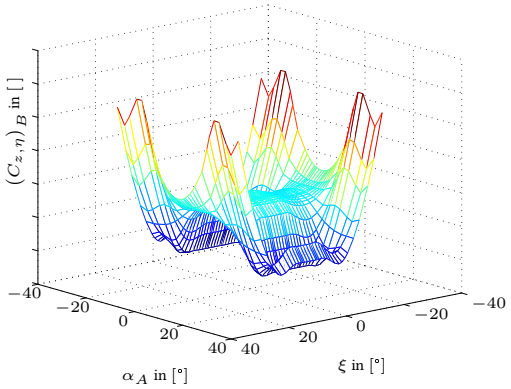

(c) Aerodynamic coefficient $(C_{z,\eta})_B$ plotted versus α_A and ξ at $\beta_A = 22.0°$, $M = 1.6$, $\eta = -15.0°$

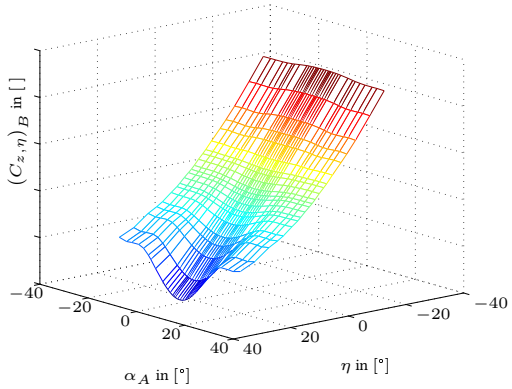

(d) Aerodynamic coefficient $(C_{z,\eta})_B$ plotted versus α_A and η at $\beta_A = 22.0°$, $M = 1.6$, $\xi = 11.0°$

Figure B.6: Aerodynamic coefficient $(C_{z,\eta})_B$ plotted versus its dependencies α_A, β_A, M, ξ, and ζ at the configuration $\beta_A = 6.0°$, $M = 1.6$, $\xi = 11.0°$, $\zeta = 2.5°$.

B.1.2 Aerodynamic Moment Coefficients

B.1.2.1 Axial Aerodynamic Moment Coefficients

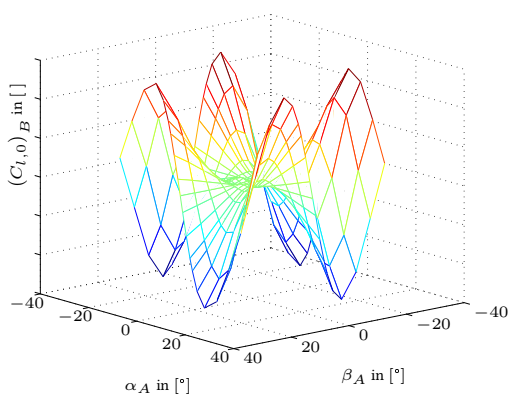

(a) Aerodynamic coefficient $(C_{l,0})_B$ plotted versus α_A and β_A at $M = 3.0$

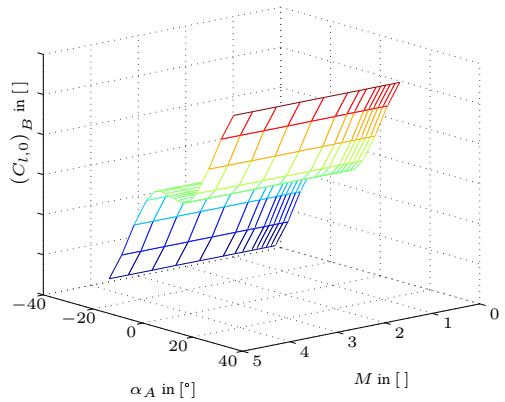

(b) Aerodynamic coefficient $(C_{l,0})_B$ plotted versus α_A and M at $\beta_A = 5.0°$

Figure B.7: Aerodynamic coefficient $(C_{l,0})_B$ plotted versus its dependencies α_A, β_A, and M at the configuration $\beta_A = 5.0°$, $M = 3.0$.

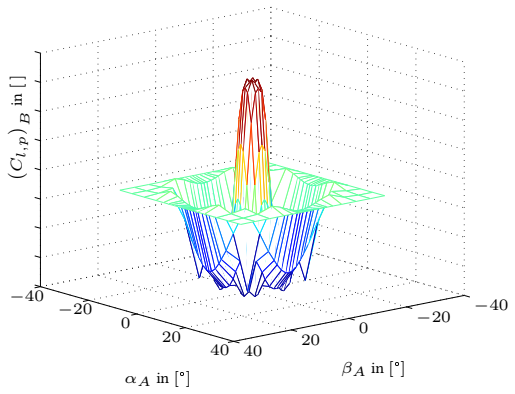

(a) Aerodynamic coefficient $(C_{l,p})_B$ plotted versus α_A and β_A at $M = 2.5$

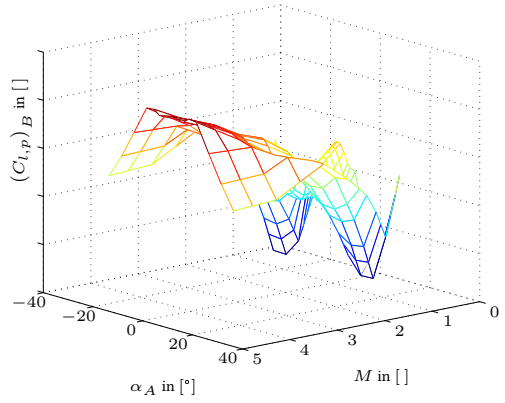

(b) Aerodynamic coefficient $(C_{l,p})_B$ plotted versus α_A and M at $\beta_A = 4.0°$

Figure B.8: Aerodynamic coefficient $(C_{l,p})_B$ plotted versus its dependencies α_A, β_A, and M at the configuration $\beta_A = 4.0°$, $M = 2.5$.

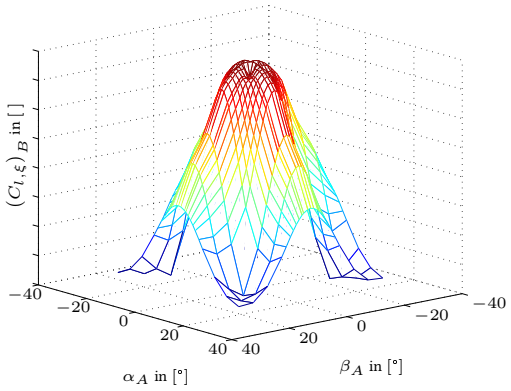

(a) Aerodynamic coefficient $(C_{l,\xi})_B$ plotted versus α_A and β_A at $M = 1.2$, $\xi = 10.0°$, $\eta = 6.0°$ $\zeta = 17.0°$

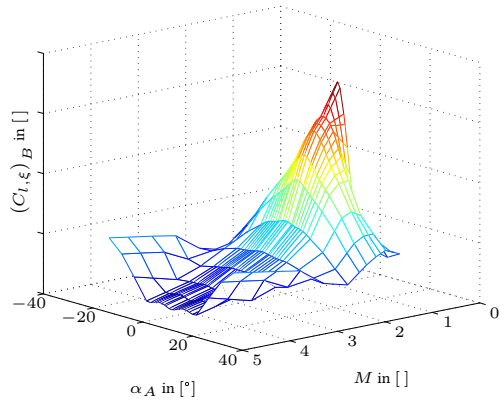

(b) Aerodynamic coefficient $(C_{l,\xi})_B$ plotted versus α_A and M at $\beta_A = 6.0°$, $\xi = 10.0°$, $\eta = 6.0°$ $\zeta = 17.0°$

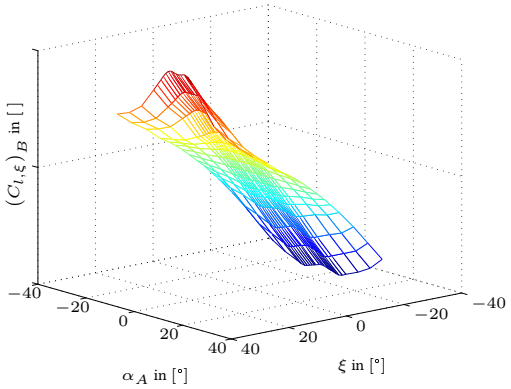

(c) Aerodynamic coefficient $(C_{l,\xi})_B$ plotted versus α_A and ξ at $\beta_A = 6.0°$, $M = 1.2$, $\eta = 6.0°$ $\zeta = 17.0°$

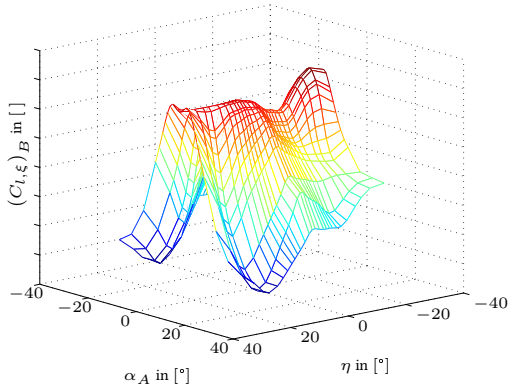

(d) Aerodynamic coefficient $(C_{l,\xi})_B$ plotted versus α_A and η at $\beta_A = 6.0°$, $M = 1.2$, $\xi = 10.0°$, $\zeta = 17.0°$

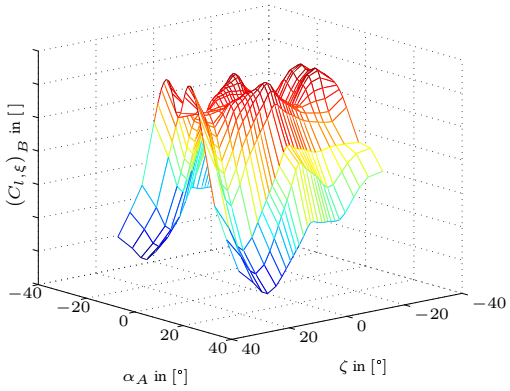

(e) Aerodynamic coefficient $(C_{l,\xi})_B$ plotted versus α_A and ζ at $\beta_A = 6.0°$, $M = 1.2$, $\xi = 10.0°$, $\eta = 6.0°$

Figure B.9: Aerodynamic coefficient $(C_{l,\xi})_B$ plotted versus its dependencies α_A, β_A, M, ξ, and ζ at the configuration $\beta_A = 6.0°$, $M = 1.2$, $\xi = 10.0°$, $\eta = 6.0°$, $\zeta = 17.0°$.

B.1.2.2 Longitudinal Aerodynamic Moment Coefficients

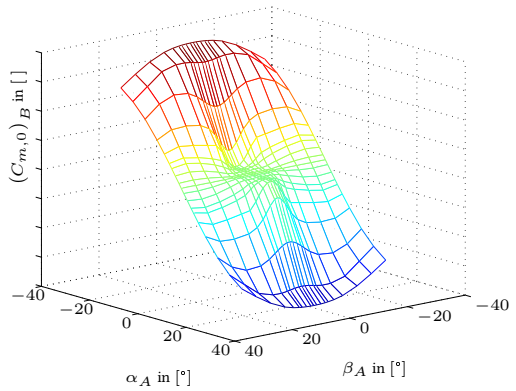

(a) Aerodynamic coefficient $(C_{m,0})_B$ plotted versus α_A and β_A at $M = 1.6$

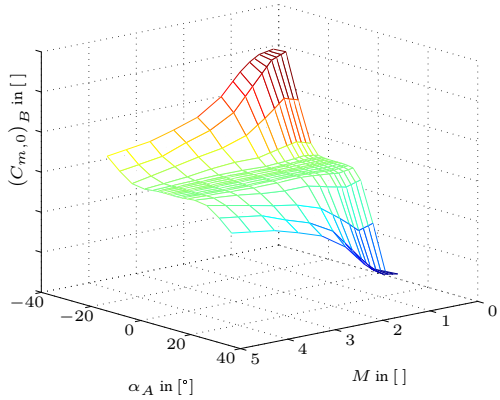

(b) Aerodynamic coefficient $(C_{m,0})_B$ plotted versus α_A and M at $\beta_A = 0.0°$

Figure B.10: Aerodynamic coefficient $(C_{m,0})_B$ plotted versus its dependencies α_A, β_A, and M at the configuration $\beta_A = 0.0°$, $M = 1.6$.

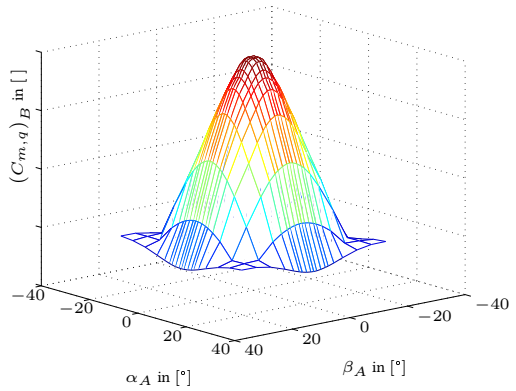

(a) Aerodynamic coefficient $(C_{m,q})_B$ plotted versus α_A and β_A at $M = 1.6$

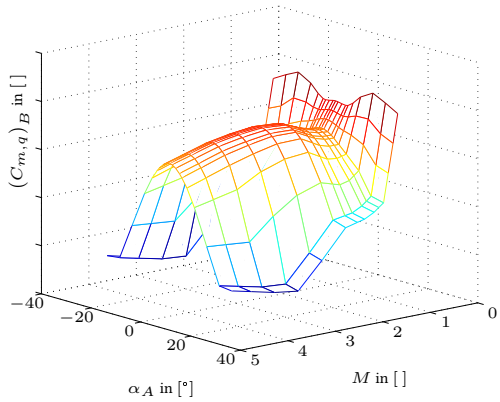

(b) Aerodynamic coefficient $(C_{m,q})_B$ plotted versus α_A and M at $\beta_A = -15.0°$

Figure B.11: Aerodynamic coefficient $(C_{m,q})_B$ plotted versus its dependencies α_A, β_A, and M at the configuration $\beta_A = -15.0°$, $M = 1.6$.

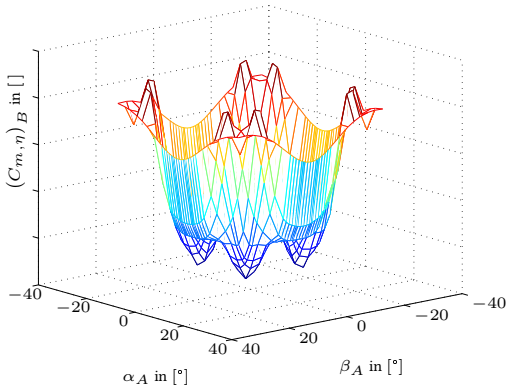

(a) Aerodynamic coefficient $(C_{m,\eta})_B$ plotted versus α_A and β_A at $M = 3.0, \xi = 8.5°, \eta = -2.5°$

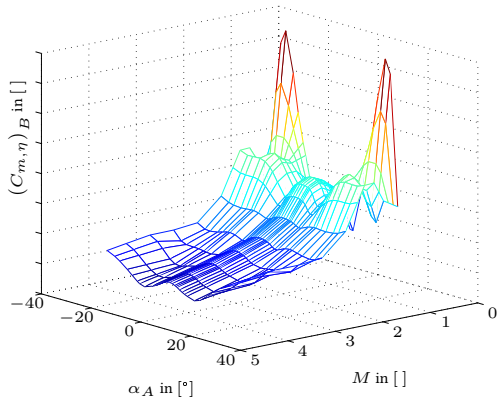

(b) Aerodynamic coefficient $(C_{m,\eta})_B$ plotted versus α_A and M at $\beta_A = 5.0°, \xi = 8.5°, \eta = -2.5°$

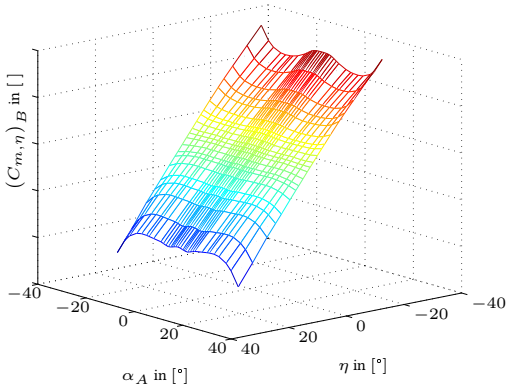

(c) Aerodynamic coefficient $(C_{m,\eta})_B$ plotted versus α_A and η at $\beta_A = 5.0°, M = 3.0, \xi = 8.5°$

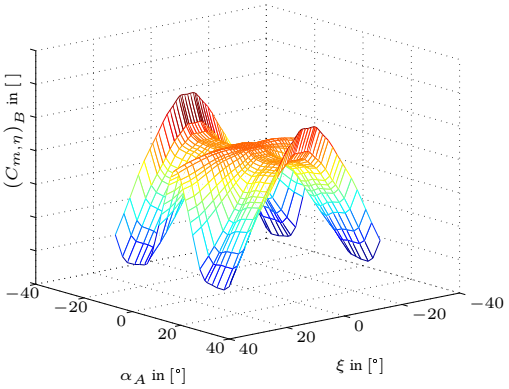

(d) Aerodynamic coefficient $(C_{m,\eta})_B$ plotted versus α_A and ξ at $\beta_A = 5.0°, M = 3.0, \eta = -2.5°$

Figure B.12: Aerodynamic coefficient $(C_{m,\eta})_B$ plotted versus its dependencies α_A, β_A, M, ξ, and ζ at the configuration $\beta_A = 5.0°, M = 3.0, \xi = 8.5°, \eta = -2.5°$.

B.1.2.3 Lateral Aerodynamic Moment Coefficients

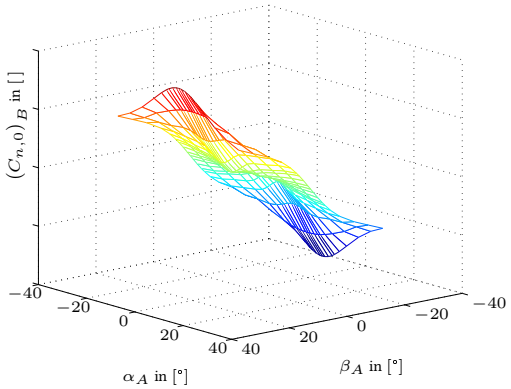

(a) Aerodynamic coefficient $(C_{n,0})_B$ plotted versus α_A and β_A at $M = 3.0$

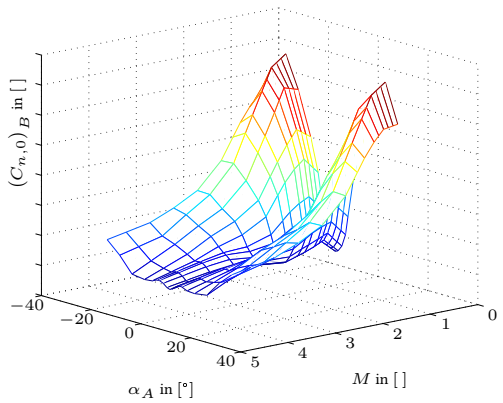

(b) Aerodynamic coefficient $(C_{n,0})_B$ plotted versus α_A and M at $\beta_A = 5.0°$

Figure B.13: Aerodynamic coefficient $(C_{n,0})_B$ plotted versus its dependencies α_A, β_A, and M at the configuration $\beta_A = 5.0°, M = 3.0$.

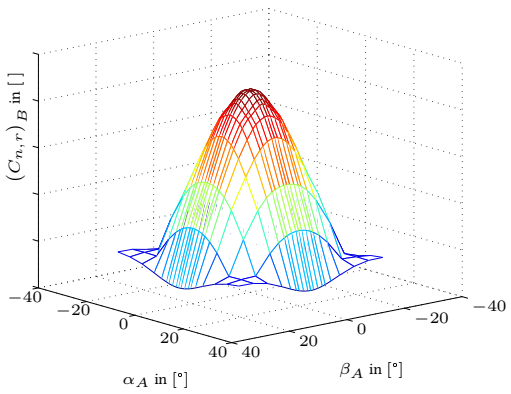

(a) Aerodynamic coefficient $(C_{n,r})_B$ plotted versus α_A and β_A at $M = 2.0$

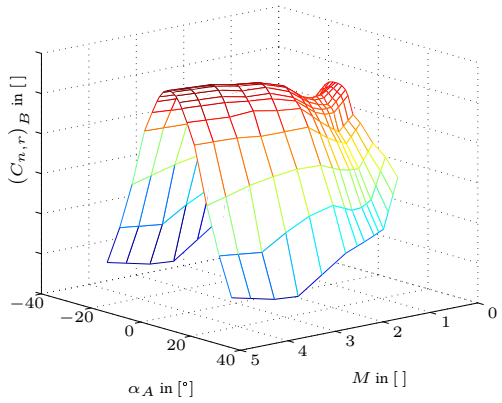

(b) Aerodynamic coefficient $(C_{n,r})_B$ plotted versus α_A and M at $\beta_A = -4.0°$

Figure B.14: Aerodynamic coefficient $(C_{n,r})_B$ plotted versus its dependencies α_A, β_A, and M at the configuration $\beta_A = -4.0°$, $M = 2.0$.

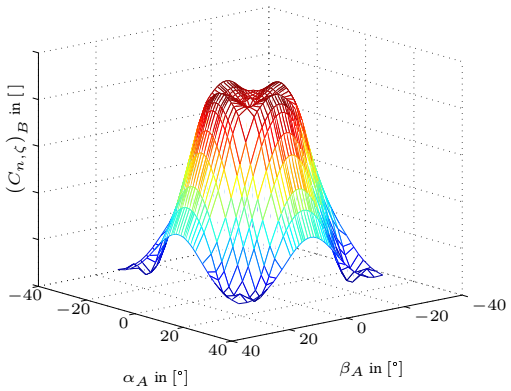

(a) Aerodynamic coefficient $(C_{n,\zeta})_B$ plotted versus α_A and β_A at $M = 4.4$, $\xi = 5.0°$, $\zeta = 12.0°$

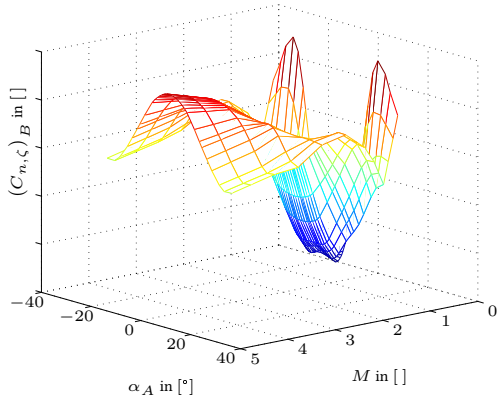

(b) Aerodynamic coefficient $(C_{n,\zeta})_B$ plotted versus α_A and M at $\beta_A = 12.0°$, $\xi = 5.0°$, $\zeta = 12.0°$

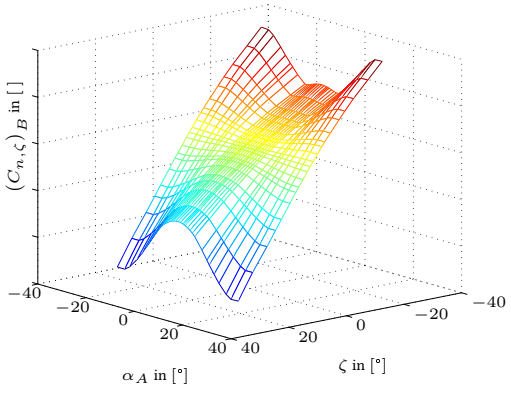

(c) Aerodynamic coefficient $(C_{n,\zeta})_B$ plotted versus α_A and η at $\beta_A = 12.0°$, $M = 4.4$, $\xi = 5.0°$

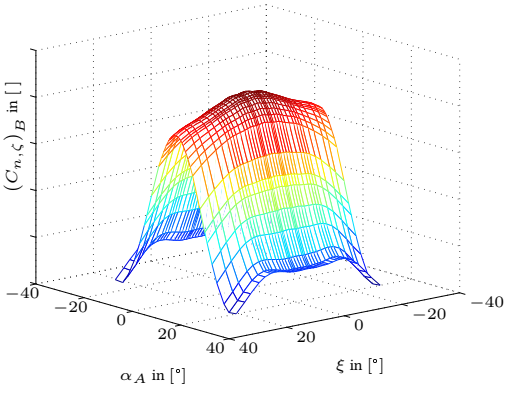

(d) Aerodynamic coefficient $(C_{n,\zeta})_B$ plotted versus α_A and ξ at $\beta_A = 12.0°$, $M = 4.4$, $\zeta = 12.0°$

Figure B.15: Aerodynamic coefficient $(C_{n,\zeta})_B$ plotted versus its dependencies α_A, β_A, M, ξ, and ζ at the configuration $\beta_A = 12.0°$, $M = 4.4$, $\xi = 5.0°$, $\zeta = 12.0°$.

Bibliography

[1] G. M. Siouris, *Missile Guidance and Control Systems.* Springer-Verlag, 2004.

[2] GlobalSecurity.org, "Appendix b - patriot system equipment." http://www.globalsecurity.org/space/library/policy/army/fm/3-01-85/appb.htm, 2014. [Online; accessed 16-January-2014].

[3] R. NOVOSTI, "Russian air force to get first t-50 fighter jet this year." http://en.ria.ru/military_news/20130806/182606552.html, 2014. [Online; accessed 16-January-2014].

[4] R. Brockhaus, W. Alles, and R. Luckner, *Flugregelung.* Springer, 2011.

[5] J. J. Jerger, *Principle of Guided Missile Design.* Systems Preliminary Design, Lancaster Press, 1960.

[6] J. Hunley, *The Development of Propulsion Technology for U.S. Space-launch Vehicles: 1926 - 1991.* Centennial of flight series, Texas A&M University Press, 2007.

[7] R. Yanushevsky, *Modern Missile Guidance.* Taylor & Francis, 2007.

[8] R. B. Dow, *Fundamentals of Advanced Missiles.* John Wiley Sons, Inc, 1958.

[9] NASA, "Rockets in ancient times (100 b.c. to 17th century)." http://history.msfc.nasa.gov/rocketry/tl1.html, 2013. [Online; accessed 09-December-2013].

[10] NASA, "Rockets as inventions (late 19th century)." http://history.msfc.nasa.gov/rocketry/tl3.html, 2013. [Online; accessed 09-December-2013].

[11] J. Crabtree, *On Air Defense.* Military profession, Praeger, 1994.

[12] M. W. Fossier, "The development of radar homing missiles," *Journal of Guidance, Control, and Dynamics*, vol. 7, no. 6, pp. 641 – 651, 1984.

[13] R. Westrum, *Sidewinder: Creative Missile Development at China Lake.* Naval Institute Press, 2013.

[14] R. Harkavy and S. I. P. R. Institute, *Bases Abroad: The Global Foreign Military Presence.* A Sipri Publication, Oxford University Press, 1989.

[15] R. Betts, *Cruise Missiles: Technology, Strategy, Politics.* Brookings Institution, 1981.

[16] J. N. Nielsen, *Missile Aerodynamics.* McGraw-Hill Book Company, Inc, 1960.

[17] N. A. Shneydor, *Missile Guidance and Pursuit.* Horwood Series in Engineering Science, 1998.

[18] N. F. Palumbo, "Guest editor's introduction: Homing missile guidance and control," *John Hopkins APL Technical Digest*, vol. 29, no. 1, pp. 2 – 8, 2010.

[19] F. W. Riedel, "Bank-to-turn control technology - survey for homing missiles," technical report, NASA, 1980.

[20] F. Peter, E. Xargay, F. Holzapfel, and N. Hovakimyan, "L1 adaptive augmentation of a missile autopilot," in *AIAA Guidance, Navigation and Control Conference*, (Minneapolis, MN), August 2012. AIAA-2012-4832.

[21] F. Peter, F. Hellmundt, F. Holzapfel, and F. Chew, "Anti-windup command filtered adaptive backstepping autopilot design for a tail-controlled air-defense missile," in *AIAA Guidance, Navigation and Control Conference*, (Boston, MA), August 2013. AIAA-2013-5013.

[22] P. B. Jackson, "Overview of missile flight control systems," *John Hopkins APL Technical Digest*, vol. 29, no. 1, pp. 9 – 24, 2010.

[23] K. A. Wise and D. J. Broy, "Agile missle dynamics and control," *AIAA Journal of Guidance, Control and Dynamics*, vol. 21, pp. 441 – 449, 1998.

[24] H. Buschek, "Full envelope missile autopilot design using gain scheduled robust control," *AIAA Journal of Guidance, Control and Dynamics*, vol. 22, no. 1, pp. 115 – 122, 1999.

[25] K. A. Wise and B. C. Mears, "Missile autopilot design using H_∞ optimal control with μ-synthesis," in *Proceedings of the American Control Conference*, (Evanston, IL), pp. 2363 – 2367, American Automatic Control Council, 1990.

[26] S. M. Yang and N. H. Huang, "Application of H^∞ control to pitch autopilot of missiles," *IEEE Transactions on Aerospace and Electronic Systems*, vol. 32, no. 1, pp. 426 – 433, 1996.

[27] P. Jackson, "Applying μ-synthesis to missile autopilot design," in *Proceedings of the 29th Conference on Decision and Control*, (Honolulu, HI), pp. 2993 – 2998, Inst. of Electrical and Electronics Engineers, 1990.

[28] G. J. Balas and A. K. Packard, "Design of robust, time-varying controllers for missile autopilots," in *IEEE International Conference on Control Applications*, (Dayton, OH), pp. 104 – 110, Inst. of Electrical and Electronics Engineers, 1992.

[29] R. T. Reichert, "Dynamic scheduling of modern-robust-control autopilot designs for missiles," *IEEE Control Systems*, vol. 12, no. 5, pp. 35 – 42, 1992.

[30] H. Pfifer and S. Hecker, "LPV controller synthesis for a generic missile model," in *IEEE International Conference on Control Applications*, (Yokohama, Japan), pp. 1838 – 1843, 2010.

[31] G. J. Balas, "Linear, parameter-varying control and its application to aerospace systems," in *23RD International Congress of Aeronautical Sciences*, (Toronto, Canada), September 2002.

[32] V. Laurain, M. Gilson, R. Toth, and H. Garnier, "Direct identification of continuous-time LPV models," in *American Control Conference*, pp. 159–164, 2011.

[33] J. Wang, F. Holzapfel, and F. Peter, "Comparison of nonlinear dynamic inversion and backstepping controls with application to a quadrotor," in *CEAS Euro GNC Conference*, (Delft, Netherlands), April 2013.

[34] J. Knöös, J. Robinson, and F. Berefelt, "Nonlinear dynamic inversion and block backstepping: A comparison," in *AIAA Guidance, Navigation and Control Conference*, (Minneapolist, MN), August 2012.

[35] M. Krstić, I. Kanellakopoulos, and P. Kokotović, *Nonlinear and adaptive control design.* Adaptive and learning systems for signal processing, communications, and control, Wiley, 1995.

[36] A. Calise, M. Sharma, and J. Corban, "Adaptive autopilot design for guided munitions," *AIAA Journal of Guidance, Control and Dynamics*, vol. 23, no. 5, pp. 837 – 843, 2000.

[37] M. McFarland and S. Hoque, "Robustness of a nonlinear missile autopilot designed using dynamic inversion," in *AIAA Guidance, Navigation and Control Conference*, (Denver, CO), August 2000.

[38] R. Hindman and W. M. Shell, "Design of a missile autopilot using adaptive nonlinear dynamic inversion," in *American Control Conference*, (Portland, OR), June 2005.

[39] L. Sonneveldt, E. van Oort, Q. Chu, and J. Mulder, "Comparison of inverse optimal and tuning functions designs for adaptive missile control," in *AIAA Guidance, Navigation and Control Conference*, (Hilton Head, SC), August 2007.

[40] R. Lange, *Nonlinear adaptive control of an endo-atmospheric dual-actuator interceptor.* Dr. Hut, 2012.

[41] J. A. Farrell, M. Polycarpou, M. Sharma, and W. Dong, "Command filtered backstepping," *IEEE Transactions on Automatic Control*, vol. 54, pp. 1391 – 1395, June 2009.

[42] S. Sastry, *Nonlinear Systems: Analysis, Stability and Control.* Springer, 2010.

[43] P. K. Menon and M. Yousefpor, "Design of nonlinear autopilots for high angle of attack missiles," in *AIAA Guidance, Navigation and Control Conference*, (San Diego, CA), July 1996.

[44] A. Narang-Siddarth, F. Peter, F. Holzapfel, and J. Valasek, "Autopilot for a nonlinear non-minimum phase tail-controlled missile," in *AIAA Guidance, Navigation and Control Conference*, (Washington, D.C.), January 2014.

[45] N. Hovakimyan, E. Lavretsky, and A. Sasane, "Dynamic inversion for nonaffine-in-control systems via time-scale separation," *AIAA Journal of Guidance, Control and Dynamics*, vol. 13, no. 4, pp. 451 – 465, 2007.

[46] P. Acquatella, E.-J. van Kampen, and Q. P. Chu, "Incremental backstepping for robust nonlinear flight control," in *CEAS Euro GNC Conference*, (Delft, Netherlands), April 2013.

[47] W. Falkena, *Investigation of Practical Flight Control Systems for Small Aircraft.* PhD thesis, TU Delft, 2012.

[48] J. Zhou and C. Wen, *Adaptive Backstepping Control of Uncertain Systems: Nonsmooth Nonlinearities, Interactions Or Time-Variations.* Lecture Notes in Control and Information Sciences, Springer, 2008.

[49] N. Hovakimyan, C. Cao, E. Kharisov, E. Xargay, and I. M. Gregory, "L1 adaptive control for safety-critical systems," *IEEE Control Systems Magazine*, vol. 31, no. 5, pp. 54 – 104, 2011.

[50] T. Leman, E. Xargay, G. Dullerud, and N. Hovakimyan, "L1 adaptive control augmentation system for the x-48b aircraft," in *AIAA Guidance, Navigation and Control Conference*, (Chicago, IL), August 2009.

[51] O. Stroosma, H. Damveld, J. Mulder, R. Choe, E. Xargay, and N. Hovakimyan, "A handling qualities assessment of a business jet augmented with an L1 adaptive controller," in *AIAA Guidance, Navigation and Control Conference*, (Portland, OR), August 2011.

[52] K. Narendra and A. Annaswamy, *Stable Adaptive Systems*. Dover Books on Electrical Engineering, Dover Publications, 1989.

[53] Z. Dydek, A. Annaswamy, and E. Lavretsky, "Adaptive control and the NASA X-15 program: A concise history, lessons learned, and a provably correct design," in *American Control Conference*, pp. 2957–2962, June 2008.

[54] P. Ioannou and J. Sun, *Robust Adaptive Control*. Dover Publications, 1996.

[55] T. Yucelen and A. J. Calise, "Derivative-free model reference adaptive control," *IEEE Control Systems Magazine*, vol. 34, no. 4, pp. 933 – 950, 2011.

[56] G. Chowdhary and E. Johnson, "Theory and flight test validation of a concurrent learning adaptive controller," *IEEE Control Systems Magazine*, vol. 34, no. 2, pp. 933 – 950, 2011.

[57] K. A. Wise, E. Lavretsky, and N. Hovakimyan, "Adaptive control of flight: Theory, applications, and open problems," in *American Control Conference*, (Minneapolis, MN), pp. 5966 – 5971, June 2006.

[58] F. Peter, M. Leitão, and F. Holzapfel, "Adaptive augmentation of a new baseline control architecture for tail-controlled missiles using a nonlinear reference model," in *AIAA Guidance, Navigation and Control Conference*, (Minneapolis, MN), August 2012. AIAA-2012-5037.

[59] G. Mattei and S. Monaco, "Nonlinear autopilot design for an asymmetric missile using robust backstepping control," *AIAA Journal of Guidance, Control and Dynamics*, vol. 37, pp. 1462 – 1476, September – October 2014.

[60] L. Sonneveldt, E. van Oort, Q. Chu, and J. Mulder, "Comparison of inverse optimal and tuning functions designs for adaptive missile control," *AIAA Journal of Guidance, Control and Dynamics*, vol. 31, pp. 1176 – 1182, July – August 2008.

[61] M. B. McFarland and A. J. Calise, "Adaptive nonlinear control of agile antiair missiles using neural networks," *IEEE Transactions on Control Systems and Technology*, vol. 8, no. 5, pp. 749 – 756, 2000.

[62] Y. Kim and B. S. Kim, "Pitch autopilot design for agile missiles with uncertain aerodynamic coefficients," *IEEE Transactions on Aerospace and Electronic Systems*, vol. 49, pp. 907 – 914, April 2013.

[63] N. Hovakimyan and C. Cao, *L1 Adaptive Control Theory*. SIAM Advances in Design and Control, 2010.

[64] P. Zipfel, *Modeling and Simulation of Aerospace Vehicle Dynamics*. AIAA education series, American Institute of Aeronautics and Astronautics, 2000.

[65] J. Blakelock, *Automatic Control of Aircraft and Missiles*. A Wiley-Interscience publication, John Wiley & Sons, 1991.

[66] F. Holzapfel, *Nichtlineare adaptive Regelung eines unbemannten Fluggerätes*. Dr. Hut, 2004.

[67] I. Newton, A. Motte, and J. Machin, *The Mathematical Principles of Natural Philosophy*, vol. 1 of *The Mathematical Principles of Natural Philosophy*. B. Motte, 1729.

[68] W. F. Phillips, *Mechanics of Flight*. Aerospace/Engineering, John Wiley & Sons, 2004.

[69] W. L. Oberkampf, S. M. DeLand, B. M. Rutherford, K. V. Diegert, and K. F. Alvin, "Estimation of total uncertainty in modeling and simulation," research report, Sandia National Laboratories, 2000.

[70] J.-Y. Choi, D. Chwa, and M.-S. Kim, "Adaptive control for feedback-linearized missiles with uncertainties," *IEEE Transactions on Aerospace and Electronic Systems*, vol. 36, pp. 467 – 481, April 2000.

[71] A. Pettersson, K. J. Åström, A. Robertsson, and R. Johansson, "Augmenting l1 adaptive control of piecewise constant type to a fighter aircraft. performance and robustness evaluation for rapid maneuvering.," in *AIAA Guidance, Navigation and Control Conference*, (Minneapolis, MN), August 2012. AIAA-2012-4547.

[72] M. D. Buhmann, *Radial Basis Functions: Theory and Implementations*. Cambridge University Press, 2004.

[73] P. Hägg, "Model based parameter estimation for a missile," Master's thesis, KTH Electrical Engineering, 2009.

[74] J. Patel and C. Read, *Handbook of the Normal Distribution, Second Edition*. Statistics: A Series of Textbooks and Monographs, Taylor & Francis, 1996.

[75] N. Grumman, "Advanced airborne IMU/AHRS." http://www.northropgrumman.com/Capabilities/LN200FOG/Documents/ln200.pdf, 2013. [Online; accessed 11-April-2014].

[76] O. J. Woodman, "An introduction to inertial navigation," technical report, University of Cambridge, Computer Laboratory, 2007.

[77] B. L. Stevens and F. L. Lewis, *Aircraft Control and Simulation*. John Wiley & Sons, 2003.

[78] D. Hinrichsen and A. Pritchard, *Mathematical Systems Theory I: Modelling, State Space Analysis, Stability and Robustness*. Texts in Applied Mathematics, Springer Berlin Heidelberg, 2006.

[79] M. Holmes, *Introduction to Perturbation Methods*. Texts in Applied Mathematics, Springer, 2012.

[80] A. Isidori, *Nonlinear Control Systems*. Communications and Control Engineering, Springer London, 1995.

[81] C. Phillips, J. Parr, and E. Riskin, *Signals, Systems, & Transforms*. Pearson Education, 2009.

[82] J. Hespanha, *Linear Systems Theory*. Princeton University Press, 2009.

[83] J. Lunze, *Regelungstechnik 1*. No. Bd. 1 in Springer-Lehrbuch, Springer, 2008.

[84] C. Grossmann, H. Roos, and M. Stynes, *Numerical Treatment of Partial Differential Equations*. Universitext, Springer, 2007.

[85] W. Levine, *Control System Fundamentals*. Taylor & Francis, 1999.

[86] M. Tahk, M. M. Briggs, P. Menon, and A. Müller, "Applications of plant inversion via state feedback to missile autopilot design," in *Decision and Control, 1988., Proceedings of the 27th IEEE Conference on*, vol. 1, pp. 730–735, December 1988.

[87] J. S. Shamma and J. R. Cloutier, "A linear parameter varying approach to gain scheduled missile autopilot design," in *American Control Conference*, pp. 1317–1321, June 1992.

[88] S. Sieberling, Q. P. Chu, , and J. A. Mulder, "Robust flight control using incremental nonlinear dynamic inversion and angular acceleration prediction," *AIAA Journal of Guidance, Control and Dynamics*, vol. 33, no. 6, pp. 1732 – 1742, 2010.

[89] G. Chowdhary, *Concurrent Learning for Convergence in Adaptive Control Without Persistency of Excitation*. PhD thesis, Georgia Institute of Technology, 2010.

[90] T. E. Gibson, A. M. Annaswamy, and E. Lavretsky, "Improved transient response in adaptive control using projection algorithms and closed loop reference models," in *AIAA Guidance, Navigation and Control Conference*, (Minneapolis, MN), August 2012. AIAA-2012-4775.

[91] T. Leman, E. Xargay, G. Dullerud, and N. Hovakimyan, "L1 adaptive control augmentation system for the X-48B aircraft," in *AIAA Guidance, Navigation and Control Conference*, (Chicago, IL), August 2009. AIAA-2009-5619.

[92] G. V. Chowdhary and E. N. Johnson, "Theory and flight-test validation of a concurrent-learning adaptive controller," *AIAA Journal of Guidance, Control and Dynamics*, vol. 34, no. 2, pp. 592 – 607, 2011.

[93] I. Gregory, E. Xargay, C. Cao, and N. Hovakimyan, "Flight test of an l1 adaptive controller on the nasa airstar flight test vehicle," in *AIAA Guidance, Navigation and Control Conference*, (Toronto, Canada), August 2010. AIAA-2010-8015.

[94] H. Khalil, *Nonlinear Systems*. Prentice Hall, 2002.

[95] J. Slotine and W. Li, *Applied Nonlinear Control*. Prentice Hall, 1991.

[96] H. Nijmeijer and A. van der Schaft, *Nonlinear Dynamical Control Systems*. U.S. Government Printing Office, 1990.

[97] P. Paraskevopoulos, *Modern Control Engineering*. Automation and Control Engineering, Taylor & Francis, 2001.

[98] G. O. Guardabassi and S. M. Savaresi, "Approximate linearization via feedback - an overview," *Automatica*, vol. 37, no. 1, pp. 1 – 15, 2001.

[99] J. Hauser, S. Sastry, and P. Kokotovic, "Nonlinear control via approximate input-output linearization: the ball and beam example," *IEEE Transactions on Automatic Control*, vol. 37, pp. 392 – 398, Mar 1992.

[100] G. Stewart, *Matrix Algorithms: Volume 1: Basic Decompositions*. Society for Industrial and Applied Mathematics, 1998.

[101] Y. Chang, "Block backstepping control of mimo systems," *IEEE Transactions on Automatic Control*, vol. 56, pp. 1191–1197, May 2011.

[102] O. Härkegård and T. Glad, "Vector backstepping design for flight control," in *AIAA Guidance, Navigation and Control Conference*, (Hilton Head, SC), August 2007. AIAA-2007-6421.

[103] E. R. van Oort, *Adaptive Backstepping Control and Safety Analysis for Modern Fighter Aircraft*. PhD thesis, Technische Universiteit Delft, 2011.

[104] M. Krstic and A. Smyshlyaev, *Boundary Control of PDEs: A Course on Backstepping Designs*. Advances in Design and Control, Society for Industrial and Applied Mathematics, 2008.

[105] P. V. Kokotovic, "The joy of feedback: nonlinear and adaptive," *IEEE Control Systems Magazine*, vol. 12, pp. 7 – 17, June 1992.

[106] P. Kokotovic, H. Khalil, and J. O'Reilly, *Singular Perturbation Methods in Control: Analysis and Design*. Classics in Applied Mathematics, Society for Industrial and Applied Mathematics, 1999.

[107] E. Johnson and A. Calise, "Limited authority adaptive flight control for reusable launch vehicles," *AIAA Journal of Guidance, Control and Dynamics*, vol. 26, pp. 906 – 913, November – December 2003.

[108] O. Wysocki and E. Schülein, "Experimental investigations on the phantom yaw effect on a maneuvering slender body," *Journal of Spacecraft and Rockets*, vol. 52, no. 1, pp. 264 – 274, 2015.

[109] S. Balakrishnan, A. Tsourdos, and B. White, *Advances in Missile Guidance, Control, and Estimation*. Automation and Control Engineering, Taylor & Francis, 2012.

[110] M. Sharma, E. Lavretsky, and K. Wise, "Application and flight testing of an adaptive autopilot on precision guided munitions," in *AIAA Guidance, Navigation and Control Conference*, (Keystone, CO), August 2006. AIAA-2006-6568.

[111] T. Bierling, L. Höcht, F. Holzapfel, R. Maier, and A. Wildschek, "Comparative analysis of mrac architectures in a unified framework," in *AIAA Guidance, Navigation and Control Conference*, (Toronto, Canada), August 2010. AIAA-2010-7536.

[112] M. Duarte and K. S. Narendra, "Indirect model reference adaptive control with dynamic adjustment of parameters," *International Journal of Adaptive Control and Signal Processing*, vol. 10, no. 6, pp. 603 – 621, 1996.

[113] E. Lavretsky, "Combined / composite model reference adaptive control," in *AIAA Guidance, Navigation and Control Conference*, (Chicago, IL), August 2009. AIAA-2009-6065.

[114] P. Ioannou and B. Fidan, *Adaptive Control Tutorial*. Advances in Design and Control, Society for Industrial and Applied Mathematics, 2006.

[115] Z. Li and N. Hovakimyan, "L1 adaptive controller for mimo systems with unmatched uncertainties using modified piecewise constant adaptation law," in *IEEE Conference on Decision and Control*, (Maui, HI), December 2012.

[116] K. Adams, *Non-functional Requirements in Systems Analysis and Design*. Topics in Safety, Risk, Reliability and Quality, Springer International Publishing, 2015.

[117] D. fo Transportation Federal Aviation Administration, "Faa writing standards," tech. rep., 2003.

[118] A. Helicopters, "Supplier quality requirements manual," tech. rep., 2014.

[119] K. J. Åström and R. M. Murray, *Feedback Systems: An Introduction for Scientists and Engineers*. Advances in Design and Control, Princeton University Press, 2010.

[120] R. Osterhuber, M. Hanel, and R. Hammon, "Realization of the eurofighter 2000 primary lateral/directional flight control laws with differential pi-algorithm," in *AIAA Guidance, Navigation and Control Conference*, (Providence, Rhode Island), August 2004. AIAA-2004-4751.

[121] C. Spitzer, ed., *The Avionics Handbook*. Advances in Design and Control, CRC Press, 2000.

[122] A. Marcos and G. J. Balas, "Gain-scheduled missile autopilot design using linear parameter varying transformation," *AIAA Journal of Guidance, Control and Dynamics*, vol. 27, no. 2, pp. 218 – 228, 2004.

[123] D. S. Naidu and A. J. Calise, "Singular perturbations and time scales in guidance and control of aerospace systems: A survey," *AIAA Journal of Guidance, Control and Dynamics*, vol. 24, no. 6, pp. 1057 – 1078, 2001.

[124] J. Wang, T. Raffler, and F. Holzapfel, "High velocity path control of quadrotors," in *AIAA Guidance, Navigation and Control Conference*, (Kissimmee, FL), January 2015.

[125] W. Falkena, C. Borst, E. R. van Oort, and Q. P. Chu, "Sensor-based backstepping," *AIAA Journal of Guidance, Control and Dynamics*, vol. 36, pp. 606 – 610, March – April 2013.

[126] I. The MathWorks, *Global Optimization Toolbox User's Guide*. 2015.

[127] A. Saltelli, M. Ratto, T. Andres, F. Campolongo, J. Cariboni, D. Gatelli, M. Saisana, and S. Tarantola, *Global Sensitivity Analysis. The Primer*. John Wiley & Sons, Ltd, 2008.

[128] T. Bierling, *Comparative Analysis of Adaptive Control Techniques for Improved Robust Performance*. Technical University of Munich, 2013.

[129] U. Mackenroth, *Robust Control Systems*. Springer Science & Business Media, Springer, 2013.

[130] C. Cao and N. Hovakimyan, "Stability margins of l1 adaptive controller: Part ii," July 2007. 1-4244-0989-6/07.

[131] C. Edwards, T. Lombaerts, and H. Smaili, *Fault Tolerant Flight Control: A Benchmark Challenge*. Lecture Notes in Control and Information Sciences, Springer, 2010.

[132] C. Z. Mooney, *Monte Carlo Simulation (Quantitative Applications in the Social Sciences)*. Quantitative Applications in the Social Sciences, SAGE Publications, Inc, 1997.